

REPORT DOCUMENTATION PAGE

AFRL-SR-BL-TR-00-
0759

Public reporting burden for this collection of information is estimated to average 1 hour per response, including the time for reviewing instructions, the collection of information. Send comments regarding this burden estimate or any other aspect of this collection of information, including Operations and Reports, 1215 Jefferson Davis Highway, Suite 1204, Arlington, VA 22202-4302, and to the Office of Management and Budget, Paperwork

and reviewing
information

1. AGENCY USE ONLY (Leave blank)		2. REPORT DATE December, 1997		3. REPORT TYPE AND DATES COVERED	
4. TITLE AND SUBTITLE 1997 Summer Research Program (SRP), Summer Faculty Research Program (SFRP), Final Reports, Volume 5C, Wright Laboratory				5. FUNDING NUMBERS F49620-93-C-0063	
6. AUTHOR(S) Gary Moore					
7. PERFORMING ORGANIZATION NAME(S) AND ADDRESS(ES) Research & Development Laboratories (RDL) 5800 Uplander Way Culver City, CA 90230-6608				8. PERFORMING ORGANIZATION REPORT NUMBER	
9. SPONSORING/MONITORING AGENCY NAME(S) AND ADDRESS(ES) Air Force Office of Scientific Research (AFOSR) 801 N. Randolph St. Arlington, VA 22203-1977				10. SPONSORING/MONITORING AGENCY REPORT NUMBER	
11. SUPPLEMENTARY NOTES					
12a. DISTRIBUTION AVAILABILITY STATEMENT Approved for Public Release				12b. DISTRIBUTION CODE	
13. ABSTRACT (Maximum 200 words) The United States Air Force Summer Research Program (USAF-SRP) is designed to introduce university, college, and technical institute faculty members, graduate students, and high school students to Air Force research. This is accomplished by the faculty members (Summer Faculty Research Program, (SFRP)), graduate students (Graduate Student Research Program (GSRP)), and high school students (High School Apprenticeship Program (HSAP)) being selected on a nationally advertised competitive basis during the summer intersession period to perform research at Air Force Research Laboratory (AFRL) Technical Directorates, Air Force Air Logistics Centers (ALC), and other AF Laboratories. This volume consists of a program overview, program management statistics, and the final technical reports from the SFRP participants at the Wright Laboratory.					
14. SUBJECT TERMS Air Force Research, Air Force, Engineering, Laboratories, Reports, Summer, Universities, Faculty, Graduate Student, High School Student				15. NUMBER OF PAGES	
				16. PRICE CODE	
17. SECURITY CLASSIFICATION OF REPORT Unclassified	18. SECURITY CLASSIFICATION OF THIS PAGE Unclassified	19. SECURITY CLASSIFICATION OF ABSTRACT Unclassified	20. LIMITATION OF ABSTRACT UL		

UNITED STATES AIR FORCE
SUMMER RESEARCH PROGRAM -- 1997
SUMMER FACULTY RESEARCH PROGRAM FINAL REPORTS

VOLUME 5C

WRIGHT LABORATORY

RESEARCH & DEVELOPMENT LABORATORIES

5800 Uplander Way
Culver City, CA 90230-6608

Program Director, RDL
Gary Moore

Program Manager, AFOSR
Major Linda Steel-Goodwin

Program Manager, RDL
Scott Licoscas

Program Administrator, RDL
Johnetta Thompson

Program Administrator, RDL
Rebecca Kelly

Submitted to:

AIR FORCE OFFICE OF SCIENTIFIC RESEARCH

Bolling Air Force Base

Washington, D.C.

December 1997

20010321 084

AQM 61-06-1281

UNITED STATES AIR FORCE
SUMMER RESEARCH PROGRAM -- 1997
SUMMER FACULTY RESEARCH PROGRAM FINAL REPORTS

VOLUME 5C

WRIGHT LABORATORY

RESEARCH & DEVELOPMENT LABORATORIES

5800 Uplander Way
Culver City, CA 90230-6608

Program Director, RDL
Gary Moore

Program Manager, AFOSR
Major Linda Steel-Goodwin

Program Manager, RDL
Scott Licoscas

Program Administrator, RDL
Johnetta Thompson

Program Administrator, RDL
Rebecca Kelly

Submitted to:

AIR FORCE OFFICE OF SCIENTIFIC RESEARCH

Bolling Air Force Base

Washington, D.C.

December 1997

SFRP FINAL REPORT TABLE OF CONTENTS

i-xviii

1. INTRODUCTION	1
2. PARTICIPATION IN THE SUMMER RESEARCH PROGRAM	2
3. RECRUITING AND SELECTION	3
4. SITE VISITS	4
5. HBCU/MI PARTICIPATION	4
6. SRP FUNDING SOURCES	5
7. COMPENSATION FOR PARTICIPATIONS	5
8. CONTENTS OF THE 1996 REPORT	6

APPENDICIES:

A. PROGRAM STATISTICAL SUMMARY	A-1
B. SRP EVALUATION RESPONSES	B-1

SFRP FINAL REPORTS

PREFACE

Reports in this volume are numbered consecutively beginning with number 1. Each report is paginated with the report number followed by consecutive page numbers, e.g., 1-1, 1-2, 1-3; 2-1, 2-2, 2-3.

Due to its length, Volume 5 is bound in three parts, 5A, 5B and 5C. Volume 5A contains #1-24. Volume 5B contains reports #25-48 and 5C contains #49-70. The Table of Contents for Volume 5 is included in all parts.

This document is one of a set of 16 volumes describing the 1997 AFOSR Summer Research Program. The following volumes comprise the set:

<u>VOLUME</u>	<u>TITLE</u>
1	Program Management Report
	<i>Summer Faculty Research Program (SFRP) Reports</i>
2A & 2B	Armstrong Laboratory
3A & 3B	Phillips Laboratory
4A & 4B	Rome Laboratory
5A , 5B & 5C	Wright Laboratory
6	Arnold Engineering Development Center, United States Air Force Academy and Air Logistics Centers
	<i>Graduate Student Research Program (GSRP) Reports</i>
7A & 7B	Armstrong Laboratory
8	Phillips Laboratory
9	Rome Laboratory
10A & 10B	Wright Laboratory
11	Arnold Engineering Development Center, Wilford Hall Medical Center and Air Logistics Centers
	<i>High School Apprenticeship Program (HSAP) Reports</i>
12A & 12B	Armstrong Laboratory
13	Phillips Laboratory
14	Rome Laboratory
15B&15B	Wright Laboratory
16	Arnold Engineering Development Center

SRP Final Report Table of Contents

Author	University/Institution Report Title	Armstrong Laboratory Directorate	Vol-Page
DR Jean M Andino	University of Florida , Gainesville , FL Atmospheric Reactions of Volatile Paint Components a Modeling Approach	AL/EQL	2- 1
DR Anthony R Andrews	Ohio University , Athens , OH Novel Electrochemiluminescence Reactions and Instrumentation	AL/EQL	2- 2
DR Stephan B Bach	Univ of Texas at San Antonio , San Antonio , TX Investigation of Sampling Interfaces for Portable Mass Spectrometry and a survey of field Portable	AL/OEA	2- 3
DR Marilyn Barger	Florida A&M-FSU College of Engineering , Tallahassee , FL Analysis for The Anaerobic Metabolites of Toulene at Fire Training Area 23 Tyndall AFB, Florida	AL/EQL	2- 4
DR Dulal K Bhaumik	University of South Alabama , Mobile , AL The Net Effect of a Covariate in Analysis of Covariance	AL/AOEP	2- 5
DR Marc L Carter, PhD, PA	Hofstra University ; Hempstead , NY Assessment of the Reliability of Ground Based Observers for the Detecton of Aircraft	AL/OEO	2- 6
DR Huseyin M Cekirge	Florida State University , Tallahassee , FL Developing a Relational Database for Natural Attenuation Field Data	AL/EQL	2- 7
DR Cheng Cheng	Johns Hopkins University , Baltimore , MD Investigation of Two Statistical Issues in Building a Classification System	AL/HRM	2- 8
DR Gerald P Chubb	Ohio State University , Columbus , OH Use of Air Synthetic Forces For GCI Training Exercises	AL/HR1	2- 9
DR Sneed B Collard, Jr.	University of West Florida , Pensacola , FL Suitability of Ascidians as Trace Metal Biosensors-Biomonitors In Marine Environments An Assessment	AL/EQL	2- 10
DR Catherine A Cornwell	Syracuse University , Syracuse , NY Rat Ultrasound Vocalization Development and Neurochemistry in Stress-Sensitive Brain Regions	AL/OER	2- 11

SRP Final Report Table of Contents

Author	University/Institution Report Title	Armstrong Laboratory Directorate	Vol-Page
DR Baolin Deng	New Mexico Tech , Socorro , NM Effect of Iron Corrosion Inhibitors on Reductive Degradation of Chlorinated Solvents	AL/EQL	2- 12
DR Micheal P Dooley	Iowa State University , Ames , IA Copulatory Response Fertilizing Potential, and Sex Ratio of Offsprings Sired by male rats Ecposed in	AL/OER	2- 13
DR Itiel E Dror	Miami University , Oxford , OH The Effect of Visual Similarity and Reference Frame Alignment on the Recognition of Military Aircraf	AL/HRT	2- 14
DR Brent D Foy	Wright State University , Dayton , OH Advances in Biologivcally-Based Kinetic Modeling for Toxicological Applications	AFRL/HES	2- 15
DR Irwin S Goldberg	St. Mary's Univ , San Antonio , TX Mixing and Streaming of a Fluid Near the Entrance of a Tube During Oscillatory Flow	AL/OES	2- 16
DR Ramesh C Gupta	University of Mainè at Orono , Orono , ME A Dynamical system approach in Biomedical Research	ALOES	2- 17
DR John R Herbold	Univ of Texas at San Antonio , San Antonio , TX A Protocol for Development of Amplicons for a Rapid and Efficient Methoiid of Genotyping Hepatitis C	AL/AOEL	2- 18
DR Andrew E Jackson	Arizona State University , Mesa , AZ Development fo a Conceptual Design for an Information Systems Infrastructure To Support the Squadron	AL/HRA	2- 19
DR Charles E Lance	Univ of Georgia Res Foundation , Athens , GA Replication and Extension of the Schmidt, Hunter, and Outerbridge (1986) Model of Job Performance R	AL/HRT	2- 20
DR David A Ludwig	Univ of N.C. at Greensboro , Greensboro , NC Mediating effect of onset rate on the relationship between+ Gz and LBNP Tolerance	AL/AOCY	2- 21
DR Robert P Mahan	University of Georgia , Athens , GA The Effects of Task Structure on Cognitive Organizing Principles Implaicatins for Complex Display	AL/CFTO	2- 22

Author	University/Institution Report Title	Armstrong Laboratory Directorate	Vol-Page
DR Phillip H Marshall	Texas Tech University , Lubbock , TX Preliminary report on the effects of varieties of feedback training on single target time-to-contac	AL/HRM	2- 23
DR Bruce V Mutter	Bluefield State College , Bluefield , WV	AL/EQP	2- 24
DR Allen L Nagy	Wright State University , Dayton , OH The Detection of Color Breakup In Field Sequential Color Displays	AL/CFHV	2- 25
DR Brent L Nielsen	Auburn University , Auburn , AL Rapid PCR Detection of Vancomycin Resistance of Enterococcus Species in infected Urine and Blood	AL/AOEL	2- 26
DR Thomas E Nygren	Ohio State University , Columbus , OH Group Differences in perceived importance of swat workload dimensions: Effects on judgment and perf	AL/CFHP	2- 27
DR Edward H Piepmeier	Oregon State University , Corvallis , OR	AL/AOHR	2- 28
DR Judy L Ratliff	Murray State Univ , Murray , KY Accumulation of Storntium and Calcium by Didemnum Conchyliatum	AL/EQL	2- 29
DR Joan R Rentsch	Wright State University , Dayton , OH the Effects of Individual Differences and Team Processed on Team Member Schema Similarity and task P	AL/CFHI	2- 30
DR Paul D Retzlaff	Univ of Northern Colorado , Greeley , CO The Armstrong Laboratory Aviation Personality Survey (ALAPS) Norming and Cross - Validation	AL/AOCN	2- 31
DR David B Reynolds	Wright State University , Dayton , OH Modeling Heat Flux Through Fabrics Exposed to a Radiant Souource and Analysis of Hot Air Burns	AL/CFBE	2- 32
DR Barth F Smets	University of Connecticut , Storrs , CT Desorption and Biodegradation of Dinitrotoluenes in aged soils	AL/EQL	2- 33

SRP Final Report Table of Contents

Author	University/Institution Report Title	Phillips Laboratory Directorate	Vol-Page
DR Graham R Allan	National Avenue , Las Vegas , NM Temporal and Spatial Characterisation of a Synchronously-Pumped Periodically-Poled Lithium Niobate O	PL/LIDD	3- 1
DR Mark J Balas	Univ of Colorado at Boulder , Boulder , CO Nonlinear Tracking Control for a Precision Deployable Structure Using a Partitioned Filter Approach	PL/SX	3- 2
DR Mikhail S Belen'kii	Georgia Inst of Technology , Atlanta , GA Multiple Aperture Averaging Technique for Measurement Full Aperture Tilt with a Laser Guide Star and	PL/LIG	3- 3
DR Gajanan S Bhat	Univ of Tennessee , Knoxville , TN Spinning Hollow Fibers From High Performance Polymers	PL/RK	3- 4
DR David B Choate	Transylvania Univ , Lexington , KY Blackhole Analysis	PL/VTMR	3- 5
DR Neb Duric	University of New Mexico , Albuquerque , NM Image Recovery Using Phase Diversity	AFRL/DEB	3- 6
DR Arthur B Edwards	9201 University City Blvd. , Charlotte , NC Theory of Protons in Buried Oxides	PL/VTMR	3- 7
DR Gary M Erickson	Boston University , Boston , MA Modeling The Magnetospheric Magnetic Field	PL/GPSG	3- 8
DR Hany A Ghoneim	Rochester Inst of Technol , Rochester , NY Focal Point Accuracy Assessment of an Off-Axis Solar Concentrator	PL/RKES	3- 9
DR Subir Ghosh	Univ of Calif, Riverside , Riverside , CA Designing Propulsion Reliability of Space Launch Vehicles	PL/RKBA	3- 10
DR George W Hanson	Univ of Wisconsin - Milwaukee , Milwaukee , WI Asymptotic analysis of the Natural system modes of coupled bodies in the large separation, Low-Frequency	AFRL/DEH	3- 11

SRP Final Report Table of Contents

Author	University/Institution Report Title	Phillips Laboratory Directorate	Vol-Page
DR Brian D Jeffs	Brigham Young University , Provo , UT Blind Bayesian Restoration of Adaptive Optics Images Using Generalized Gaussian Markov Random Field	AFRL/DES	3- 12
DR Christopher H Jenkins	S Dakota School of Mines/Tech , Rapid City , SD Mechnics of Surface Precosion for Membrane Reflectors	PL/VTVS	3- 13
DR Dikshitulu K Kalluri	University of Lowell , Lowell , MA Mode Conversion in a Time-Varying Magnetoplasma Medium	PL/GPID	3- 14
DR Aravinda Kar	University of Central Florida , Orlando , FL Measurement of the Cutting Performance of a High Beam Quality Chemical Oxygen-Iodine Laser on Aerosp	AFRL/DEO	3- 15
DR Bernard Kirtman	Univ of Calif, Santa Barbara , Santa Barbara , CA Quantum Chemical Characterization of the elكتروnic Structure and Reactions of Silicon Dangling Bon	PL/VTMR	3- 16
DR Spencer P Kuo	Polytechnic University , Farmingdale , NY Excitation of Oscillating Two Stream Instability by Upper Hybrid Pump Waves in Ionospheric Heating	PL.GPI	3- 17
DR Henry A Kurtz	Memphis State University , Memphis , TN H2 Reactions at Dangling Bonds in SIO2	PL/VTMR	3- 18
DR Min-Chang Lee	Massachusetts Inst of Technology , Cambridge , MA Laboratory Studies of Ionospheric Plasma Effects Produced by Lightning-induced Whistler Waves	PL/GPSG	3- 19
DR Donald J Leo	University of Toledo , Toledo , OH Microcontroller-Based Implementation of Adaptive Structural Control	AFRL/VSD	3- 20
DR Hua Li	University of New Mexico , Albuquerque , NM	PL/LIDD	3- 21
DR Hanli Liu	Univ of Texas at Arlington , Arlington , TX Experimental Validation of Threc-Dimensional Reconstruction of Inhomogenety Images in Turbid Media	AFRL/DEB	3- 22

SRP Final Report Table of Contents

Author	University/Institution Report Title	Phillips Laboratory Directorate	Vol-Page
DR M. Arfin K Lodhi	Texas Tech University , Lubbock , TX Thermoelectric Energy Conversion with solid Electrolytes	PL/VTRP	3- 23
DR Tim C Newell	University of New Mexico , Albuquerque , NM Study of Nonlinear Dynamics in a Diode Pumped Nd:YAG laser	PL/LIGR	3- 24
DR Michael J Pangia	Georgia College & State University , Milledgeville , GA Preparatory Work Towards a Computer Simulation of Electron beam Operations on TSS 1	PL/GPSG	3- 25
DR Vladimir O Papitashvili	Univ of Michigan , Ann Arbor , MI Modeling of Ionospheric Convection from the IMF and Solar Wind Data	PL/GPSG	3- 26
DR Jaime Ramirez-Angulo	New Mexico State University , Las Cruces , NM	PL/VTMR	3- 27
DR Louis F Rossi	University of Lowell , Lowell , MA Analysis of Turbulent Mixing in the Stratosphere & Troposphere	PL/GPOL	3- 28
DR David P Stapleton	University of Central Oklahoma , Edmond , OK Atmospheric Effects Upon Sub-Orbital Boost glide Spaceplane Trajectories	PL/RKBA	3- 29
DR Jenn-Ming Yang	Univ of Calif, Los Angeles , Los Angeles , CA Thermodynamic Stability and Oxidation Behavior of Refractory (Hf, Ta, Zr) Carbide/boride Composites	PL/RKS	3- 30

SRP Final Report Table of Contents

Author	University/Institution Report Title	Rome Laboratory Directorate	Vol-Page
DR A. F Anwar	University of Connecticut , Storrs , CT Properties of Quantum Wells Formed In AlGaIn/GaN Heterostructures	RL/ERAC	4- 1
DR Milica Barjaktarovic	Wilkes University , Wilkes Barre , PA Assured Software Design: Privacy Enhanced Mail (PEM) and X.509 Certificate Specification	AFRL/IFG	4- 2
DR Stella N Batalama	SUNY Buffalo , Buffalo , NY Adaptive Robust Spread-Spectrum Receivers	AFRL/IFG	4- 3
DR Adam W Bojanczyk	Cornell University , Ithaca , NY Lowering the Computational Complexity of Stair Radar Systems	RL/OCSS	4- 4
DR Nazeih M Botros	So. Illinois Univ-Carbondale , Carbondale , IL A PC-Based Speech Synthesizing Using Sinusoidal Transform Coding (STC)	RL/ERC-1	4- 5
DR Nikolaos G Bourbakis	SUNY Binghamton , Binghamton , NY Eikones-An Object-Oriented Language For Image Analysis & Process	AFRL/IF	4- 6
DR Peter P Chen	Louisiana State University , Baton Rouge , LA Reconstructing the information Warfare Attack Scenario Guessing what Actually Had Happened Based on	RL/CA-II	4- 7
DR Everett E Crisman	Brown University , Providence , RI A Three-Dimensional, Dielectric Antenna Array Re-Configurable By Optical Wavelength Multiplexing	RL/ERAC	4- 8
DR Digendra K Das	SUNYIT , Utica , NY A Study of the Emerging Diagnostic Techniques in Avionics	RL/ERSR	4- 9
DR Venugopala R Dasigi	Southern Polytechnic State Univ , Marietta , GA Information Fusion for text Classification-an Experimental Comparison	AFRL/IFT	4- 10
DR Richard R Eckert	SUNY Binghamton , Binghamton , NY Enhancing the Rome Lab ADII virtual environment system	AFRL/IFSA	4- 11

SRP Final Report Table of Contents

Author	University/Institution Report Title	Rome Laboratory Directorate	Vol-Page
DR Micheal A Fiddy	University of Lowell , Lowell , MA Target Identification from Limited Backscattered Field Data	RL/ERCS	4- 12
DR Lili He	Nothern Illinois University , Dekalb , IL the Study of Caaractreistics of CdS Passivation on InP	RL/EROE	4- 13
DR Edem Ibragimov	Michigan Tech University , Houghton , MI Effects of Surface Scattering in 3-D Optical Mass Storage	RL/TRAP	4- 14
DR Phillip G Kornreich	Syracuse University , Syracuse , NY Analysis of Optically Active Material Layer Fibers	RL/OCPA	4- 15
DR Kuo-Chi Lin	University of Central Florida , Orlando , FL A Study on The Crowded Airspace Self Organized Criticality	AFRL/IFSB	4- 16
Dr. Beth L Losiewicz	Colorado College , Colorado Spring , CO The Miami Corpus Latin American Dialect Database continued Research and Documentation	RL/IRAA	4- 17
DR John D Norgard	Univ of Colorado at Colorado Springs , Colorado Spring , CO Microwave Holography using Infrared Thermograms of Electromagnetic Fields	RL/ERST	4- 18
DR Jeffrey B Norman	Vassar College , Poughkeepsie , NY Gain Spectra of Beam-Coupling In Photorefractive Semiconductors	RL/OCPA	4- 19
DR Dimitrios N Pados	State Univ. of New York Buffalo , Buffalo , NY Joint Domain Space-Time Adaptive Processing w/Small Training Data Sets	AFRL/SNR	4- 21
DR Brajendra N Panda	University of North Dakota , Grand Forks , ND A Model to Attain Data Integrity After System Invasion	AFRL/IFG	4- 22
DR Michael A Pittarelli	SUNY OF Tech Utica , Utica , NY Phase Transitions in probability Estimation and Constraint Satisfaction Problems	AFRL/IFT	4- 23

SRP Final Report Table of Contents

Author	University/Institution Report Title	Rome Laboratory Directorate	Vol-Page
DR Salahuddin Qazi	SUNY OF Tech Utica , Utica , NY Low Data rate Multimedia Communication Using Wireless Links	RL/IWT	4- 24
DR Arindam Saha	Mississippi State University , Mississippi State , MS An Implementationa of the message passing Interface on Rtems	RL/OCSS	4- 25
DR Ravi Sankar	University of South Florida , Tampa , FL A Study ofIntegrated and Intelligent Network Management	RL/C3BC	4- 26
DR Mark S Schmalz	University of Florida , Gainesville , FL Errors inherent in Reconstruction of Targets From multi-Look Imagery	AFRL/IF	4- 27
DR John L Stensby	Univ of Alabama at Huntsville , Huntsville , AL Simple Real-time Tracking Indicator for a Frequency Feedback Demodulator	RL/TRAP	4- 28
DR Micheal C Stinson	Central Michigan University , Mt. Pleasant , MI Destructive Objects	RL/CAII	4- 29
DR Donald R Ucci	Illinois Inst of Technology , Chicago , IL Simulation of a Robust Locally Optimum Receiver in correlated Noise Using Autoregressive Modeling	RL/C3BB	4- 30
DR Nong Ye	Arizona State University , Tempe , AZ A Process Engineering Approach to Continuous Command and Control on Security-Aware Computer Networks	AFRL/IFSA	4- 31

SRP Final Report Table of Contents

Author	University/Institution Report Title	Wright Laboratory Directorate	Vol-Page
DR William A Baeslack	Ohio State University , Columbus , OH	WL/MLLM _____	5- 1
DR Bhavik R Bakshi	Ohio State University , Columbus , OH Modeling of Materials Manufacturing Processes by NonlinearContimuum Regression	WL/MLIM _____	5- 2
DR Brian P Beecken	Bethel College , St. Paul , MN Contribution of a Scene Projector's Non-Uniformity to a Test Article's Output Image Non-Uniformity	AFRL/MN _____	5- 3
DR John H Beggs	Mississippi State University , Mississippi State , MS The Finite Element Method in Electromagnetics For Multidisciplinary Design	AFRL/VA _____	5- 4
DR Kevin D Belfield	University of Detroit Mercy , Detroit , MI Synthesis of Novel Organic Compounds and Polymers for two Photon Asorption, NLO, and Photorefractive	WL/MLBP _____	5- 5
DR Raj K Bhatnagar	University of Cincinnati , Cincinnati , OH A Study of Intra-Class Variability in ATR Systems	AFRL/SN _____	5- 6
DR Victor M Birman	Univ of Missouri - St. Louis , St Louis , MO Theoretical Foundations for Detection of Post-Processing Cracks in Ceramic Matrix Composites Based o	WL/FIBT _____	5- 7
DR Gregory A Blaisdell	Purdue University , West Lafayette , IN A Review of Benchmark Flows for Large EddySimulation	AFRL/VA _____	5- 8
DR Octavia I Camps	Pennsylvania State University , University Park , PA MDL Texture Segmentation Compressed Images	WL/MNGA _____	5- 9
DR Yiding Cao	Florida International Univ , Miami , FL A Feasibility Study of Turbine Disk Cooling by Employing Radially Rotating Heat Pipes	WL/POTT _____	5- 10
DR Reaz A Chaudhuri	University of Utah , Salt Lake City , UT A Novel Compatibility/Equilibrium Based Iterative Post-Processing Approach For Axisymmetric brittle	WL/MLBM _____	5- 11

SRP Final Report Table of Contents

Author	University/Institution Report Title	Wright Laboratory Directorate	Vol-Page
DR Mohamed F Chouikha	Howard University , Washington , DC Detection Techniques Use in Forward-Looking Radar Signal Procesing a Literature Review	WL/AAMR _____	5- 12
DR Milton L Cone	Embry-Riddle Aeronautical University , Prescott , AZ Scheduling in the Dynamic System Simulation Testbed	WL/AACF _____	5- 13
DR Robert C Creese	West Virginia University , Morgantown , WV Feature Based Cost Modeling	WL/MTI _____	5- 14
DR William Crossley	Purdue University , West Lafayette , IN Objects and Methods for Aircraft Conceptual Design and Optimization in a Knowledge-Based Environment	WL/FIBD _____	5- 15
DR Gene A Crowder	Tulane University , New Orleans , LA Vibrational Analysis of some High-Energy Compounds	WL/MNM _____	5- 16
DR Richard W Darling	University of South Florida , Tampa , FL Geometrically Invariant NonLinear recursive Filters, with Applicaation to Target Tracking	WL/MNAG _____	5- 17
DR Robert J DeAngelis	Univ of Nebraska - Lincoln , Lincoln , NE Quantitative Description of Wire Tecxtures In Cubic Metals	WL/MNM _____	5- 18
DR Bill M Diong	Pan American University , Edinburg , TX Analysis and Control Design for a Novel Resonant DC-DC Converter	WL/POOC _____	5- 19
DR John K Douglass	University of Arizona , Tucson , AZ Guiding Missiles "On The Fly:" Applications of Neurobiologica Princioles to Machine Vision For Arma	AFRL/MN _____	5- 20
DR Mark E Eberhart	Colorado School of Mines , Golden , CO Modeling The Charge Redistribution Associated with Deformation and Fracture	WL/MLLM _____	5- 21
DR Gregory S Elliott	Rutgers:State Univ of New Jersey , Piscataway , NJ On the Development of Planar Doppler Velocimetry	WL/POPT _____	5- 22

SRP Final Report Table of Contents

Author	University/Institution Report Title	Wright Laboratory Directorate	Vol-Page
DR Elizabeth A Ervin	University of Dayton , Dayton , OH Eval of the Pointwise K-2 Turbulence Model to Predict Transition & Separtion in a Low Pressure	WL/POTT _____	5- 23
DR Altan M Ferendeci	University of Cincinnati , Cincinnati , OH Vertically Interconnected 3D MMICs with Active Interlayer Elements	WL/AADI _____	5- 24
DR Dennis R Flentge	Cedarville College , Cedarville , OH Kinetic Study of the Thermal Decomposition of t-Butylphenyl Phosphate Using the System for Thermal D	WL/POSL _____	5- 25
DR George N Frantziskonis	University of Arizona , Tuson , AZ Multiscale Material Characterization and Applications	WL/MLLP _____	5- 26
DR Zewdu Gebeyehu	Tuskegee University , Tuskegee , AL Synthesis and Characterization of Metal-Xanthic Acid and -Amino Acid Com[lexes Useful Ad Nonlinear	WL/MLPO _____	5- 27
DR Richard D Gould	North Carolina State U-Raleigh , Raleigh , NC Reduction and Analysis of LDV and Analog Raw Data	WL/POPT _____	5- 28
DR Michael S Grace	University of Virginia , Charlottesville , VA Structure and Function of an Extremely Sensitive Biological Infrared Detector	WL/MLPJ _____	5- 29
DR Gary M Graham	Ohio University , Athens , OH Indicial Response Model for Roll Rate Effects on A 65-Degree Delta wing	WL/FIGC _____	5- 30
DR Allen G Greenwood	Mississippi State University , Mississippi Sta , MS An Object-Based approach for Integrating Cost Assessment into Product/Process Design	WL/MTI _____	5- 31
DR Rita A Gregory	Georgia Inst of Technology , Atlanta , GA Range Estimating for Research and Development Alternatives	WL/FIVC _____	5- 32
DR Mark T Hanson	University of Kentucky , Lexington , KY Anisotropy in Epic 96&97: Implementation and Effects	WL/MNM _____	5- 33

SRP Final Report Table of Contents

Author	University/Institution Report Title	Wright Laboratory Directorate	Vol-Page
DR Majeed M Hayat	University of Dayton , Dayton , OH A Model for Turbulence and Photodetection Noise in Imaging	WL/AAJT	5- 34
DR Larry S Helmick	Cedarville College , Cedarville , OH NMA Study of the Decomposition Reaction Path of Demnum fluid under Tribological Conditions	WL/MLBT	5- 35
DR William F Hosford	Univ of Michigan , Ann Arbor , MI INTENSITY OF [111]AND [100] TEXTURAL COMPONENTS IN COMPRESSION-FORGED TANTALUM	AFRL/MN	5- 36
DR David E Hudak	Ohio Northern University , Ada , OH A Study fo a Data-Parallel Implemmentation of An Implicit Solution fo the 3D Navier-Stokes Equations	WL/FIMC	5- 37
DR David P Johnson	Mississippi State University , Mississippi , MS An Innovative Segmented Tugsten Penetrating Munition	WL/MNAZ	5- 38
DR Ismail I Jouny	Lafayette College , Easton , PA	WL/AACT	5- 39
DR Edward T Knobbe	Oklahoma State University , Stillwater , OK Organically Modified silicate Films as Corrosion Resistant Treatments for 2024-T3 Alumium Alloy	WL/MLBT	5- 40
DR Seungug Koh	University of Dayton , Dayton , OH Numerically Efficinet Direct Ray Tracing Algorithms for Automatic Target Recognition using FPGAs	WL/AAST	5- 41
DR Ravi Kothari	University of Cincinnati , Cincinnati , OH A Function Approximation Approach for Region of Interest Selection in synthetic Aperture Radar Image	WL/AACA	5- 42
DR Douglas A Lawrence	Ohio University , Athens , OH On the Analysis and Design of Gain scheduled missile Autopilots	WL/MNAG	5- 43
DR Robert Lee	Ohio State University , Columbus , OH Boundary Conditions applied to the Finite Vlume Time Domain Method for the Solution of Maxwell's Equ	WL/FIM	5- 44

SRP Final Report Table of Contents

Author	University/Institution Report Title	Wright Laboratory Directorate	Vol-Page
DR Junghsen Lich	Wright State University , Dayton , OH Develop an Explosive Simulated Testing Apparatus for Impact Physics Research at Wright Laboratory	WL/FIV	5- 45
DR James S Marsh	University of West Florida , Pensacola , FL Distortion Compensation and Elimination in Holographic Reocnstruction	WL/MNSI	5- 46
DR Mark D McClain	Cedarville College , Cedarville , OH A Molecular Orbital Theory Analysis of Oligomers of 2,2'-Bithiazole and Partially Reduced 3,3'-Dimet	WL/MLBP	5- 47
DR William S McCormick	Wright State University , Dayton , OH Some Observations of Target Recognition Using High Range Resolution Radar	WL/AACR	5- 48
DR Richard O Mines	University of South Florida , Tampa , FL Testing Protocol for the Demilitarization System at the Eglin AFB Herd Facility	WLMN/M	5- 49
DR Dakshina V Murty	University of Portland , Portland , OR A Useful Benchmarking Method in Computational Mechanics, CFD, adn Heat Tansfer	WL/FIBT	5- 50
DR Krishna Naishadham	Wright State University , Dayton , OH	WL/MLPO	5- 51
DR Serguei Ostapenko	University of South Florida , Tampa , FL	WL/MLPO	5- 52
DR Yi Pan	University of Dayton , Dayton , OH Improvement of Cache Utilization and Parallel Efficiency of a Time-Dependnet Maxwell Equation Solver	AFRL/VA	5- 53
DR Rolfe G Petschek	Case Western Reserve Univ , Cleveland , OH AB INITIO AUANTUM CHEMICAL STUDIES OF NICKEL DITHIOLENE COMPLEX	WL/MLPJ	5- 54
DR Kishore V Pochiraju	Stevens Inst of Technology , Hoboken , NJ Refined Reissner's Variational Solution in the Vicinity of Stress Singularities	AFRL/ML	5- 55

SRP Final Report Table of Contents

Author	University/Institution Report Title	Wright Laboratory Directorate	Vol-Page
DR Muhammad M Rahman	University of South Florida , Tampa , FL Computation of Free Surface Flows with Applications in Capillary Pumped Loops, Heat Pipes, and Jet I	WL/POOB	5- 56
DR Mateen M Rizki	Wright State University , Dayton , OH Classification of High Range Resolution Radar Signatures Using Evolutionary Computation	WL/AACA	5- 57
DR Shankar M Sastry	Washington University , St Louis , MO	WL/MLLM	5- 58
DR Martin Schwartz	University of North Texas , Denton , TX Computational Studies of Hydrogen Abstraction From Haloalkanes by the Hydroxyl Radical	WL/MLBT	5- 59
DR Rathinam P Selvam	Univ of Arkansas , Fayetteville , AR Computation of Nonlennear Viscous Panel Flutter Using a Full-Implicit Aeroelastic Solver	WL/FIMC	5- 60
DR Yuri B Shtessel	Univ of Alabama at Huntsville , Huntsville , AL Smoothed Sliding Mode control Approach For Addressing Actuator Deflection and Deflection Rate Saturata	AFRL/VA	5- 61
DR Mario Sznaier	Pennsylvania State University , University Park , PA Suboptimal Control of Nonlennear Systems via Receding Horizon State Dependent Riccati Equations	WL/MNAG	5- 62
DR Barney E Taylor	Miami Univ. - Hamilton , Hamilton , OH Photoconductivity Studies of the Polymer 6FPBO	WLMLBP	5- 63
DR Joseph W Tedesco	Auburn University , Auburn , AL high Velocity Penetration of Layered Concrete Targets with Small Scale Ogive-nose Steel projectiles	WL/MNSA	5- 64
DR Krishnaprasad Thirunarayan	Wright State University , Dayton , OH A VHDL MODEL SYNTHESIS APPLLET IN TCL/TK	WL/AAST	5- 65

SRP Final Report Table of Contents

Author	University/Institution Report Title	Wright Laboratory Directorate	Vol-Page
DR Karen A Tomko	Wright State University , Dayton , OH Grid Level Parallelization of an Implicit Solution of the 3D Navier-Stokes Equations	WL/FIMC _____	5- 66
DR Max B Trueblood	University of Missouri-Rolla , Rolla , MO A Study of the Particulate Emissions of a Well-Stirred Reactor	WL/POSC _____	5- 67
DR Chi-Tay Tsai	Florida Atlantic University , Boca Raton , FL Dislocation Dynamics in Heterojunction Bipolar Transistor Under Current Induced Thermal St	WL/AA _____	5- 68
DR John L Valasek	Texas A&M University , College Station , TX Two Axis Pneumatic Vortex Control at High Speed and Low Angle-of-Attack	WL/FIMT _____	5- 69
DR Mitch J Wolff	Wright State University , Dayton , OH An Experimental and Computational Analysis of the Unsteady Blade Row Potential Interaction in a Tr	WL/POTF _____	5- 70
DR Rama K Yedavalli	Ohio State University , Columbus , OH Improved Aircraft Roll Maneuver Performance Using Smart Deformable Wings	WL/FIBD _____	5- 71

SRP Final Report Table of Contents

Author	University/Institution Report Title	Arnold Engineering Development Center Directorate	Vol-Page
DR Csaba A Biegl	Vanderbilt University , Nashville , TN Parallel processing for Turbine Engine Modeling and Test Data validation	AEDC/SVT _____	6- 1
DR Frank G Collins	Tennessee Univ Space Institute , Tullahoma , TN Design of a Mass Spectrometer Sampling Probe for The AEDC Impulse Facility	AEDC _____	6- 2
DR Kenneth M Jones	N Carolina A&T State Univ , Greensboro , NC	AEDC/SVT _____	6- 3
DR Kevin M Lyons	North Carolina State U-Raleigh , Raleigh , NC Velocity Field Measurements Using Filtered-Rayleigh Scattering	AEDC/SVT _____	6- 4
DR Gerald J Micklow	Univ of Alabama at Tuscaloosa , Tucasloosa , AL	AEDC/SVT _____	6- 5
DR Michael S Moore	Vanderbilt University , Nashville , TN Extension and Installation of the Model-Integrated Real-Time Imaging System (Mirtis)	AEDC/SVT _____	6- 6
DR Robert L Roach	Tennessee Univ Space Institute , Tullahoma , TN Investigation of Fluid Mechanical Phenomena Relating to Air Injection Between the Segments of an Arc	AEDC _____	6- 7
DR Nicholas S Winowich	University of Tennessee , Knoxville , TN	AEDC _____	6- 8
DR Daniel M Knauss	Colorado School of Mines , Golden , CO Synthesis of salts With Delocalized Anions For Use as Third Order Nonlinear Optical Materials	USAF/DF _____	6- 9
DR Jeffrey M Bigelow	Oklahoma Christian Univ of Science & Art , Oklahoma City , OK Raster-To-Vector Conversion of Circuit Diagrams: Software Requirements	OCALC/TI _____	6- 10

SRP Final Report Table of Contents

Author	University/Institution Report Title	Arnold Engineering Development Center Directorate	Vol-Page
DR Paul W Whaley	Oklahoma Christian Univ of Science & Art , Oklahoma City , OK A Probabilistic framework for the Analysis of corrosion Damage in Aging Aircraft	OCALC/L _____	6- 11
DR Bjong W Yeigh	Oklahoma State University , Stillwater , OK Logistics Asset Management : Models and Simulations	OCALC/TI _____	6- 12
DR Michael J McFarland	Utah State University , Logan , UT Delisting of Hill Air Force Base's Industrial Wastewater Treatment Plant Sludge	OC-ALC/E _____	6- 13
DR William E Sanford	Colorado State University , Fort Collins , CO Nuerical Modeling of Physical Constraints on in-Situ Cosolvent Flushing as a Groundwater Remedial Op	OO-ALC/E _____	6- 14
DR Sophia Hassiotis	University of South Florida , Tampa , FL Fracture Analysis of the F-5, 15%-Spar Bolt	SAALC/TI _____	6- 15
DR Devendra Kumar	CUNY-City College , New York , NY A Simple, Multiversion Concurrency Control Protocol For Internet Databases	SAALC/LD _____	6- 16
DR Ernest L McDuffie	Florida State University , Tallahassee , FL A Proposed Exjpert System for ATS Capability Analysis	SAALC/TI _____	6- 17
DR Prabhaker Mateti	Wright State University , Dayton , OH How to Provide and Evaluate Computer Network Security	SMALC/TI _____	6- 18
DR Mansur Rastani	N Carolina A&T State Univ , Greensboro , NC Optimal Structural Design of Modular Composite bare base Shelters	SMALC/L _____	6- 19
DR Joe G Chow	Florida International Univ , Miami , FL Re-engineer and Re-Manufacture Aircraft Sstructural Components Using Laser Scanning	WRALC/TI _____	6- 20

1. INTRODUCTION

The Summer Research Program (SRP), sponsored by the Air Force Office of Scientific Research (AFOSR), offers paid opportunities for university faculty, graduate students, and high school students to conduct research in U.S. Air Force research laboratories nationwide during the summer.

Introduced by AFOSR in 1978, this innovative program is based on the concept of teaming academic researchers with Air Force scientists in the same disciplines using laboratory facilities and equipment not often available at associates' institutions.

The Summer Faculty Research Program (SFRP) is open annually to approximately 150 faculty members with at least two years of teaching and/or research experience in accredited U.S. colleges, universities, or technical institutions. SFRP associates must be either U.S. citizens or permanent residents.

The Graduate Student Research Program (GSRP) is open annually to approximately 100 graduate students holding a bachelor's or a master's degree; GSRP associates must be U.S. citizens enrolled full time at an accredited institution.

The High School Apprentice Program (HSAP) annually selects about 125 high school students located within a twenty mile commuting distance of participating Air Force laboratories.

AFOSR also offers its research associates an opportunity, under the Summer Research Extension Program (SREP), to continue their AFOSR-sponsored research at their home institutions through the award of research grants. In 1994 the maximum amount of each grant was increased from \$20,000 to \$25,000, and the number of AFOSR-sponsored grants decreased from 75 to 60. A separate annual report is compiled on the SREP.

The numbers of projected summer research participants in each of the three categories and SREP "grants" are usually increased through direct sponsorship by participating laboratories.

AFOSR's SRP has well served its objectives of building critical links between Air Force research laboratories and the academic community, opening avenues of communications and forging new research relationships between Air Force and academic technical experts in areas of national interest, and strengthening the nation's efforts to sustain careers in science and engineering. The success of the SRP can be gauged from its growth from inception (see Table 1) and from the favorable responses the 1997 participants expressed in end-of-tour SRP evaluations (Appendix B).

AFOSR contracts for administration of the SRP by civilian contractors. The contract was first awarded to Research & Development Laboratories (RDL) in September 1990. After completion of the

1990 contract, RDL (in 1993) won the recompetition for the basic year and four 1-year options.

2. PARTICIPATION IN THE SUMMER RESEARCH PROGRAM

The SRP began with faculty associates in 1979; graduate students were added in 1982 and high school students in 1986. The following table shows the number of associates in the program each year.

YEAR	SRP Participation, by Year			TOTAL
	SFRP	GSRP	HSAP	
1979	70			70
1980	87			87
1981	87			87
1982	91	17		108
1983	101	53		154
1984	152	84		236
1985	154	92		246
1986	158	100	42	300
1987	159	101	73	333
1988	153	107	101	361
1989	168	102	103	373
1990	165	121	132	418
1991	170	142	132	444
1992	185	121	159	464
1993	187	117	136	440
1994	192	117	133	442
1995	190	115	137	442
1996	188	109	138	435
1997	148	98	140	427

Beginning in 1993, due to budget cuts, some of the laboratories weren't able to afford to fund as many associates as in previous years. Since then, the number of funded positions has remained fairly constant at a slightly lower level.

3. RECRUITING AND SELECTION

The SRP is conducted on a nationally advertised and competitive-selection basis. The advertising for faculty and graduate students consisted primarily of the mailing of 8,000 52-page SRP brochures to chairpersons of departments relevant to AFOSR research and to administrators of grants in accredited universities, colleges, and technical institutions. Historically Black Colleges and Universities (HBCUs) and Minority Institutions (MIs) were included. Brochures also went to all participating USAF laboratories, the previous year's participants, and numerous individual requesters (over 1000 annually).

RDL placed advertisements in the following publications: *Black Issues in Higher Education*, *Winds of Change*, and *IEEE Spectrum*. Because no participants list either *Physics Today* or *Chemical & Engineering News* as being their source of learning about the program for the past several years, advertisements in these magazines were dropped, and the funds were used to cover increases in brochure printing costs.

High school applicants can participate only in laboratories located no more than 20 miles from their residence. Tailored brochures on the HSAP were sent to the head counselors of 180 high schools in the vicinity of participating laboratories, with instructions for publicizing the program in their schools.

High school students selected to serve at Wright Laboratory's Armament Directorate (Eglin Air Force Base, Florida) serve eleven weeks as opposed to the eight weeks normally worked by high school students at all other participating laboratories.

Each SFRP or GSRP applicant is given a first, second, and third choice of laboratory. High school students who have more than one laboratory or directorate near their homes are also given first, second, and third choices.

Laboratories make their selections and prioritize their nominees. AFOSR then determines the number to be funded at each laboratory and approves laboratories' selections.

Subsequently, laboratories use their own funds to sponsor additional candidates. Some selectees do not accept the appointment, so alternate candidates are chosen. This multi-step selection procedure results in some candidates being notified of their acceptance after scheduled deadlines. The total applicants and participants for 1997 are shown in this table.

1997 Applicants and Participants			
PARTICIPANT CATEGORY	TOTAL APPLICANTS	SELECTEES	DECLINING SELECTEES
SFRP	490	188	32
(HBCU/MI)	(0)	(0)	(0)
GSRP	202	98	9
(HBCU/MI)	(0)	(0)	(0)
HSAP	433	140	14
TOTAL	1125	426	55

4. SITE VISITS

During June and July of 1997, representatives of both AFOSR/NI and RDL visited each participating laboratory to provide briefings, answer questions, and resolve problems for both laboratory personnel and participants. The objective was to ensure that the SRP would be as constructive as possible for all participants. Both SRP participants and RDL representatives found these visits beneficial. At many of the laboratories, this was the only opportunity for all participants to meet at one time to share their experiences and exchange ideas.

5. HISTORICALLY BLACK COLLEGES AND UNIVERSITIES AND MINORITY INSTITUTIONS (HBCU/MIIs)

Before 1993, an RDL program representative visited from seven to ten different HBCU/MIIs annually to promote interest in the SRP among the faculty and graduate students. These efforts were marginally effective, yielding a doubling of HBCU/MI applicants. In an effort to achieve AFOSR's goal of 10% of all applicants and selectees being HBCU/MI qualified, the RDL team decided to try other avenues of approach to increase the number of qualified applicants. Through the combined efforts of the AFOSR Program Office at Bolling AFB and RDL, two very active minority groups were found, HACU (Hispanic American Colleges and Universities) and AISES (American Indian Science and Engineering Society). RDL is in communication with representatives of each of these organizations on a monthly basis to keep up with their activities and special events. Both organizations have widely-distributed magazines/quarterlies in which RDL placed ads.

Since 1994 the number of both SFRP and GSRP HBCU/MI applicants and participants has increased ten-fold, from about two dozen SFRP applicants and a half dozen selectees to over 100 applicants and two dozen selectees, and a half-dozen GSRP applicants and two or three selectees to 18 applicants and 7 or 8 selectees. Since 1993, the SFRP had a two-fold applicant increase and a two-fold selectee increase. Since 1993, the GSRP had a three-fold applicant increase and a three to four-fold increase in selectees.

In addition to RDL's special recruiting efforts, AFOSR attempts each year to obtain additional funding or use leftover funding from cancellations the past year to fund HBCU/MI associates. This year, 5 HBCU/MI SFRPs declined after they were selected (and there was no one qualified to replace them with). The following table records HBCU/MI participation in this program.

SRP HBCU/MI Participation, By Year				
YEAR	SFRP		GSRP	
	Applicants	Participants	Applicants	Participants
1985	76	23	15	11
1986	70	18	20	10
1987	82	32	32	10
1988	53	17	23	14
1989	39	15	13	4
1990	43	14	17	3
1991	42	13	8	5
1992	70	13	9	5
1993	60	13	6	2
1994	90	16	11	6
1995	90	21	20	8
1996	119	27	18	7

6. SRP FUNDING SOURCES

Funding sources for the 1997 SRP were the AFOSR-provided slots for the basic contract and laboratory funds. Funding sources by category for the 1997 SRP selected participants are shown here.

1997 SRP FUNDING CATEGORY	SFRP	GSRP	HSAP
AFOSR Basic Allocation Funds	141	89	123
USAF Laboratory Funds	48	9	17
HBCU/MI By AFOSR (Using Procured Addn'l Funds)	0	0	N/A
TOTAL	9	98	140

SFRP - 188 were selected, but thirty two canceled too late to be replaced.

GSRP - 98 were selected, but nine canceled too late to be replaced.

HSAP - 140 were selected, but fourteen canceled too late to be replaced.

7. COMPENSATION FOR PARTICIPANTS

Compensation for SRP participants, per five-day work week, is shown in this table.

1997 SRP Associate Compensation

PARTICIPANT CATEGORY	1991	1992	1993	1994	1995	1996	1997
Faculty Members	\$690	\$718	\$740	\$740	\$740	\$770	\$770
Graduate Student (Master's Degree)	\$425	\$442	\$455	\$455	\$455	\$470	\$470
Graduate Student (Bachelor's Degree)	\$365	\$380	\$391	\$391	\$391	\$400	\$400
High School Student (First Year)	\$200	\$200	\$200	\$200	\$200	\$200	\$200
High School Student (Subsequent Years)	\$240	\$240	\$240	\$240	\$240	\$240	\$240

The program also offered associates whose homes were more than 50 miles from the laboratory an expense allowance (seven days per week) of \$50/day for faculty and \$40/day for graduate students. Transportation to the laboratory at the beginning of their tour and back to their home destinations at the end was also reimbursed for these participants. Of the combined SFRP and GSRP associates, 65 % (194 out of 286) claimed travel reimbursements at an average round-trip cost of \$776.

Faculty members were encouraged to visit their laboratories before their summer tour began. All costs of these orientation visits were reimbursed. Forty-three percent (85 out of 188) of faculty associates took orientation trips at an average cost of \$388. By contrast, in 1993, 58 % of SFRP associates took

orientation visits at an average cost of \$685; that was the highest percentage of associates opting to take an orientation trip since RDL has administered the SRP, and the highest average cost of an orientation trip. These 1993 numbers are included to show the fluctuation which can occur in these numbers for planning purposes.

Program participants submitted biweekly vouchers countersigned by their laboratory research focal point, and RDL issued paychecks so as to arrive in associates' hands two weeks later.

This is the second year of using direct deposit for the SFRP and GSRP associates. The process went much more smoothly with respect to obtaining required information from the associates, only 7% of the associates' information needed clarification in order for direct deposit to properly function as opposed to 10% from last year. The remaining associates received their stipend and expense payments via checks sent in the US mail.

HSAP program participants were considered actual RDL employees, and their respective state and federal income tax and Social Security were withheld from their paychecks. By the nature of their independent research, SFRP and GSRP program participants were considered to be consultants or independent contractors. As such, SFRP and GSRP associates were responsible for their own income taxes, Social Security, and insurance.

8. CONTENTS OF THE 1997 REPORT

The complete set of reports for the 1997 SRP includes this program management report (Volume 1) augmented by fifteen volumes of final research reports by the 1997 associates, as indicated below:

1997 SRP Final Report Volume Assignments

LABORATORY	SFRP	GSRP	HSAP
Armstrong	2	7	12
Phillips	3	8	13
Rome	4	9	14
Wright	5A, 5B	10	15
AEDC, ALCs, WHMC	6	11	16

APPENDIX A – PROGRAM STATISTICAL SUMMARY

A. Colleges/Universities Represented

Selected SFRP associates represented 169 different colleges, universities, and institutions,
GSRP associates represented 95 different colleges, universities, and institutions.

B. States Represented

SFRP -Applicants came from 47 states plus Washington D.C. Selectees represent 44 states.

GSRP - Applicants came from 44 states. Selectees represent 32 states.

HSAP - Applicants came from thirteen states. Selectees represent nine states.

Total Number of Participants	
SFRP	189
GSRP	97
HSAP	140
TOTAL	426

Degrees Represented			
	SFRP	GSRP	TOTAL
Doctoral	184	0	184
Master's	2	41	43
Bachelor's	0	56	56
TOTAL	186	97	298

SFRP Academic Titles	
Assistant Professor	64
Associate Professor	70
Professor	40
Instructor	0
Chairman	1
Visiting Professor	1
Visiting Assoc. Prof.	1
Research Associate	9
TOTAL	186

Source of Learning About the SRP		
Category	Applicants	Selectees
Applied/participated in prior years	28 %	34 %
Colleague familiar with SRP	19 %	16 %
Brochure mailed to institution	23 %	17 %
Contact with Air Force laboratory	17 %	23 %
<i>IEEE Spectrum</i>	2 %	1 %
<i>BIIHE</i>	1 %	1 %
Other source	10 %	8 %
TOTAL	100 %	100 %

APPENDIX B – SRP EVALUATION RESPONSES

1. OVERVIEW

Evaluations were completed and returned to RDL by four groups at the completion of the SRP. The number of respondents in each group is shown below.

Table B-1. Total SRP Evaluations Received

Evaluation Group	Responses
SFRP & GSRPs	275
HSAPs	113
USAF Laboratory Focal Points	84
USAF Laboratory HSAP Mentors	6

All groups indicate unanimous enthusiasm for the SRP experience.

The summarized recommendations for program improvement from both associates and laboratory personnel are listed below:

- A. Better preparation on the labs' part prior to associates' arrival (i.e., office space, computer assets, clearly defined scope of work).
- B. Faculty Associates suggest higher stipends for SFRP associates.
- C. Both HSAP Air Force laboratory mentors and associates would like the summer tour extended from the current 8 weeks to either 10 or 11 weeks; the groups state it takes 4-6 weeks just to get high school students up-to-speed on what's going on at laboratory. (Note: this same argument was used to raise the faculty and graduate student participation time a few years ago.)

2. 1997 USAF LABORATORY FOCAL POINT (LFP) EVALUATION RESPONSES

The summarized results listed below are from the 84 LFP evaluations received.

1. LFP evaluations received and associate preferences:

Table B-2. Air Force LFP Evaluation Responses (By Type)

Lab	Evals Recv'd	How Many Associates Would You Prefer To Get ?								(% Response)			
		SFRP				GSRP (w/Univ Professor)				GSRP (w/o Univ Professor)			
		0	1	2	3+	0	1	2	3+	0	1	2	3+
AEDC	0	-	-	-	-	-	-	-	-	-	-	-	-
WHMC	0	-	-	-	-	-	-	-	-	-	-	-	-
AL	7	28	28	28	14	54	14	28	0	86	0	14	0
USAF A	1	0	100	0	0	100	0	0	0	0	100	0	0
PL	25	40	40	16	4	88	12	0	0	84	12	4	0
RL	5	60	40	0	0	80	10	0	0	100	0	0	0
WL	46	30	43	20	6	78	17	4	0	93	4	2	0
Total	84	32%	50%	13%	5%	80%	11%	6%	0%	73%	23%	4%	0%

LFP Evaluation Summary. The summarized responses, by laboratory, are listed on the following page. LFPs were asked to rate the following questions on a scale from 1 (below average) to 5 (above average).

2. LFPs involved in SRP associate application evaluation process:
 - a. Time available for evaluation of applications:
 - b. Adequacy of applications for selection process:
3. Value of orientation trips:
4. Length of research tour:
5.
 - a. Benefits of associate's work to laboratory:
 - b. Benefits of associate's work to Air Force:
6.
 - a. Enhancement of research qualifications for LFP and staff:
 - b. Enhancement of research qualifications for SFRP associate:
 - c. Enhancement of research qualifications for GSRP associate:
7.
 - a. Enhancement of knowledge for LFP and staff:
 - b. Enhancement of knowledge for SFRP associate:
 - c. Enhancement of knowledge for GSRP associate:
8. Value of Air Force and university links:
9. Potential for future collaboration:
10.
 - a. Your working relationship with SFRP:
 - b. Your working relationship with GSRP:
11. Expenditure of your time worthwhile:

(Continued on next page)

12. Quality of program literature for associate:
13. a. Quality of RDL's communications with you:
 b. Quality of RDL's communications with associates:
14. Overall assessment of SRP:

Table B-3. Laboratory Focal Point Responses to above questions

	<i>AEDC</i>	<i>AL</i>	<i>USAFA</i>	<i>PL</i>	<i>RL</i>	<i>WHMC</i>	<i>WL</i>
<i># Evals Recv'd</i>	0	7	1	14	5	0	46
<i>Question #</i>							
2	-	86 %	0 %	88 %	80 %	-	85 %
2a	-	4.3	n/a	3.8	4.0	-	3.6
2b	-	4.0	n/a	3.9	4.5	-	4.1
3	-	4.5	n/a	4.3	4.3	-	3.7
4	-	4.1	4.0	4.1	4.2	-	3.9
5a	-	4.3	5.0	4.3	4.6	-	4.4
5b	-	4.5	n/a	4.2	4.6	-	4.3
6a	-	4.5	5.0	4.0	4.4	-	4.3
6b	-	4.3	n/a	4.1	5.0	-	4.4
6c	-	3.7	5.0	3.5	5.0	-	4.3
7a	-	4.7	5.0	4.0	4.4	-	4.3
7b	-	4.3	n/a	4.2	5.0	-	4.4
7c	-	4.0	5.0	3.9	5.0	-	4.3
8	-	4.6	4.0	4.5	4.6	-	4.3
9	-	4.9	5.0	4.4	4.8	-	4.2
10a	-	5.0	n/a	4.6	4.6	-	4.6
10b	-	4.7	5.0	3.9	5.0	-	4.4
11	-	4.6	5.0	4.4	4.8	-	4.4
12	-	4.0	4.0	4.0	4.2	-	3.8
13a	-	3.2	4.0	3.5	3.8	-	3.4
13b	-	3.4	4.0	3.6	4.5	-	3.6
14	-	4.4	5.0	4.4	4.8	-	4.4

3. 1997 SFRP & GSRP EVALUATION RESPONSES

The summarized results listed below are from the 257 SFRP/GSRP evaluations received.

Associates were asked to rate the following questions on a scale from 1 (below average) to 5 (above average) - by Air Force base results and over-all results of the 1997 evaluations are listed after the questions.

1. The match between the laboratories research and your field:
2. Your working relationship with your LFP:
3. Enhancement of your academic qualifications:
4. Enhancement of your research qualifications:
5. Lab readiness for you: LFP, task, plan:
6. Lab readiness for you: equipment, supplies, facilities:
7. Lab resources:
8. Lab research and administrative support:
9. Adequacy of brochure and associate handbook:
10. RDL communications with you:
11. Overall payment procedures:
12. Overall assessment of the SRP:
13.
 - a. Would you apply again?
 - b. Will you continue this or related research?
14. Was length of your tour satisfactory?
15. Percentage of associates who experienced difficulties in finding housing:
16. Where did you stay during your SRP tour?
 - a. At Home:
 - b. With Friend:
 - c. On Local Economy:
 - d. Base Quarters:
17. Value of orientation visit:
 - a. Essential:
 - b. Convenient:
 - c. Not Worth Cost:
 - d. Not Used:

SFRP and GSRP associate's responses are listed in tabular format on the following page.

Table B-4. 1997 SFRP & GSRP Associate Responses to SRP Evaluation

	Arnold	Brooks	Edwards	Eglin	Griffin	Hanscom	Kelly	Kirtland	Lackland	Robins	Tyndall	WPAFB	average
# res	6	48	6	14	31	19	3	32	1	2	10	85	257
1	4.8	4.4	4.6	4.7	4.4	4.9	4.6	4.6	5.0	5.0	4.0	4.7	4.6
2	5.0	4.6	4.1	4.9	4.7	4.7	5.0	4.7	5.0	5.0	4.6	4.8	4.7
3	4.5	4.4	4.0	4.6	4.3	4.2	4.3	4.4	5.0	5.0	4.5	4.3	4.4
4	4.3	4.5	3.8	4.6	4.4	4.4	4.3	4.6	5.0	4.0	4.4	4.5	4.5
5	4.5	4.3	3.3	4.8	4.4	4.5	4.3	4.2	5.0	5.0	3.9	4.4	4.4
6	4.3	4.3	3.7	4.7	4.4	4.5	4.0	3.8	5.0	5.0	3.8	4.2	4.2
7	4.5	4.4	4.2	4.8	4.5	4.3	4.3	4.1	5.0	5.0	4.3	4.3	4.4
8	4.5	4.6	3.0	4.9	4.4	4.3	4.3	4.5	5.0	5.0	4.7	4.5	4.5
9	4.7	4.5	4.7	4.5	4.3	4.5	4.7	4.3	5.0	5.0	4.1	4.5	4.5
10	4.2	4.4	4.7	4.4	4.1	4.1	4.0	4.2	5.0	4.5	3.6	4.4	4.3
11	3.8	4.1	4.5	4.0	3.9	4.1	4.0	4.0	3.0	4.0	3.7	4.0	4.0
12	5.7	4.7	4.3	4.9	4.5	4.9	4.7	4.6	5.0	4.5	4.6	4.5	4.6
Numbers below are percentages													
13a	83	90	83	93	87	75	100	81	100	100	100	86	87
13b	100	89	83	100	94	98	100	94	100	100	100	94	93
14	83	96	100	90	87	80	100	92	100	100	70	84	88
15	17	6	0	33	20	76	33	25	0	100	20	8	39
16a	-	26	17	9	38	23	33	4	-	-	-	30	
16b	100	33	-	40	-	8	-	-	-	-	36	2	
16c	-	41	83	40	62	69	67	96	100	100	64	68	
16d	-	-	-	-	-	-	-	-	-	-	-	0	
17a	-	33	100	17	50	14	67	39	-	50	40	31	35
17b	-	21	-	17	10	14	-	24	-	50	20	16	16
17c	-	-	-	-	10	7	-	-	-	-	-	2	3
17d	100	46	-	66	30	69	33	37	100	-	40	51	46

4. 1997 USAF LABORATORY HSAP MENTOR EVALUATION RESPONSES

Not enough evaluations received (5 total) from Mentors to do useful summary.

5. 1997 HSAP EVALUATION RESPONSES

The summarized results listed below are from the 113 HSAP evaluations received.

HSAP apprentices were asked to rate the following questions on a scale from
1 (below average) to 5 (above average)

1. Your influence on selection of topic/type of work.
2. Working relationship with mentor, other lab scientists.
3. Enhancement of your academic qualifications.
4. Technically challenging work.
5. Lab readiness for you: mentor, task, work plan, equipment.
6. Influence on your career.
7. Increased interest in math/science.
8. Lab research & administrative support.
9. Adequacy of RDL's Apprentice Handbook and administrative materials.
10. Responsiveness of RDL communications.
11. Overall payment procedures.
12. Overall assessment of SRP value to you.
13. Would you apply again next year? Yes (92 %)
14. Will you pursue future studies related to this research? Yes (68 %)
15. Was Tour length satisfactory? Yes (82 %)

	Arnold	Brooks	Edwards	Eglin	Griffiss	Hanscom	Kirtland	Tyndall	WPAFB	Totals
# resp	5	19	7	15	13	2	7	5	40	113
1	2.8	3.3	3.4	3.5	3.4	4.0	3.2	3.6	3.6	3.4
2	4.4	4.6	4.5	4.8	4.6	4.0	4.4	4.0	4.6	4.6
3	4.0	4.2	4.1	4.3	4.5	5.0	4.3	4.6	4.4	4.4
4	3.6	3.9	4.0	4.5	4.2	5.0	4.6	3.8	4.3	4.2
5	4.4	4.1	3.7	4.5	4.1	3.0	3.9	3.6	3.9	4.0
6	3.2	3.6	3.6	4.1	3.8	5.0	3.3	3.8	3.6	3.7
7	2.8	4.1	4.0	3.9	3.9	5.0	3.6	4.0	4.0	3.9
8	3.8	4.1	4.0	4.3	4.0	4.0	4.3	3.8	4.3	4.2
9	4.4	3.6	4.1	4.1	3.5	4.0	3.9	4.0	3.7	3.8
10	4.0	3.8	4.1	3.7	4.1	4.0	3.9	2.4	3.8	3.8
11	4.2	4.2	3.7	3.9	3.8	3.0	3.7	2.6	3.7	3.8
12	4.0	4.5	4.9	4.6	4.6	5.0	4.6	4.2	4.3	4.5
Numbers below are percentages										
13	60%	95%	100%	100%	85%	100%	100%	100%	90%	92%
14	20%	80%	71%	80%	54%	100%	71%	80%	65%	68%
15	100%	70%	71%	100%	100%	50%	86%	60%	80%	82%

TESTING PROTOCOL FOR THE DEMILITARIZATION
SYSTEM AT THE EGLIN AFB HERD FACILITY

Richard O. Mines, Jr., Ph.D., P.E.
Assistant Professor
Department of Civil & Environmental Engineering

University of South Florida
4202 East Fowler Avenue, ENG 118
Tampa, FL 33620

Final Report for:
Summer Faculty Research Program
Wright Laboratory

Sponsored by:
Air Force Office of Scientific Research
Bolling Air Force Base, DC

and

Wright Laboratory

August 1997

TESTING PROTOCOL FOR THE DEMILITARIZATION SYSTEM AT THE EGLIN AFB HERD FACILITY

Richard O. Mines, Jr., Ph.D., P.E.
Assistant Professor
Department of Civil & Environmental Engineering
University of South Florida

Abstract

A sampling and testing protocol was developed for evaluating the three-stage wastewater filtration system and slurry feed injection system to the molten salt destruction unit at the High Explosive Research and Development (HERD) demilitarization facility at Eglin Air Force Base in Florida. Both systems are to be evaluated for their effectiveness in treating the wastewater and high explosive solids. The wastewater or "pink water" generated from washing out warheads will be treated by a three-stage filtration system consisting of sand filters, a fabric filter, and activated carbon filters so that it can be reused in the high-pressure water washout system. The slurry containing high explosive material will be oxidized to carbon dioxide, nitrogen and water vapor using the molten salt destruction process (MSD). Grab samples will be collected on the influent and effluent wastewater streams to the sand filters, fabric filter, and activated carbon filters. It is anticipated that approximately 99 percent of both the influent suspended solids and organic material as measured by chemical oxygen demand (COD) will be removed by the three-stage filtration system. Various air flow rates, slurry injection rates, and slurry compositions will be evaluated using the feed system test apparatus (FSTA) so that optimum rates can be determined to prevent plugging of the slurry feed injection tube to the molten salt destruction process. The molten salt destruction process is expected to achieve greater than 99.9 percent oxidation of the organic components in the slurry to carbon dioxide and water.

TESTING PROTOCOL FOR THE DEMILITARIZATION SYSTEM AT THE EGLIN AFB HERD FACILITY

Richard O. Mines, Jr.

Introduction

Since the end of the cold war, there has been an increased interest in the reuse and destruction of obsolete munition and propulsion systems. Smaller defense budgets necessitate that excess munitions stockpiles be eliminated by demilitarizing operations and open detonation. With the increase in environmental awareness, regulatory agencies have placed more stringent requirements on the discharge of air and water pollutants. In particular, permits for open burning /open detonation (OB/OD) and incinerators have become more difficult to obtain. Wastewater that is generated during demilitarization (demil) operations must be properly treated before discharging to a municipal sewer system or to a surface water. All wastewater treatment facilities that discharge into surface waters are required to have a National Pollution Discharge Elimination System (NPDES) permit. Wastewater facilities that discharge to surface waters in the Tampa Bay, Florida area must meet effluent limits of approximately 5 mg/L biochemical oxygen demand (BOD), 5 mg/L suspended solids (SS), 3 mg/L total nitrogen (TN), and 1 mg/L total phosphorus (TP), respectively. To meet such low limits, advanced wastewater treatment (AWT) processes are required (Mines {1}). Innovative and cost efficient processes must be used for reducing and destroying the wastes associated with demilitarization operations and treating the wastewater generated at these facilities.

Numerous studies have been conducted on the use of high-pressure water washout systems for cutting and removing explosive materials from warheads (Giltner, Meschberger, and Worsey {2}, Giltner, Sitton, and Worsey {3}, Summers, Worsey, Blaine, Fossey, Burch, and Johnson {4}, Fossey,

Rankin, Klosterman, and Craig {5}, and Craig, Short, Summers, and Worsey {6} Other investigators have focused their research efforts on the destruction of explosives and hazardous wastes using molten salt technology (Upadhye, Brummond, and Pruneda {7}, Bechtel {8}, and Consaga and Heslop {9}). Research conducted at Lawrence Livermore National Laboratories (LLNL) has been performed at both bench-scale and pilot-scale levels on slurries containing high explosives (Upadhye, Brummond, and Pruneda {10}). The molten salt destruction process at the Naval Surface Warfare Center Indian Head, Maryland (NSWC - IH) is a pilot-scale unit to which explosive solids are fed to the process rather than using a slurry (Consaga {9}).

This report describes the sampling and testing protocol that was developed for evaluating the effectiveness of the demilitarization system at the High Explosive Research and Development (HERD) demilitarization facility at Eglin Air Force Base, Florida. The next section discusses the demilitarization process that is being installed at Eglin.

Discussion of Problem

The Armament Directorate of Wright Laboratory at Eglin Air Force Base, Florida is in the process of installing a pilot-scale high-pressure water washout system followed by a molten salt destruction process (MSD) for treating high explosives produced at the High Explosive Research and Development (HERD) facility. The HERD facility at Eglin generates an average of approximately 300 pounds of explosive waste per month. Explosive wastes, contaminated hardware, and personal protective equipment are currently disposed of on Eglin ranges using OB/OD. Waste streams consisting of water and explosive cuttings from machining operations are treated by gravity settling basins prior to discharge to the bases' wastewater treatment facility.

A demilitarization facility has been constructed for washing out the explosive materials from various warhead sizes. This is accomplished with a high-pressure water washout system (14.5 gallon per minute at 15,000 pounds per square inch) followed by high-pressure water maceration to achieve a reduction in particle size. The macerator reduces explosive materials to a particle size range of 0.140 millimeter (149 micron) to 3.17-mm (3170 micron) in diameter. The wastewater or “pinkwater” that is generated contains suspended explosive particles less than 149 micron in diameter, soluble organics, halides (ammonium perchlorate for example) and metals such as aluminum or tungsten. The wastewater is physically treated by passing through a three-stage filtration system consisting of sand filters, a fabric filter, and activated carbon filters. The reclaimed water is sent to a storage tank prior to being reused in the high-pressure washout system. The warhead casing can be reused, retained for study or sold for scrap metal.

The high-pressure water washout system is used as a tool for cutting and removing explosive material from warheads. After maceration, the explosive solids fall through a chute into the slurry surge tank where make-up water is added to achieve a slurry concentration of approximately 30 percent high explosive by mass. A diaphragm pump is used for pumping the slurry from the slurry surge tank to the slurry holding tank. The slurry is pumped by a diaphragm pump to the molten salt destruction process (MSD). The Molten Salt Destruction Process was originally developed by Rockwell International as a single-stage coal gasification process. Lawrence Livermore National Laboratory (LLNL) has developed a pilot-scale unit for treating approximately 5 kilograms per hour of high explosive wastes using MSD (Upadhye, Brummond, and Pruneda {10}). The waste is injected into the reactor along with air which acts as the carrier gas and provides air for oxidation. The reactor contains molten salt which may consist of a single salt or a low melting eutectic mixture of salts such as sodium carbonate, potassium carbonate, and/or lithium carbonate. The temperature of the reactor is normally maintained between 400 to 1000 °

C. The combustible organic components in the waste react with the oxygen to produce carbon dioxide, nitrogen, and steam. The inorganic components, in the form of ash, are captured in the molten salt bed as a result of wetting and dissolution of the ash (Upadhye, Brummond, and Pruneda {7}). During the pyrolysis and combustion of halogenated hydrocarbons, acidic gases are produced that are neutralized by the alkaline carbonates. If required, off-gases from the process may be cleaned with fabric and HEPA filters prior to discharge. At the end of the process runs, the salt is separated into carbonates, non-carbonate salts, and ash. The carbonates are recycled back to the process and the stable salts and ash are disposed of appropriately. Explosive wastes containing, 2,4,6-trinitrotoluene (TNT), 1,3,5-trinitro-1,3,5-triazocyclohexane (RDX), and 1,3,5,7-tetranitro-1,3,5,7-tetraazocyclooctane (HMX) have been successfully treated using the MSD (Jeffers and Corley {10}).

Objectives

The major objectives to be accomplished in this study are as follows:

1. Characterize the wastewater following maceration, sand filtration, fabric filtration, and carbon filtration.
2. Characterize the slurry containing high explosives that is fed to the molten salt destruction process.
3. Determine the efficiency of the three-stage filtration system for removing suspended solids and soluble organics as measured by the chemical oxygen demand (COD).
4. Determine the quantity of water that can be processed by the sand filters prior to initiating a backwash and the time interval between backwashings.

5. Determine the appropriate slurry feed rate, percent solids in slurry, and air flow rate that can be applied to the molten salt destruction process without plugging up the feed injection tube.
6. Develop system operating data on the molten salt destruction process: slurry feed rate, percent solids in the slurry, composition and purity of salt bed, and concentration and composition of off-gases from the molten salt destruction process for the four types of high explosives.

Methodology

The proposed research will be carried out at the HERD facility's Demil Building (1233). A three phased approach will be used in performing the proposed research. Phase I of the study will involve the evaluation of the three-stage filtration system for treating the wastewater generated from the high-pressure water warhead washout system. Phase II of this study will utilize the feed system test apparatus (FSTA) for assessing appropriate slurry feed rates and air flow rates that will be applied to the molten salt destruction process using a high explosive simulant. Phase III will focus on the collection of system operating data with regard to slurry feed rates and air flow rates, percent solids in the slurry, and concentration and composition of off-gases from the molten salt destruction process for the four types of high explosives evaluated.

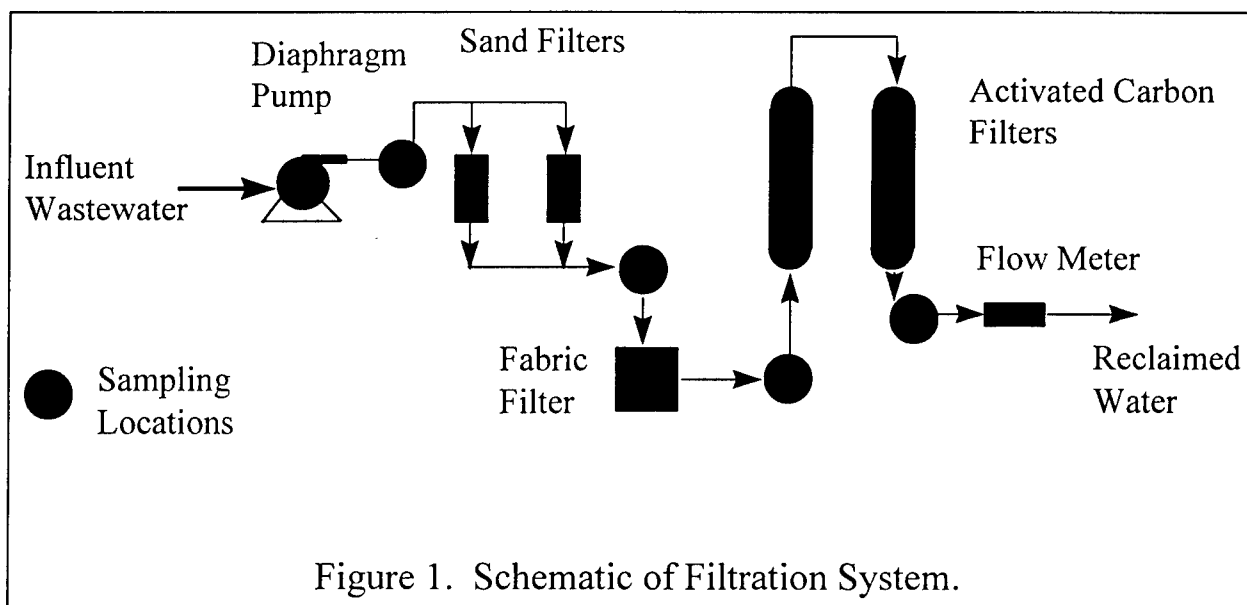
Wastewater Treatment

To determine the effectiveness of the three-stage wastewater filtration system, a sampling and testing program will be conducted. Phase I-A will involve tests performed on a high explosive simulant whereas, Phase I-B will utilize four different types of high explosives as discussed below. Phase I-A of the testing will be performed on a high explosive simulant to collect preliminary data with regard to the anticipated time interval between backwashings and the volume of water that can be treated between backwashings.

Percent suspended solids removal through the sand filters, fabric filter, and through the carbon filters will be determined. A particle size distribution of the wastewater entering and exiting the sand, fabric, and carbon filters will be performed. Phase I-B will be similar to Phase I-A, however, four types of explosive materials (TNT, RDX, HMX, and tritonal or Tung-5) will be evaluated and more emphasis will be placed on the chemical characteristics of the wastewater throughout the three-stage filtration process. A warhead casing containing a high explosive simulant will be used in Phase I-A, and four warhead casings with the different types of explosive materials will be used in Phase I-B. During the Phase I-A testing, grab samples of approximately 1.0 liter will be manually collected in glass bottles or polytetrafluoroethylene (TFE) containers and analyses performed as soon as possible after collection. Samples shall be preserved in accordance with Section 1060 C of Standard Methods {12} and the maximum sample holding times as presented in Table 1060 of Standard Methods {12} should be followed. Samples collected during Phase I-A may be collected while the macerator is in operation. During Phase I-B, samples must be collected after the macerator has been turned-off, since personnel are not allowed in the Demil Building when high explosive wastes are being processed. Alternatively, automatic samplers may be installed to collect the samples during actual processing of the "pink water". This would provide more representative samples, however, this approach may not be cost-effective.

Influent and effluent grab samples to the sand filters, fabric filter, and activated carbon filters will be collected during each run. A minimum of two runs will be made for each type of explosive and simulant tested. Figure 1 is a schematic showing the proposed sampling locations. Wastewater flowrate will be measured by a Venturi flowmeter and the time between backwashings the filters will be monitored. The volume of water filtered prior to backwashing will also be determined based on the flow measurement readings. The analytical procedures will be in accordance with Standard Methods {12}. The specific method to be used from Standard Methods {12} is listed in parentheses following the specific parameter

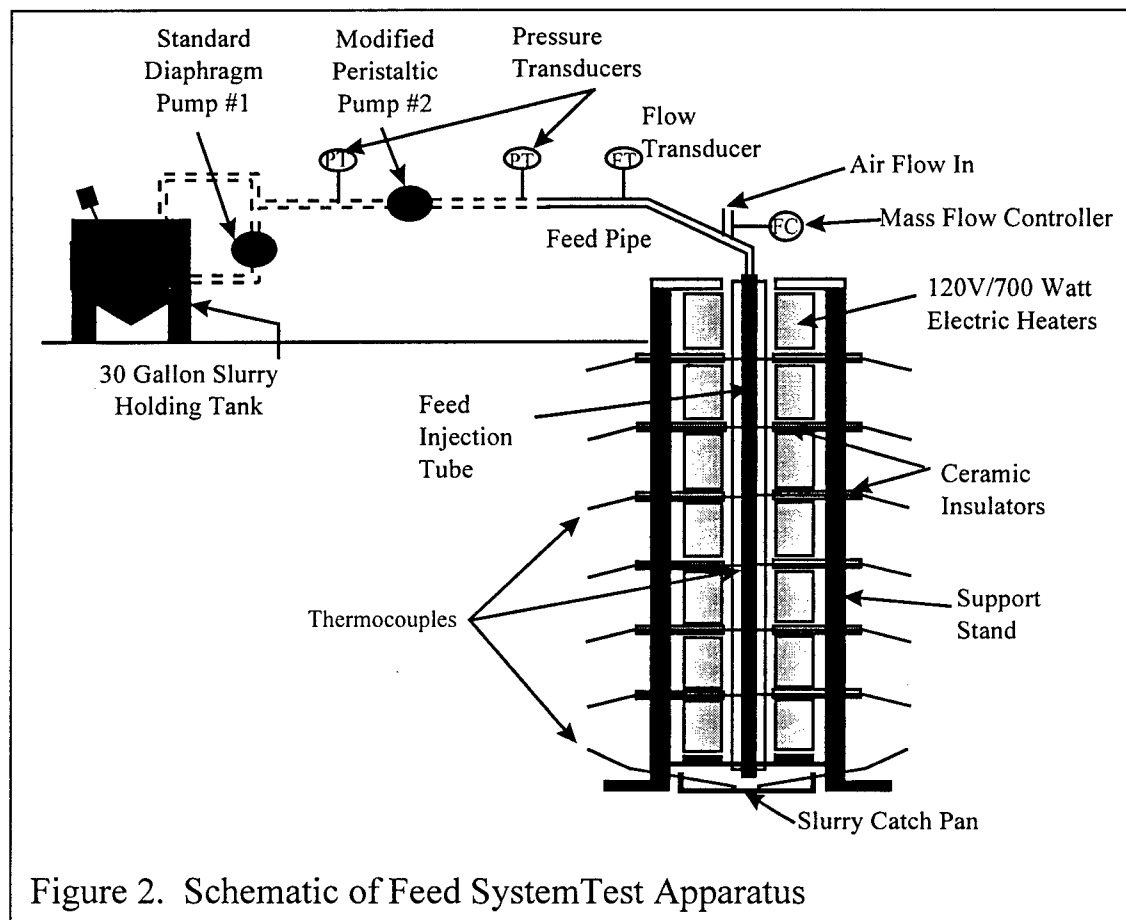
to be measured. Analytical tests to be performed on the samples include: total solids (2540 B), suspended solids, (2540 D), and dissolved solids (2540 C); temperature (2550 B), pH (4500 - H^+ B), total alkalinity (2320 B), chemical oxygen demand (COD) (5220 B or 5220 C), total Kjeldahl nitrogen (TKN) (4500 - N_{org} C), and ammonia (NH_3) (4500 - NH_3 F). In Phase I-A, only the solids analyses will be performed on the wastewater samples. During Phase I-B, the complete set of analyses will be performed on the wastewater samples collected. The particle size distribution of the wastewater entering and exiting the sand filters, fabric filters, and carbon filters will be determined for each simulant and high explosive evaluated. Particle size and distribution will be measured by a Coulter particle counter.



MSD Feed System Test Apparatus

The molten salt destruction process was originally developed by Rockwell International. Lawrence Livermore National Laboratory has developed bench-scale and pilot-scale units for destroying high explosive wastes. Their bench-scale unit was capable of handling 1 to 1.5 kilograms per hour of high explosive material (Upadhye, Brummond, and Pruneda {10}) whereas the pilot-scale unit could process 5.0 kg per hour. Problems with their pilot-scale unit's feed injection system led to the plugging of the feed injection tube leading to a non-energetic steam explosion and the release of molten salt from the

reactor (AI Committee {13}). To overcome these problems, a feed system test apparatus (FSTA) is to be constructed to investigate various high explosive injection feed rates and air flow rates that can be utilized in the pilot-scale molten salt destruction process that will be installed in the Demil Building (1233) at the HERD facility. Figure 2 is a schematic of the FSTA.



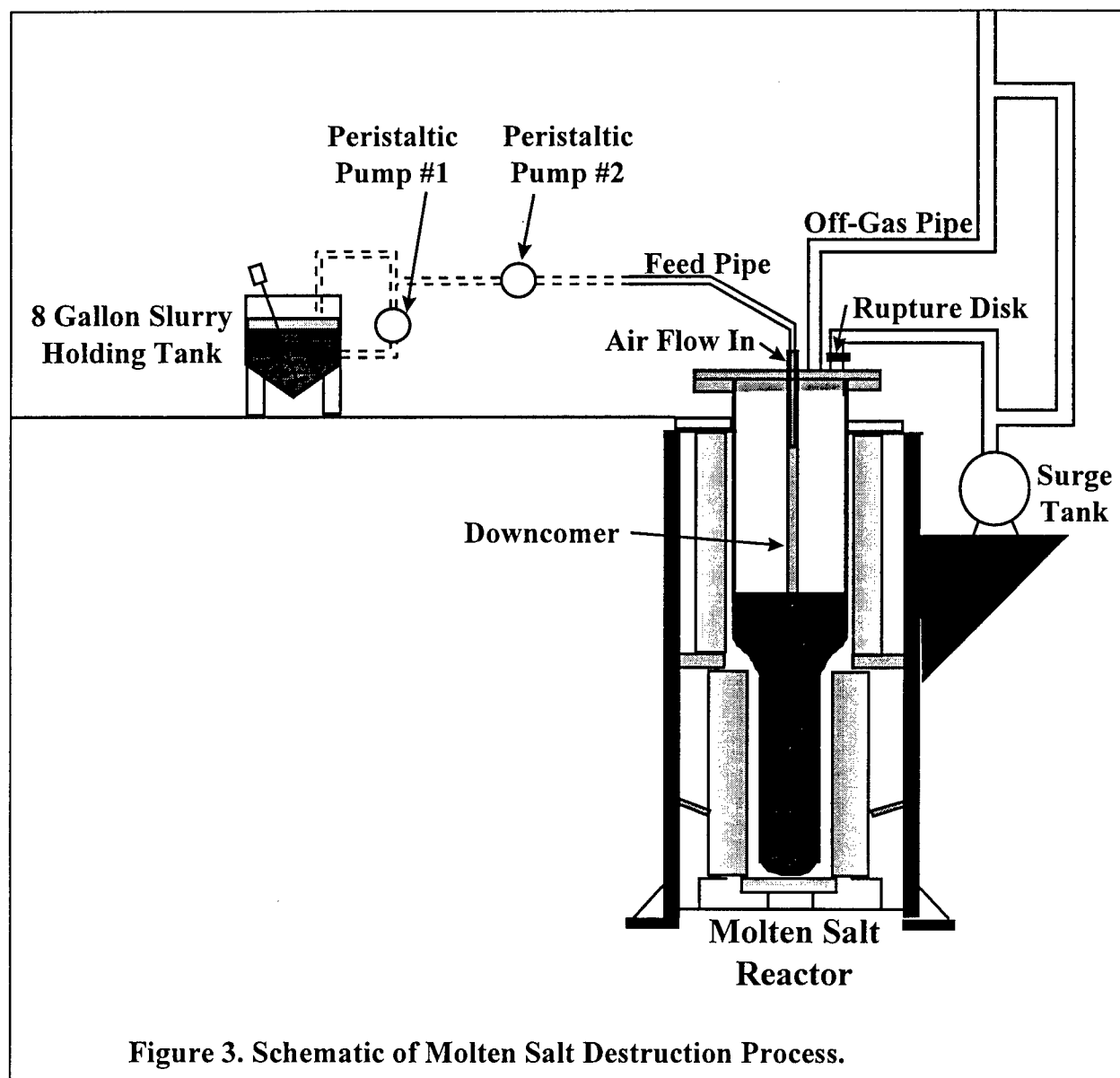
The characterization and testing protocol to be followed for the feed system test apparatus is described below. Phase II will involve feeding a high explosive simulant through the feed system test apparatus. The temperature of the reactor will be monitored in the feed injection tube from top to bottom by thermocouples (approximately at 6 locations). The slurry feed rate and discharge pressure from the peristaltic pump will be measured by a flow transducer and pressure transducer, respectively. The percent solids concentration and particle size distribution of the slurry fed to the molten salt destruction process will be measured. Percent solids will be measured by drying approximately 25 to 50 grams of

slurry at 103 to 105 °C (2540 G, Standard Methods {12}). Particle size and distribution will be accomplished by running an aqueous sample through the Coulter particle counter. The air mass flow rate is to be measured by a flow transducer. Major parameters that will be examined include: temperature of the slurry at the bottom of the feed injection tube, influent feed pressure, percent solids concentration of slurry feed, slurry feed rate, and air flow mass rate.

Molten Salt Destruction Process

Phase III will focus on developing operational parameters for the molten salt destruction process. Figure 3 is a schematic of the molten salt destruction process. Four types of explosives, TNT, RDX, HMX, and tritonal or Tung-5 will be evaluated. The following parameters were identified as those that have the most significant impact on the design and operation of the molten salt destruction process. Major parameters that will be examined include: temperature of the reactor, influent feed pressure, percent solids concentration of slurry feed, slurry feed rate, air flow rate, off-gas composition and concentration, and composition of salt bed. These parameters will be evaluated during Phase III of this research program so that the appropriate ranges can be established for proper destruction of the explosives. Analyses will be performed in accordance to the procedures outlined in Standard Methods {12} or EPA approved methods. A gas chromatograph/mass spectrometer (GC/MS) will be used for identifying the various components in the off-gas. It may be necessary to use Fourier transform infrared spectroscopy (FTIR) to determine the concentration of nitrogen dioxide (NO₂) in the off-gas. High performance liquid chromatography (HPLC) will be used for identifying the specific components (i.e. TNT, HMX, RDX) in the slurry feed and in the salt bed. Section 6010 B Standard Methods {12} discusses sample collection and preservation of samples whereas, Section 6010 C describes the analytical methods that can be used for the HPLC analyses. An ion chromatograph will be used for determining the concentration of

metal ions (sodium, potassium, lithium, etc.) in the salt bed. The composition and concentration of the off-gases, and the organics and inorganics in the salt bed will be measured for each run.



Testing Schedule

The wastewater sampling and testing program is expected to begin in early August and be completed at the end of September. It is anticipated that it will take approximately four months to complete Phase I

and Phase II of this project. A minimum of two runs will be made for each type of explosive or simulant tested during Phase I and II. Phase III is expected to take approximately six months to complete.

Conclusions

A sampling and testing program was developed for evaluating the HERD's Demil facility at Eglin AFB in Florida. Phase I of the program focused on evaluating the three-stage filtration system for treating the wastewater or "pink water" generated during demiling operations. Warheads containing high explosive simulant and high explosive material will be evaluated during this phase. Grab samples will be collected on the influent and effluent to the sand filters, fabric filter, and activated carbon filters. A minimum of two runs will be made for each type of explosive or simulant tested. It is anticipated that one simulant and four types of high explosives consisting of TNT, RDX, HMX, and tritonal or Tung-5 will be evaluated.

Phase II of the program will involve an evaluation of the feed system test apparatus (FSTA) using a high explosive simulant to determine appropriate air flow rates and slurry feed rates that can be safely applied to the molten salt destruction process. It is anticipated that a minimum of two runs will be made for each set of parameters evaluated.

Phase III will focus on developing operating parameters for the actual molten salt destruction process. Major parameters that will be examined include: temperature of the reactor, influent feed pressure, percent solids concentration of slurry feed, slurry feed rate, air flow rate, off-gas composition and concentration, and composition of salt bed. Four types of high explosives consisting of TNT, RDX, HMX, and tritonal or Tung-5 will be evaluated during Phase III.

It will take approximately four months to complete Phase I and II, and six additional months to complete Phase III.

References

1. Mines, R. O. Assessment of AWT Systems in the Tampa Bay Area. *J. Environ. Eng. (NY)* 1996; 122(7): 605-611.
2. Giltner, S. G., Meschberger, J. and Worsey, P. N., "Overview of the Demilitarization Program for Class 1.1 Warheads and Rocket Motors Using High Pressure Waterjets at the University of Missouri-Rolla".
3. Giltner, S. G., Sitton, O. C., and Worsey, P. N., The Reaction of Class 1.1 Propellants and Explosive to Water Jet Impact.
4. Summers, D. A. , Worsey, P. N., Blaine, J. G., Fossey, R. D, Burch, D., and Johnson, M., "Waterjet Cutting Parameterization Test for the Programmed Extraction of Explosive and Propellant from Military Casings", p 487-492.
5. Fossey, R. D., Rankin, J., Klosterman, J., and Craig, L. E., "Propellant Sensitivity to Waterjet Impact: Preliminary Research on the Feasibility of Downloading Propellant from Rocker Motors via Waterjet", Naval Weapons Support Center, Crane Indiana, NWSC/CR/RDTR-511, March 1990, p 1-32
6. Craig, L. E., Short, J. E., Summers, D. A., and Worsey, P. N., "Evaluation of Washout Procedures for Missile Casings", Naval Weapons Support Center, Crane, Indiana, NWSC/CR/RDTR-291, July 1986, p 1-64.

7. Upadhye, R. S., Brummond, W. A., and Pruneda, C. O. , “Destruction of High Explosives and Wastes Containing High Explosives using the Molten Salt Destruction Process”. *Proc. 23rd International Annual Conf. Of ICT: Waste Management of Energetic Materials and Polymers, June 30 - July 3, 1992., Karlsruhe, Germany, May 1992.*
8. Bechtel, “Review and Evaluation of Alternative Technologies for Demilitarizing High Explosives”, prepared for Lawrence Livermore National Laboratory, Livermore, CA 9450, June 1994.
9. Consaga, J. P. and Heslop, J. M. , “NSWC/IHD MSO Process”, 4th Global Demil Symposium, May 13-17, 1996, John Ascuaga’s Nugget, Sparks, NV, pp 870- 883.
10. Upadhye, S. Watkins, B. E., and Pruneda, C. O., “Recent Advances in the Molten Salt Technology for the Destruction of Energetic Materials”, 27th International Annual Conference of ICT, June 25- 28, 1996, Karlsruhe, Federal Republic of Germany, pp 110-1 to 110-13.
11. Jeffers, S. R. and Corley, J. C., “Memo: Molten Salt Destruction Experiments Lawrence Livermore National Laboratory, Livermore, California”, Wright Laboratory, HERD Facility, Eglin AFB, FL, January 1995.
12. Standard Methods for the Examination of Water and Wastewater, 19th Edition, American Public Health Association, Washington, DC (1992).
13. IA Committee, “Incident Analysis Report Incident No. 0477”, Lawrence Livermore National Laboratory, UCRL-AR-12658, March 1997.

**A USEFUL BENCHMARKING METHOD IN COMPUTATIONAL
MECHANICS, CFD. AND HEAT TRANSFER**

**V. Dakshina Murty
Professor
Department of Mechanical Engineering**

**University of Portland
5000 N. Willamette Blvd.
Portland, OR 97203**

**Final Report for:
Summer Research Program
Wright Laboratory**

**Sponsored by:
Air Force Office of Scientific Research
Bolling Air Force Base, Washington, DC**

And

Wright Laboratory

September 1997

A USEFUL BENCHMARKING METHOD IN COMPUTATIONAL MECHANICS, CFD, AND HEAT TRANSFER

V. Dakshina Murty
Professor
School of Engineering
University of Portland

Abstract

A procedure for efficient benchmarking of computer solutions in the fields of computational mechanics including computational fluid mechanics, heat transfer, and k- ϵ turbulence models is presented. It consists of using assumed solutions to calculate the required source terms and use the resulting source terms as inputs to back calculate the displacements, velocities, temperature, etc. The procedure works for nonlinear problems also. Examples are provided from elasticity, Navier-Stokes equations, nonlinear heat conduction, convective heat transfer, and k- ϵ turbulence modeling.

A USEFUL BENCHMARKING METHOD IN COMPUTATIONAL MECHANICS, CFD, AND HEAT TRANSFER

V. Dakshina Murty

Introduction

The field of computational mechanics (including computational fluid dynamics, heat transfer) has matured in the past several years. This is evident from the amount of software in the form of commercial codes available for solving every conceivable problem in mechanics. Yet one of the questions that appears to remain unanswered or perhaps even unaddressed is efficient benchmarking of these codes. One procedure is to compare the numerical solutions against experimental data available in the literature. This procedure though convenient, leaves a lot to be desired. For one thing, the computer solutions do not simulate the physical problem directly. Rather, they solve the governing equations, which are often partial differential equations. In this note, we will present an efficient procedure for benchmarking computational solutions. In the rest of the paper, the philosophy behind numerical solutions will be presented followed by detailed exact solutions of two dimensional elasticity, Navier-Stokes equations, nonlinear heat transfer, and $k-\epsilon$ turbulence models.

Many physical laws encountered in applied mechanics/heat transfer can be modeled in the form of differential equations, either ordinary or partial. These equations are often nonlinear and coupled, and as such are difficult to solve exactly. Hence one has to resort to numerical methods. The situation surrounding the physical problem and the resulting mathematical models along with their verification mechanisms is shown in Fig. 1.

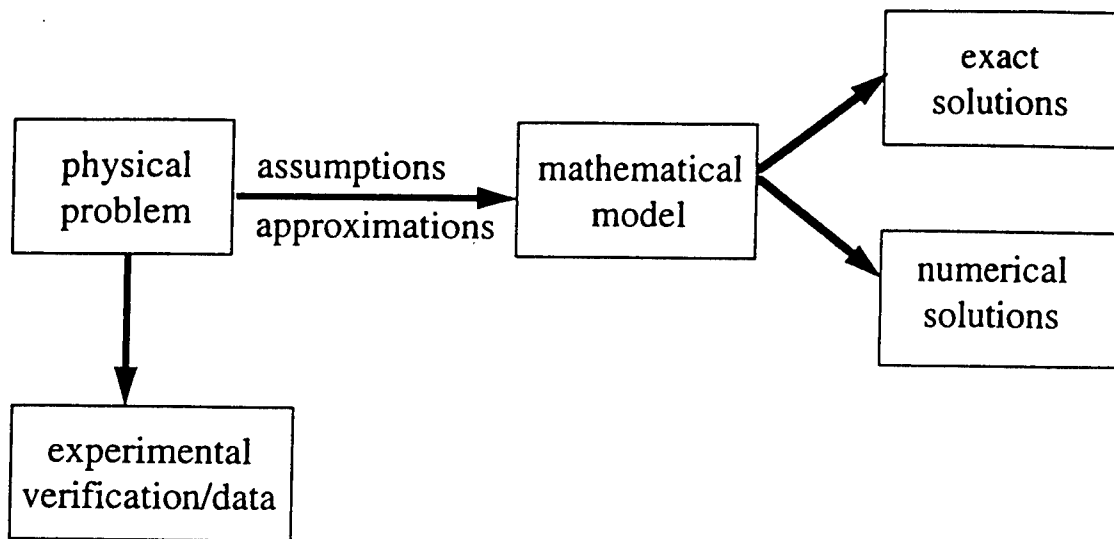


Fig. 1: Steps leading to numerical solutions of boundary value problems in engineering.

The starting point is the physics of the problem. This could be the determination of stresses in a composite plate, temperature distribution around a space module, or flow and turbulence variables in reacting diffusion flames. The physical model is converted into a mathematical model through suitable assumptions. The mathematical model often consists of coupled nonlinear partial differential equations which are difficult to solve analytically. Hence numerical methods, be they finite element, finite difference, finite volume, have to be used. The numerical algorithms which are developed based on these methods need to be tested as to their accuracy, stability, and convergence behaviour. Very often, these numerical solutions are tested against experimental data since exact solutions are not always available except for simple linearized problems. We strongly believe that this procedure of comparing numerical solutions with experiments is at best inadequate and leads to a misleading sense of accuracy of the numerical algorithms. The reasons are as follows: first of all, as shown in the Fig. 1, the computer model is solving (often approximating) the mathematical model and not the physics of the problem. In fact, even to obtain the mathematical model, several assumptions need to be made. Thus the best computer solution (if one such could be found) is merely as good as the mathematical model. Secondly, not all the physical variables that are simulated by the computer are easily measurable. For example, the displacement field on the interior of a solid (in solid mechanics), flow and temperature fields (in high temperature reacting flows), and k and ε in the entire flow (for turbulence modeling) are difficult to measure accurately. Thirdly, most of the comparisons made between the experimental measurements and computer results are for the

secondary variables (stresses, heat transfer rates, etc.) and not for the primary variables (like displacements, velocities, temperatures, etc.). Finally, the true test of the robustness of an algorithm or a code is how well the numerical solutions compare with exact solutions. After all, the commercial codes are black boxes for the end users. Hence, it is of paramount importance that the engineer who is often such an end user, knows not only the strengths but also the limitations of the algorithms. Even if the code is unable to produce the exact solution for a test problem, this inability in itself would be very useful information, since it tells the limits of applicability of the algorithm. For the above reasons we believe that it is of utmost importance that any numerical algorithm should be tested against exact solutions and not experiments. If exact solutions are not available in the literature, then they should be constructed (which is usually possible for several nonlinear problems also) and used as test cases. In the remainder of the paper, we will demonstrate a procedure by which exact solutions can be constructed, as long as the governing equations are derived from some kind of a conservation principle. This condition is met in most applications in mechanics/heat transfer.

Linear Elasticity

Let us start with boundary value problems in linear elasticity. A typical problem consists of a continuum which is subjected to a set of body forces and surface tractions and/or displacements, as shown in Fig. 2a.

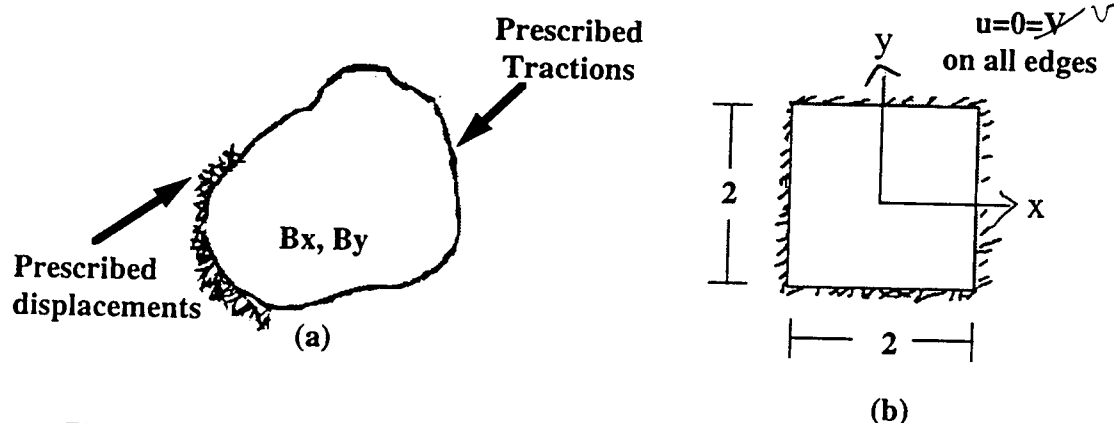


Fig. 2: a) Boundary value problem in solid mechanics and b) example problem in elasticity.

The problem consists of finding a displacement field (from which strains and stresses can be obtained later) which takes on the prescribed values of

displacements and stresses on the boundary, when the body is subjected to the given body forces and surface tractions. For simplicity, we will concentrate on two dimensional plane elasticity, in particular plane strain. The governing equations are then the equilibrium equations (derived from the conservation of momentum principle), strain displacement relations, and stress strain relations. For a plane strain problem, they can be written as [1]:

$$\frac{\partial \sigma_{xx}}{\partial x} + \frac{\partial \tau_{xy}}{\partial y} + B_x = 0 \quad (1)$$

$$\frac{\partial \tau_{xy}}{\partial x} + \frac{\partial \sigma_{yy}}{\partial y} + B_y = 0 \quad (2)$$

$$\epsilon_{xx} = \frac{\partial u}{\partial x}; \quad \epsilon_{yy} = \frac{\partial v}{\partial y}; \quad \gamma_{xy} = \frac{\partial u}{\partial y} + \frac{\partial v}{\partial x} \quad (3)$$

$$\epsilon_{zz} = \gamma_{xz} = \gamma_{yz} = 0 \quad (3a)$$

$$\sigma_{xx} = (2G + \lambda) \epsilon_{xx} + \lambda \epsilon_{yy} \quad (4)$$

$$\sigma_{yy} = (2G + \lambda) \epsilon_{yy} + \lambda \epsilon_{xx} \quad (5)$$

$$\sigma_{zz} = -\nu(\sigma_{xx} + \sigma_{yy}) \quad (6)$$

$$\gamma_{xy} = \tau_{xy}/G \quad (7)$$

The exact solution for the above set of equations can be constructed as follows. First, assume any displacement field on the interior of the solid. From the displacement field, the strains and the corresponding stresses can be calculated. These stresses when substituted into the equilibrium equations, Eqs. (1), (2), result in a set of body forces B_x and B_y . Now if the solid is subjected to the prescribed body forces and displacements and tractions on the surface (the values taken by the assumed fields), and the equations solved, the solutions obtained should precisely be the assumed displacements. To illustrate the ideas, let us consider the plate shown in Fig. 2b. The assumed displacement fields and the resulting body forces are given below:

$$u = (1-x^2)^2(1-y^2); \quad v = (1-y^2)^2(1-x^2); \quad w = 0 \quad (8)$$

$$B_x = 4(2G + \lambda)(1-3x^2)(1-y^2) - 8\lambda xy(1-y^2) + 2G(1-x^2)^2 - 8Gxy(1-x^2) \quad (9a)$$

$$B_y = 4(2G + \lambda)(1-3y^2)(1-x^2) - 8\lambda xy(1-x^2) + 2G(1-y^2)^2 - 8Gxy(1-y^2) \quad (9b)$$

$$B_z = 0 \quad (9c)$$

Thus the plate if it is subjected to the boundary conditions of vanishing u and v along the edges and $w = 0$ everywhere, along with the body force field described above, we would get the displacement field as given in Eq. (8). The stresses and strains can be calculated from the displacement field. Notice, that the body force field as shown in Eq. (9) cannot be simulated in a laboratory. However, this is of little consequence for the computer solution which is after all simulating the mathematical model and not the physics of the problem *directly*.

Navier Stokes Equations

Now we consider the exact solutions for Navier-Stokes equations. For steady, laminar, incompressible flow of a Newtonian fluid in two dimensions the equations are the conservation of mass and linear momentum in x and y directions. They can be written as follows [2]:

$$\frac{\partial u}{\partial x} + \frac{\partial v}{\partial y} = 0 \quad (10)$$

$$\rho(u \frac{\partial u}{\partial x} + v \frac{\partial u}{\partial y}) = -\frac{\partial p}{\partial x} + \mu \nabla^2 u + B_x \quad (11)$$

$$\rho(u \frac{\partial v}{\partial x} + v \frac{\partial v}{\partial y}) = -\frac{\partial p}{\partial y} + \mu \nabla^2 v + B_y \quad (12)$$

The above set of equations is nonlinear and coupled. Thus, it is difficult to obtain exact solutions for arbitrary geometries and flow situations. However, as in the case of boundary value problems in solid mechanics, the exact solutions can be constructed by first assuming a velocity field which satisfies conservation of mass and using this in conjunction with an assumed pressure field to obtain the required body forces to satisfy the momentum equations. The resulting body forces and surface tractions would then be the inputs into the Navier-Stokes equations, which when solved should give the assumed velocity and pressure fields in the interior of the fluid. The boundary value problem is shown in Fig. 3. The corresponding exact solution along with the body force terms is given in the following equations.

$$u = x(1-x); \quad v = -(1-2x)y; \quad p = 1-y \quad (13)$$

$$B_x = 2 + x(1-x)(1-2x) \quad (14a)$$

$$B_y = -2xy(1-x) + y(1-2x)^2 - 1 \quad (14b)$$

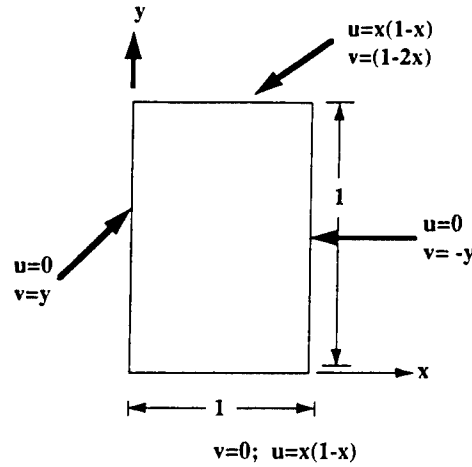


Fig. 3: Problem involving Navier-Stokes equations.

with $\mu = \rho = 1$. We again wish to point out that the problem presented in Eqs. (13), (14) makes little sense physically (*it is not even possible to visualize the corresponding boundary value problem*), but it certainly tests the robustness of the numerical solution.

Nonlinear Heat Conduction

Next we consider the unsteady heat conduction problem. The governing equation which is derived from conservation of energy is as follows:

$$\rho C \frac{\partial T}{\partial t} = \nabla \cdot (k \nabla T) + Q \quad (15)$$

Here we shall consider the nonlinear transient version of the problem. The physical problem is given in Fig. 3, which consists of a plate whose boundaries are maintained at all time at $T = 0$. The nonlinearity appears in the form of dependence of the thermal conductivity (k) on temperature. The exact solutions along with the source terms are given below. It can be seen that since the temperature is time dependent, the resulting source term is also time dependent. Thus, if the plate as shown in Fig. 4, is subjected to the volumetric heat source given and the boundaries are held at $T = 0$ for all time, with the given initial conditions and nonlinear thermal conductivity, the resulting temperature distribution would be as given by Eq. (16).

$$T(x,y,t) = e^{-t}(1-x^2)(1-y^2) \quad (16)$$

$$k = T + T^2 \quad (17a)$$

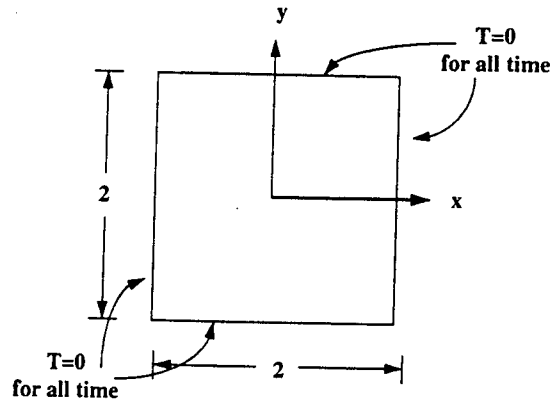


Fig. 4: Transient nonlinear heat conduction problem description with the Boundary conditions

$$T(x,y,0) = (1-x^2)(1-y^2) \quad (17b)$$

$$\begin{aligned} Q(x,y,t) = & -e^{-t}(1-x^2)(1-y^2) \\ & + 2e^{-2t}(1-x^2)(1-y^2)(2-x^2-x^2) + 2e^{-3t}(1-x^2)^2(1-y^2)^2(2-x^2-x^2) \\ & - 4x^2e^{-2t}(1-y^2)^2 - 8x^2e^{-3t}(1-x^2)(1-y^2)^3 \\ & - 4y^2e^{-2t}(1-x^2)^2 - 8y^2e^{-3t}(1-y^2)(1-x^2)^3 \end{aligned} \quad (18)$$

Convective Heat Transfer

The next example to be considered is forced convection heat transfer in two dimensions. The governing equations for incompressible flows of Newtonian fluids are the continuity equation, Navier-Stokes equations (Eqs. (10) - (12)), and the thermal energy balance equation which is given below [2]:

$$\rho C_p \left(\frac{\partial T}{\partial t} + u \frac{\partial T}{\partial x} + v \frac{\partial T}{\partial y} \right) = \nabla \cdot (k \nabla T) + S \quad (19)$$

Notice that we have removed the viscous dissipation term from the energy equation. However, it can be included into the formulation without modifying the procedure of constructing exact solutions. From Eqs. (10) - (12) and (19) it is clear that the coupling between the hydrodynamic equations and thermal energy balance is only one way, in that once the velocity field (and of course the pressure field) is known, the temperature equation can be solved, i.e., the velocity field determines the temperature field, but not vice versa. Here too, the

problem is nonlinear, since the thermal conductivity is dependent on temperature. The boundary value problem which again cannot be simulated in a laboratory is shown in Fig. 5. The exact solutions, along with the corresponding source term are given below:

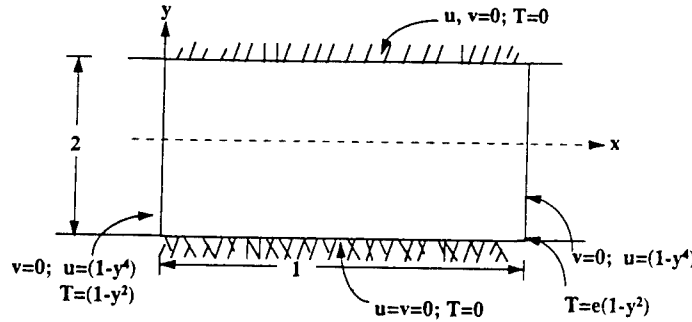


Fig. 5: Computational domain with boundary conditions for convective heat transfer

$$u = (1-y^4); \quad v = 0; \quad p = \text{constant} \quad (20)$$

$$B_x = 12y^2; \quad B_y = 0 \quad (21)$$

$$T = e^x(1-y^2) \quad (22)$$

with $\rho = C_p = 1$ and k , thermal conductivity being temperature dependent as $\kappa = T + T^2$.

Turbulence Modeling

As a final example, exact solutions to the a class of turbulent flows are considered. Turbulence modeling has been one area where extensive literature on CFD solutions is available. There are several areas of turbulence modeling like one and two equation models, direct numerical simulation, Reynolds stress models, large eddy simulations, etc. We will however, concentrate on the $k-\epsilon$ model, for among other things it has found extensive use not only in commercial software but also in academic research. The governing equations [3,4] are given below (the continuity equation, given by Eq. (10) is not repeated here).

$$\begin{aligned} \rho(u \frac{\partial u}{\partial x} + v \frac{\partial u}{\partial y}) = & -\frac{\partial p}{\partial x} + \frac{\partial}{\partial x}[(\mu_l + \mu_t) \frac{\partial u}{\partial x}] + \frac{\partial}{\partial y}[(\mu_l + \mu_t) \frac{\partial u}{\partial y}] \\ & + \frac{\partial}{\partial x}[(\mu_l + \mu_t) \frac{\partial u}{\partial x}] + \frac{\partial}{\partial y}[(\mu_l + \mu_t) \frac{\partial v}{\partial x}] + B_x \end{aligned} \quad (24)$$

$$\rho(u \frac{\partial v}{\partial x} + v \frac{\partial v}{\partial y}) = -\frac{\partial p}{\partial y} + \frac{\partial}{\partial x}[(\mu_l + \mu_t) \frac{\partial v}{\partial x}] + \frac{\partial}{\partial y}[(\mu_l + \mu_t) \frac{\partial v}{\partial y}] + \frac{\partial}{\partial x}[(\mu_l + \mu_t) \frac{\partial u}{\partial y}] + \frac{\partial}{\partial y}[(\mu_l + \mu_t) \frac{\partial v}{\partial y}] + B_y \quad (25)$$

$$\rho(u \frac{\partial k}{\partial x} + v \frac{\partial k}{\partial y}) = \frac{\partial}{\partial x}[(\mu_l + \frac{\mu_t}{\sigma_k}) \frac{\partial k}{\partial x}] + \frac{\partial}{\partial y}[(\mu_l + \frac{\mu_t}{\sigma_k}) \frac{\partial k}{\partial y}] + G - \rho \epsilon + S_k \quad (26)$$

$$\rho(u \frac{\partial \epsilon}{\partial x} + v \frac{\partial \epsilon}{\partial y}) = \frac{\partial}{\partial x}[(\mu_l + \frac{\mu_t}{\sigma_\epsilon}) \frac{\partial \epsilon}{\partial x}] + \frac{\partial}{\partial y}[(\mu_l + \frac{\mu_t}{\sigma_\epsilon}) \frac{\partial \epsilon}{\partial y}] + C_1 G \frac{\epsilon}{k} - C_2 \rho \frac{\epsilon^2}{k} + S_\epsilon \quad (27)$$

$$\mu_t = C_\mu \rho \frac{k^2}{\epsilon}$$

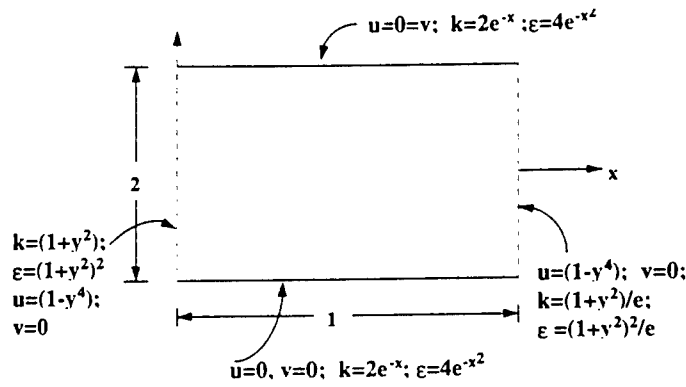
$$G = \mu_t \left[2 \left(\left(\frac{\partial u}{\partial x} \right)^2 + \left(\frac{\partial v}{\partial y} \right)^2 + \left(\frac{\partial u}{\partial y} + \frac{\partial v}{\partial x} \right)^2 \right) \right]$$

and C_1 , C_2 , C_μ are constants and σ_k and σ_ϵ are turbulent Prandtl/Schmidt numbers. S_k and S_ϵ are the source terms similar to body force terms in the momentum equations. For the sake of convenience the values of C_1 , C_2 , C_μ , σ_k and σ_ϵ are taken to be 1 and μ_l , the laminar viscosity is set equal to 0. The similarities between the momentum and energy balance equations and the k - ϵ equations (26), (27) are striking. All the terms can be classified into three broad categories, namely, convection, diffusion, and source terms. The difficulty in solving the k - ϵ equations is mainly due to the stiff nonlinearity of the source terms. This makes convergence of any numerical scheme not only difficult, but also unstable and heavily dependent on the boundary (or inlet) values of k and ϵ . This necessitates the adjustment of the numerical constants of the model or boundary/inlet values of the variables to get converged solutions, which appear reasonable. *It is due to this reason that we firmly believe that turbulent flow algorithms and/or codes should be tested against as many exact solutions as possible and the researchers not be content with comparing them with experimental data only. It should be pointed out that accurate matching between numerical and exact solutions is not a cure for all the difficulties associated with CFD turbulence modeling. However, it certainly provides a measure of confidence in later predictions made by the algorithm.* The numerical problem for the test case is described in Fig. 6 followed by the exact solutions along with the source terms.

$$u = (1-y^4); \quad v = 0; \quad p = \text{constant} \quad (28)$$

$$B_x = 12y^2; \quad B_y = 0 \quad (29)$$

$$k = e^{-x} (1+y^2) \quad 50-11 \quad (30)$$



$$\epsilon = e^{-x^2} (1 + y^2)^2 \quad (31)$$

$$S_k = -(1 - y^4)e^{-x}(1 + y^2) - e^{-x}(1 + y^2) - 2e^{-x} - 32y^6 + e^{-x^2}(1 + y^2)^2 \quad (32)$$

$$S_\epsilon = -2x(1 - y^4)e^{-x^2}(1 + y^2)^2 - 2e^{-x^2}(1 + y^2)^2(2x^2 - 1) - 32y^6e^{-x+x^2}(1 + y^2) - e^{-x^2}(12y^2 + 4) + e^{-2x^2+x}(1 + y^2)^3 \quad (33)$$

Conclusions

We have presented a technique for constructing exact solutions for several nonlinear boundary value problems in computational mechanics and heat transfer. It is shown that for those equations which are derived from conservation principles, exact solutions can be constructed. Such solutions, although not verifiable experimentally, provide valuable insights into the underlying numerical methods. The same procedure can be extended to other areas like compressible flows, forced vibrations of plates and shells, modeling of non-Newtonian fluids, and other areas of engineering.

References

1. Shames, I. H., Mechanics of Deformable Solids, Prentice-Hall, 1964.
2. Roshenow, W. M. and Hatrnett, J. P., Handbook of Heat Transfer, McGraw-Hill, 1973.
3. Vanka, S. P., Block-implicit Calculation of Steady Turbulent Recirculating Flows, International Journal of Heat and Mass Transfer, Vol. 28, No. 11, pp. 2093-2103.

4. Vanka, S. P., Calculation of Axisymmetric, Turbulent, Confined Diffusion Flames, AIAA Journal, Vol. 24, No. 3, pp. 462-469.

Associate did not participate in the program.

Associate did not participate in the program.

**IMPROVEMENT OF CACHE UTILIZATION AND PARALLEL EFFICIENCY
OF A TIME-DEPENDENT MAXWELL EQUATION SOLVER**

**Yi Pan
Associate Professor
Department of Computer Science**

**University of Dayton
300 College Park
Dayton, OH 45469**

**Final Report for:
Summer Research Program
Wright Laboratory**

**Sponsored by:
Air Force Office of Scientific Research
Bolling Air Force Base, Washington, DC**

And

Wright Laboratory

September 1997

Improvement of Cache Utilization and Parallel Efficiency of a Time-Dependent Maxwell Equation Solver

Yi Pan
Associate Professor
Department of Computer Science
The University of Dayton

Abstract

Performance improvement is achieved for a sequential Fortran time-dependent Maxwell equations solver through improved cache utilization and manual tuning of parallelization. This report describes the background of the project, the theory behind the improvement being achieved, the methodologies employed, and the experimental results obtained on the SGI Origin 2000.

Through loop fusion, loop interchange, loop index shift, and other loop transformations, we are able to enhance the cache locality in the program and to reduce the cache misses drastically. We also add several Power Fortran directives in the Fortran program to instruct the parallel compiler how to parallelize the code efficiently.

Experimental runs show that the execution time is reduced from 28 hours to about 3 hours on one Origin 2000 processor using loop transformations alone. The final version of our code runs efficiently on the Origin 2000 using up to 16 processors. In fact, our program uses less time than the corresponding MPI program when running on the SGI Origin 2000 using six processors, while the coding time involved is much shorter than the time used to develop the MPI code. Based on the experience learned during the summer, we believe that a high level parallel programming language such as the Power Fortran or High Performance Fortran is a viable and alternative way to parallelize many existing Maxwell equations solvers.

Improvement of Cache Utilization and Parallel Efficiency of a Time-Dependent Maxwell Equation Solver

Yi Pan

1 Introduction

A lot of efforts are directed towards the development of high performance portable electromagnetics codes for scalable architectures as part of the Department of Defense High Performance Computing Modernization Program's (DoD HPCMP) Common High Performance Software Support Initiative (CHSSI). The effort is part of the Computational Electromagnetics and Acoustics (CEA) Computational Technology Area (CTA) lead by Dr Joseph J.S. Shang at Wright Laboratory at the Wright-Patterson Air Force Base.

At present, high numerical efficiency of CEM simulation procedures can be attained either by algorithmic improvements to solve the Maxwell equations or by using scalable parallel distributed memory computer systems. Since the massive volume of data processing involved in solving the Maxwell equations, distributed memory computer systems are viable means to solve the memory shortage problem on workstations or vector computer systems. The other advantage is reduced time when parallel processing is employed to solve the Maxwell equations. Hence, parallelization of existing sequential Fortran code for solving Maxwell equations is an important effort towards developing efficient and accurate CEM code in analyzing refraction and diffraction phenomena for aircraft signature technology.

Currently, two versions of the solver are available. One is the sequential Fortran version developed by Dr Joseph J.S. Shang for vector machine such as the CRAY C90. The other is the MPI (Message Passing Interface) implemented by Dr. Marcus Wagner of IBM. Our main objective of this research is to investigate the possibility of improving the sequential code and parallelize it efficiently. The other objective is to seek possible improvement space for the MPI code.

In this research, we partially accomplish the objectives stated above. We improve the cache utilization of the sequential code and use the Power Fortran compiler directives to parallelize the sequential Fortran code. The optimization steps adopted in this research are:

1. Locate the "hot spot" of the sequential code via profiling tools;
2. Study these subroutines identified in step 1 carefully for performance improvement;
3. Improve the cache locality behavior of these subroutines through a series of systematic loop transformations;
4. Study the listing file produced by the PFA compiler and locate the overhead caused by inefficient parallel loops;
5. Insert Power Fortran compiler directives to direct the compiler to parallelize the parallel code so that most overhead is eliminated.

Notice that some of the goals may conflict each other. Hence, the above steps may be repeated several times to achieve an overall good performance. Although our effort is mainly to improve the sequential code, the lesson learned can also be applied to improve the MPI code.

This report is organized as follows. Methodologies used in this research is discussed in Section 2. Section 3 presents in details the loop transformations used to improve cache utilization and to reduce cache misses. Hand parallelization for the code is treated in section 4. We conclude with some suggested next steps to be taken toward achieving a more efficient and general parallel Maxwell equation solver.

2 Methodologies

When optimizing the performance of programs, the most gains will come from optimizing the regions of the program that require the most time - the repetitive regions of the program. These correspond either to iterative loops or recursive procedures. In the MAX3D program, the most time consuming regions are the loop which calls subroutines FXI, GETA, HZETA, and SUM. We used profiling tools on the SGI Origin 2000 and got it confirmed. Hence, we focused our efforts on those procedures which do the bulk of computation load.

A parallel program can not achieve high performance without making efficient use of each individual processor. To do so, the program must be able to efficiently access program data (i.e. make efficient use of cache memory). In fact, cache behavior continues to be the largest single factor affecting performance in both sequential and parallel computations. Origin 2000 provides cache-coherent, shared memory in the hardware. As shown in Table 1, Origin 2000 has two levels of cache memory. The difference between the speeds of cache memory and local memory is larger than 5 times. Hence, programs with good locality behavior will be executed much faster than programs without good locality behavior, even though they perform the same amount of computations. Memory is physically distributed across processors. Consequently, references to locations in the remote memory of another processor take substantially longer (by a factor of two or more) to complete than references to locations in local memory. In fact, the latency is even getting larger when more processors are used as seen from Table 1, because Origin 2000 adopts the Non-Uniform Memory Access (NUMA) model [12]. This can severely affect the performance of programs that suffer from a large number of cache misses. Therefore, reducing cache misses is crucial in improving a program's performance. On Origin 2000, the first level data cache contains only 32 kbytes. The secondary level cache size is 4 mbytes. Our focus is on the secondary cache in the hope that most data will be repeatedly used in the secondary cache before they are forced out of it.

Power Fortran Accelerator (PFA) is available on the SGI Origin 2000 and is a source-to-source optimizing Fortran preprocessor that discovers parallelism in Fortran code and converts those programs to parallel code. PFA is normally invoked as an option to f77, although it can be run separately. The PFA preprocessor allows you to apply the capabilities of a Silicon Graphics multiprocessor system to the execution of a single job. It splits the job into concurrently executing pieces, thereby decreasing the wall-clock run time of the job. Although the PFA preprocessor uses a lot of complicated analysis tools to analyze the user program and can produce a corresponding parallel version without user intervention, the quality of the parallel code produced in such a way is usually very poor. The compiler is simply not

Memory Level	Latency (ns)
L1 cache	5.1
L2 cache	56.4
Local Memory	310
4P Remote Memory	540
8P Avg Remote Memory	707
16P Avg. Remote Memory	726
32P Avg. Remote Memory	773

Table 1: Cache Latencies on Origin 2000

intelligent enough to make a smart decision. Hence, automatical parallelization has to be combined with hand tuning to produce more efficient code.

The best way to use the PFA preprocessor is to inform the compiler about the sequential program, such as data dependence, which loop to parallelize, which variables are local, which variables are shared by all processors, etc. By coding a few simple directives, the compiler uses the information provided by the user and makes smart decisions. Directives allow you to enable, disable, or modify a feature of the compiler in addition to, or instead of, command line options. In the following section, we describe in details what we have done to improve the performance of the Maxwell equations solver MAX3D through a series of loop transformations to improve cache utilization and several PFA directives to improve parallel efficiency.

3 Cache Utilization Improvement

If a data item is in cache or a register and it is reused later in the application, it is desirable for the reuse to occur while the value is still in a register or in the cache. If we reference a data item which has remained in a register or cache the reference is said to exhibit *locality*. There are many techniques which have been developed to transform loops to help increase locality. A thorough discussion on optimizing for uniprocessor caches is given by Wolf [11]. The first step in this research is to investigate the possibility of improving the cache utilization of the subroutines used in MAX3D. The purpose is to enhance the program locality via a series of loop transformations. After carefully examining the loops in subroutine HZETA, we made the following changes:

3.1 Loop Index Shift

In order to fuse the loops in subroutine HZETA, we have to remove data dependence between consecutive iterations. In loop 7 of HZETA, we have the following statement:

$$H(I, J, K, 1) = SSZT * (HP(J, K, 1) + HM(J, KP, 1))$$

Clearly, this requires the availability of $HM(J, KP, 1)$ before calculating $H(I, J, K, 1)$. In the original code, all HM values are computed first in loop 5. Then loop 7 computes the H values. Hence, this presents no problem. But this makes loop fusion impossible since in the same iteration when calculating

$H(I, J, K, 1)$, we do not have the $HM(J, KP, 1)$ value yet. To solve the problem, we use loop index shift in loop 7 to avoid the problem. In other words, when we finish the computation of $HM(J, K, 1)$ in an iteration, we calculate the $H(I, J, K-1, 1)$ value instead of the $H(I, J, K, 1)$ value. Thus, we eliminate the data dependence problem.

3.2 Loop Fusion

Loop fusion is an important loop restructuring method. When two adjacent countable loops have the same loop limits, they can sometimes be *fused* into a single loop. Originally, loop fusion was developed as a way of reducing the cost of the test and branch code for the loop itself. The recent development of deep memory hierarchies has made it more important to take advantage of memory locality. Fusing loops that refer to the same memory locations enhances temporal locality, and can have a significant impact on cache memory and virtual memory performance.

Another benefit of loop fusion is that the larger loop body may allow the compiler to do more effective scalar optimization, such as common subexpression elimination and instruction scheduling. We used the highest optimization level -O3, and the results are significant.

Note that loop fusion increases the size of a loop, which can potentially reduce instruction locality. In our case, we fuse 5 loops into one loop. Since the new loop does not contain a very large number of instructions, it will fit into the instruction cache in a reasonable cache memory. The experimental runs confirm our conjecture.

3.3 Loop Interchange

It is always a good policy to write loops that take the effect of the cache into account, with or without parallelism. The technique for the best cache performance is also quite simple: make the loop step through the array in the same way that the array is laid out in memory. For Fortran program, this means stepping through the array without any gaps and with the leftmost subscript varying the fastest. Note that this does not depend on multiprocessing, nor is it required in order for multiprocessing to work correctly. However, multiprocessing can affect how the cache is used. Hence, small stride cache access is important for both sequential and parallel codes.

Perhaps the single most important loop structuring transformation is loop interchanging. Interchanging two tightly nested loops switches the inner and outer loops; Interchanging can change the spatial and sequential cache locality characteristics of the program. In particular, interchanging can affect spatial locality by changing the stride of array accesses in the inner loop. In the original code, Loop I is the outermost loop, and loop J is the innermost loop. When accessing array element $U2(I, J, K, L)$ between consecutive iterations, the stride is not 1. In fact, when we access the element $U2(I+1, J, K, L)$, all the array elements brought in by $U2(I, J, K, L)$ have been flushed out of cache long time ago because between iteration I and $I+1$, almost $JL \times KL$ iterations have been executed. The result is that each element along with its cache line is brought the cache and only used once and kicked out of cache. This makes the cache utilization low and increases cache misses tremendously.

After careful examination of the loops in HZETA, we found only one data dependence relation existing

among the loops. Once the data dependence relation is eliminated through index shift as described above, we are free to interchange the three loops. Certainly, the best way to restructuring the loops is to make loop *I* the innermost loop, and loop *K* the outermost loop. After this change, we have stride 1 access of the arrays, and reduce the cache misses in the subroutine.

3.4 Loop Fission

A single loop can be broken into two or more loops; this is the inverse of loop fusion, and is called *loop fission*. In the HZETA subroutine, loop 8 uses loop indices *I*, *K*, and *L*, and hence cannot be fused with loops 2, 3, 5, and 7. A solution is found to split loop 8 into independent segment outside of loop 2.

3.5 Cache Blocking

Cache blocking is a technique to reduce cache or TLB (Table Lookahead Buffer) misses in nested array-processing loops, by processing data in blocks or strips small enough to fit in the cache or TLB. Blocking is also referred to as *strip mining*. The principal behind blocking is that every array element brought into the cache is processed as fully as possible before it is forced out of the cache by computations requiring other data to be read in.

The technique could be applied to MAX3D to reduce cache misses. For example, in the subroutine HZETA, we need to access $U1(I, J, K, L)$, $U1(I, J, K+1, L)$, and $U1(I, J, K-1, L)$ in an iteration. Without cache blocking, these array values are used only once before they are forced out of the cache. Through cache blocking, we can access these elements several times in the cache and hence reduce the cache misses. This technique is tested for the HZETA subroutine and have not been incorporated into the final version of the PFA code.

After all these transformation steps, subroutine HZETA runs much faster than the original version due to reduced cache misses on a single processor. Similar transformations are carried out in subroutines GETA. Figure 1 shows the original loops and the transformed loops within HZETA.

4 Parallelization

The model of parallelism used focuses on the Fortran DO loop. The compiler executes different iterations of the DO loop in parallel on multiple processors. The processes that participate in the parallel execution of a task are arranged in a master/slave organization. The original process is the master. It creates zero or more slaves to assist. When a parallel DO loop is encountered, the master asks the slaves for help. When the loop is complete, the slaves wait on the master, and the master resumes normal execution. The master process and each of the slave processes are called a thread of execution or simply a thread. By default, the number of threads is set to the number of processors on the machine.

For multiprocessing to work correctly, the iterations of the loop must not depend on each other; each iteration must stand alone and produce the same answer regardless of when any other iteration of the loop is executed. Not all DO loops have this property, and loops without it cannot be correctly executed

Original Loops	Optimized Loop
<pre> DO 1 I=1,ILM DO 2 K=1,KLM DO 2 J=1,JLM SSZT=SQRT(SZT(I,J,K,1)**2+SZT(I,J,K,2)**2+SZT(I,J,K,3)**2) SSZT=AMAX1(SSZT,SS) RSSZT=1.0/SSZT UK1(J,K)=SZT(I,J,K,1)*RSSZT 2 CONTINUE DO 3 K=2,KLM KM=K-1 KP=K+1 DO 3 J=1,JLM UP1(J,K)=U1(I,J,K,1)+0.25*RP*((1.0-RK)* 1 (U1(I,J,K,1)-U1(I,J,KM,1)) 1 +(1.0+RK)*(U1(I,J,KP,1)-U1(I,J,K,1))) UC1=UI1(J,K)*UP1(J,K)+UI2(J,K)*UP2(J,K)+UI3(J,K)*UP3(J,K) HP1= 0.5*(C1*UC1-C2*UC5) HP(J,K,1)=UI1(J,K)*HP1+UJ1(J,K)*HP2 3 CONTINUE DO 5 K=2,KLM KM=K-1 KP=K+1 DO 5 J=1,JLM UP1(J,K)=U1(I,J,K,1)-0.25*RP*((1.0+RK)* 1 (U1(I,J,K,1)-U1(I,J,KM,1)) 1 +(1.0-RK)*(U1(I,J,KP,1)-U1(I,J,K,1))) 1 +(1.0-RK)*(U1(I,J,KP,2)-U1(I,J,K,2))) UC1=UI1(J,KM)*UP1(J,K)+UI2(J,KM)*UP2(J,K)+UI3(J,KM)*UP3(J,K) HM1=-0.5*(C1*UC1+C2*UC5) HM(J,K,1)=UI1(J,KM)*HM1+UJ1(J,KM)*HM2 5 CONTINUE DO 7 K=2,KLM KP=K+1 DO 7 J=1,JLM SSZT=SQRT(SZT(I,J,K,1)**2+SZT(I,J,K,2)**2+SZT(I,J,K,3)**2) H(I,J,K,1)=SSZT*(HP(J,K,1)+HM(J,KP,1)) 7 CONTINUE DO 8 L=1,6 DO 8 J=1,JLM H(I,J,1,L)=H(I,J,KL-3,L) H(I,J,KL,L)=H(I,J,4,L) 8 CONTINUE 1 CONTINUE </pre>	<pre> DO 2 J=1,JLM DO 2 K=1,KLM KM=K-1 KP=K+1 DO 2 I=1,ILM SSZT=SQRT(SZT(I,J,K,1)**2+SZT(I,J,K,2)**2+SZT(I,J,K,3)**2) SSZT=AMAX1(SSZT,SS) RSSZT=1.0/SSZT UK1(I,K)=SZT(I,J,K,1)*RSSZT UI1(I,K)=UIX*RSUI C UP1(I,K)=U1(I,J,K,1)+0.25*RP*((1.0-RK) 1 * (U1(I,J,K,1)-U1(I,J,KM,1)) 1 +(1.0+RK)*(U1(I,J,KP,1)-U1(I,J,K,1))) UC1=UI1(I,K)*UP1(I,K)+UI2(I,K)*UP2(I,K)+UI3(I,K)*UP3(I,K) HP1= 0.5*(C1*UC1-C2*UC5) HP(I,K,1)=UI1(I,K)*HP1+UJ1(I,K)*HP2 UP1(I,K)=U1(I,J,K,1)-0.25*RP*((1.0+RK)* 1 (U1(I,J,K,1)-U1(I,J,KM,1)) 1 +(1.0-RK)*(U1(I,J,KP,1)-U1(I,J,K,1))) UC1=UI1(I,KM)*UP1(I,K)+UI2(I,KM)*UP2(I,K)+UI3(I,KM)*UP3(I,K) HM1=-0.5*(C1*UC1+C2*UC5) HM(I,K,1)=UI1(I,KM)*HM1+UJ1(I,KM)*HM2 C C Loop index shift to eliminate data dependence C SSZT=SQRT(SZT(I,J,K-1,1)**2+SZT(I,J,K-1,2)**2+SZT(I,J,K-1,3)**2) H(I,J,K-1,1)=SSZT*(HP(I,K-1,1)+HM(I,K,1)) 2 CONTINUE C C Peeling off loop 8 from loop 1 C DO 8 I=1,ILM DO 8 K=1,KLM KRF=K+KN IF(K.GT.KH) KRF=K-KN DO 8 L=1,6 G(I,1,K,L)=G(I,4,KRF,L) G(I,JL,K,L)=G(I,JL-5,KRF,L) 8 CONTINUE </pre>

Figure 1: Cache locality enhancing transformation of HZETA loops.

in parallel. However, many of the loops encountered in practice fit this model. Further, many loops that cannot be run in parallel in their original form can be rewritten to run wholly or partially.

The essential compiler directive for multiprocessing is `C$DOACROSS`. This directive directs the compiler to generate special code to run iterations of a DO loop in parallel. The `C$DOACROSS` directive applies only to the next statement (which must be a DO loop) in parallel.

The `LOCAL`, `SHARE`, and `LASTLOCAL` clauses specify lists of variables used within parallel loops. A variable can appear in only one of these lists. To make the task of writing these lists easier, there are several defaults. The loop-iteration variable is `LASTLOCAL` by default. All other variables are `SHARE` by default.

Many loops that have data dependencies can be rewritten so that some or all of the loop can be run in parallel. The essential idea is to locate the statement(s) in the loop that cannot be made parallel and try to find another way to express it that does not depend on any other iteration of the loop.

A certain amount of overhead is associated with multiprocessing a loop. If the work occurring in the loop is small, the loop can actually run slower by multiprocessing than by single processing. Roughly speaking, the amount of overhead is about 500 arithmetic operations. After examining the listing file of the program with improved cache utilization, we found that the compiler always parallelize the innermost loops within subroutines `FXI`, `GETA`, and `HZETA`. Because the two outermost loops in each subroutine is very large (for example 60 and 96 in `HZETA`), the program will incur this overhead 5760 times. Hence, the overhead alone will be 5760×500 operations in `HZETA`. This will certainly cause the program slow down. This problem is associated with the modified code with cache improvement due to the loop fusion. This problem in the original code is not so severe since the middle loops are parallelized in `HZETA`. Hence, the overhead is about 72×500 operations since the outermost loop executes 72 times.

To avoid this, we have to make the amount of work inside the multiprocessed region as large as possible. After carefully examining the code, we find that we have two choices: parallelize the *J* loop or the *I* loop in `HZETA`. We cannot parallelize the *K* loop because different iterations of the *K* loop have data dependence for the *HP*, *HM* and *H* arrays. In other words, the results produced in the current iteration *K* are used in the next iteration *K* + 1. Here we try to parallelize the outermost DO loop possible, because it encloses the most work. In this example, that is the *J* loop. After inserting the PFA directives, the parallelized loop encloses more work and shows better performance than the original version, as discussed in the next section.

5 Experimental Results

Based on the above analysis, several experiments are carried out. Most of the results are obtained via hardware counters `ssrun` and profiling tool `prof` available on the SGI Origin 2000.

Table 2 lists the secondary data cache misses, the secondary instruction cache misses, and the table lookahead buffer (TLB) misses in the `HZETA` subroutine with `NEND=10`. The test is run for three different cases: the original code, the code with fused loops, and the code with all loop transformations done. As seen from the table, the secondary data cache misses is reduced by more than 95% after loop optimization. The secondary instruction cache misses is also reduced drastically. We are not sure about

Performance Measures	Original Code	Fused Loop	Final Version
Data Cache Misses	1644954	1293716	62962
Instruction Cache Misses	6339	4726	284
TLB Misses	82444	120986	171188
Execution Time (seconds)	87	68	21

Table 2: Performance Comparisons of Before and After Loop Transformations

Original Code	Fused Loop	Cache Blocking $8 \times 10 \times 8$	Cache Blocking $18 \times 10 \times 16$
1644954	1293716	173514	107848

Table 3: Effect of Cache Blocking on Cache Misses

the reason why the TLB misses are increased about twice after the loop transformation. It deserves further investigation. However, compared with the number of the secondary data cache misses, the number of TLB misses is relatively small, and hence it will not affect the overall performance too much. This is confirmed by execution times shown in the table. The execution time in HZETA is reduced from 87 seconds to 68 seconds after loop fusion and is further reduced to 21 seconds after loop interchange and other loop optimization.

We also performed some experiments to measure the effect of cache blocking strategy on the cache misses. Table 3 shows the effect of cache blocking in the HZETA subroutine with NEND=10. Here, two blocking sizes are tested: $8 \times 10 \times 8$ and $18 \times 10 \times 16$. The conclusions are that cache blocking is effective in reducing the cache misses by at least 10 times and bigger blocking sizes are more effective than smaller sizes.

Table 4 shows the execution times of the original sequential code with automatic parallelization, the code after loop transformations with automatic parallelization, and the code after loop transformations and hand parallelization. The timings are also shown in Figure 2. From Figure 2, we see that the execution time of the original code reaches its minimum when 8 processors are used on the Origin 2000. On the contrast, the execution time reaches its minimum when 20 processors are used. Clearly, the new code not only reduces the total execution time, but also is more scalable than the original code.

Because of the loop fusion, the PFA preprocessor always parallelize the innermost loops within subroutines FXI, GETA, and HZETA in the code with loop optimization. As described before, the overhead alone will be 5760×500 operations in HZETA. Therefore, parallelization of the code only hurts its performance, as seen from the table. In the original code, the middle loops are parallelized in HZETA and GETA. Hence, the overhead is about 72×500 operations and hence is not so severe. However, the scalability is still poor because of the large overhead involved in the parallelization process. In the final version of our code, we insert several PFA directives to force the compiler to parallelize the outermost loops in HZETA and GETA. Therefore, the overhead incurs only once for each calling of FXI, HZETA and GETA, and hence the execution time is much smaller than the counterparts of the other two versions. This also explains the fact that the final version is more scalable than the original version.

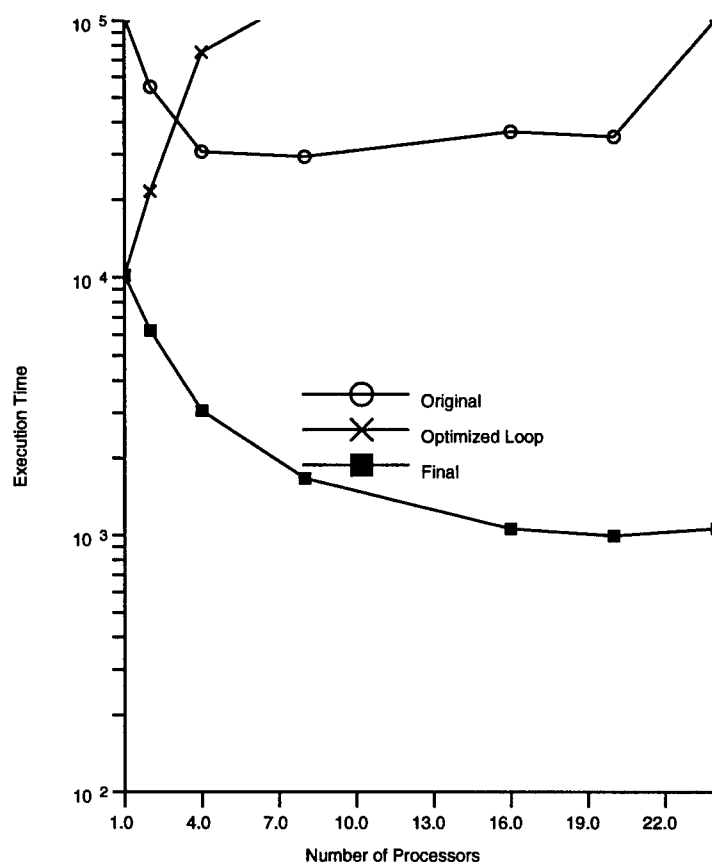


Figure 2: Execution Times of Three Different Versions of MAX3D

No. of Processors	Execution Time (seconds)		
	Original	Optimized Loop Only	Final Version
1	102,974	10,191	10,191
2	55,003	21,567	6,222
4	30,739	75,052	3,063
8	29,399	> 126,000	1,667
16	36,686	∞	1,060
20	35,060	∞	993
24	101,433	∞	1,061

Table 4: Execution Times of Three Different Versions of MAX3D

No. of Processors	Speedup
1	1
2	1.638
4	3.327
8	6.113
16	9.614
20	10.263
24	9.605

Table 5: Speedups of the Final Version of MAX3D

Table 5 shows the speedups of the final code after loop transformations and hand parallelization. The speedups are also shown in Figure 3. It is clear that the code is still quite scalable when the number of processors used is 16.

Finally, we want to compare the performance of the MPI code and the PFA code. Table 6 lists the execution times for the three programs: the original sequential Fortran code implemented by Dr. Joseph Shang, the MPI code implemented by Dr. Marcus Wagner and the final optimized PFA code. The times are obtained on the Origin 2000 using 6 processors for the MIP code and the PFA code and 8 processors for the sequential code.

6 Conclusions and Future Work

In this report we have demonstrated that the sequential MAX3D code can improved drastically via loop transformations to reduce cache misses and can be parallelized efficiently using high level parallel

Original Code	MPI code	PFA code
29,399 (sec)	2421 (sec)	2180 (sec)

Table 6: Execution Times for Three Different Implementation

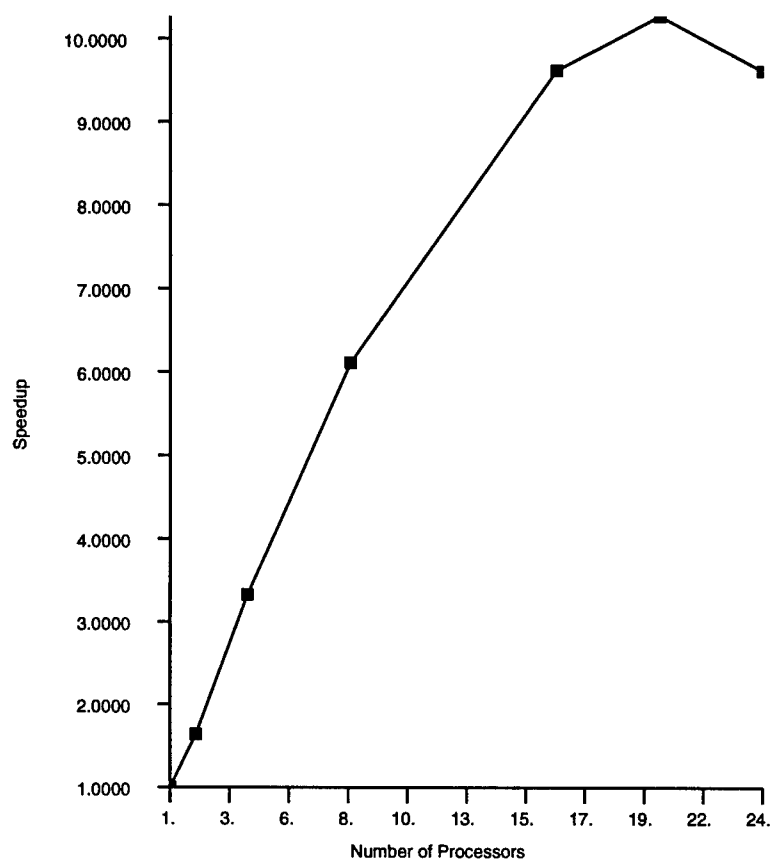


Figure 3: Speedup of the Final Version of MAX3D

languages such as the PFA preprocessor with hand tuning and intervention. Many sequential CEM codes are written for vector machines. When running them on parallel computer systems, their cache locality behavior is not always good, and there is a lot of space to make improvement in this respect. Hence, enhancing program reference locality is the first step to parallelize a CEM code.

The popular model used in today's massively parallel computer systems is the data-parallel **Single-Program-Multiple-Data (SPMD)** programming model, in which data are distributed across the processors of the machine, and each processor essentially executes the same code, on different portions of the data domain. The current programming paradigm associated with this model is the message passing approach, in which existing high-level sequential languages such as Fortran and C are combined with a standard interface to a message passing subsystem such as PVM or MPI.

Using the message passing paradigm has several disadvantages: the cost of producing a message passing code may be between 5 and 10 times that of its serial counterpart, the length of the code grows significantly, and it is much less readable and less maintainable than the sequential version. For these reasons, it is widely agreed that a higher level programming paradigm is essential if parallel systems are to be widely adopted. The results obtained in this research show that the performance of the parallel code is even better than the MPI counterpart besides the advantages stated above. This suggests that a higher level programming paradigm is a viable and alternative way to parallelize CEM codes.

The results achieved in this research is only a preliminary step in achieving a scalable version of the MAX3D code. Due to the time limit, we did not investigate all the subroutines in the code and other possibilities of improving the code performance. We believe that more performance improvement is possible. For example, currently, data allocation is done by compiler. If we manually allocate the data arrays, maybe we can get a further reduction in execution time. Another example is that the minimum computation used in the code is not parallelized. We need to insert some PFA directives to parallelize the loop. Several nested loops are not parallelized efficiently.

The experiments conducted in this research are limited to a fixed problem size ($73 \times 61 \times 97$). When the problem size changes, the scalability and efficiency may also change. Theoretically, when the problem size is bigger, the ratio of computation over communication is also getting bigger. This implies that the communication overhead becomes relatively smaller. It is our conjecture that the parallel code will be more scalable and efficient when computing larger problems. However, more experiments are needed to confirm our conjecture.

The current version is implemented in Power Fortran and is only available on certain parallel computer systems such as Origin 2000. On the other hand, High Performance Fortran (HPF) is becoming a widely accepted standard for high level parallel language and many systems such as CRAY T3E, SGI Origin 2000, and IBM SP2 run HPF. Many other systems are also moving in this direction. The next step is to investigate the possibility of implementing the Maxwell equation solvers efficiently in HPF. In this way, the parallel code produced will be portable on many popular parallel computer systems. All these deserve further investigation.

7 Acknowledgements

Thanks to Dr. Joseph Shang for providing the original source code MAX3D, and answering numerous questions which made this work possible. Thanks to Dr. Marcus Wagner for his help and answers regarding his MPI code. I also appreciate the help from Prof. Karen Tomko, Prof. Robert Lee, Prof. Dave Hudak, and Dr. Doug Blake during the last two months.

Computational resources for the work presented here were supported in part by a grant of HPC time from the DOD ASC MSRC Center, WPAFB, Dayton, Ohio. Additional computer resources were provided by the Ohio Super Computer Center, Columbus OH.

References

- [1] Joseph S. Shang and Datta Gaitonde and K. Wurtzler. Scattering Simulations of Computational Electromagnetics. 27th AIAA Plasmadynamics and Lasers Conference, AIAA-96-2337, AIAA, 1996.
- [2] Joseph S. Shang and Datta Gaitonde. High-Order Finite-Volume Schemes in Wave Propagation Phenomena. 27th AIAA Plasmadynamics and Lasers Conference, AIAA 96-2335, AIAA, 1996.
- [3] Joseph S. Shang and Datta Gaitonde. On High Resolution Schemes for Time-Dependent Maxwell Equations. 34th Aerospace Sciences Meeting and Exhibit, AIAA 96-0832, AIAA, 1996.
- [4] Joseph S. Shang and Robert M. Fithen. A Comparative Study of Characteristic-Based Algorithms for the Maxwell Equations Journal of Computational Physics, 125: 378 - 394, 1996.
- [5] Joseph S. Shang and S.J. Scherr. Time-Domain Electromagnetic Scattering Simulations on Multi-computers. 26th AIAA Plasmadynamics and Lasers Conference , AIAA 95-1966, AIAA, 1995.
- [6] Joseph S. Shang and D.A. Calahan and B Vikstrom. Performance of a Finite Volume CEM Code on Multicomputers. Computing Systems in Engineering, 6(3): 241 - 250, 1995.
- [7] Joseph S. Shang and Datta Gaitonde. Scattered Electromagnetic Field of a Re-Entry Vehicle. Journal of Spacecraft and Rockets, 32(2) : 294 - 301, 1995.
- [8] Joseph S. Shang and Datta Gaitonde. Characteristic-Based, Time-Dependent Maxwell Equation Solvers on a General Curvilinear Frame. AIAA Journal, 33(3): 491 - 498, 1995.
- [9] Joseph S. Shang. A Fractional-Step Method for Solving 3-D Time-Domain Maxwell Equations. 31th Aerospace Sciences Meeting and Exhibit, AIAA 93-0461, AIAA, 1993.
- [10] Joseph S. Shang. Characteristics Based Methods for the Time-Domain Maxwell Equations. 29th Aerospace Sciences Meeting, AIAA 91-0606, AIAA, 1991.
- [11] Michael Wolfe. High Performance Compilers for Parallel Computing, Addison-Wesley Publishing Company, 1996.
- [12] James Laudon and Daniel Lenoski. The SGI Origin: A ccNUMA Highly Scalable Server, the 1997 International Symposium on Computer Architectures, Denver, Co, pp. 241-251.

**AB INITIO QUANTUM CHEMICAL STUDIES OF NICKEL DITHIOLENE
COMPLEX**

**Rolfe G. Petschek
Professor
Department of Engineering**

**Case Western Reserve University
Cleveland, OH 44106**

**Final Report for:
Summer Research Program
Wright Laboratory**

**Sponsored by:
Air Force Office of Scientific Research
Bolling Air Force Base, Washington, DC**

And

Wright Laboratory

September 1997

AB INITIO QUANTUM CHEMICAL STUDIES OF
NICKEL DITHIOLENE

Rolfe G. Petschek
Case Western Reserve University
Cleveland Oh. 44106-7079

Abstract

Nickel dithiolene $\text{Ni}(\text{S}_2\text{C}_2\text{H}_2)_2$, was studied theoretically using *ab initio* quantum chemistry through the GAMESS quantum chemistry package. Only the neutral oxidation state was studied. It was found that the bonding pattern in this dye is complex and that an accurate description of the electronic state requires a multi-configurational-self-consistent-field (MCSCF) description. The electronic configuration of the nickel was found to be 8d in every important configuration. The electronic configurations, degree of approximation required, geometry, bonding structure and electronically excited states were studied, primarily using effective-core-potential basis sets in which the core electrons are not considered. The possibility of a distortion from the assumed D_{2h} geometry associated with these low-lying states was examined. These results will make possible further studies of similar molecules, different oxidation states and other molecules with partially filled d orbitals.

I) Introduction:

Nickel dithiolene complexes are of great interest for a variety of reasons[1-3]. They are important commercial dyes. They have strong absorption bands in the near infrared that makes them useful for laser hardening, Q-switching near infrared lasers, and a variety of other applications. They are also easily oxidized and reduced and, with appropriate substituents, have stable anions and/or cations. However in these initial studies only neutral molecules were examined. The objective of this study was to calculate the electronic structure and properties of these dyes. It was found that the electronic structure is quite complex. Considerable progress was made in elucidating this structure. Unfortunately there was inadequate time to complete the calculations which were more complex than expected. Thus the results reported below are preliminary and somewhat incomplete.

Nickel dithiolene consists of a Nickel atom with approximately square-planar bonds to two thiolenes. The nature of this bonding to the ligands is not immediate. One possibility is coordinate covalent bonds in which the lone pair electrons on the sulfurs that are in pi orbitals approximately perpendicular to the plane of the molecule are donated to form bonds with neutral nickel. Another possibility is four sigma bonds between the ligands and a nickel with formal charge +2. There are a variety of possible intermediate forms. It is also possible for a pi bond to form involving the Nickel d-orbitals, two of which have pi-like symmetry. In this work we found that none of these points of view is correct rather the electronic structure is viewed correctly (even quite approximately) only as an amalgamation of these views. This, particularly the participation of Nickel d orbitals in the pi bonding, has important consequences for the optical properties of these complexes. This understanding may assist in the design of dyes that are superior for various purposes.

Another interesting aspect of these molecules that they have very low-lying electronic excited states which have large extinction coefficients and, in consequence, must be electric dipole transition matrix element allowed. If the molecule has (as usually hypothesized) D_{2h} symmetry this implies that there must be two different, relatively closely spaced states of this molecule which transform like different irreducible representations of the symmetry group of the molecule. This would be unusual as if (as in this case) there is a molecular displacement which transforms like a representation contained in the symmetric product of these two representations then such a displacement will cause these two states to mix with each other. This mixing will lower the energy of the lower lying state, by an amount proportional to the square of a coupling between the displacements and the electronic states and inversely proportional to the energy difference between the two states. Thus, if the energy difference between two electronic states is small, it is reasonable to suppose that this energy lowering will be large; larger than the energy increase in the state generally associated with the a molecular displacement. This would imply that at least one displacement transforming like a non-trivial representation of the group decreases the energy so that the actual symmetry of the system should be lower. It is, of course, possible that either the coupling between all such electronic states and all possible displacements is small or the energy change associated with a displacement in the absence of such coupling is large. However calculations in D_{2h} geometry suggested that there was a low-lying electronic excited state for *all* irreducible representations of D_{2h} . Thus we explored the possibility that the actual ground state has a lower symmetry. This work is still in progress. Only preliminary results can be presented.

This report is organized as follows. The next section introduces our findings for D_{2h} molecules through a simple molecular orbital discussion of the bonding structures and electronic states. A detailed discussion of the quantum chemical calculations in D_{2h} symmetry that support this discussion is deferred until the third section. Preliminary results in lower symmetries are presented in the fourth section. A brief review and discussion is given in the last section. All quantum chemical calculations were done using the GAMESS[4] quantum chemistry package.

II) Bonding, Symmetry, and Orbital considerations

The central nickel atom in a nickel dithiolene is in an approximately D_{4h} environment consisting of the ligand sulfurs which are arranged approximately in a square and, prior to bonding to the nickel, have sp bonds to the carbons. The largest overlaps between the nickel and sulfur atomic orbitals are between the sulfur p orbitals perpendicular to the plane of the molecule and s, p and d orbitals of the nickel. There are four such sulfur orbitals with essentially identical energies. These orbitals transform like the A_{1g} , E_u and B_{1g} representations of D_{4h} . The nickel d orbitals transform like the A_{1g} , E_g , B_{1g} and B_{2g} representations, the nickel p orbitals transform like the E_u and A_{2u} representations of D_{4h} and the nickel s orbitals like the A_g . It is naively expected that bonding between the sulfur and the nickel should involve mixing of nickel and sulfur orbitals with the same symmetry. As the nickel d orbitals initially have the same energy this the resultant splittings should determine which nickel d orbitals are occupied, bearing in mind that the nickel s orbital does not directly couple to (any) nickel d orbital.

The nickel 3p orbitals are significantly lower in energy and the nickel 4p orbitals significantly higher in energy than the sulfur p (or other) orbitals and in consequence there is relatively little relevant mixing involving these orbitals. The energies of the sulfur E_u orbitals are appreciably decreased by the nickel. This results in coordinate covalent bonds between the sulfur and the nickel consisting of two electrons in each of the E_u states. The nickel B_{2g} d orbital (which has A_g symmetry in the actual D_{2h} symmetry group) does not mix appreciably with other orbitals or participate in the bonding and is expected to be filled. The nickel E_g orbitals couple relatively weakly to the ligand pi orbitals and are also expected to be filled. The A_g and B_{1g} sulfur orbitals are expected to mix with the nickel orbitals of the same symmetry, lowering the energy of one of each pair of orbitals and raising the energy of the other. There are two B_{1g} orbitals (ligand, nickel d) and three A_g orbitals (ligand, nickel s, nickel d). The largest mixing is expected between the B_{1g} orbitals because this nickel d orbital has a larger amplitude in the plane of the molecule and the nickel s orbital has a rather higher energy. Thus the ordering of these states (lowest to highest energy) is expected to be B_{1g} , A_g , A_g , B_{1g} , and A_g . If the highest lying A_g and B_{1g} states are above the ligand pi states then it follows that two A_g and one B_{1g} states should be filled. If the empty B_{1g} is approximated by the nickel d orbital the nickel state is $8d Ni^{++}$. Given a Ni^{++} the ligands must each be radical anions (or together they must be a dianion). More precisely this must be the pi configuration of the ligands, independent of the charge on the nickel and character of the filled sigma orbitals discussed above.

If all orbitals are doubly occupied or unoccupied then the highest occupied pi orbital (in D_{2h} symmetry) is a B_{1u} orbital (we will take the z-axis normal to the molecular plane and the y-axis along the long axis of the molecule e.g. from one ligand to the other). If all the orbitals

are doubly occupied or unoccupied – that is in a restricted (close shell) Hartree-Fock calculation - the above is a reasonable description of our results for the electronic structure of the A_g electronic state. However this filled B_{1u} orbital is even under all symmetry operations which leave the plane of the molecule fixed and is expected to be essentially degenerate with the next pi orbital, a B_{2g} . This is because the ligand pi electrons are expected to couple only weakly to the sulfur d B_{2g} and B_{3g} and the sulfur p orbitals have quite different energies. Thus pi orbitals which are even under exchange of the ligands are expected to be close in energy to those which are odd under exchange of the ligands. Thus it is reasonable to suppose that it is more correct to view this state as a singlet biradical in which each ligand is essentially a biradical. This was confirmed by a two component self consistent field calculation (TCSCF) in which allows either this B_{1u} or this B_{2g} orbital to be doubly occupied when the other is unoccupied.

The above discussion omits the rather large coupling between the nickel d orbitals. Here and below the term “nickel d orbitals” is to be construed “molecular orbitals having appreciable nickel d character”. The nickel d orbitals were found to be largely localized on the nickel, although there is appreciable mixing of the A_g orbitals. Hund's rule informs us that the interactions between electrons in these orbitals will tend to result in high angular momentum, high spin configurations. The 8d configuration with two empty B_{1g} orbitals has zero spin and large fractions of low angular momentum components. In fact there is at least one restricted open shell Hartree-Fock calculation which results in a lower energy than this one – the quintet B_{3u} in which an A_g and the B_{1g} nickel d orbitals and these B_{1u} and B_{3g} pi orbitals are all singly occupied. This is unsurprising on the basis of the above discussion: these d orbitals should be essentially degenerate, as are these pi orbitals. This configuration has higher spin on the d orbitals and has a large fraction of high angular momentum components therein. Thus rather little mixing energy is sacrificed for a relatively large decrease in the interaction energy between the nickel d electrons. This was a puzzle as the molecule is known to be a singlet and, while the singlet B_{3u} (with the same configuration) has a lower energy than the RHF or TCSCF A_g described above, it has a higher energy than the corresponding quintet. This in turn suggests that more complicated orbital configurations in which the number of electrons in several of the nickel d orbitals is allowed to vary should be considered as these will also allow for a larger fraction of high angular momentum contributions to the d configuration around the nickel. A larger fraction of high angular momentum contributions is more important in lowering the energy than higher spin so that this program was expected to be consistent with the lowest energy state being a singlet. This also changes the energies of various states, particularly the configurations in which one of the d electrons has B_{3g} symmetry result in significantly lower energies for (and large occupations for) the pi state with this symmetry.

It is important to remark that this intuitive discussion (which we believe is correct) is only poorly reflected in the RHF or TCSCF calculations of the A_g state. It is, of course, the case that doubly occupied orbitals have (Koopman's Theorem) energies appreciably below those of unoccupied orbitals. This is particularly true of the Nickel d orbitals, presumably because of the relatively large interactions between them, so that the filled nickel d orbitals are of order the 15th highest occupied orbitals. Thus one standard method of checking for the importance of non-RHF configurations – including a number of frontier orbitals in a Configuration-Interaction (CI) calculation – fails in this case. The strong interactions that result in the

importance of other configurations also result in these orbitals do not seem to be "frontier" orbitals.

On the basis of the above discussion and calculations a number of CI and (primarily) MCSCF calculations with active spaces including various nickel d orbitals were pursued. These calculations largely confirm the (partly *a posteriori*) discussion above. Detailed results are given in the next section.

III) Detailed description of the calculations in D_{2h}

In this section we will give a detailed description of the calculations performed in D_{2h} symmetry, including the basis sets used, the orbitals which were filled and partially filled in the MCSCF calculations. We will also describe briefly the orbitals and nature of the states that result in these energies, the importance of various levels of calculation to both the nature of the states, energies and energy differences.

Three basis sets were used for the final calculations. The first used the SBK effective core potentials and the corresponding 31* basis functions including polarization functions. Some exploratory work (which will not be reported) was performed using this basis excluding the diffuse functions discussed next. A diffuse (6 component) d basis function with the exponent 0.04 was added to the Nickel and diffuse s and p functions with the exponent 0.0564 were added to the sulfur. These exponents are given in atomic units. The sulfur basis had been optimized for the Dunning-Hays basis set except that we discarded the corresponding d functions and used the s exponent for both of the (very similar) s and p functions. The diffuse nickel d function was not optimized in any sense but was included when it became evident that relatively subtle effects of the environment might be crucial to the behavior. This basis will be symbolized SBK⁺⁺. Another basis set was the all electron triple zeta valence (TZV^{*}) basis set with p and d polarization functions. The final TZV⁺⁺ basis set was the TZV^{*} basis set augmented by a (10 component) polarization f function with the exponent 0.8 and a (15 component) g function with exponent 1.0. Again these exponents were not in any sense optimized – they were used only to explore the importance of polarization functions on the nickel.

Several calculational methods were used and will be symbolized as follows. ROHF5 symbolizes a calculation in which the electronic state had multiplicity 5. The converged wavefunction had B_{3u} symmetry. However, in initial phases of these calculations it was necessary to restrict changes in the symmetry of the wavefunction. Later (MCSCF) results suggest that similar wavefunctions with different symmetries (different nickel d orbitals are involved) have similar energies. However they have rather different orbitals and might not have been obtained when the restriction on symmetry change was removed. TCSCF symbolizes a two-component-self-consistent field calculation for an A_g state in which either the RHF B_{1u} HOMO or the B_{3g} LUMO can be doubly occupied. Mnxm+qA symbolizes an MCSCF calculation with *n*, *m* and *q* specifying the orbitals in the active space, and A specifies the symmetry of the electronic state. Specifically in the reference-state for A_g symmetry there are *n* doubly occupied orbitals from which electrons can be excited to other orbitals. There are *m* orbitals to which any number of electrons can be excited and an additional *q* orbitals to which a single electron can be excited. Thus M7x5+0 B_{3u} symbolizes a complete active space / fully optimized reaction space calculation in which fourteen electrons can be distrib-

uted in any way consistent with B_{3u} symmetry and multiplicity one among twelve orbitals. Similarly $M13x2+7A_g$ symbolizes a calculation in which twenty-six electrons can be distributed in any way among fifteen orbitals and, additionally, all configurations in which can be constructed by exciting a single electron from one of these configurations to an additional 7 orbitals are included consistent with A_g symmetry and multiplicity one. An additional class of MCSCF calculations is symbolized by $Mnxm/q$. These were done only for A_g symmetry. Here n and m have the same meaning as above but q specifies the number of electrons that can be excited from the doubly occupied orbitals to the singly occupied ones.

A few exploratory MCSCF calculations were done on electronic states with spin multiplicities different from one, exclusively for the B_{3u} state. The singlet state with this symmetry, at all levels of calculation we have performed, consists largely of a configuration with four singly occupied orbitals and the remaining orbitals either doubly occupied or unoccupied. In all such calculations we found that the energy of the triplet and quintet were lower than that of the singlet. The lowest lying singlet states we have found for certain other symmetries are also dominated by such configurations. We speculate that the quintet is the lowest-energy state for these symmetries. These calculations will not be reported further. However, the lowest lying state we have found (at high levels of calculation) is an A_g state. Examination of this state shows that it contains large (indeed the largest) contributions from configurations in which all orbitals are doubly occupied or unoccupied, and thus is unlikely to have nearby non-singlet states. Thus high levels (and only high levels) of calculation seem to agree with the experimental prediction that the ground state is a singlet

The symbols given above are inadequate to determine the nature of the wavefunctions as we did not systematically examine what symmetries the orbitals considered should have for the best (potentially lowest energy) state. Orbital symmetries were chosen on an *ad hoc* basis, partly including CI calculations that will not be reported on. Thus completeness requires reporting the symmetries of the orbitals involved. While we believe that reporting the symmetry of the orbitals involved should be adequate for converged MCSCF calculations initial orbitals with a large nickel d character potentially result in different states than orbitals without substantial nickel d character. Thus we give in Table 1 a list of the MCSCF calculations that will be reported on together with the symmetries of the orbitals. The orbitals with and without substantial nickel d character are given separately, as are those that are occupied and empty in the A_g reference-state, as are the orbitals which can only be singly occupied. The orbitals without substantial d character were initially the orbitals of that symmetry closest to the frontier orbitals in a lower level (e.g. TCSCF or ROHF5 or smaller active space MCSCF) calculation. There are initially 6 orbitals with substantial nickel d character. There are two ambiguities in reporting them as there are three such orbitals with A_g symmetry. A_{g2} is the nickel d orbital, which essentially does not mix with the ligand orbitals, and A_{g1} and A_{g3} are the two orbitals, which are mixtures of nickel d and ligand. Examination of the converged A_g orbitals with appreciable nickel d character shows very appreciable change in these orbitals during the MCSCF convergence. Thus we do not believe that the nature of these initial orbitals is at all important to the results.

It should be remarked that the *ad hoc* choice of orbital symmetries was guided largely by calculations on the A_g electronic state. This may have introduced a bias to make this the lowest lying state. Some exploratory calculations were also performed on the B_{3u} state.

However it was not possible to use these as a guide for choosing orbital symmetries as no orbitals were found which, when added to the active space, resulted in appreciable dynamic correlation. However, in the largest calculations orbitals of essentially all symmetries were included in the active space. No calculation resulted in occupation numbers appreciably different from an integer for any orbital of a symmetry not included in the completely active space of all each of the MCSCF calculations.

The geometry of this molecule, if it has D_{2h} symmetry, can be specified by placing the nickel nucleus at the origin and giving the coordinates of one sulfur, carbon and hydrogen. Each optimized geometry is given in Table 2. The final converged energies of various MCSCF calculations that we performed in the SBK** basis are reported in Table 3. We also report the occupation numbers for natural orbitals for four orbitals (B_{2g} , A_g , B_{3g} and B_{1g}) which are largely nickel d-like, two pi orbitals (B_{1u} and B_{3g}) and a sigma orbital (B_{1g}). These always include those orbitals with occupation numbers substantially different from integers. We calculated the optimum geometries only for a small number of states. Thus we also report in table 3 the calculation which was used to optimize the geometry. Some MCSCF calculations we have performed using the TZV bases are reported in Table 4.

Examination of these tables strongly suggests that simple RHF calculations are inadequate to describe this molecule. In particular at the single-configuration or even two-configuration level the lowest-lying energy state is a quintet. Moreover the degree of dynamic correlation in calculations with different symmetries is substantially different. Thus multi-configurational calculations are particularly important for calculating energy differences. Therefore it is important to ask how much correlation is required. It seems clear that for accurate calculation of the wavefunctions and energies of this molecule it is necessary to use an MCSCF that allows more than two electrons to be excited from the A_g reference configuration. It seems likely that exciting four electrons is adequate. Unfortunately such calculations converge only rather slowly compared to CAS/FORS type calculations. We have not performed the calculations that would tell us if exciting three electrons is adequate. We believe that such calculations would also converge slowly. It also seems clear that those approximate natural orbitals, which have occupation numbers significantly different from the appropriate integers, must be included. The most important of these would seem to be the nickel d B_{1g} and B_{3g} and the ligand B_{1g} and B_{3g} orbitals. This suggests that the ligand-nickel bond has partial sigma and partial pi character, with this character changing with changing symmetry of the state. These calculations also suggest that the most important remaining orbitals are the other orbitals with substantial nickel d character. However, it may be that these are sufficiently uncorrelated that they can be treated within perturbation theory. Calculations that would confirm or deny this possibility have not been performed.

Possibly the most interesting thing to predict from these calculations would be the absorption spectrum, which is the quantity of most interest for applications. We believe that this can be done even qualitatively correctly only using a high level MCSCF calculation with many orbitals in the active space and the possibility of exciting a large number of electrons. In the process of doing the MCSCF calculations reported above it was routinely necessary to take orbitals from calculations that had converged with different geometries and calculate new orbitals germane to other symmetries. A typical energy change during the orbital optimization process was 0.05 H or 100% of the energy difference between the lowest lying state and the first excited state. While we will not document this in detail it implies that it is at least

necessary to do a separate MCSCF calculation for each symmetry (or to use a yet larger active space.) Additionally, given the plethora of low lying excited states it seems important to examine the possibility that coupling between these states and nuclear coordinates results in distortions from D_{2h} symmetry. This would be expected to radically change the energy differences between excited states. This is discussed in the next section.

IV Preliminary calculations with lower symmetry

As we argued in the introduction the presence of a number of low-lying excited states with differing symmetries suggests that there may be distortions from the D_{2h} geometry. However it is known that this molecule has low-lying states. There are also exceptions to this argument. One exception to the argument that might be important in this molecule is the singlet biradical. Consider a molecule that has two identical molecular orbitals localized to different parts of the molecule and which are not conjugated terribly well to each other. Suppose electron-electron repulsion results in one electron in each of these orbitals - at least in many configurations - so that each part of the molecule can be considered a radical. Then there are two nearly degenerate singlet states of this molecule, one that is even under interchange of the electrons in these orbitals, another that is odd under this interchange. However it is also clear that these states will not mix appreciably when the symmetry is changed so these orbitals are not identical - the electron-electron repulsion and weak conjugation result in little mixing. Some of the states discussed above have considerable biradical character. On the other hand this simple argument works only for one pair of states and we found relatively low lying states of all symmetries. However such pairs of states are also (for identical reasons) not expected to have large transition dipole matrix elements. The molecule is known experimentally to have a strong optical absorption band so this is inconsistent with this biradical mechanism.

We have done two calculations to test the hypothesis that this molecule has a lower symmetry than D_{2h} . Both have used the SBK⁺⁺ basis. First we took the optimized coordinates and orbitals from the A_g state of the D_{2h} M13x2+7 calculation. We changed the molecular symmetry to C_s , with the mirror plane chosen to be the plane of the molecule. This choice seemed consistent with preliminary calculations and the nature of the lowest lying excited states, which are multiplied by unity by the action of this mirror reflection. Some of the orbitals were then modified to distort them from representations of D_{2h} to representations of C_s . An M13x2+7 MCSCF calculation was then run starting from these orbitals. It was observed that the energy decreased by 0.03 H and that there was a dipole of 1.24 D. This dipole moment was primarily along the long axis of the molecule. This state was then optimized in C_s , resulting in a final energy of -232.68686 H and a dipole of 1.29D. The dipole moments and other molecular asymmetries of this state - e.g. the optimized atomic separations - are consistent with numerical and optimization error and C_{2v} symmetry with the rotation axis along the long axis of the molecule. It seems reasonable to conclude that the symmetry of this molecule is less than D_{2h} . However when excited states of this molecule were calculated it was observed that the lowest lying excited state transformed like a non-trivial representation of C_{2v} . The first excited state changes sign under the action of the mirror plane that was preserved in the calculation. This suggested to us that the actual molecule might have still lower symmetry. Therefore we decided to distort the molecule to C_1 symmetry by moving the nickel and sulfur nuclei by about .01 angstroms in various directions to decrease the apparent C_{2v} symmetry to C_1 and perform another M13x2+7

calculation to find if this lowered the energy. This did, in fact, lower the energy by about .01 H. The subsequent geometry calculation has not yet converged – in fact only two geometry steps (using rather good initial positions and the Hessian available from the D_{2h} MCSCF geometry optimization) have been taken. All the properties that we have examined for this incomplete run are consistent with a final symmetry of C_s with the mirror plane passing through the nickel and the midpoints between identical particles (e.g. the two sulfurs) in each ligand. These properties include the gradients, predicted positions of the particles, the electric dipole moments of the state and some components of the wave function and some of the larger CI coefficients. These properties may also be consistent with C_{2v} with the rotation axis perpendicular to the plane of the molecule, or with yet another symmetry. The present lowest energy we have achieved with this basis for this molecule this symmetry-less calculation, with the energy -232.69721 H. The CI energy for the lowest lying excited state using the same active space and MCSCF orbitals optimized for the ground state is -232.64424 H. The energy difference between these states is roughly consistent with experimental results. Essentially no orbital configurations that contribute to the ground state also contribute to this excited state.

We believe that we have convincing evidence that at this (relatively high) level of theory this molecule does not have D_{2h} symmetry. However we do not at this time believe that we have convincing evidence for the actual symmetry. We note that the symmetry of the molecule in the crystal structure from which experimental (D_{2h}) coordinates have been derived is actually C_1 . This is inconsistent with either of our current predictions of C_s or C_{2v} .

V) Discussion

We have done several calculations on nickel dithiolene. We found that if the system is constrained to have D_{2h} geometry then the state with the lowest calculated energy is a singlet A_g state. However this energy state is very complicated in the sense that it can not be described in terms of a small number of configurations / Slater determinants. In striking contrast when identical configurations are allowed states with certain other symmetries have higher energies but are well approximated by a single configuration. Thus (the relatively easy) calculations which include no dynamic correlation or only a small number of conformations give result in these states with other symmetries having higher apparent energies than the A_g state. It is also the case that the excitation energies and particularly the near infrared absorption band which is of great practical interest require a good evaluation of the ground state energy and, particularly, of the energy differences between the ground and excited state energies. Unfortunately we have found that these energy differences depend strongly on the degree of dynamic correlation considered in the system. Increasing the dynamic correlation to verify that the calculation has converged is a relatively difficult task, particularly given the rather small energy differences that are considered. However it seems likely that the degree of correlation considered in this work is adequate to give reasonable results for energy differences as these seem not to be terribly different for various high levels of correlation we have considered.

We believe that we have correctly identified the states that need to be included in a MCSCF calculation with D_{2h} symmetry. Most importantly these include molecular orbitals which have a strong nickel d contribution and the frontier pi orbitals. It seems plausible that these orbitals are also important in other situations in which a transition metal has a partially filled

d or f band. It may be that the results we have found for this compound are unusually complicated because there are two nearly degenerate configurations of the ligand pi orbitals that have rather different conjugation to the d orbitals – specifically to the B_{2g} d orbital. However there are also significant contributions (CI coefficients close to .05) from configurations involving other d orbitals. Thus we hypothesize that even molecules that do not have pi system degeneracies but have partially filled d or f orbitals, the energies of which are not too strongly modified by mixing with other molecular orbitals may require (and should at least be examined for) considerable dynamic electron correlation involving these partially filled orbitals.

Acknowledgements: This work supported by the AFOSR and through the summer faculty program and the DOD high performance computer program. It is a pleasure to thank both my Airforce contacts, Ruth Pachter and Douglas Dudis who suggested this problem and who provided valuable suggestions of how to achieve various objectives. I would also like to thank Robert Zellmer his collaborative work and many suggestions and discussions.

References:

- 1) K.H. Brexhage and U.T. Muller-Westerhoff IEEE J. Quantum Elect. **QE-8** 759 (1972) and U.S. Patent 3,743,964
- 2) S.M. Kuebler and R.G. Deming Chem. Phys. Lett. **250** 120 (1994)
- 3) J.-L. Zuo, T.-M. Yao, F. You, X.-Z. You, H.-K. Fun and B.-C. Yip J. Mater. Chem. **6** 1633 (1996)
- 4) M.W. Schmidt *et al.* J. Comp. Chem. **14**, 1347 (1993)

Table 1

Name	Occupied non-d	Unoccupied non-d	D	Singly occupied
M10x8+0	$A_u B_{1g} B_{3u} B_{1u}$	$B_{3g} B_{2g} A_g A_u$	$A_{g3} B_{1g} B_{2g} B_{3g}$	None
M13x2+7	$A_g A_u 2B_{1u} B_{2u}$ $B_{3u} B_{1g} B_{2g} B_{3g}$	B_{3g}	$A_{g2} A_{g3} B_{1g} B_{2g}$ B_{3g}	$A_g A_u B_{1u} B_{2u}$ $B_{3u} B_{1g} B_{2g}$
M14x2+6	$A_g A_u 2B_{1u} B_{2u}$ $B_{3u} 2B_{1g} B_{2g} B_{3g}$	B_{3g}	$A_{g2} A_{g3} B_{1g} B_{2g}$ B_{3g}	$A_g A_u B_{1u} B_{3u}$ $B_{1g} B_{2g}$
M7x2+0		B_{3g}	$A_{g3} B_{1g} B_{2g} B_{3g}$	None

This table defines the calculational schemes discussed in the text and other tables. Listed are the name and the symmetries of various orbitals in the active space. The second column are those orbitals not having significant Nickel d character which are doubly occupied in the A_g reference state, the third symmetries and sequence numbers of those orbitals having substantial nickel d character. The B_{1g} orbital is always empty in the A_g reference state, the others are invariably filled. The final column is the symmetries of the orbitals that can be singly occupied.

Table 2

Name	Sx	Sy	Cx	Cy	Hx	Hy
ROHF5	1.6954	1.7903	0.7092	3.1540	1.1990	4.1302
TCSCF	1.6502	1.6663	0.7069	3.0581	1.2162	4.0240
M14x2+6 Ag	1.5664	1.5319	0.6894	2.9907	1.2516	3.9258
M10x8+0 Ag	1.5724	1.5484	0.6893	3.0042	1.2505	3.9400

This table gives the equilibrium coordinates calculated with various calculational techniques in D_{2h} . As the nickel is at the origin and the molecule is in the xy -plane only six coordinates need to be specified. The x coordinate is given first, then the y . The sulfur, carbon and hydrogen coordinates are given in that order. All distances are given in Angstroms.

Table 3

Name	Geometry	Energy	CSF-S	B _{1g}	B _{2g}	B _{3g}	A _g	B _{1u}	B _{2u}	B _{3u}
ROHF	ROHF	.55029	1	2	2	2	1	1	1	1
TCSCF	TCSCF	.47664	2	2	2	2	2	2	1.309	0.6904
M14x2 +6A _g	M14x2+6 A _g	.65304	29192	1.9047	1.9811	1.8638	1.9792	0.1176	1.9708	0.1768
M14x2 +6A _g	M10x8+0 A _g	.65281	29192	1.9007	1.9807	1.8583	1.9786	0.1230	1.9669	0.1864
M14x2 +6A _u	M10x8+0 A _g	.60899	29192	1.9935	1.9703	1.4416	1.9710	1.0267	1.0034	0.5863
M14x2 +6B _{1g}	M10x8+0 A _g	.59504	29272	1.8784	1.0498	1.9686	1.9867	0.1571	1.9851	1.0240
M14x2 +6B _{2u}	M10x8+0 A _g	.57387	29192	1.8836	1.9763	1.0308	1.9783	0.1366	1.0070	1.9851
M14x2 +6B _{3u}	M10x8+0 A _g	.58384	29248	1.9962	1.9910	1.9971	0.9981	1.0046	1.0021	1.0046
M13x2 +6A _g	M10x8+0 A _g	.63706	24444	1.8777	1.9779	1.8192	1.9806	0.1464	1.9621	0.2335
M13x2 +7A _u	M10x8+0 A _g	.60641	24416	1.9930	1.9696	1.4371	1.9703	1.0259	1.0038	0.5921
M10x8 +0A _g	M10x8+0 A _g	.59437	21578	1.8806	1.9687	1.8191	1.9670	0.1623	1.9345	0.2518
M10x8/ 2A _g	M10x8+0 A _g	.56137	101	1.9477	1.9792	1.9463	1.9744	0.0703	1.9897	0.0559
M10x8/ 4A _g	M10x8+0 A _g	.59234	3221	1.8827	1.9698	1.8281	1.9698	0.1552	1.9405	0.2367
M10x8 +0A _u	M10x8+0 A _g	.55034	21168	1.9905	1.9644	1.4321	1.9627	1.0293	1.0004	0.5899
M10x8 +0B _{1g}	M10x8+0 A _g	.53194	21228	1.8527	1.0260	1.9702	1.9525	0.2278	1.9492	1.0451
M10x8 +0B _{2g}	M10x8+0 A _g	.48116	21278	1.9824	1.9753	1.0531	1.9708	1.0264	1.4650	0.5018
M10x8 +0B _{3g}	M10x8+0 A _g	.53783	21228	1.8457	1.9845	1.9941	0.9954	0.2057	1.9506	1.0489
M10x8 +0B _{1u}	M10x8+0 A _g	.51637	21168	1.9929	1.0474	1.9507	1.9362	1.0555	1.0008	1.0001
M10x8 +0B _{2u}	M10x8+0 A _g	.52636	21168	1.8495	1.9685	1.0025	1.9671	0.2908	1.1211	1.8851
M10x8 +0B _{3u}	M10x8+0 A _g	.51984	21168	1.9943	1.9884	1.9974	0.9967	1.0050	1.0002	1.0030

This table gives the energies and parameters related to the wave function of various calculations that have been performed. These calculations all used the SBK⁺⁺ basis as described in the text. The names given in the first two columns are as described in the text. The energies have been truncated. The actual energy involved is $-232.x$ Hartrees where x is the given energy. The numbers given in subsequent columns are the occupation numbers of approximate natural orbitals of various symmetries.

Table 4

Name	Geometry	Energy	CSF-S	B _{1g}	B _{2g}	B _{3g}	A _g	B _{1g}	B _{1u}	B _{3g}
M10x8/ 4A _g	M10x8+0 A _g	.59234	3221	1.8827	1.9698	1.8281	1.9698	0.1552	1.9405	0.2367
M7x2+ 0A _g	M10x8+0 A _g	.82992	91	1.8374	1.9770	1.7702	1.9733	0.2091	1.9186	0.3260
M7x2+ 0A _g /fg	M10x8+0 A _g	.84848	91	1.8300	1.9768	1.7240	1.9973	0.2511	1.9224	0.3837

This table gives results for two calculations done in different electron basis sets and the same geometry for the (highly correlated) A_g state. The energy in the SBK⁺⁺ basis is -232.59234 H, those in the TZV^{*} and TZV⁺⁺ bases described in the text are -3250.82992 H and -3250.84848 H. Note that the occupation numbers are similar and that the dynamic correlation seems to increase with increasing quality of the basis set.

REFINED REISSNER'S VARIATIONAL SOLUTION IN THE VICINITY
OF STRESS SINGULARITIES

Kishore V. Pochiraju
Assistant Professor
Department of Mechanical Engineering

Stevens Institute of Technology
Castle Point on Hudson
Hoboken, NJ 07030

Final Report for:
Summer Faculty Research Program
Wright Laboratory

Sponsored by:
Air Force Office of Scientific Research
Bolling Air Force Base, DC

And

Wright Laboratory

September, 1997

Refined Reissner's Variational Solution in the Vicinity of Stress Singularities

Kishore V. Pochiraju
Assistant Professor
Department of Mechanical Engineering
Stevens Institute of Technology
Castle Point on Hudson
Hoboken, NJ 07030

Abstract

The prediction of micro-mechanical damage initiation and growth in composite materials requires accurate stress and deformation analyses. Prior research at Wright Laboratories established the effectiveness of Reissner's variational method in determining the detailed stress fields in composite structures and for studying the micro-mechanical damage mechanisms. The present effort investigates the ability of this variational method to capture the details of the stress fields in the vicinity of bi-material cracks and corners in a single-fiber axisymmetric (concentric cylinder) model. The singular stress fields in these local regions drive the initiation and/or propagation of damage in the composite.

The results of this project are two-fold. First, several example problems varying the local geometry and boundary conditions are studied and the stress distributions obtained from asymptotic analyses are compared with the variational solutions. The variational solution is shown to accurately capture two of the three stress components within the meridian plane, namely the opening stress component and the shear stress component. The axial stress component, however, was significantly different from the asymptotic variation, possibly due to the influence of the boundary condition coincident with the singular point. This prompted modifications of the variational solution procedure to accommodate the exact singular behavior. Modifications without a fundamental changes (stress function assumptions) to the variational formulation are investigated. A method, named the Interior Point Matching (IPM), which replaces a selected area around the singular point with asymptotic stress fields, ensures the continuity of the stress fields at an interior point, and satisfies the global equilibrium and boundary conditions with the embedded singular fields is developed. The Axisymmetric Damage Model (ADM) implementation of Wright Laboratories is enhanced to include local asymptotic solutions (the power of singularity and the angular variations), the software implementation of Interior Point Matching Method is completed and tested, and the example problems are solved to determine the extent of refinement and limitations of the modified solution. This report summarizes the results of the initial comparison and IPM development.

Refined Reissner's Variational Solution in the Vicinity of Stress Singularities

Kishore V. Pochiraju

1 Introduction

The ability to predict damage initiation and growth in composite structures relies on accurate stress solutions and simulation of micro-mechanical damage processes. Pagano [1] applied the approximate elasticity model based on Reissner's variational formulation [2] for the prediction of micro-mechanical failure modes in brittle matrix composites. Tandon and Pagano [3] recently investigated the failure modes and stress states of a single fiber pullout model. The solution technique, based on Reissner's variational formulation, entails dividing the structure into regions, assuming the distribution of some components of a stress field within a region, determining the spatial structure of the other components that satisfy the equilibrium and boundary conditions, and inter-region continuity conditions. Pagano [4], Kurtz and Pagano [5], and Brown [6] describe the extension of this technique to axisymmetric concentric cylinder model.

The single fiber axisymmetric model was also investigated earlier by Pochiraju [7] using a local asymptotic and a global finite element analysis. This effort employs a local-global matching method to effectively determine the detail spatial structure and magnitude of the locally singular stress field as well as the complete global stress distribution in the single fiber concentric cylinder model. The local-global matching method consists of three components: a local analysis, a global analysis, and proper matching of the local asymptotic field to the global complete stress field. (Pochiraju, Lau, Wang [8]). The local regions are identified as the areas where the geometry and the presence of interface leads to stress accentuation and possibly a singularity. In such local regions, asymptotic solutions are obtained for several fiber-matrix interface conditions. In order to determine the effects of applied thermal residual loading, mechanical pulling and boundary conditions on the local fields, a global finite element analysis is performed with mesh refinement in the local regions. No singularity information is embedded into the finite element analysis. Matching the angular variation and radial variation of stress fields obtained from the finite element analysis and with those obtained from asymptotic analysis determines the nature of the local stress fields in the local regions. The method as developed is applicable for various fiber-matrix interface conditions: namely perfectly bonded interface, partially debonded interface with interfacial crack, or debonded interface with frictional interface sliding [9].

The motivation to solve for the local stress field is that these accentuated stresses, strains and energies are likely to induce damage. The research presented in this report is motivated to include the characteristics of asymptotically singular stress fields within the Reissner's variational solution. There are several significant differences in the nature of the variational and asymptotic solutions and are listed below:

- The variational solution solves the axisymmetric equilibrium, boundary conditions and the constitutive relationships. Separable solutions with power type of radial singularities exist for plane strain problems. However, Zak [10] showed, that through the transformation of coordinates from global to local systems, that the axisymmetric solution degenerates (curvature terms become insignificant) to the plane strain solutions in small local regions around a point.
- The variational solution for axisymmetric problems is separable in the axial (Z) and radial (R) directions. The asymptotic stress fields are the solutions separable in the polar coordinate system (ρ, θ) with the origin at the point of singularity.
- The variational solution is determined by assuming the radial (R) distribution of two of the four stress components and determining the functional form of the other components by the minimization of the potential energy. This is a complete solution and satisfies the equilibrium and boundary conditions. The asymptotic solution is a partial solution and consists of undetermined coefficients. These coefficients may be obtained from loading and boundary conditions or by comparison with a global complete solution.

The variational formulation, as implemented in the Axisymmetric Damage Model, assumes a linear radial variation of the axial and hoop stresses within any solution element (Layer) and the axial variation is determined as a solution to a first order differential equation. It may be conceptualized that an assumption of stress fields of the type given in Eq. (1) for M singular fields and with N terms/field expansion of asymptotic solution for two stress components and deriving the nature of the other components using the variational technique, but such an effort would be algebraically tedious, requiring lengthy development for concept validation.

$$\sigma_{\theta\theta} = \sum_{j=1}^M \left(\sum_{i=1}^{N_j} K_i \rho_j^{\lambda_i} \langle \tilde{\sigma}_{\theta\theta}(\theta_j) \rangle \right), \sigma_{zz} = \sum_{j=1}^M \left(\sum_{i=1}^{N_j} K_i \rho_j^{\lambda_i} \langle \tilde{\sigma}_{zz}(\theta_j) \rangle \right) \quad (1)$$

Methods for enhancing the solutions near bi-material cracks and corners by selectively using the asymptotic solution are investigated.

2 Comparison of Asymptotic and Variational Solutions

In this section, the asymptotic and axisymmetric variational solutions are compared for several crack and corner problems. Figure 1 shows schematics of the concentric cylinder model along with the R-Z meridian plane for the axisymmetric problem, and the local solution for a typical fiber pullout problem. A local region is shown in the detail-A which surrounds the point of singularity, O. First a short description of the asymptotic solutions in the local region along with a method of matching the local solution with a global numerical solution is presented. The variational solution is summarized in the second sub-section. An algorithm for determining the angular variation of stresses around the singular point from the variational solution is presented. A series of problems involving cracks and corner singularities are investigated. A comparison angular variation of the stress distributions obtained from the variational solution and asymptotic analyses is presented. This comparison is conducted at a selected radius where the leading singular term in the asymptotic analysis is believed to be dominant. A second global solution from Finite Element Method (FEM) is also presented for reference.

2.1 Local Asymptotic Solution

The point, O, is the location of material and geometric discontinuity. The local stresses at O may be singular in nature depending upon the fiber and matrix properties and the fiber-matrix interface conditions. In order to determine the spatial distributions of the stress fields in the local region, the governing equations are formulated for axisymmetric stresses in {R, Z, Φ } coordinates and then transformed to the local { ρ , θ } coordinates, retaining only terms valid as $\rho \rightarrow 0$. Stress fields separable in the ρ & θ coordinates and with radial power-type of singularities are considered. Eq. (2) shows the function form of stress components near the point of singularity as determined from the asymptotic analysis.

$$\sigma_{ij}(\rho, \theta) = k \rho^\lambda \tilde{\sigma}_{ij}(\theta) \quad (\lambda < 0; \rho \rightarrow 0) \quad (2)$$

The angular distribution functions, $\tilde{\sigma}_{ij}(\theta)$, for the matrix-domain and fiber-domain are determined from the Williams[11] type of stress functions. Eq. (3) shows the typical stress function required to derive the stress components for axisymmetric problem.

$$\varphi(\theta) = A \cos(\lambda + 3)\theta + B \sin(\lambda + 3)\theta + C \cos(\lambda)\theta + D \sin(\lambda)\theta \quad (3)$$

The traction free boundary conditions at $\theta=0$ and $\theta=3\pi/2$, and the perfectly-bonded fiber-matrix interface conditions at $\theta=\pi/2$, form a system of eight homogeneous equations ([7]):

$$[C_{ij}(\lambda)] A = 0 \quad (4)$$

where λ is the eigenvalue, and $A = [A^m, B^m, C^m, D^m, A^f, B^f, C^f, D^f]^T$ is its associated eigenvector. For nontrivial solution, the determinant of $[C_{mn}(\lambda)]$ must vanish. The eigenpair $\{\lambda, A\}$ determined from Eq. (4) provides the ρ - and θ -dependent structure, ρ^λ and $\tilde{\sigma}_{ij}(\theta)$, of the singular field. A determinant search algorithm was used to find the eigenvalue λ within the admissible range of $0 > \lambda > -1$. For some fiber-matrix combinations, there can be more than one solution for λ in the admissible range. We are concerned with the smallest admissible λ , which gives rise to the most dominant singular stresses. The θ -dependence of the singular field, $\tilde{\sigma}_{ij}(\theta)$, is determinable from solution of the eigenvector A to within an arbitrary constant. We normalized $\tilde{\sigma}_{ij}(\theta)$ by choosing the arbitrary constant so that $\tilde{\sigma}_{\theta\theta}(\theta^*) = 1$, where θ^* is the angular position of points on the interface.

The amplitude factor k of Eq. (2) is to be determined from the full-field solution. This is accomplished by appropriately matching the singular field with the full-field stress distribution provided by an analyses methods such as FEM or other variational methods. This matching was carried out earlier [8,9] using the FEM. A displacement-based axisymmetric finite element model, as shown in Figure 2, with quadratic Lagrange elements was used to compute the global full-field solution. Near the fiber-protrusion point O , elements were arranged in concentric rings with boundaries given by: $(\rho/R_O)_n = 10^{-8} \{1 + (10^{0.2})^{n-1}\}$ where n denotes the n -th ring. The first ring encircling the fiber-protrusion point consisted of quadratic triangular elements degenerated from Lagrange quadrilateral elements which formed the rest of the mesh. No special implementation for singularity was imposed on these elements. Within the finite element spatial domain, we searched for a sub-region where the full-field stresses, $\sigma_{ij}(r, \theta)$ FEM, have the identical θ -dependence as that of the singular solution, $\tilde{\sigma}_{ij}(\theta)$. If the finite element stresses match $\tilde{\sigma}_{ij}(\theta)$, then they also match the eigenvector A and its associated eigenvalue λ . One may choose any stress component, say $\sigma_{\theta\theta}$, at any angle, say θ^* , to determine k :

$$k = \frac{\sigma_{\theta\theta}(\rho, \theta^*)^{FEM}}{\rho^\lambda \tilde{\sigma}_{\theta\theta}(\theta^*)} \quad (5)$$

However, starting from the second ring of elements, results show good matching characteristics typical of Figure 2. It is expected that as ρ/R_O increases, the one-term singular solution will deviate from the full-field solution, resulting in less spectacular angular matching at sampling points with large ρ/R_O . A root-mean-square error parameter, E , was developed to quantify mismatching along any arc of constant radius ρ . Finite element results were sampled at N points of varying θ -value along the arc. At each sampling point p (at θ_p), the average of the squares of the mismatch for three stress components. The expression for the error measure is shown in Eq.(6). E is zero when there is a perfect match. K is determined from the regions where E is minimum.

$$E = \sqrt{\frac{\sum_{p=1}^N \text{Average} \left\{ \left[\frac{\sigma_{ij}(\rho, \theta_p)^{FEM}}{k \rho^\lambda} - \tilde{\sigma}_{ij}(\theta_p)^{asympt} \right]^2 \right\}}{N}} \quad (6)$$

2.2 Variational Solution

The axisymmetric damage model was developed in order to approximate the elastic stress field and energy release rates of bodies in the form of concentric cylinders and contains damaged regions in the form of annular or penny-shaped cracks in the constituents and/or debonds between them. The model is generated by subdividing the body into regions consisting of a core and a number of shells of constant length and satisfying the Reissner variational equation with an assumed stress field in each region. That is, we set

$$\delta J = 0 \quad (7)$$

$$J = \int_V F dV - \int_{S'} \tilde{T}_i U_i ds \quad (8)$$

$$F = \frac{1}{2} \tau_{ij} (U_{i,j} + U_{j,i}) - W(\tau_{ij}, e_{ij}) \quad (9)$$

In these equations, W is the complementary energy, τ_{ij} and U_i are the stress and displacement components, respectively, in Cartesian coordinates, e_{ij} are the mathematical free expansional or non-mechanical strains, V is the volume enclosed by S , S' is the part of S on which one or more traction components are prescribed and \tilde{T}_i are the Cartesian components of the prescribed tractions. Further, a comma followed by a subscript(s) implies differentiation with respect to the appropriate coordinate(s) and the summation convention is understood.

Reissner (1950) has shown that the governing equations of elasticity can be obtained as a consequence of the variational equation provided both stresses and displacements are subject to variation in the application of (7). The stress field is assumed such that σ_{zz} and $\sigma_{\theta\theta}$ are linear in R within each region, while the forms of σ_{RR} and σ_{RZ} are chosen to satisfy the axisymmetric equilibrium equations of linear elasticity. Letting,

$$\sigma_i = \sigma_{zz}, \sigma_i = \sigma_{\theta\theta}, \sigma_i = \sigma_{RR}, \sigma_i = \sigma_{RZ} \quad (10)$$

(and the analogous relation for the engineering strain components ϵ_i ($i=1, 2, 3, 5$) and hygrothermal free expansional strain components e_i ($i = 1, 2, 3$)), we arrive at the relations in the region $R_1 \leq R \leq R_2$:

$$\sigma_i = p_{ij} f_j^{(i)} \quad (i = 1, 2, 3, 5; J=1, 2, \dots, 5) \quad (11)$$

where $f_j^{(i)}$ are known shape functions of R defined such that:

$$p_{i\alpha} = \sigma_i(R_\alpha, Z) \quad (i = 1, 2, 3, 5; J=1, 2, \dots, 5) \quad (12)$$

In order to maintain consistency with our postulated stress field, we further assume that eqs. (11) hold on the boundaries, as well as within the medium itself. The remaining dependent variables follow directly from the mathematics without further assumptions. They are the weighted displacements:

$$(\bar{u}, u^*, \hat{u}, \bar{\bar{u}}) = \int_{r_1}^{r_2} u(1, r, r^2, r^3) dr \quad (13)$$

$$(w^*, \hat{w}) = \int_{r_1}^{r_2} w(r, r^2) dr \quad (14)$$

The interfacial displacements u_α , w_α ($\alpha = 1, 2$), or displacements on the radial boundaries $R = r_1, r_2$, only enter the formulation if they are prescribed or if we have relative slip with friction at the interface. For a body composed of a core region plus N shells, the formulation leads to the solution of $18N + 16$ algebraic and ordinary differential equations in Z . On planes,

$Z=\text{constant}$, the weighted displacement or traction quantities are specified in certain pairs. Furthermore, continuity conditions can be written for the surfaces $R = \text{constant}$ which are internal to the medium. Finally, the boundary conditions on $z = z_1, z_2$, or end conditions, can be expressed by prescribing one term from each of the following products. The regions are selected such that the thermoelastic properties are constant and the boundary conditions do not change character on any of the bounding surfaces (i.e., traction and/or displacement components prescribed or continuity prescribed) within each region. The number of regions, in particular in the r direction, can be increased in order to improve the solution accuracy.

Since the field equations within each material are linear differential equations with constant coefficients, the general form of the solution for any of the dependent variables $P(z)$ is expressed by:

$$P(Z) = P_h(Z) + \sum_i A_i e^{\lambda_i Z} + P_p(Z) \quad (15)$$

within each layer where A_i are constants, λ_i are eigenvalues of a determinant, $P_h(z)$ is the polynomial type of homogenous solution (repeated roots), and $P_p(z)$ is a particular solution, which in the present case is a simple polynomial. This completes the boundary value problem formulation with the variational model.

2.3 Angular variation determination from variational solution

To tabulate the stress fields in the ADM solution in a region, following algorithm is used.

1. Given the point of singularity, R_0 and Z_0
2. Given ρ , generate a series of θ values from θ_1 start to θ_2 at $\Delta\theta$ increment
3. For every ρ and θ :
 4. Determine the global coordinate R and Z

$$R = R_0 + \rho \cos(\theta)$$

$$Z = Z_0 - \rho \sin(\theta)$$
 5. Determine the section number, i_{sec} , based on the Z value
 6. Determine the section properties for i_{sec}
 7. Determine the layer number, i_{layer} , based on the R value
 8. Do a transformation of Z to local coordinate, Z_{local} of the section and layer.
 9. Construct the solution for the unknown quantities [4] for that layer at $Z = Z_{local}$
 10. Store the solution quantities and their derivatives
11. Do radial interpolation using the appropriate equations for core and coating:

For core:

$$\begin{aligned} \sigma_{zz}(r) &= \sigma_{zz}(r_1) \frac{(r_2 - r_1)}{(r_1 - r_2)} + \sigma_{zz}(r_2) \frac{(r - r_1)}{(r_1 - r_2)} \\ \sigma_{\theta\theta}(r) &= \sigma_{\theta\theta}(r_1) \frac{(r_2 - r_1)}{(r_1 - r_2)} + \sigma_{\theta\theta}(r_2) \frac{(r - r_1)}{(r_1 - r_2)} \\ \sigma_{RZ}(r) &= \sigma_{RZ}(r_2) \frac{(r - r_1)}{(r_1 - r_2)} + \sigma_{RZ}^I (r - r_2) r \\ \sigma_{RR}(r) &= \sigma_{RR}(r_1) \frac{(r_2 - r_1)}{(r_1 - r_2)} + \sigma_{RR}(r_2) \frac{(r - r_1)}{(r_1 - r_2)} + \sigma_{RR}^I (r^2 - r_2^2) r + \sigma_{RR}^{II} (r^2 - r_2) r \end{aligned}$$

For Coating:

$$\begin{aligned}
\sigma_{zz}(r) &= \sigma_{zz}(r_1) \frac{(r_2 - r_1)}{(r_1 - r_2)} + \sigma_{zz}(r_2) \frac{(r - r_1)}{(r_1 - r_2)} \\
\sigma_{\theta\theta}(r) &= \sigma_{\theta\theta}(r_1) \frac{(r_2 - r_1)}{(r_1 - r_2)} + \sigma_{\theta\theta}(r_2) \frac{(r - r_1)}{(r_1 - r_2)} \\
\sigma_{RR}(r) &= \sigma_{RR}(r_1) \frac{(r_2 - r_1)}{(r_1 - r_2)} + \sigma_{RR}(r_2) \frac{(r - r_1)}{(r_1 - r_2)} + \sigma_{RR}^I (r^2 - r_2^2)(r^3 - r_1^3 r_2^3 r + r_1 r_2 (r_1 + r_2)) \\
&\quad + \sigma_{RR}^{II} (r^2 - (r_1 + r_2)r + r_1 r_2) + \sigma_{RR}^{III} \frac{(r^2 - (r_1 + r_2))}{r_1 r_2 r} \\
\sigma_{RZ}(r) &= \sigma_{RZ}(r_1) \frac{r}{r_1} + \sigma_{RZ}(r_2) \frac{(r - r_1)}{r_2 (r_1 - r_2)} + \sigma_{RZ}^I \left\{ (r_1 + r_2)r - \frac{(r_1^2 + r_1 r_2 + r_2)r}{r_1^2 + r_2^2} + \frac{1}{r} \right\}
\end{aligned}$$

where σ^I , σ^{II} , and σ^{III} correspond to the solution quantities as given in Eq. (11) [4].

12. Increment θ by $\Delta\theta$

13. Check if $\theta = \theta_2$, YES: Stop, NO: goto 3

Table 1: Material properties and power of singularity for configuration in Problem-A

Material	E_f	ν_f	E_m	ν_m	λ
Polyester/Epoxy	3.25 GPa	0.35	4.0 GPa	0.35	-0.00463
Silicon Carbide/ Borosilicate	410 GPa	0.2	63 GPa	0.2	-0.11206

2.4 Comparison of ADM and Asymptotic Solutions

The algorithm presented in the previous section was implemented into the current axisymmetric damage model. The results presented in this section are for unmodified variational solution. Several problem involving crack and corner geometry were then investigated to determine the radial and angular distribution of the stresses predicted by the variational model. In this report, the following four case studies are presented.

Problem A: Corner singularity in the single fiber push-out model: Figure 3 shows the geometry of the axisymmetric concentric cylinder model typically employed to simulate fiber push-in experiments. The singularity at the ends of the model is material dependent is given for two material combinations in Table 1.

Problem B: The problem of an interface crack with the debonded faces sliding with friction is considered. The local coordinate system at the crack tip and the geometry of the model is shown in Figure 4. The fiber and matrix materials are taken to be Polyester and Epoxy, respectively. The coefficient of friction is assumed to be 0.52. These values correspond to recent push-in tests conducted by Bechel [12]. The power of the stress singularity for this case is -0.49605.

Problem C: The penny shaped crack in a fiber is considered as the third example. For this case the stress singularity is -0.5 and is material independent. The mode-1 loading case is considered and for this case the exact stress intensity factor for the infinite body is also known. Figure 5 shows the local coordinate system.

Problem D: The problem of a bi-material crack with open, traction-free, crack faces is considered. This is the case where the stress singularity is complex-valued. ($\lambda = -0.5 \pm 0.0076i$) Again polyester-epoxy system is considered. The local coordinate system is shown in Figure 6.

The comparison of angular variation for problem A reveals the nature of the variational solution around the corner singularities. The asymptotic behavior of the opening stress ($\sigma_{\theta\theta}$) and the shear stress ($\sigma_{\rho\theta}$) are captured by the variational solution. Figure 7 and Figure 8 show the comparison of the variational and asymptotic solution for problem A. The comparison is conducted at a distance of 1 μm from the singular point and the variational solution shows a good correlation with the field obtained from asymptotic analysis. Figure 9 shows the angular distribution of the radial stress (corresponds to the axial stress σ_{zz} in the axisymmetric coordinate system) for asymptotic and variational solutions. The variation of the radial stress (σ_r) significantly differs from the asymptotic behavior. The variational solution tends to a zero value at the interface consistent with the boundary condition imposed at that point in the solution. Figure 10 shows the radial variation of the axial stress component (σ_{zz}) in the fiber and matrix. This plot compares the stress distributions obtained from the FEM and variational solutions. There is a good correlation of the stress distributions between the two solutions in regions away from the singular point (at $z = 0$). This behavior is due to the boundary conditions imposed in the variational solution which require that the axial stress component (σ_{zz}) should vanish in both fiber and matrix at $z = 0$.

Problem-B is the frictional crack problem. The angular variation matching is conducted comparing asymptotic (Comninou-type of crack [13]), FEM and variational solutions. Again the opening stress ($\sigma_{\theta\theta}$) and the shear stress ($\sigma_{\rho\theta}$) are compared. The comparison shows additional characteristics of the variational solution. The opening stress, Figure 11, shows a good match between all the three cases though the FEM analysis is an incremental analysis and the variational and asymptotic analyses are independent of the load history. The shear stress, Figure 12, shows that the overall distribution of the stress component in the vicinity of the stress singularity is comparable, the discontinuities in the shear stress component in the ADM solutions correspond to the jump between the sections where shear stress continuity is not imposed.

The penny shaped crack in a polyester fiber is considered. The applied loading was pure mode-I and the exact stress intensity factor is known. Figure 13 shows the comparison of the opening stresses between asymptotic and ADM solutions. There is a good correlation between the ADM and asymptotic solutions. The shear stress angular distribution is shown in Figure 14. Once again the jump across the sections in the variational model causes the discontinuity of the shear stress. The results of the angular variation comparisons are presented for the bi-material interface crack problem in Figures Figure 15 and Figure 16. The variational solution captures the opening and shear stress distributions as predicted by the asymptotic solution for this case also.

Stress intensity (Scale) factors can be obtained by single point matching method as described in the previous sub-section. However, since an error basis was not developed for matching using the variational solution, the radius and the component of matching is arbitrary and may be subjected to a large error. Therefore, the work on stress intensity factor determination is not presented here.

3 Refining Variational Solution with Asymptotics

In this section a technique for embedding the asymptotic solutions within selected regions of the model is described. This technique modifies the variational solution while ensuring that the global equilibrium, boundary conditions and the constitutive relationships are satisfied and

maintaining stress continuity between the asymptotic and variational solution at a selected point inside the domain.

3.1 Modified Variational Solution

Consider the axisymmetric model, corresponding to Problem-A, as shown in Figure 17. In obtaining the refined solution, a region, of radius ρ^* , is identified around the singular point and in this region the asymptotic solution determined by solving the local homogenous problem prevails and the obtained variational solution is ignored. The local asymptotic solution however is determined with unknown scale coefficient(s) which depend upon the global solution. This scale factor needs to be determined using a global solution.

Since a small region around the singular point is excluded in the variational solution, several boundary conditions are also excluded in this region. This requires additional equations so that the undetermined coefficients in the variational formulation can be computed. These additional equations are obtained by matching the asymptotic and variational solutions at selected radius

A point on the boundary between the variational and asymptotic solution is identified (ρ^* , θ^*). At this point continuity conditions are imposed such that the normal, shear and radial stresses are continuous between the variational solution and the asymptotic analysis. If there are 'M' boundary conditions associated with the singular point in the variational solution (thus determining M undetermined constants), and a 'N' term expansion of the asymptotic solution is considered, then N+M independent matching conditions are required to determine both the local and global solutions. For example in Problem-A, there are three boundary conditions associated with the singular point in the variational formulation. They are the axial stress in the fiber (σ_{zz}^f), the axial stress in the matrix (σ_{zz}^m), the shear stress (σ_{RZ} , continuous on fiber and matrix side) vanish. These conditions determine three unknown coefficients in the variational solution. If a one term asymptotic solution is considered, then one undetermined scale constant needs to be obtained by matching. Thus there are four unknown coefficients requiring four matching conditions. Following four conditions can be written at the matching radius, r^* . Replace these conditions at $R=R_f$, $Z=0$ by following conditions at $R=R_F$, $Z=Z^*$

@ $R=R_f$ & $Z=Z^*$ ($Z^* \neq 0$)

$$\begin{aligned}\sigma_{ZZ}(\text{ADM}) &= \sigma_{ZZ}(\text{ASYMP}) \text{ in fiber} \\ \sigma_{ZZ}(\text{ADM}) &= \sigma_{ZZ}(\text{ASYMP}) \text{ in matrix} \\ \sigma_{RZ}(\text{ADM}) &= \sigma_{RZ}(\text{ASYMP}) \\ \sigma_{RR}(\text{ADM}) &= \sigma_{RR}(\text{ASYMP})\end{aligned}\tag{16}$$

3.2 Software Implementation

The current ADM software implementation was modified to include the asymptotic behavior. Following enhancements were made to the software to include the asymptotic analysis and the refinement to the solution by embedding the asymptotic solution within the variational solution.

- A **framework** for handling several singular points within a model was implemented. Each of the singular points can have different powers of singularities and angular variations. This enables the solution modifications described in the previous section to be applied at several spatial locations simultaneously.
- A local homogenous problem can be described so that power of the stress singularity and the angular distributions can be computed within the ADM solution. The user identifies the point of singularity and describes the local homogenous boundary

conditions. The eigenvalue and eigenvectors for the local problems are computed from within the software.

- The computation of the unknown coefficients of the solution (Eq. 15) is modified so that the boundary conditions corresponding to the singular point are removed and the equations corresponding to the matching conditions shown in Eq. (16) are formulated. The solution of the **new system of the equilibrium equations** is carried out *simultaneously* determining the unknown coefficients in the variational solution as well as the **scale factors** for the asymptotic fields.
- A **post-processing** enhancements to determine the modified solution by considering the presence of the asymptotic solution within a small region is also developed.

Table 2 : Asymptotic Solution

POWER OF SINGULARITY: $\lambda = -.1121$	
COEFFICIENTS OF ANGULAR VARIATION	
1	1.0000 (Arbitrarily Set)
2	1.8428
3	-1.3832
4	-1.3019
5	4.9462
6	1.0667
7	-6.2097
8	0.2440
Mixity = .1567	

Table 3: Original and modified stresses at the matching point

Stress	Original (MPa)	Modified (MPa)
σ_{zz}	-0.00002	-0.00835
$\sigma_{\phi\phi}$	0.01834	0.01345
σ_{RR}	0.03112	0.02339
σ_{RZ}	0.00085	0.00315

3.3 Characteristics of the refined solution

Using example problem-A, the original and modified solutions are compared. An arbitrary matching distance of $\rho^* = 1\text{E-}04$ mm is chosen for this example. The results of the local asymptotic solution is given in Table 2. This problem has a fixed mixity of normal and shear stresses and hence has one undetermined scaling constant for the local asymptotic solution.

A eleven layer variational model has 86 coefficients determined through the global equilibrium solution. In this system, three relations corresponding to the boundary conditions at the point of singularity are identified in the software as equations 18, 20 and 21. Following the method presented earlier, three equations are replaced with the matching equations given in Eq. (16). The fourth relation in Eq. (16) is written as an additional equation (87th) into the equilibrium solution. The variational equilibrium solution is solved along with the additional equation that determines the scale factor. Table 3 presents the original and modified state of stress at the matching point ($\rho^*, \theta=90$).

Figure 18 shows the axial variation of the original and modified solution plotted along the fiber-matrix interface. It can be seen that the solution away from the local singular point is

unaffected and the solution in the singular region corrects towards correct asymptotic behavior. This plot also shows that the matching distance from the variational solution perspective should be larger as the influence of the boundary condition (as seen as a local maximum near the singular point in the axial and shear stresses) seem to be of the order of $\rho = 0.1$ mm. The appropriate distance for the matching is currently being investigated.

4 Summary and suggested future work

In this summer project period, the characteristics of the variational solution in the vicinity of a stress singularity are investigated. Though the variational formulation does not contain any features of the asymptotic solution, the solution reflects the asymptotic nature in two of the three components. Effort was also focused on refining the solution near the stress singularities. This resulted in a technique that modifies the global equilibrium solution in the variational formulation such that an exact asymptotic solution is embedded near the point of singularity, continuity of stresses is maintained between the asymptotic solution and the variational solution. It is also shown that such modification effects only the local regions of the global solution and does not influence the solutions in the regions away from the singular points.

The modification to the variational solution presented here requires detailed investigation of several important issues.

- First is the determination of the radius, ρ^* , where both asymptotic solution and the ADM solutions are effective. In the proof of concept investigation presented here, this distance is specified arbitrarily based on the prior experience with the angular variation matching. Identification and validation of the error measures which can be used to establish an effective radial matching distance is crucial.
- The second investigation required is to generalize the methodology several types of singular fields within the ADM model. The boundary conditions corresponding to the variational solution differs from crack problems to corner problems. Based on the findings and the development presented in this report, a general procedure of modifying the global equilibrium system of equations within in the variational formulation can be established.
- As mentioned in the report, for some problems there are several terms in the asymptotic expansion which could be singular. Considering the powers of the asymptotic expansion higher than the most dominant singular term may be required. Considering the additional terms in the asymptotic solution will increase the domain in which the solution prevails. This creates additional flexibility in accurately finding a matching radius.
- The variational solution as implemented in the ADM model considered orthotropic materials. The asymptotic expansion presented here is valid for isotropic methods. A preliminary investigation into the nature of stress fields near the interfaces of the orthotropic materials and its effect on the presented methodology may be addressed.

5 Acknowledgements

Thanks are due to AFOSR for providing the financial support through the summer research program and to RDL for effectively administrating the program. Author wishes to thank Dr. N. Pagano of the Materials Laboratories and Dr. G. P. Tandon of Ad Tech Systems Research for their help and collaboration during this effort. Thanks are due to Maj. Paul Hesse, Branch Chief, MLBM and all the members of the MLBM group for helpful discussions and cooperation during my stay at the Wright Laboratories. Thanks to Mr. Milton (Dan) Danishek for assistance at the base.

6 References

1. Pagano, N.J., "On the micromechanical failure modes in a class of ideal brittle matrix composites," Wright Laboratories Report, to be published., 1997.
2. Reissner, E., "On a variational theorem in elasticity," J. Math. Phys, 29, 1950, pp. 90-95.
3. Tandon, G. P., and Pagano, N. J., "Micro-mechanical analysis of fiber push-out and re-push test," to be published, personal communication, 1997.
4. Pagano, N. J., "Axisymmetric micromechanical stress fields in composites," Proceedings 1991 IUTAM symposium on local mechanics concepts for composite material systems, Springer Verlag, 1991, pp. 1-26
5. Kurtz, R. D. and Pagano, N. J., Analysis of the deformation of a symmetrically loaded fiber embedded in a matrix material, Composites Engineering, 1 [1] (1991), pp. 13-27.
6. Brown, H. W., "Analysis of axisymmetric micro-mechanical concentric cylinder model," Wright Laboratories Report.
7. Pochiraju, K. V., "Mechanics of the fiber pullout problem with several fiber-matrix interface conditions," Ph.D. dissertation, Drexel University, Philadelphia, PA, 1993
8. Pochiraju, K.V., A. C. W. Lau and A. S. D. Wang, "A local-global matching method for the single fiber pullout problem with perfectly bonded interface," Computational Mechanics, 14, 1994, pp. 84-89
9. Pochiraju, K.V., A. C. W. Lau and A. S. D. Wang, "Analysis of fiber pullout or push-in with frictional sliding at the fiber-matrix interface," Composites Engineering, V 5, No. 6, 1995, pp 611-631
10. Zak, A. R., "Stress in the vicinity of boundary discontinuities in bodies of revolution", Journal of Applied Mechanics, 33 (1964), pp.150-152.
11. Williams, M. L., Stress singularities resulting from various boundary conditions at angular corners of plates in extension, Journal of Applied Mechanics, 74 (1952), pp. 526.
12. Bechel, V., & Sottos, N., "Application of debond length measurements to examine the mechanics of fiber pushout", to be published in J. Mech. Phys. Solids, 1997,
13. Comninou, M., Interface crack with friction in contact zone, Journal of Applied Mechanics, 44 (1977), pp. 780-781.

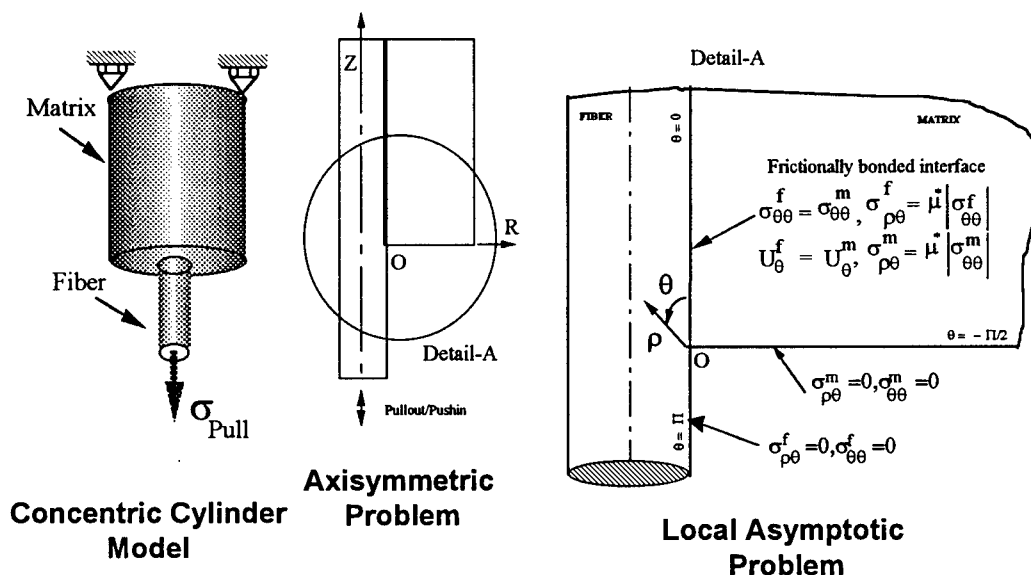


Figure 1: Concentric Cylinder Model - Global axisymmetric and local asymptotic problems

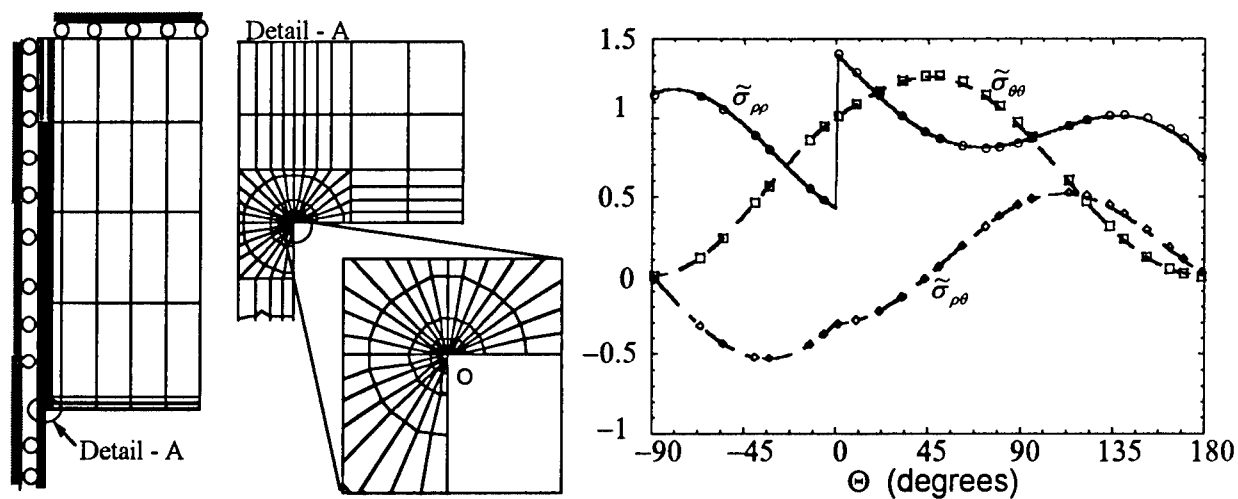


Figure 2: FEM mesh and angular variation matching.
(Discrete symbols are FEM, lines are asymptotic solutions)

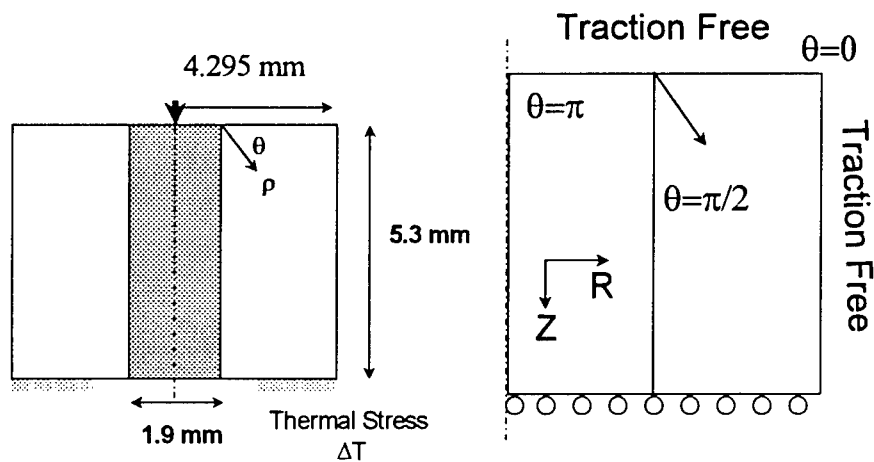


Figure 3: Problem A: Bi-material corner problem

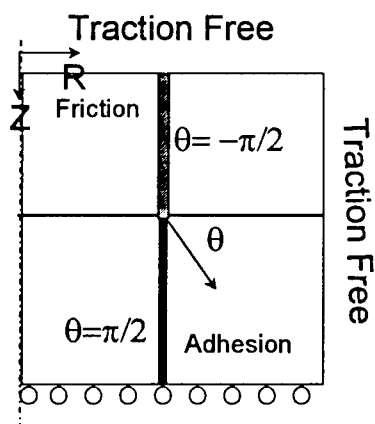


Figure 4: Problem B - Frictional Crack problem

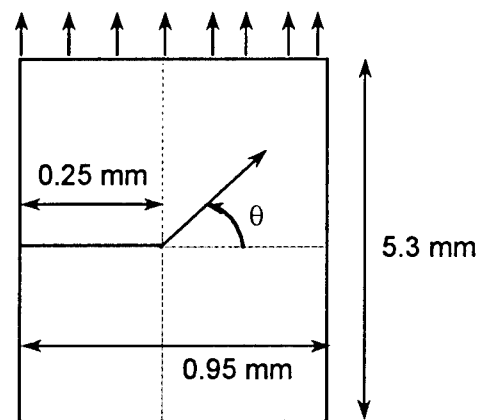


Figure 5: Problem C- Penny shaped crack

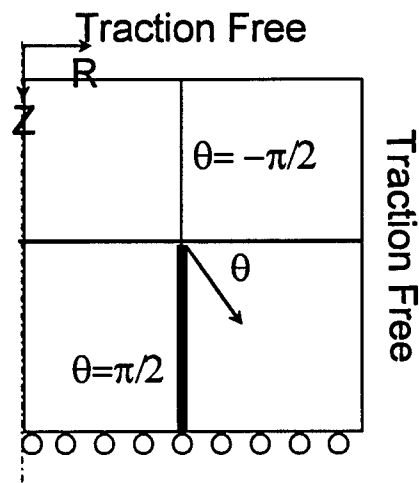


Figure 6: Problem-D: Bi-material interface crack. (Complex singularity)

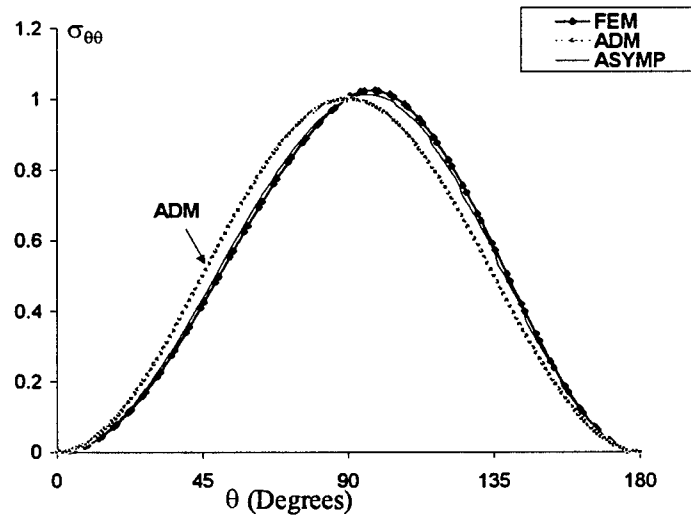


Figure 7: Opening stress angular variation comparison for problem - A

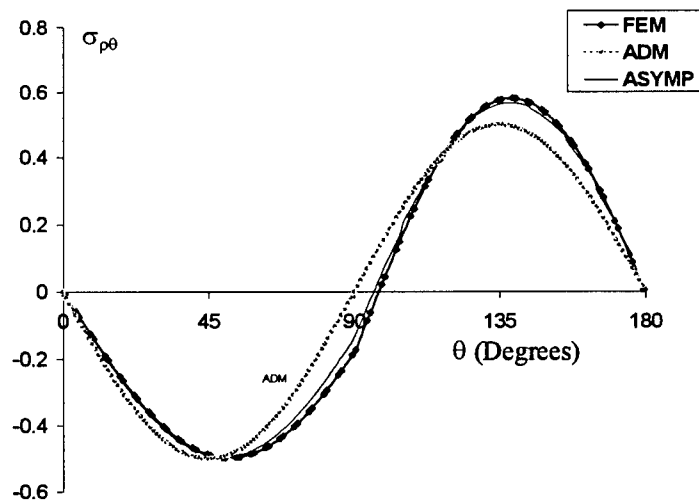


Figure 8: Shear stress angular variation comparison for problem - A

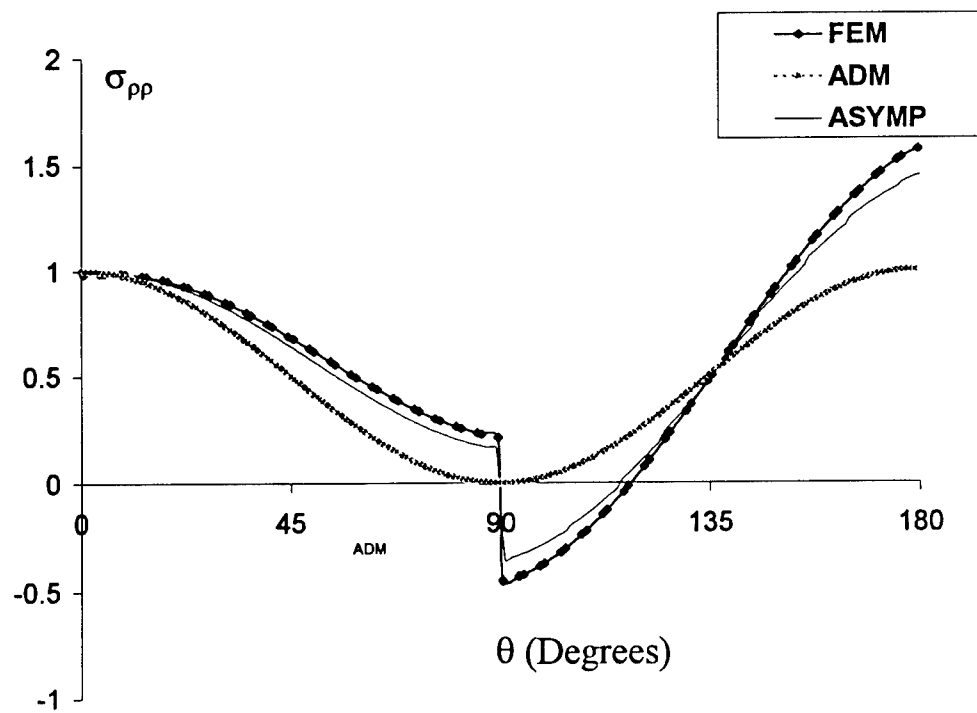


Figure 9: Radial stress angular variation comparison for problem - A

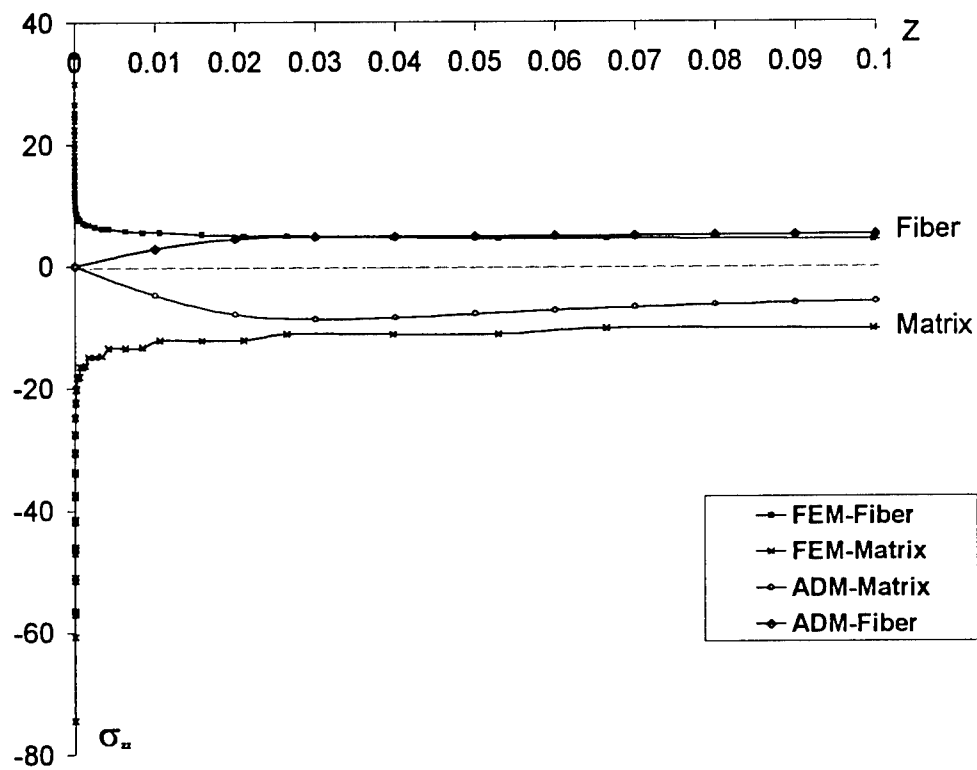


Figure 10: Radial variation of the axial stress

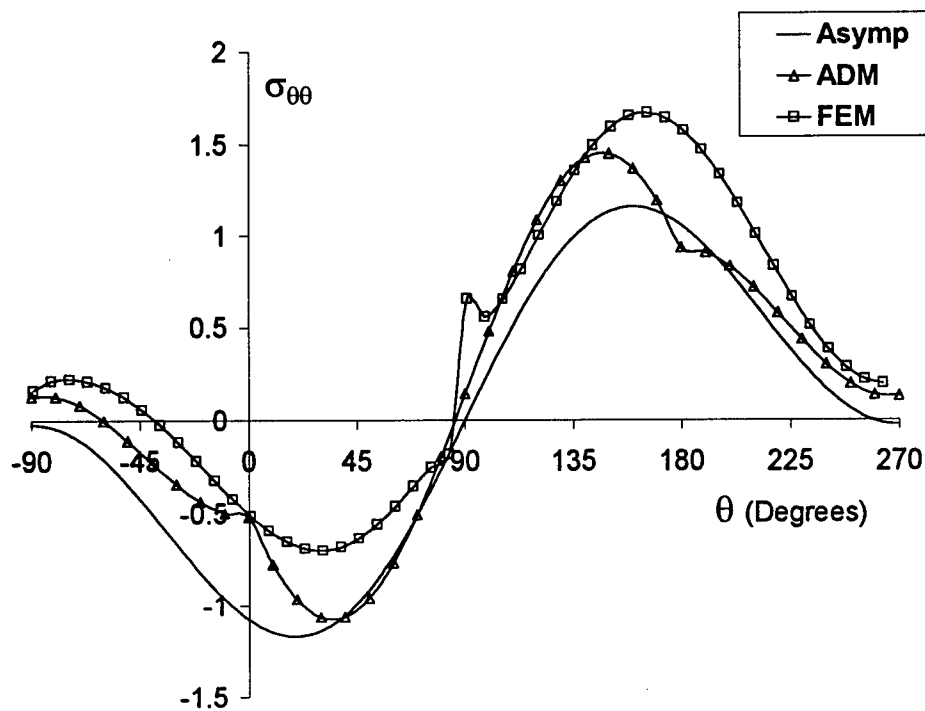


Figure 11: Angular variation matching for normal stress, ADM, FEM and Asymptotic Solutions

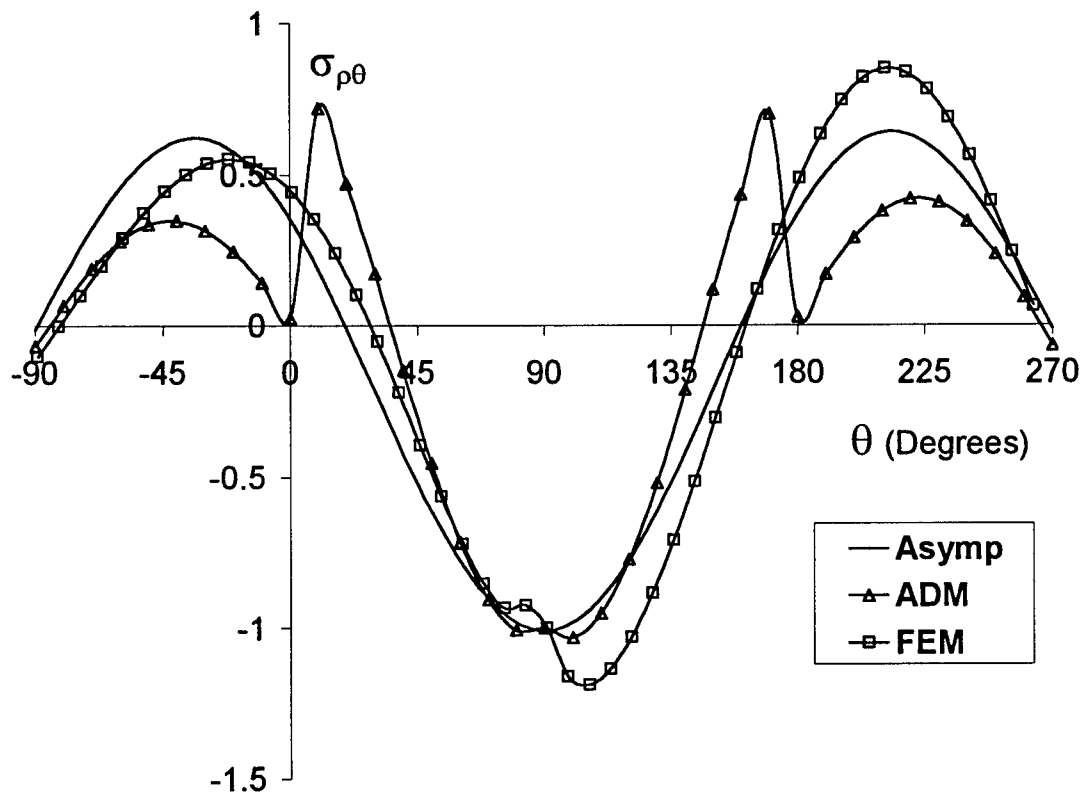


Figure 12: Angular variation matching for shear stresses ADM, FEM and Asymptotic solutions

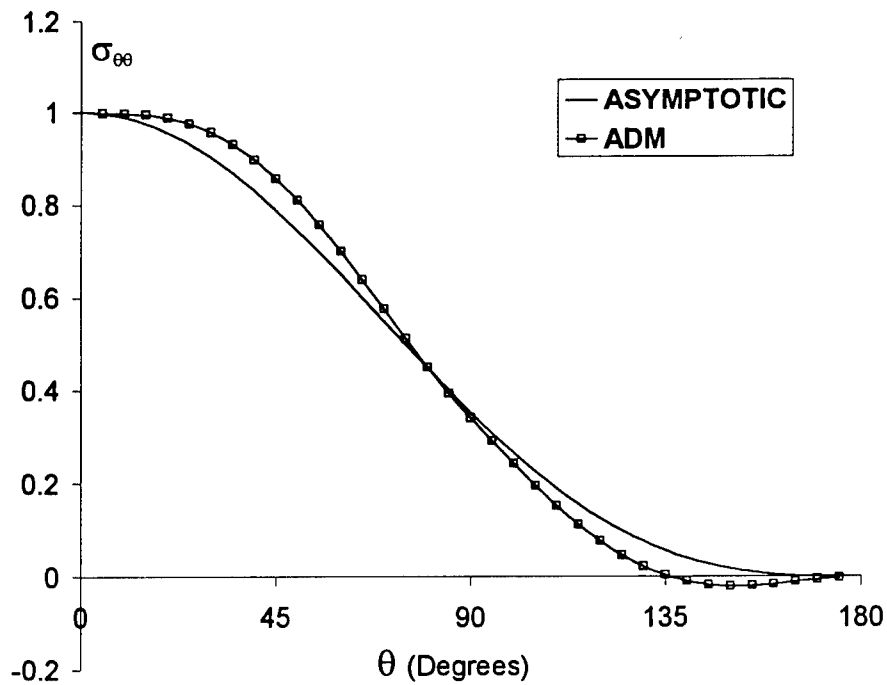


Figure 13: Angular variation matching for penny shaped crack problem (Problem-C)

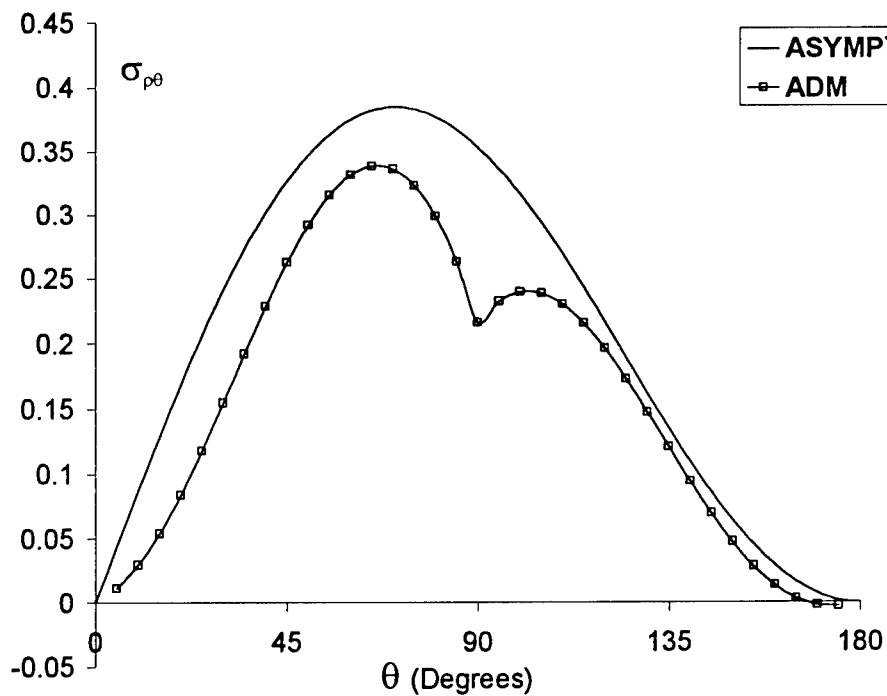


Figure 14: Angular variations of the shear stress for the penny shaped crack problem

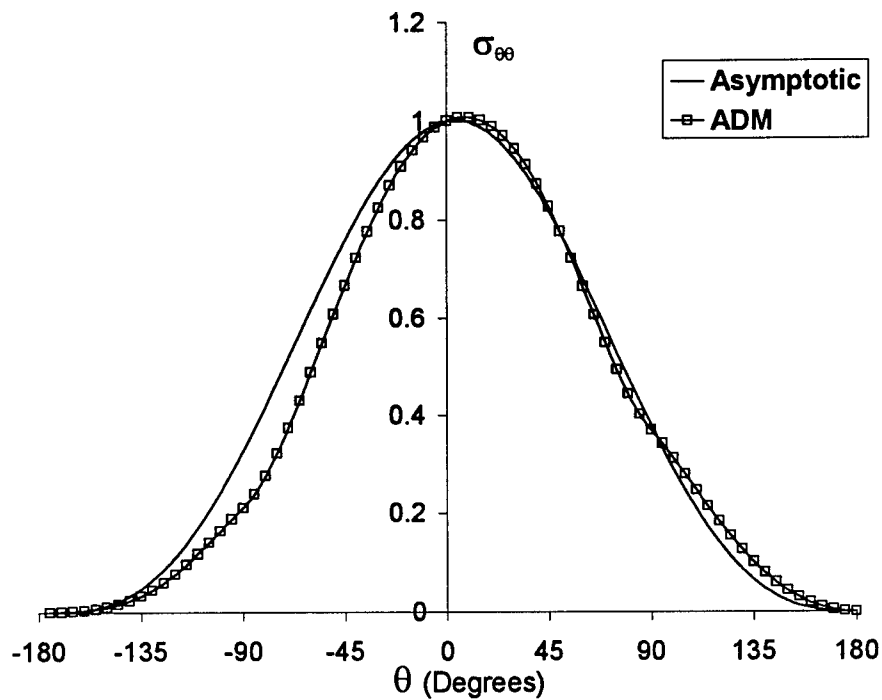


Figure 15: Normal stress distribution for the interfacial crack problem. (Problem-D)

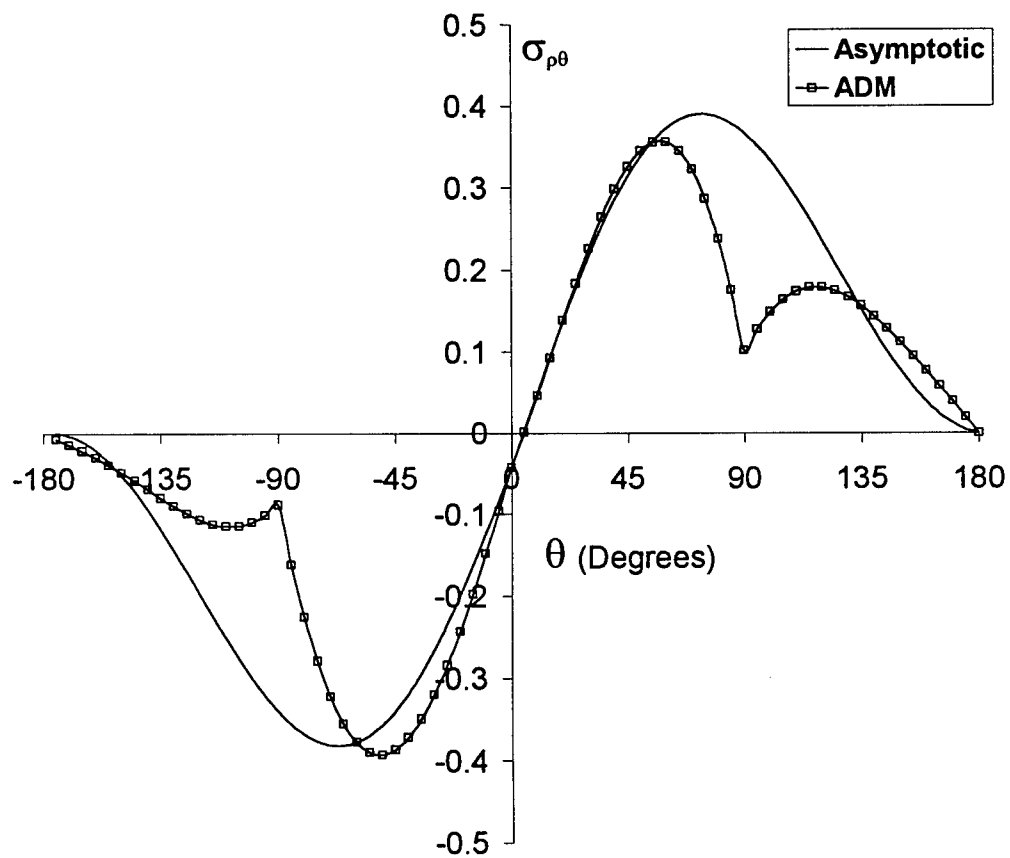


Figure 16: Shear Stress distribution comparison for problem-D.

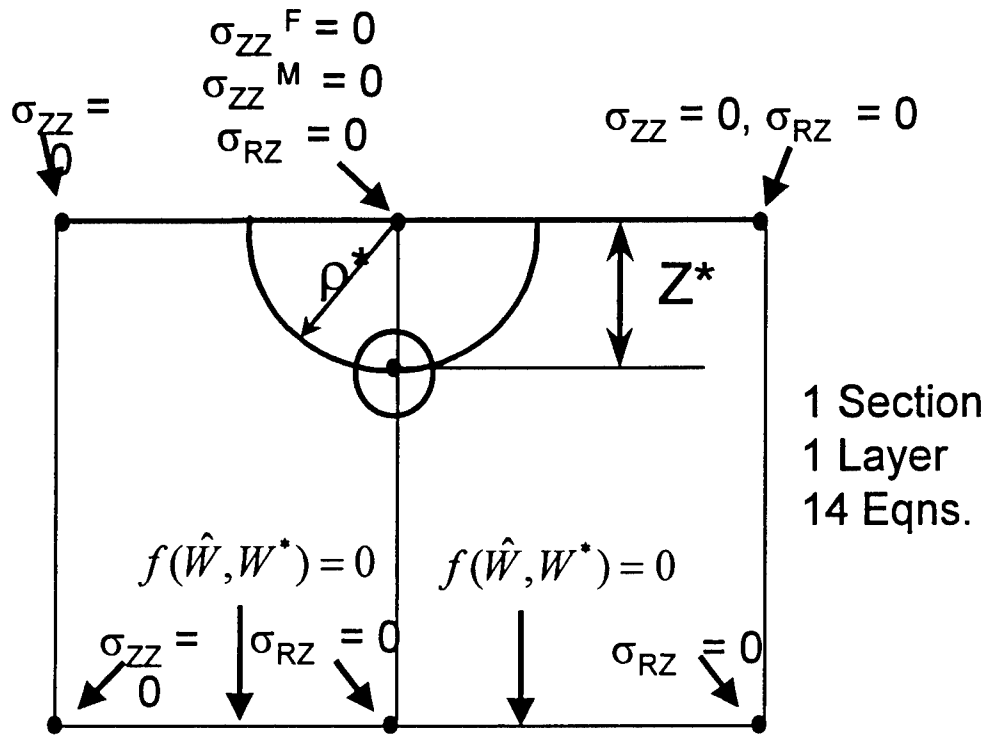


Figure 17: Refining the variational solution by embedding asymptotic solution

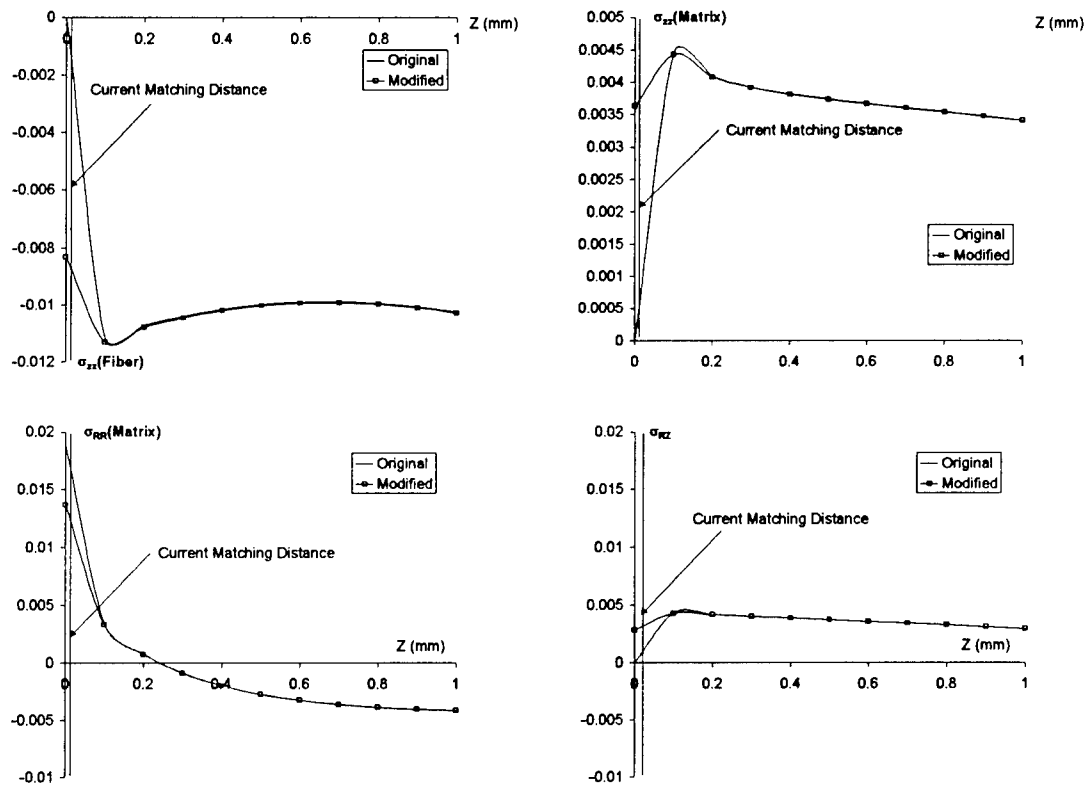


Figure 18: Original and modified solutions for problem - A

**COMPUTATION OF FREE SURFACE FLOWS WITH APPLICATIONS IN
CAPILLARY PUMPED LOOPS, HEAT PIPES, AND JET IMPINGMENT
COOLING ELECTRONICS**

**Muhammad Mustafizur Rahman
Assistant Professor
Department of Mechanical Engineering**

**University of South Florida
4202 E. Fowler Avenue, ENB 118
Tampa, Florida 33620**

**Final Report for:
Summer Research Program
Wright Laboratory**

**Sponsored by:
Air Force Office of Scientific Research
Bolling Air Force Base, Washington, DC**

And

Wright Laboratory

August 1997

COMPUTATION OF FREE SURFACE FLOWS WITH APPLICATIONS IN CAPILLARY PUMPED LOOPS, HEAT PIPES, AND JET IMPINGEMENT COOLING OF ELECTRONICS

Muhammad Mustafizur Rahman
Assistant Professor
Department of Mechanical Engineering
University of South Florida

ABSTRACT

The numerical modeling and computation of free surface flows associated with the development of advanced thermal control devices for aircraft is the objective of the present investigation. Three important physical problems were studied. These are: (1) Prediction of free surface dynamics during vibration of a capillary pumped loop, (2) Prediction of liquid return flow in a helically-grooved heat pipe under high acceleration loading, and (3) Computation of heat transfer during liquid jet impingement on a horizontal surface. The numerical modeling was done by considering the governing transport equations and boundary conditions representing each physical problem and the computation was carried out using the computational fluid dynamics code FIDAP. Several interesting results were obtained. It was found that an extended meniscus is formed at the liquid-vapor interface when a capillary tube is subjected to vibration in the transverse direction. The computation of free surface flow in a helically grooved revolving heat pipe showed that a larger body force in the direction of the flow decreases the film thickness and increases the flow velocity providing the possibility of larger fluid transport through the groove and higher capillary limit. During jet impingement of a large Prandtl number fluid, the local heat transfer coefficient is maximum at the center of the disk and decreases gradually with radius as the flow moves downstream. The average heat transfer coefficient decreases with increase of disk thickness and increase of thermal conductivity of the disk material. A minimum temperature at the heat source can be realized for a disk thickness of about 1 mm. This maximum temperature can be reduced by increasing the thermal conductivity of the disk material. The temperature variation at the solid-fluid interface becomes larger with decrease of thermal conductivity of disk material and disk thickness.

COMPUTATION OF FREE SURFACE FLOWS WITH APPLICATIONS IN CAPILLARY PUMPED LOOPS, HEAT PIPES, AND JET IMPINGEMENT COOLING OF ELECTRONICS

Muhammad Mustafizur Rahman

INTRODUCTION

Free surface flow occurs in nature and in several technological applications. Many of these applications are related to the thermal management of high performance aircraft. In this class of flow, a liquid medium is in direct contact with a gaseous medium and the interface between the two mediums is free to deform and can assume any shape to satisfy the equilibrium of all forces acting on the surface. Computations of flow involving a free surface is difficult because the boundary of the computation domain is not known apriori, and therefore the discretized equations have to be updated at each computational step to satisfy the new position of the free boundary. In addition, the shape and location of the free surface have to be determined as a part of the solution scheme. The objective of the present investigation was to explore the capabilities of the computational fluid dynamics software FIDAP to numerically model and solve free surface problems. The present work was intended to develop basic numerical models and compare them with available experimental data and analytical solution for limiting conditions. The complete exploration of the numerical models to understand the fundamental physics of the transport mechanisms and the prediction of the effects of different transport parameters will require huge computational efforts and will be carried out as a follow up study of this research effort. The following three problems were investigated.

1. Free surface dynamics during vibration of a capillary pumped loop.
2. Liquid flow in a helically-grooved heat pipe under high acceleration loading.
3. Liquid jet impingement cooling of electronics.

FREE SURFACE COMPUTATION USING FIDAP

A free surface boundary occurs when there is an interface between a liquid and a gas, with the gas being treated as an effective vacuum. The interface is a region of molecular thickness where the intermolecular or van der Waals forces are significant. In macroscopic sense, the interface has associated with it a surface tension which, in the event that the interface is curved, accounts for the pressure difference between the liquid and the gas. The interface, represented by the equation $S(x_i, t) = 0$, always remains an interface (kinematic condition), and stress on this surface is continuous. The kinematic condition and the dynamic balance of forces at the interface lead to the following three equations.

$$\frac{\partial S}{\partial t} + u_j S_j = 0 \quad (1)$$

$$\sigma_n = 2\gamma\kappa - p_a \quad (2)$$

$$\sigma_t = t_j \gamma_j \quad (3)$$

In these equations, σ_n and σ_t are normal and tangential components of the shear stress, γ is the surface tension, κ is the mean Gaussian curvature of the surface, and p_a is the ambient pressure.

The approach adopted by FIDAP to simulate free surface problems is to introduce a new degree of freedom at the nodes on the free surface. This degree of freedom represents the position of the free surface, S . This position degree of freedom is introduced as a new unknown into the global system of equations that FIDAP solves. The discretization of governing transport equations and boundary conditions are carried out using the Galerkin finite-element method. The solution of the resulting algebraic equations can be carried out using either a coupled (Newton-Raphson or Quasi-Newton) or uncoupled (segregated) solver. In a coupled solver, all degrees of freedom are solved simultaneously. It has the advantage of faster convergence and the position of the free surface is determined explicitly as a part of the solution scheme. A coupled solver, however, requires a good starting guess and it is storage (both memory and disk) intensive.

In an uncoupled method, each degree of freedom is solved separately. Because of larger radius of convergence and smaller memory requirements, all three-dimensional problems are limited to this solver. Since the solution of the momentum equation requires only two out of the three boundary conditions at the free surface, the third condition is used to upgrade the position of the free surface at the end of each iteration step. When the kinematic condition (Equation. 1) is used to update the free surface location, it is called the Kinematic Update Approach and when the normal stress condition (Equation. 2) is used to update the free surface location, it is called the Normal Stress Update Approach.

In FIDAP, the coupled or Newton-based solvers utilize spines to track or guide the free surface. Spines are straight lines passing through the free surface nodes and connecting the nodes underneath the free surface. Only nodes along a spine are affected by the free surface movement. The segregated solver allows a broader freedom on the remeshing of nodes to accommodate the movement of the free surface during computation. By choosing a MAPPED option, all nodes in the region below the free surface can be updated. The direction of movement of the nodes is specified by choosing STRAIGHT, NORMAL, or PREFERRED keyword. The movement along a spine is denoted by the STRAIGHT keyword. The NORMAL keyword is used to specify the movement of the free surface along the local normal on the surface. The movement of nodes in any other direction can be specified by using the PREFERRED keyword along with a direction vector. To effectively remesh the computation domain below the free surface, a MAPPED mesh is required at least for that region.

Since the free surface position (S) is treated like any other degree of freedom, an initial condition (initial displacement) of free surface nodes can be specified. In addition, any free surface node can be constrained to be fixed or changing position with time via a user specified time function. The contact angle at the solid-liquid-gas interface needs to be specified for all three dimensional problems and for two dimensional problems with both ends free to move. The surface tension can be specified as a constant value or as a function of temperature or species concentration.

FREE SURFACE DYNAMICS DURING VIBRATION OF A CAPILLARY PUMPED LOOP

Capillary pumped loops are used in high heat flux thermal management applications due to benefits of large rate of heat transfer by phase change without significant variation of temperature for the thermal transport. This passive heat transfer device has great potential for application in the development of novel thermal management techniques for more electric aircraft. For more rigorous application of this device for the cooling of electronics onboard an aircraft, it will be very important to identify the effects of transient acceleration load and vibration on the performance of a capillary pumped loop.

One of the crucial elements determining the performance of a capillary pumped loop is the evaporating meniscus in the capillary tube. The wetting behavior of a liquid on a heated surface significantly affects the evaporation and therefore heat transfer from a meniscus. It has been shown in past studies that the meniscus shape influences evaporation rates with very high heat transfer rates near a contact line. The evaluation of the dynamic structure of the free surface in a capillary tube will demonstrate the potential for enhanced heat transfer from the region where there is an elongated liquid film in contact with the solid wall.

The objective of the present investigation was to model the free surface motion of the evaporating meniscus in a capillary tube under transient acceleration loading and compare with the previous experimental observations of Brown (1995). Of particular interest in these tests, which used water as the working fluid in a 1 mm ID capillary tube, was the response at the contact line. Video was taken using a high speed camera in conjunction with a long-working distance microscope, to demonstrate the extension of the contact line region as the tube is vibrated at a frequency of 200 Hz transverse to its axis. It was seen that the liquid near the contact line is thrown against the walls of the tube as would be expected in a typical sloshing action. However, at these small dimensions and high peak accelerations, the liquid sticks to the wall and causes an extension of the contact region. As the vibrations continue, additional fluid is pumped into this region.

The three dimensional problem of free surface movement under transverse body force was simplified to a two dimensional problem of a meniscus contained in between two parallel walls. The gap between these walls was assumed to be 1 mm (same as capillary tube diameter) and the height of the fluid column was assumed to be 5 mm. Water was used as the working fluid. A sinusoidal variation of body force in the direction perpendicular to the walls was imposed. The amplitude of variation was 196.2 m/s^2 (20-g) and its frequency was 200 Hz. The initial condition of the fluid in the tube was assumed to be static with a meniscus shape determined by a balance of surface tension and gravitational forces. This initial shape of the free surface between the walls was calculated by solving the Young-Laplace equation. Figure 1 shows the initial free surface height distribution and the mesh structure used for the computation. It can be noticed that the mesh was graded towards the free surface and towards the walls to better capture the variation of free surface near the contact line. It may be mentioned that the computational mesh was updated several times during a time step as new location of the free surface was calculated by solving the transport equations.

Figures 2-5 show the velocity distribution in the liquid at four different time instants during vibration. At

$t=0.00625$ s, the body force in the positive x-direction has induced a motion in the fluid contained between the walls in that direction. The shape of the free surface has not changed at this early instant of time. At $t=0.0175$ s, the sinusoidal body force has already completed 3 cycles and half of a cycle in the positive x-direction. It can be noticed that the free surface has deformed significantly from its initial condition. The motion of the fluid towards the positive x-direction and a thinner meniscus at the left wall is due to the positive body force over the last half cycle. At $t=0.03$ s, the fluid is moving in the negative x-direction. At this point, the body force has just completed 6 cycles. The inertia of the fluid is keeping motion in the negative x-direction when the body force is actually zero. The free surface has become thinner near the walls and extended down into the capillary tube. Further deformation and thinning of the meniscus is noticed at the snapshot at $t=0.0625$ s. The variation of free surface shape with time qualitatively supports the experimental observations of Brown (1995).

To quantitatively compare the film height at the extended meniscus during vibration, a three-dimensional simulation of the capillary tube will be needed. Further, the effect of bottom wall and the size of computational mesh will be evaluated to independently validate the accuracy of the numerical results. These will be carried out during a follow up study of this research project.

LIQUID FLOW IN A HELICALLY-GROOVED HEAT PIPE UNDER HIGH ACCELERATION LOADING

The analysis of heat pipes has usually been restricted to the inclusion of a relatively small acceleration field, such as that due to gravity. While this type of analysis is appropriate for many applications, it may not be valid in the assessment of the thermal performance of heat pipes in acceleration fields which are significantly greater than 1-g. For instance, heat pipes have been proposed to be used aboard fighter aircraft such as the Navy F/A-18 to act as heat sinks for electronics packages which drive aileron or trailing edge flap actuators (Yerkes and Hager, 1992). During combat, transient acceleration fields of up to 9-g could be present on the aircraft. Therefore, the knowledge of the thermal performance of heat pipes under significant acceleration fields is of importance to designers of electronics packages for aircraft.

A revolving heat pipe rotates about an axis other than its own. Even with high potential for application in aircraft and in the cooling of rotating machinery, there have been only a few studies on the performance of a revolving heat pipe. In a recent study by Thomas et al. (1997), it has been shown that a helically grooved revolving heat pipe can overcome the deficiencies of depriming of wicks at high acceleration loading and can provide much superior performance at high transient body force environment. The steady-state performance of a helically-grooved copper-ethanol heat pipe when subjected to constant heat input and constant radial acceleration fields was determined experimentally using a horizontal centrifuge table. The heat input ranged from 10 to 250 W and the magnitude of radial acceleration ranged up to 10-g. An one-dimensional mathematical model to determine the capillary limit of helically grooved heat pipes was developed and the analytical predictions were compared with experimental data.

The objective of the present investigation was to develop a complete mathematical model for liquid flow in

helical grooves of a revolving heat pipe using FIDAP and compare the numerical results with the experimental data and analytical predictions of Thomas et al. (1997). In order to adequately handle the complex three dimensional flow in a helically-grooved passage and the motion of the free surface at the vapor-liquid interface, it was decided to build and test the model at several steps.

First, the flow in curved channel simulating a groove of the heat pipe was investigated. To simplify the problem, the presence of the free surface was ignored and all the sides of the channel were assumed to be rigid and fixed in space. In the experiments of Thomas et al. (1997) the heat pipe was bent to match the radius of the centrifuge table to assure an uniform radial acceleration field over the length of the pipe. The radius of the table was 122 cm, length of the pipe was 50 cm, and its radius was 0.635 cm. Using these dimensions and assuming a square groove of 0.04 cm side, a geometric model of the heat pipe groove was developed in FIDAP. Essentially, the mesh over the cross-section at one end of the groove was developed using Cartesian coordinates and it was projected along a curve defined along the helical path. For an uniform velocity defined at the inlet of the channel, the velocity and pressure distribution in the channel was calculated. Figure 6 shows the velocity vectors along a section of the channel towards its outlet. The velocity is maximum at the center and decreases to zero at the walls. Due to large length to hydraulic diameter ratio, the uniform entrance flow becomes fully-developed within a short length from the entrance.

To explore the characteristics of the free surface at the liquid-vapor interface, a two-dimensional model of the groove along its flow length was developed neglecting the curvature of the pipe as well as that of the groove. The characteristics of the flow in the adiabatic section of the heat pipe was investigated assuming that the flow enters this section with a uniform velocity and with a film height equal to the height of the groove. The actual height (0.442 mm) and width (0.474 mm) of the groove used in the experiments of Thomas et al. (1997) was used. Ethanol was used as the working fluid. Computations were first carried out over a length of 10.16 mm and then extended over the entire length of the adiabatic section (101.6 mm). Even though only steady state results were desired, computations were carried out as a transient problem to make the free surface computation somewhat more stable. To achieve faster convergence, the Newton-Raphson solver was used. Calculations were done for different imposed acceleration fields on the fluid in the groove.

Figure 7 shows the velocity distribution in the liquid film when the acceleration is 1-g in the axial direction. This also simulates a falling film if the channel is oriented in the vertical direction. The flow velocity at the entrance to the adiabatic section corresponded to a thermal load of 14.6 W for the heat pipe. It can be noticed that the uniform flow at the entrance gradually develops into a parabolic flow further downstream. As expected, the velocity is maximum at the free surface and decreases to zero at the solid wall. The height of the film at the exit of the computation domain was compared to the equilibrium film height for a falling film (Bird et al., 1960), and they were found to be within 0.2 percent.

Figure 8 shows the film height distribution for different combinations of axial and normal components of the body force on the film. The axial component seem to have much greater impact on the film height compared to the component perpendicular to the solid wall. When the axial acceleration is increased from 1-g to 10-g, the film height

decreases to a much smaller value. In addition, the film approaches the equilibrium height within a much shorter distance. The equilibrium film height for 10-g acceleration in the axial direction compared to the analytical solution of Bird et al. (1960) within 4%. The body force normal to the wall had the effect of slightly increasing the film height when the force is applied in the direction away from the wall, and slightly decreasing the height when it is applied in the opposite direction. The normal acceleration in excess of 3-g away from the wall, however made the film detach from the wall and the solution of the flow was not possible. The above two-dimensional model ignored the side walls of the heat pipe and surface tension forces at the contact lines along these walls may be quite significant to hold the liquid in the groove to a larger value of the acceleration perpendicular to the bottom wall.

Figure 9 shows the liquid film height distribution over the full length of the adiabatic section of the heat pipe for a heat load of 8 W and for an acceleration of 1.6 m/s^2 in the axial direction and 28 m/s^2 across the thickness of the film directed towards the wall. These conditions relate to the average acceleration in the adiabatic section and the capillary limit of the heat pipe tested by Thomas et al. (1997) when revolving with a 6-g radial acceleration. It can be noticed that under these conditions the height of the free surface approaches an equilibrium value within a short length indicating that the groove will run only partially filled.

To investigate the effects of the side walls on the structure of the liquid film, computations were carried out over a two-dimensional cross section of the groove using a static model of the free surface but including the accelerations induced in the actual heat pipe. Figure 10 shows the cross-section of the liquid film under an acceleration loading of 53 m/s^2 in the x-direction and -28 m/s^2 in the y-direction. The body force in the positive x-direction pushes the meniscus up along the side wall in that direction. It was observed that when a large acceleration in the positive y-direction is applied, the film cannot be contained within the groove and tears apart overcoming the surface tension forces.

The simplified three-dimensional model for the curved channel simulating the flow in a helically coiled heat pipe groove and the two-dimensional free surface models along the length and cross-section of the groove provided some basic insight into the liquid return flow in a helically grooved revolving heat pipe. However, to simulate the actual physical scenario, a three-dimensional model of the heat pipe with the free surface will be required. The condensation and evaporation of fluid at the free surface has to be accounted for in this model. It is expected that this work will be continued over in a follow up research project where the three-dimensional model of the heat pipe groove will be developed and the numerical predictions will be compared with experimental data presented by Thomas et al. (1997). It is anticipated that the computations for the full three-dimensional model will require a supercomputer and the computational facilities at the Shared Resource Center at the Wright-Patterson Air Force Base will be used for this work.

LIQUID JET IMPINGEMENT COOLING OF ELECTRONICS

Jet impingement heat transfer is known for its ease of implementation and high heat transfer coefficients. It has been employed for the drying of paper and textiles, tempering glass, bearing cooling, turbine blade cooling, and electronics cooling. Even though there has been a large number of research work on free and submerged jets, a literature

review presented by Leland and Pais (1997) showed that very little experimental data or analyses for free surface liquid jet impingement using high Prandtl number fluids is currently available in the open literature. In addition, the change of fluid properties during jet impingement heat transfer process for a high Prandtl number fluid has not been investigated in any previous work.

Although a poor heat transfer fluid, lubricating oil is an attractive coolant for aircraft applications because it is generally in close proximity to the electrical generating equipment. It is also pre-existing in the aircraft and therefore does not require: (1) flight qualification, (2) new maintenance procedures, (3) additional inventory space and logistics procedures, and (4) additional environmental protection guidelines. These four advantages translate into greatly reduced operational costs which may far outweigh the loss in cooling efficiency. Lubricating oils are generally known for their large Prandtl number and strong dependence of viscosity on temperature. Coolanol and its replacement PAO are also used as coolants aboard aircraft and have Prandtl number and viscosity profiles similar to lubricating oil. Even the aircraft fuel is being considered as a coolant alternative because of the same four reasons stated above although it carries the obvious safety concerns associated with the use of fuel. The fuels used also have high Prandtl numbers. Therefore, the investigation of jet impingement heat transfer for a high Prandtl number fluid taking into account the effects of property variation with temperature is of great importance to the military and commercial aircraft industry.

The present study aimed towards the development of a free surface model for a liquid jet impinging on a solid disk and to use the numerical model to parametrically study the effects of disk thickness and disk thermal conductivity on the heat transfer process. The conditions corresponding to one of the experimental data presented by Leland and Pais (1997) was used for the numerical simulation. The diameter of the jet was 0.17 cm and that of the disk was 1.295 cm. The orifice was located at a distance of 0.85 cm from the disk. The jet velocity at the exit of the orifice was 280 cm/s. The velocity distribution at this location was assumed to be uniform over the jet cross-section. Fluid properties used for the computation corresponded to Mil-7808 used in the experiments of Leland and Pais (1997). This fluid had a density of 0.966 gm/cm³, viscosity of 0.3421 gm/cm.s, thermal conductivity of 0.0003384 cal/cm.s.^oC, and specific heat of 0.4957 cal/gm.^oC. In order to converge to the final free surface height distribution within a reasonable number of iterations, the initial shape of the free surface was approximately calculated by looking into the physics of the flow and the conservation of mass as the film spreads over the disk after impingement. The Newton-Raphson solver was used for the calculation of flow and the free surface location. Figure 11 shows the final free surface structure and the velocity distribution in the jet as well as in the film. The velocity remains almost uniform in the earlier part of the jet and effect of the impingement surface is felt when the jet reaches close to the wall. Beyond the stagnation region, the film spreads out, decreases in velocity and increases in thickness. The velocity is small in regions away from the center of the disk because of loss of momentum to counteract the shear forces from the solid wall of the disk and due to increase of flow area because of radial spreading. The velocity is always maximum at the free surface and decreases gradually to zero at the solid disk.

The heat transfer was investigated for two different materials: copper ($k=393$ W/m.K) and constantan ($k=17$ W/m.K). The computation domain was extended to include the solid disk and computations were carried out for both

solid and liquid regions simultaneously as a conjugate problem. The disk thickness was varied between 0.002 cm and 0.5 cm. An uniform heat flux of 33000 W/m^2 was imposed at the bottom of the disk. The distribution of local heat transfer coefficient at the interface for a copper disk of 0.5 cm thickness is shown in Figure 12. The heat transfer coefficient is maximum at the stagnation region and gradually decreases with radius. Due to large flow velocity at smaller radii just beyond the stagnation region, the heat transfer coefficient holds to a higher value. Beyond that, the heat transfer coefficient decreases as the thermal boundary layer increases in thickness.

Figure 13 shows the temperature contours for a constantan disk of 0.5 cm thickness. It can be noticed that the highest temperature is encountered at the largest radius on the heater surface. The temperature in the solid region decreases gradually towards the axis of the disk and towards the solid-fluid interface. The minimum disk temperature is reached right at the impingement location of the jet. The existence of a thermal boundary layer in the fluid region is seen in the figure. The fluid temperature at jet locations far away from the disk and at the free surface remains approximately constant at its incoming value confirming the adequacy of the assumed adiabatic condition at the free surface for the heat transfer model.

Figure 14 shows the variation of average heat transfer coefficient with disk thickness. The average heat transfer coefficient decreases with disk thickness. The effect is particularly significant at smaller thicknesses. The constantan disk seems to provide a larger average heat transfer coefficient compared to a copper disk of the same thickness. The maximum temperature in the solid is plotted in figure 15. A larger maximum temperature in the constantan may be attributed to a smaller thermal conductivity of this material. The difference is fairly significant for any given thickness. This indicates that for electronics cooling, the thermal conductivity of the substrate material may play a very crucial role in transporting heat from the electronics to the coolant keeping the temperature of the electronics to an acceptable level. It is also interesting to note that the best performance is realized for a disk thickness of about 1 mm for both copper and constantan. Due to smaller thermal conductivity, the maximum temperature in the constantan disk increases rapidly if the disk thickness is increased beyond 1 mm. The increase is small in copper under the same range of disk thicknesses.

Figure 16 shows the minimum surface temperature at the disk which always happens at the impingement location. This temperature is somewhat higher in copper than in constantan. The minimum temperature increases with increase of disk thickness. Figure 17 shows the variation of surface temperature over the disk surface. The variation decreases with increase of disk thickness because of larger conduction within the solid. The magnitude of variation is fairly significant for constantan under all conditions. For copper, the surface temperature may be assumed approximately constant for a disk thickness of higher than 1 mm. By adding values of temperatures plotted in figures 16 and 17, the maximum surface temperature of the disk can be calculated. This is shown in figure 18. The maximum surface temperature decreases with increase in disk thickness. The magnitudes of the maximum surface temperature are somewhat larger for constantan than for copper.

CONCLUSIONS

This research investigation focused on the modeling and computation of a number of free surface problems

using the commercially available computer code FIDAP. The problems related to the development of novel thermal management techniques for future high performance aircraft. The following conclusions can be made based on the computational results.

1. An extended meniscus is formed at the liquid-vapor interface when a capillary tube is subjected to vibration in the transverse direction. This shows the possibility of enhancement of the performance of a capillary pumped loop under vibration loading.
2. The flow in a helically grooved revolving heat pipe is highly affected by magnitude and direction of the resultant body force. A larger body force in the direction of the flow decreases the film thickness and increases the flow velocity showing the possibility of larger fluid transport through the groove and higher capillary limit. A body force directed downward into the groove simply helps retain the fluid in the groove but does not significantly affect the flow velocity. A large body force directed upward from the groove may force the fluid out of the groove resulting in local dryout.
3. During jet impingement of a large Prandtl number fluid, the local heat transfer coefficient is maximum at the center of the disk and decreases gradually with radius as the flow moves downstream. The average heat transfer coefficient decreases with increase of disk thickness and increase of thermal conductivity of the disk material. A minimum temperature at the heat source can be realized for a disk thickness of about 1 mm. This maximum temperature can be reduced by increasing the thermal conductivity of the disk material. A smaller minimum surface temperature during jet impingement can be realized for a smaller thermal conductivity and smaller thickness of the disk. The variation of temperature at the solid-fluid interface becomes larger with decrease of thermal conductivity of disk material and disk thickness. For copper, the surface temperature becomes practically uniform when the disk thickness is more than 1 mm.

REFERENCES

- Bird, R.B., Stewart, W.E., and Lightfoot, E.N., *Transport Phenomena*, John Wiley & Sons, New York, 1960.
- Brown, J.R., "Effect of Interfacial Dynamics on the Heat Transfer of an Evaporating Meniscus," Ph.D. Thesis, University of Dayton, Dayton, Ohio, 1995.
- Leland, J.E. and Pais, M.R., "Free Jet Impingement Heat Transfer of a High Prandtl Number Fluid with Large Surface to Jet Temperature Variation," paper under preparation for *ASME Journal of Heat Transfer*, 1997.
- Thomas, S.K., Klasing, K.S., and Yerkes, K.L., "Experimental and Analytical Prediction of the Capillary Limit of Helically-Grooved Revolving Heat Pipes," accepted for ASME International Mechanical Engineering Congress and Exposition, Dallas, Texas, November, 1997.
- Yerkes, K.L. and Hager, B., "Transient Response of Heat Pipes for Actuator Thermal Management," *Proc. of the Aerospace Atlantic Conference*, Dayton, Ohio, SAE Paper Number 921024, 1992.

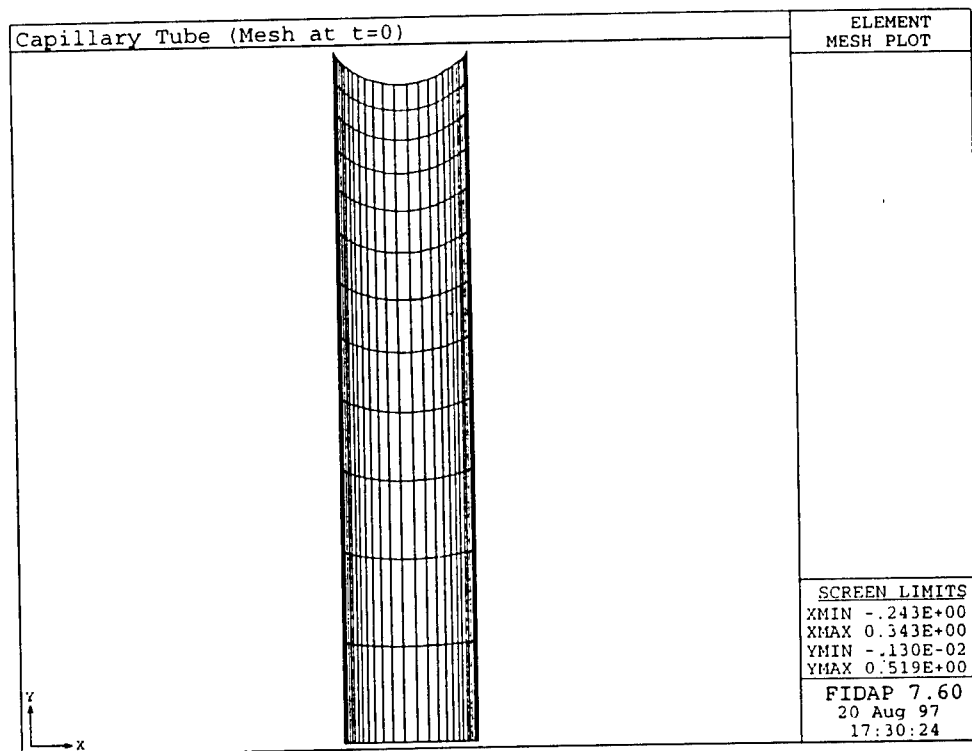


Figure 1.Mesh distribution in the capillary at t=0

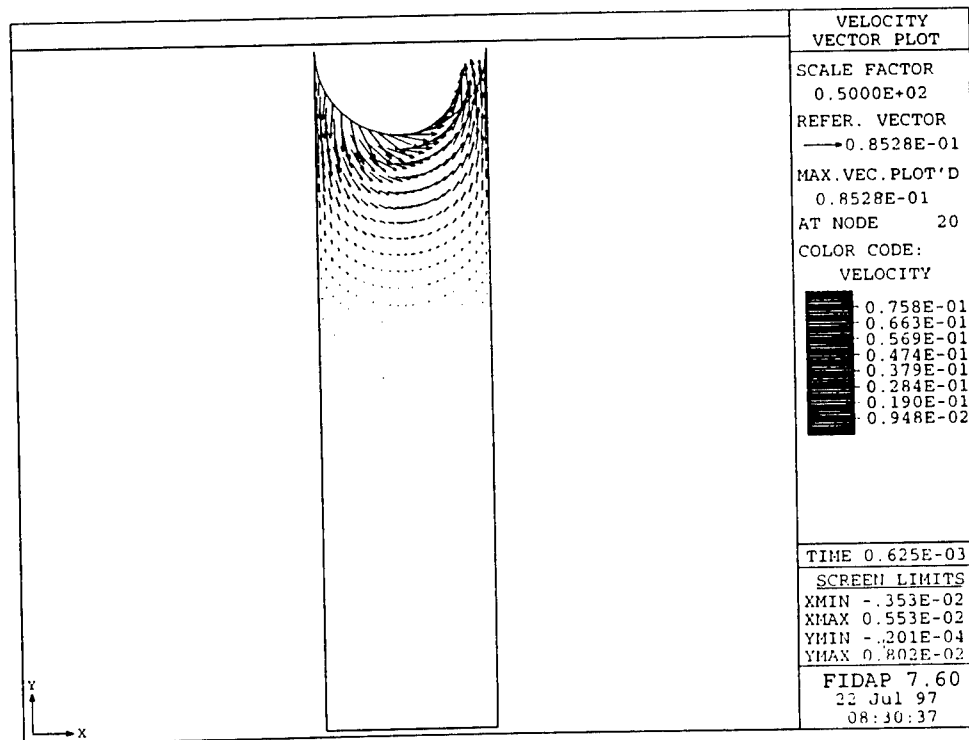


Figure 2.Velocity distribution in the capillary under vibration at t=0.000625 s

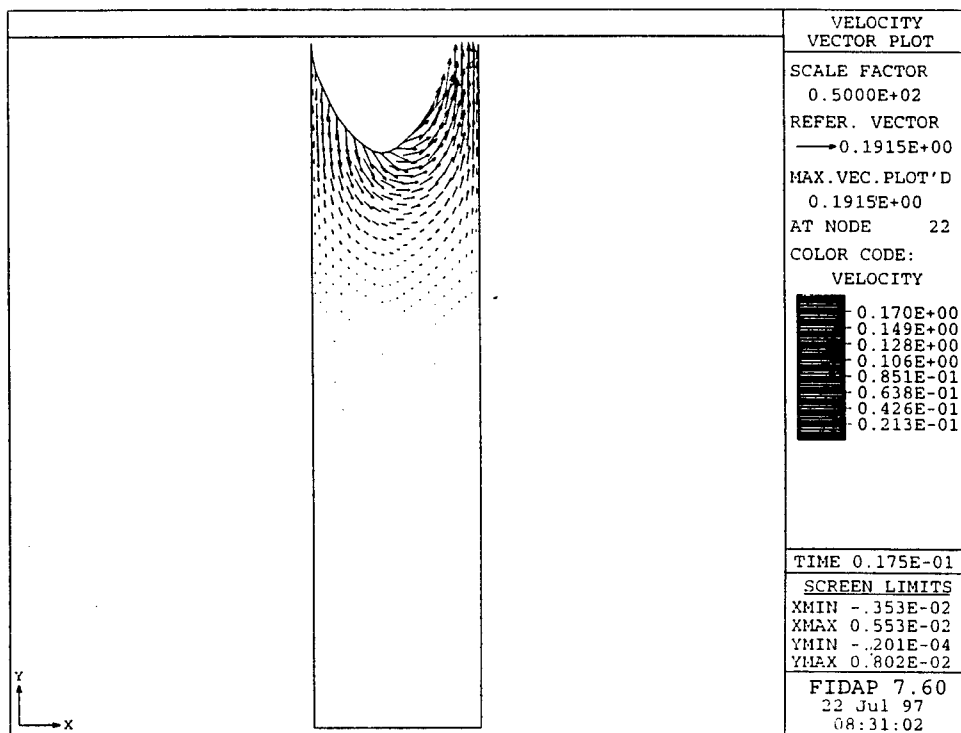


Figure 3.Velocity distribution in the capillary under vibration at $t=0.0175$ s

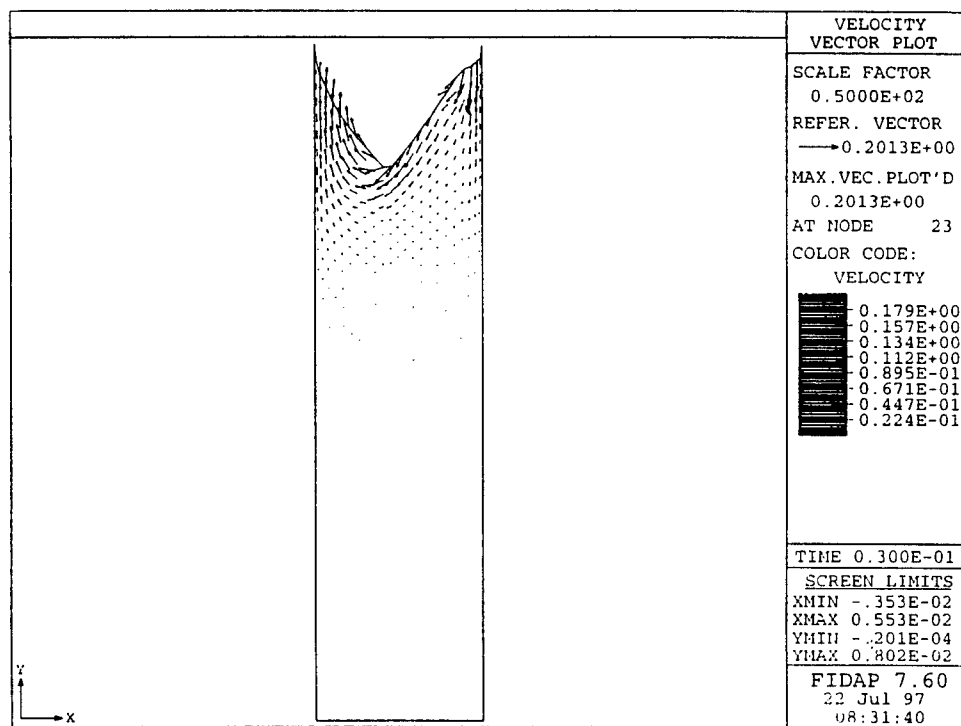


Figure 4.Velocity distribution in the capillary under vibration at $t=0.03$ s

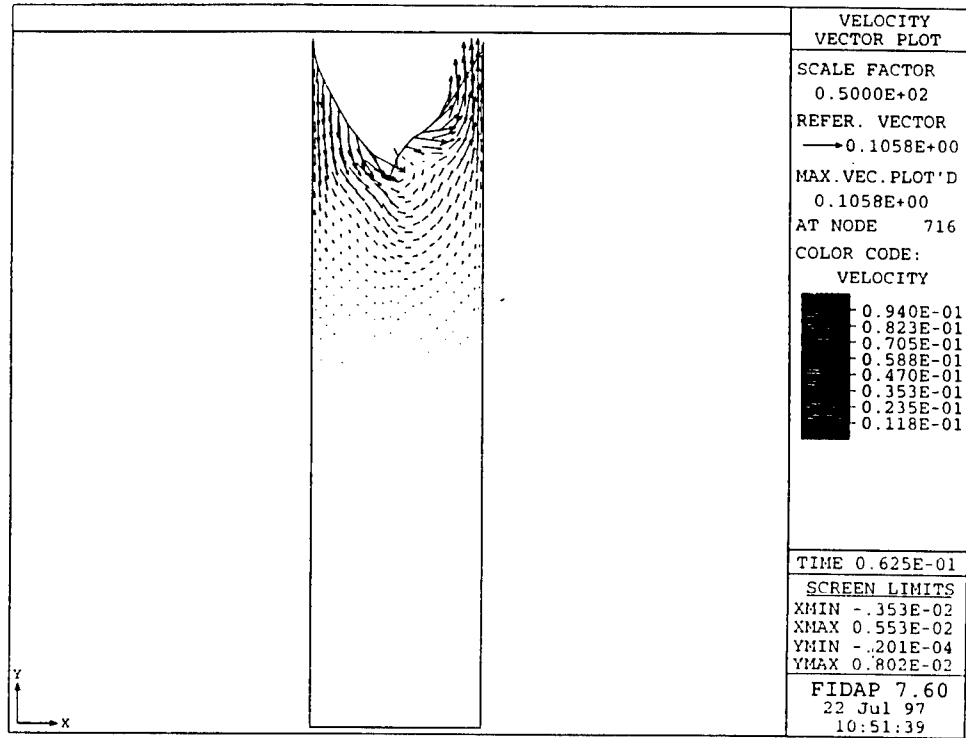


Figure 5.Velocity distribution in the capillary under vibration at $t=0.0625$ s

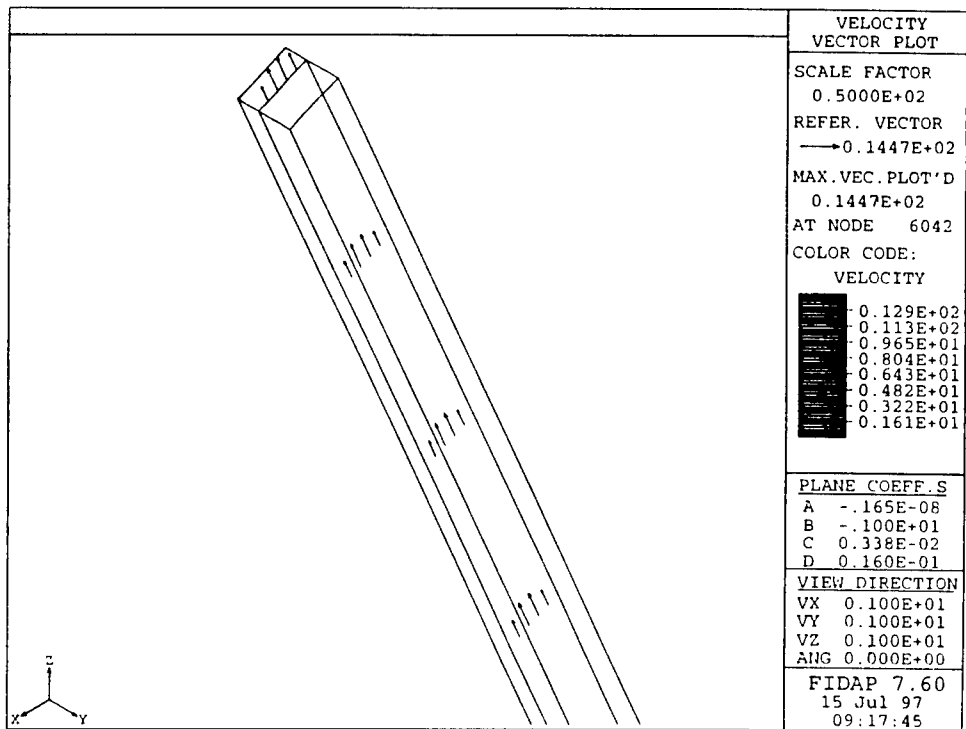


Figure 6.Velocity distribution in a curved channel simulating the heat pipe groove

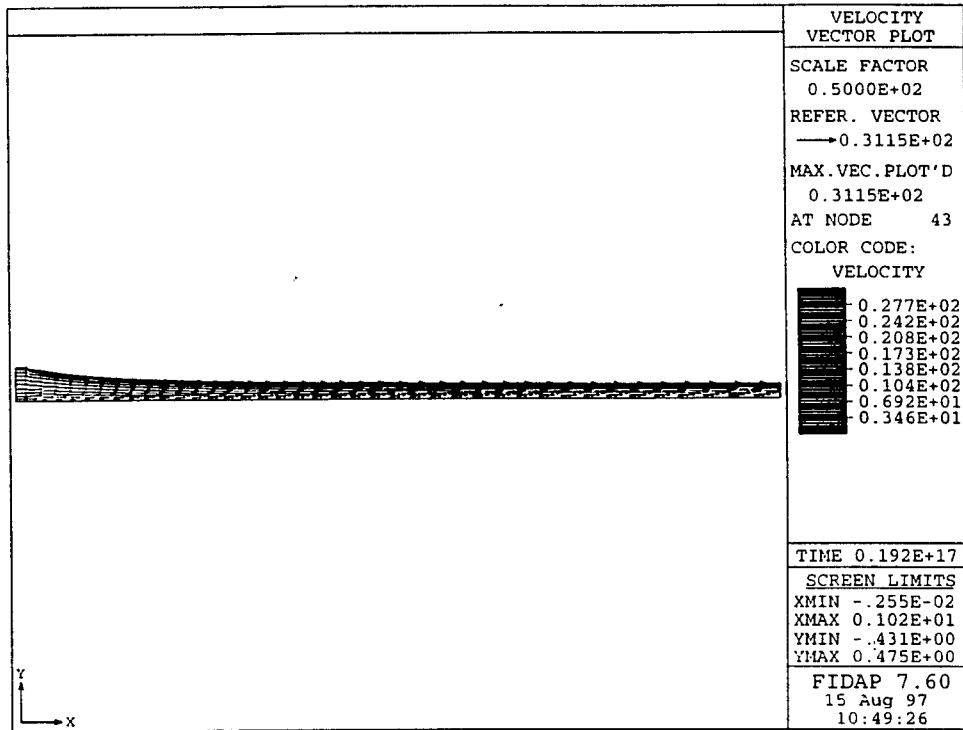


Figure 7.Velocity distribution in the adiabatic section of the heat pipe for 1-g axial acceleration

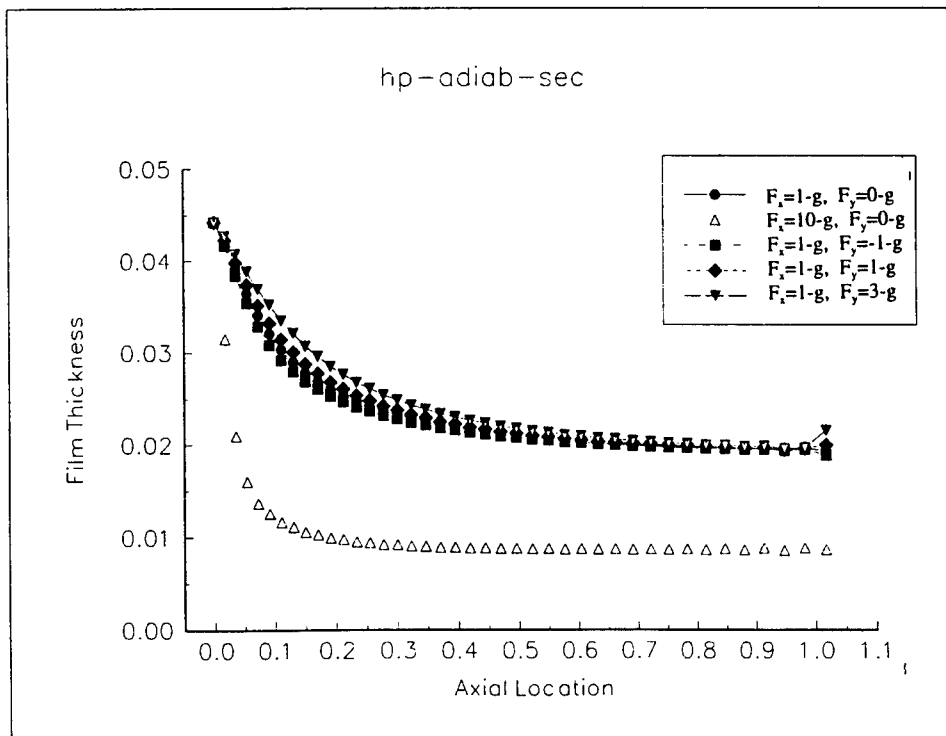


Figure 8.Film height in the adiabatic section of the heat pipe under different acceleration field

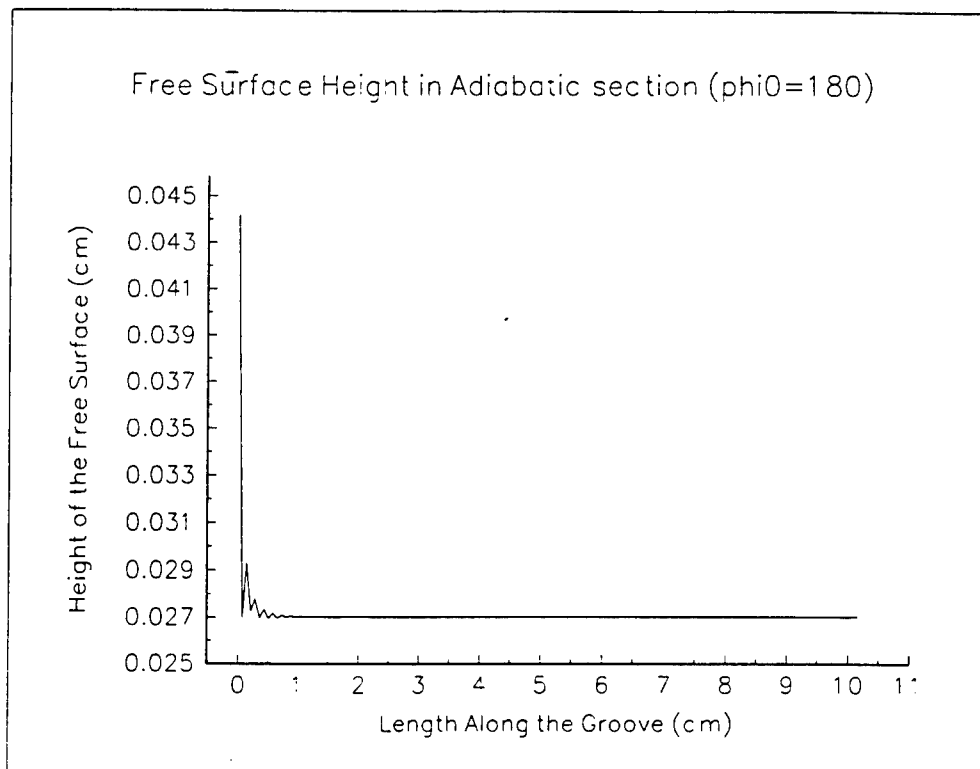


Figure 9. Film height in the adiabatic section of the heat pipe for 6-g acceration towards the axis of revolution

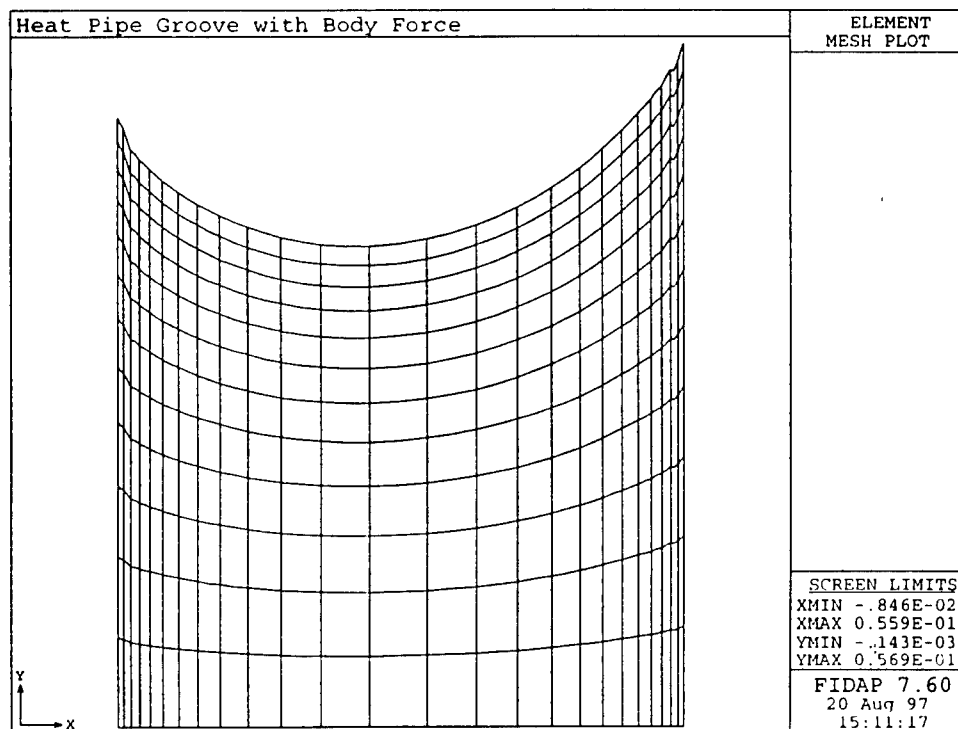


Figure 10. Cross-section of a liquid film in the heat pipe groove

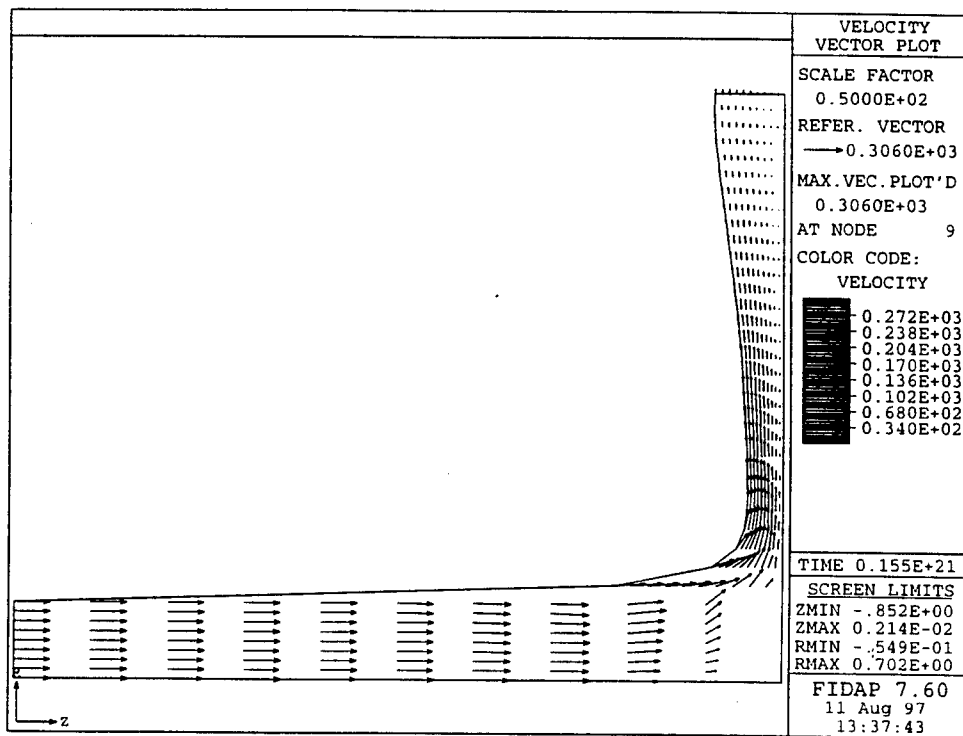


Figure 11.Velocity distribution in the impinging jet

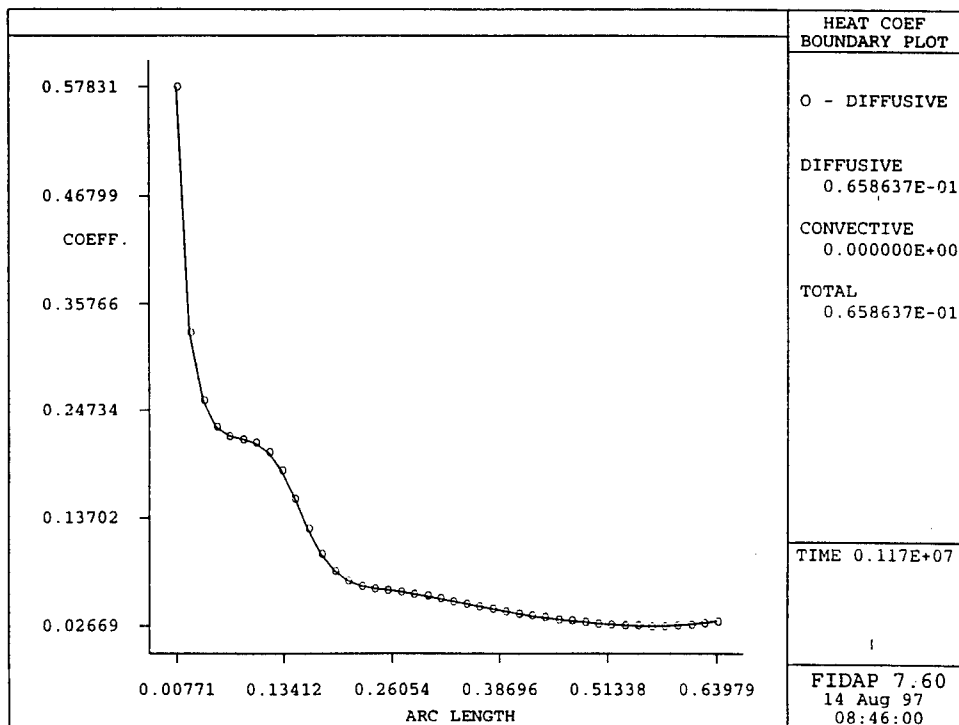


Figure 12.Local heat transfer coefficient at the solid-fluid interface during jet impingement

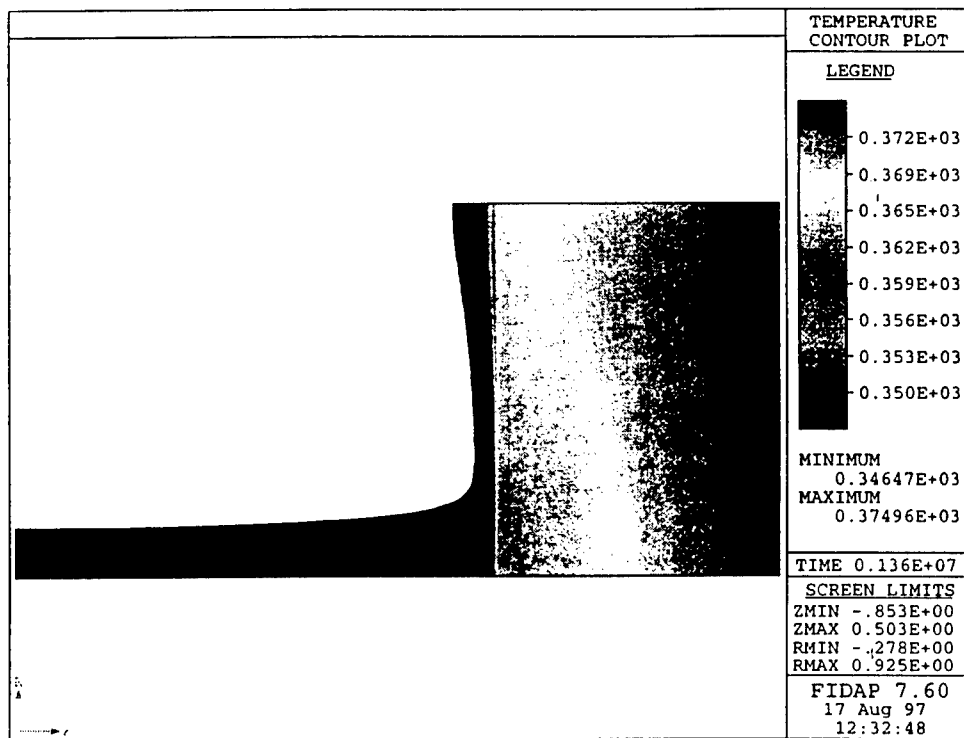


Figure 13. Temperature contours in the disk and the fluid during jet impingement

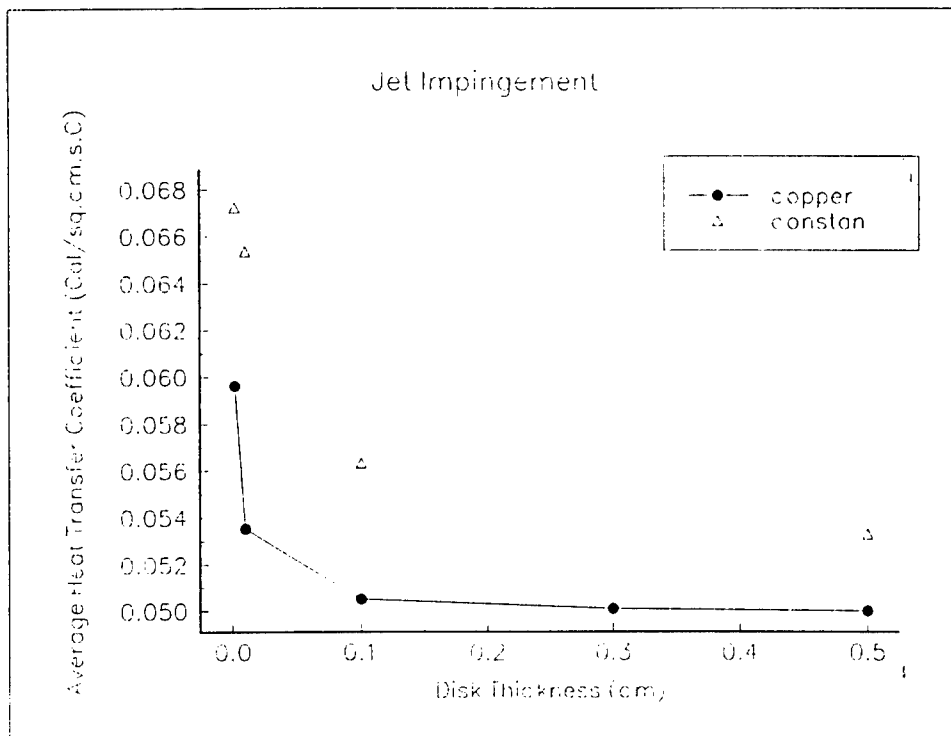


Figure 14. Average heat transfer coefficient over the disk during jet impingement

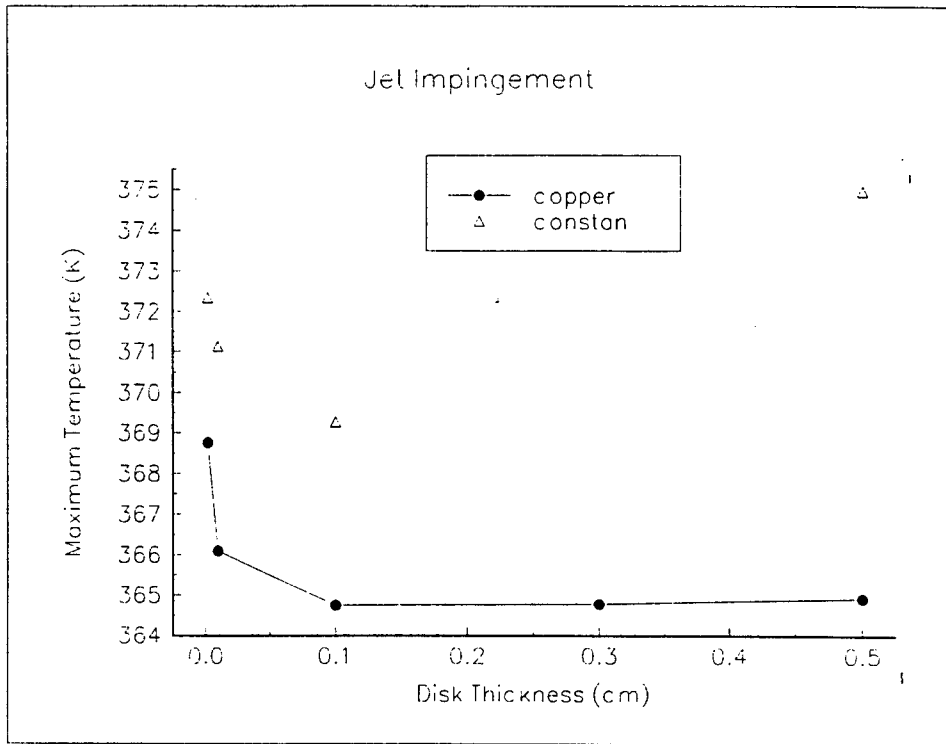


Figure 15. Maximum temperature in the solid during jet impingement cooling

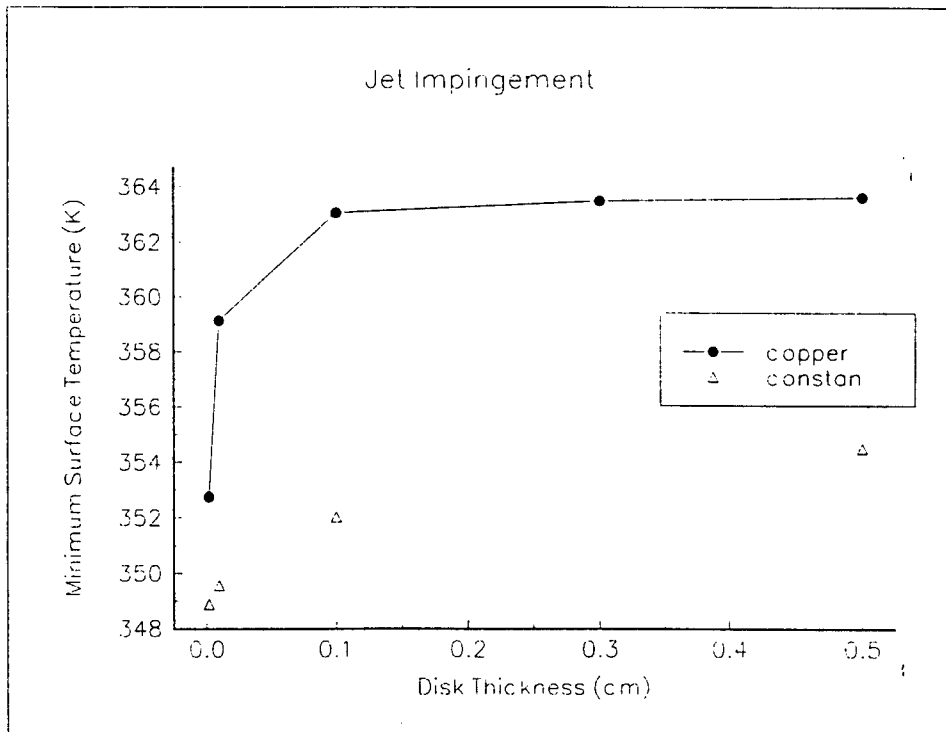


Figure 16. Minimum surface temperature during jet impingement cooling

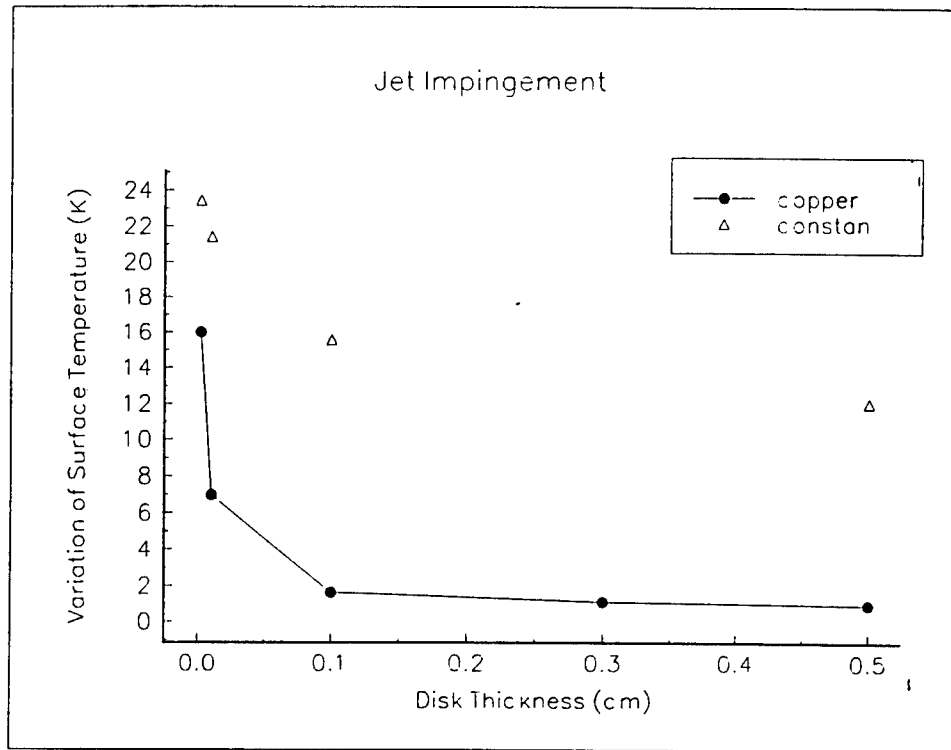


Figure 17. Variation of surface temperature during jet impingement cooling

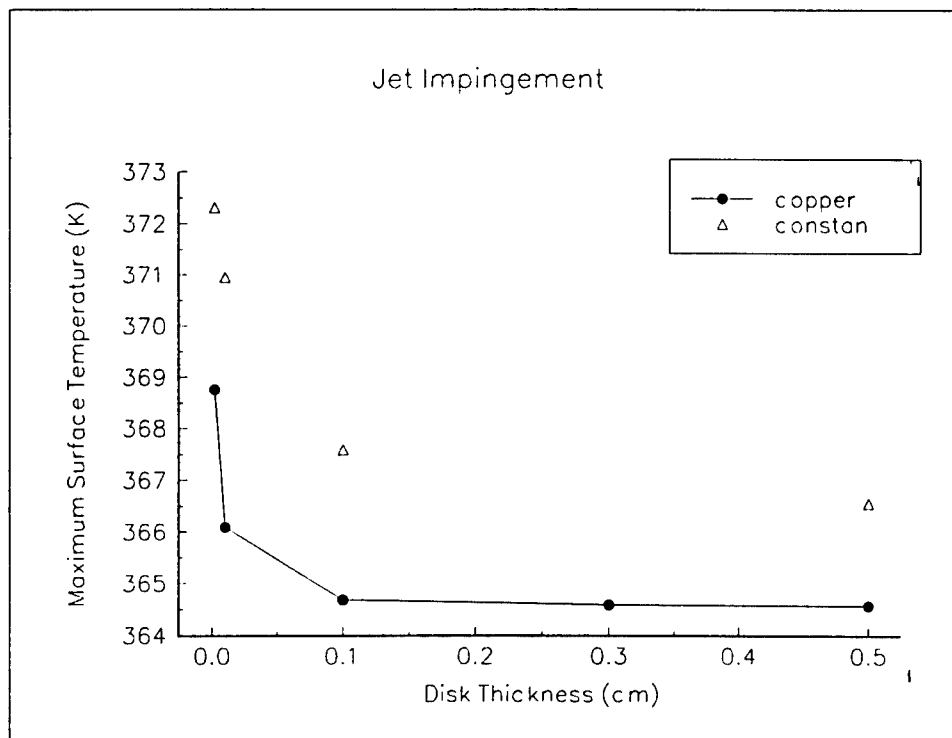


Figure 18. Maximum surface temperature during jet impingement cooling

**CLASSIFICATION OF HIGH RANGE RESOLUTION RADAR SIGNATURES
USING EVOLUTIONARY COMPUTATION**

**Mateen M. Rizki
Associate Professor
Department of Computer Science**

**Wright State University
Dayton Ohio 45435**

**Final Report for:
Summer Research Program
Wright Laboratory**

**Sponsored by:
Air Force Office of Scientific Research
Bolling Air Force Base, Washington, DC**

And

Wright Laboratory

September 1997

CLASSIFICATION OF HIGH RANGE RESOLUTION RADAR SIGNATURES USING EVOLUTIONARY COMPUTATION

Mateen M. Rizki
Associate Professor
Department of Computer Science and Engineering
Wright State University

Abstract

E-MORPH is multi-phase evolutionary learning system that evolves cooperative sets of feature detectors and combines their response using a simple linear classifier to form a complete pattern recognition system. The learning system evolves registered sets of primitive morphological detectors that directly measure normalized radar signatures. A special convolution kernel evolves simultaneously to extract information from the output of the primitive detectors to form real valued feature vectors. Starting with a population of trivial randomly generated detector sets, EMORPH uses a novel combination of three evolutionary learning techniques, genetic programming (GP), evolutionary programming (EP), and genetic algorithms (GA) to evolve increasingly complex detectors. The GP grows complex mathematical expressions that perform signal-to-signal transformations, EP optimizes convolution templates to process the results of these transformations, and the GA recombines sets of feature detectors to form orthogonal features. A simple linear Perceptron is trained to classify the resulting features forming a complete pattern recognition system. This report provides a brief description of E-MORPH and presents recognition results for the problem of classifying high range resolution radar signatures. This problem is challenging because the data sets exhibit a large within class variation and poor separation between classes. The specific data set used in this experiment consists of 100 signatures of six airborne targets drawn from a $10^\circ \times 10^\circ$ (azimuth x elevation) view window. The best recognition system evolved using EMORPH accurately classified 98.7% of the training signatures (6 targets x 50 samples = 300 signatures) and 95.7% of the signatures in an independent test set (6 targets x 50 samples = 300 signatures). This result is based on a preliminary experiment that did not involve tuning EMORPH's control parameters for this specific problem. This suggests that even better performance can be achieved in future experiments. The techniques used in E-MORPH are not tied to radar signals. The approach is generic and readily transitions to many different problems in automatic target recognition.

CLASSIFICATION OF HIGH RANGE RESOLUTION RADAR SIGNATURES USING EVOLUTIONARY COMPUTATION

Mateen M. Rizki
Associate Professor
Department of Computer Science and Engineering
Wright State University

INTRODUCTION

The foundation of a robust pattern recognition system is the set of features used to distinguish among the given patterns. In many problems, the features are predetermined and the task is to build a system to extract the selected features and then classify the resultant measurements. In automatic target recognition problems, the identification of a set of robust, invariant features is complicated because the shape and orientation of the objects of interest are often not known *a priori*. As a result, a human expert is responsible of examining each problem to formulate an effective set of features and then build a system to perform the recognition task. An alternative to this labor intensive approach of building recognition systems has emerged in the past ten years that uses learning algorithms such as neural networks and genetic algorithms to automate the process of feature extraction. There are many advantages to the automated construction of recognition systems over techniques that rely solely on human expertise. Automated approaches are not problem specific. Consequently, once an automated system is developed, it can be readily applied to similar problems greatly reducing the time needed to solve new recognition problems. Automated systems are capable of producing solutions that are comparable to the customized solutions created by human experts, but the solutions formed by these systems are often non-intuitive and quite different from the solutions formed by human experts. In many applications, this is a drawback because it is not possible to describe how the solution is obtained. This is also a strength of the automated approach. Automated techniques are unbiased. The features selected to solve problems represent alternative designs based on the structural and statistical attributes of the data. The fact that different features are selected suggests that automated systems are capable of exploring different regions of the space of potential solutions.

Several automated target recognition systems exist that use evolutionary learning to extract features from raw data and perform classification [Rizki et. al. 1993, 1994]. Early experiments with EMORPH, a system developed to evolve morphological algorithms, demonstrated that hybrid evolutionary learning systems are capable of generating pattern recognition systems to automatically perform feature extraction and classification from grey-scale images. In this system, a robust set of features is identified using a population of pattern recognition systems. Each system is composed of a collection of cooperative feature detectors and a classifier that evolves under the control of a user provided performance measure. The performance measure is tied to recognition accuracy, but additional constraints are included such as complexity measures to sculpt specific types of solutions. The recognition systems compete for

survival based on their performance. Successful systems have a higher probability of survival and contribute more information to future generations. The structural and statistical information gathered by each recognition system during the evolutionary process is passed to the next generation through a process of reproduction with variation. The most successful recognition systems are combined to form new recognition systems that are often superior to either parental unit. Two opposing forces operate in the evolutionary process: exploration and exploitation. By recombining successful solutions during reproduction, each generation contains recognition systems that are more capable of exploiting the performance measure and solving the recognition task. The reproductive process is imperfect, variations in the new recognition systems are created by mutating the structure of the feature detectors. Each new recognition system contains pieces of past successful designs with variations that explore alternative designs. The process of reproduction with variation and selection continues until the best recognition system in the population achieves a satisfactory level of performance.

This report describes experiments conducted using a modified version of EMORPH to evolve pattern recognition systems to classify high range resolution radar cross sections. This version of EMORPH blends three evolutionary learning paradigms: evolutionary programming [Fogel et. al., 1966; Fogel, 1991], genetic algorithms [Holland, 1975; Goldberg, 1989], and genetic programming [Koza, 1992] to form a hybrid learning system. The system extracts features from a training set of radar cross sections, assembles cooperative sets of features, and forms a single layer Perceptron [Papert and Minsky, 1988] to classify targets. A minimum amount of effort was devoted to tuning the EMORPH for the specific problem of classifying radar target, yet the evolved pattern recognition systems accurately classify an independent test set of radar cross sections.

THE EVOLUTIONARY LEARNING SYSTEM

The overall design of the EMORPH generated recognition system is shown in Figure 1. A recognition system is composed of a feature extraction module and a classification module. The feature extraction module applies a set of feature detectors to each radar cross section to form a feature vector. The classifier then assigns a target label to each feature vector. A feature detector is composed of two components, a transformation and a cap. Transformations are networks of morphological and arithmetic operations that alter the signal in an attempt to enhance the most discriminating regions of the radar cross sections while suppressing noise. Caps are convolution kernels or templates composed of a collection of positive and negative Gaussian probes that are used to explore both the geometrical structure and contrast variation of the transformed signal. The convolution operator produces its strongest response when all of the positive and negative probe points align with similar regions in the signal. Consequently, when a cap produces a strong response, it indicates that geometry and contrast variation embodied in the cap also exists in the transformed signal. By adjusting the positions, values, and spread of the probe points, complex structural relationships are readily identified. The output of a detector set is a registered stack of processed radar cross sections. The set of caps present in a single recognition system is a registered set of convolution templates that serves as a 3D

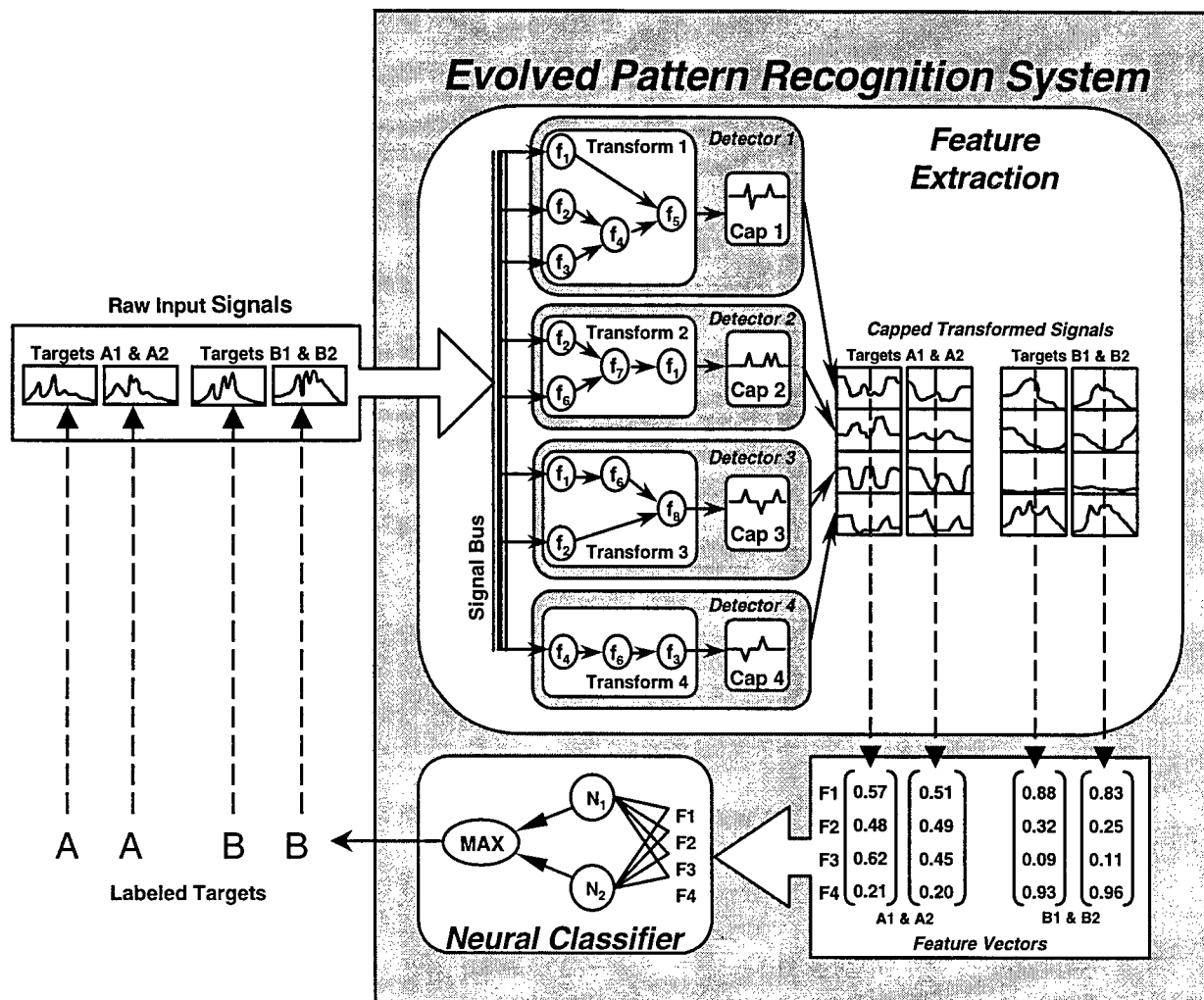


Figure 1. Overview of an evolved pattern recognition system.

probe. This probe allows the recognition system to explore relationships within a single stack-plane (transformed view of the input signal) or across several stack-planes. By varying the parameters of each transform, the feature extraction module can decompose a signal into different spatial frequencies creating a pseudo-wavelet transformation. When this occurs, the 3D probe can exploit multiple resolution levels to selectively mask noisy high frequency spikes leaving only the most prominent structures for further analysis. When the full set of detectors is applied to a radar signal, a real valued feature vector is produced. Each detector contributes one component to the vector. By repeating this process for all the signals, a feature matrix is created that is passed to a neural network for classification.

The E-MORPH system maintains a population of candidate recognition systems as shown in Figure 2. The performance of each member of the population is evaluated by using the recognition system to classify a training set of radar signals. After each recognition system is assigned a performance measure, it competes for survival with other members of the population. The competition is organized as a tournament that ranks each recognition system

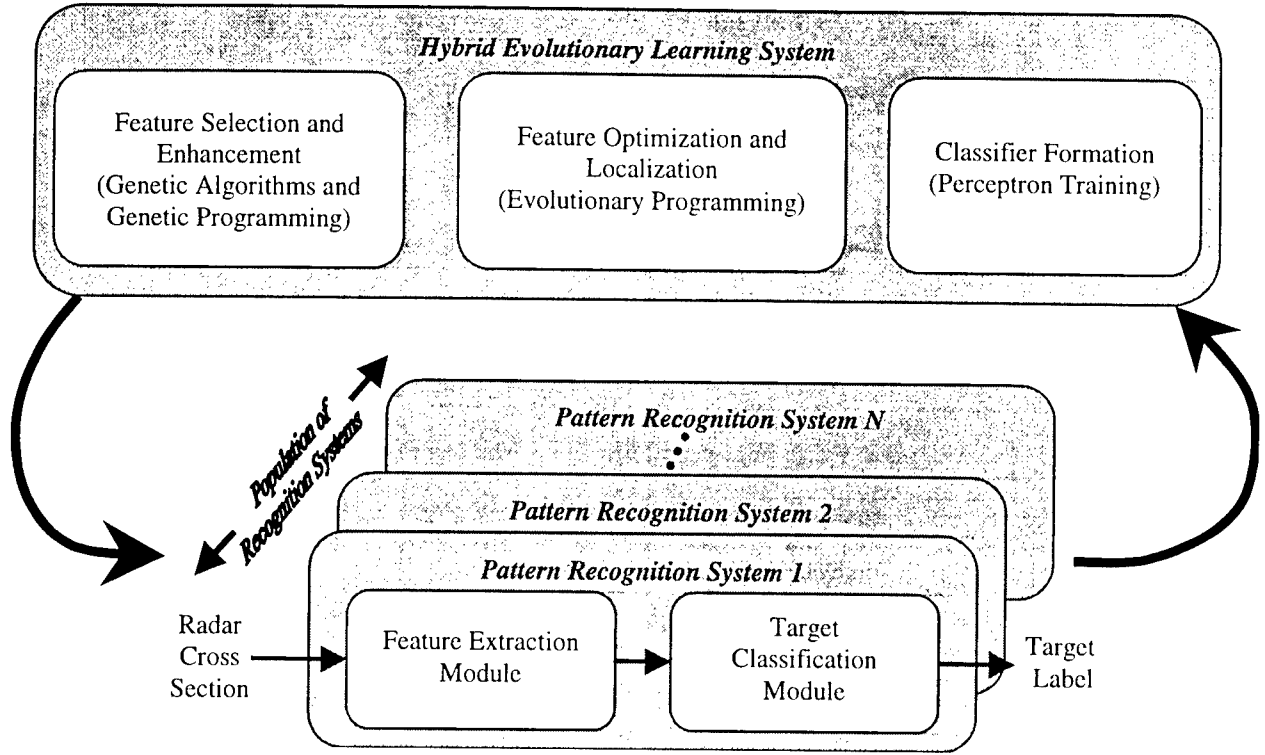


Figure 2. Overview of the EMORPH system.

based on its performance relative to the performance of other systems in the population. The size of the tournament changes throughout the evolutionary process and is based on the average performance of the population as shown in Equation 1.

$$NC = \max \left(1, M \cdot \frac{\sum_{i=1}^N pm_i}{N} \right) \quad \text{Equation 1}$$

In this Equation, NC is the number of competitors in each tournament, N is the population size, and M is a user imposed upper limit on the number of competitions ($M \leq N$). Each recognition system must win as many conflicts as possible to increase its chance for survival. The number of competitions won or lost is calculated using Equation 2.

$$win_i = \sum_{k=1}^{NC} \left[\left(\frac{pm_i}{pm_i + pm_{2 \cdot N \cdot U(0,1)}} \right) < U(0, 1) \right] \quad \text{Equation 2}$$

In these local competitions, the chance of winning is proportional to the ratio of the performance measure of the recognition system and its competitor. For example, if a recognition system's performance (pm_i) is high and a randomly selected competitor's performance ($pm_{2 \cdot N \cdot U(0,1)}$) is low, then the probability that the ratio is greater than a value drawn from a uniformly distributed random variable $U(0, 1)$ is also high. When the relationship shown in Equation 2 is satisfied, the recognition system wins the pairwise competition. Limiting the tournaments to a subset of

the population reduces the possibility of premature convergence of the evolutionary process. When the average performance of the population is poor, the number of individuals in each tournament is small and a marginally better recognition system does not have the opportunity to dominate the population. The pairwise competition used within each tournament tends to maintain a diverse population of recognition systems because marginal individuals always have a small probability of survival. The final selection for survival is based on a ranking of the number of conflicts won by each recognition system. The sets with the greatest number of victories survive to the next learning cycle.

E-MORPH uses three different techniques to alter the structure of the detector set contained in each recognition system. The position of the Gaussian points in the convolution templates within a detector set are varied using evolutionary programming [Fogel, 1991], the functional form of the transformation is modified using genetic programming [Koza, 1992], and the collection of detectors that form the basis of the feature extraction module are selected using a genetic algorithm [Holland, 1975]. These techniques are combined to exploit the strengths of each paradigm.

The purpose of the EP algorithm is to systematically improve the position, type, and number of probe points in the convolution templates. This is accomplished using a controlled vibration of the position of the Gaussian points in each template followed by a series of random mutations that add and/or delete points (see Figure 3). The EP phase manipulate each recognition system independently. To begin, a member of the population of recognition systems is cloned to form an extended clonal population of C recognition systems. The caps in each detector set in the extended population are subjected to random variations. The amount of variation is inversely proportional to the performance of the parental detector set and controlled by Equation 3. The value $x_{j,k}$ is the central position of the k th Gaussian

$$x_{j,k} = \max\left(\min\left(x_{j,k} + \left(\frac{X_{size_j}}{2} \cdot (1 - pm_i)\right) \cdot N(0, 1)\right), X_{max_j}\right), X_{min_j}\right) \quad \text{Equation 3}$$

point in the j th convolution template, X_{size} is the size of the template, X_{min} is the location of the left side of the template, X_{max} is the location of the right side of the template, $(1 - pm_i)$ is the complement of the performance measure of the i th detector set, and $N(0,1)$ is a normally distributed random variable with a mean of zero and a variance of one. To update a probe point's position, the mean of the random variable is set to the value of the initial position of the

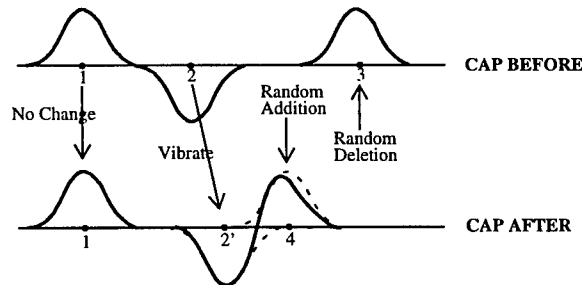


Figure 3. Evolving a convolution template.

probe point and the variance is scaled to fall into the range from zero to half the template size. Using this technique, when the performance measure is low, the potential extent of variation in the position of a probe point is high. The potential for variation is reduced as the performance increases. If the performance reaches one, the potential for variation is zero and the template's point configuration is frozen. This approach to adjusting the structure of a template is similar to the process of simulated annealing where gradual improvements in the population performance shut down the process of random variation as a solution is formed.

The vibration process is only capable of adjusting the position of existing probe points. The second step of the EP phase is mutation that adds and/or deletes probe points to alter the complexity of the templates. Point mutation occurs immediately after the template points are vibrated. The amount of each type of mutation is controlled by a user selected probability. As a rule, if the detector set is initialized with a limited number of probe points, the probability of addition should be larger than the probability of deletion. This will bias the mutation rate toward addition and cause the detectors to grow in complexity.

In addition to the type and placement of the Gaussian points in a template, the variance (spread) of Gaussian probes change during the evolutionary process. The extent of each probe point is determined using an Equation 4. The

$$\sigma = \sigma_{min} + (1 - pm_i) \cdot (\sigma_{max} - \sigma_{min}) \quad \text{Equation 4}$$

limits on the spread of a single Gaussian point are set by the user to $(\sigma_{min}, \sigma_{max})$. The actual size of the probe point is then adjusted relative to the performance of the i th recognition system (pm_i). If the system exhibits poor performance, the points increase in size to become less sensitive to the environment. If the recognition system is very accurate, the points become smaller and more sensitive to variations in the signals.

The decision to accept a mutated cap is based on a local performance measure. A value for the Fisher's Discriminant [Fisher, 1936] is calculated for the original capped detector and the mutated detector. This is a measure of the detector's ability to increase the separation between the means of the response for each class of target while simultaneously reducing the variance in the response for each class. If the mutated detector is more discriminating than the original detector, it replaces the parental unit. After all of the templates in a detector set are mutated and the successful caps have replaced their parental caps, the complete set of detectors is placed in the recognition module and a Perceptron [Minsky and Papert, 1988] is trained to classify the targets. The error vector returned by the recognition module is used to assign a performance measure to the modified detector set. This process is repeated for each detector set in the clonal population. Finally, the C parental detector sets compete with the C offspring detector sets for survival in a tournament. The top ranked C detectors are preserved and the evolutionary programming cycle begins again. After a fixed number of EP cycles, the performance of the best recognition system evolved during the EP phase is compared to the original parental recognition system. If the best evolved recognition system is more

accurate than its parent, it replaces its parent in the base population. This process is repeated for each member of the base population. When the EP phase terminates, the base population contains optimized sets of convolution templates specifically tuned to the transforms contained in the individual recognition systems.

EMORPH uses genetic programming (GP) to grow the transformations and a genetic algorithm (GA) to mix detector sets. The actions of GP and GA are blended together into one process. The GA is responsible for recombining detector sets and components of detector sets (see Figure 4). Parental units are selected from the base population using roulette wheel sampling where the probability of selection is proportional to the recognition system's accuracy. Once a pair of parents is selected, their detectors are exchanged using a uniform crossover. The detector set is analogous to a biological chromosome and the individual detectors are similar to genes. During crossover, each detector position in the parental set contributes some portion of each of its detectors to a pair of offspring detector sets. There is a 0.5 probability that the first parent places its information in the first offspring and the second parent places its detector in the second offspring. Similarly, there is a 0.5 probability that the first parent places its information in the second offspring and the second parent places its detector in the first offspring. As shown in Figure 4, the information placed in the offspring can vary. In some cases, a parental unit simply copies its whole detector into the selected offspring. In other cases, one parent contributes a transform and the other contributes a cap. There are user defined probabilities for each type of exchange. Typically, there is a higher probability of exchanging complete detectors and a lower probability of exchanging caps and transforms. Since caps are customized to the transformation during the EP phase, exchanging whole detectors is not as disruptive as recombining transforms and

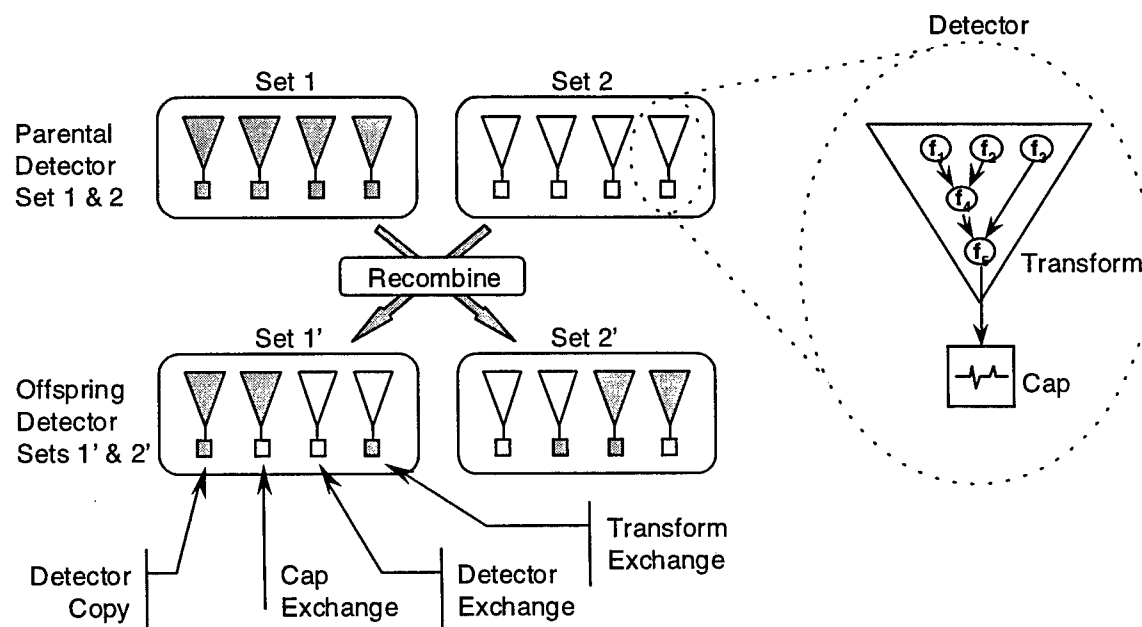


Figure 4. Action of the GA process. The GA takes pairs of detector sets and recombines components of each parental set to form pairs of offspring. This process can result in combinations of different caps on transforms or whole detectors being exchanged between sets.

caps. At the same time, since the detectors are at fixed positions in the set, the transforms and caps at a given position are similar so mixing caps and transform is not unreasonable.

The GP and GA are concurrent processes. When an exchange of detectors occurs, there is a small probability that the internal structure of the underlying transforms are also recombined using GP as shown in Figure 5. The transformations are represented as expression trees. The input patterns flow from the leaves of the tree through the operators to the root of the tree. The GP algorithm exchanges sub-trees between pairs of transformations. In Figure 5, transform one (dark grey) contains a root and two sub-trees labeled S1 and S2 while transform two (stippled grey) consists of a root and two different sub-trees labeled T1 and T2. Recombination forms two new transformations where the sub-trees S1 and T1 are exchanged in the offspring. In addition to exchanging information by recombination, sub-trees can be added, deleted, or replaced. Mixing the structure of expressions produces radical changes in the operation of the offspring transform. This disruptive process facilitates the search for new functions. The probability of each type of action is defined by the user. Usually, the probability of mutation (addition, deletion, replacement) is lower than the probability of recombination because recombination preserves larger pieces of the structure and therefore is slightly less disruptive than mutation.

EMORPH uses a combination of morphological and arithmetic operators as a basis for its functional transformations. Mathematical morphology is a technique for probing the structure of signals or images using set theoretic operations

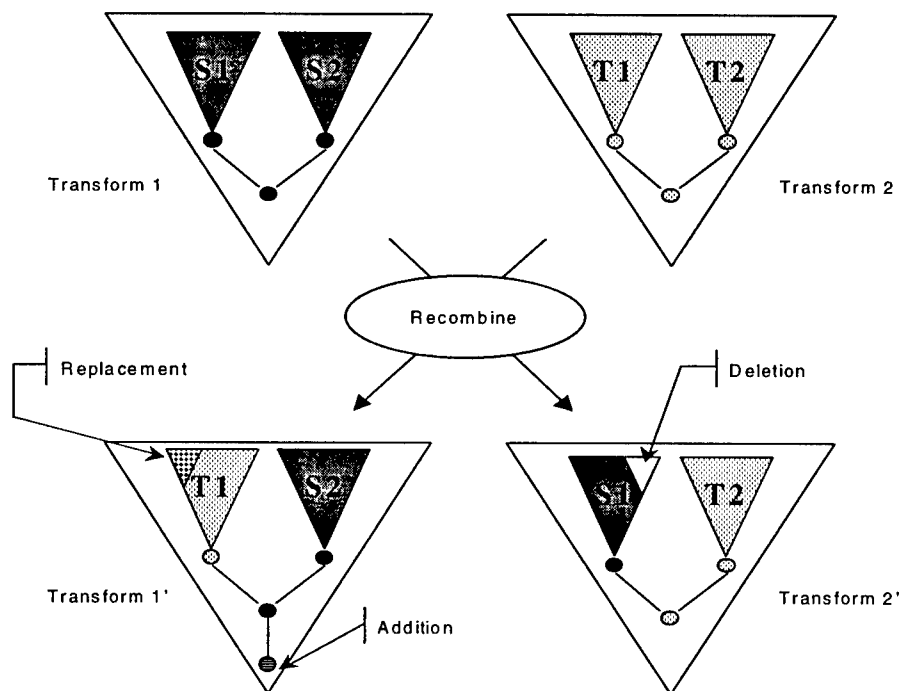


Figure 5. The GP process applied to transformation. Parental transformations are defined as expression trees. Sub-trees are recombined to form new transformations. During this process, some new operators are introduced (addition), some are removed (deletion), and some sub-trees are replaced with randomly generated sub-trees.

[Serra, 1982; Haralick et. al. 1987]. Each morphological operation is a signal-to-signal transformation that applies a probe-like pattern, referred to as a structuring element, to an input signal to produce an output signal. By selecting the correct algebraic form and structuring elements, specific objects can be isolated or enhanced, but finding the combination of operators and probes to perform a given task is difficult even for an experienced morphological analyst. EMORPH solves this problem using GP to generate, evaluate, and select suitable morphological transformations to accomplish the desired classification. To begin the evolutionary process, the detector sets that form the basis for the population of recognition systems are initialized with small randomly generated expression trees. Each node in the trees contains an operator drawn from the set: erosion, dilation, opening, closing, band-opening, band-closing, complement, addition, subtraction, minimum, maximum, and threshold. Most of the operators require some type of parameter. The morphological operators (erosion, dilation, opening, closing, band-opening, band-closing) use structuring elements that are selected at random from a standard library consisting of three basic shapes (e.g. 1-D cross section of a cone, a bar, a ball). A scale factor is also included to alter the size of the structuring element. Some of the arithmetic operators (minimum, maximum, threshold) also use a parameter to control the behavior of the operation. These parameters are selected from a uniformly distributed random variable ($U(0,1)$). Detailed examples of morphological operations, library structuring elements, and the process of generating expressions are described by Zmuda et al. [1992]. When each expression is generated, it is applied to the input signals. If it produces an extreme effect (e.g., the output of the operation is a constant value), it is considered a lethal form and discarded. Transforms are generated until an acceptable set is found for each member of the initial population.

The GP/GA phase begins with N detector sets and combines $N/2$ pairs of parental sets to form an extended population of $2N$ sets. Each member of the extended population is evaluated using the same procedure described for the EP phase. A tournament selection process is applied to rank the entire population and the N top-ranked detector sets are preserved for the next cycle of the GP/GA algorithm. When the GP/GA phase is complete, each detector set consists of combinations of transforms and caps that proved useful in the recognition process.

The overall flow of the EMORPH evolutionary process is shown in Figure 6. To summarize, EMORPH generates N random recognition systems. Then the learning cycles begin. Each pass through a learning cycle consists of one application of the EP phase where the caps within each detector set are adjusted and several passes through the GP/GA phase where the transformations are restructured. The EP phase is applied to each recognition system in the base population of size N . The i th recognition system ($i=1,2,3,...,N$) is cloned C times. The detector set caps within each clonal recognition system are then mutated to produce C mutated recognition systems. Then C recognition systems are selected from the expanded population of size $2C$ using tournament selection and the process repeats. After a user specified number of cycles, the best recognition system in the final set of C competes to replace its ancestor (the i th recognition system) in the base population. The GP/GA phase then begins. In this phase, the base population of N recognition systems are repeatedly recombined using the hybrid GP/GA technique described earlier. The $N/2$ pairs

```

//GENERATE INITIAL POPULATION OF N RECOGNITION SYSTEMS
FOREACH recognition system DO
    FOREACH detector in the recognition system DO
        randomly generate a transform
        randomly generate a cap
    ENDFOR
    apply the detector set to the training data (produce a feature matrix)
    calculate the performance measure (classify the training data set)

FOR 1 to the desired number of learning cycles DO
    // ACTIVATE THE EP PHASE
    FOREACH recognition system DO
        generate a clonal population of size C
        FOR 1 to the desire number of ep cycles DO
            FOREACH recognition system in the clonal population DO
                copy the recognition system
                FOREACH detector in the copied recognition system DO
                    vibrate the cap
                    mutate the cap
                    compute the Fisher's discriminant
                    IF the Fisher's value of mutated detector is better
                        THEN replace the detector
                ENDFOR
            apply the detector set to the training data (produce a feature matrix)
            calculate the performance measure (classify the training data set)
            perform tournament selection (reduce 2C --> C)
        ENDFOR
        IF the best detector is more accurate than the original parental unit
            THEN replace the parental unit
    ENDFOR
ENDFOR
// ACTIVATE THE GP/GA PHASE
FOR 1 to the desired number of ga/gp cycles DO
    select parents using roulette wheel sampling
    // recombine parental sets using modified uniform crossover to form two offspring
    FOREACH position in the detector sets DO
        SELECT type of exchange with a user specified probability
        1:    exchange whole detector
        2:    exchange caps
        3:    exchange transforms
        4:    recombine transforms (gp)
              (a) crossover sub-trees
              (b) extend trees with randomly selected operators
              (c) delete randomly selected sub-trees
    ENDFOR
    apply the detector set to the training data (produce a feature matrix)
    calculate the performance measure (classify the training data set)
    perform tournament selection (reduce 2N --> N)
ENDFOR
IF the maximum performance is unchanged for several generation
    THEN IF the maximum performance is less than 100%
        THEN add a randomly generated detector to the end of every detector set
        ELSE select a random position and delete the detector in the position in all detector sets
ENDFOR

```

Figure 6. An overview of the EMORPH algorithm.

of recognition systems are selected using roulette wheel sampling to form N new recognition systems. The recognition accuracy of these new systems is then calculated using a linear Perceptron classifier, and a tournament is conducted to reduce the population from 2N to N recognition systems. This process repeats for a user selected number of cycles. Since the number of detectors in each member of the population is fixed, it is possible to have too

many detectors to solve the given recognition task. To overcome this difficulty, EMORPH tracks the performance of the best member of the base population during the course of the evolutionary process. If there is no improvement in the accuracy of the best recognition system for several generations, a new detector is added to the end of every detector set in the base population. If EMORPH generates a perfect system (100% accurate), then periodically a detector is deleted from every recognition system in an attempt to locate a less complex solution.

The user can set parameters to control the number of EP and GP/GA sub-cycles that occur within each E-MORPH learning cycle. There is a trade-off between the EP and GP/GA phases. The user can increase the sensitivity of the individual detectors by increasing the number of passes through the EP phase relative to the number of passes through the GP/GA phase. Alternatively, the user may elect to spend more computational resources adjusting the average complexity of the detector sets by increasing the number of passes through the GP/GA phase. It is difficult to select an appropriate mixture of passes because the evolutionary learning process is dynamic. During the early stages of evolution, it is not likely that the complexity and number of detectors in the population is suitable for the recognition task. If the user arbitrarily increases the number of EP passes, the probe point density will increase to compensate for the lack of complexity in the transforms and limited number of detectors. This will produce customized solutions that tend to perform well on training sets and poorly on test sets. If the number of GP/GA cycles is too large, the transform can become too complex to compensate for the inadequate distribution of probe points within each cap. A good compromise would be to implement an adaptive control mechanism that evaluates the relative contribution of each phase throughout the evolutionary process and dynamically adjust the length of each phase appropriately.

EXPERIMENTAL DESIGN

To demonstrate how EMORPH generates pattern recognition systems, the results of a target recognition task in high range resolution radar are presented. Specifically, the problem is to classify a set of airborne targets from their radar cross sections. For this experiment, a sample of 600 radar signatures were extract from a large database of signals. Each radar signature is one view of a target at a specific azimuth and elevation. The selected data set contains six targets at azimuths that range from -25° to -16° and elevations that range from -20° to -11° in increments of 1° . Thus, there are one hundred samples of each target in the data set. These were divided into a training set of 300 radar signatures that contain 50 samples of each target and a test set of 300 cross sections that also contain 50 samples of each target. The data was not placed in the sets at random. The training set contains all targets with odd values of azimuth while the test set contains the remaining signatures. This amounts to placing every other signature in the view volume (azimuths x elevations) into one set and the remaining signatures into the other. A few sample signatures are plotted in Figure 7. Notice the signatures have been normalized into 128 range bins with the maximum value (255) placed in bin 63. Looking down the column of data it is easy to see there are characteristic features in each target that persist through a few degrees of change in azimuth, but then rapidly disappear. Also note the similarity in the signatures between targets making the classification task quite difficult. In Figure 8, the full

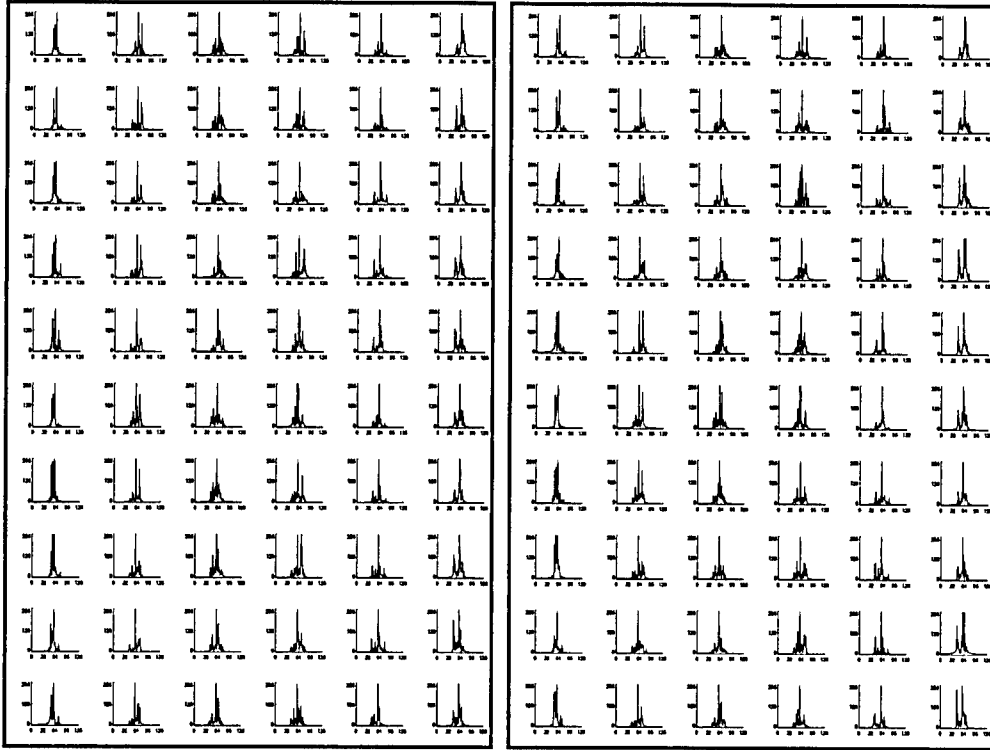


Figure 7. Sample radar cross sections. The box to the left contains training data. The column are targets 1-6 and the rows are various changes in azimuth and elevation (az=-25° to -17° in increments of -2° at elevation -20° followed by az=-25° to -17° in increments of -2° at elevation -19°). The box to the right contains test data. Again, the column are targets 1-6 and the rows are various changes in azimuth and elevation (az=-24° to -16° in increments of -2° at elevation -20° followed by az=-24° to -16° in increments of -2° at elevation -19°).

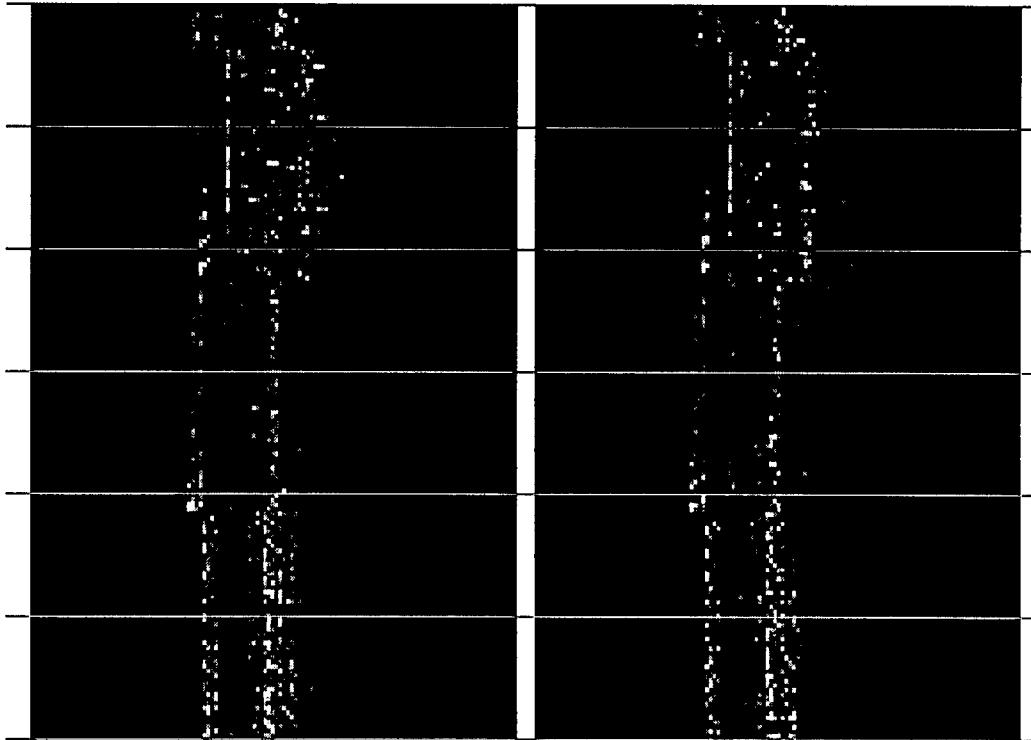


Figure 8. Training and test data sets. The complete training set is displayed as an image in the box to the left and the test data set is displayed to the right. Each row in these images represent one radar signature at a given azimuth and elevation. The intensity of each pixel represents the magnitude of the range bin at the given location. The horizontal white lines were added to divide the data sets into six groups that represent the six different targets.

training and test data sets are displayed as images. A set of horizontal white lines are inserted into the figure to separate the different targets, but it is possible to see the general location of the sets of targets without the lines. This suggests that there are some invariant aspects to each target.

To begin the learning experiment, a population of 10 pattern recognition systems is generated. Each system is initialized with three randomly generated detectors consisting of a transform containing one to three operators and a cap with one or two Gaussian points. The accuracy of each detector is evaluated by training a single layer Perceptron to classify the training data set. The initial population contains recognition systems that range in accuracy from 40.7% to 57.7% on the training data set.

An E-MORPH learning cycle consists of five EP sub-cycles followed by five GA sub-cycles. A pass through the EP phase consists of processing each member of the base population of 10 recognition systems. Each member of the base population is used to produce 10 clones that are then mutated to produce an additional 10 recognition systems. This extended population of 20 systems is pruned back to 10 individual using tournament selection. The process is repeated five times and the best recognition system found competes to replace its ancestor in the base population. Similarly, the GP/GA phase begins with the base population of 10 recognition systems. Copies of these base systems are mutated and recombined to create an extended population of 20 systems (10 parents + 10 offspring). The extended population is ranked using tournament selection and the top 10 systems are saved to start the next GP/GA sub-cycle.

For the EP phase, the probabilities of vibration, addition, and deletion are 0.6, 0.3, 0.1 respectively. When a Gaussian point is added to a cap, there is a 0.67 probability that the point is positive and a 0.33 probability that the point is negative. The range of a Gaussian probe point is 4 to 12 range bins (i.e. pixels) and the maximum weight of a point is limited to the range of 1 to 3. In the GP/GA phase there is a 0.3 probability that a detector set is mutated and a 0.7 probability that a pair of sets is recombined. If a set is selected to undergo mutation, there is a 0.2 probability that an individual transform passes to the offspring unchanged; a 0.7 probability that the transform is extended with a randomly selected operator, and a 0.1 probability that a random tree is added to the transform. If a pair of detector sets are combined, there is a 0.4 probability that the complete detectors are exchanged, a 0.4 probability that only the caps are exchanged; a 0.1 probability that sub-trees within the transforms are exchanged; and a 0.1 probability that transforms are joined at the root with a randomly selected operator (a special form of exchange).

The experiment consists of a total of 50 learning cycles where each cycle consists of one application of EP (5 sub-cycle) followed by one application of GP/GA (5 sub-cycles). The average recognition accuracy for the population produced during the evolutionary learning process is shown in Figure 9a. The performance is displayed at the end of each EP and GP/GA phase ($50 * (1 + 1) = 100$ generations). The average recognition accuracy rises from a low of 49.5% in generation 0 (before applying EP or GP/GA) to 93.7% in generation 100. Notice, the curve is not

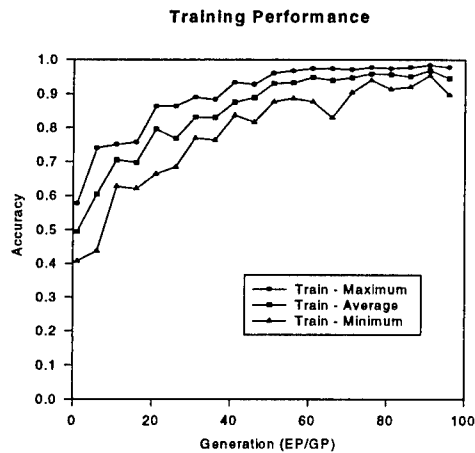


Figure 9a. Average performance for the training set.

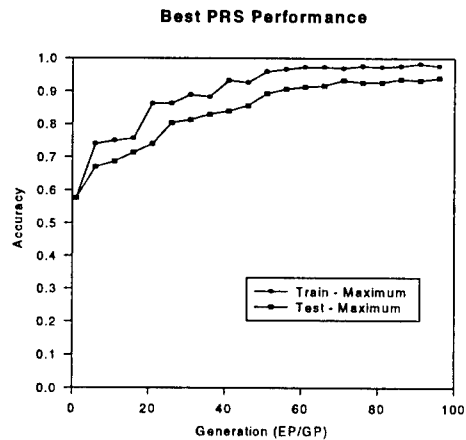


Figure 9b. Performance of the best recognition system for the training and test data sets.

monotonically increasing. This is because detectors are added to each detector set in generations 15, 33, 49, 73, and 93. When a new detector is added, the performance of some of the recognition systems is disrupted and performance fluctuates until the new detector is optimized. There are other disruptive influences that are not visible in this graph. After each application of the GP/GA phase, the overall system performance decreases slightly, but usually bounces back after the next application of the EP phase. This is not surprising, the GP/GA phase tends to disrupt the underlying transformations and EP adjusts the caps to compensate. This disruptive influence is often beneficial, leading to better performance in later learning cycles. The performance of the best recognition system in each generation is shown in Figure 9b. The accuracy of the best system rises from approximately 57% on the training and test data sets using 3 detectors to a maximum level of 97% on the training set and 95.7% on the independent test set. The best recognition system uses 8 detectors. A higher training score (98.7%) appears in generation 84 using only 7 detectors, but it is associated with a slightly lower test set performance of 94.7%.

The response vectors produced by the best recognition system are shown in Figure 10. The plots in the left-most column represent the output response of the eight detectors in the best recognition system to the training data set. The x-axis of each plot is numbered in units of 50 that correspond to groups of data of the same class (e.g. 0-49 are examples of target 1, 50-99 are examples of target 2, etc.). The jagged nature of the response vectors makes it difficult to judge how much overlap there is between the responses for different classes. The plots in the second column from the left depict the range of the response for each class as a horizontal line (class one is at the bottom and class six is at the top). For example, the first detector's plot (row 1, column 2) shows there is no overlap between the response for target 1 and target 6 and there is a slight overlap between the responses for targets 2-4 and target 6. Consequently, detector 1 is effectively separating class 1 from class 6 and almost separating classes 2-4 from class 6. Essentially, this is a target 6 detector. Each detector's response to the test data set is shown in the third column of

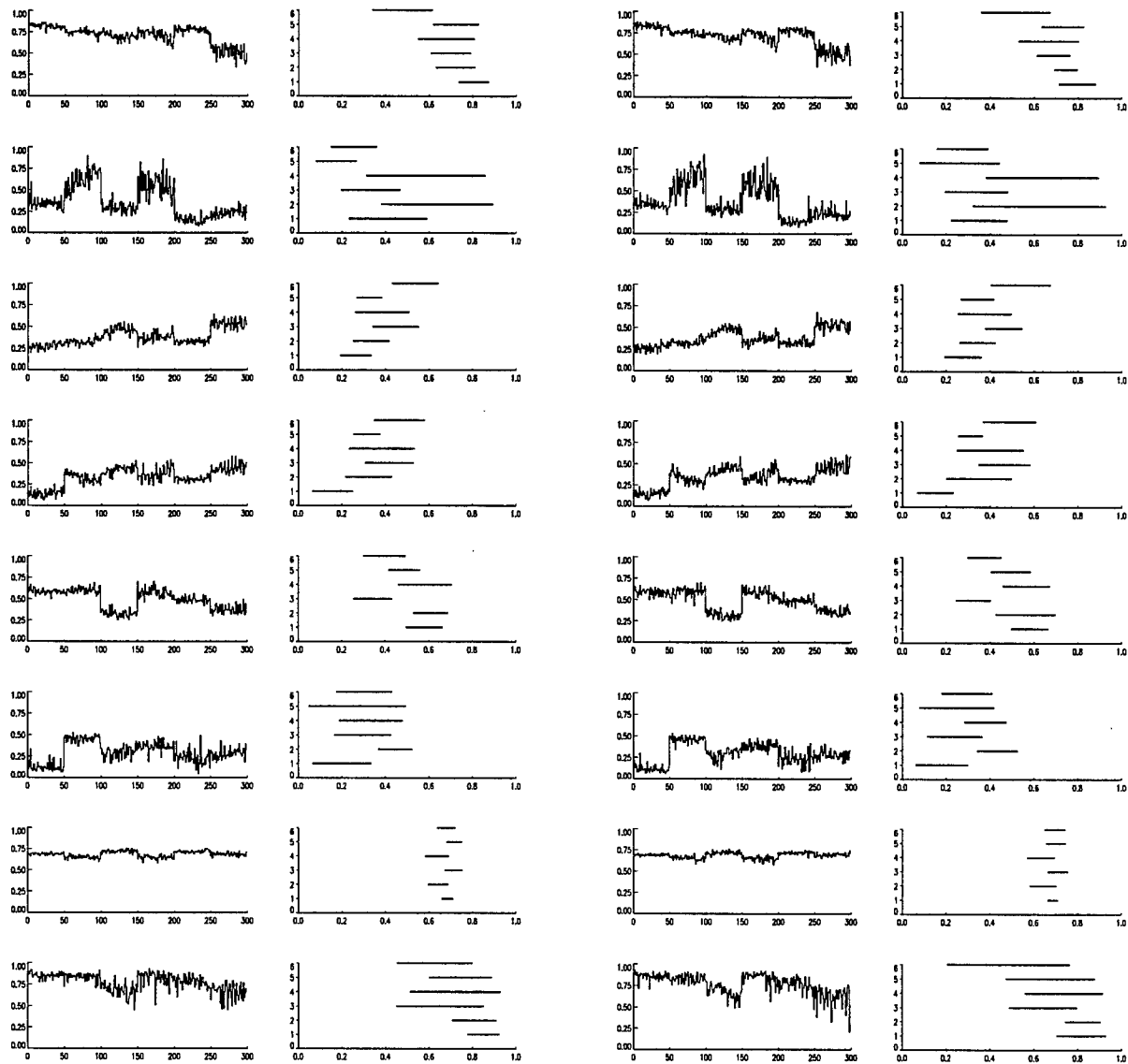


Figure 10. Response vectors produce by the best recognition system in generation 100.

plots, and the range of these responses are shown in the right-most column. There is some variation in the range of responses of the detector to the training and test data sets, but the overall the behavior is quite similar. The detectors form an ordered set (1-8). The detectors in the higher numbered positions are younger in terms of the evolutionary process so it is not surprising that they do not exhibit as much separation among the class responses. The older detector positions (1-6) all contain at least one pair of completely separated classes, while the less optimized detectors (7-8) do not. If the evolutionary process was allowed to continue, these responses could be refined producing better separation among the classes.

A more detailed examination of the best recognition system reveals that it contains detectors with different levels of complexity (see Figure 11). The transforms are displayed in a LISP-like format where expressions are parenthesized

DISCUSSION

E-MORPH successfully generated a pattern recognition system to classify high range resolution radar signatures. The evolved recognition system achieved a classification accuracy of 98.7% when applied to a training data set consisting of 300 radar signatures (50 samples of six targets) and 95.7% accuracy on an independent set of 300 additional signatures. The best recognition system contained eight feature detectors composed of primitive morphological and arithmetic operators capped by a special convolution template containing an evolved distribution of Gaussian-shaped probe points. The response of these detectors are processed by a simple linear classifier that labels each signature. The use of morphological operators in the construction of primitive feature detectors allows EMORPH to evolve wavelet-like transformations that eliminate noise from the signatures and suppress information at various spatial frequencies to facilitate the process of classifying targets.

Although EMORPH achieves excellent recognition results, its performance can be improved. Inspection of the evolved feature detectors suggests that various redundant sub-expressions within the detector transformations can be eliminated to accelerate the evolutionary search process. This also implies that adjusting the library of operators and parameters used to grow feature detectors may improve both accuracy and the robustness of the evolved recognition systems. In addition, EMORPH's control parameters were not carefully tuned for this specific problem. Consequently, even better performance can be achieved in future experiments by adjusting the library of morphological operators, structuring elements, and distribution of the computation resource among the different phases of the evolutionary process.

The techniques used in EMORPH are not tied to radar signal processing. The approach is generic and can be readily transitioned to many different problems in automatic target recognition. No single approach solves all problems in automatic target recognition, EMORPH represents one viable alternative. The solutions generated using our evolutionary learning algorithm are quite different than the solutions produced by human experts. This indicates that human experts may not be using all of the available information to develop robust pattern recognition systems. In future work, we hope to tune EMORPH, perform a more definitive set of experiments, and explore the possibility of combining human expertise with the evolutionary search process to access alternative designs. This hybrid approach to design may ultimately produce recognition systems with performance superior to any in use today.

ACKNOWLEDGMENT

I would like to express my appreciation to Dr. Louis Tamburino for serving as my laboratory focal point for the Summer Faculty Research Program. His total commitment to this research made my stay at Wright-Patterson Air Force Base a pleasure. I enjoyed his many helpful ideas and stimulating discussions throughout the summer. I would also like to thank Dale Nelson and Jerry Covert for again allowing me the opportunity to participate in the summer program and providing a stimulating environment in which to work.

REFERENCES

- Fisher, R. A., (1936). "The use of multiple measurements in taxonomic problems," *Ann. Eugenics*, 7, Part II, 179-188.
- Fogel, D. B. (1991). *System Identification Through Simulated Evolution: A Machine Learning Approach to Modeling*, Needham, MA: Ginn Press.
- Fogel, L. J., A. J. Owens, and M. J. Walsh (1966). *Artificial Intelligence Through Simulated Evolution*. New York, NY: John Wiley & Sons.
- Goldberg, D. E. (1989). *Genetic Algorithms in Search, Optimization, and Machine Learning*, Reading, MA: Addison-Wesley.
- Haralick, R. M., S. R. Sternburg, and X. Zhuang, (1987). "Image Analysis Using Mathematical Morphology", *IEEE Trans. on Pattern Analysis and Machine Intelligence*, PAMI-9:532-550.
- Holland, J. H. (1975). *Adaptation in Natural and Artificial Systems*, Ann Arbor, MI: The University of Michigan Press.
- Koza, J. R. (1992). *Genetic Programming: On the Programming of Computers By Means of Natural Selection*. Cambridge, MA: The MIT Press.
- Minsky, M. L. and S. A. Papert (1988). *Perceptrons*, Cambridge, MA: The MIT Press.
- Rizki, M. M., L. A. Tamburino, and M. A. Zmuda (1993) Evolving multi-resolution feature detectors. In *Proceedings of the Second Annual Conference on Evolutionary Learning*, eds. D.B. Fogel and W. Atmar, La Jolla, CA: Evolutionary Programming Society, 57-66.
- Rizki, M. M., L. A. Tamburino, and M. A. Zmuda (1994) E-MORPH: A two-phased learning system for evolving morphological classification systems. In *Proceedings of the Third Annual Conference on Evolutionary Learning*, eds. A. V. Sebald and L. J. Fogel, River Edge, NJ: World Scientific, 60-67.
- Serra, J., (1982). *Image Analysis and Mathematical Morphology*, London: Academic Press.
- Zmuda, M. A., M. M. Rizki, and L. A. Tamburino, (1992). Automatic generation of morphological sequences, In *SPIE Conference on Image Algebra and Morphological Image Processing III*, pp. 106- 118.

Associate did not participate in the program.

**COMPUTATIONAL STUDIES OF HYDROGEN ABSTRACTION FROM
HALOALKANES BY THE HYDROXYL RADICAL**

**Martin Schwartz
Regents Professor
Department of Chemistry**

**University of North Texas
215 W. Sycamore
Denton, TX 76203**

**Final Report for:
Summer Research Program
Wright Laboratory**

**Sponsored by:
Air Force Office of Scientific Research
Bolling Air Force Base, Washington, DC**

And

Wright Laboratory

October 1997

COMPUTATIONAL STUDIES OF HYDROGEN ABSTRACTION FROM HALOALKANES BY THE HYDROXYL RADICAL

Martin Schwartz
Regents Professor
Department of Chemistry
University of North Texas

Abstract

One of the most efficient steps in the initial decomposition of HFCs under combustion conditions is proton abstraction by hydroxyl radicals. We have utilized *ab initio* quantum mechanics and Transition State Theory (TST) to calculate the temperature dependence of rate constants for the reactions, $\text{CH}_x\text{F}_{4-x}$ ($x=1$ to 4) + OH \rightarrow $\text{CH}_{x-1}\text{F}_{4-x}$ + H_2O . Rate constants calculated using HF/6-31G(d) frequencies and MP2/6-31G(d) structures to calculate reactant and transition state partition functions and the Hartree Fock imaginary frequency, ω_i , to compute the tunneling factors, Γ , yielded rate constants which were substantially greater than experiment. Adjustment of the energy barrier to effect agreement between experimental and calculated rate constants at 298 K gave Arrhenius plots that exhibited markedly greater curvature than measured rate constants.

When the imaginary frequency and barrier height were calculated by fitting high level (G2) energies along the reaction path with a semi-empirical Eckart function, it was found that the calculated imaginary frequency is a factor of 2.5 lower than the HF/6-31G(d) value, indicating that the energy barrier is considerably broader than predicted by the latter frequency. When the new imaginary frequencies and barrier heights were used to calculate rate constants, it was found that $k_{\text{TST}} < k(\text{exp})$, but that lowering the barrier height (by an average of 4.7 kJ/mol for the four reactions) yields calculated rate constants which are in excellent agreement with experiment at all temperatures.

COMPUTATIONAL STUDIES OF HYDROGEN ABSTRACTION
FROM HALOALKANES BY THE HYDROXYL RADICAL

Martin Schwartz

TABLE OF CONTENTS

	page
I. Introduction	4
II. Computational Methods	5
III. Results and Discussion	7
A. Transition State Geometries	7
B. Rate Constants	7
C. A Revised Procedure	8
IV. Summary and Conclusions	12
REFERENCES	14
TABLES	16
Table 1. Selected Transition State Geometric Parameters and Vibrational Frequencies	16
Table 2. Transition State Energies, Classical Energy Barriers and Imaginary Frequencies	17
Table 3. Calculated Tunneling Factors	18
FIGURES	19
Figure 1. Temperature Dependence of the Rate Constant for the CH ₄ + OH Reaction	19
Figure 2. Potential Energy Diagram for the CH ₄ + OH Reaction	20

COMPUTATIONAL STUDIES OF HYDROGEN ABSTRACTION FROM HALOALKANES BY THE HYDROXYL RADICAL

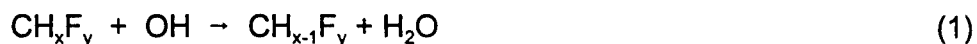
Martin Schwartz

I. INTRODUCTION

Halons (bromofluorocarbons), including CF_3Br , are excellent fire suppression agents. However, it has been well documented in recent years that they very efficiently catalyze destruction of stratospheric ozone;^{1,2} hence, their further commercial production has been severely restricted.^{2,3} Partially hydrogenated hydrofluorocarbons (HFCs) are more efficiently destroyed in the troposphere, which results in a diminished ozone depletion potential. Therefore, these compounds have been proposed as transitional replacements for the perhalogenated Halons.^{2,4}

Evaluation of the efficacy of these compounds to serve as alternative fire suppressants can, in principle, be greatly aided by high temperature computational kinetic modeling of the interactions of HFCs and their decomposition products with the species present in hydrocarbon fires. The reliability of this modeling is critically dependent upon the accuracy of estimated rate constants for the various reactions involving these species under combustion conditions (≥ 2000 K). Unfortunately, the required kinetic data are often unavailable or else have been measured only at temperatures below 1000 K.

One of the most important species responsible for flame propagation is the hydroxyl radical, which can also act to initiate decomposition of the proposed extinguishment agent via proton abstraction:



During the past summer, we utilized *ab initio* quantum mechanics and Canonical Transition State Theory (TST) to calculate the rate constants for proton abstraction from methane and the three fluoromethanes containing hydrogen at temperatures ranging from

250 K to 2000 K. The computational methods, results and comparison to experimental rate constants are presented below.

II. COMPUTATIONAL METHODS

Ab Initio molecular orbital calculations were performed using the Gaussian-94 suite of programs;⁵ TST rate constant computations were performed using a FORTRAN program written by the authors.

Geometries, frequencies and energies were determined for the reactants and products using the G2⁶ and related G2(MP2)⁷ and G2(ZPE=MP2) procedures.

Transition state geometries were optimized at the UHF/6-31G(d) and UMP2(full)/6-31G(d) levels and verified to be first order saddle points by observation of a single imaginary frequency. The Intrinsic Reaction Coordinate⁸ (IRC) was then determined using the UMP2(full)/6-31G(d) basis at increments of approximately 0.10 reduced mass units. Single point G2 energies were calculated at selected points along the IRC.

Rate constants were evaluated using the standard Eyring TST expression:⁹

$$k_{TST} = \Gamma \frac{k_B T}{h} \frac{Q_{TS}}{Q_{Rct}} e^{-\frac{\Delta E_0^\ddagger}{RT}} \quad (2)$$

in which ΔE_0^\ddagger is the classical energy barrier, Q_{TS} and Q_{Rct} are the partition functions of the transition state and reactants, and Γ is the tunneling factor. The partition functions were evaluated using MP2/6-31G(d) moments of inertia and HF/6-31G(d) frequencies (scaled by 0.8929) using standard formulae.¹⁰ Vibrations were treated as harmonic oscillators with the exception of the $X_3C \cdots H \cdots OH$ torsional mode of the transition state, which was treated as a hindered internal rotor using the new polynomial expression proposed by Ayala and Schlegel¹¹ to compute Q_{HR} . There are at least two ways to determine the reduced moment of inertia, I_r , required to evaluate this partition function. The first method involves the

intuitively straightforward calculation of the X_3C and $O-H$ group moments about the approximately linear $C\cdots H\cdots O$ axis. This yields $I_r = 1.20 \times 10^{-47} \text{ kg}\cdot\text{m}^2$ for the CH_4 reaction and a nearly constant value of $I_r = 1.46 \times 10^{-47} \text{ kg}\cdot\text{m}^2$ for reactions of the three fluoromethanes. In the second method, proposed by Truhlar,¹² the internal rotation axis is adjusted to require cancellation of the internal angular momentum of the two groups. However, application of this method (as implemented in a subroutine of the POLYRATE program¹³) yielded reduced moments which were one to two orders of magnitude greater than values obtained with the first method and effective internal rotation axes lying as much as 80° away from the $C\cdots H\cdots O$ axis. Therefore, the values of I_r obtained with the former procedure were utilized in the evaluation of Q_{HR} .

In order to evaluate the tunneling factor, Γ , we used an Eckart potential function,¹⁴ which yields an analytical expression for the transmission coefficient that can then be integrated to obtain Γ .¹⁵ The Eckart potential is a function of the forward and reverse energy barriers, V_1 and V_2 , the reaction coordinate corresponding to the barrier maximum, x_o , and a parameter characterizing the barrier width, Δ , and is given by:

$$V(x) = \frac{A e^{\frac{x-x_o}{\Delta}}}{\left[1 + e^{\frac{x-x_o}{\Delta}}\right]^2} + \frac{B e^{\frac{x-x_o}{\Delta}}}{1 + e^{\frac{x-x_o}{\Delta}}} \quad (3a)$$

where $A = [(V_1)^{1/2} + (V_2)^{1/2}]^2$ and $B = V_2 - V_1$. The width parameter is related to the imaginary frequency, ω_i , via the relations

$$\omega_i = \frac{1}{2\pi c} \sqrt{\frac{f}{\mu}} \quad , \quad f = \frac{[B^2 - A^2]^2}{8A^3\Delta^2} \quad (3b)$$

where f and μ are the vibration's force constant and reduced mass.

Initial tunneling calculations were performed using the HF/6-31G(d) imaginary frequency and barriers determined from G2 energies of the reactants and products and at

the maximum in the MP2/6-31G(d) IRC. As discussed below, this procedure yielded unrealistic values of Γ , leading to an alternative method for determination of the tunneling factor.

III. RESULTS AND DISCUSSION

A. Transition State Geometries. Selected transition state geometric parameters for the four reactions are presented in Table 1. Also shown in the table are the inertia products and scaled frequencies, required for evaluation of the transition state partition functions.

One observes from the table that the MP2/6-31G(d) values of $R(C\cdots H)$ and $R(H\cdots O)$ are shorter and longer, respectively, than the HF/6-31G(d) bond lengths (in parentheses) for all reactions. There have been a number of earlier studies of the transition state geometries and kinetics of the $CH_4 + OH$ reaction, utilizing a variety of basis sets.^{16,17,18,19,20} In all cases, earlier transition states are reported for the correlated energy geometries. One observes also that, as reported earlier for the CH_4 reaction, the $C\cdots H\cdots O$ angle's deviation from linearity in all four transition states is somewhat greater when electron correlation is included in the optimization. The earlier reported changes in the $H_3C\cdots H\cdots OH$ transition state geometry, from staggered to eclipsed with the inclusion of electron correlation, is also found here. However, this trend does not extend to other members of the series since, as seen in the table, one finds eclipsed conformations at both the HF and MP2 levels for both the $H_2FC\cdots H\cdots OH$ and $F_3C\cdots H\cdots OH$ transition states.

B. Rate Constants. Displayed in the third column of Table 2 are the forward and reverse classical energy barriers (excluding vibrational ZPE, which is included in the vibrational partition functions) for the four reactions calculated from G2 energies of the reactants and products and at the MP2/6-31G(d) transition states. The table also contains the HF/6-31G(d) imaginary frequencies at the transition state (required for the tunneling

calculations). These parameters together with transition state and reactant inertia products and frequencies were used to calculate the rate constants via eq. (2). Displayed in Fig. (1a) is an Arrhenius plot of the temperature dependence of k_{TST} for the reaction, $\text{CH}_4 + \text{OH}$ [dashed line], for which there is the most accurate experimental data [symbols] over the broadest range of temperature. One sees that the calculated rate constants are considerably greater than measured values at low to moderate temperatures (as much as an order of magnitude or more at room temperature and below). It is not uncommon to observe significant deviations of TST rate constants from experiment, which are often attributed to the exponential dependence of k_{TST} on the calculated energy barrier. For example, an error of only 5 kJ/mol in ΔE_0^\ddagger would yield a value of $k_{\text{TST}}/k(\text{exp}) \approx 7.5$ at room temperature (not considering changes in Γ with barrier height).

A common remedy for this problem is to arbitrarily adjust the barrier height to effect equality of the calculated and experimental k 's at a reference temperature (often taken to be 298 K). The barrier height was adjusted iteratively [the required recalculation of Γ prohibits direct determination of $\delta(\Delta E_0^\ddagger)$] and it was found that $k_{\text{TST}}=k(\text{exp})$ at 298 K when the *ab initio* barrier is increased by 7 kJ/mol (to 39.2 kJ/mol). The calculated rate constants using the higher value of ΔE_0^\ddagger are plotted in Fig. (1A) [solid curve]. One observes clearly from this plot that the calculated rate constants exhibit markedly greater curvature over the complete temperature range than do the experimental k 's. Therefore, it may be concluded that errors in k_{TST} **cannot** be attributed primarily to incorrect *ab initio* barrier heights.

Although not shown, calculated rate constants for reactions of the three fluoromethanes show the same trends; i.e. values of k_{TST} are significantly greater than experiment when the *ab initio* barriers are used and exhibit too much curvature when the barrier is raised to produce agreement between k_{TST} and $k(\text{exp})$ at 298 K.

C. A Revised Procedure. In order to investigate further the source(s) of error in

the calculated rate constants, we decided to explore the reaction path energies at a higher level of theory. As reported by one of the authors,¹⁵ when the IRC for a reaction is determined at various levels of theory, the shape of the PES, including its breadth, peak position and barrier height are sensitive to the chosen basis set. However, the reaction path geometries are comparatively independent of basis. Accordingly, one may efficiently calculate a reasonably accurate high level IRC utilizing geometries determined with a smaller basis. Therefore, in order to obtain better characterizations of the PES, we have calculated G2 energies (excluding ZPE) at various points along the MP2/6-31G(d) IRC for all four reactions. The results for $\text{CH}_4 + \text{OH}$ are displayed in Fig. (2).

The diamonds in this figure are the MP2/6-31G(d) energies. The dashed line represents the curve one obtains when the HF/6-31G(d) imaginary frequency and the G2 energy at the MP2/6-31G(d) maximum are used to characterize the shape and position of the energy barrier, and the circles are G2 energies (without ZPE) determined at points along the MP2 IRC. The solid curve represents the fit of an Eckart function [eqs. (3)] to the G2 energies subject to the constraint that $V_1 - V_2 = \Delta E_{\text{rxn}}$ (i.e. the forward and reverse barriers must be consistent with the calculated overall energy change for the reaction).

One sees several significant differences in the shape of the new G2 PES compared to that of the lower level curve. In addition to a shift in the barrier maximum (which has no impact on calculated rate constants), the new barrier height is somewhat greater and the breadth of G2 IRC is substantially greater than the curve generated using $\omega_i(\text{HF})$. These differences are quantified for all four reactions in Table 2. $\Delta E_0^*[\text{Eck.}]$ and $\omega_i[\text{Eck.}]$ are the barrier height and imaginary frequency determined by the Eckart function fit to the G2 energies. One finds that, in every case, the fitted barrier height is somewhat greater than the value determined at the MP2/6-31(d) transition state. Even more significantly, the fitted imaginary frequencies, $\omega_i[\text{Eck.}]$, are much lower than values of $\omega_i[\text{HF/6-31G(d)}]$, by

approximately a factor of 2.5 for all four reactions, indicating the much greater breadth of the higher level G2 IRC. As shown below, this large change in ω_i has a major impact on the calculated tunneling factors, which are quite sensitive to the PES curvature.

The values of V_1 , V_2 and Δ (and, hence, ω_i) obtained from a fit of the G2 energies along the reaction path characterize the classical PES without vibrational zero point energy. However, it is important to include the ZPE when calculating the tunneling factor, Γ .²¹ Therefore, V_1 and V_2 (and thus A and B in Eq. (3)) were adjusted by adding in the ZPE's calculated for the reactants, products and transition states, and then Γ was evaluated as described elsewhere.¹⁵ Since the zero point energy of the transition state for the reactions studied here is lower than for either the products or reactants, this adjustment lowers the barriers somewhat, which corresponds to a lower curvature and, hence, a somewhat diminished imaginary frequency, which is shown in the last column of Table 2 [$\omega_i(\text{Adj.})$].

As shown in Table 3, the effect of using the revised parameters from the higher level G2 IRC on the calculated tunneling factors is quite striking. Whereas, the Hartree Fock imaginary frequencies and barriers heights calculated at the MP2 IRC maximum yielded a change in Γ [in square brackets] of at least three orders of magnitude over the range from 200 K to 2000 K, the variation in the tunneling efficiency is a much more modest factor of 10-20 when using the fitted values of the imaginary frequency and barrier heights. From these results, it is apparent that the excess curvature in the Arrhenius plot of the calculated rate constants (*vide supra*) results from calculated tunneling efficiencies that are far too high at the lower temperatures.

We have recalculated rate constants for the four proton abstraction reactions using the new fitted PES parameters from Table 2. The results for the $\text{CH}_4 + \text{OH}$ reaction are shown in Fig. (1B) [dashed line]. One observes that now k_{TST} is significantly lower than $k(\text{exp})$ at most temperatures. Once again, though, assuming that the deviations are due

predominantly in errors in the calculated barrier heights, the value of ΔE_0^\ddagger was adjusted to require that $k_{\text{TST}} = k(\text{exp})$ at 298 K; the adjusted values of the barrier for the four reactions are given in Table 2 ($\Delta E_0^\ddagger[\text{RT Fit}]$). Unlike the earlier results using $\omega_1(\text{HF})$, this time the adjusted rate constants are in close to perfect agreement with experiment at all temperatures. Although not shown, excellent agreement between calculated and experimental rate constants is also observed for reactions of the three fluoromethanes with OH.

One finds from Table 2 that errors in the *ab initio* barriers are systematic since the barrier heights required to obtain agreement with experiment at room temperature, $\Delta E_0^\ddagger[\text{RT Fit}]$ are lower than $\Delta E_0^\ddagger[\text{Eck.}]$ for all reactions in the series; the average decrease in barrier height is 4.7 ± 1.6 kJ/mol. This trend is not surprising and is in good agreement with the recent results of one of the authors, who studied energy barriers of a series of ten reactions using a variety of *ab initio* methods. In that investigation, it was found that the calculated G2 barrier height (as well as barriers determined with a number of other bases) was substantially greater than (a) the exact energy barrier for the $\text{H} + \text{H}_2$ reaction,²² and (b) calculated barriers for all 10 reactions using the more accurate CBS-QCI/APNO method²³ (calibrated to produce agreement with the exact barrier for the $\text{H} + \text{H}_2$ reaction). Indeed, the recommended G2 energy barrier correction of -5.2 kJ/mol is rather close to the average required adjustment of -4.7 kJ/mol found for the four reactions studied here.

A commonly utilized procedure in the calculation of transition state energies is to compute a high level energy barrier at the maximum in a lower level IRC. As found here (Table 2) the actual G2 barrier heights ($\Delta E_0^\ddagger[\text{Eck.}]$) are higher than barriers obtained at the MP2 IRC maximum ($\Delta E_0^\ddagger[\text{G2/MP2(max)}]$) since the maxima of the two PESs do not coincide [Fig. (2)]. Yet as found here and elsewhere,¹⁵ most methods, including G2, tend to overestimate the true energy barriers. Hence, the above simple procedure benefits from a

fortuitous partial cancellation of error.

It is straightforward to show that incorrect values of the reaction path's imaginary frequency form the greatest source of error calculation of the tunneling factor for proton abstraction reactions since the barrier's curvature, $\partial^2 V / \partial x^2$, is proportional to ω_i^2 . In principle, a less computationally intensive procedure than fitting high level energies along the IRC to obtain an accurate measure of PES curvature would be to perform the frequency analysis with a larger basis set and higher level treatment of electron correlation. Accordingly, we have reoptimized the $\text{CH}_4 + \text{OH}$ transition state at the QCISD/6-311G(d,p) level, and obtained a value of $\omega_i = 1885 \text{ cm}^{-1}$. While clearly an improvement over the HF/6-31G(d) result, the higher level frequency is still more than 60% greater than the value obtained from the Eckart fit. This frequency yields a room temperature tunneling factor of approximately $\Gamma \approx 20$, which is still almost an order of magnitude greater than the value obtained using the fitted frequency (Table 3). Similarly high values of $\omega_i(\text{QCISD})$ and Γ were obtained for reactions of the fluoromethanes. Hence, we must conclude that fitting the high level PES is the only currently feasible procedure for calculating accurate tunneling factors.

SUMMARY AND CONCLUSIONS

Transition states for the proton abstraction reactions by the OH radical from CH_4 and the three fluoromethanes were located at the HF/6-31G(d) and MP2/6-31G(d) levels and the MP2/6-31G(d) Intrinsic Reaction Coordinate was obtained. Rate constants were initially calculated using the Hartree Fock frequencies and MP2 moments of inertia and G2 energy barriers calculated via the standard Transition State Theory equation with the tunneling factor calculated using a one dimensional Eckart potential. Calculated rate constants were too high by approximately one order of magnitude at room temperature. Adjustment of the energy barrier to effect agreement between experimental and calculated rate constants at

298 K yielded Arrhenius plots that exhibited significantly greater curvature than measured rate constants.

Acquisition of high level (G2) energies at various points along the IRC revealed that the breadth of the barrier is markedly higher than that which is predicted by the HF/6-31G(d) imaginary frequency. The G2 PES was fit by an Eckart function to obtain new values for the barrier maximum and for ω_i . When these values were used to calculate the rate constants, it was found that $k_{\text{TST}} < k(\text{exp})$, but that lowering the barrier height (by an average of 4.7 kJ/mol for the four reactions) to yields calculated rate constants which are in excellent agreement with experiment at all temperatures.

REFERENCES

1. Baes, G. *ANPI Mag.* **1992**, 112, 43.
2. Banks, R. E. *J. Fluorine Chem.* **1994**, 67, 193.
3. Rowland, F. S. *Environ. Sci. Technol.* **1991**, 25, 622.
4. Grosshandler, W. L.; Gann, R. G.; Pitts, W. M. (Eds.) 'Evaluation of Alternative In-Flight Fire Suppressants for Full-Scale Testing in Simulated Aircraft Engine Nacelles and Dry Bays.' *NIST Special Publication* **1994**, 861.
5. *Gaussian 94*, Revision A.1, Frisch, M. J.; Trucks, G. W.; Schlegel, H. B.; Gill, P. M. W.; Johnson, B. G.; Robb, M. A.; Cheeseman, J.R.; Keith, T. A.; Petersson, G.A.; Montgomery, J. A.; Raghavachari, K.; Al-Laham, M. A.; Zakrzewski, V. G.; Ortiz, J. V.; Foresman, J. B.; Cioslowski, J.; Stefanov, B. B.; Nanayakkara, A.; Challacombe, M.; Peng, C. Y.; Ayala, P. Y.; Chen, W.; Wong, M. W.; Andres, J. L.; Replogle, E. S.; Gomperts, R.; Martin, R. L.; Fox, D. J.; Binkley, J. S.; Defrees, D. J.; Baker, J.; Stewart, J. J. P.; Head-Gordon, M.; Gonzalez, C.; Pople, J. A. Gaussian, Inc., Pittsburgh, PA, 1995.
6. Curtiss, L. A.; Raghavachari, K.; Trucks, G. W.; and Pople, J. A. *J. Chem. Phys.* **1991**, 94, 7221.
7. Curtiss, L. A.; Raghavachari, K.; Pople, J. A. *J. Chem. Phys.* **1993**, 98, 1293.
8. Gonzalez, C.; Schlegel, H. B. *J. Phys. Chem. (a)* **1989**, 90, 2154; (b) **1990**, 94, 5523.
9. Eyring, H. *J. Chem. Phys.* **1935**, 35, 107.
10. Hill, T. L. *An Introduction to Statistical Thermodynamics*; Addison-Wesley Publishing Co.: Reading, MA, 1960; Chap. 9.
11. P. Y. Ayala, Ph.D. Dissertation, Wayne State University, 1997.
12. Truhlar, D. G. *J. Comput. Chem.* **1990**, 12, 266.
13. Lu, D.-H.; Truong, T. N.; Melissas, V. S.; Lynch, G. C.; Liu, Y.-P.; Garret, B. C.; Steckler, R.; Isaacson, A. D.; Rai, S. N.; Hancock, G. C.; Lauderdale, J. G.; Joseph, T.; Truhlar, D. G. *Comput. Phys. Commun.* **1992**, 71, 235.
14. Eckart, C. *Phys. Rev.* **1930**, 35, 1303.

15. "Complete Basis Set Thermochemistry and Kinetics," Petersson, G. A., in *Computational Thermochemistry: Prediction and Estimation of Molecular Thermodynamics*, K. Irikura and D. Frurip, Eds., ACS Symposium Series, American Chemical Society, Washington, D. C. (in Press).
16. Bottoni, A.; Poggi, G.; Emmi, S. S. *J. Molec. Struct.(Theochem)* **1993**, 279, 299.
17. Gonzalez, C.; McDouall, J. J. W.; Schlegel, H. B. *J. Phys. Chem.* **1990**, 94, 7467.
18. Truong, T. N.; Truhlar, D. G. *J. Chem. Phys.* **1990**, 93, 1761.
19. Dobbs, K. D.; Dixon, D. A.; Komornicki, A. *J. Chem. Phys.* **1993**, 98, 8852.
20. Melissas, V. S.; Truhlar, D. G. *J. Chem. Phys.* **1993**, 99, 1013.
21. Truhlar, D. G.; Kuppermann, A. *J. Am. Chem. Soc.* **1971**, 93, 1840.
22. Diedrich, D. L.; Anderson, J. B. *Science* **1992**, 258, 786.
23. Montgomery, J. A., Jr.; Ochterski, J. W.; Petersson, G. A. *J. Chem. Phys.* **1994**, 101, 5900.

Table 1. Selected Transition State Geometric Parameters and Vibrational Frequencies.^{a,b}

Param.	H ₃ C..H..OH	H ₂ FC..H..OH	HF ₂ C..H..OH	F ₃ C..H..OH
R(C..H)	1.226 (1.313)	1.224 (1.311)	1.222 (1.312)	1.243 (1.334)
R(H..O)	1.269 (1.200)	1.274 (1.196)	1.271 (1.186)	1.229 (1.155)
Θ(CHO)	168.5 (175.9)	158.6 (171.0)	160.6 (174.9)	163.1 (171.1)
Φ(HO..CX) ^c	0.0 (60.4)	0.0 (0.0)	15.5 (78.9)	0.0 (0.0)
10 ⁴⁶ (I _A I _B I _C) ^{1/3, d}	0.530	8.717	15.58	21.61
Frequencies ^e	43(IR), 343 347, 495, 867 1097, 1184, 1392 1411, 1445, 2899 3014, 3017, 3608	108, 140(IR) 323, 512, 768 1097, 1097, 1194 1203, 1450, 1502 2936, 3029, 3604	40(IR), 118 158, 452, 543 797, 1028, 1129 1168, 1198, 1362 1502, 2991, 3602	79(IR), 101 106, 346, 493 493, 715, 778 998, 1119, 1267 1283, 1497, 3601

a) Bond lengths in Angstroms, angles in degrees and frequencies in wavenumbers.

b) The top number in each entry is the MP2/6-31G(d) parameter.

The second number (in parentheses) is the HF/6-31G(d) parameter.

c) X=F except for H₃C..H..OH.

d) from the MP2/6-31G(d) geometries, in kg-m².

e) HF/6-31G(d) frequencies, scaled by 0.8929.

The frequency of the internal rotation (torsion) is denoted by (IR).

Table 2. Transition State Energies, Classical Energy Barriers and Imaginary Frequencies.^a

Reaction	E(G2) ^b	$\Delta E^{\ddagger, c, d}$ [G2/MP2(max)]	$\Delta E^{\ddagger, c, e}$ [Eck.]	$\Delta E^{\ddagger, c, f}$ [RT Fit]	ω_i [HF/6-31G(d)]	ω_i [Eck.]	ω_i [Adj.]
CH ₄ + OH	-116.092559	31.2 [82.9]	34.2 (3.0)	27.4 (-6.8)	2836	1165	1084
CH ₃ F + OH	-215.233865	24.6 [91.1]	27.0 (2.4)	21.5 (-5.5)	2872	1175	986
CH ₂ F ₂ + OH	-314.391201	25.4 [91.6]	28.7 (3.3)	26.2 (-2.5)	2942	1375	1162
CHF ₃ + OH	-413.556555	37.1 [83.4]	37.2 (0.1)	33.2 (-4.0)	3023	1382	1196
		Avg. Change:	+2.2	-4.7			
		Std. Deviation:	1.3	1.6			

a) TS Energies in a.u., Energy Barriers in kJ/mol and Frequencies in wavenumbers.

b) G2 energies do not include the ZPE.

c) Classical energy barriers do not include the ZPE.

d) Quantities in brackets are energy barriers for the reverse reaction

e) Quantities in parentheses represent $\Delta E^{\ddagger}[\text{Eck.}] - \Delta E^{\ddagger}[\text{G2/MP2(max)}]$

f) Quantities in parentheses represent $\Delta E^{\ddagger}[\text{RT Fit}] - \Delta E^{\ddagger}[\text{Eck.}]$

Table 3. Calculated Tunneling Factors (Γ).^a

T (K)	CH ₄ + OH	CH ₃ F + OH	CH ₂ F ₂ + OH	CHF ₃ + OH
200	15 [8550]	7.1 [2010]	16.8 [9340]	34 [181,000]
250	5.2 [2840]	3.5 [230]	6.0 [650]	8.6 [4830]
298	3.1 [360]	2.4 [61]	3.5 [130]	4.4 [540]
400	1.9 [32]	1.7 [13]	2.0 [19]	2.2 [40]
700	1.2 [3.3]	1.2 [2.6]	1.3 [2.9]	1.3 [3.6]
2000	1.03 [1.2]	1.03 [1.2]	1.04 [1.2]	1.04 [1.2]

a) The first number is the value of Γ obtained with HF/6-31G(d) imaginary frequencies.
The second number (in brackets) is the value obtained with Eckart fitted frequencies.

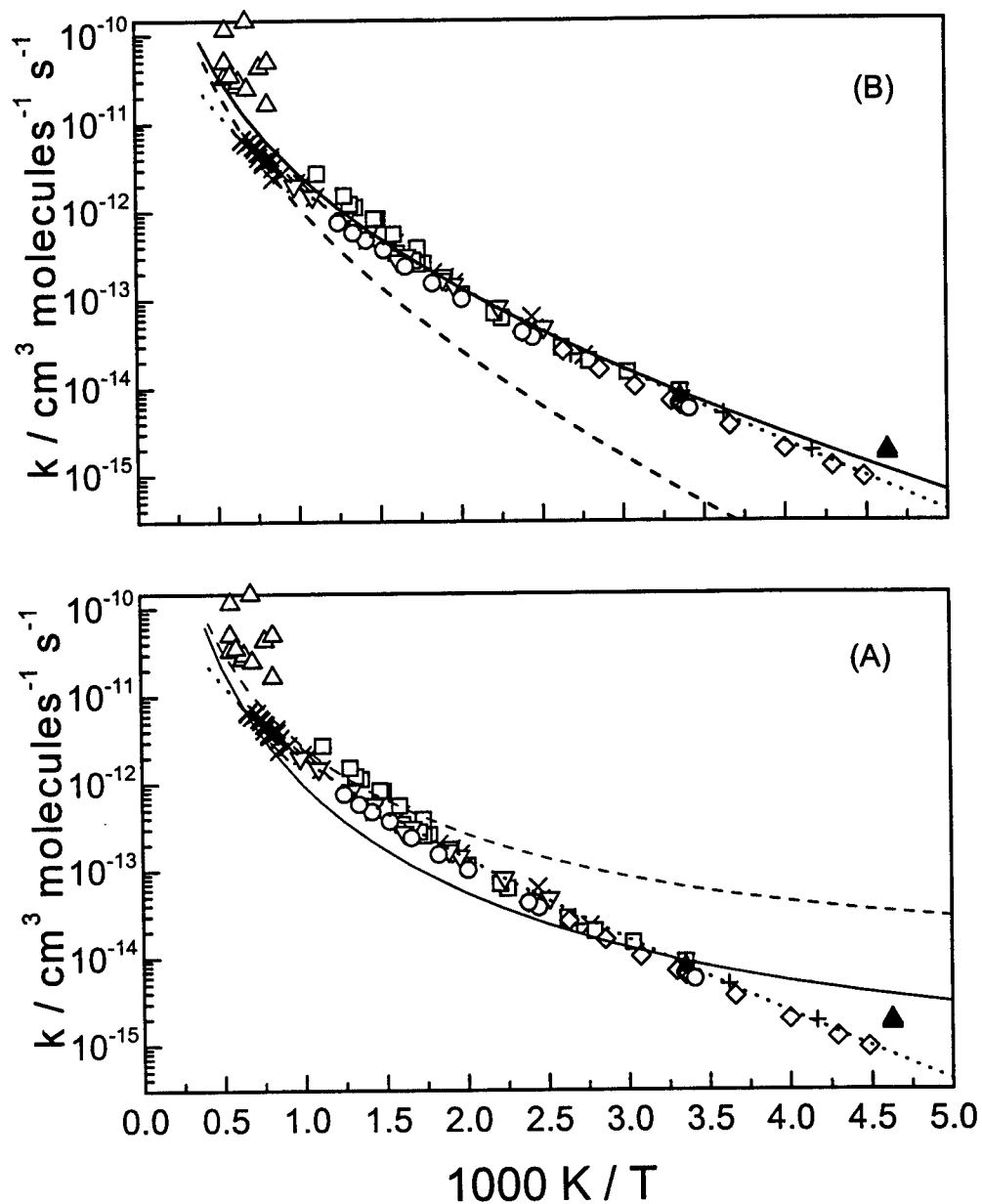


Fig. 1 Temperature dependence of the rate constant for the $\text{CH}_4 + \text{OH}$ reaction.
 (A) HF/6-31G(d) imaginary frequency used for tunneling calculation; (B) Eckart fit
 imaginary frequency used for tunneling calculation.
 Symbols - Experimental rate constants; Dashed Line - calculated rate constant using
 Eckart energy barrier; Solid Line - calculated rate constant using barrier adjusted to
 fit experimental rate constant at 298 K.

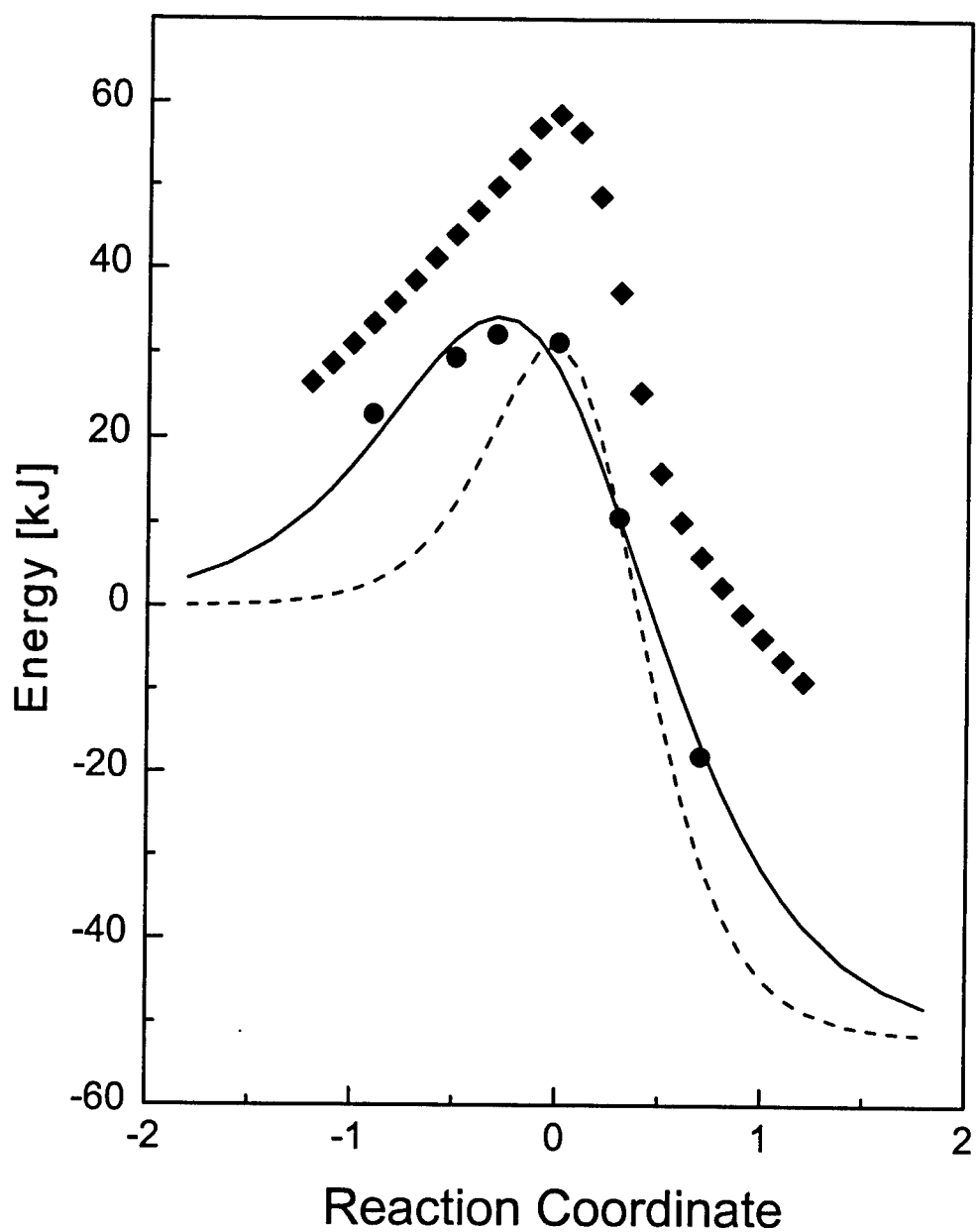


Fig. 2 Potential Energy Diagram for the $\text{CH}_4 + \text{OH}$ reaction.
 ♦ - MP2/6-31G(d) IRC; • - G2 energies at points along the MP2 IRC; Dashed line - PED calculated using the G2 energy barrier at the maximum in the MP2 IRC ($\Delta E^\ddagger = 31.2$ kJ/mol) and the HF/6-31G(d) imaginary frequency ($\omega_i = 2836$ cm^{-1}); Solid line - PED calculated by fitting an Eckart function to the G2 energies along the IRC ($\Delta E^\ddagger = 34.2$ kJ/mol and $\omega_i = 1165$ cm^{-1}).

**COMPUTATIONAL OF NONLINERAR VISCOUS PANEL FLUTTER USING A
FULLY-IMPLICIT AEROELASTIC SOLVER**

**R. Panneer Selvam
Assistant Professor
Department of Civil Engineering**

**University of Arkansas
BELL 4190
Fayetteville, AR 72701**

**Final Report for:
Summer Research Program
Wright Laboratory**

**Sponsored by:
Air Force Office of Scientific Research
Bolling Air Force Base, Washington, DC**

And

Wright Laboratory

October 1997

Computation of Nonlinear Viscous Panel Flutter Using a Fully-Implicit Aeroelastic Solver

R. Panneer Selvam
Associate Professor
Department of Civil Engineering
University of Arkansas

Abstract

The implicit time-accurate approach developed by Morton, Melville and Visbal (1997) for aeroelastic application is used here to study the flutter of a panel in the transonic regime. The phenomenon is modeled by coupling either Euler or Navier-Stokes equations for the fluid with the nonlinear plate deformation equations. The flow equations are solved at each time step by the Beam-Warming, alternate-direction, implicit scheme. The plate equation is solved by the Newmark- β method in time and a finite difference method in space. Lagging errors between the fluid and the structure are eliminated with Newton-like subiterations allowing the coupled system to achieve second-order temporal accuracy. The model is applied to compute the flutter stability boundary for simply supported and fixed panels. The stability boundary is computed for both Euler and viscous flow. The time response of the panel in stable and unstable regimes for various Mach numbers are presented. The effect of boundary layer in the production and suppression of the flutter is also investigated. The computed results are compared with available numerical results.

Computation of Nonlinear Viscous Panel Flutter Using a Fully-Implicit Aeroelastic Solver

R. Panneer Selvam

1 Nomenclature

D	=	plate stiffness, $E_s h^3 / 12(1 - \nu^2)$
E	=	total specific energy
E_s	=	modulus of elasticity
F, G, \hat{F}, \hat{G}	=	flux vectors
h	=	thickness of the panel
H_{GCL}	=	GCL source vector term
J	=	Jacobian of coordinate transformation
l	=	length of the panel
λ	=	nondimensional dynamic pressure $\rho_\infty u_\infty^2 l^3 / D$
m	=	panel mass per unit area
M_∞	=	free stream Mach number
ν	=	Poisson's ratio
p	=	non dimensional static pressure
Pr	=	Prandtl number, 0.73 for air
q_x, q_y	=	components of heat flux vector
Re	=	reference Reynolds number, $\rho_\infty u_\infty D / \mu_\infty$
S	=	structural variables
t^*	=	non dimensional time, $u_\infty \bar{t} / l$
t	=	transformed time
t_1	=	non dimensional coefficient for the nonlinear term in the plate equation
T	=	nondimensional static temperature
u, v	=	nondimensional Cartesian velocity components in x, y directions
U, \hat{U}	=	vector of dependent variables
\bar{u}	=	reduced velocity
x, y	=	nondimensional coordinates in streamwise and normal directions
$x_t, y_t,$	=	grid velocities

γ	=	specific heat ratio, 1.4 for air
δ_{ij}	=	Kronecker delta function
δ_ξ, δ_η	=	central difference operators
$\Delta t, \Delta t_s$	=	time step sizes
ΔU	=	$U^{p+1} - U^p$
μ	=	molecular viscosity
μ_s	=	mass ratio
ξ, η	=	computational coordinates
$\xi_t, \xi_x, \xi_y,$	=	metric coefficients of the coordinate
η_t, η_x, η_y	=	transformation
ρ	=	nondimensional fluid density
$\tau_{xx}, \tau_{xy},$	=	components of viscous stress tensor
τ_{yx}, τ_{yy}		
<i>Subscripts</i>		
b	=	evaluated at the surface
v	=	viscous
∞	=	dimensional freestream value
<i>Superscript</i>		
n	=	time level
p	=	subiteration level

2 Introduction

An important goal of computational aeroelasticity is to impact the design process with simulations of full aircraft configurations. One challenging aspect of this goal is computing time-accurate aeroelastic solutions in the nonlinear flow regimes associated with transonic conditions, high angle of attack, or maneuvering flight. Although the well established aeroelastic solvers represent great progress in fluid-structure interaction research, improvements in efficiency and accuracy must be pursued to allow full aircraft time-accurate nonlinear aeroelastic simulations to influence the design cycle.

Historically, researchers interested in dynamic aeroelastic computations have taken well-validated, implicit Navier-Stokes algorithms developed to solve complex flows over three-dimensional, rigid bodies, and extended them to include aeroelastic effects. The most common method of extending these algorithms is to simply lag the effects of moving/deforming structures by one time step [13, 8, 9], allowing current algorithms to be used in updating the aerodynamic variables. After the aerodynamic loads are determined, a structural module is called to update the position and shape of the body. A disadvantage of this strategy is the fact that regardless of the temporal accuracy of the aerodynamic and structural algorithms independently, the coupling introduces an $O(\Delta t)$ error, necessitating small time steps. Overcoming this error requires the coupled scheme to be fully implicit.

One attractive method of converting an alternating direction implicit (ADI) scheme to a fully implicit algorithm is by implementing Newton-like subiterations [12, 10]. Subiterations can eliminate errors from

linearization, factorization, lagged boundary condition, and lagged turbulence models. This strategy is attractive since only minor modifications are made to the baseline solver. The added computational cost of subiterations is typically an additional solution vector storage, and each subiterate is equivalent in workload to a time step of the baseline algorithm. This approach was demonstrated for instance in reference [12] for time-accurate pitching airfoil computations utilizing the $k - \epsilon$ turbulence equations. Stability enhancement was found to be an added benefit of subiteration documented in reference [12, 10]. The current research uses this subiteration methodology to reduce the structural coupling errors and allow higher order accurate time-integration schemes to be used with relatively minor changes to the baseline aerodynamic solver.

The purpose of the present work is to improve the efficiency of existing coupled Navier-Stokes/structural dynamics algorithms and also to address accuracy issues of dynamic computations on deforming meshes. There are five main issues addressed in the current research: temporal accuracy, spatial accuracy, deforming mesh induced errors, structural coupling, and the effect of considering viscous as opposed to inviscid flow during flutter. To reduce the computational resource requirements and limit the flowfield physics to phenomena relatively well understood, a two-dimensional aeroelastic panel shown in Figure 1 is used to analyze the aforementioned issues. The nonlinear effect of the plate in-plane forces due to stretching is also considered in the analysis. Here the flow as well as the structure have nonlinear behavior, yet the geometrical configuration is kept simple. Only a few studies consider the nonlinear effect of the flow in panel flutter [5, 4]. Davis and Bendiksen used an Euler solver and a finite element procedure for the plate equation. To the authors' knowledge, none have considered so far the effect of the viscous flow on the panel flutter. This work will investigate viscous flow effects on panel flutter in detail.

A first or second order temporally accurate Beam-Warming algorithm with Newton subiterations is used to compute the flowfield. The issues of temporal accuracy and coupling are addressed by time step and maximum subiterate number studies. The error in grid refinement is studied using three different grids. The overall solution accuracy for the inviscid case is verified through comparison with the work of Davis and Bendiksen [5, 4]. The viscous flow is used to compute the boundary layer depth required for flutter at various Mach numbers for simply supported and fixed end panels. The difference in the computed viscous and inviscid flutter stability boundary is analyzed.

3 Method of Solution

In this section, the aerodynamic governing equations and boundary conditions, as well as the structural governing equations are presented.

3.1 Aerodynamic Governing Equations

The aerodynamic governing equations are the unsteady compressible two-dimensional Navier-Stokes equations written in nondimensional strong-conservation law form employing a general time dependent transformation of the form

$$\xi = \xi(x, y, t^*), \quad (1)$$

$$\begin{aligned}\eta &= \eta(x, y, t^*), \\ t &= t^*.\end{aligned}$$

The resulting system of governing equations is expressed as

$$\frac{\partial \hat{U}}{\partial t} + \frac{\partial}{\partial \xi}(\hat{F} - \frac{1}{Re}\hat{F}_v) + \frac{\partial}{\partial \eta}(\hat{G} - \frac{1}{Re}\hat{G}_v) = H_{GCL}. \quad (2)$$

The source vector term, H_{GCL} , is a term to enforce the geometric conservation law for moving meshes. This term is defined [14]

$$H_{GCL} = U \left[\frac{\partial J^{-1}}{\partial t} + \left(\frac{\xi_t}{J} \right)_\xi + \left(\frac{\eta_t}{J} \right)_\eta \right]. \quad (3)$$

A discussion and derivation of this term is provided in the following section.

Vector quantities appearing in (2) are defined as

$$\hat{U} = \frac{1}{J}U \quad (4)$$

$$\hat{F} = \frac{1}{J}(\xi_t U + \xi_x F + \xi_y G) \quad (5)$$

$$\hat{G} = \frac{1}{J}(\eta_t U + \eta_x F + \eta_y G) \quad (6)$$

$$\hat{F}_v = \frac{1}{J}(\xi_x F_v + \xi_y G_v) \quad (7)$$

$$\hat{G}_v = \frac{1}{J}(\eta_x F_v + \eta_y G_v). \quad (8)$$

With this formulation, the vector of dependent variables U is given as

$$U = \begin{bmatrix} \rho \\ \rho u \\ \rho v \\ \rho E \end{bmatrix} \quad (9)$$

and the flux vectors as

$$F = \begin{bmatrix} \rho u \\ \rho u^2 + p \\ \rho uv \\ (\rho E + p)u \end{bmatrix}, G = \begin{bmatrix} \rho v \\ \rho uv \\ \rho v^2 + p \\ (\rho E + p)v \end{bmatrix} \quad (10)$$

$$F_v = \begin{bmatrix} 0 \\ \tau_{xx} \\ \tau_{xy} \\ u\tau_{xx} + v\tau_{xy} - q_x \end{bmatrix} \quad (11)$$

$$G_v = \begin{bmatrix} 0 \\ \tau_{yx} \\ \tau_{yy} \\ u\tau_{yx} + v\tau_{yy} - q_y \end{bmatrix} \quad (12)$$

where

$$E = \frac{T}{(\gamma - 1)M_\infty^2} + (u^2 + v^2)/2. \quad (13)$$

All variables have been normalized by representative freestream values except for p which has been nondimensionalized by $\rho_\infty u_\infty^2$. Components of the stress tensor and heat flux vector may be expressed as

$$\tau_{x_i x_j} = \mu \left(\frac{\partial u_i}{\partial x_j} + \frac{\partial u_j}{\partial x_i} - \frac{2}{3} \delta_{ij} \frac{\partial u_k}{\partial x_k} \right) \quad (14)$$

$$q_{x_i} = - \left[\frac{1}{(\gamma - 1)M_\infty^2} \right] \left(\frac{\mu}{Pr} \right) \frac{\partial T}{\partial x_i} \quad (15)$$

where $u_1, u_2 = u, v$ and $x_1, x_2 = x, y$. Sutherland's law for the molecular viscosity coefficient μ and the perfect gas relationship

$$p = \frac{\rho T}{\gamma M_\infty^2} \quad (16)$$

are also employed, and Stokes' hypothesis for the bulk viscosity coefficient is assumed.

3.2 Geometric Conservation Law

This section describes the relationship between the governing equations and the geometric conservation law. The nondimensional Cartesian governing equations can be expressed

$$\frac{\partial U}{\partial t^*} + \frac{\partial}{\partial x} \left(F - \frac{1}{Re} F_v \right) + \frac{\partial}{\partial y} \left(G - \frac{1}{Re} G_v \right) = 0. \quad (17)$$

Using the chain-rule differentiation expressions

$$\frac{\partial(\cdot)}{\partial t^*} = \frac{\partial(\cdot)}{\partial t} + \xi_t \frac{\partial(\cdot)}{\partial \xi} + \eta_t \frac{\partial(\cdot)}{\partial \eta}, \quad (18)$$

$$\frac{\partial(\cdot)}{\partial x} = \xi_x \frac{\partial(\cdot)}{\partial \xi} + \eta_x \frac{\partial(\cdot)}{\partial \eta}, \quad (19)$$

$$\frac{\partial(\cdot)}{\partial y} = \xi_y \frac{\partial(\cdot)}{\partial \xi} + \eta_y \frac{\partial(\cdot)}{\partial \eta}, \quad (20)$$

and premultiplying by the inverse of the transformation Jacobian, J , equation (17) becomes

$$\begin{aligned} \frac{\partial \hat{U}}{\partial t} + \frac{\partial}{\partial \xi} \left(\hat{F} - \frac{1}{Re} \hat{F}_v \right) + \frac{\partial}{\partial \eta} \left(\hat{G} - \frac{1}{Re} \hat{G}_v \right) = \\ U \left[\frac{\partial J^{-1}}{\partial t} + \left(\frac{\xi_t}{J} \right)_\xi + \left(\frac{\eta_t}{J} \right)_\eta \right] + \end{aligned}$$

$$\begin{aligned} & \left(F - \frac{1}{Re} F_v\right) \left[\left(\frac{\xi_x}{J}\right)_\xi + \left(\frac{\eta_x}{J}\right)_\eta \right] + \\ & \left(G - \frac{1}{Re} G_v\right) \left[\left(\frac{\xi_y}{J}\right)_\xi + \left(\frac{\eta_y}{J}\right)_\eta \right]. \end{aligned} \quad (21)$$

All three terms on the right hand side of (21) vanish analytically. The difficulty arises when discrete representations of the temporal and spatial derivatives are used. The discrete form of the last two terms are zero when central differences are used for all metric calculations in 2-D. Unfortunately this is not true for the first term due to the mixed temporal and spatial derivatives. The first term is referred to in the literature as the geometric conservation law [14]. The most straightforward approach of accounting for this term is to simply include it in the discrete governing equations, more accurately representing the non-transformed governing equations.

3.3 Aerodynamic Boundary Conditions

Numerical boundary conditions for the plate provide the connection between the aerodynamic and structural equations. On the plate surface, for viscous flow computations the no slip condition is implemented. This requires that

$$u = \dot{x}_b, \quad v = \dot{y}_b \quad (22)$$

where \dot{x}_b and \dot{y}_b denote the velocity of the moving boundary, with $\dot{x}_b = \dot{y}_b = 0$ in the static case. For the current problem $\dot{x}_b = 0$. The remaining two conditions are the adiabatic wall condition and the normal momentum equation:

$$\frac{\partial T}{\partial \eta} = 0, \quad \frac{\partial p}{\partial \eta} = - \left(\frac{\rho}{\eta_x^2 + \eta_y^2} \right) (\eta_x \ddot{x}_b + \eta_y \ddot{y}_b). \quad (23)$$

Along the inflow boundary, all dependent variables are assigned their respective freestream values for supersonic flow whereas for subsonic flow characteristics boundary conditions are applied [15]. On the top boundary, either extrapolation or characteristic conditions are specified for supersonic or subsonic flows respectively. On the outflow boundary, first-order accurate extrapolation of the dependent variables is employed in all cases, corresponding to the condition

$$\frac{\partial U}{\partial x} = 0. \quad (24)$$

For inviscid flows, the boundary conditions along the plate are modified by setting the fluid velocity component normal to the surface equal to the corresponding value for the moving plate. Finally, a slip condition is implemented by using second-order extrapolation for the tangential velocity component.

3.4 Structural Dynamic Governing Equations

The governing equation for the plate lateral deflection, w , can be written as:

$$D \frac{\partial^4 w}{\partial x^4} - (N_x + N_{x0}) \frac{\partial^2 w}{\partial x^2} + m \frac{\partial^2 w}{\partial t^2} = p_\infty - p \quad (25)$$

Here, N_{x0} , is the initial in-plane loading due to external forces, and N_x is the in-plane force induced by deflection of the panel. N_x is given by

$$N_x = \frac{E_s h}{2l} \int_0^l \left(\frac{\partial w}{\partial x} \right)^2 dx \quad (26)$$

D is the plate stiffness and m is the mass of the plate per unit area. The above two equations are the two dimensional equivalent of the von Karman plate equations. The equations are nondimensionalized by the aerodynamic scales and the nondimensional equation is

$$\left(\frac{\mu}{\lambda} \right) \frac{\partial^4 w}{\partial x^4} - (N_x) \frac{\partial^2 w}{\partial x^2} + \frac{\partial^2 w}{\partial t^2} = \mu(p_\infty - p) \quad (27)$$

$$N_x = t1 \int_0^1 \left(\frac{\partial w}{\partial x} \right)^2 dx \quad (28)$$

where $t1 = \frac{E_s}{2\rho_s U_\infty^2}$ and $\mu_s = \frac{\rho_\infty l}{\rho_s h}$. For simply supported case the following boundary conditions are used at both ends:

$$w = 0, \quad \frac{\partial^2 w}{\partial x^2} = 0 \quad (29)$$

For fixed end case the following boundary conditions are used:

$$w = 0, \quad \frac{\partial w}{\partial x} = 0 \quad (30)$$

4 Numerical Procedure

This section describes the numerical procedure for time integration of the aerodynamic equations, as well as the structural dynamic equations. Also, the grid deformation strategy is presented.

4.1 Time Integration Scheme

Solutions to equation (2) are obtained numerically using the implicit approximately-factored finite-difference algorithm of Beam and Warming [3], employing a Newton-like subiteration procedure [12]. The numerical algorithm is obtained from (2) by utilizing either a two- or three-point backward time differencing and linearizing about the solution at subiteration level p . The choice of first or second-order temporal accuracy is retained in the following iterative approach by specifying either $\phi = 0$ or $\phi = 1/2$, respectively. The approximate factored numerical algorithm is written in delta form as

$$\begin{aligned} & \left[J^{-1} + \phi^i \Delta t_s \delta_\xi \left(\frac{\partial F^p}{\partial U} - \frac{1}{Re} \frac{\partial F_v^p}{\partial U} \right) \right] \times \\ & \left[J^{-1} + \phi^i \Delta t_s \delta_\eta \left(\frac{\partial G^p}{\partial U} - \frac{1}{Re} \frac{\partial G_v^p}{\partial U} \right) \right] \Delta U \\ & = -\phi^i \Delta t_s \left[J^{-1} \frac{(1 + \phi)U^p - (1 + 2\phi)U^n + \phi U^{n-1}}{\Delta t} \right] \end{aligned}$$

$$\begin{aligned}
& -U^p \left(\left(\frac{\xi_i}{J} \right)_\xi + \left(\frac{\eta_i}{J} \right)_\eta \right) + J^{-1} \delta_\xi \left(F^p - \frac{1}{Re} F_v^p \right) \\
& + J^{-1} \delta_\eta \left(G^p - \frac{1}{Re} G_v^p \right) \Big].
\end{aligned} \tag{31}$$

where

$$\phi^i = \frac{1}{1 + \phi}, \quad \Delta U = U^{p+1} - U^p \tag{32}$$

and for $p = 1$, $U^p = U^n$. Here U^p is the subiteration approximation to U^{n+1} so that as $p \rightarrow \infty$, $U^p \rightarrow U^{n+1}$. It should be noted that with this subiteration approach the right-hand side of (31) represents the numerical approximation to the governing equation, while the left-hand side vanishes as $p \rightarrow \infty$. The left-hand side then, may be modified without loss of formal accuracy provided a sufficient number of subiterates is employed. In particular, a time step on the left-hand side of the equation Δt_s , may be chosen independently from the physical time step Δt on the right-hand side, thereby enhancing stability. Also the right hand side of (31) can be modified to include a higher order upwind algorithm, lagged boundary conditions or lagged $k - \epsilon$ turbulence modeling without destroying the implicit nature of the algorithm. Left hand side efficiency improvements can also be implemented. The numerical procedure has been modified to include diagonalization, following the approach of reference [11]. Although the diagonalized form of the ADI scheme is only first-order time-accurate, when coupled with subiterations, higher order time accuracy may be recovered. The diagonal scheme provides a 32% reduction in CPU time in two spatial dimensions relative to the block tridiagonal scheme. In three spatial dimensions the savings would be on the order of 50%. The numerical scheme (31) reverts to the standard first-order Beam-Warming procedure for $\phi = 0$, $\Delta t_s = \Delta t$, and $p = 1$.

In equation (31) all spatial derivatives are approximated by second-order accurate central differences, and common forms of both implicit and explicit nonlinear dissipation [7] are employed in order to preserve numerical stability. The temporal metric derivatives are discretized in a manner consistent with the temporal derivative of the conserved variables in equation (31).

The structural equation (27) is discretized using finite difference procedure in space and the Newmark- β method in time. The five and three point finite difference stencils [1] are used to approximate the fourth and second order space derivatives. The implementation of the Newmark- β method is discussed in detail in [2]. This is second order accurate in time and unconditionally stable. The following simultaneous equations are formed after discretizing equation (27) with proper boundary conditions:

$$Aw^{n+1} = B^{n+1} \tag{33}$$

The equation is solved by the preconditioned conjugate gradient iterative procedure at this time. At each time step and for each iteration the structural nonlinearity term N_x is computed and the matrix A is updated. Then solved until the difference between each iteration for N_x divided by N_x is less than 0.001 or maximum of 20 iterations. From experience it is found that about 10 iteration is enough for convergence. For a safer convergence an under-relaxation factor of 0.7 is used. In addition to improve the accuracy of the fluid-structure interaction solution, minimum three subiterations are done. This modifies the vector B. Thus a fully implicit coupling between the aerodynamic and the structural model

is accomplished.

5 Results

For the present computations, an aluminum plate with $h/l = .00271$, $E_s = 10^7 \text{ psi}$, and $\rho_s = .1 \text{ lb/in}^3$ is employed. The fluid properties at a height of 20,000 feet from sea level are $u_\infty = 1037 M_\infty \text{ ft/sec.}$ and $\rho_\infty = .046751 \text{ lb/ft}^3$. These values yields $\mu_s = .1$ and $t1 = 125/M_\infty^2$.

The effects of both spatial and temporal resolution on panel flutter are considered first. Three different grids are employed in order to assess spatial resolution effects. These meshes have 25, 50 and 100 equal intervals on the plate respectively. In all cases, the grid is stretched away from the plate in both the horizontal and vertical directions, and the computational domain farfield boundaries are located 25 plate lengths away from the panel. This is done in order to mitigate the effects of spurious reflections from the boundaries. The mesh distribution in the vertical direction is the same for all grids, with a minimum spacing next to the plate of 0.001l and a stretching factor of approximately 1.2. The panel flutter case corresponding to $M_\infty = 1.2$, $\lambda = 374$ and $\mu_s = 0.1$ was computed using all three grids. The three computed solutions were found to be in close agreement in terms of frequency and amplitude of the panel midpoint displacement. The variation in flutter frequency between the coarse and medium grids was 0.66%, whereas the corresponding difference between the medium and fine grids was 0.27%. The non-dimensional frequency on the fine mesh $St = 0.117$ is also in agreement with the value of $St = 0.12$ predicted by Davis and Bendiksen [5].

The effects of temporal resolution were also considered for the $M_\infty = 1.2$ case. Calculations were performed on the medium mesh using the second-order accurate time marching scheme with 3 subiterations and with time step values ranging from $\Delta t = 0.005$ to $\Delta t = 0.12$. Figure 2 shows the effect of time step on the computed non-dimensional frequency demonstrating convergence with decreasing Δt . It should be noted that Figure 2 displays an enlarged scale, and the change in frequency between the smallest and largest time step shown is less than 1%. A phase plot of the midpoint deflection and velocity is shown in Figure 3 for various Δt . In all cases a periodic solution is obtained, with all phase trajectories in excellent agreement. In the final paper, a comparison of the first and second order accurate time-marching schemes will be provided.

The panel stability boundary for Mach number 1.2 and $\mu_s = .1$ is computed to compare with the Bendiksen [4, 5] Euler solution and Dowell's [6] potential solution. For this case similar to the medium grid and a $\Delta t = 0.05$ is employed. The difference between the medium grid to this is, the fluid is extended in the y-direction for about 10l and in the x-direction about 5l on both sides of the plate. The grid size is 103x101 mesh. This grid is used to save computer time. The computed critical $\lambda = 19.2$ is in good agreement with the available results as shown in Figure 4. The critical λ is computed by computing the time response in stable and unstable region and plotting the amplification factor as shown in Figure 5. The amplification factor of the response is defined here as the ratio of the magnitude of a peak with respect to the preceding peak. Similarly $M_\infty = 0.9, 1., 1.1 \text{ and } 1.3$ are considered for computation. For $M_\infty = 0.9$ either stable or divergence condition occurred. For $M_\infty = 1.$ only divergence occurred for any range of λ from .5 to 250. Where as Davis and Bendiksen [5] could simulate flutter for $\lambda = 260$. For M_∞ greater than one the computed stability boundary is in good agreement with Bendiksen and Dowell as

shown in Figure 4.

For $M_\infty = 1.2$ the corresponding critical λ for viscous flow is 50. To compute this stability boundary a boundary layer depth of .0211 is used at the center of the plate. Using the same boundary layer depth the stability boundary for M_∞ ranging from 1.1 to 1.3 are computed and plotted in Figure 4. It is expected that depending upon the boundary layer depth different stability curve can be computed. For this boundary layer depth divergence occurred for M_∞ less than 1.1. For viscous flow, flutter occurs only if the boundary layer thickness is less than a critical value, beyond which only static divergence occurs. The time response of the midchord and quarter-chord point displacements are plotted both for stable and flutter region in Figures 6-9. It can be seen that the critical dynamic pressure is higher for viscous flow compared to the inviscid case.

6 Conclusions and Future Work

The flutter phenomena for a two-dimensional nonlinear panel is simulated using a fully-implicit aeroelastic solver. The panel is considered to be simply supported at this time. The time and space accuracy are studied in detail and documented. The computed stability boundary for Euler flow is in agreement with Bendiksen's finite element Euler solution and Dowell's potential flow solution. The stability boundary for viscous flow and for a boundary layer depth of .0211 is also reported.

Further work is needed to study the flutter condition for fixed panel, interaction of moving vortex on the panel, and flutter condition for plate in three-dimensional flow. The effects of the Geometric Conservation Law and of structural lagging needs to be investigated. The critical boundary layer thickness beyond which no flutter occurs needs to be computed for various Mach numbers. In this work, the number of points used for fluid and structure are the same. If less number of points are used on the structure, the effect of different interpolation technique on the accuracy is also needs to be investigated.

6.1 Acknowledgments

The author acknowledges the summer support provided by the Air Force Office of Scientific Research through the Summer Faculty Research Program. My sincere thanks to Dr. Miguel Visbal for giving me the opportunity to work on this problem and helping me during the process of this research. Thanks also to Capt. Scott A. Morton, Ph.D. for answering questions with the 2D fluid-structure interaction code.

References

- [1] Anderson, D.A., Tannehill, J.C. and Pletcher, R.H., *Computational Fluid Mechanics and Heat Transfer*, Hemisphere Publishing Corporation, New York, 1984
- [2] Bathe, K.J., *Finite Element Procedures in Engineering Analysis*, Prentice Hall, Englewood Cliffs, N.J., 1982
- [3] Beam, R. and Warming, R., "An Implicit Factored Scheme for the Compressible Navier-Stokes Equations," *AIAA Journal*, Vol.16, April 1978, pp. 393-402.
- [4] Bendiksen, O.O. and Davis, G.A., "Nonlinear Traveling Wave Flutter of Panels in Transonic Flow," AIAA Paper 95-1486, April 1995

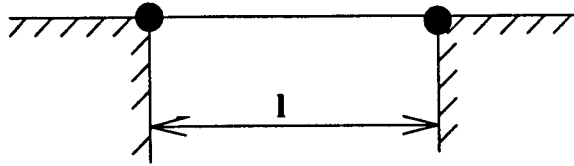


Figure 1: Two-Dimensional Panel

- [5] Davis, G.A. and Bendiksen, O.O., "Transonic Panel Flutter," AIAA Paper 93-1476, April 1993
- [6] Dowell, E.H., *Aeroelasticity of Plates and Shells*, Noordhoff International Publishing, The Netherlands, 1975
- [7] Jameson, A., Schmidt, W., and Turkel, E., "Numerical Solutions of the Euler Equations by Finite Volume Methods Using Runge-Kutta Time Stepping Schemes," AIAA Paper 81-1259, June 1981.
- [8] Guruswamy, G. P., "Unsteady Aerodynamic and Aeroelastic Calculations for Wings Using Euler Equations," AIAA Journal, Vol 28, No 3, pp. 461-469, March 1990.
- [9] Morton, S.A., Beran, P.S., "Nonlinear Analysis of Airfoil Flutter at Transonic Speeds," *AIAA 13th AIAA Applied Aerodynamics Conference, San Diego, CA June 19-22, 1995.* AIAA-95-1905.
- [10] Morton, S.A., Melville, R.B., and Visbal, M.R., "Accuracy and Coupling Issues of Aeroelastic Navier-Stokes Solutions on Deforming Meshes," *AIAA 38th AIAA Structures, Structural Dynamics, and Materials Conference, Kissimmee, FL April 7-10, 1997.* AIAA-97-1085.
- [11] Pulliam, T.H. and Chaussee, D.S., "A Diagonal Form of an Implicit Approximate-Factorization Algorithm," Journal of Computational Physics, Vol 39, No 2, pp. 347-363.
- [12] Rizzetta, D.P. and Visbal, M. R., "Comparative Numerical Study of Two Turbulence Models for Airfoil Static and Dynamic Stall," AIAA Paper 92-4649, June 1992.
- [13] Smith, M.J. *Flight Loads Prediction Methods for Aircraft: Vol I. Euler/Navier-Stokes Aeroelastic Method (ENS3DAE) Technical Development Summary: Version 4.0* (to be published: supersedes WRDC-TR-89-3104, Nov 1989, D.M. Schuster, J. Vadyak, E.H. Alta.),
- [14] Thomas, P.D. and Lombard, C.K., "Geometric Conservation Law and Its Application to Flow Computations on Moving Grids," *AIAA Journal*, Vol. 17, No. 10, pp. 1030-1037.
- [15] Whitfield, David L., "Three-Dimensional Unsteady Euler Equation Solutions using a Flux Vector Splitting", Short Course on Numerical Grid Generation at Mississippi State University, June, 1984.

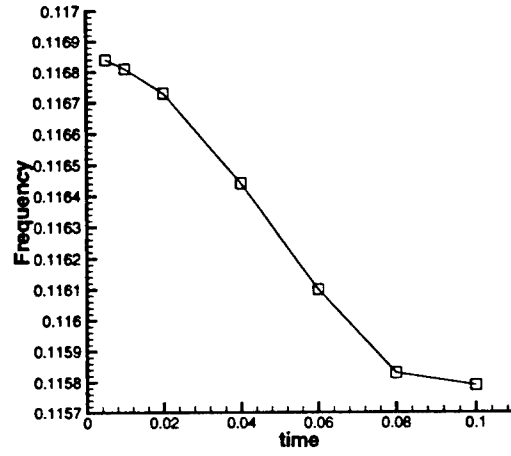


Figure 2: Effect of Time Step on Flutter Frequency for $M_\infty = 1.2$, $\mu_s = .1$ and $\lambda = 374$

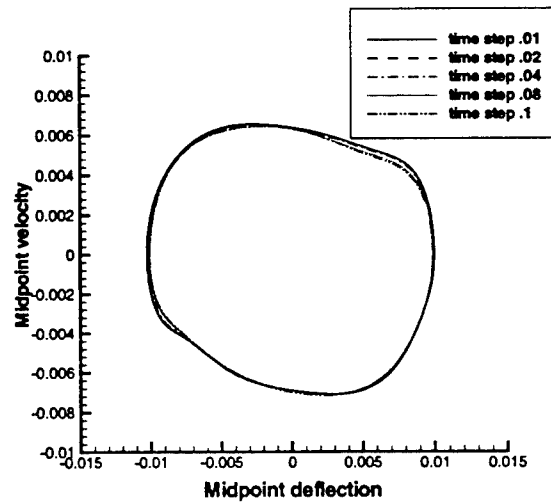


Figure 3: Phase Plot of Midpoint Oscillations for $M_\infty = 1.2$, $\mu_s = .1$ and $\lambda = 374$

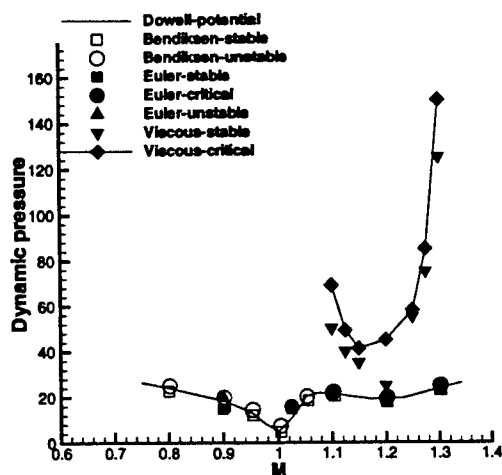


Figure 4: Stability Boundary for Simply Supported Panels for $\mu_s = .1$

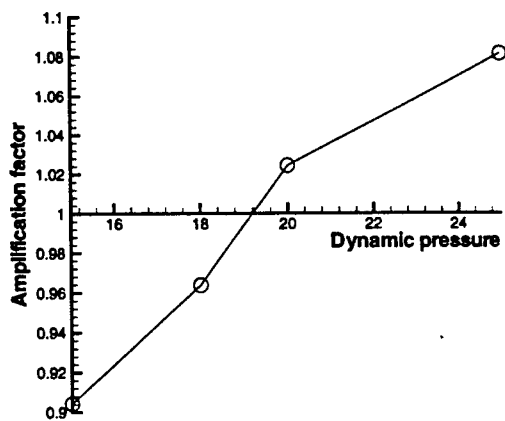


Figure 5: Computation of Dynamic Pressure for Flutter at $M_\infty = 1.2$ Using Euler Flow. For $\mu_s = .1$

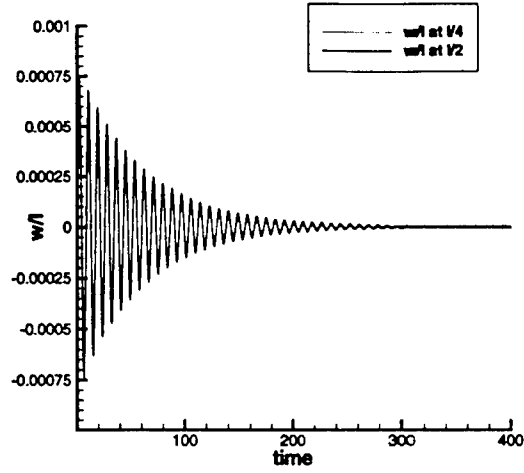


Figure 6: Panel Response in the Stable Region for $M_\infty = 1.2$ Using Euler Flow. Simply supported panel, $\mu_s = .1$ and $\lambda = 15$

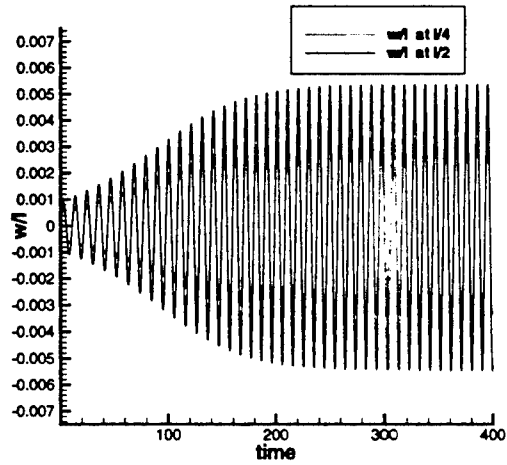


Figure 7: Panel Response During Flutter at $M_\infty = 1.2$ Using Euler Flow. Simply supported panel, $\mu_s = .1$ and $\lambda = 25$

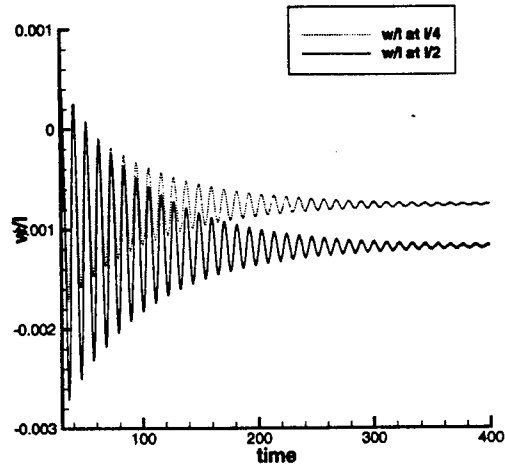


Figure 8: Panel Response in the Stable Region for $M_\infty = 1.2$ Using Viscous Flow. Simply supported panel, $\mu_s = .1$ and $\lambda = 25$

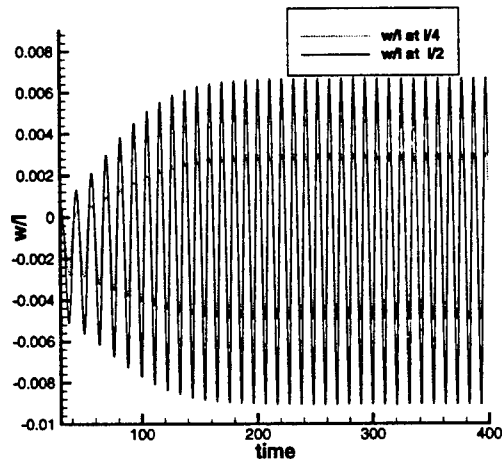


Figure 9: Panel Response During Flutter at $M_\infty = 1.2$ Using Viscous Flow. Simply supported panel, $\mu_s = .1$ and $\lambda = 100$

SMOOTHED SLIDING MODE CONTROL APPROACH FOR ADDRESSING
ACTUATOR DEFLECTION AND DEFLECTION RATE SATURATION IN TALESS
AIRCRAFT CONTROL AND RECONFIGURABLE FLIGHT CONTROL

Yuri B. Shtessel
Associate Professor
Department of Electrical and Computer Engineering

The University of Alabama in Huntsville
Huntsville, AL 35899

Final Report for:
Summer Faculty Research Program
Wright Laboratory

Sponsored by:
Air Force Office of Scientific Research
Bolling Air Force Base, DC

And

Wright Laboratory

September, 1997

SMOOTHED SLIDING MODE CONTROL APPROACH FOR ADDRESSING ACTUATOR DEFLECTION AND DEFLECTION RATE SATURATION IN TALESS AIRCRAFT CONTROL AND RECONFIGURABLE FLIGHT CONTROL

Yuri B. Shtessel
Associate Professor
Department of Electrical and Computer Engineering
The University of Alabama in Huntsville

Abstract

The following flight sliding mode control problems are considered: *tailless aircraft control, reconfigurable control of a traditional aircraft addressing actuator deflections and deflection rates saturation without damage identification, and control allocation and reconfiguration for damaged tailless aircraft*. Solving tailless aircraft control problem smoothed sliding mode virtual controllers are designed. A detailed investigation of properties of a smoothed sliding mode controller is accomplished. The sliding mode controller design is tailored to control allocation algorithm developed in the Wright Laboratory. The reconfigurable on-line sliding mode control strategy is developed for aircraft with “square “ configuration to address actuator deflections and deflection rates saturation without damage identification . This strategy guarantees a high accuracy tracking performance of pilot’s angular rates commands with given flying qualities before and after damage to an aircraft. The developed reconfigurable control strategy implies a smoothed sliding mode controller with a boundary layer reconfiguration. On-line explicit system (damage) identification is not required. Computer simulation sdemonstarted efficiency of the designed reconfigurable smoothed sliding mode controller.

SMOOTHED SLIDING MODE CONTROL APPROACH FOR ADDRESSING ACTUATOR DEFLECTION AND DEFLECTION RATE SATURATION IN TALESS AIRCRAFT CONTROL AND RECONFIGURABLE FLIGHT CONTROL

Yuri B. Shtessel

Introduction

The following flight control problems are considered

1. ***Tailess aircraft control.*** A tailess aircraft is characterized by a significant control redundancy: number of control effectors is larger than number of control variables. Solving flight control problem redundant control effectors must be allocated to maintain performance of a jet fighter preventing actuator deflections and deflection rates saturation. Employing the control allocation algorithm developing by Dr. Jim Buffington¹, we plan to design the virtual controllers using the Sliding Mode Control technique. The expected advantage from the virtual sliding mode controller design is in its inherent robustness. In addition using the new insight into the virtual controller design we expect to improve the existing prioritization algorithm¹.

2. ***Reconfigurable control of a traditional aircraft addressing actuator deflections and deflection rates saturation without damage identification.*** Control reconfiguration responding to aircraft damage in order to recover the loss of aircraft tracking performance is one of the contemporary control tools which needs development. The “bottle-neck” of a control reconfiguration is on-line damage (system) identification. Limitations to an actuator’s deflection and deflection rate usually lead to loss of stability and must be taken into account during reconfigurable controller design. The flight control reconfiguration problem was intensively investigated at Wright-Patterson Air Force Base by Drs. Banda, Chandler, Pachter, Mears, and Buffington²⁻⁵.

Well-known insensitivity and robustness of Variable Structure (Sliding Mode) Controllers (VSC) to plant disturbances and uncertainties¹¹⁻¹³ makes VSC attractive for application to tailess aircraft control and flight control reconfiguration. The system’s motion on the sliding surface is called a *sliding mode*. The chattering phenomenon¹⁴, associating with a VSC and consisting in high frequency control oscillations, can lead to unwanted mechanical distortions in plant actuators (control surfaces). However, the chattering issue can be easily addressed in flight control systems by including the actuator description (low-pass filter) in the system’s equations and utilizing smoothed (saturation) realization of the discontinuous control functions¹⁴⁻¹⁶. VSC has been applied already to output tracking in linearized^{17,18} and nonlinear^{15,16} flight control systems and demonstrated high accuracy robust de-coupled tracking performance of angular rates and trajectory angles in a broad flight domain^{15,16}. Control reconfiguration in sliding modes without on-line damage identification was addressed in the work¹⁹ as well.

I. Tailess aircraft control

Problem formulation

Mathematical model of an aircraft dynamics, linearized along some trajectory, is taken in the following format¹:

$$\begin{bmatrix} \dot{z} \\ \dot{y} \end{bmatrix} = \begin{bmatrix} A_{zz} & A_{zy} \\ A_{yz} & A_{yy} \end{bmatrix} \begin{bmatrix} z \\ y \end{bmatrix} + \begin{bmatrix} B_z \\ B_y \end{bmatrix} u + \begin{bmatrix} b_z \\ b_y \end{bmatrix} \quad (1)$$

where matrices $A_{zz}, A_{zy}, A_{yz}, A_{yy}, B_z, B_y$ and the vectors b_z, b_y are the functions of time, $y(t) \in \mathbb{R}^3$ is a control output, $z(t) \in \mathbb{R}^{n-3}$ is a state vector, $u(t) \in \mathbb{R}^k, k > 3$ is a control vector, $\text{rank}(B_y) = 3$.

It is shown¹ that the control dimension may be reduced by introducing a control allocation function $\rho(d_y(t))$:

$$d_z = B_z \rho(d_y(t)), \quad d_y = B_y \rho(d_y(t)) \equiv B_y u \quad (2)$$

and the system (1a) can be rewritten as follows:

$$\begin{bmatrix} \dot{z} \\ \dot{y} \end{bmatrix} = \begin{bmatrix} A_{zz} & A_{zy} \\ A_{yz} & A_{yy} \end{bmatrix} \begin{bmatrix} z \\ y \end{bmatrix} + \begin{bmatrix} B_z \rho(d_y(t)) \\ d_y(t) \end{bmatrix} + \begin{bmatrix} b_z \\ b_y \end{bmatrix} \quad (3)$$

The problem is: given in a real time a command output profile $y_c(t)$ design the control function $d_y(t)$ to provide

$$\lim_{t \rightarrow \infty} |y_{ci}(t) - y_i(t)| = 0 \quad \forall i = 1, 3 \quad (4)$$

to the system (1) using a Sliding Mode Control technique.

Assumptions

- Assuming stability of the internal dynamics of the system (1), i.e. the equation

$$\dot{z} = A_{zz}z + A_{zy}y + B_z \rho(d_y(t)) + b_z \text{ is stable, only the second part of the system (1)}$$

$$\dot{y} = A_{yz}z + A_{yy}y + d_y(t) + b_y \quad (5)$$

will be taken into consideration during the sliding mode controller design.

- We assume that the expression $A_{yz}z + A_{yy}y + b_y$ is only partially known and can be approximately estimated.

Discontinuous Sliding Mode Controller Design

At the first step of the sliding mode controller design such a sliding surface is designed. This is

$$\sigma = y_c(t) - y(t) = 0, \quad \sigma \in \mathbb{R}^3. \quad (6)$$

It is obvious that while in the surface the output tracking errors are de-coupled and identically equal to zero.

At the second step a control function $d_y(t)$ is identified to move the system to the sliding surface in a finite time

and to retain the system in this surface thereafter. The motion of the system in the σ -subspace is described

$$\dot{\sigma} = \dot{y}_c(t) - A_{yz}z - A_{yy}y - d_y(t) - b_y \quad (7)$$

The following equivalent control^{11,12} is identified

$$d_{yeq}(t) = \dot{y}_c(t) - A_{yz}z - A_{yy}y - b_y \quad (8)$$

Substituting the expression (8) into the equation (7) the following equation is obtained

$$\dot{\sigma} = d_{yeq}(t) - d_y(t) \quad (9)$$

Asymptotic stability of the system (9) must be provided via the control function $d_y(t)$. Introducing a candidate to the Lyapunov function as

$$V = \frac{1}{2} \sigma^T \sigma > 0 \quad (10)$$

its derivative is identified as follows:

$$\dot{V} = \sigma^T \dot{\sigma} = \sigma^T (d_{yeq}(t) - d_y(t)) \quad (11)$$

Assuming $d_y(t) = \hat{d}_{yeq}(t) + u$, where $\hat{d}_{yeq}(t)$ estimates $d_{yeq}(t)$, and $\Delta_{eq}(t) = d_{yeq}(t) - \hat{d}_{yeq}(t)$ we obtain

$$\dot{V} = \sigma^T (\Delta_{eq}(t) - u) = \sum_{i=1}^3 \sigma_i (\Delta_{eq_i}(t) - u_i) = \sum_{i=1}^3 (\sigma_i \Delta_{eq_i}(t) - \sigma_i u_i) \quad (12)$$

Assuming $|\Delta_{eq_i}(t)| < L_i < \infty$ and $u_i = \rho_i \text{sign} \sigma_i$ the expression (12) is transformed to the following one:

$$\dot{V} < \sum_{i=1}^3 (|\sigma_i| L_i - \rho_i |\sigma_i|) = \sum_{i=1}^3 |\sigma_i| (L_i - \rho_i) < 0 \quad (13)$$

In order to provide a negative definiteness to the quadratic form (13) the following obvious inequalities must be met

$$\rho_i > L_i \quad \forall i = \overline{1,3} \quad (14)$$

It can be easily shown that the sliding surfaces are reached if finite time $t_{reach_i} = \frac{|\sigma_i(0)|}{\rho_i - L_i} \quad \forall i = \overline{1,3}$.

In order to avoid a control chattering a smoothed implementation of this sliding mode controller is developed.

Smoothed Sliding Mode Controller Design. First scenario: perfect knowledge of an aircraft model

Assumption. Assume the equivalent control $d_{yeq}(t)$ is perfectly estimated, i.e. $\Delta_{eq}(t) = d_{yeq}(t) - \hat{d}_{yeq}(t) = 0$.

The smoothed sliding mode controller is proposed to design in the following format

$$d_{y_i}(t) = d_{yeq_i}(t) + \rho_i \text{sat} \frac{\sigma_i}{\varepsilon_i} \quad \forall i = \overline{1,3} \quad (15)$$

Substituting the formula (15) into the expression (12) we obtain

$$\dot{V} = \sum_{i=1}^3 \left(-\sigma_i \rho_i \text{sat} \frac{\sigma_i}{\varepsilon_i} \right) = -\sum_{i=1}^3 k_i |\sigma_i| < 0, \quad \rho_i > 0 \quad \forall i = \overline{1,3} \quad (16)$$

where

$$k_i = \begin{cases} \rho_i, & \text{if } |\sigma_i| > \varepsilon_i \\ \frac{\rho_i |\sigma_i|}{\varepsilon_i}, & \text{if } |\sigma_i| \leq \varepsilon_i \end{cases} \quad (17)$$

Remark 1, The origin of the σ - subspace is asymptotically stable with no finite reaching time.

Smoothed Sliding Mode Controller Design. Second scenario: Robust Smoothed Sliding Mode Controller

Now, let's assume the equivalent control $d_{yeq}(t)$ is not perfectly estimated, i.e. $\Delta_{eq}(t) = d_{yeq}(t) - \hat{d}_{yeq}(t) \neq 0$ and

$|\Delta_{eq_i}(t)| \leq L_i < \infty \quad \forall i = \overline{1,3}$. The question is whether the sliding mode controller

$$d_{y_i}(t) = \hat{d}_{yeq_i}(t) + \rho_i \text{sat} \frac{\sigma_i}{\varepsilon_i} \quad \forall i = \overline{1,3} \quad (18)$$

provides the asymptotic stability to the system's motion in the σ - subspace. The following expression is obtained

$$\dot{V} = \sum_{i=1}^3 \left(\sigma_i \Delta_{eq_i}(t) - \rho_i \sigma_i \text{sat} \frac{\sigma_i}{\varepsilon_i} \right) < \sum_{i=1}^3 (L_i |\sigma_i| - k_i |\sigma_i|) = \sum_{i=1}^3 (L_i - k_i) |\sigma_i| < 0 \quad (19)$$

where the gains $k_i \forall i = \overline{1,3}$ are defined by the formulas (17). Inequality (19) implies the following inequalities:

$$L_i - k_i < 0 \quad \forall i = \overline{1,3} \quad (20)$$

Substituting the formulas (17) in to inequalities (19) the following inequalities are obtained

$$\begin{cases} \rho_i > L_i, & \text{if } |\sigma_i| > \varepsilon_i \\ |\sigma_i| > \frac{L_i \varepsilon_i}{\rho_i}, & \text{if } |\sigma_i| \leq \varepsilon_i \end{cases} \quad \forall i = \overline{1,3} \quad (21)$$

In order to provide asymptotic output tracking $\lim_{t \rightarrow \infty} |y_{ci}(t) - y_i(t)| = 0$ we assume $\lim_{t \rightarrow \infty} \Delta_{eq}(t) = l = \text{const}$, where

$\Delta_{eq}(t) = d_{yeq}(t) - \hat{d}_{yeq}(t)$, for instance (can be unknown). In this case the sliding surfaces must be redesign.

Smoothed Sliding Mode Controller Design. Third Scenario: Robust Smoothed Asymptotic Sliding Mode Controller

Assumption. It is assumed that $|\Delta_{eq_i}| \leq L_i = \text{cons}$, if $|\sigma_i| > \varepsilon_i$, and $\Delta_{eq_i} = l_i = \text{cons}$, $|l_i| \leq L_i$ if $|\sigma_i| \leq \varepsilon_i \quad \forall i = \overline{1,3}$.

At the first step the sliding surfaces are redesigned as follows:

$$\sigma = e + C \int_0^t e d\tau = 0, \quad e = y_c(t) - y(t), \quad C = \text{diag}\{c_i\}, \quad \forall i = \overline{1,3}, \quad \sigma, e \in \mathbb{R}^3, \quad (22)$$

At the second step the control function $d_y(t)$ is selected in the "saturation" format (18). However, the equivalent control term $d_{yeq}(t)$ is augmented comparing with the expression (8), and is formed as follows

$$d_{yeq}(t) = \dot{y}_c(t) + C y_c(t) - A_{yz} z - (A_{yy} + C) y - b_y \quad (23)$$

The evolution of σ is described as follows:

$$\dot{\sigma}_i = \Delta_{eq_i} - \rho_i \text{sat} \frac{\sigma_i}{\varepsilon_i}, \quad \sigma_i(0) = \sigma_{i0} \quad \forall i = \overline{1,3} \quad (24)$$

It is clear that the conditions $\rho_i > L_i \quad \forall i = \overline{1,3}$ yield asymptotic convergence of the system's trajectory to the

boundary of the domain $|\sigma_i| \leq \frac{L_i \varepsilon_i}{\rho_i} \quad \forall i = \overline{1,3}$ in the σ -subspace, or to the boundary of the domain

$\left| e_i + c_i \int_0^t e d\tau \right| \leq \frac{L_i \varepsilon_i}{\rho_i} \quad \forall i = \overline{1,3}$ in the errors-and-their-derivatives (integrals) subspace. However, the system's motion

in this domain is defined only in sense of above inequalities. Assuming

$$\Delta_{eq_i} = l_i = \text{cons}, \quad |l_i| \leq L_i \quad \forall t \geq t_{ri} \quad \forall i = \overline{1,3}. \quad (25)$$

the boundaries of the domain $|\sigma_i| \leq \varepsilon_i \quad \forall i = \overline{1,3}$ will be reached at finite moments of time $t_{ri} \quad \forall i = \overline{1,3}$. Now, assuming $t \geq t_{ri}$, evolution of σ_i is described as follows:

$$\dot{\sigma}_i = l_i - \rho_i \frac{\sigma_i}{\varepsilon_i}, \quad |\sigma_i(t_{ri})| = \varepsilon_i \quad \forall i = \overline{1,3} \quad (26)$$

It is obvious that the equations (26) are asymptotically stable and $\lim_{t \rightarrow \infty} \sigma_i = \frac{l_i \varepsilon_i}{\rho_i} \neq 0 \quad \forall i = \overline{1,3}$. The values $\frac{l_i \varepsilon_i}{\rho_i}$ will

be reached by $\sigma_i(t)$ with a 2% accuracy due settling times $t_{si} = \frac{4\varepsilon_i}{\rho_i} \quad \forall i = \overline{1,3}$. Then, the sliding modes start in the

close vicinities of the sliding surfaces $\sigma_i = \frac{l_i \varepsilon_i}{\rho_i} \quad \forall i = \overline{1,3}$ and is described as follows:

$$\sigma_i(t) = \varepsilon_i + c_i \int_0^t e_i d\tau = \frac{l_i \varepsilon_i}{\rho_i} \quad \forall i = \overline{1,3} \quad (27)$$

or

$$\dot{e}_i + c_i e_i = 0 \quad \forall i = \overline{1,3} \quad (28)$$

The solutions to the equations (28) are

$$e_i(t) = e_i(t_{si}) \exp\{-c_i(t - t_{si})\} \quad \forall t \geq t_{si} \quad \forall i = \overline{1,3} \quad (29)$$

with settling times $\tilde{t}_{si} \geq \frac{4}{c_i}$. A geometric interpretation of the sliding mode control with the “nonsaturating”

continuous sliding mode controller is shown in Fig. 1

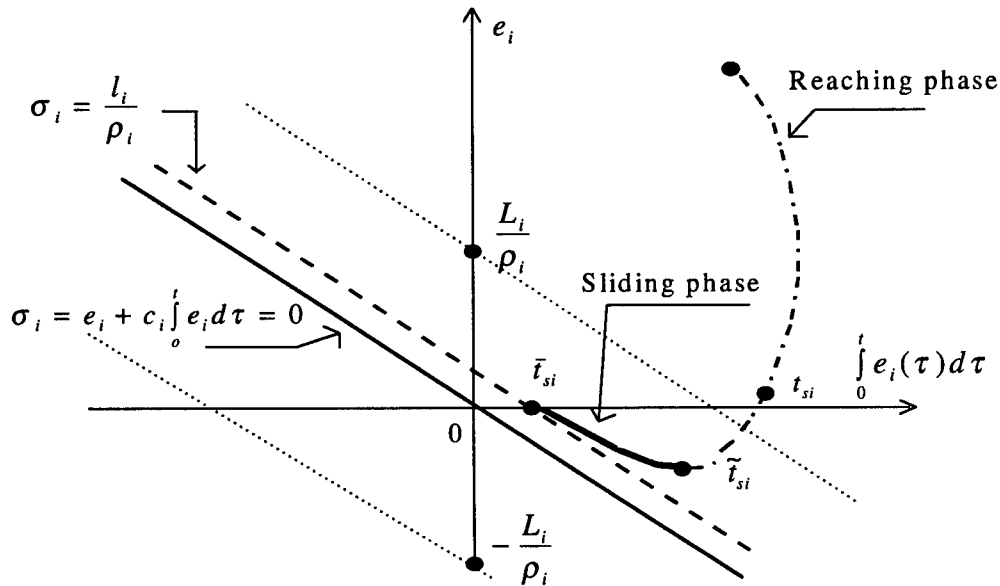


Fig. 1 Sliding mode control with continuous “nonsaturating sliding mode controller

Smoothed Sliding Mode Controller Design. Fourth scenario: linear asymptotic controller

This scenario is based on the consideration of the evolution of the system's tracking errors e_i as one asymptotic motion from an initial condition to the origin via continuous "nonsaturating" sliding mode controller $d_{y_i}(t) = \hat{d}_{y_{eq_i}}(t) + \rho_i \sigma_i \quad \forall i = \overline{1,3}$. It is assumed that $\Delta_{eq_i} = l_i = \text{cons}$, $|l_i| \leq L_i \quad \forall t \geq 0 \quad \forall i = \overline{1,3}$. This evolution is described by the equations

$$\dot{\sigma}_i = l_i - \rho_i \sigma_i, \quad \sigma_i = e_i + c_i \int_0^t e_i d\tau, \quad \forall i = \overline{1,3} \quad (30)$$

The equations (30) can be rewritten in the state-variable format as follows:

$$\begin{cases} \dot{\xi}_{1,i} = \xi_{2,i} \\ \dot{\xi}_{2,i} + c_i \xi_{1,i} = l_i - \rho_i (\xi_{2,i} + c_i \xi_{1,i}) \\ \sigma_i = \xi_{2,i} + c_i \xi_{1,i} \end{cases} \Rightarrow \begin{cases} \dot{\xi}_{1,i} = \xi_{2,i} \\ \dot{\xi}_{2,i} = l_i - \rho_i c_i \xi_{1,i} - (\rho_i + c_i) \xi_{2,i} \\ \sigma_i = \xi_{2,i} + c_i \xi_{1,i} \end{cases} \quad \forall i = \overline{1,3}, \quad (31)$$

where $\xi_1 = \int_0^t e d\tau$, $\xi_2 = e$, $\xi_1, \xi_2 \in \mathbb{R}^3$. The equations (31) are rewritten as the second order differential equations

$$\ddot{\xi}_{2,i} + (\rho_i + c_i) \dot{\xi}_{2,i} + \rho_i c_i \xi_{2,i} = 0, \quad \forall i = \overline{1,3} \quad (32)$$

The equations (32) are asymptotically stable $\forall \rho_i > 0, c_i > 0 \quad \forall i = \overline{1,3}$, and their solutions are

$$\xi_{2,i} = e_i(t) = a_i \exp(-\rho_i t) + b_i \exp(-c_i t) \quad (33)$$

A geometrical interpretation is given in fig. 2.

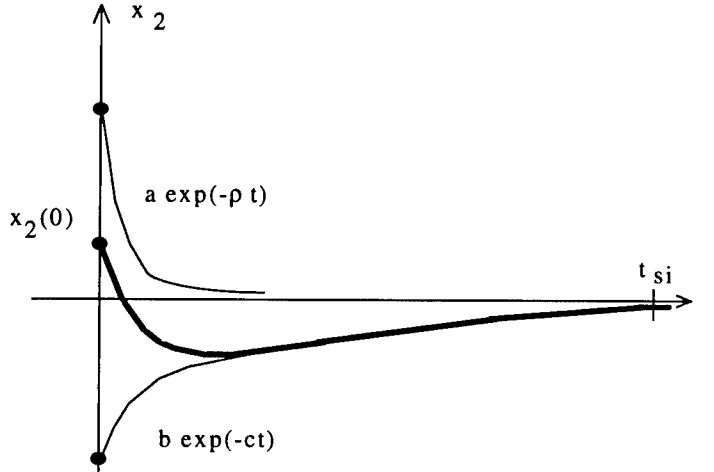


Fig. 2 Linear asymptotic controller

Conclusions

1. Smoothed sliding mode virtual controller was designed for tailless aircraft. Asymptotic output tracking is guaranteed upon certain conditions.

2. In order to apply the control allocation algorithm¹ a controller is designed in a nonsaturating format. This control allocation algorithm provide optimal control effector commands that prevent actuator deflection and deflection rate saturation. The sliding mode controller is designed for the system (5) in the following format

$$d_y = \hat{d}_{yeq} + \rho\sigma, \quad \sigma = e + c \int_0^t e d\tau, \quad \hat{d}_{yeq} = -A_{yz}z - A_{yy}y - b_y(t) + \dot{y}_c + cy_c - cy \quad (34)$$

which can be reformatted as follows

$$\begin{cases} d_y = -A_{yz}z - A_{yy}y - b_y + \dot{y}_c + \rho y_c + cy_c - cy - \rho y + \rho c x_i \\ \dot{x}_i = y_c - y \end{cases} \quad (35)$$

It is obvious that the nonsaturating sliding mode controller in the format (35) is pretty much similar to the feedback linearization controller, developed by Dr. Buffington¹

$$\begin{cases} d_y = -A_{yz}z - A_{yy}y - b_y + \omega_c f_c y_c - \omega_c y + \omega_c^2 f_i x_i \\ \dot{x}_i = y_c - y \end{cases} \quad (36)$$

We expect to gain some advantage using sliding mode controller (35). The sliding mode control philosophy provides insight into control partition priority for unachievable control commands

$$d_y = \lambda_1 d_1 + \lambda_2 d_2 + \lambda_3 d_3 + \lambda_4 d_4 \quad (37)$$

This insight is.

- At the reaching (beginning) phase it is important to retain the ρ – terms, which are responsible for reaching time. At the sliding (finale) phase it is important to retain the c – terms , which are responsible for transient in the vicinity of the sliding surface.
- The largest terms in the distribution (37) must be relaxed first. It is hard to identify a term which will have the largest value all the time, because the terms depend on time. This logic leads us to the dynamic priority schemes, which were not examined yet.

For instance, looking for sliding mode controller allocation we examine now the following “static” priority

$$\begin{cases} d_1 = \rho e \\ d_2 = c(\rho x_i + e) \\ d_3 = -A_{yz}z - A_{yy}y - b_y(t) \\ d_4 = \dot{y}_c \end{cases} \quad (38)$$

II. Reconfigurable control of a traditional aircraft addressing actuator deflections and deflection rates saturation without damage identification

Problem Formulation

Mathematical model of an aircraft is taken in a following generic format

$$\begin{cases} \dot{z} = f_1(z, y, t) + \Delta f_1(z, y, t) + (B_1(z, y, t) + \Delta B_1(z, y, t))\delta \\ \dot{y} = f_2(z, y, t) + \Delta f_2(z, y, t) + (B_2(z, y, t) + \Delta B_2(z, y, t))\delta \\ \dot{\delta} = -A_\delta(\delta - u) \end{cases} \quad (39)$$

where $y \in \mathbb{R}^3$ is an output vector (without loss of generality it is assumed that $y = \{p, q, r\}^T$ with p, q, r standing for roll, pitch and yaw rates correspondingly); $z \in \mathbb{R}^k$ is a vector which coordinates do not contain the coordinates to be controlled, $\delta = \{\delta_A, \delta_E, \delta_R\}^T$, $u \in \mathbb{R}^3$ is a control vector, $f_1(z, y, t) \in \mathbb{R}^k$, $f_2(z, y, t) \in \mathbb{R}^3$ are partially known vector-functions, $B_1(z, y, t) \in \mathbb{R}^{k \times 3}$, $B_2(z, y, t) \in \mathbb{R}^{3 \times 3}$ are known matrices, $\Delta f_1 \in \mathbb{R}^k$, $\Delta f_2 \in \mathbb{R}^3$, $\Delta B_1 \in \mathbb{R}^{k \times 3}$, $\Delta B_2 \in \mathbb{R}^{3 \times 3}$ are unknown bounded smooth perturbations, caused by an aircraft damage, $\det B_2(z, y, t) \neq 0$, $\det(B_2(z, y, t) + \Delta B_2(z, y, t)) \neq 0 \quad \forall z, y, t$ from a reasonable flight domain, $A_\delta \in \mathbb{R}^{3 \times 3}$, $A_\delta = \text{diag}\{a_\delta\}$, $a_\delta > 0$.

The deflections and deflection rates of the actuators are assumed to be bounded as $|\delta_i| \leq \delta_m$, $|\dot{\delta}_i| \leq \bar{\delta}_m \quad \forall i = \overline{1, 3}$

The problem is: given in real time a command reference profile $y_c(t)$ design a control function u to provide

$$\lim_{t \rightarrow \infty} |y_{ci} - y_i| = 0 \quad \forall i = \overline{1, 3} \quad (40)$$

taking into account the actuators' deflection and deflection rate limits via the sliding mode control.

Problem 1. Design the sliding mode controller without reconfiguration providing robust tracking of the pilot's angular rates commands insensitive to aircraft damage and taking into account limitations to the actuator's deflection and deflection's rate.

Designing the control law we will use the following equations

$$\begin{cases} \dot{y} = f_2(z, y, t) + \Delta f_2(z, y, t) + (B_2(z, y, t) + \Delta B_2(z, y, t))\delta \\ \dot{\delta} = -A_\delta(\delta - u). \end{cases} \quad (41)$$

In order to make the designed control law operational it is assumed that any solution of the equations

$$\dot{z} = f_1(z, y, t) + \Delta f_1(z, y, t) + (B_1(z, y, t) + \Delta B_1(z, y, t))\delta \quad (42)$$

is bounded if the vector-deflection δ is bounded. The sliding surface is designed

$$\sigma = \dot{e} + C^1 e + C^2 \int_0^t e d\tau = 0, \quad e_i = y_{ci} - y_i \quad \forall i = \overline{1, 3} \quad (43)$$

The system's (41) motion in the σ - subspace is described by the following equations:

$$\dot{\sigma} = F(.) - (B_2 + \Delta B_2)v, \quad (44)$$

where

$$F(.) = \ddot{y}_c + C^1 \dot{y}_c + C^2 e - \frac{d}{dt}(f_2 + \Delta f_2) - C^1(f_2 + \Delta f_2) - \left[\frac{d}{dt}(B_2 + \Delta B_2) + C^1(B_2 + \Delta B_2) \right] \delta \quad (45)$$

$$v = -A_\delta(\delta - u). \quad (46)$$

Assuming the matrix B_2 symmetric and positive definite, the candidate to the Lyapunov function is formed

$$V = \frac{1}{2} \sigma^T Q \sigma = \frac{1}{2} \sigma^T (B_2)^{-1} \sigma > 0 \quad (47)$$

The derivative of the candidate to the Lyapunov function (47) is identified as:

$$\dot{v} = \sigma^T (B_2)^{-1} \dot{\sigma} + \frac{1}{2} \sigma^T \frac{d}{dt} (B_2)^{-1} \sigma = \sigma^T (B_2)^{-1} \left[F(\cdot) - \frac{(B_2)^{-1}}{2} \frac{d}{dt} (B_2) \sigma - (B_2 + \Delta B_2) v \right] \quad (48)$$

The equivalent control^{11,12} v_{eq} is identified as follows:

$$v_{eq} = (B_2 + \Delta B_2)^{-1} \left[F(\cdot) - \frac{(B_2)^{-1}}{2} \frac{d}{dt} (B_2) \sigma \right] \quad (49)$$

The following discontinuous control function is designed

$$v = \hat{v}_{eq} + \rho \text{SIGN} \sigma, \quad (50)$$

where $\rho = \text{diag}\{\rho_i\}, \rho_i > 0 \forall i = \overline{1,3}$, $\text{SIGN} \sigma = \{\text{sign} \sigma_1, \text{sign} \sigma_2, \text{sign} \sigma_3\}^T$, \hat{v}_{eq} is an estimate of the v_{eq} .

Denoting $\Delta_{eq} = v_{eq} - \hat{v}_{eq}$ and $\Delta_v = (B_2)^{-1} \Delta B_2$ the following formula is obtained

$$\dot{v} = \sigma^T (I + \Delta_v) (\Delta_{eq} - \rho \text{SIGN} \sigma) = - \sum_{i=1}^3 \rho_i (1 + \Delta_{v_i} + \xi_i) |\sigma_i| + \sum_{i=1}^3 (\Delta_{eq_i} + \Delta_{eq_i} \Delta_{v_i} + \psi_i) \sigma_i, \quad (51)$$

where

$$\xi_1 = \frac{\Delta_{v_{21}} \sigma_2 + \Delta_{v_{31}} \sigma_3}{\sigma_1}, \quad \xi_2 = \frac{\Delta_{v_{12}} \sigma_1 + \Delta_{v_{32}} \sigma_3}{\sigma_2}, \quad \xi_3 = \frac{\Delta_{v_{23}} \sigma_2 + \Delta_{v_{13}} \sigma_1}{\sigma_3}, \quad \psi_1 = \Delta_{v_{12}} \Delta_{eq_2} + \Delta_{v_{13}} \Delta_{eq_3}, \quad (52)$$

$$\psi_2 = \Delta_{v_{21}} \Delta_{eq_1} + \Delta_{v_{23}} \Delta_{eq_3}, \quad \psi_3 = \Delta_{v_{31}} \Delta_{eq_1} + \Delta_{v_{32}} \Delta_{eq_2}$$

Assume the following inequalities are met

$$|\xi_i| \leq w_i, \quad |\psi_i| \leq r_i, \quad |\Delta_{v_{ii}}| \leq \lambda_i, \quad |\Delta_{eq_i}| \leq L_i \quad \forall i = \overline{1,3}, \quad (53)$$

where w_i, r_i, λ_i are proportional to perturbations (damages), and L_i are positive numbers which are proportional to the estimation errors of the equivalent control terms. The following inequality is obtained

$$\dot{v} \leq - \sum_{i=1}^3 |\sigma_i| [\rho_i (1 - \lambda_i - w_i) - L_i (1 + \lambda_i) - r_i] < 0. \quad (54)$$

In order to meet the inequality (54) the values of ρ_i must satisfy the conditions

$$\rho_i > \frac{(1 + \lambda_i) L_i + r_i}{1 - \lambda_i - w_i} \quad \forall i = \overline{1,3} \quad (55)$$

The final formula for the control law is derived

$$u_i = \begin{cases} \delta_m, & \text{if } g_{1_i} > \delta_m \\ \delta_i + \frac{\bar{\delta}_m}{a_\delta}, & \text{if } |g_{1_i}| \leq \delta_m \& g_{2_i} > \bar{\delta}_m \\ \delta_i + \frac{1}{a_\delta} (\hat{v}_{eq_i} + \rho_i \text{sign} \sigma_i), & \text{if } |g_{1_i}| \leq \delta_m \& |g_{2_i}| \leq \bar{\delta}_m \\ \delta_i - \frac{\bar{\delta}_m}{a_\delta}, & \text{if } |g_{1_i}| \leq \delta_m \& g_{2_i} < -\bar{\delta}_m \\ -\delta_m, & \text{if } g_{1_i} < -\delta_m \end{cases} \quad (56)$$

where $g_{1_i} = \delta_i + \frac{1}{a_\delta}(\hat{v}_{eq_i} + \rho_i \text{sign} \sigma_i)$, $g_{2_i} = \hat{v}_{eq_i} + \rho_i \text{sign} \sigma_i \quad \forall i = \overline{1,3}$

Avoiding a control chattering and saturation of actuator deflections or deflection rates, the following smoothed sliding mode controller with a boundary layer is proposed.

$$v = \hat{v}_{eq} + \rho SAT \frac{\sigma}{\varepsilon}, \quad SAT \frac{\sigma}{\varepsilon} = \left\{ sat \frac{\sigma_1}{\varepsilon_1}, sat \frac{\sigma_2}{\varepsilon_2}, sat \frac{\sigma_3}{\varepsilon_3} \right\}^T \quad (57)$$

The derivative of the candidate to the Lyapunov function is calculated

$$\dot{V} = \sigma^T (I + \Delta_v) \left(\Delta_{eq} - \rho SAT \frac{\sigma}{\varepsilon} \right) = - \sum_{i=1}^3 k_i (1 + \Delta_{v_i} + \xi_i) |\sigma_i| + \sum_{i=1}^3 (\Delta_{eq_i} + \Delta_{eq_i} \Delta_{v_i} + \psi_i) \sigma_i, \quad (58)$$

where

$$k_i = \begin{cases} \rho_i, & \text{if } |\sigma_i| > \varepsilon_i \\ \frac{\rho_i |\sigma_i|}{\varepsilon_i}, & \text{if } |\sigma_i| \leq \varepsilon_i \end{cases} \quad (59)$$

The conditions which provide negative definiteness of the candidate to the Lyapunov function are obtained. They are

$$\rho_i > R_i, \quad \text{if } |\sigma_i| > \varepsilon_i \quad (60)$$

$$|\sigma_i| > \frac{R_i \varepsilon_i}{\rho_i}, \quad \text{if } |\sigma_i| \leq \varepsilon_i \quad (61)$$

where $R_i = \frac{(1 + \lambda_i)L_i + r_i}{1 - \lambda_i - w_i} \quad \forall i = \overline{1,3}$. After the boundary $|\sigma_i| = \frac{R_i \varepsilon_i}{\rho_i} \quad \forall i = \overline{1,3}$ of the domain (61) is reached)probably

asymptotically) , the system's (41) motion will obey the inequalities

$$\left| \dot{e}_i + c_i^1 e + c_i^2 \int_0^t e_i d\tau \right| \leq \frac{R_i \varepsilon_i}{\rho_i}, \quad e_i = y_{ci} - y_i \quad \forall i = \overline{1,3}, \quad (62)$$

and we can talk about an ε -robustness of the smoothed sliding mode controller.

Problem 2. *Design the sliding mode controller with on-line reconfiguration providing robust high accuracy tracking of the pilot's angular rates commands in a damaged regime without system (damage) on-line identification and taking into account limitations to the actuator's deflection and deflection's rate.*

The sliding mode controller (56) is rewritten in a smoothed format

$$u_i = \begin{cases} \delta_m, & \text{if } g_{1_i} > \delta_m \\ \delta_i + \frac{\bar{\delta}_m}{a_\delta}, & \text{if } |g_{1_i}| \leq \delta_m \& g_{2_i} > \bar{\delta}_m \\ \delta_i + \frac{1}{a_\delta} \left(\hat{v}_{eq_i} + \rho_i sat \frac{\sigma_i}{\varepsilon_i} \right), & \text{if } |g_{1_i}| \leq \delta_m \& |g_{2_i}| \leq \bar{\delta}_m \\ \delta_i - \frac{\bar{\delta}_m}{a_\delta}, & \text{if } |g_{1_i}| \leq \delta_m \& g_{2_i} < -\bar{\delta}_m \\ -\delta_m, & \text{if } g_{1_i} < -\delta_m \end{cases} \quad (63)$$

where $g_{1i} = \delta_i + \frac{1}{a_\delta} \left(\hat{v}_{eq_i} + \rho_i \text{sat} \frac{\sigma_i}{\varepsilon_i} \right)$ and $g_{2i} = \hat{v}_{eq_i} + \rho_i \text{sat} \frac{\sigma_i}{\varepsilon_i} \quad \forall i = \overline{1,3}$

Concept. If one of the following conditions

$$|g_{1i}| \leq \delta_m, \quad |g_{2i}| \leq \bar{\delta}_m \quad \forall i = \overline{1,3} \quad (64)$$

is violated, then the originally selected values ε_i of the corresponding boundary layers must be increased.

Remark 2. Increase of ε_i leads to a corresponding gain $\frac{\rho_i}{\varepsilon_i}$ reduction.

Algorithm of reconfiguration (direct adaptation) of a thickness of a boundary layer

Assume that the reaching phase is over, and the system moves in the ε_i -vicinities of the sliding surfaces (43). In this case saturation functions in the smoothed sliding mode controller (63) can be substituted by the linear functions

$\frac{\rho_i}{\varepsilon_i} \sigma_i \quad \forall i = \overline{1,3}$. The inequalities (64) are written as follows:

$$\left| \delta_i + \frac{1}{a_\delta} \left(\hat{v}_{eq_i} + \rho_i \frac{\sigma_i}{\varepsilon_i} \right) \right| \leq \delta_m, \quad \left| \hat{v}_{eq_i} + \rho_i \frac{\sigma_i}{\varepsilon_i} \right| \leq \bar{\delta}_m \quad \forall i = \overline{1,3} \quad (65)$$

In case of an aircraft damage the nonlinear vector- and matrix- functions $\Delta f_1 \in \mathfrak{R}^k$, $\Delta f_2 \in \mathfrak{R}^3$, $\Delta B_1 \in \mathfrak{R}^{k \times 3}$, $\Delta B_2 \in \mathfrak{R}^{3 \times 3}$ are not equal to zero and can lead to increase of the absolute values of \hat{v}_{eq_i} , σ_i , δ_i , which can cause saturation of the actuator deflections or deflection rates. In order to prevent such a system's performance the thickness of the boundary layers ε_i will be changed on-line. A solution to the inequalities (65) is obtained

$$\varepsilon_i = \max \{ \varepsilon_i^1, \varepsilon_i^2, \varepsilon_i^3 \} \quad (66)$$

where

$$\varepsilon_i^1 = |\sigma_i| + r_i^1, \quad \varepsilon_i^2 = \frac{|\sigma_i| \rho_i}{\bar{\delta}_m - \hat{v}_{eq_i} \text{sign} \sigma_i} + r_i^2, \quad \varepsilon_i^3 = \frac{|\sigma_i| \rho_i}{a_\delta \bar{\delta}_m - (a_\delta \delta_i + \hat{v}_{eq_i}) \text{sign} \sigma_i} + r_i^3 \quad (67)$$

and r_i^1, r_i^2, r_i^3 are small positive numbers $\forall i = \overline{1,3}$.

Example 1

The pitch rate command tracking problem is considered. The aircraft model of the linearized second-order pitch plane dynamics for F-16 at Mach = 0.7, h = 10000 ft flight condition is taken as follows^{4,5}:

$$\begin{bmatrix} \dot{\alpha} \\ \dot{q} \end{bmatrix} = \tilde{A} \begin{bmatrix} \alpha \\ q \end{bmatrix} + \tilde{B} \delta \quad (68)$$

where $\tilde{A} = A_n + \Delta A$, $\tilde{B} = B_n + \Delta B$, and

$$A_n = \begin{bmatrix} Z_\alpha & Z_q \\ M_\alpha & M_q \end{bmatrix}, \quad \Delta A = \begin{bmatrix} \Delta Z_\alpha & \Delta Z_q \\ \Delta M_\alpha & \Delta M_q \end{bmatrix}, \quad B_n = \begin{bmatrix} Z_\delta \\ M_\delta \end{bmatrix}, \quad \Delta B = \begin{bmatrix} \Delta Z_\delta \\ \Delta M_\delta \end{bmatrix} \quad (69)$$

where α is angle of attack (rad), q is pitch rate (rad/s), δ is an elevator deflection (rad).

The actuator's model is taken as follows:

$$\dot{\delta} = -20\delta + 20u \quad (70)$$

where u is the control input of the actuator (*rad*), and

$$v = -20\delta + 20u \quad (71)$$

is a "virtual" control function. The actuator's output is rate limited to $|\dot{\delta}| \leq b$, ($b = 1 \text{ rad/s}$), and its deflection is limited to $|\delta| \leq a$, ($a = 0.37 \text{ rad}$). It is obvious that $|v| \leq b$. The failure is modeled as a 50% loss of horizontal tail area which occurs 5 sec into the simulation. The reference model, the nominal and failure values of parameters are taken as in the papers^{4,5}. The pilot's commands u_{com} are 1.0 s duration pitch rates pulses of 0.1 rad/s amplitude, and input polarities of -, +, -, and + at times of 0.0, 3.0, 6.0, and 9.0 respectively.

Design of a Smoothed Reconfigurable Sliding Mode Controller

We assume that

- $\hat{v}_{eq} = 0$, and $L > |v_{eq}|$, $\lambda > \left| \frac{\Delta B_2}{B_2} \right| = 0.5$, (72)
- the system's motion is already in the close vicinity of the boundary layer.

The formula (63) is reduced to

$$u = \delta + 0.05 \rho \text{sat} \frac{\sigma}{\varepsilon} \quad (73)$$

and the constraints to the actuator deflection and deflection rate are relaxed. A value of the gain ρ must be identified in accordance with the formula (55) with $w_i = r_i = 0$, as

$$\rho > \frac{(1+\lambda)}{(1-\lambda)} L = 3.0L. \quad (74)$$

The equivalent control can be identified as

$$v_{eq} = v_{eq_{nom}} + \Delta v_{eq}, \quad (75)$$

where $v_{eq_{nom}}$ corresponds to the equivalent control in nominal (undamaged) case, Δv_{eq} is due an aircraft damage.

Estimating $|\Delta v_{eq}| < 0.16$ the value of ρ is identified as follows:

$$\rho > 3.0L > 3.0(|v_{eq_{nom}}| + |\Delta v_{eq}|) = 3.0|v_{eq_{nom}}| + 0.5, \quad (76)$$

$$v_{eq_{nom}} = -0.05128(\ddot{q}_r + 10\dot{q}_r) + 1.45\alpha - 9.729q - 8.774\delta. \quad (77)$$

Substituting $\delta_m = 0.37$, $\bar{\delta}_m = 1.0$ and $r^1 = r^2 = r^3 = 0.02$ into formulas (67) we obtain

$$\varepsilon^2 = |\sigma|\rho + 0.02, \quad \varepsilon^3 = \frac{0.05|\sigma|\rho}{0.37 - \delta \text{sign}\sigma} \quad (78)$$

The results of the system's simulation are shown in Fig. 3-6. The reference profile is tracked perfectly before and after a 50% loss of horizontal tail area. The actuator deflection and deflection's rate are within the imposed limits.

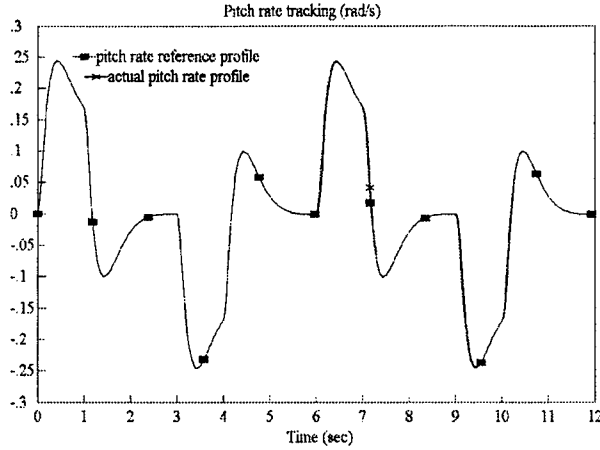


Fig. 3 Pitch rate reference profile tracking

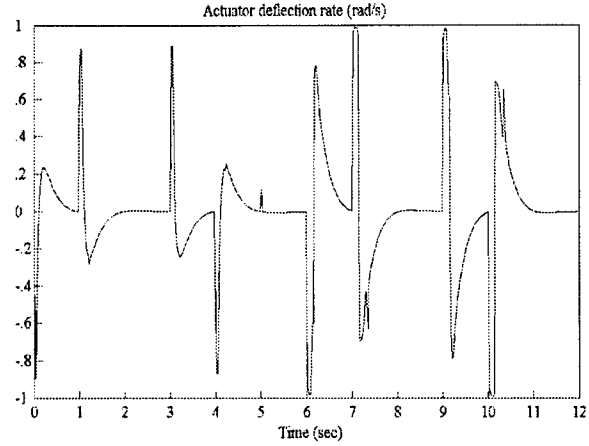


Fig. 4 Actuator's deflection rate

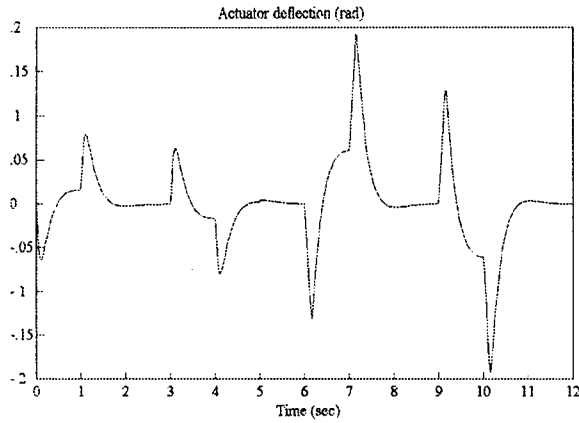


Fig. 5 Actuator's deflection

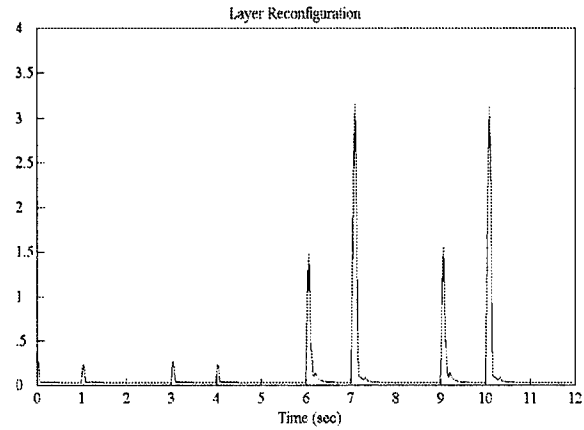


Fig. 6 Boundary layer reconfiguration

Example 2

The mathematical model of an F-16 jet fighter at $Mach = 0.7$, $h = 10000 \text{ ft}$ $\alpha_{trim} = \theta_{trim} = 0.106803 \text{ rad}$,

$\delta_{e_{trim}} = -0.0295 \text{ rad}$, $\beta_{trim} = p_{trim} = q_{trim} = r_{trim} = \varphi_{trim} = \delta_{a_{trim}} = \delta_{r_{trim}} = 0$ flight condition is taken as follows:

$$\begin{cases} \dot{\theta} = q \cos \varphi - r \sin \varphi \\ \dot{\varphi} = p + q \sin \varphi \tan \theta + r \cos \varphi \tan \theta \end{cases} \quad (79)$$

$$\begin{cases} \dot{\alpha} = 0.9939q - \beta p + 0.0427 \cos \theta \cos \varphi + 0.083589 - 1.2295\alpha - 0.1786\delta_e \\ \dot{\beta} = -0.9973r + \alpha p + 0.0427 \cos \theta \sin \varphi - 0.2971\beta + 0.000851p + 0.03723\delta_r + 0.002466\delta_a \end{cases} \quad (80)$$

$$\begin{cases} \dot{p} = -0.1345pq - 0.8225qr - 53.48\beta - 4.3242p - 0.2237r - 50.933\delta_a + 10.177\delta_r \\ \dot{q} = 0.9586pr - 0.0833(r^2 - p^2) - 1.94166 + 12.886\alpha - 1.083q - 19.166\delta_e \\ \dot{r} = -0.7256pq + 0.1345qr + 17.671\beta + 0.2339p - 0.6487r + 4.125\delta_a - 6.155\delta_r \end{cases} \quad (81)$$

$$\dot{\delta}_a = 20(u_1 - \delta_a), \quad \dot{\delta}_e = 20(u_1 - \delta_e), \quad \dot{\delta}_r = 20(u_1 - \delta_r) \quad (82)$$

Actuator deflection limits are $|\delta_i| \leq 0.3 \text{ rad}$, $|\dot{\delta}_i| \leq 1 \text{ rad/s} \quad \forall i = a, e, r$. Flying qualities are defined by the filters:

$$\begin{aligned} \frac{p}{p^*} &= \frac{1.25}{s+1.25} \text{ for ingoing pilot command, } \frac{p}{p^*} = \frac{1.25}{s+1.25} \text{ for outgoing pilot command,} \\ \frac{\alpha}{\alpha^*} &= \frac{4}{s^2+3s+4}, \quad \frac{\beta}{\beta^*} = \frac{16.98}{s^2+6.18s+16.98} \end{aligned} \quad (83)$$

Problem is to design a sliding mode controller to provide de-coupling tracking of angles α, β and roll rate p commands addressing the actuator deflection and deflection rates limits in accordance with the flying qualities (83). The functional diagram of the flight control system is shown in fig. 7.

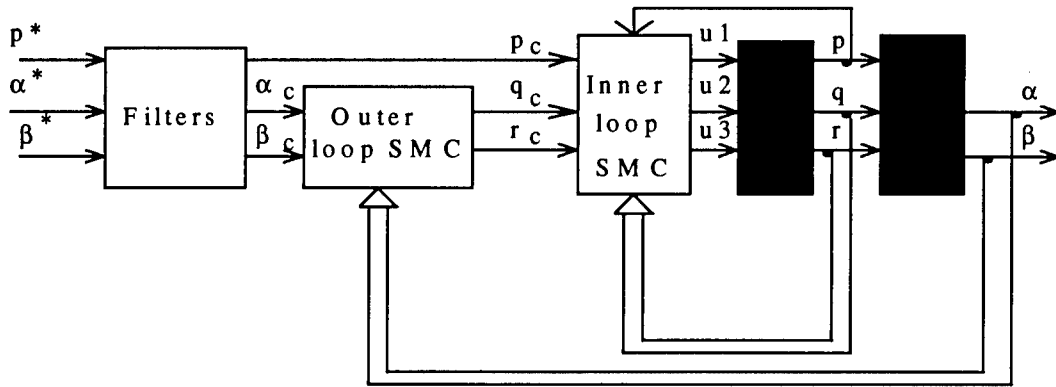


Fig. 7 The functional diagram of the two-loop flight control system

Inner-loop sliding mode controller design

Assuming given the reference profiles for angular rates p_c, q_c, r_c the sliding surfaces are designed as follows:

$$\sigma_1 = \dot{e}_1 + 8e_1 + 16 \int_0^t e_1 d\tau, \quad \sigma_2 = \dot{e}_2 + 100e_2 + 2500 \int_0^t e_2 d\tau, \quad \sigma_3 = \dot{e}_3 + 16e_3 + 64 \int_0^t e_3 d\tau \quad (84)$$

where $e_1 = p_c - p$, $e_2 = q_c - q$, $e_3 = r_c - r$, and p_c, q_c, r_c are reference profiles.

The control functions are designed. They are

$$u_i = \delta_i + \frac{1}{a_{\delta}} \left(\hat{v}_{eq_i} + \rho_i \text{sat} \frac{\sigma_i}{\varepsilon_i} \right) \quad \forall i = 1, 2, 3 \quad (85)$$

Assuming $\hat{v}_{eq_i} = 0$ the formulas (85) are implemented to the inner-loop smoothed sliding mode controller design

$$u_i = \delta_i + 0.05 \rho_i \text{sat} \frac{\sigma_i}{\varepsilon_i}, \quad \rho_i > |v_{eq_i}| \quad \forall i = 1, 2, 3. \quad (86)$$

The boundary layer are reconfigured (adapted). They are

$$\varepsilon_i = \max\{\varepsilon_i^1, \varepsilon_i^2, \varepsilon_i^3\} \quad \forall i = 1, 2, 3 \quad (87)$$

$$\varepsilon_i^1 = |\sigma_i| + 0.02, \quad \varepsilon_i^2 = |\sigma_i| \rho_i + 0.02 \quad \varepsilon_i^3 = \frac{0.05 |\sigma_i| \rho_i}{(0.3 - \delta_i \text{sign } \sigma_i)} + 0.02 \quad (88)$$

Outer-loop sliding mode controller design

Assuming the tracking errors in inner loops rapidly tend to zero, and $p \approx p_c$, $q \approx q_c$, $r \approx r_c$, the unknown angular rates command profiles q_c and r_c are considered as the virtual controls for the mission variables α and β .

The outer-loop sliding mode controllers design started with sliding surfaces identification. They are.

$$\sigma_4 = e_4 + 20 \int_0^t e_4 d\tau, \quad \sigma_5 = e_5 + 25 \int_0^t e_5 d\tau, \quad e_4 = \alpha_c - \alpha, \quad e_5 = \beta_c - \beta. \quad (89)$$

The outer-loop sliding mode controllers are designed in the smoothed nonsaturating format:

$$q_c = \hat{q}_{eq} + 50\sigma_4, \quad r_c = \hat{r}_{eq} - 6\sigma_5, \quad (90)$$

where

$$\begin{cases} \hat{q}_{eq} = 1.0061(\dot{\alpha}_c + 20\alpha_c - 18.7705\alpha + \beta p - 0.0427 \cos \theta \cos \varphi - 0.083589 + 0.1786\delta_e) \\ \hat{r}_{eq} = 1.0027(-\dot{\beta}_c - 25\beta_c + 2.2029\beta + \alpha p + 0.0427 \cos \theta \sin \varphi + 0.000851 + 0.03723\delta_r + 0.002466\delta_a) \end{cases}$$

Two different maneuvers are simulated. In the first maneuver the angle of attack and sideslip angle profiles are tracked. In the second maneuver the angle of attack profile and maximum-then-zero roll rate profile are tracked until the 90 degrees roll angle is achieved. The results of simulations are shown in fig.8-19.

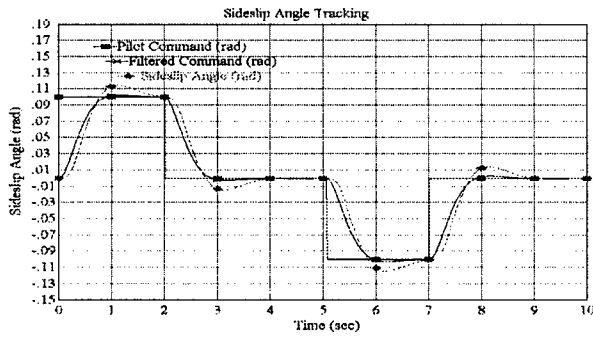


Fig. 8 Tracking of angle of attack

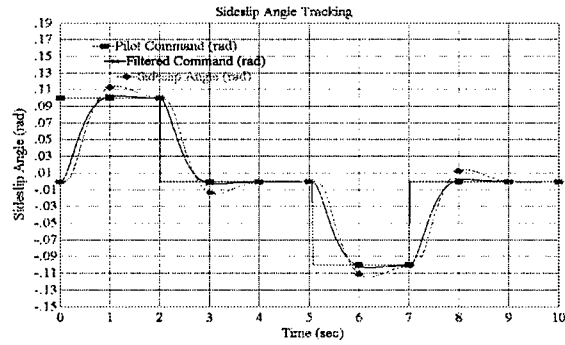


Fig. 9 Tracking of a sideslip angle

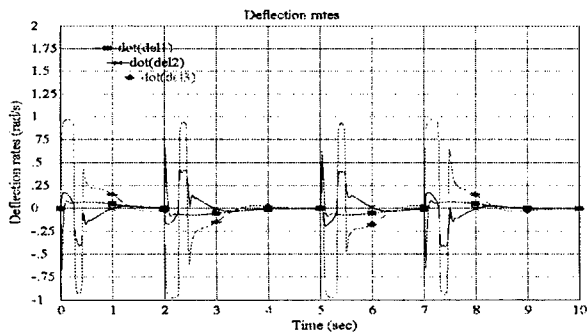


Fig. 10 Deflection rates

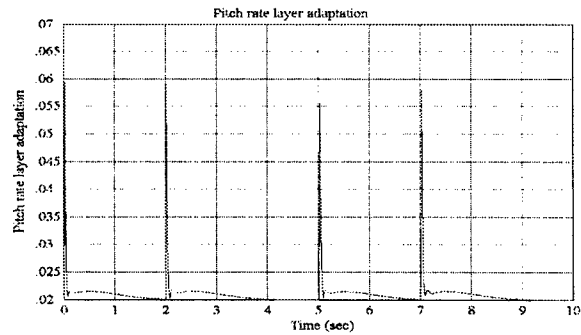


Fig. 11 First boundary layer

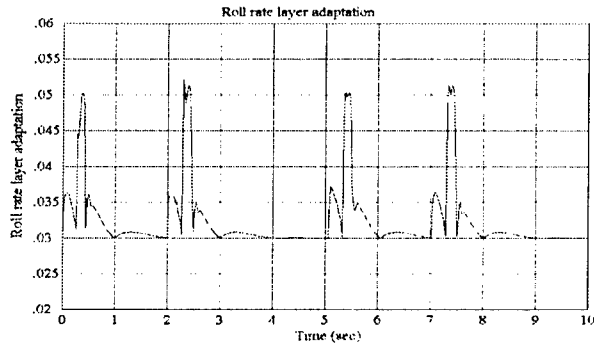


Fig. 12 Second boundary later

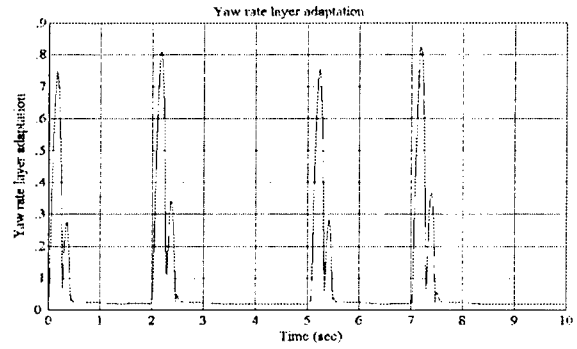


Fig. 13 Third boundary layer

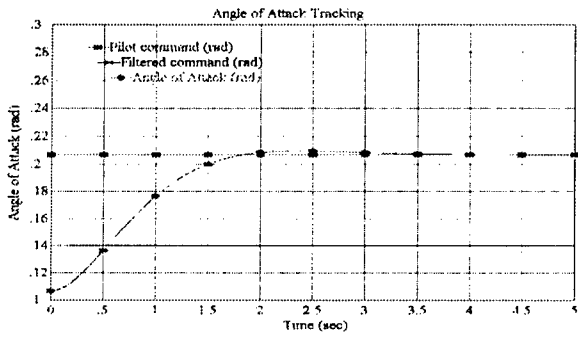


Fig. 14 Tracking of angle of attack

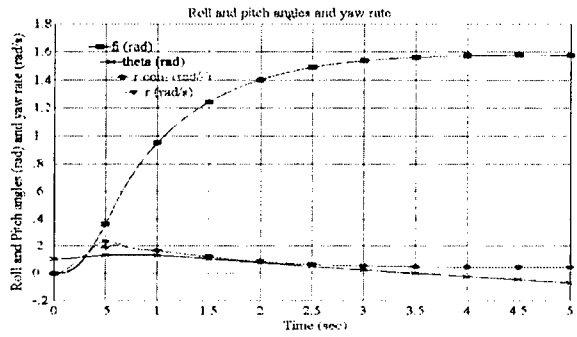


Fig. 15 Roll angle

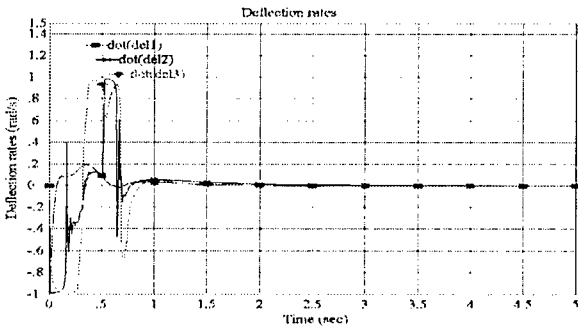


Fig. 16 Deflection rates

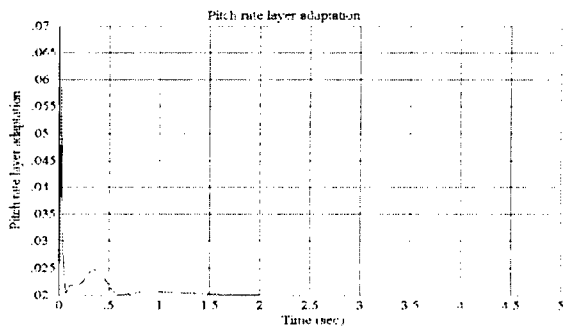


Fig. 17 First boundary layer

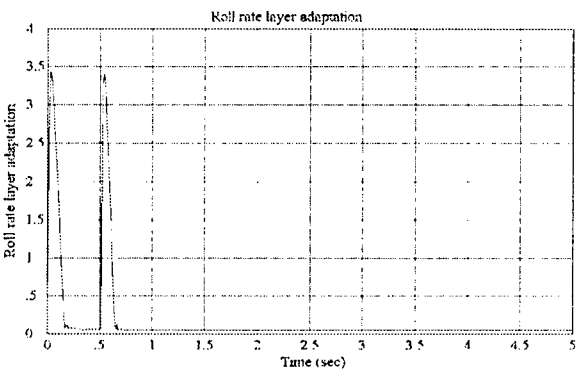


Fig. 18 Second boundary layer

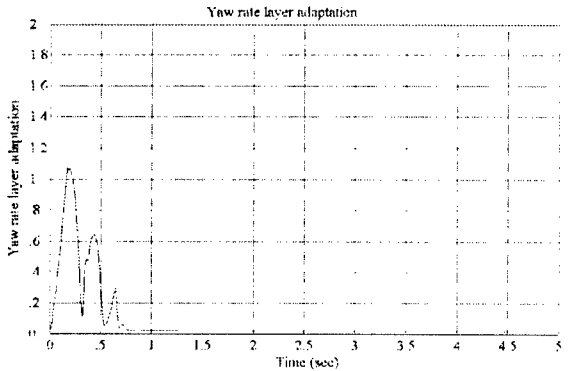


Fig. 19 Third boundary layer

Conclusion

A smoothed sliding mode controller preventing actuator deflections and deflection rates saturation is developed for tailless aircraft. The designed sliding mode controller is tailored to the control allocation algorithm developing by Dr. Jim Buffington¹. A reconfigurable on-line sliding mode control strategy without on-line system (damage) identification is developed for an aircraft with a "square" configuration. The developing sliding mode control strategy with reconfiguration guarantees a high accuracy tracking performance of the pilot's angular rates commands with given flying qualities before and after damage to an aircraft without on-line damage identification. The limitations to the actuator's deflection and deflection rate are addressed.

Future research

1. *Tailless Aircraft*

- design smoothed nonlinear virtual sliding mode controller to provide finite reaching time,
- develop priority schemes on the basis of the new insight into the control partition priority providing by the sliding mode controller,
- develop dynamic priority schemes,
- study overall stability of the system with "static" and "dynamic" priorities.

2. *Reconfigurable control of an aircraft with "square" configuration*

- develop **direct adaptation** algorithm of the boundary layers in inner- and outer loop smoothed sliding mode controllers,
- study overall stability of the two-loop flight control system with the boundary layers direct adaptation,
- design a nonlinear observer,
- incorporate noise reduction requirements into the boundary layer direct adaptation algorithm.

3. *Control allocation and reconfiguration for damaged tailless aircraft*

- develop algorithm of an optimal allocation matrix design,
- merge the boundary layer **direct adaptation** algorithm for an aircraft with "square" configuration and the algorithm of the optimal allocation matrix design into reconfigurable smoothed sliding mode controller design algorithm for a tailless aircraft.

4. *General problem*

- improving a flight control system performance incorporate some indirect adaptation control algorithms into the developing direct adaptation control algorithms.

References

- [1] Buffington, J. M., "Tailless Aircraft Control Allocation," *Proceedings of AIAA GNC*, New Orleans, 1997.
- [2] Chandler, R. P. "Self-Repairing Flight Control System Reliability and Maintainability. Program Executive Overview," *Proceedings of National Aerospace and Electronics Conference*, Dayton, 1984, pp. 586-590.

- [3] Adams, R. J., Buffington, J. M., Sparks, A. G., Banda, S. S., Robust Multivariable Flight Control, Springer-Verlag, New York 1994.
- [4] Pachter, M., Chandler, P. R., and Mears, M., "Re-configurable Tracking Control with Saturation," *Journal of Guidance, Control and Dynamics*, Vol. 18, No 5, September-October 1995, pp. 1016-1022.
- [5] Pachter, M., Chandler, P. R., and Mears, M., "Control Reconfiguration with Actuator Rate Saturation," *Proceedings of American Control Conference*, Seattle, Washington, June 1995, pp. 3495-3499.
- [6] Napolitano, M., and Swaim, R., "Redesign of the Feedback Structure Following a Battle Damage and/or A Failure on a Control Surface by Eigenstructure Assignment," *Proceedings of the Guidance , Navigation, and Control Conference*, August 1991, pp. 247-254.
- [7] Gao, Z., and Antsaklis, P. J., "Stability of the Pseudo-Inverse Method for Re-configurable Control Systems," *International Journal of Control*, Vol. 53, No. 3, 1991, pp. 717-729.
- [8] Huang, C. Y., and Stengel, R. F., "Reconfigurable Control Using Proportional-Integral Implicit Model Following," *Journal of Guidance, Control, and Dynamics*, Vol. 13, No. 2, March-April 1990, pp. 303-309.
- [9] Huang, C. Y., "Analysis and Simulation of Control Distributor Concept for a Control-Reconfigurable Aircraft," *Proceedings of GNC*, MN, August 15-17, 1988, pp. 726-735.
- [10] Ochi, Y., Kanai, K., "Design of Restructurable Flight Control Systems Using Feedback Linearization," *Journal of Guidance, Control and Dynamics*, Vol. 14, No 5, September-October 1991, pp. 903-911.
- [11] Utkin, V. I., Sliding Modes in Control Optimization, Springer-Verlag, Berlin, 1992.
- [12] DeCarlo, R. A., Zak, S. H. and Matthews, G. P., "Variable structure control of nonlinear multivariable systems: a tutorial," *IEEE Proceedings*, Vol. 76, 1988, pp. 212-232.
- [13] Fernandez, B. R., Hedrick, K. J., "Control of multivariable non-linear systems by the sliding mode method," *International Journal of Control*, Vol. 46, No 3, 1987, pp. 1019-1040.
- [14] Slotine, J., Weiping, Li., Applied non Linear Control, Prentice Hall, Englewood Cliffs, N J, 1991.
- [15] C. Tournes, and Y. Shtessel, "Aircraft Control Using Sliding Mode Control," *Proceedings of AIAA Guidance, Navigation, and Control Conference*, San Diego, CA, July 29-31, paper # AIAA 96-3692, 1996.
- [16] Shtessel, Y. B., Tournes, C., "Non Linear Flight Control Problem on Decentralized Sliding Modes," *Proceedings of The Fourth IEEE CCA*, September 27-29, 1995, Albany, NY. pp. 488-493.
- [17] Calise, A. J., and Kramer, F. S., "A Variable Structure Approach to Robust Control of VTOL Aircraft," *Journal of Guidance, Control, and Dynamics*, Vol. 7, No. 5, 1984, pp. 620-626.
- [18] Thukral, A., and Innocenty, M., "Control Design Challenge: A Variable Structure Approach," *Journal of Guidance, Control, and Dynamics*, Vol. 17, No. 5, September-October, 1994, pp. 942-949.
- [19] C. Tournes, and Y. Shtessel, "Flight Control Reconfiguration on Sliding Modes," *Proceedings of AIAA Guidance, Navigation, and Control Conference*, New Orleans, , paper # AIAA 97-3632, 1997.
- [20] "Military Standard-Flying Qualities of Piloted Vehicles," MIL-STD-1797A, January 1990.

SUBOPTIMAL CONTROL OF NONLINEAR SYSTEMS VIA RECEDING HORIZON
STATE DEPENDENT RICCATI EQUATIONS

Mario Sznaier
Associate Professor
Department of Electrical Engineering

The Pennsylvania State University
University Park, PA 16802

Final Report for:
Summer Faculty Research Program
Wright Laboratory

Sponsored by:
Air Force Office of Scientific Research
Bolling Air Force Base, DC

And

Wright Laboratory

August, 1997

Suboptimal Control of Nonlinear Systems via Receding Horizon State Dependent Riccati Equations

Mario Sznaier
Associate Professor
Department of Electrical Engineering
The Pennsylvania State University
University Park, PA 16802,
email: msznaier@frodo.ee.psu.edu

Abstract

The problem of rendering the origin an asymptotically stable equilibrium point of a nonlinear system while, at the same time, optimizing some measure of performance has been the object of much attention in the past few years. In contrast to the case of linear systems where several optimal synthesis techniques (such as \mathcal{H}_∞ , \mathcal{H}_2 and l^1) are well established, their nonlinear counterparts are just starting to emerge. Moreover, in most cases these tools lead to partial differential equations that are difficult to solve. In this research we developed a suboptimal regulator for nonlinear affine systems based upon the combination of receding horizon and state dependent Riccati equation techniques. Our main result shows that this controller is nearly optimal provided that a certain finite horizon problem can be solved on-line. Additional results include conditions guaranteeing closed loop stability even in cases where this fails, and an analysis of the suboptimality level of the proposed method.

Contents

1	Introduction	62-4
2	Preliminaries	62-5
2.1	Notation and Definitions	62-5
2.2	The Nonlinear Regulator Problem	62-6
2.3	The SDRE approach to nonlinear regulation	62-6
3	An Equivalent Finite Horizon Regulation Problem	62-7
4	A Modified Receding Horizon Controller	62-10
5	Illustrative Examples	62-13
6	Conclusions	62-15

1 Introduction

A large number of control problems involve designing a controller capable of rendering some point an asymptotically stable equilibrium point of a given time invariant system while simultaneously optimizing some performance index. This problem is relevant for disturbance rejection, tracking and robustness to model uncertainty [19]. In the case of linear dynamics this problem has been thoroughly explored during the past decade, leading to powerful formalism such as μ -synthesis and l^1 optimal control theory that have been successfully employed to solve some hard practical problems. More recently, these techniques have been extended to handle multiple, perhaps conflicting, performance specifications (see for example [18, 6, ?] and references therein).

In the case of nonlinear dynamics, popular design techniques include feedback linearization (FL) [11], the use of control Lyapunov functions (CLF) [10, 15], recursive backstepping [11], and recursive interlacing [13]. While these methods provide powerful tools for designing globally (or semi-globally) stabilizing controllers, performance of the resulting closed loop systems can vary widely. To illustrate this point consider the following system [10]

$$\begin{aligned} \dot{x}_1 &= x_2 \\ \dot{x}_2 &= -e^{x_2} \left(x_1 + \frac{1}{2}x_2 \right) + \frac{1}{2}x_2 e^{4x_1+3x_2} + e^{2x_1+2x_2}u \end{aligned} \quad (1)$$

with initial condition $[-2 \ 0]'$. It can be shown that the optimal control law that minimizes the performance index

$$J = \int_0^{\infty} (x_2^2 + u^2) dt$$

is given by $u^* = -x_2 e^{2x_1+x_2}$, with the corresponding value of $J^* = 4$. On the other hand, FL and CLF designs yield the values $J_{FL} = 238$ and $J_{CLF} = 390$ (see [10] for details). Indeed, a recent workshop on nonlinear control [8] has shown that while the methods mentioned above can recover the optimal under certain conditions, in general there are no guarantees on the performance of the resulting system.

As an alternative, during the past few years nonlinear counterparts of \mathcal{H}_{∞} and l^1 have started to emerge. While these theories are appealing since they guarantee optimal performance (at least in a given sense), from a practical standpoint they suffer from the fact that they lead to Hamilton-Jacobi-Isaacs type partial-differential equations that are hard to solve, except in some restrictive, low-dimensional cases.

Finally, there are two methods that which do not guarantee in general global stability, but work well in practice. The first is the State Dependent Riccati Equation methods (SDRE) developed by Cloutier and coworkers ([3]), based upon recasting the nonlinear plant into a linear-like, state dependent form and solving at each point a Riccati equation. While at the present time only local stability of the resulting system has been formally established, consistent experience indicates that the method works well, often outperforming other techniques ([8]). For instance, it gives the optimal solution in the simple example (1), even though in this case the level sets of the optimal return function are not compact [10]. The second method, receding horizon (RH) control, is based upon the on-line solution of a finite-horizon optimal control problem at each sampling instant k . The first element of the resulting (open-loop) control sequence is implemented over the interval $[k, k+1]$. At time $k+1$ the process is repeated with the new initial condition x_{k+1} . RH methods

are appealing since they allow for explicitly handling constraints and guarantee optimality in some sense. Moreover, since the optimization is carried only along the present trajectory of the system (i.e. “locally”) the resulting computational complexity is far less than that associated with finding the true global optimal control (a task that entails solving a Hamilton–Jacobi type equation). However, stability of the resulting closed-loop systems has been established only for the case of linear plants ([17, 14], although a modified RH formulation has been recently proposed, achieving stability at the expense of optimality [8].

In this research we developed an alternative controller for suboptimal regulation of non-linear affine systems. This controller is based upon the combination of receding horizon and SDRE ideas, and follows in the spirit of a similar controller successfully used in the case of constrained linear systems [16, 17]. The main result of the research shows that this controller is nearly optimal and globally stabilizes the plant, provided that enough computational power is available to solve on-line a *finite horizon* optimization problem. In cases where this condition fails, we show how to modify the proposed controller to guarantee stability (possibly at the expense of optimality) and we establish a connection with the well known CLF methodology. Additional results include an analysis of the suboptimality of the proposed method and show that if an approximate solution to the problem is known in a set containing the origin, then our controller yields an extension of this solution with the same suboptimality level.

This report is organized as follows: In section 2 we introduce the notation to be used and some preliminary results. In section 3 we show that the infinite horizon regulation problem is approximately equivalent to a finite horizon problem and we analyze the properties of this approximation. In section 4 we describe the new controller and we analyze the properties of the resulting closed loop. Section 5 illustrates the synthesis method with two simple examples. Finally, in section 6 we summarize our results and we indicate directions for future research.

2 Preliminaries

2.1 Notation and Definitions

Consider the control-affine nonlinear system:

$$\dot{x} = f(x) + g(x)u \quad (2)$$

where $x \in R^n$, $u \in R^m$, the vector fields $f(\cdot)$ and $g(\cdot)$ are known C^1 functions, and where $f(0) = 0$. Given a function $V: R^n \rightarrow R$ its Lie derivative along f is defined as

$$L_f V(x) = \frac{\partial V}{\partial x} f(x)$$

Definition 1 A positive definite C^1 function $V: R^n \rightarrow R_+$ is a Control Lyapunov function for the system (2) if

$$\inf_u [L_f V(x) + L_g V(x)u] < 0, \quad \forall x \neq 0 \quad (3)$$

It is well known ([15, 1]) that existence of a control Lyapunov function is equivalent to the existence of a smooth globally stabilizing feedback control law $u(x)$.

The nonlinear system (2) can be represented (in a non-unique way) by the following linear-like structure: [3]

$$\dot{x} = A(x)x + B(x)u \quad (4)$$

Definition 2 *The state dependent coefficient (SDC) representation (4) is a stabilizable parametrization of the nonlinear system (2) in a region Ω if the pair $(A(x), B(x))$ is pointwise stabilizable for all $x \in \Omega$.*

2.2 The Nonlinear Regulator Problem

Consider the nonlinear system (2). Our goal is to find a feedback control law $u(x)$ that minimizes the following performance index

$$J(x_o, u) = \int_0^\infty [x'Q(x)x + u'R(x)u] dt, \quad x(0) = x_o \quad (5)$$

where $Q(\cdot)$ and $R(\cdot)$ are C^1 , positive definite matrices.¹ It is well known [2] that this problem is equivalent to solving the following Hamilton–Jacobi–Bellman partial differential equation:

$$0 = \frac{\partial V}{\partial x} f - \frac{1}{4} \frac{\partial V}{\partial x} g R^{-1} g' \frac{\partial V'}{\partial x} + x'Q(x)x, \quad V(0) = 0 \quad (6)$$

If this equation admits a C^1 nonnegative solution V , then the optimal control is given by $u = -\frac{1}{2}R^{-1}g'\frac{\partial V'}{\partial x}$ and $V(x)$ is the corresponding optimal cost (or storage function), i.e.

$$V(x) = \min_u \int_0^\infty (x'Qx + u'Ru) dt$$

2.3 The SDRE approach to nonlinear regulation

Unfortunately, the complexity of equation (6) prevents its solution except in some very simple, low dimensional cases. This has prompted the search for alternative, suboptimal solutions to the problem. In this section we briefly cover the details of the SDRE approach developed by Cloutier and coworkers [3]. The main idea of the method is to use the linear-like parametrization (4) to obtain a control law by solving pointwise along the trajectory a steady-state Riccati equation. Specifically, the nonlinear system (2) is recast into the SDC form (4) and the following state-dependent Riccati equation is solved

$$A'(x)P(x) + P(x)A(x) - P(x)B(x)R^{-1}(x)B'(x)P(x) + Q(x) = 0 \quad (7)$$

The suboptimal control law is given by $u_{sdre} = -R^{-1}(x)B'P(x)x$ where $P(x)$ is the positive definite (pointwise stabilizing) solution of (7). In the sequel we briefly review the properties of this control law. The corresponding proofs can be found in [3]

¹This condition can be relaxed to $Q(x) \geq 0$

Lemma 1 Assume that the parametrization (4) is stabilizable, $Q(x) > 0$ for all x , and all the matrix functions involved are smooth. Then the control law u_{sdre} is locally optimal and renders the origin a locally asymptotically stable equilibrium point of the closed-loop system.

Lemma 2 If the parametrization (4) is stabilizable and all the matrices involved along with their gradients are bounded along trajectories, then the SDRE control law satisfies the (first order) necessary conditions for optimality asymptotically as $\mathcal{O}(\|x\|^2)$.

Lemma 3 If $\frac{\partial}{\partial x} [P(x)x]$ is symmetric and $\int_0^y y' P(y) dy > 0$ then u_{sdre} is the globally optimal control law.

Corollary 1 If the conditions in Lemma 3 hold then the control law u_{sdre} globally stabilizes system (2).

3 An Equivalent Finite Horizon Regulation Problem

In this section we introduce a finite horizon approximation of the nonlinear regulation problem stated in section 2.2 and we analyze its properties. This approximation forms the basis of the proposed method.

Lemma 4 Consider an compact set S containing the origin in its interior and assume that the optimal storage function $V(x)$ is known for all $x \in S$. Let $c = \min_{x \in \partial S} V(x)$ where ∂S denotes the boundary of S . Finally, define the set $S_v = \{x: V(x) < c\}$. Consider the following two optimization problems:

$$\min_u \left\{ J(x, u) = \int_0^\infty [x' Q(x)x + u' R u] dt \right\} \quad (8)$$

$$\min_u \left\{ J_T(x, u) = \int_0^T (x' Q(x)x + u' R u) dt + V[x(T)] \right\} \quad (9)$$

subject to (2). Then the following facts hold:

1. An optimal solution of problem (9) is also optimal for (8) in the interval $[0, T]$ provided that $x(T) \in S_v$.
2. Consider now $T_1 > T$. If $x(T) \in S_v$ then a controller that optimizes J_T is also optimal with respect to J_{T_1} in $[0, T]$.

Proof: Consider first the following free terminal time problem:

$$\begin{aligned} J^o(x, t) &= \min_u \left\{ V[x(t_f)] + \int_t^{t_f} [x' Q x + u' R u] dt \right\} \\ &\text{subject to:} \\ x(t_f) &\in S_v \end{aligned} \quad (10)$$

Let x°, u° denote the optimal trajectory. The optimal return function satisfies [2]:

$$0 = \frac{\partial J}{\partial t} + \frac{\partial J}{\partial x} f - \frac{1}{4} \frac{\partial J}{\partial x} g R^{-1} g' \frac{\partial J}{\partial x} + x' Q(x) x, \quad (11)$$

with boundary condition $J(x, t) = V(x)$ for $x \in S_v$. Clearly this equation admits as solution $J(x, t) \equiv V(x)$. Thus problems (8) and (10) are equivalent. To establish the first claim we will show that an optimal solution u° of (9) is also optimal for (10) (and thus (8)), provided that $x^\circ(T) \in S_v$. To this effect note that the Euler-Lagrange optimality conditions for problems (9) and (10) are identical, except for the additional transversality condition $H[u^\circ, x^\circ(t_f), \lambda^\circ(t_f)] = 0$ that appears in the latter, where $\lambda(t)$ denotes the co-states. The boundary condition for λ in problem (9) is given by

$$\lambda^\circ(T) = \frac{\partial V}{\partial x} |_{x(T)} \quad (12)$$

Since $x(T) \in S_v$ it follows that $x^\circ(T), u^\circ(T), \lambda^\circ(T)$ satisfy the HJB equation (6), or equivalently $H[u^\circ, x^\circ(T), \lambda^\circ(T)] = 0$. Thus, an optimal solution of (9) is also optimal for (10).

To establish the second claim note that the set S_v is positively invariant with respect to the optimal control law. Consider now the following control law:

$$u^* = \begin{cases} u^\circ(t) & \text{for } t \in [0, T] \\ -R^{-1} g' \frac{\partial V}{\partial x} & t > T \end{cases} \quad (13)$$

Since $V(x)$ is the optimal return function in S_v and this set is invariant, it follows that $V[x(T_1)] = V[x(T)] + \int_T^{T_1} (x'^* Q x^* + u'^* R u^*) dt$. Thus $J_{T_1}(x, u^*) = J_T$. From the equivalence of (9) and the free terminal time problem (10) it follows that $J_{T_1} \geq J_T$. Hence $\min_u J_{T_1} = J_T$ and u^* is the corresponding optimal control law.

□

This Lemma shows that if a solution to the HJB equation (6) is known in a neighborhood of the origin, then it can be extended via an explicit finite horizon optimization, well suited for an on-line implementation. This suggests a receding horizon type control combining an on-line optimization with an off-line phase to find a local solution to (6). However, finding (and storing) this local solution can be very computationally demanding in cases where the dimension of the problem is not low. Thus it is of interest to consider the case where an approximation $\Psi(x)$ rather than the true storage function is used in (9). The next result shows that in this case the approximation error *does not grow* (to the first order). In other words, the difference between the true optimal $V[x(0)]$ and $J_T[x(0)]$ is approximately equal to the difference between $V[x(T)]$ and $\Psi[x(T)]$.

Theorem 1 *Let $\Psi: R^n \rightarrow R_+$ be a positive definite function and consider the following optimization problem:*

$$J_\Psi(x, t) = \min_u \int_t^T (x' Q x + u' R u) dt + \Psi[x(T)] \quad (14)$$

subject to (2). Then $J_\Psi(x, t) - V[x(t)] \cong \Psi[x(T)] - V[x(T)]$.

Proof: Define $e(x, t) \doteq J_\Psi(x, t) - V(x)$. By considering the Hamilton Jacobi equations for J_Ψ and V it can be easily shown that $e(t, x)$ satisfies the following equation:

$$0 = \frac{\partial e}{\partial t} + \frac{\partial e}{\partial x} \left(f - \frac{1}{2} g R^{-1} g' \frac{\partial J_\Psi}{\partial x} \right) + \frac{1}{4} \frac{\partial e}{\partial x} g R^{-1} g' \frac{\partial e}{\partial x} \quad (15)$$

By exploiting the fact that the optimal control law for (14) is given by

$$u_\psi = -\frac{1}{2} R^{-1} g' \frac{\partial J_\Psi}{\partial x} \quad (16)$$

equation (15) can be rewritten as:

$$\begin{aligned} 0 &= \frac{\partial e}{\partial t} + \frac{\partial e}{\partial x} (f - g u_\psi) + \frac{1}{4} \frac{\partial e}{\partial x} g R^{-1} g' \frac{\partial e}{\partial x} \\ &= \frac{\partial e}{\partial t} + \frac{\partial e}{\partial x} \dot{x} + \frac{1}{4} \frac{\partial e}{\partial x} g R^{-1} g' \frac{\partial e}{\partial x} \\ &= \dot{e} + \frac{1}{4} \frac{\partial e}{\partial x} g R^{-1} g' \frac{\partial e}{\partial x} \end{aligned} \quad (17)$$

Thus, along the trajectories $\dot{e} = 0$ (to the first order) and hence $J(x, t) - V(x)$ is approximately constant.

□

From Lemma 4 it follows that, given an initial condition $x(0)$, problem (8) can be solved by solving a sequence of problems of the form (9) with increasing T until a solution such that $x(T) \in S_v$. Moreover, once such a solution is obtained, no further improvement of the cost can be achieved by increasing the horizon T . These results suggest the following receding-horizon type control law. Let $x(t)$ denote the current state of system (2). Then:

1. If $x(t) \in S_v$, $u = -\frac{1}{2} R^{-1} g' \frac{\partial V}{\partial x}$
2. If $x(t) \notin S_v$ then solve a sequence of optimization problems of the form (9) until a solution such that $x(T) \in S_v$ is found. Use the corresponding control law $u(t)$ in the interval $[t, t + dt]$.

From the results above it is clear that the resulting control law is globally optimal and thus globally stabilizing. However, as we indicated before, the computational complexity associated with finding $V(x)$ (even only in the region S_v) may preclude the use of this control law in many practical cases. Thus, it is of interest to consider a modified control law where an approximation $\Psi(x)$ (rather than $V(x)$) is used. To this effect consider a compact set S containing the origin in its interior and let $\Psi: S \rightarrow R_+$, $\Psi \in C^1$ be a Control Lyapunov Function for system (2). Denote by u_ψ the corresponding control law. Finally, let $c = \min_{x \in \partial S} \Psi(x)$ and define the set $S_\Psi \subseteq S = \{x: \Psi(x) \leq c\}$. Then we propose the following modified control law:

1. If $x \in S_\psi$, $u_\psi(x) \doteq \underset{u}{\operatorname{argmin}} \{L_f \Psi + L_g \Psi u\}$

2. If $x \notin S_\Psi$ then consider an increasing sequence T_i . Let

$$u_T^* = \operatorname{argmin} \left\{ \int_0^T (x' Q x u' R u) dt + \Psi[x(T)] \right\}$$

Denote by $x^*(.)$ the corresponding optimal trajectory and define: $T(x) = \inf \{T : x^*(T) \in S_\Psi\}$. Then $u_\psi(x) \doteq u_{T(x)}^*(t)$, $t \in [t, t + dt]$.

Note that from Theorem 1 it follows that the suboptimality associated with the modified algorithm is approximately given by $e_\Psi = \sup_{x \in S_\Psi} |\Psi(x) - V(x)|$. In the sequel we show that the control law u_ψ also globally stabilizes system (2).

Theorem 2 *The control law u_ψ globally stabilizes (2)*

Proof: Consider first an initial condition $x(0) = x_o \notin S_\Psi$. Let $J(x_o) = \int_0^{T(x_o)} (x^{*'} Q x^* + u^{*'} R u^*) dt + \Psi\{x^*[T(x_o)]\}$. Clearly $J(x_o) > 0$ outside S_Ψ and thus it is a candidate Lyapunov function there. Next we show that $\dot{J} < 0$ along the trajectories. Consider the trajectory starting at x_o . Let $x_1 \doteq x^*(dt)$ (with dt small enough so that $x^*(dt) \notin S_\Psi$). Since $x^*(t)$, $t \in [dt, T]$ is also a feasible trajectory starting from x_1 we have that:

$$\begin{aligned} J(x_1) &= \inf_u \left\{ \int_{dt}^{T(x_1)} (x' Q x + u' R u) dt + \Psi\{x[T(x_1)]\} \right\} \\ &\leq \int_{dt}^{T(x_o)} (x^{*'} Q x^* + u^{*'} R u^*) dt + \Psi\{x^*[T(x_o)]\} \\ &= J(x_o) - [x_o' Q x_o + u(x_o)' R u(x_o)] dt \leq J(x_o) - x_o' Q x_o dt \end{aligned} \quad (18)$$

Thus

$$\dot{J} = \lim_{dt \rightarrow 0} \frac{J(x(t+dt)) - J(x(t))}{dt} \leq -x(t)' Q x(t) < 0$$

Hence trajectories starting outside S_Ψ reach this set in a finite time. Asymptotic stability now follows from the facts that S_Ψ is invariant with respect to u_ψ (i.e. trajectories starting in the set never leave it) and that $\Psi(x)$ is a CLF there.

□

4 A Modified Receding Horizon Controller

In the last section we outlined a receding horizon type law, that under certain conditions, is nearly optimal and globally stabilizes system (2). While most of these conditions are rather mild (essentially equivalent to the existence of a CLF), the requirement that T should be large enough so that $x(T) \in S_\Psi$ could pose a problem, specially in cases where the system has fast dynamics. In this section we propose a modified control law that is guaranteed to stabilize the system, even when this condition fails, and that takes into account computational time constraints.

Consider the following receding horizon control law:

Algorithm 1

0.- Data: a CLF $\Psi(x)$, an invariant region S_Ψ such that $0 \in \text{int}\{S_\Psi\}$, a horizon T .

1.- If $x(t) \in S_\Psi$, $u_\Psi(x) = \underset{u}{\operatorname{argmin}} \{L_f \Psi + L_g \Psi u\}$

2.- If $x(t) \notin S_\Psi$ then

$$u_\Psi = \underset{u}{\operatorname{argmin}} \left\{ \int_t^{T+t} (x'Qx + u'Ru) dt + \Psi[x(T+t)] \right\} \quad (19)$$

subject to:

$$\begin{aligned} -\sigma[x(t+T)] &> x(t+T)'Qx(t+T) + L_f \Psi \Big|_{x(t+T)} \\ &+ \min_u \left\{ u'(t+T)Ru(t+T) + L_g \Psi \Big|_{x(t+T)} u \right\} \\ &- x(t)'Qx(t) - u'(t)Ru(t) \end{aligned} \quad (20)$$

where $\sigma(x)$ is some positive definite function such that $\sigma(x) \leq x'Qx$.

Theorem 3 The control law u_Ψ generated by Algorithm 1 has the following properties:

1. It renders the origin a globally stable equilibrium point of (2)
2. Coincides with the globally optimal control law when $\Psi(x) = V(x)$.
3. Is nearly optimal (in the sense of Theorem 1) when $x(T) \in S_\Psi$.

Proof: To prove stability, proceeding as in Theorem 2, consider first an initial condition $x_0 \notin S_\Psi$. Denote by u^*, x^* the optimal control and associated trajectory respectively. Then

$$\begin{aligned} J[x(t+dt)] &= \min_u \left\{ \int_{t+dt}^{T+t+dt} (x'Qx + u'Ru) dt + \Psi[x(T+t+dt)] \right\} \\ &\leq \int_{t+dt}^{T+t} (x^{*'}Qx^* + u^{*'}Ru^*) dt + \Psi[x^*(T)] \\ &+ \min_u \left\{ x'(T+t)Qx(T+t) + u'(T+t)Ru(t+T) + \dot{\Psi}[x(T+t)] \right\} \\ &= J[x(t)] - x(t)'Qx(t) - u^{*'}(t)Ru^*(t) \\ &+ \min_u \left\{ x'(T+t)Qx(T+t) + u'(T+t)Ru(t+T) + \dot{\Psi}[x(T+t)] \right\} \end{aligned} \quad (21)$$

Therefore, if (20) holds then we have that

$$\dot{J} = \lim_{dt \rightarrow 0} \frac{J[x(t+dt)] - J[x(t)]}{dt} \leq -\sigma(x) < 0 \quad (22)$$

Hence the trajectories starting outside S_Ψ reach this set in a finite time. As in the proof of Theorem 2, once there, asymptotic stability is guaranteed by the control Lyapunov function Ψ .

To prove item 2.- note that when $\Psi(x) = V(x)$ then from the Hamilton Jacobi equation (6) we have that

$$x(t+T)'Qx(t+T) + L_f\Psi\big|_{x(t+T)} + \min_u \left\{ u'(t+T)Ru(t+T) + L_g\Psi\big|_{x(t+T)}u \right\} \leq 0 \quad (23)$$

Thus in this case the constraints (20) are redundant. The proof follows now immediately from Lemma 4. Finally, the proof of item 3.- follows from Theorem 1.

Corollary 2 *Let $\Psi(x) = x'P(x)x$, where P denotes the solution to the SDRE introduced in section 2.3. Then There exists T_o such that for all $T > T_o$ the constraints (20) are feasible.*

Remark 1 *From Corollary 2 it follows that $\Psi(x) = x'P(x)x$ is a suitable choice for the terminal penalty. Moreover from the properties of the SDRE method (see section 2.3) it follows that with this choice, the control law satisfies all the necessary conditions for optimality as $\mathcal{O}[\|x(t+T)\|^2]$*

Finally, before closing this section we consider a modified control law that takes into account the sample and hold nature of receding horizon implementations.

Algorithm 2

0.- *Data: a CLF $\Psi(x)$, an invariant region S_Ψ such that $0 \in \text{int}\{S_\Psi\}$, a horizon T , a sampling interval T_s .*

1.- *If $x(t) \in S_\Psi$, $u_s(x) = \underset{u}{\operatorname{argmin}} \{L_f\Psi + L_g\Psi u\}$*

2.- *If $x(t) \notin S_\Psi$ then*

$$u_s = \underset{u}{\operatorname{argmin}} \left\{ \int_t^{T+t} (x'Qx + u'Ru) dt + \Psi[x(T+t)] \right\} \quad (24)$$

subject to:

$$\begin{aligned} -\sigma[x(\tau+T)] &> x(\tau+T)'Qx(\tau+T) + L_f\Psi\big|_{x(\tau+T)} \\ &+ \min_u \left\{ u'(\tau+T)Ru(\tau+T) + L_g\Psi\big|_{x(\tau+T)}u \right\} \\ &- x(t)'Qx(t) - u'(t)Ru(t), \quad t \leq \tau t + T_s \end{aligned} \quad (25)$$

Lemma 5 *The control law u_s renders the origin a globally stable equilibrium point of (2). Moreover, it is nearly optimal and coincides with the globally optimal control law when $\Psi(x) = V(x)$.*

Proof: The proof, omitted for space reasons follows along the same lines of the proof of Theorem 3.

5 Illustrative Examples

From the results of the previous section, we will expect that the Algorithm 2 using $\Psi(x) = x'P(x)x$ will generate a nearly optimal control law, even when T is relatively small. In this section we show that this is indeed the case with two examples.

Example 1 Consider the following regulation problem:

$$\min_u \left\{ J = \int_0^\infty x_2^2 + u^2 dt \right\} \quad (26)$$

subject to

$$\begin{aligned} \dot{x}_1 &= x_2 \\ \dot{x}_2 &= -x_1 e^{x_1} + \frac{1}{2}x_2^2 + e^{x_1}u \end{aligned} \quad (27)$$

It can be shown that the optimal control law is given by:

$$u_{opt} = -x_2 \quad (28)$$

with the corresponding optimal storage function:

$$V(x) = x_1^2 + x_2^2 e^{-x_1} \quad (29)$$

Consider now the following SDC parametrization:

$$A = \begin{bmatrix} 0 & 1 \\ -e^{x_1} & \frac{1}{2}x_2 \end{bmatrix}; \quad B = \begin{bmatrix} 0 \\ e^{x_1} \end{bmatrix} \quad (30)$$

It can be shown that the solution to the corresponding SDRE is given by:

$$P(x) = \begin{bmatrix} e^{x_1} & 0 \\ 0 & 1 \end{bmatrix} p \quad (31)$$

where

$$p = 0.5 * \left(x_2 + \sqrt{x_2^2 + 4e^{2x_1}} \right) e^{-2x_1} \quad (32)$$

with associated control action:

$$u_{sdre} = -x_2 \left[\left(\frac{x_2}{2e^{x_1}} \right) + \sqrt{1 + \left(\frac{x_2}{2e^{x_1}} \right)^2} \right] \quad (33)$$

Thus $u_{sdre} \cong u_{opt}$ only when $\left(\frac{x_2}{2e^{x_1}} \right) \ll 1$. On the other hand, if $e^{x_1} \rightarrow 0$ then $\frac{u_{sdre}}{u_{opt}} \rightarrow \infty$. Finally, it can also be shown that

$$x'P(x)x = pe^{x_1}V(x) \quad (34)$$

Thus $x'P(x)x$ gives a good estimate of $V(x)$ only when $\left(\frac{x_2}{2e^{x_1}} \right) \ll 1$. Figures 1 and 2 show the trajectories and optimal cost corresponding to the initial condition $x(0) = [-2 \ 2]$. In this case $J_{optimal} = 33.55$ and $J_{sdre} = 154.73$. Note that here $\frac{x_2}{2e^{x_1}} = e^2 \cong 7.4$ so the difference between u_{sdre} and $u_{optimal}$ is not surprising.

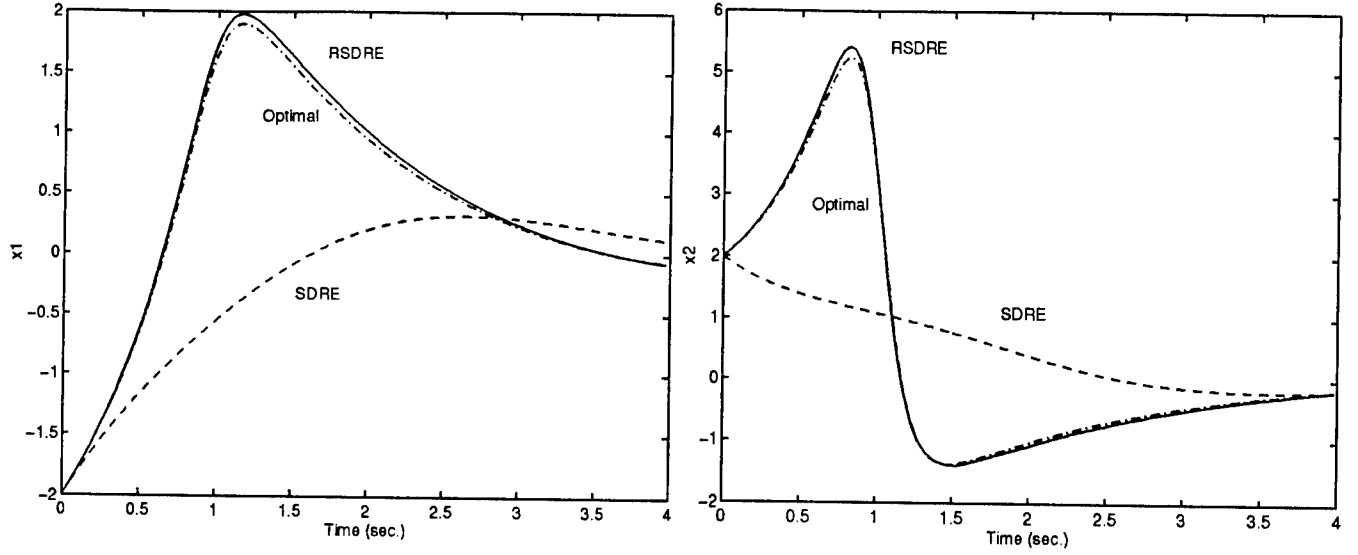


Figure 1: State trajectories for example 1

Example 2 The second example consists of a planar ducted fan (a simplified model of a thrust vectored aircraft). The dynamics are given by (see [13, 8] for details)

$$\begin{bmatrix} \ddot{x} \\ \ddot{y} \\ \ddot{\theta} \end{bmatrix} = \begin{bmatrix} -g \sin \theta \\ g (\cos \theta - 1) \\ 0 \end{bmatrix} + \begin{bmatrix} \frac{\cos \theta}{m} & -\frac{\sin \theta}{m} \\ \frac{\sin \theta}{m} & \frac{\cos \theta}{m} \\ \frac{r}{J} & 0 \end{bmatrix} \begin{bmatrix} u_1 \\ u_2 \end{bmatrix} \quad (35)$$

where x, y and θ denote horizontal, vertical and angular position respectively and where u_1 and u_2 are the control inputs. The numerical values of the parameters are $m = 4 \text{ Kg}$, $J = 0.0475 \text{ Kg m}^2$ and $r = 0.26 \text{ m}$. The goal is to minimize a performance index of the form (5) with:

$$Q = \text{diag}[5 \quad 5 \quad 1 \quad 1 \quad 1 \quad 5], \quad R = I_{2 \times 2}$$

corresponding to the following choice of state variables: $\xi = [x \quad y \quad \theta \quad \dot{x} \quad \dot{y} \quad \dot{\theta}]$.

method	V
LQR [8]	1.1×10^5
CLF [8]	2.53×10^4
LPV [8]	1833
SDRE	1646
RSDRE	1140

Table 1: Comparison of different methods

Table 1 shows the result corresponding to the initial condition $\xi(0) = [0 \quad 0 \quad 0 \quad 12.5 \quad 0 \quad 0]$. Note that in this case the SDRE solution yields the second lowest cost.

Figure 3 shows a comparison of the trajectories generated by the SDRE and RSDRE method, with $T = 1 \text{ sec}$ and $T_s = 0.5 \text{ sec}$. In this case the RSDRE method produced a cost virtually equal to the global optimal (found off-line by numerical optimization). This can be explained by looking

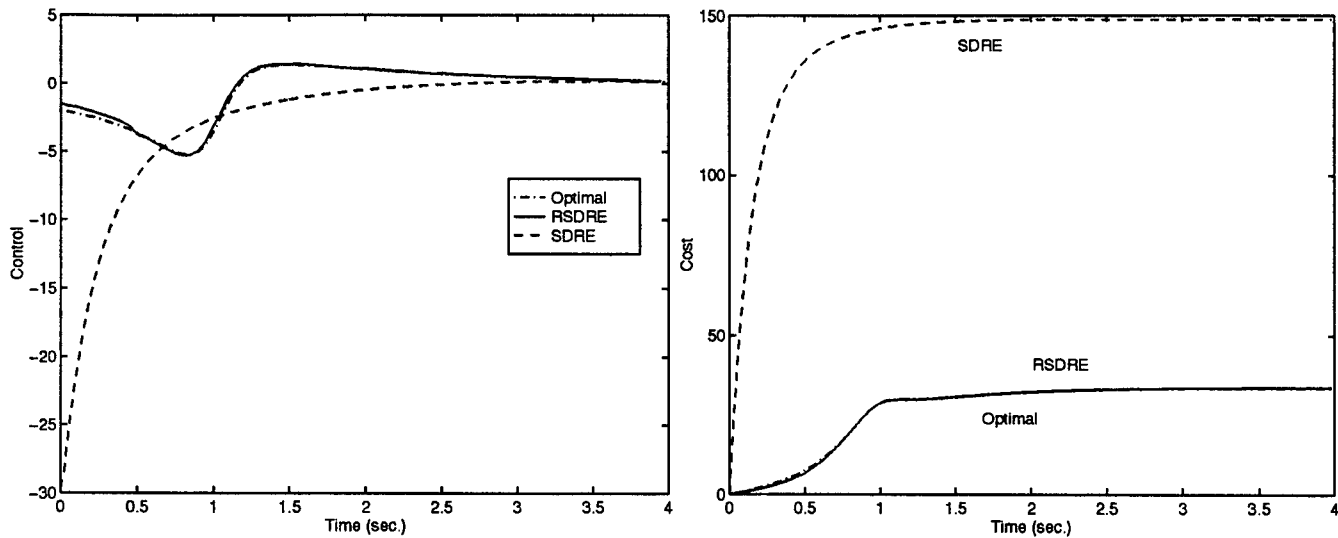


Figure 2: Control effort and cost for example 1

at the plots in Figure 4. These plots show that while $\Psi(x) = x'P(x)x$ gives initially a very poor estimate of the cost-to-go, the combination of $\Phi(x)$ and the explicit integral in (24) give a very good estimate if T is chosen ≥ 1 sec. It is worth mentioning that a conventional receding horizon controller (i.e. one obtained by setting $\Psi \equiv 0$ in (24)) with the same choice of horizon and sampling time fails to stabilize the system.

6 Conclusions

In contrast with the case of linear plants, tools for simultaneously addressing performance and stability of nonlinear systems have emerged relatively recently. Recent counterexamples [7, 8] illustrated the fact that while several commonly used techniques can successfully stabilize nonlinear systems, the resulting closed-loop performance varies widely. Moreover, these performance differences are problem dependent, with performance of a given method ranging from (near) optimal to very poor.

In this research effort we have developed a new suboptimal regulator for affine nonlinear systems, based upon the combination of receding horizon and state dependent Riccati equation techniques. Under certain relatively mild conditions this regulator renders the origin a globally asymptotically stable equilibrium point. In the limit as the horizon $T \rightarrow 0$, the proposed control law reduces to the inverse optimal controller proposed by Freeman and Kokotovic [9]. Thus, these conditions are essentially equivalent to the existence of a Control Lyapunov Function. Additionally our research has shown that the regulator is near optimal, provided that a good approximation to the optimal storage function is known in a neighborhood of the origin. These results were illustrated in this report with two examples. In both cases our controller outperformed several other commonly used techniques. Finally, note in passing that the finite approximation (14) is also valuable as a tool to speed-up off line numerical computation of near optimal solutions, for instance when combined with conjugate gradient type algorithms [4].

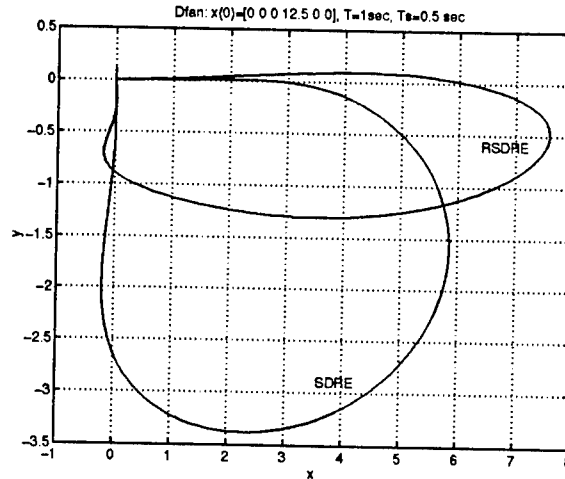


Figure 3: SDRE and RSDRE trajectories for the Dfan example

An issue that was beyond the scope of this research is that of the computational complexity associated with solving the nonlinear optimization problem (24). Following [8] this complexity could be reduced by exploiting differential flatness to perform the optimization in flat space. Additional research being pursued includes the explicit incorporation of state and control constraints into the formalism and its extension to handle model uncertainty.

Manuscripts resulting from this research:

1. M. Sznaier, J. Cloutier, R. Hull, D. Jacques and C. Mracek, "A Receding Horizon State Dependent Riccati Equation Approach to Suboptimal Regulation of Nonlinear Systems," submitted for publication, 1997.

Acknowledgements

The author is indebted to Major David R. Jacques, Lt. Col. Curtis Mracek, Dr. J. Cloutier and Dr. Richard Hull (Navigation and Control Branch, USAF Armament Directorate, Eglin AFB) for many suggestions and discussions during the course of this research.

References

- [1] Z. Artstein, "Stabilization with Relaxed Controls," *Nonlinear Anal.*, 7, 11, pp. 1163-1173, 1983.
- [2] A. E. Bryson and Y. C. Ho, *Applied Optimal Control*, Hemisphere Publishing Corp., Washington, D.C., 1975.

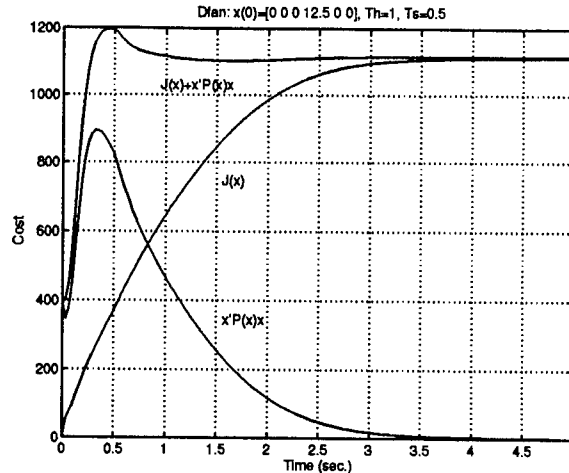


Figure 4: The terms of the cost as function of the horizon

- [3] J. R. Cloutier, C. N. D'Souza and C. P. Mracek, "Nonlinear Regulation and Nonlinear \mathcal{H}_∞ Control Via the State- Dependent Riccati Equation Technique: Part 1, Theory; Part 2, Examples." *Proceedings of the International Conference on Nonlinear Problems in Aviation and Aerospace*, Daytona Beach, FL, May 1996, pp 117-142.
- [4] J. R. Cloutier and R. A Hull, "Periodically Preconditioned Conjugate Gradient Restoration Algorithm for Optimal Control: The Hybrid Approach," *Proceedings of the 1997 AIAA GNC Conf.*, New Orleans, August 1997, to appear.
- [5] M. A. Dahleh and I. J. Diaz-Bobillo, "Control of Uncertain Systems, A Linear Programming Approach", Prentice Hall, 1994.
- [6] P. Dorato, "A Survey of Robust Multiobjective Design Techniques," in Control of Uncertain Dynamic Systems, S. P. Bhattacharyya and L. H. Keel editors, CRC Press, Boca Raton, FL, 1991, pp. 249-259.
- [7] J. Doyle, J. A. Primbs, B. Shapiro and V. Nevistic, "Nonlinear Games: Examples and Counterexamples," *Proc. 35th IEEE CDC*, Kobe, Japan, Dec. 1996, pp. 3915-3920.
- [8] J. Doyle et. al., "Nonlinear Control: Comparisons and Case Studies, *Workshop #7, 1997 ACC*, Albuquerque, N. M., June 1997.
- [9] R. A. Freeman and P. V. Kokotovic, "Inverse Optimality in Robust Stabilization," *SIAM J. Contr. Opt.*, 34, pp. 1365-1391, July 1996.
- [10] R. A. Freeman and J. A. Primbs, "Control Lyapunov Functions, New Ideas From an Old Source," *Proc. of the 35th IEEE CDC*, Kobe, Japan, Dec. 1996, pp. 3926-3931.
- [11] M. Krstic, I. Kanellakopoulos and P. Kokotovic, *Nonlinear and Adaptive Control Design*, John Wiley, New York, 1995.
- [12] H. Choi, P Sturdza and R. M. Murray, "Design and Construction of a Small Ducted Fan Engine for Nonlinear Control Experiments," *Proc. 1994 ACC*, Baltimore, Md, June 1994, pp. 2618- 2622.

- [13] Z. Qu, "Robust Control of Nonlinear Uncertain Systems Without Generalized Matching Conditions," *IEEE Trans. Autom. Contr.*, 1994.
- [14] J. B. Rawlings and K. R. Muske, "Stability of Constrained Receding Horizon Control," *IEEE Trans. Autom. Contr.*, 38, 10, pp 1512–1516, 1993.
- [15] E. D. Sontag, "A 'Universal' Construction of Artstein's Theorem on Nonlinear Stabilization," *Syst. & Contr. Letters*, 13, 2, pp. 117–123, 1989.
- [16] M. Sznaier and M. J. Damberg, *Suboptimal Control of Linear Systems with State and Control Inequality Constraints*, "Proc of the 26th IEEE CDC, Los Angeles, CA, Dec. 1987, pp. 761–762.
- [17] M. Sznaier and M. Damberg, "Heuristically Enhanced Feedback Control of Constrained Discrete Time Linear Systems," *Automatica*, Vol 26, 3, pp 521–532, May 1990.
- [18] M. Sznaier and P. Dorato, Organizers, Invited Session on Multiobjective Robust Control, *Proc. of the 33 IEEE CDC*, Lake Buena Vista, Fl, December 14–16, 1994.
- [19] M. Vidyasagar, "Optimal Rejection of Persistent Bounded Disturbances," *IEEE Trans. Automat. Contr.*, Vol. AC-31, no. 6, pp. 527–535, 1986.

PHOTOCONDUCTIVITY STUDIES OF THE POLYMER 6FPBO

Barney E. Taylor
Associate Professor
Department of Physics

Miami University - Hamilton
1601 Peck Blvd.
Hamilton, OH 45011

Final Report for:
Summer Faculty Research Program
Wright Laboratory

Sponsored by:
Air Force Office of Scientific Research
Bolling Air Force Base, DC

And

Wright Laboratory

August, 1997

PHOTOCONDUCTIVITY STUDIES OF THE POLYMER 6FPBO

Barney E. Taylor
Visiting Assistant Professor
Department of Physics
Miami University - Hamilton

The polymer 6FPBO is the subject of an intense investigation by the Physics Group of the Polymer Branch of the Materials Laboratory at Wright Patterson AFB. Successful blue electroluminescent devices have been fabricated and the underlying physics is being pursued in continuing studies. This report summarizes a complementary study of the photoconductivity measurements on the electroluminescent devices and samples made from the starting materials.

An experimental system was put in place to acquire the photoconductivity spectra using equipment available in the Physics Group. The necessary software to control the experiment was developed. A methodology of normalizing the photoconductivity data was put in place, and 6FPBO devices were studied.

6FPBO samples produce a weak but measurable photoconductivity spectrum. The spectrum shows multiple peaks with two prominent features at about 340 and 405 nm. Preliminary investigations were made of the effect of bias voltage, probe beam intensity and the effect of chopping of the probe beam at different frequencies.

Difficulties with the normalization data preclude definitive assignment of the spectral shape. However, it is clear that the dependence of the photoconductivity on the probe intensity is linear - independent of uncertainties in normalization. Further, the dependence of the photoconductivity on the bias is supralinear for forward biased samples. (The electroluminescent devices may be considered to be Schottky diodes - by their structure and by their current-voltage characteristics). Two types of electroluminescent devices are routinely fabricated - monolayer devices using only 6FPBO and bilayer devices using 6FPBO with a PVK hole transport layer. In the case of monolayer devices, reverse bias caused an increase in photoconductivity with increasing reverse bias (although the total intensity was less than for the same forward bias). In the bilayer devices the photoconductivity was quenched with increasing bias. Chopping frequency studies were inconclusive.

PHOTOCONDUCTIVITY STUDIES OF THE POLYMER 6FPBO

Barney E. Taylor

Introduction

The physics group of the Polymer Branch of WL/MLBP supports the synthetic chemists by electrically and optically evaluating the prototype polymers in order to meet the needs of the Air Force. A successful program in the physics group is the fabrication and characterization of electroluminescent (EL) devices from the polymeric family known as 6FPBO [1], whose structure is shown in Figure 1 a). 6FPBO is one member of the polybenzozoles with 6F moieties which break up conjugation along the backbone and alkoxy pendants ($\text{OC}_{10}\text{H}_{21}$) to increase solubility. In an attempt to understand the physics involved, complimentary studies have also been a part of the continuing studies. Optical absorption and photoluminescence (PL) data are routinely taken on polymers of interest as potential EL materials. EL spectral characterization, PL, quantum efficiency, and current-voltage studies are normally performed on EL devices in order to understand the effect of experimental refinements and/or processing changes. Still, the discovery of the underlying photophysics of 6FPBO is a challenging task. It was thought that photoconductivity studies might be a useful complementary study to augment the knowledge base of 6FPBO EL devices.

A system to allow photoconductivity (PC) measurements to be routinely performed on EL and other polymeric samples was implemented, the software developed, baseline studies performed, and preliminary characterization of the EL devices was accomplished. The implementation of the experimental system will be discussed in the next section along with the necessary control software and baseline studies. The preliminary studies of 6FPBO will be described in the following sections.

EXPERIMENTAL

Photoconductivity Measurement System

Several years ago, this investigator had performed PC studies on the ladder polymer BBL. The experimental system was quite good, but it consumed much of the real estate available in the physics lab. In the ensuing interval, PL, a nitrogen pumped-dye laser, EL and other experiments had taken over the area where the PC had previously been measured. Hence, it was desired to make a more compact arrangement for measuring PC that could be continually available. Further, it was desired to have the experiment be a routine measurement that technicians from other groups could use without extensive training. This meant that a greater degree of automation of the experimental process was necessary along with more sophisticated data acquisition / experimental control software. A detailed description of the experimental PC system is given in the following paragraphs.

An block diagram is shown in Figure 1 b). The light source, which is attached to the monochromator, contains both a deuterium and a tungsten-halogen lamp that can be selected by computer control. The monochromator is an Acton SpectraPro™ 275 monochromator with a triple grating turret containing gratings blazed at 300 nm, 500 nm, and 800 nm. The exit slit of the monochromator is coupled directly into the sample box, without the beam being exposed to ambient light. A lens at the front of the sample box focuses the light on the sample, which is located near the back wall. The chopper is inserted between the lens and the sample. The sample chamber has numerous portals that can be sealed with magnetic plugs. Further, heavy black cloth is draped over the entire sample chamber area when measurements are being performed to minimize stray light from the area where the electrical cables enter the sample chamber. The current from the PC sample is measured synchronously with the chopping rate by the PAR 5210 Lock-In Amplifier. A PAR 581 Current to Voltage amplifier is used to convert the raw current into a voltage measurable by the 5210. Although the 5210 possesses a current mode, that mode does not allow monitoring of the dc current level using an oscilloscope (that is not indicated on the block diagram). The oscilloscope proved useful in several cases when the sample was undergoing breakdown or EL devices were beginning to glow. The entire optical assembly was bolted to the optical table to maintain alignment and light tightness for the system in the event of accidental 'bumps' of the sample chamber or monochromator.

Data from the 5210 is passed to the computer via the GPIB bus. The computer exercises GPIB control of the settings of the monochromator, the selection of the lamp to be used, and the settings of the 5210. Only a few, very important, quantities must be entered manually. One of these is the gain of the 581 preamp. It determines the overall gain of the system. Another is the bias applied to the PC sample which is necessary if one wishes to convert the photocurrent into a photoconductivity.

Control software was developed in Visual Basic™ to control the experiment, to acquire the data, and to maintain a database of experimental settings along with a description of the sample. The process of developing the software was to start with the most rudimentary control of the monochromator and reading of the 5210. The program was successively revised adding increased functionality at each step. Once the control/data acquisition functionality was in place the user interface for that part was polished to make the program accessible to 'non experts' such as summer students or technicians from other groups.

A major effort was required in performing the baseline calibration of the PC to account for the differing number of photons from the lamp at various wavelengths. A PAR 4000 Optical Multichannel Analyzer (OMA) was used along with an Oriel 63358, NIST traceable, calibrated tungsten lamp. The lamp was set up distant from the entrance slit of the OMA and allowed to stabilize in temperature. A spectrum of the calibrated lamp was taken and saved along with a dark background. Then the lamp was turned off, and the Acton monochromator with its integral lamps was placed on jacks near the entrance slit of the OMA. It was discovered that the beam was sufficiently intense, so that focusing of the light onto the entrance slit was not required. The Acton was set to a wavelength shorter than the shortest measurable by the OMA, and a continuous scan was initiated that ended at a longer wavelength than the OMA was set to measure. A background was also taken with the exit slit of the Acton monochromator blocked. The relative intensity of the light from the Acton was calculated as follows:

$$\text{Rel Intensity} = \text{NIST Response} \frac{\text{Acton} - \text{Acton}_{\text{background}}}{\text{Cal Lamp} - \text{Cal Lamp}_{\text{background}}}$$

The monochromator was much closer to the OMA than the calibrated lamp. It was decided to use a relative intensity, due to the difficulty of gating the exit slit on the Acton for a known period of time. Such a measurement could be performed as part of a very comprehensive study. The relative intensity was converted into the number of photons at each wavelength. That function was then fit using non-linear least squares techniques to determine the best fit function to the data for a particular lamp and grating in the Acton monochromator. The best fit function was used to normalize the raw PC data into the form of relative PC/photon.

It was fortunate to have both the tungsten and deuterium lamps attached to the Acton monochromator. The deuterium is very bright in the near UV, but it glows very faintly in the visible. The tungsten lamp is very bright in the visible and near IR, but falls off very rapidly at wavelengths shorter than about 400 nm. It is much more likely that a suitably strong excitation can be obtained for a given material's PC response than with one lamp only.

Sample Preparation:

All of the samples investigated were prepared by Dr. Gang Du, a NRC Fellow in the physics group. Two types of samples were studied: monolayer EL devices consisting of 6FPBO as the active layer, and bilayer devices consisting of a 6FPBO active layer and a PVK hole transport layer to balance the charge flow in the device [2,3]. The active layer is typically 300 to 500 Angstroms thick. A schematic of the sample is shown in Figure 2. The samples consisted of a glass substrate with conducting indium-tin oxide (ITO) on it. On bilayer samples, the PVK was spin coated on the ITO, followed by spin coating the 6FPBO. Finally metal electrodes, usually aluminum, were evaporated on top of the 6FPBO. Monolayer samples were made in an identical manner with the exception of omitting the PVK layer. Dr. Du typically makes 8 samples on a 2.0 by 2.0 cm substrate. The substrate was mounted in a holder, and fine copper or gold wires were attached to the ITO (after scraping away the polymer layers) and to the metallized regions using high purity silver paint. The fine wires went to turret posts, to which heavier wires were then attached. The holder was then mounted on an adjustable stage to position the desired sample area in the exit beam of the Acton monochromator. All illumination was performed through the ITO coated glass.

One sample, a monolayer, was constructed specifically for PC measurements. It was spin coated 5 times to get a thicker active region. Otherwise, it was made in an identical fashion to the monolayer EL devices.

Due to the difference in work function between the ITO and the Al, there were sufficient internal electric fields to allow the EL samples to function in a photovoltaic mode - i.e. without external bias. Indeed, some of the cleanest spectra were obtained in this method. Other measurements were performed under bias. Initially, a Keithley 237 Source Measurement Unit was used to bias the sample using either constant voltage or constant current modes. The 237 apparently has internal operations in the 100 Hz frequency range that caused interference to the PC measurement. The data was much, much noisier than the photovoltaic mode data. Other bias experiments were performed using 1.5 volt dry cells in series up to 6 volts. The polarity of the bias voltage is referenced to that of active EL devices. An EL device is forward biased and glows when the ITO is made sufficiently positive with respect to the Al. Hence, we will refer to forward biased for cases where the ITO is positive and reverse biased for cases where the ITO is negative with respect to the metal electrode.

Data and Discussion:

Figure 3 shows the raw (unnormalized) PC spectrum obtained for a monolayer 6FPBO sample under photovoltaic conditions (zero external bias) for both the tungsten and deuterium lamp. It is quite obvious that the spectrum contains two or more features that contribute to the spectrum. The difference in relative height is due to the differing brightness profiles of the two lamps used to excite the sample. The small dips and upturns at about 300 nm (and 450 nm for the D₂ lamp) are artifacts of the lock-in amplifier. There is a significant drop in the noise level when the lock-in acquires a signal and a corresponding increase as it loses the signal. The data plotted is the magnitude of the lock-in signal measured in volts. The photocurrent is that value multiplied by the conversion gain of the 581 current to voltage pre-amp. The total photocurrent is about 20 times greater for the tungsten lamp than the deuterium lamp. This can be understood in terms of the decreasing

brightness of the D₂ lamp in the 300 to 450 nm region. The inset on the right hand graph of Figure 3 shows the transmittance of the ITO coated glass used as a substrate. The transmittance is for the as received material. During the preparation of samples, Dr. Du performs some processing of the glass that leads to a better device yield. While the processing should not alter the shape of the ITO absorption, it could increase the transmittance by making the ITO layer thinner in the samples relative to the as received material - assuming the absorption is due to the ITO. In any case, the loss of PC spectrum at about 300 nm can easily be understood. Effectively none of the probe beam is penetrating the ITO-glass substrate to impinge upon the polymer. Hence the drop of PC signal near 300 nm must be further investigated using a different substrate or a different sample arrangement. This topic will be addressed in the next section.

Figure 4 shows the raw PC of a bilayer EL device (consisting of ITO/PVK/6FPBO/metal contact) for various experimental conditions. The left graph demonstrates the effect of the grating used to collect the PC data. Both gratings are about equally efficient at the long wavelength edge for 6FPBO PC, but the 300 nm blaze grating is substantially more efficient at the shorter wavelength peak. Otherwise, the two spectra have the same shape. This data was taken at a chopping frequency of 14 Hz to reduce the noise level on the signal. The right graph of Figure 4 shows two different effects: The first is the minimal effect of changing the chopping frequency. The noise level increases substantially at 414 Hz, and the signal is slightly smaller. Other than chopping frequency, the two runs were made under identical conditions. The sample was biased at a voltage of 1.5 V using a dry cell battery. The second observation is that the relative intensity of the two peaks has shifted relative to zero bias. The data was taken using the 500 nm blaze grating, so the filled squares on the two graphs are comparable. We see that the shorter wavelength feature is depressed relative to the longer wavelength feature, and that the entire PC response is greatly enhanced by the biasing. This is not too surprising since the increased electric field will tend to sweep carrier pairs to opposite electrode, preventing their recombination and reducing the photoluminescence of the device. The left hand graph of Figure 5 shows the same device under 3 volts of forward and reverse bias. The effect of further increasing the forward bias voltage is shown in

the right hand graph of Figure 5. The 3V curve represented by the open circles is the same data on both sides. The effect of reversing the bias is dramatic. The forward biased (3 V) peak is approximately 30 times larger than the reverse biased peak at 405 nm. The 340 nm peak is only about 4.5 times larger under forward bias. At 4.5 V forward bias, the device is unstable, most likely due to the fact that it is nearing its turn on state. While the peak is much noisier, it is indeed much larger. The amplitude of the 405 nm peak is increased by a factor of 3 when increasing the bias from 3.0 to 4.5 V. The increase in amplitude (or total area) is definitely not linear. A 50% increase in the bias leads to a 300 % increase in the PC with an overall degradation of the signal quality.

Figure 6 shows the dependence of the PC of a forward biased 6FPBO bilayer device upon probe intensity. Neutral density filters were inserted between the chopper and the sample and the spectra recorded. The average value of the 3 points centered on 404 nm was computed and plotted against the fractional transmittance of the neutral density filter. It is quite apparent that the PC scales linearly with probe intensity for this device. The dependence on bias voltage of the bilayer is different from that of the 5 times spun monolayer sample that was prepared exclusively for PC measurements. Figure 7 shows the response of the monolayer under comparable reverse and forward bias voltages. The scales are identical, the curves were plotted separately as an aid to the eye. The amplitudes of the peak at 404 nm and the total area were plotted as functions of bias. The curves resulting plots grew monotonically, but were not well described by parabolic or exponential functions. With only 4 points, it seemed improper to try to find a fit to a more complicated function without sound theoretical backing of that function.

Figure 8 presents prototypical PC/photon and 6FPBO absorbance as a function of photon energy for both bilayer and monolayer devices. The left graph is for the bilayer 6FPBO/PVK device probed using the D₂ lamp. The scales were chosen to make the amplitude of the 3.1 eV features comparable in the absorbance and the PC/photon. The PC exhibits less well defined structure than the absorbance. Additionally, the PC seems to lead the absorbance at the band edge. The right graph is for the monolayer device probed with a tungsten lamp. The two curves represent possible normalized results. Unfortunately, several of the OMA files needed for normalization were accidentally rewritten

or recopied. It is not possible to determine which file is associated with which grating on the Acton monochromator. This misfortune severely limits the ability to meaningfully analyze the PC data until the calibration measurements are repeated.

The cutoff of the PC around 300 nm appears to be an artifact of the transmittance of the ITO coated glass. While the glass has been processed before making devices, the transmittance should be similar to that of virgin ITO coated glass (shown in Figure 3). Transmittance data taken locally on the as received ITO material indicates that the substrate material ceases to transmit by 4 eV. Hence the PC would naturally go to zero, as the probe intensity goes to zero. The process of normalizing the data will need to be amended to include the transmittance of the processed ITO glass.

SUMMARY AND SUGGESTIONS FOR FURTHER STUDY

The photoconductivity of 6FPBO devices is very interesting. Although the PC response is weak, the PC mimics the shape of the absorption of 6FPBO. This would indicate the absence of significant trapping levels that would remove carriers from the PC process, yet be able to absorb the incident photons. The linear dependence of the PC on the probe intensity suggests that the probe beam is not sufficiently intense to alter the PC spectrum. The PL of 6FPBO has been measured using a nitrogen pulsed laser as the pump, and an intensity dependent PL profile has been observed [4]. It was observed that the baseline noise in the PC measurements increased with chopping frequency. Normally the noise decreases with increasing frequency - up to about 400 Hz. 390 Hz is often chosen as the optimum choice for minimizing the noise in lock-in with an input impedance of 1 megohm. However, the PC noise level increases with chopping frequency above about 40 Hz. The data presented earlier hints that there might be a slight dependence on the chopping frequency, but it is possible that the sensitivity of the system is falling at higher chopping frequencies and the result is not valid. In any case, the dependence of the PC on chopping frequency is slight as compared to the extreme dependence in the polymer PPV [5].

The bias results are very interesting. The PC of the bilayer device is quite distinct from that of the monolayer. At zero external bias, the bilayer

device has a very clean PC spectrum while the 5 times spun monolayer spectrum is hidden in the noise. For the bilayer device, the built in electric fields associated with the difference in the work function of ITO and Al provide the electric field gradient, and the PVK layer provides a mechanism to facilitate the transport of holes. The monolayer device would have a smaller gradient (due to the increased sample thickness), and would have no layer to facilitate the transport of holes at zero bias. Hence, the lack of a zero bias PC spectrum above the noise level is not surprising. As increasing forward bias is applied to each sample, the electric fields increase in each device and the amount of charge transported increases. Under reverse bias, the bilayer device almost ceases to function, probably because the PVK hole transport layer would need to transport electrons instead. The monolayer device experiences a field that is opposite of the built in field and shows a net PC under reverse bias that is smaller than under the same forward bias. It seems that one should be able to learn something about the nature of the built in potential by comparing PC spectra that have comparable maximum amplitudes. From Figure 7, this would be on the order of one volt. The PC grows supralinearly with increasing bias. With only 4 data points, it was not possible to determine the best empirical fit to the data.

It is planned to revisit the calibration of the raw data using the OMA and the calibrated light. Once this has been completed, the existing data can be properly normalized and interpreted. Several interesting prospects exist for further study. The PC could be measured as a function of temperature. A cryostat exists that is capable of spanning the range from about -160°C to 250°C . With full PC spectra at a number of temperatures between those limits, one could determine whether thermally activated processes are present, and, if present, what the activation energy is.

In other polymeric systems, a stark contrast has been observed between the sandwich structure (used in this study) and the surface cell structure of a polymer film on a nonconducting substrate with metallic electrodes applied adjacent to each other. Rather than crossing predominantly from chain to chain, the carriers could move along the chains more with less interchain hopping. Also the surface cell geometry should reveal the true shape of the 6FPBO PC for shorter wavelengths. In the surface cell geometry, the 6FPBO can be illuminated directly, without having to pass through the ITO-glass

substrate. Frequently, there are differences in the shape of PC spectra from surface and sandwich geometries. Hence, the final spectral profile might not be that of the sandwich configuration. Perhaps a sample could be spun using a much thinner ITO layer on a quartz substrate to see if the shape of the PC line in the two geometries is the same.

Finally, a suitably quiet bias source is needed so that PC measurements can be made at other bias voltages than those obtained from electrochemical batteries.

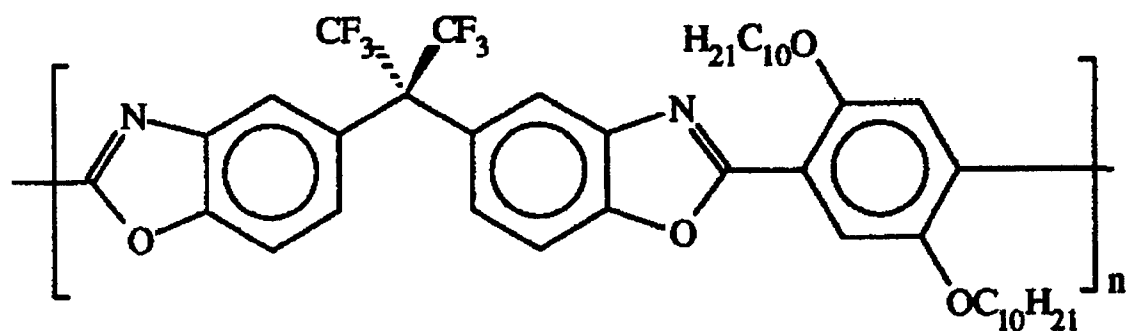
Acknowledgments

The author is grateful to Dr. Gang Du, NRC Fellow, for providing the EL devices and for fabricating the 5 spun monolayer PC sample. The author would also like to thank Mr. Robert Dollinger, a SOCHE student during this tenure for his assistance in taking data and coding the PC software. We are grateful to the Polymer Branch, AFOSR, and Dr. Robert Spry for the opportunity of performing this investigation.

REFERENCES

- 1 B. E. Taylor, Final Report, AFOSR SFRP Program, Sept., 1996.
- 2 G. Du, M. D. Alexander Jr., J. B. Ferguson, B. A. Reinhardt, R. J. Spry, B. E. Taylor, J. L. Burkett, Bull. Am. Phys. Soc. 42, 1, 539 (1977)
- 3 G. Du, et al, to be published.
- 4 Gang Du, Private Communication.
- 5 K. S. Narayan, K. S. Gautam, J. Appl. Phys. 79 (4), p 1935, 1996.

a) Structure of 6FPBO



b) Block diagram of the experimental PC system.

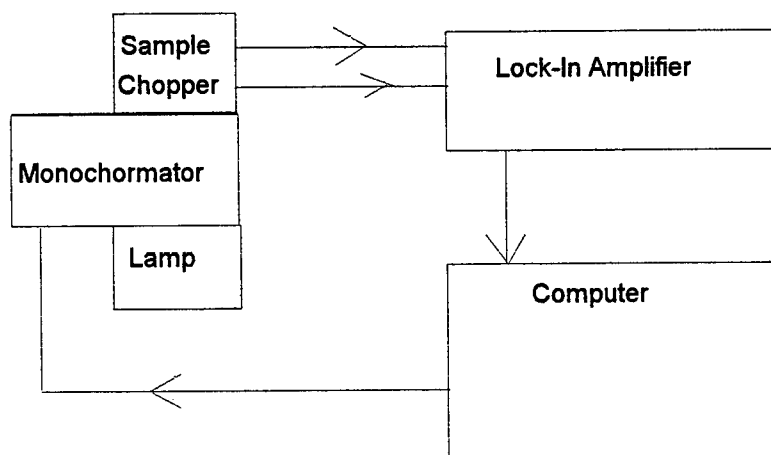


Figure 1. a) The structure of the polymer 6FBO used in this investigation.
b) A block diagram of the experimental system for measuring photoconductivity.

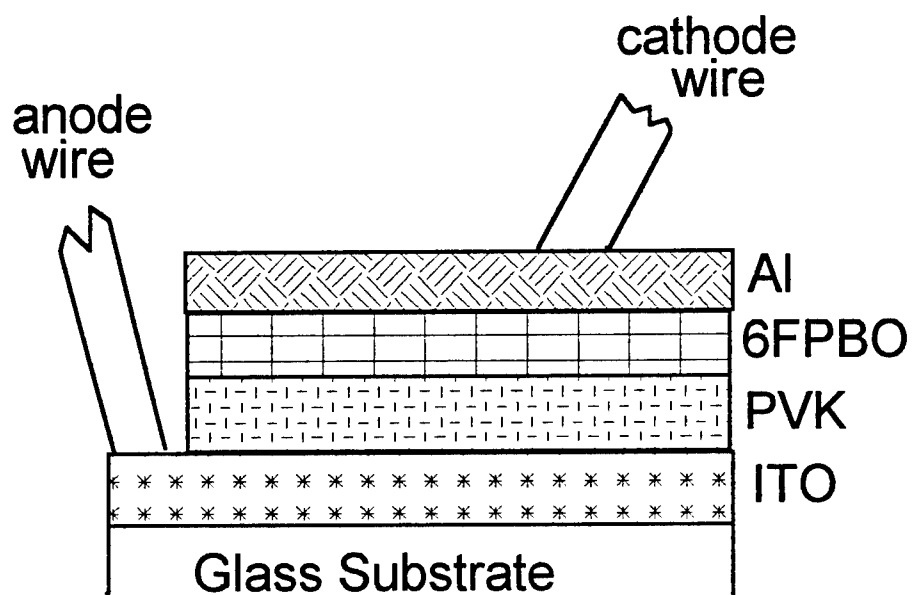


Figure 2.. Schematic of the EL device structure. The layers are not to scale.

Unnormalized (Raw) PC of 6FPBO Monolayer vs Wavelength

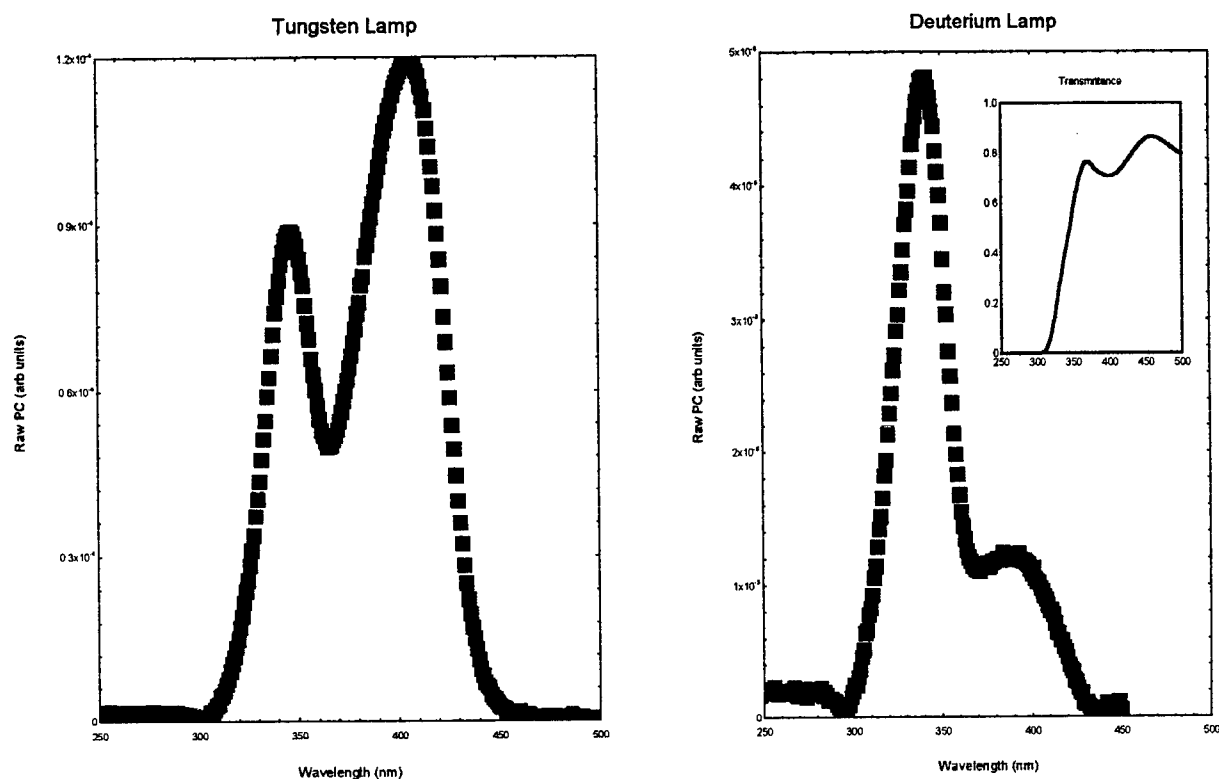


Figure 3. Unnormalized PC data for a 6FPBO monolayer obtained using the deuterium and the tungsten lamps. The inset shows the transmittance of the ITO coated glass used as a substrate for the samples.

Raw Photocurrent of 6FPBO Bilayer vs Wavelength

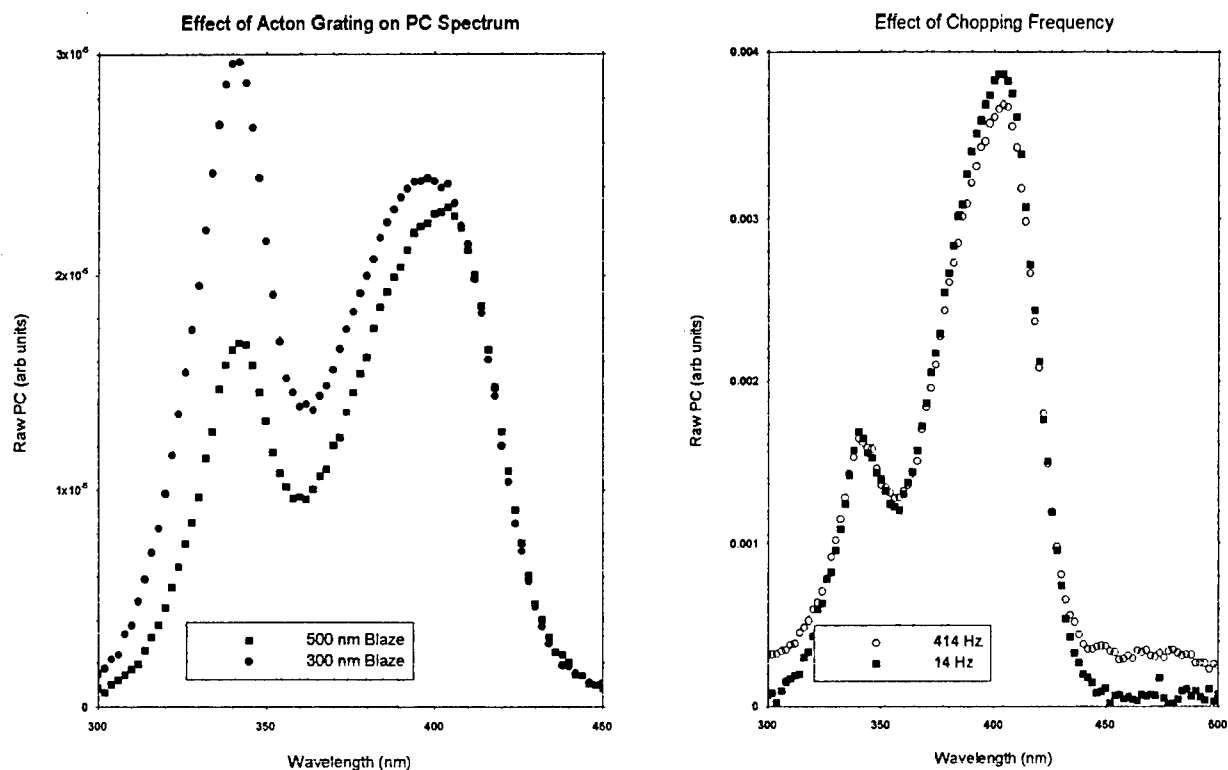


Figure 4. The effect of the Acton's grating on the Raw PC of a 6FPBO bilayer device, and the effect of changing the chopping frequency while the sample is under 1.5 V bias.

Raw Photocurrent of 6FPBO Bilayer vs Wavelength

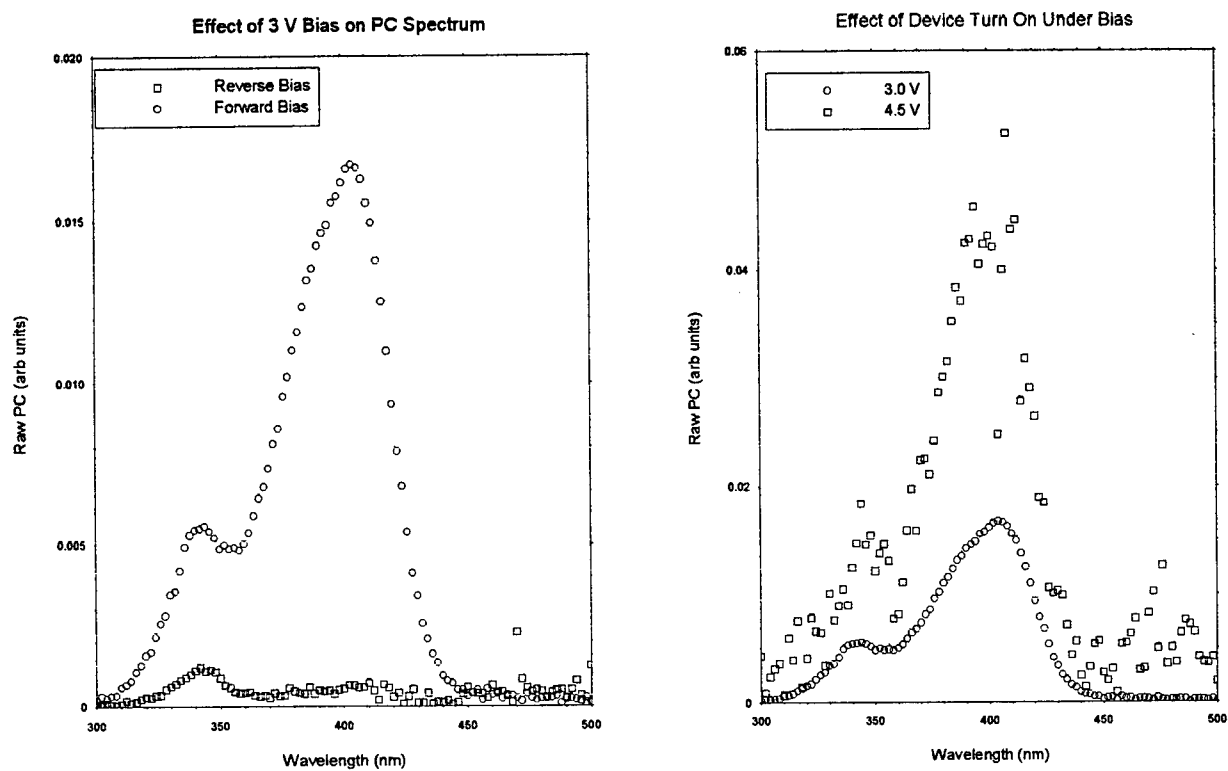


Figure 5. The effect of bias on the raw PC of the bilayer 6FPBO EL device.

Probe Intensity Effects on Photocurrent of 6FPBO Bilayer

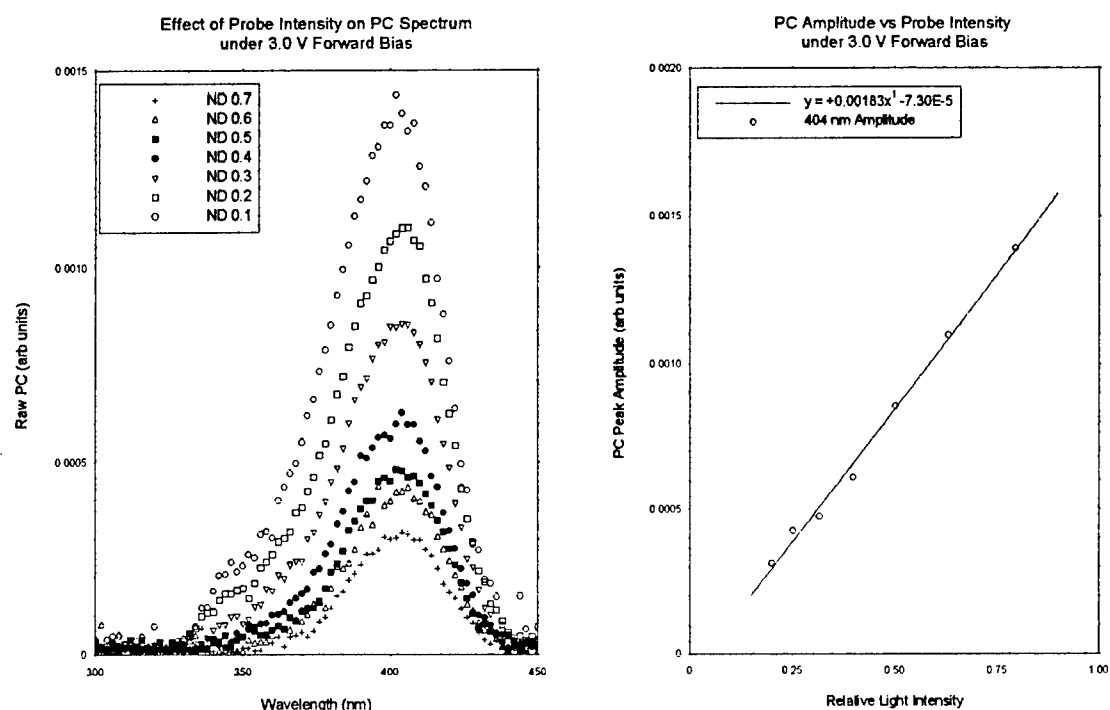


Figure 6. The raw PC vs. wavelength of a 6FPBO bilayer for various probe intensities, and the peak PC amplitude as a function of probe intensity.

Photocurrent vs Wavelength of 5 Spun 6FPBO Monolayer

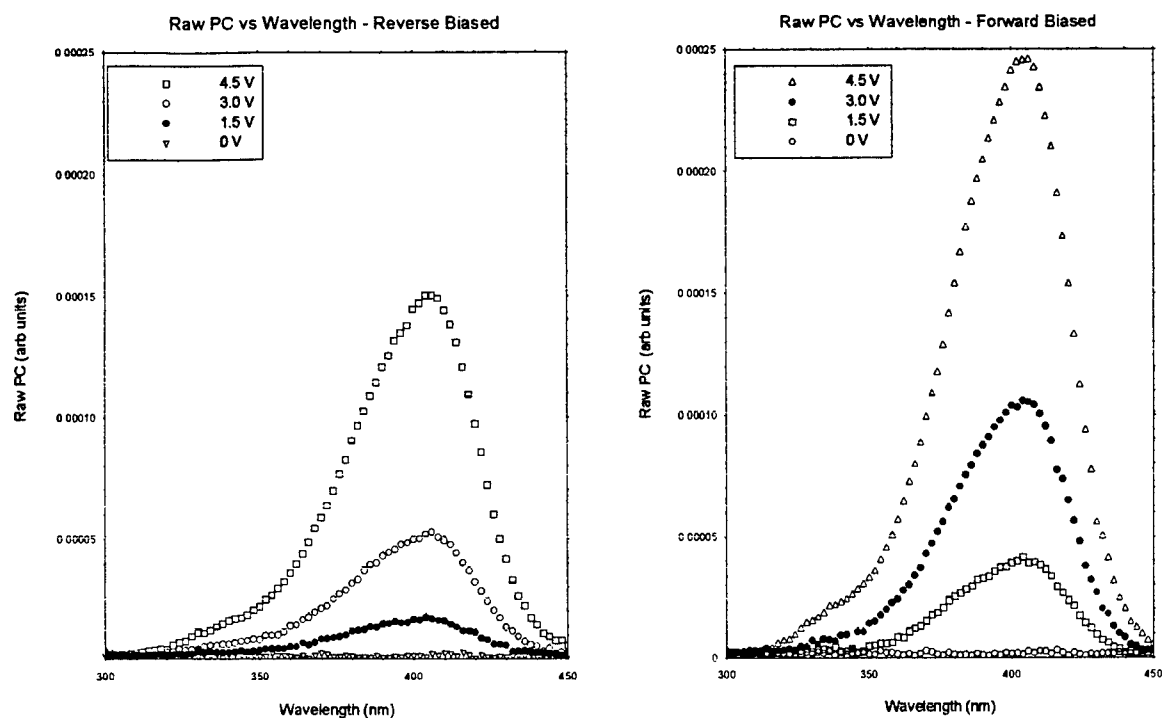


Figure 7. The PC of a 5 times spin cast monolayer 6FPBO sample made specifically for PC studies. A family of curves is shown for various bias voltages in both forward and reverse bias conditions.

Absorbance and PC per Photon versus Photon Energy for 6FPBO Devices

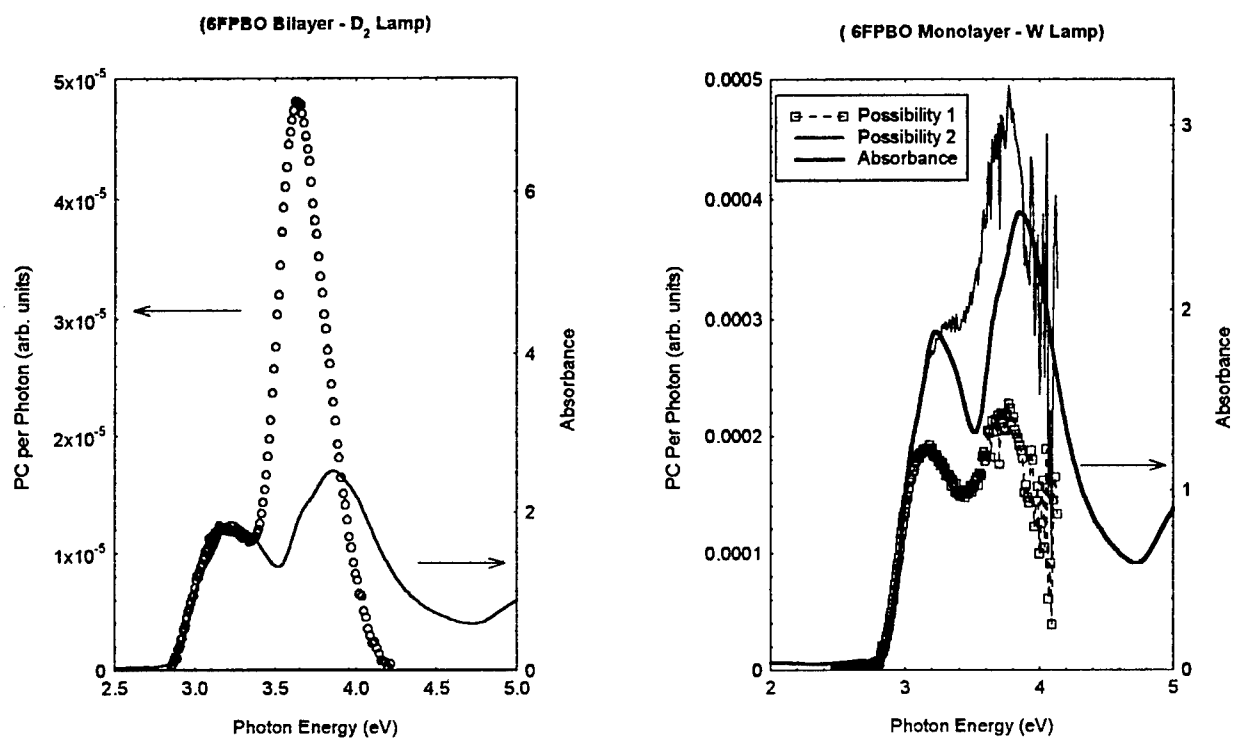


Figure 8. Representative plots of normalized PC/photon and absorbance of 6FPBO versus photon energy.

**HIGH VELOCITY PENETRATION OF LAYERED CONCRETE TARGETS
WIGH SMALL SCALE OGIVE-NOSE STEEL PROJECTILES**

**Joseph W. Tedesco
Professor
Department of Civil Engineering**

**Auburn University
Auburn, AL 36849**

**Final Report for:
Summer Research Program
Wright Laboratory**

**Sponsored by:
Air Force Office of Scientific Research
Bolling Air Force Base, Washington, DC**

And

Wright Laboratory

September 1997

HIGH VELOCITY PENETRATION OF LAYERED CONCRETE TARGETS WITH SMALL SCALE OGIVE-NOSE STEEL PROJECTILES

Joseph W. Tedesco
Professor
Department of Civil Engineering
Auburn University

Abstract

New Air Force designs for manned aircraft continue to follow the recent trend of internal weapon carriage for RCS considerations. Therefore, future penetrator designs must accommodate reduced mass and volume constraints. To meet these requirements the Air Force is focusing on smaller penetrators. A key technical issue associated with the small penetrators is high velocity impact phenomenology, especially into layered concrete targets. This report summarizes the results of a preliminary study to evaluate the effects of layering on the penetration of small scale projectiles. The results of the study indicate that layered targets experience a significantly larger amount of penetration than the corresponding monolithic target. A small scale testing program is recommended to investigate the problem further.

HIGH VELOCITY PENETRATION OF LAYERED CONCRETE TARGETS WITH SMALL SCALE OGIVE-NOSE STEEL PROJECTILES

Joseph W. Tedesco

Introduction

New designs for manned Air Force aircraft continue to follow the recent trend of internal weapon carriage due to reduced radar cross-section (RCS) and stealth considerations. For example, the F-22 currently has two weapon bays, each having a capacity of 1000 lbs. Therefore, future penetrator designs must accommodate these mass and volume constraints, and large externally mounted penetrators may eventually be phased out.

To meet these requirements, the Air Force is focusing on smaller penetrators (e.g. the 250 lb class MMT), with the ability to maintain or exceed the performance criteria of the currently deployed 2000 lb penetrator. These performance criteria raise several key technical issues which must be addressed. One of the most important of these issues is the increased striking velocity requirement for the smaller penetrator. Current focus is on high velocity impact phenomenology in the range of 3000 to 8000 fps.

Over the past 40 years a large database for projectile penetration into geological materials and concrete has been developed by Sandia National Laboratories (SNL) and the Waterways Experimentation Station (WES). However, until recently, the issues concerning high velocity penetration into concrete targets has not been addressed.

The most comprehensive studies of high velocity penetration into concrete targets have been conducted at SNL by Forrestal et al [1, 2, 3, 4, 5]. All tests were performed using the small scale penetrators shown in Figure 1 and monolithic concrete or grout targets. Consequently, a database for high velocity penetration into layered concrete targets does not exist. Interest in penetration into layered targets has recently been piqued for several reasons: 1) cold joint construction of hardened facilities and 2) construction of multiple burster slab layers. However, of more significance is the fact that the majority of full scale testing on concrete targets employ some type of multiple layer target configuration to depict a monolithic target. This procedure may result in significant error with respect to assessments of penetration effectiveness.

Objectives and Scope

The objectives of this study are to provide a preliminary quantification of the effects of layering on penetration into concrete targets by using existing analytical techniques and to design a test matrix for high velocity penetration of small scale ogive-nose steel projectiles into layered concrete targets. The physical characteristics of the small scale projectile are illustrated in Figure 1 and summarized in Table 1. The inventory of existing targets is presented in Table 2. All targets are 30 in square plates of variable thickness.

Table 1. Steel Projectile Data

Weight	0.15 lb
Length	3.5 in
Diameter	0.5 in
CRH	3.0
Yield Stress	180000 psi
Elongation	18%

Table 2. Existing Targets ($f_c=8000$ psi)

Number	Thickness (in)
20	1.375
14	2.75
8	4.125
2	4.375
10	5.5
6	8.25

Prediction Methods for Extrapolating Experimental Results

There are three basic approaches to predicting penetration of projectiles into geological materials and concrete [6]: 1) empirical methods, 2) analytical methods and 3) numerical modeling techniques. The level of sophistication for use of these methods varies from very simplistic to extremely complex.

The empirical methods trace their development to either SNL or WES. The SNL empirical methods development are attributed to either Young [7] or Forrestal [4]. WES also proposed several empirical methods, but the one most applicable to concrete was that developed by Bernard [8]. Of these methods, only Young's, which is embodied in the SAMPLL [7] computer program can accommodate layered target structures.

The analytical methods developed for penetration are based upon either the cavity expansion theory (CET) or the differential area force law (DAFL). The CET (either spherical or cylindrical) assumes the resistance to penetration to be the sum of the shear resistance of the target, and of the inertial effects of projectile movement in the target. The alternate analytical method, the DAFL, provides for explicit formulations for the normal stress and tangential stress at every point on the

external surface of a penetrator. WES has adopted and modified both these analytical techniques and subsequently implemented them in computer programs [9, 10]. Unfortunately, neither the CET or DAFL methods can represent layered target systems.

Numerical modeling techniques include a wide variety of finite element, finite difference and discrete element methods. The most commonly employed of these numerical techniques are Lagrangian finite element codes such as EPIC3 [11] or Eulerian finite difference codes such as Hull [12]. Evaluation of penetration phenomena via these codes is generally very computationally intense, even for monolithic structures. Numerical simulations of layered structures without experimental data to corroborate the results would be extremely difficult, if possible at all.

Concrete Penetration Using SAMPLL

Before attempting to assess the effects of layering on penetration, a limited parametric study of high velocity small projectile penetration into monolithic concrete targets was conducted using the empirically based penetration code SAMPLL. The basic SAMPLL penetration equation into a semi-infinite half space of concrete is given by

$$D = 0.0008SN(W/A)^{.7}(V-100) \quad (1)$$

where

- D = penetration distance (ft)
- S = penetrability of target (dimensionless)
- N = nose performance coefficient (dimensionless)
- W = penetrator weight (lbs)
- A = cross-sectional area (in²)
- V = impact velocity (fps)

The S term in Eq (1) is an empirical measure of concrete target penetrability; the higher the S number, the greater the projectile penetration into the target. The S number is given by the expression

$$S = 0.085K_1K_2(11-P)(CT \times TH)^{-.06} \left(\frac{5000}{UNC} \right)^{0.3} \quad (2)$$

where

- P = reinforcement index (0=no reinforcement; 3=heavy reinforcement)
- CT = cure time in years (CT ≤ 1.0)
- TH = thickness of target in penetrator diameters
- UNC = unconfined compressive strength (psi)
- K₁ = (F/W₁)^{0.5}, F=20 for reinforced concrete, F=30 for unreinforced concrete
- W₁ = target width in penetrator diameters (note that K₁=1.0 for W₁>F)
- K₂ = 2/D₁
- D₁ = lateral distance to nearest edge in penetrator diameters (note that K₂=1.0 for D₁>2)

Close scrutiny of Eq (2) reveals that the target penetrability (S-number) is a function of the concrete compressive strength, amount of steel reinforcement, cure time and the relative thickness of the target. A very obvious omission in the S-number equation is a term to account for the density of the target material.

In applying this expression to small scale projectiles several important observations can be made. First, the K_1 and K_2 terms in Eq (2), which account for target edge effects, generally maximize at 1.0. Second, the TH term which specifies the relative thickness of the target may be unusually high for small scale penetrators. The combination of these effects can result in an unrealistic S-number for small scale penetrators. For example, suggested S-numbers for concrete and competent rock are presented in Table 3. In Table 4, S-number calculated for the 0.5 in diameter projectile penetrating a 30 in diameter by 36 in long cylindrical unreinforced concrete target are presented for several different values of UNC. A comparison of these Tables indicates a discernible discrepancy between the suggested and calculated S-numbers.

Table 3. Suggested S-Numbers

Material	S-Number
hard rock	0.7
strong reinforced concrete	0.8
weak unreinforced concrete	1.1

Table 4. Calculated S-Numbers (30 in diameter by 36 in long cylindrical target)

UNC (psi)	S-Number
5000	0.72
6000	0.68
7000	0.65
8000	0.63

To calibrate the SAMPLL code for the small scale projectile, a family of penetration curves were generated for a wide range of S-numbers. Since the SAMPLL code can only accommodate penetrator weights in increments of 0.1 lbs, two sets of penetration curves had to be generated to predict the penetration of the 0.15 lb projectile. Penetration curves for 0.1 lb and 0.2 lb penetrators are presented in Figures 2 and 3, respectively. The penetration of the 0.15 lb penetrator can then be estimated by averaging the results obtained from the 0.1 lb and 0.2 lb penetration curves.

To illustrate the use of the penetration curves, consider the case of the 0.15 lb projectile impacting the 30 in diameter cylindrical target at a velocity of 1.5 km/s (4900 ft/sec). The penetration results for both the 0.1 lb and 0.2 lb penetrator are summarized in Table 5 for a wide range of S-numbers. The average penetration depth, which represents the penetration of 0.15 lb projectile, is presented in the last column of Table 5.

The actual penetration depth for this test was measured to be 19.84 in. For a UNC of 6000 psi for the target concrete, the calculated S-number is 0.68. For this S-number the penetration depth estimated from Table 5 is approximately 15 in, which underestimates the measured penetration by approximately 25%. However, for an S-number of 0.9, which would be representative of the suggested S-number for a strong unreinforced concrete, then the penetration depth estimated from Table 5 is approximately 20.3 in, which is within 2% of the measured value. This example clearly indicates the importance of selecting the appropriate S-number in estimating penetration depth.

Table 5. Penetration into Cylindrical Target (Import Velocity=4900 ft/sec).

W (lbs)	S	D (in)	D _{ave} (in)
0.1	1.2	19.0	27.0
0.2	1.2	35.0	
0.1	1.1	17.5	24.8
0.2	1.1	32.0	
0.1	1.0	16.0	22.5
0.2	1.0	29.0	
0.1	0.9	14.5	20.3
0.2	0.9	26.0	
0.1	0.8	12.5	18.0
0.2	0.8	23.5	
0.1	0.7	11	15.5
0.2	0.7	20	
0.1	0.6	10	13.8
0.2	0.6	17.5	

Penetration of Layered Concrete Targets

In an attempt to lend some insight to the effects of layering on penetration, a series of penetration simulations of a variety of layered targets was conducted using the SAMPLL code. For a target system comprised of multiple layers, several modifications of the basic penetration expression given by Eq (1) are employed by the SAMPLL code. First, the S-number is calculated for each individual layer in the target, rather than the S-number for the corresponding monolithic target. Second, as the projectile exits a layer, an exit velocity is calculated. This exit velocity is then employed as the impact velocity for the next layer. This recalculated impact velocity is then substituted for V in Eq (1) to determine the penetration into the layer. The exit velocity from any layer is calculated as

$$V_{exit} = \left[V^2 - 2ga \left(T - \frac{L_n}{K_3} \right) \right]^{0.5} \quad (3)$$

where

- V_{exit} = exit velocity from layer (fps)
- V = impact velocity at layer
- g = 32.2 ft/sec²
- a = average acceleration of projectile
- T = thickness of layer (ft)
- L_n = nose length of projectile (ft)
- K_3 = constant = (a) 2, for no soil over or under concrete
(b) 3, for soil under concrete only
(c) 4, for soil over concrete only

The average acceleration term, a, in Eq (3) is estimated as

$$a = \frac{V^2}{2gD} \quad (4)$$

where V is the impact velocity for the layer and D is the calculated penetration into the layer.

To quantify the effects of layering on penetration, two series of layered target systems were investigated using the SAMPLL code. The baseline monolithic systems for the layered systems investigated were a 16.5 in thick concrete target having a UNC of 8000 psi and a 24 in thick concrete target having a UNC of 5000 psi. All targets investigated were 30 in square. Penetration curves for the monolithic 16.5 in thick and 24 in thick targets are presented in Figures 4 and 5, respectively.

For the 16.5 in thick target, two layered systems were investigated. The first system consisted of two layers, each having a thickness of 8.25 in; the second system investigated consisted of four layers, each having a thickness of 4.125 in. Penetration curves for the two layer system and four layer system are presented in Figures 6 and 7, respectively. The corresponding percent increase in penetration curves are presented in Figures 8 and 9, respectively.

For the 24 in thick target, three layered systems were investigated. The first system consisted of two layers, each having a thickness of 12 in; the second system investigated consisted of three layers, each having a thickness of 8 in; and the third system investigated consisted of six layers, each having a thickness of 4 in. Penetration curves for the two layer system, three layer system and six layer system are presented in Figures 10, 11 and 12, respectively. The corresponding percent increase in penetration curves are presented in Figures 13, 14 and 15, respectively.

Close scrutiny of the percent increase in penetration curves indicates that layering the target structure may yield a significantly greater amount of penetration compared to the corresponding monolithic target. For the 16.5 in thick targets, the two layer system can experience an increase in penetration in excess of 25% (refer to Figure 8) and the four layer systems can experience an increase in penetration that approaches 50% (refer to Figure 9). For the 24 in thick targets, the two layer system can experience an increase in penetration in excess of 25% (refer to Figure 13), the three layer system can experience an increase in penetration exceeding 40% (refer to Figure 14), and the six layer system can experience an increase in penetration approaching 70% (refer to Figure 15).

Conclusions and Recommendations

Indeed, penetration of layered concrete target structures is a very complex phenomenon which is not well defined and poorly understood. Moreover, due to the lack of experimental data pertinent to the subject, the problem may not be conducive to a reliable analytical formulation and solution at the present time.

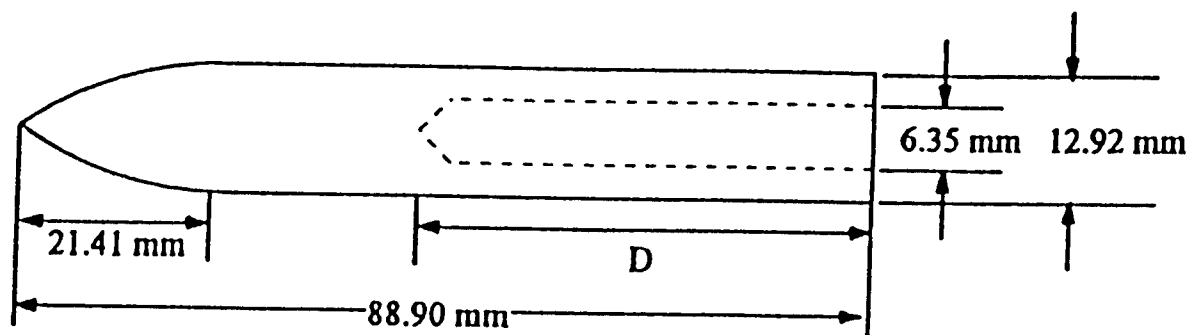
To establish a preliminary database for penetration into layered concrete target systems, a small scale test program is recommended. The projectile to be used in the experiments is described in Table 1 and Figure 1. The existing 30 in x 30 in plate targets, summarized in Table 2, shall be used in the study. A test matrix for the experimental program is presented in Table 6. The test matrix was constructed to deploy 100% of the inventory of the existing targets. An impact velocity of 1 km/s (3000 fps) is recommended for the projectile in all tests.

Table 6. Test Matrix For Existing Targets (Import Velocity=3000 fps).

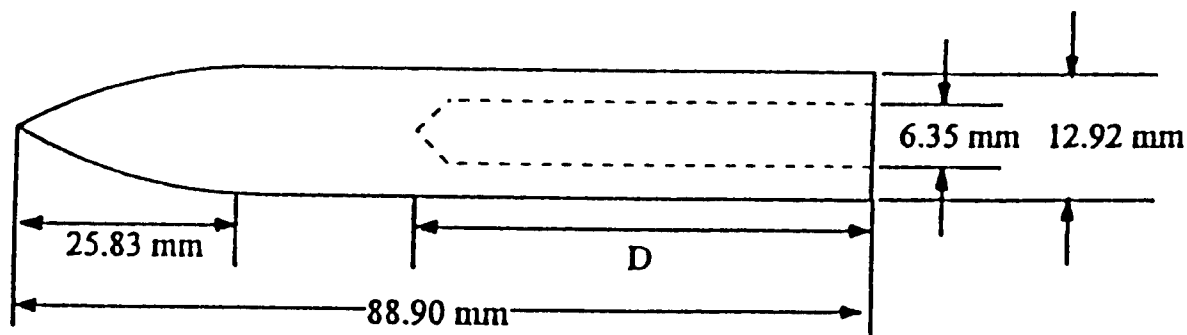
Plate Combinations						No. of Plates	Total t (in)	No. of Tests
1.375 (in)	2.75 (in)	4.125 (in)	4.375 (in)	5.5 (in)	8.25 (in)			
					2	2	16.5	3
12						12	16.5	1
	6					6	16.5	2
		4				4	16.5	2
				3		3	16.5	2
8				1		9	16.5	1
	2		1	1		4	15.375	1
			1	2		3	15.375	1

References

1. Forrestal, M.J., Frew, D.J., Hanchak, S.J. and Brar, N.S., "Penetration of Grout and Concrete Targets With Ogive-Nose Steel Projectiles", International Journal of Impact Engineering, submitted for publication.
2. Forrestal, M.J., Brar, N.S. and Hanchak, S.J., "Penetration of Grout Targets With Ogive-Nose Steel Projectiles", International Journal of Impact Engineering, submitted for publication.
3. Lak, V.K. and Forrestal, M.J., "Penetration Into Semi-Infinite Reinforced Concrete Targets With Spherical and Ogival Nose Projectiles", International Journal of Impact Engineering, Vol. 6, No. 4, pp. 291-301, 1987.
4. Forrestal, M.J., Altman, B.S., Cargile, J.D. and Hanchak, S.J., "An Empirical Equation For Penetration Depth Of Ogive-Nose Projectiles Into Concrete Targets", International Journal of Impact Engineering, Vol. 15, No. 4, pp. 345-405, 1994.
5. Frew, D.J., Forrestal, M.J., Hanchak, S.J. and Green, M.L., "Penetration into Limestone Targets With Ogive-Nose Steel Projectiles", The 14th U.S. Army Symposium on Solid Mechanics, Oct. 16-18, 1996, Myrtle Beach, SC.
6. Heuze, F.E., "An Overview of Projectile Penetration Into Geological Materials, With Emphasis on Rocks", International Journal of Rock Mechanics, Mineral Science and Geomechanical Abstracts, Vol. 27, No. 1, pp. 1-14, 1990.
7. Young C.W., Simplified Analytical Model of Penetration with Lateral Loading (SAMPLL), Sandia National Laboratories, Albuquerque, NM, Report SAND 88-0013, 1988.
8. Bernard, R.S. and Creighton, D., Projectile Penetration in Soil and Rock: Analysis for Non-Normal Impact, U.S. Army Waterways Experiment Station, Vicksburg, MS, Technical Report SL-79-15, 1979.
9. Bernard, R.S. and Creighton, D., Projectile Penetration in Earth Materials: Theory and Computer Analysis, U.S. Army Waterways Experiment Station, Vicksburg, MS, Report S-76-13, 1976.
10. Creighton, D.C., Non-Normal Projectile Penetration in Soil and Rock: User's Guide for Computer Code PENCOZD, U.S. Army Waterways Experiment Station, Vicksburg, MS, Technical Report SL-87-7, 1982.
11. Belytschko, T. and Lin, J.L., "A Three-Dimension Impact-Penetration Algorithm with Erosion", Computers and Structures, Vol. 25, pp. 95-104, 1987.
12. Matsuka, D.A., HULL User's Manual, Orlando Technologies Inc., Shalimar, FL, Report to Air Force Armament Laboratory, Eglin AFB, FL, AD-A145000, 1984.



(a)



(b)

Fig. 1. Projectile geometries for the grout targets. Caliber-radius-head $\psi = 3.0$ for (a) and $\psi = 4.25$ for (b). $D =$ approximately 50.8 mm, adjusted to obtain 0.064 kg.

Velocity Vs. Penetration

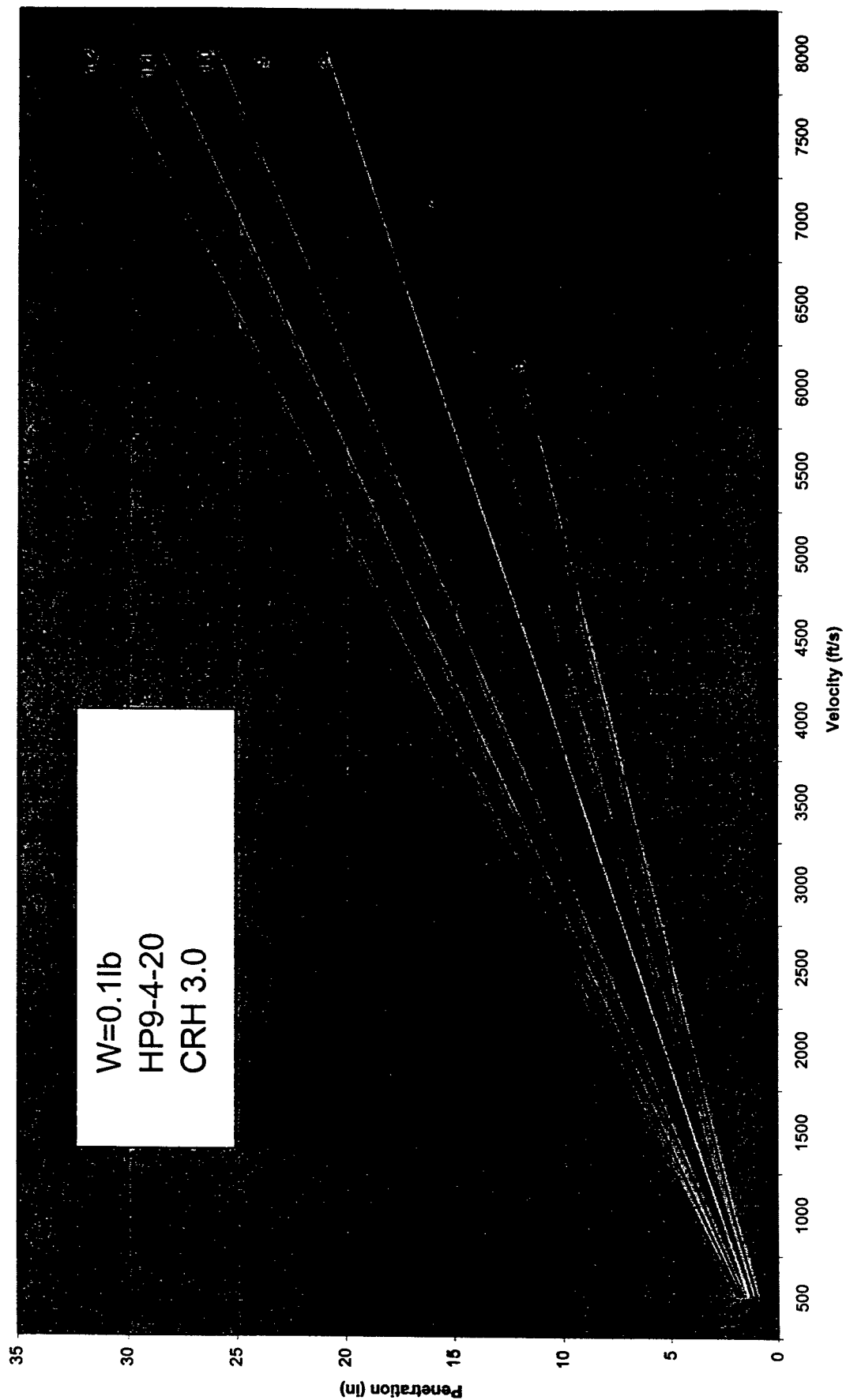


Fig. 2. Penetration curves for 0.1 lb projectile.

Velocity Vs. Penetration

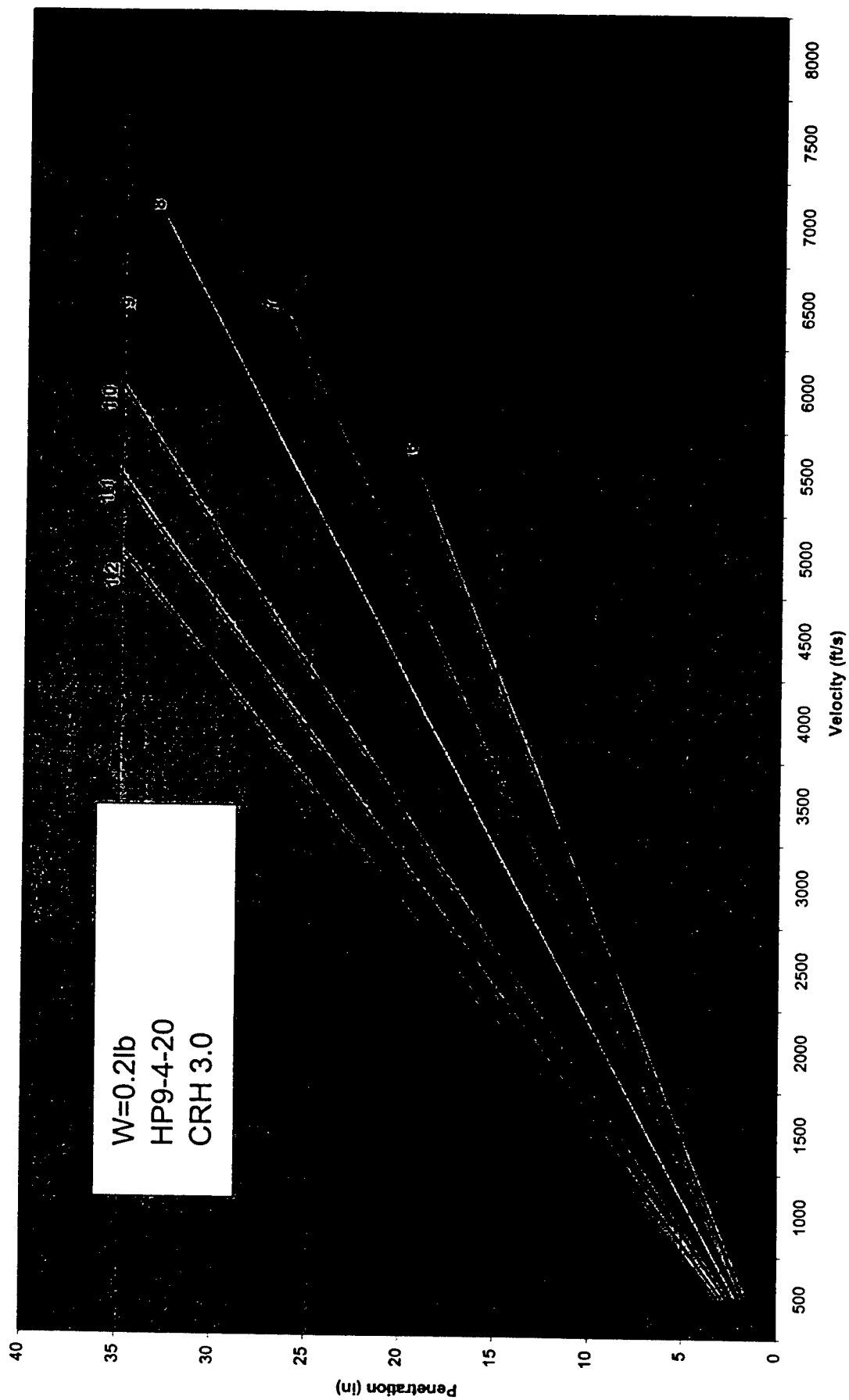


Fig. 3 Penetration curves for 0.2 lb projectile.

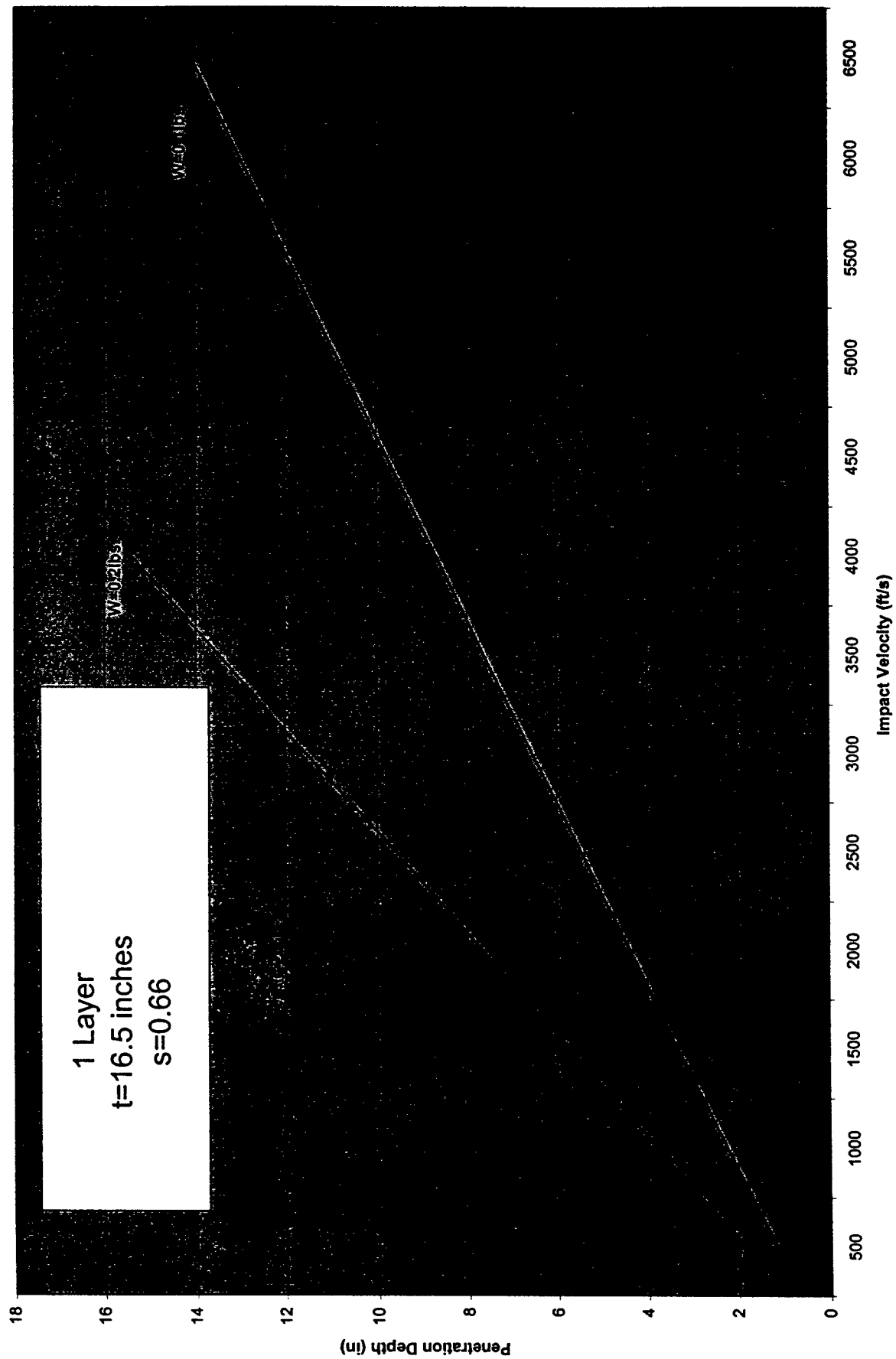


Fig. 4. Penetration curves for 16.5 in. monolithic target.

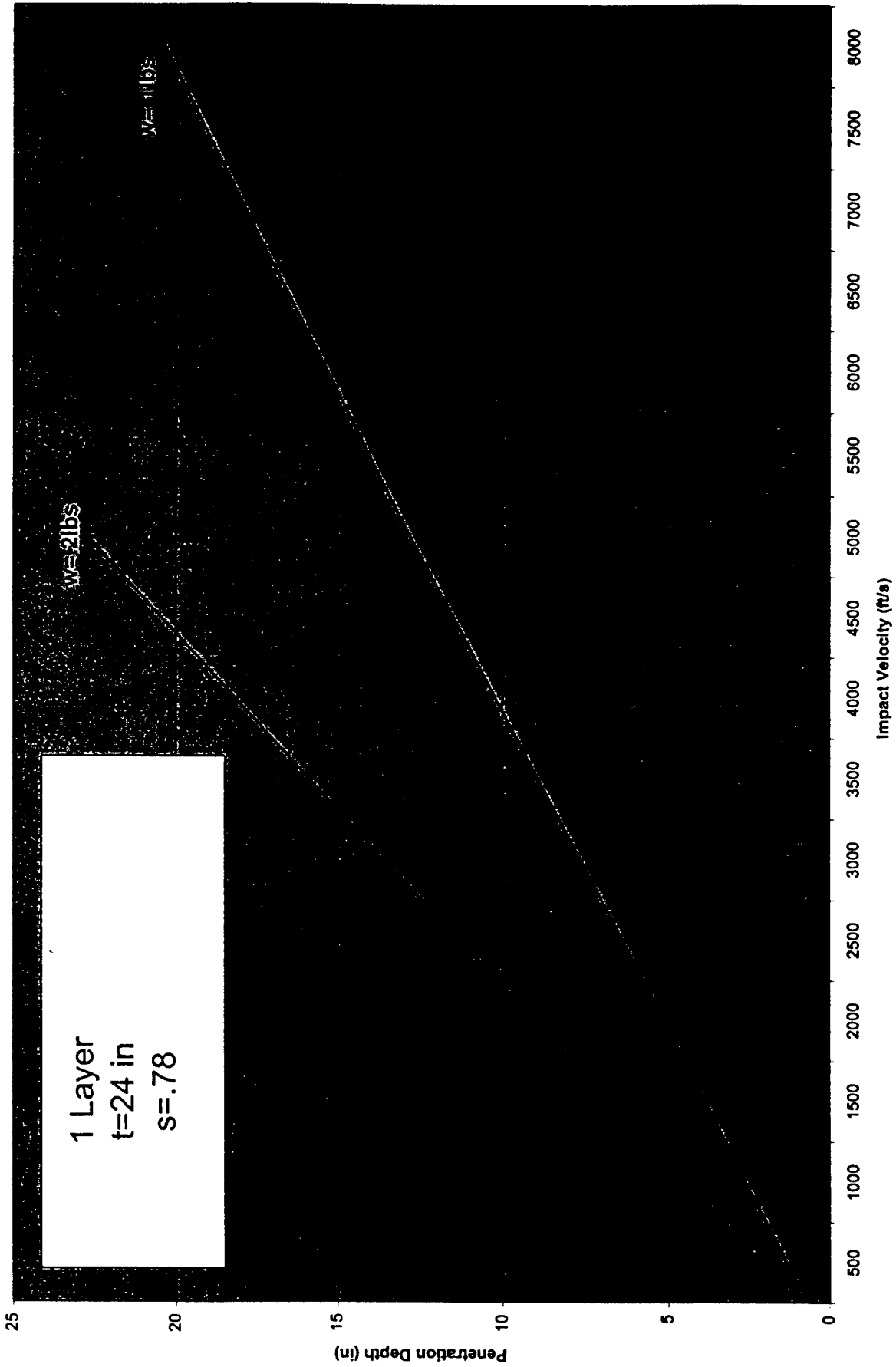


Fig. 5. Penetration curves for 24.0 in. monolithic target.

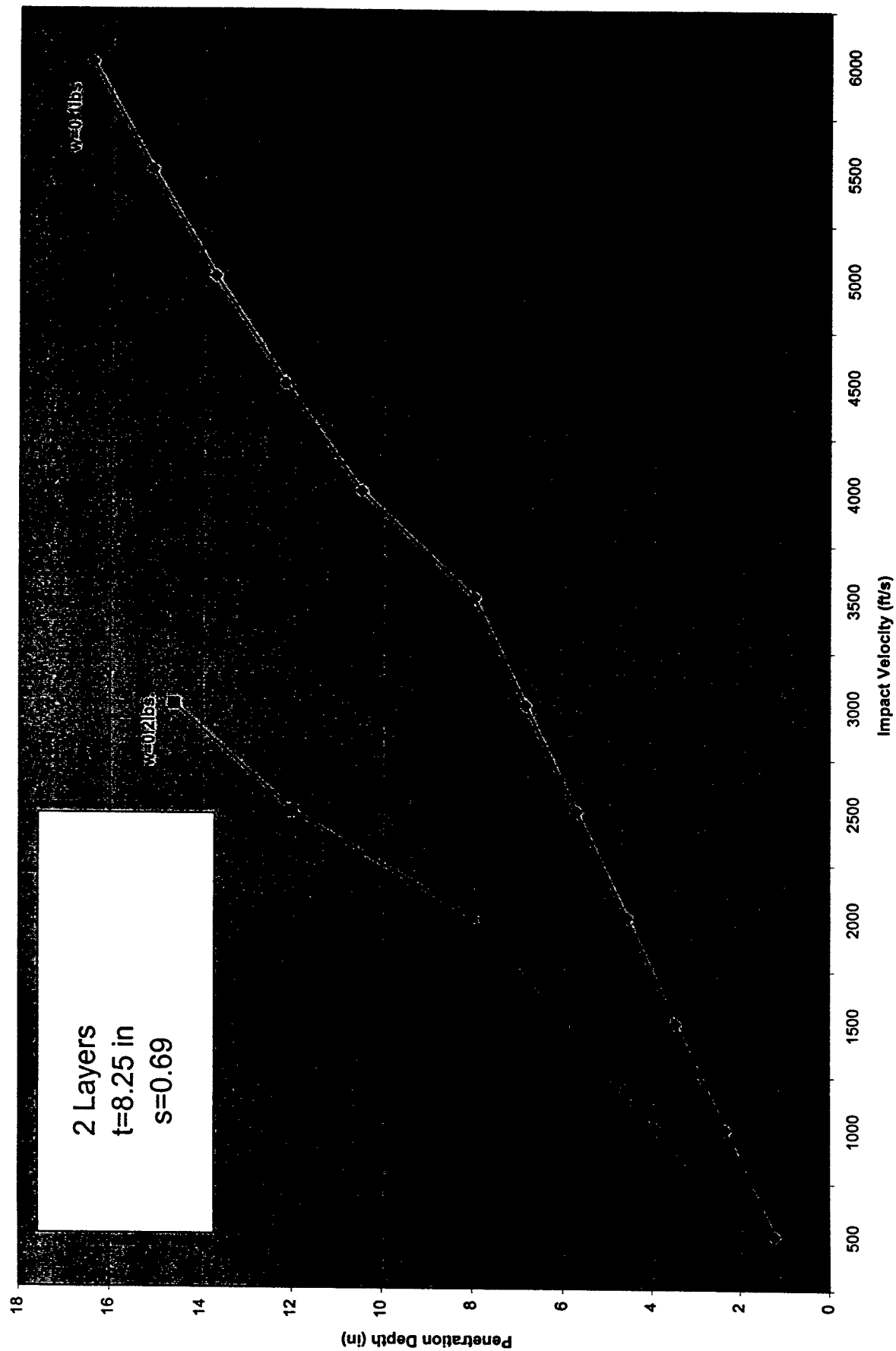


Fig. 6. Penetration curves for two-layer system (16.5 in).

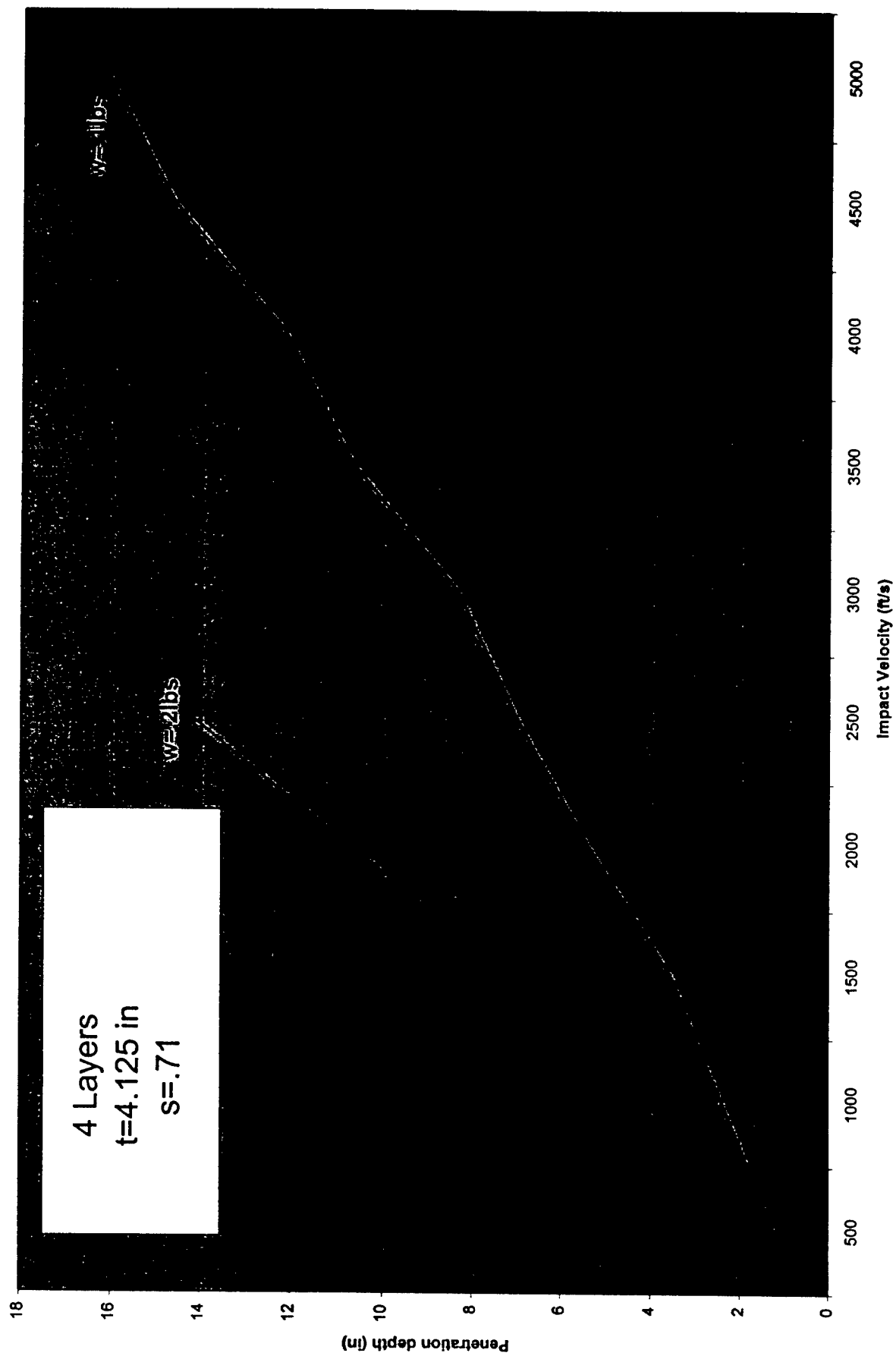


Fig. 7. Penetration curves for four-layer system (16.5 in).

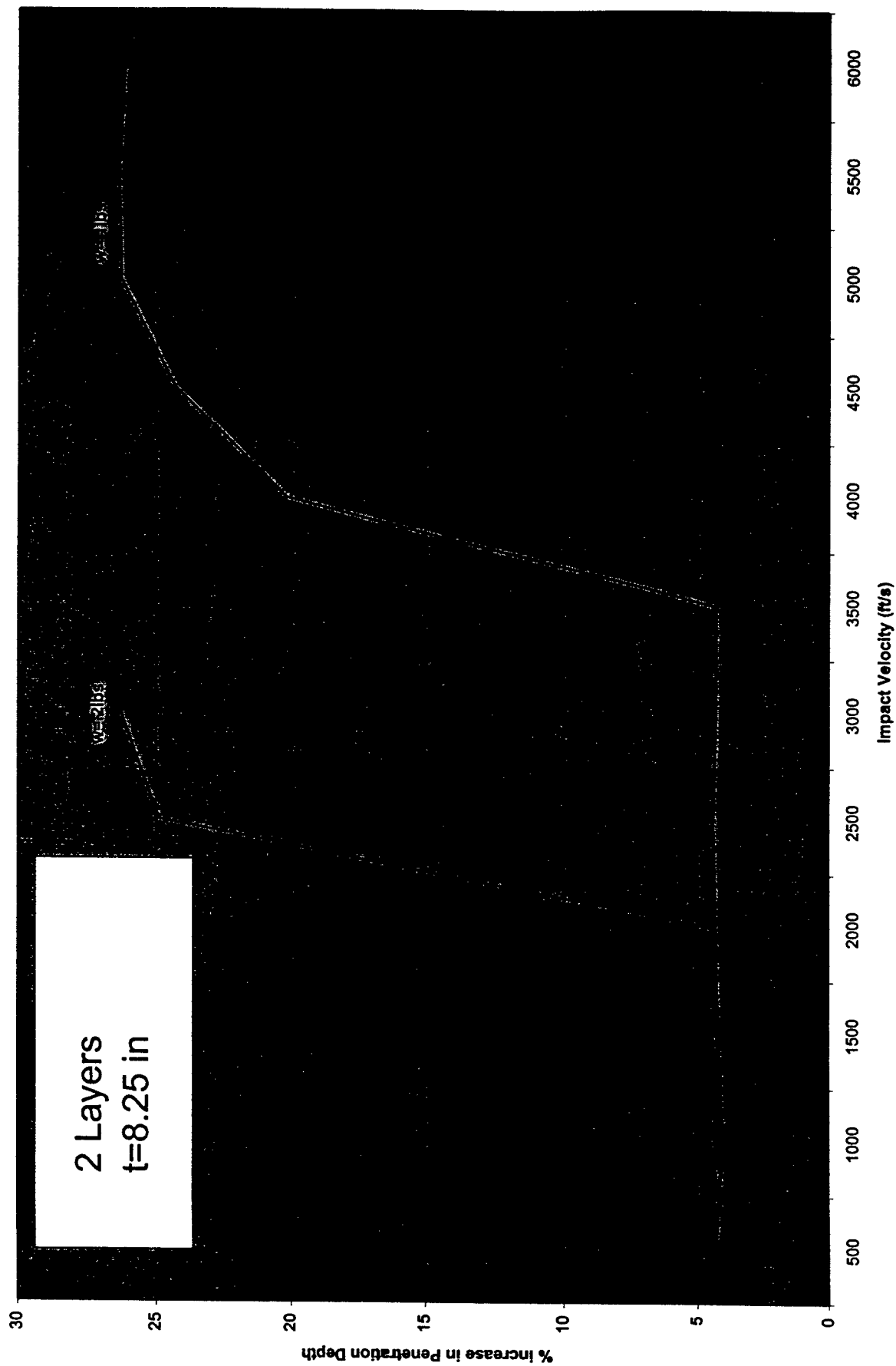


Fig. 8. Percent increase in penetration for two-layer system (16.5 in).

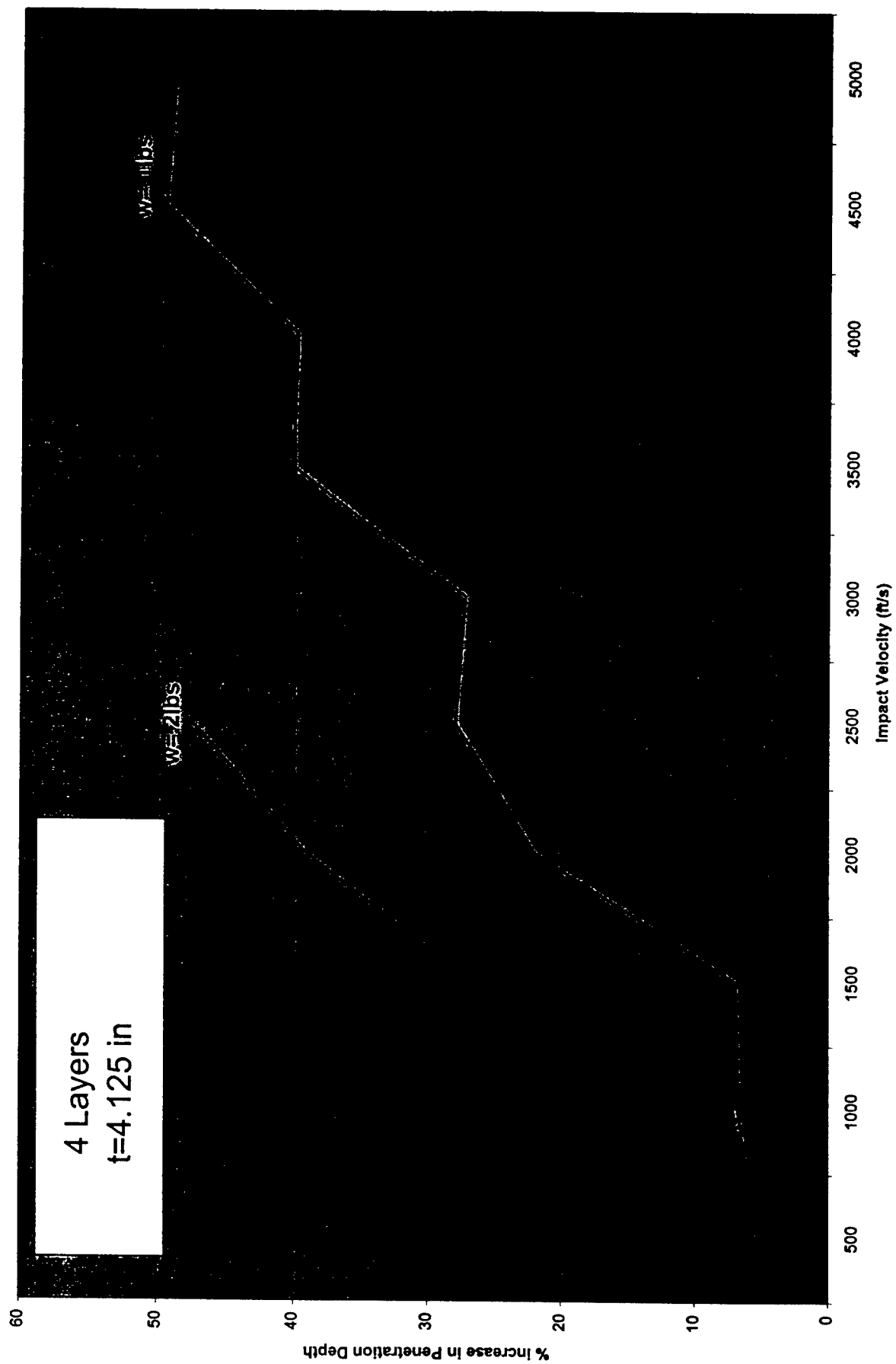


Fig. 9. Percent increase in penetration for four-layer system (16.5 in).

A VHDL MODEL SYNTHESIS APPLET IN TCL/TK

Krishnaprasad Thirunarayan
Associate Professor
Department of Computer Science and Engineering

Wright State University
3640, Col. Glenn Hwy
Dayton, OH 45435.

Final Report for:
Summer Faculty Research Program
Wright Laboratory

Sponsored by:
Air Force Office of Scientific Research
Bolling Air Force Base, DC

and

Wright Laboratory

September 1997

A VHDL MODEL SYNTHESIS APPLET IN TCL/TK

Krishnaprasad Thirunarayan
Associate Professor
Department of Computer Science and Engineering
Wright State University

Abstract

VHDL Model Synthesizer is a tool that enables a circuit designer to generate VHDL descriptions by customizing entity-architecture templates residing in the design database. Currently, the tool, written in Tcl/Tk, is distributed in the standard “*.tar.gz” format that must be downloaded and installed locally by each user. The goal of our work is to convert this tool into an applet in Tcl/Tk (called a *tclet*) residing on a web-server, to enable users to run it remotely in a web-browser (such as Netscape Navigator). The main benefit of this work is that only the master copy needs to be maintained, and the users are always guaranteed to have access to the latest version of the tool and the design database.

An effort is also underway to improve and port the VHDL-93 Design Description Browser tool, implemented using SWI-Prolog and Tcl/Tk, from the UNIX environment to the Windows-95/NT environment. This is being done by converting the TeX files (containing the parser code) into HTML documents, and rewriting the filter program and the Graphical User Interface in Java.

A VHDL MODEL SYNTHESIS APPLLET IN TCL/TK

Krishnaprasad Thirunarayan

Introduction

VHDL Model Synthesis Tool, written in Tcl/Tk by James Todd of OSU, enables a circuit designer to pick from a number of entity-architecture templates residing in the design database, and generate a customized VHDL design description by supplying values for the relevant parameters. Currently, this tool is distributed in the standard “*.tar.gz” format, and must be downloaded and installed locally by each user. The goal of our work is to convert this tool into an applet in Tcl/Tk and place it on a web-server so that it can be run via a web-browser (such as Netscape Navigator) remotely. The main benefit of this approach is that only one master copy of the tool and the design database need to be created and updated.

We are also trying to port the VHDL-93 Design Description Browser tool, implemented using SWI-Prolog and Tcl/Tk, from the UNIX environment to the Windows-95/NT environment. This is being done by converting the TeX files (containing the parser code) into HTML documents, and then rewriting the “filter” program (currently implemented in *lex* and requiring *flex/gcc* or *lex/cc* to run) and the Graphical User Interface part (currently implemented in Tcl/Tk) uniformly in Java.

Discussion of the Problem

To enable the browser to run Tcl/Tk code, a suitable *plug-in* needs to be installed in the browser. However, we were swamped with a host of problems, in part due to the diversity of the browsers and the platforms, and the subtle differences between the various versions of the plug-in even for the same browser and the platform.

The Tcl/Tk plug-in is readily available for Netscape Navigator 3.01 installed on SPARC/SUN-OS 4.1.4 and we confined our attention to it for starters. Even here, there are two versions of the plug-in: Version 1.1 and Version 2.0. The former plug-in implements *Safe-Tcl*, a severely restricted subset of Tcl. This subset is inadequate for our purposes because the VHDL Model Synthesizer tool uses Tcl commands such as *source*, *exec*, *open*, etc that are not permitted in Safe-Tcl, and the tclet requires primitives for downloading files from a URL and manipulating them locally. So, we experimented with Tcl/Tk Version 2.0 (*Alpha release*) plug-in.

We now describe the conversion of the VHDL Model Synthesizer into a *tclet*, and the configuration of the Tcl/Tk plug-in Version 2.0 (*Alpha*) to run the tclet.

Methodology

The Tcl/Tk Version 2.0 (*Alpha*) plug-in extends Safe-Tcl in a controlled fashion by supporting various different *Security Policies*. Each security policy introduces or reinstates an additional set of Tcl-commands (over and above those of the Safe-Tcl) for use in the tclet. For security reasons, these policies cannot be composed freely. That is, even though the individual sets of commands are reasonably safe, their union is potentially unsafe.

We first present some useful (albeit general) information we gleaned out of the sparse documentation available with the plug-in, and from email correspondences with Jacob Levy, the technical contact at SUN Microsystems responsible for the plug-in. We believe that these remarks will be helpful to those who wish to convert a Tcl/Tk application into a tclet.

- To allow a tclet to use all the commands in Tcl/Tk, both the “*server*” tclet and the client-site plug-in need to be changed. Each tclet requests the desired level of access using “package require Trusted”. The client-site grants the tclet the desired permissions by adding the tclet’s URL to “trusted_tclet” array in the file “\$HOME/shared/policies/trusted.data”.

- For the policy files to be loaded correctly, the environment variable **TCLLIBPATH** needs to be set to “*\$HOME/shared/policies*” in the client shell before it fires up the browser. The **auto_path** variable of the plug-in contains the directories from which Tcl-scripts are automatically loaded on demand. The **auto_path** variable is initialized using **TCLLIBPATH**.
- For debugging purposes, one can create a *Tcl Plug-in console* by setting the environment variable **TCL_PLUGIN_CONSOLE** to 1.

```
setenv TCLLIBPATH $HOME/shared/policies
setenv TCL_PLUGIN_CONSOLE 1
netscape &
```

\$HOME is the default location for the *shared*-directory.

- In the console, one can *echo* the value of **auto_path** and print the value of **trusted_tclets** array.

```
echo $auto_path
parray trusted_tclets
```

For proper installation, the former must contain “*\$HOME/shared/policies*” and the latter must contain URLs for the trusted hosts.

- Typically, one can develop the code using local files and then run it finally from the web-server. This approach is *not* feasible for our case because the URL’s that start with “*ftp://**” cannot be used with these security policies.
- Our web-server, called **Webstar**, runs on a Macintosh. This initially identified a “**.tcl*” file as a *text/plain*, rather than as *application/x-tcl*, causing the browser to misbehave even when the plug-in was installed correctly.
- Transferring files to/from the Mac using *ftp* must be done in binary mode. Otherwise, the browser displays the text of the “**.tcl*”-file, rather than interpret it as a script. Use *ncftp* to improve matters.

- The Netscape Navigator 3.01 on SPARC/SUN-OS 4.1.4 (violin.cs.wright.edu) behaves differently from Navigator 3.0 on SPARC/SUN-OS 4.1 (fleetwood.aa.wpafb.af.mil) even when both have the plug-in installed. In particular, the latter still displays the tcl-file rather than running it, even when the web-server identifies the file correctly. The Tcl/Tk plug-in for Navigator 3.01 and Explorer 4.0 on Windows 95 PCs do not seem to have customizable security policy yet.
- Eventually, we feel we may need a UNIX-based web-server, in order to use standard UNIX utilities in a Client-Server mode through CGI-scripting.

We now describe, in sufficient detail, all the changes made to the VHDL Model Synthesizer code to turn it into a tclet.

- Concatenate all the three tcl-files vhd_gui.tcl, vhd_proc.tcl, and common.tcl into one file called gui.tcl. This eliminates “source”-lines in vhd_gui.tcl.

```
cat vhd_gui.tcl vhd_proc.tcl common.tcl > gui.tcl
```

- Make gui.tcl executable, and replace the first “#!”-line in gui.tcl (due to vhd_gui.tcl) by

```
#!/apps/tcl_tk/tcl/tk8.0b2/unix/wish -f (on hustler)
```

```
#!/usr/local/bin/wish -f (o/w)
```

- ◆ Many UNIX systems do not allow the “#!”-line to exceed about 30 characters in length. So a better approach is to start the script files with the following three lines:

- ◆ `#!/bin/sh`
- ◆ `# the next line restarts using wish \`
- ◆ `exec wish "$0" "$@"`

For details, look at the man-page for wish.

- Hard-code global(environment) variable values by redefining `proc SetPaths` as follows:

```
proc SetPaths {} {
    # Set global env variables.
    global VMGD_LIB VMGS_LIB
    set VMGS_LIB /usr/export/home/ele2/tkprasad/osu_stuff
        # on: fleetwood/hustler.aa.wpafb.af.mil
    #set VMGS_LIB /nfs/valhalla/users26/cs/tkprasad/osu_stuff
        # on: violin.cs.wright.edu
    #set VMGS_LIB http://www.cs.wright.edu/people/faculty/tkprasad/osu_stuff
        # on: www.cs.wright.edu
    set VMGD_LIB $VMGS_LIB/lib
    return 0
}
```

- ◆ VMG_OUTPUT has been deleted. Instead, the VHDL output is stored on the client site at a fixed location determined by the plug-in and the embed-statement in the file “gui.html” as explained later.
- The *Browser Security Policy* of the plug-in supports additional primitives to download files over the web from a given URL, and manipulate them locally. To enable this policy, modify the file “*../shared/policies/browser.data*” by adding the tclet URL as follows.

```
array set browser_tclets {
    ...
    http://130.108.20.20/*      1
    http://www.cs.wright.edu/*  1
}
```

- The tclet must now request *Browser Security Policy* as follows.

```
package require Browser
```

- ◆ We illustrate this further using the following scenerio. To create the GUI window, the tclet requires

`http://www.cs.wright.edu/people/faculty/tkprasad/osu_stuff/lib/database.txt`

It first downloads this file to the local disk over the web and stores it as “*database.txt*” in the directory “*VHDL*” created inside “*\$HOME/.browserTmp/public/*”. The directory name is specified in the embed-statement in “*gui.html*” as

```
<embed
src=http://www.cs.wright.edu/people/faculty/tkprasad/osu_stuff/gui.tcl
width=1400 height=700 directory=VHDL>
```

The actual downloading is accomplished using the primitive

`browser_getURL $fileURL FileReadCallback`

defined for the Browser Security Policy. The *callback* stores the data read into a local file (whose name is the part of the URL following the last “/”) after replacing CNTL-M’s in the data by *newlines*.

```
proc FileReadCallback {URL Reason Contents} {
    CallBackCheck $URL $Reason
    CacheData $Contents [index [split $URL /] end] w
}

proc CacheData {Data FileName Mode} {
    regsub -all "^M" $Data "\n" Lines
    set FileID [open $FileName $Mode]
    puts $FileID $Lines
    close $FileID
}
```

- The following code exhibits very different behavior when run using standalone *wish* from that using the Tcl/Tk plug-in for Netscape 3.01.

```
while {[gets $FileID line] >= 0} {
```

```

        if {[index $line 0] == "class"} {
            } else {
        }}

```

In particular, the plug-in generates an “*unmatched brace error*” at [index \$line 0] when the line is bound to the incomplete command “if {} {”, while the *wish* works fine. This situation arises when reading a multi-line conditional from a file.

This problem can be fixed by ensuring that a complete tcl-command, rather than just a line, is read before invoking lindex as follows.

```

while {[info complete $line] == 0} {
    append line [gets $FileID]
}

```

- The entry boxes in the GUI-area of the Netscape window (due to Tcl/Tk) can be filled in only after moving the mouse away from the GUI-area. The cause of this bizzare behavior is unclear.
- Finally, after garnering all the relevant information about the entity-architecture pair from the user through the GUI, the tclet can download relevant VHDL-template files from the web-server and run the pre-processor to customize them.
 - ◆ Due to a bug in the plug-in, primitives such as tkwait and vwait are not available. So there is no simple way of making the main program wait for the download to complete and the callback to return. (This problem is going to be rectified in a future release of the plug-in.) The precise cause of race condition is unclear, but it may be that the callback is executed in a separate thread.
 - ◆ As a temporary “fix”, we can get by with the following hack: Repeatedly press the “OK” button on the GUI to enable it to download all the relevant files. At the end, it will synthesize the relevant VHDL file. However, it will also create a bunch of windows, one for each VHDL template file downloaded, heralding *error* about the premature death of the interpreter. This is very likely generated because the main thread exited before the callback threads (that were busy downloading) return later. We can safely

ignore the error messages because the downloading has been completed and the final result has been generated. All these problems will go away once we have access to tkwait.

- The C pre-processor `cpp` is used to generate the VHDL code from the templates. Typically, the pre-processor binaries are located at “usr/lib/cpp”. In the tclet, it is not reasonable to expect `cpp` to be available on the client-site at a standard location. Instead, we wrote the required pre-processor in Tcl to support commands such as `ifdef`, `ifndef`, `else`, `endif`, `include`, etc and strip off C-style comments. This code integrates smoothly with the rest of the Tcl/Tk code.

```
proc tclpp {inFile loadDir} {
    global defineArray definedNames
    set inFileId [open $loadDir/$inFile r]
    set outStr ""
    set copyFlag 1
    while {[gets $inFileId line] >= 0} {
        set keyword [lindex $line 0]
        if {[string match $keyword "#include"]} {
            append outStr [tclpp [lindex $line 1] $loadDir]
        } elseif {[string match $keyword "#ifdef"]} {
            set copyFlag [info exists defineArray([lindex $line 1])]
        } elseif {[string match $keyword "#ifndef"]} {
            set copyFlag [expr ![info exists defineArray([lindex $line 1])]]
        } elseif {[string match $keyword "#else"]} {
            set copyFlag [expr !($copyFlag)]
        } elseif {[string match $keyword "#endif"]} {
            set copyFlag 1
        } elseif {[string first "/" $line] != -1} {
            # C-style comments must begin with /* and end with */
            # and can span several lines. However, the C-directives,
            # tcl-commands and VHDL-code must be on separate lines.
            while {[string first "/" $line] == -1} {
                gets $inFileId line
            }
        }
    }
}
```

```

    } elseif { $copyFlag } {
        set modLine $line
        foreach name $definedNames {
            set temp $modLine
            regsub -all $name $temp $defineArray($name) modLine
        }
        append outStr $modLine "\n"
    } else {
    }
}
close $inFileId
return $outStr
}

```

- To replace `cpp` with `tcldpp`, we need to modify the format of “*defines*”. In particular, the flag “*-D*” is stripped off, and the default value of *I* is made explicit. That is, “*-D_STD*” is turned into “*_STD=I*”. This is finally translated as

```
defineArray(_STD) = 1
```

- This pre-processor can be further modified to run with the `tclet` by changing the action for `#include`. The `tcldpp` takes a file name as input, and downloads it from the URL (obtained by concatenating the URL for the `tclet` directory, followed by `lib`, followed by the file name). It can be easily modified to cache downloaded files locally or store its contents internally as a string, for efficiency reasons.

```

proc tcldpp {inFile} { ...
    browser_getURL $VMGD_LIB/$inFile FileReadCallback
    # pre-processing steps as described earlier
}

```

Methodology : Porting VHDL-93 Parser to Windows-95 Environment

The original VHDL parser has been distributed as a *TeX*-document containing the design and implementation of the VHDL-87 parser and pretty printer in Quintus Prolog (by Peter Reintjes). A *lex*-filter extracts the Prolog code from the *tex*-document.

This system was subsequently ported to SWI-Prolog and upgraded to IEEE 1076-1993 Standard of VHDL-93 by K. Thirunarayan et al. The overall system requires languages and utilities that are typically available on a UNIX system and are in the public domain (e.g., *lex*, *gcc*, *tex*, *swi_prolog*, etc.). L. DeBrock designed and implemented a VHDL-93 Design Browser by adding a graphical user interface written in Tcl/Tk to compose the queries, and a suitable Prolog search engine to execute the queries.

To enable this VHDL-93 Design Browser to be usable in both the UNIX and the Windows-95 environment, and for the ease of dissemination through the World-Wide Web, the original *TeX*-document is being converted into an HTML document. To achieve platform independence, the program to extract the parser code from the HTML document and the GUI, is being re-written in Java.

The earlier version of the lexer stripped off the comments in the VHDL source code. To enable browser to display the source text of the VHDL-93 code, the lexer now maintains an association of the source files with the design units. The `assoc_file_design_unit/4` facts are asserted when a file is loaded. Each fact contains the name of the design unit, the name of the associated file, and the beginning and the ending character positions of the design unit in the file. This also includes the comments that precede the text of the design unit declaration (that were not stored in the parse tree.)

Conclusion

The VHDL Model Synthesis tool has been converted into a *tclet* and is now available from the URL http://www.cs.wright.edu/people/faculty/tkprasad/osu_stuff/gui.html.

It can be run in Netscape Navigator 3.01 (with the Tcl/Tk plugin Version 2) on SPARC/SUNOS 4.1.4. The plug-in must be customized to support the "*Browser Security Policy*" for the tclet. The tclet runs satisfactorily with the remaining problems attributable to the bugs in the alpha-release of the plug-in.

In the future, the tclet will be made to work with Netscape Navigator and Microsoft Explorer on Windows-95 after the corresponding Tcl/Tk plug-in Version 2.0 becomes available for them. (The future releases of the plug-in also promise to fix the bugs we encountered.) The tclet will also be enhanced to accommodate the new features as the Model Synthesizer evolves.

Grid Level Parallelization of an Implicit Solution of the 3D
Navier-Stokes Equations

Karen A. Tomko
Associate Professor
Department of Computer Science and Engineering

Wright State University
3640 Colonel Glen Highway
Dayton, OH 45435-0001

Final Report for:
Summer Faculty Research Program
Wright Laboratory

Sponsored by:
Air Force Office of Scientific Research
Bolling Air Force Base, DC

And

Wright Laboratory

September, 1998

Grid Level Parallelization of an Implicit Solution of the 3D Navier-Stokes Equations

Karen A. Tomko
Assistant Professor
Department of Computer Science and Engineering
Wright State University

Abstract

The objective of my summer faculty project was to work in collaboration with the computational scientists in the CFD Research Branch of Wright Laboratory to develop a parallel implementation of FDL3DI and related tools to support the parallel solution of the Navier-Stokes Equations for unsteady and vortical flows. My time was spent on two primary tasks: 1) Integrating the grid parallel FDL3DI, developed in 1996, with a simulation of the tail buffet phenomenon. 2) Develop a utility to split a single grid into overlapped subgrids to increase the exploitable parallelism for the grid parallel FDL3DI.

The tail buffet application, performs a numerical simulation of the impingement of a streamwise vortex on a plate. The initial grid system employed 4 grids with large size discrepancies. The grid system was manually subdivided to get 11 grids ranging to improve the processor load balance. Both configurations were executed in parallel on the IBM SP2 at the ASC MSRC system, using 4 and 11 processors respectively. The 11 processor run on the IBM SP2 is within 17% of the run time of the four grid serial execution on the Cray C916 system.

In an effort to provide a convenient mechanism for decomposing a grid system into subgrids, I developed the GridSplit utility, which decomposes a single rectangular grid into overlapped subgrids. This tool was used to perform a preliminary scalability study of the grid parallel FDL3DI application for uniform flow.

Grid Level Parallelization of an Implicit Solution of the 3D Navier-Stokes Equations

Karen A. Tomko

1 Introduction

Despite progress in parallel compiler technology, parallel aerospace applications are still primarily hand-crafted. This need for hand-crafting bars many computational scientist from utilizing the computational power of modern parallel systems. The objective of my summer faculty project was to work in collaboration with the computational scientists in the CFD Research Branch of Wright Laboratory to develop tools and techniques which will allow them to take advantage of the computational potential offered by the IBM SP2 and Cray/SGI Origin 2000 which have recently become available at the Aeronautical Systems Center (ASC) Major Shared Resource Center (MSRC) at Wright Patterson Air Force base.

During the summer of 1996, as an AFOSR Summer Faculty Associate, I developed a parallel version of the FDL3DI application. FDL3DI solves the three-dimensional Navier-Stokes equations using the approximate-factorization algorithm of Beam and Warming in conjunction with a newton subiteration procedure to enhance the accuracy for rapid fluid motion. I parallelized the Chimera version of FDL3DI which solves the Navier-Stokes equations for multiple overlapped grids. A simple approach to parallelizing the Chimera method was taken. Each grid is assigned to a separate processor and the interpolated boundary points are exchanged between processors as necessary. This approach requires few modifications to the source and relatively little communication between processors [11].

During the summer of 97, again as an AFOSR Summer Faculty Associate with the CFD Research Branch, I worked on two tasks.

1. Utilize the grid parallel FDL3DI for a simulation of the tail buffet phenomenon.
2. Develop a utility to split a single grid into overlapped subgrids to increase the exploitable parallelism for the grid parallel FDL3DI.

The tail buffet application, developed by Raymond Gordnier and Miguel Visbal [5] performs a numerical simulation of the impingement of a streamwise vortex on a plate. The initial grid system employed 4 grids ranging in size from 69,630 grid points to 1,004,562 grid points. The grid system was manually subdivided to get 11 grids ranging in size from 69,630 points to 207,090. Both configurations were executed in parallel on the IBM SP2 at the ASC MSRC system, using 4 and 11 processors respectively. The 11 processor run on the IBM SP2 is within 17% of the run time of the four grid serial execution on the Cray C916 system.

However, due to the size discrepancies between the grids this initial parallelization of the application is poorly load balanced, and thus underutilizes the parallel computer resources. To address this problem, a tool to split multiple overset grids of varying size into an arbitrary number of equivalently sized subgrids is under development. During July and August I developed the core module of this tool, the GridSplit

utility, which decomposes a single rectangular grid into overlapped subgrids. This tool was used to perform a preliminary scalability study of the grid parallel application.

The rest of this report provides a more in depth discussion of the two tasks outlined above and is organized as follows. Related research is presented in Section 2. A description of the parallelization approach is given in Section 3. It is followed by an account of using this parallel solver for the simulation of the tail buffet phenomenon in Section 4 and a description of the preliminary automatic grid decomposition tool, GridSplit, in Section 5. We conclude with some suggested next steps to be taken toward achieving a scalable parallel FDL3DI.

2 Related Work

FDL3DI has been used by many scientist to compute a variety of unsteady, vortical flows. The application is currently being used to study the aerodynamics of a full F-22 aircraft. A grid parallel version of FDL3DI has been implemented by Tomko and is described in Section 3. In Section 4 we discuss the use the grid parallel FDL3DI to study tail buffet. More Specifically, a numerical simulation of the impingement of a streamwise vortex on a plate was conducted using the model and grid structure described in [5]. Parallel FDL3DI is also being used by Donald Rizzetta to study a synthetic jet.

Many research and industrial groups have parallelized their Navier-Stokes equation solvers for parallel machines. Several of these groups have used a grid level and/or solver level parallel approach similar to that used in the Chimera version of FDL3DI for their multiple grid applications [1, 3, 4, 10, 12]. Ryan and Weeratunga use a hybrid or hierarchical approach, exploiting parallelism at both the grid level and at the solver level. Each grid is assigned some number of processors proportional to its size[10].

For implicit applications, some form of compensation code may be required to maintain numerical accuracy when grids are broken into subgrids for parallelization. Meakin [9] and Lutton and Visbal [8] discuss the numerical accuracy of Chimera (or overset) grid solutions for unsteady flows. Both agree that using Chimera grid methods can compute flow fields with acceptable accuracy. However, the timestep size may have to be reduced or the number of Newton subiterations increased as the number of subgrids is increased.

Many grid partitioning algorithms have been developed for unstructured grids requiring non-overlapped domains. Two software tools providing such algorithms are Chaco [6] and Metis [7]. Blake adapts unstructured grid techniques to overset (overlapped) grids in [2].

3 Grid Parallel FDL3DI

As reported in [11], a simple approach has been taken for parallelizing FDL3DI. Each input grid is assigned to a separate processor. The flow equations for each grid are solved independently in parallel and the interpolated boundary values are also updated in parallel. The boundary data is exchanged between processors then, on each processor, the Chimera boundary conditions and the physical boundary conditions are applied to the assigned grid.

The Single Program Multiple Data (SPMD) parallel programming style is use. The code running on

each processor is identical and the processor identification number is used to determine which grid is assigned to each processor. The MPI message passing library is used for interprocessor communication. Point-to-point communication using send and receive calls are used to exchange the Chimera boundary data between processors.

The parallel algorithm is sketched out below.

Algorithm 1 (Parallel FDL3DI) *Calculate, in parallel, the three-dimensional compressible Navier-Stokes equations with the implicit Beam-Warming algorithm using the Chimera method for overlapped grids. This algorithm runs simultaneously on each processor. Grids are assigned to processors by a mapping between processor id numbers and grid numbers.*

1. *Initialize message passing system*
2. *Read in the program parameters file and the restart file (the entire restart file is read in redundantly on each processor.)*
3. *Determine which boundary data elements must be exchanged between processors*
4. *Increment the time step*
5. *For the grid assigned to this processor*
 - (a) *Perform initialization*
 - (b) *Solve flow equation for current grid*
 - (c) *Calculate flow values for interpolated Chimera boundary points*
 - (d) *Send flow values for interpolated Chimera boundary points to each processor requiring the data*
 - (e) *Wait until all Chimera boundary data are received from other processors*
 - (f) *Update flow values for Chimera boundaries with data from donor grids*
 - (g) *Apply physical boundary conditions to non-Chimera boundaries.*
6. *Repeat Step 5 for each newton subiteration*
7. *Repeat Steps 4 thru 6 for each timestep*
8. *Send final flow results for each grid to processor 0 for output*
9. *Output results to a new restart file*

4 Tail Buffet Simulation

The parallel implementation of the numerical simulation of the impingement of a streamwise vortex on a plate, was developed based on the vectorized version of the simulation which utilizes the sequential FDL3DI application on a Cray C916 system [5]. The simulation model consisted of a delta wing that generated a vortex which subsequently impinged on a thin plate placed downstream of the delta wing.

Grid Number	Grid Dimensions	Grid Size	Grid Solution Time (seconds)
1	$117 \times 54 \times 159$	1,004,562	515.78
2	$65 \times 54 \times 53$	186,030	84.07
3	$35 \times 54 \times 37$	69,930	30.45
4	$112 \times 54 \times 65$	393,120	190.49

Table 1: Grid Sizes and Execution Times for the 4 grid simulation

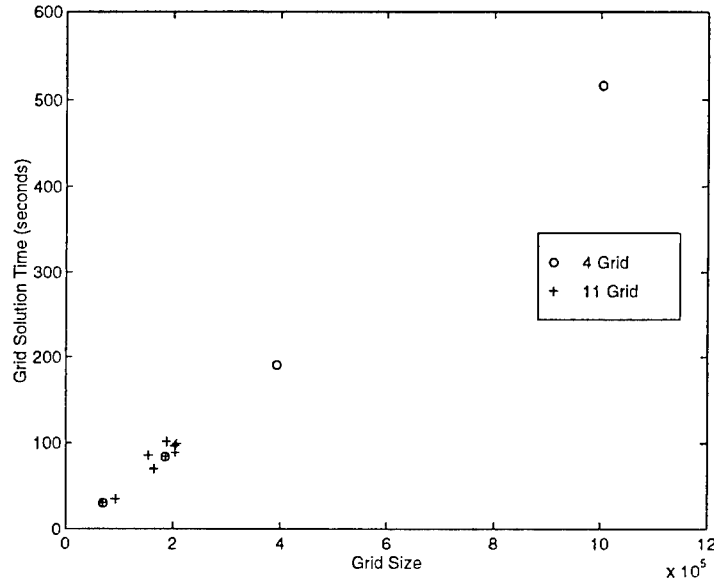


Figure 1: Time taken for solving flow equations on a single grid (NS3D subroutine) as a function of grid size.

A Chimera grid approach in which separate overlapping grids are used for the delta wing and plate has been used for these computations. Four grids, totaling to 1.65 million grid points, were initially employed for this simulation. The grid dimensions and sizes are given in Table 1.

This 4 grid configuration, based on the model configuration, provides very poor load balancing for a parallel implementation since grid 1 makes up 60.7% of the entire grid system. Since the computation time of the FDL3DI algorithm is linear in gridsize (See Figure 1), the parallel 4 grid implementation is limited to a speedup of 1.65 over the serial 4 grid solution.

In order to improve the parallel efficiency, Raymond Gordnier, manually decomposed the 4 grid configuration into the 11 grid configuration described in Table 2. The delta wing grid (grid 1 in the original 4 grid configuration) was split into grids 1-7 in the 11 grid configuration. The original delta wing grid, an H-H grid, was split along the delta wing surface, to simplify the programming for the 11 grid case. Grids 2 and 3 of the 4 grid case are unchanged and map to grids 8 and 9 in the 11 grid configuration. Finally, the O grid surrounding the flat plate was split into two grids, 10 and 11 in the 11 grid configuration. While still not perfectly balanced the 11 grid configuration can potentially achieve a

Grid Number	Grid Dimensions	Grid Size	Grid Solution Time (seconds)
1	22 × 54 × 159	188,892	101.63
2	86 × 30 × 36	92,880	35.11
3	86 × 30 × 64	165,120	70.29
4	86 × 30 × 64	165,120	70.75
5	86 × 29 × 82	204,508	89.27
6	86 × 29 × 82	204,508	88.83
7	18 × 54 × 159	154,548	86.20
8	65 × 54 × 53	186,030	84.28
9	35 × 54 × 37	69,930	30.67
10	58 × 54 × 65	203,580	96.98
11	59 × 54 × 65	207,090	99.35

Table 2: Grid Sizes and Execution Times for the 11 grid simulation

Computer System	Number of Grids	Number of Processors	Execution Time (minutes)	Parallel Speedup
Cray C916	4	1	90	-
IBM SP2	4	1	888	1
IBM SP2	4	4	498	1.8
IBM SP2	11	11	105	8.4

Table 3: A Comparison of Execution Times

speedup of 8.0 over the serial 4 grid version when executed on 11 processors.

A comparison of run times for the configurations described above are given in Table 3. The execution times have been normalized and reflect the time taken to execute 111 timesteps of the tail buffet simulation, with NSUBMX = 2 and no turbulence modeling. For the parallel runs on the SP2 time was measured using MPI_TIME. For the serial runs the time reported by the batch system was used. The xlf and mpixlf compilers with the flags -O3 -qarch=pwr2 -autodbl=dbl4 were used on the SP2 for serial and parallel programs respectively. Additionally, imprecise floating point exception handling was turned on for the parallel runs.

Figure 2 gives the execution times taken on each processor for a 2 timestep simulation of the 11 grid configuration. The bar chart shows how much time is spent computing the flow equations for each grid (black), the time spent exchanging data between grids and waiting for data from other grids (light gray) and time spent reading and writing data files (dark gray). Note small grids spend a lot of time waiting for data from neighboring grids and overall runtime is limited by the processors with the large grids.

In the course of porting the tail buffet application from the C916 to the SP2 a few issues came up. The first is the differences in the default size of an integer between the two systems. The C916 uses eight byte integers while SP2 uses four byte integers. As a result of this difference some of the common block variables were reordered to prevent misalignment on the SP2. Additionally, the floating point representations are

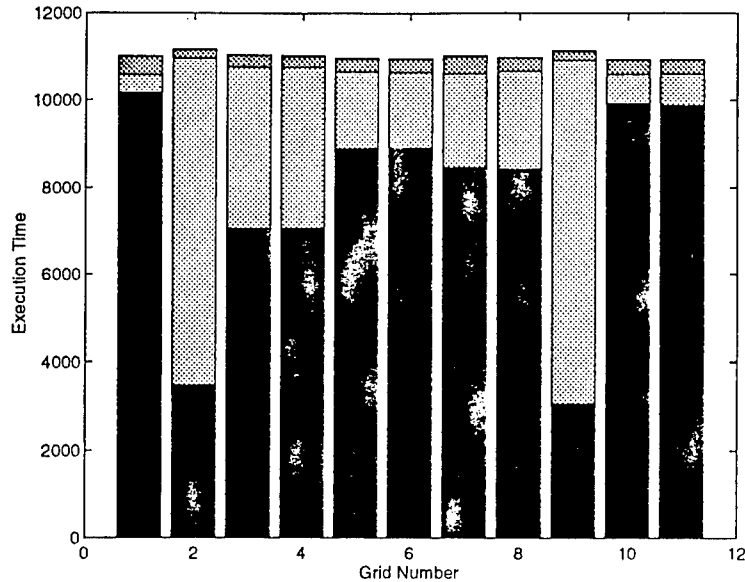


Figure 2: Time taken 11 grid solution broken down by components (I/O time, Communication and wait time, computation time).

different so numerical results vary some between the C916 and the SP2. All of the above make it difficult to translate data files between the two systems. Some translation utilities were written in order to use the C916 generated restart files on the SP2.

5 Automatic Grid Partitioning

The range of experimental cases evaluated for the tail buffet simulation in Section 4 is limited by our inability to quickly decompose grids into equal sized subgrids. An automatic decomposition package is needed to split the regular grids into any number of subgrids. This tool should allow the user control over the degree to which each dimension is split and the amount of overlap between subgrids. In addition the external boundary conditions of the original grid need to be appropriately applied to subgrid boundaries.

GridSplit, a grid partitioning tool for single rectangular grids, was developed this summer. It allows the user to cut the grid in as many locations in each dimension as desired. The input to GridSplit is a restart file (*rstin*) and a parameter file which gives the initial grid dimensions and the number and location of cuts in each dimension of the grid. GridSplit produces a new restart file consisting of the x,y,z coordinates and flow variables for each subgrid and an *intout* file which is compatible with the *intout* file which is generated by Pegsus. The algorithm is outlined below.

Number of Grids	2D or 3D Decomposition	IDIM	JDIM	KDIM
2	2D	100	53	100
4	2D	100	53	53
8	2D	100	29	53
16	2D	100	29	29
32	2D	100	17	29
8	3D	53	53	53
16	3D	53	53	29
32	3D	53	29	29

Table 4: Grid Dimensions for Automatically generated grids

Algorithm 2 (GridSplit) *Split a single rectangular grid into several subgrids.*

1. *Read parameter file*
2. *Determine number of subgrids*
3. *For each subgrid*
 - *determine dimensions*
 - *store interpolation points into hash table*
4. *For each subgrid*
 - *determine boundary points for inter-subgrid boundary*
 - *for each boundary point identify donor subgrid*
5. *For each subgrid*
 - *create list of interpolation points that will be supplied to other grids.*
6. *Read original rstin file*
7. *Write the new rstin file*
8. *Write the new intout file*

GridSplit was used to split a $100 \times 100 \times 100$ grid into 2, 4, 8, 16 and 32 subgrids. Two types of decomposition were performed 1) 2-Dimensional decompositions which only split the J and K dimensions and 2) 3-Dimensional decomposition which split along I, J and K dimensions. The grid sizes and execution times for the various decompositions are given in Table 4 and Figure 3.

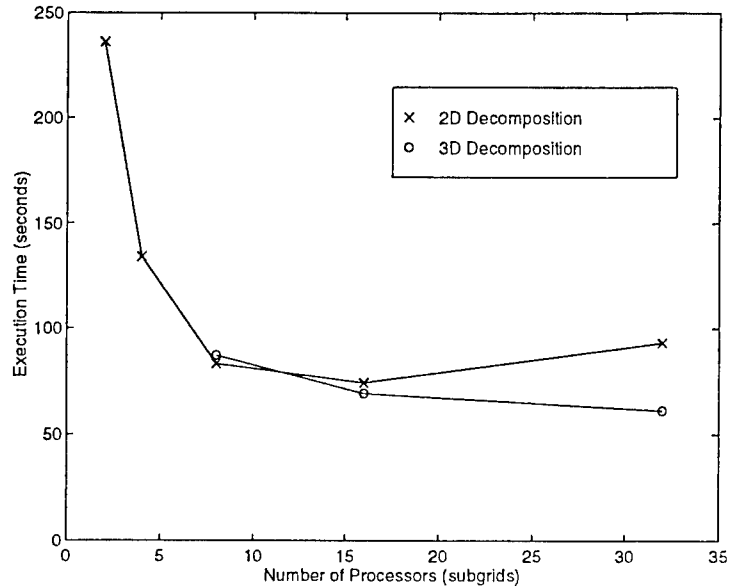


Figure 3: Execution time for a single rectangular grid, decomposed into a varying number of subgrids.

6 Conclusion and Future Work

In this report we have demonstrated that the IBM SP2 is a viable platform for the solution of the 3D Navier-Stokes Equations using the grid parallel FDL3DI application. An 11 grid tail buffet simulation achieved an execution time within 17% of the Cray C916 execution time.

A preliminary GridSplit utility has been developed and demonstrated which provides a convenient means of splitting a single rectangular grid into several subgrids. Using this tool, execution times for 2 to 32 processors were analyzed. Our example decompositions which partition in 3 dimensions exhibit greater scalability than 2 dimensional decompositions. Additional scalability tests on a variety of grid sizes and a larger number of processors are required for a more complete view of the scalability of the application.

The GridSplit tool has many limitations which have not yet been addressed. Currently it only supports rectangular grids. Support for O grids, C grids, H-H grids and possibly others needs to be incorporated to make it generally useful. It also must allow for multiple overset grids as input. Additionally a more convenient user interface should be supplied which provides the ability to display subgrids.

7 Acknowledgements

Thanks to Raymond Gordnier for his assistance with the tail buffet simulation, thanks to Donald Rizzetta for asking and answering several questions pertaining to the grid parallel FDL3DI, and thanks to Douglas Blake for discussions and source code pertaining to grid partitioning. Thanks also to Miguel Visbal for giving me the opportunity to work with the FIMC research group.

Computational resources for the work presented here were supported in part by a grant of HPC time from the DOD HPC Major Shared Resource Center, ASC, Wright-Patterson Air Force Base, Ohio. Additional computer resources were provided by the Ohio Super Computer Center, Columbus OH.

References

- [1] David Bailey, Tim Harris, William Saphir, Rob van der Wijngaart, Alex Woo, and Maurice Yarrow. The NAS parallel benchmarks 2.0. Technical Report NAS-95-020, NASA Ames Research Center, December 1995.
- [2] Douglas C. Blake. Application of unstructured grid domain decomposition techniques to overset grids. In *Eighth SIAM Conference on Parallel Processing for Scientific Computing*, March 1997.
- [3] Rob F. Van der Wijngaart. Efficient implementation of a 3-dimensional adi method on the iPSC/860. In *Proceedings of Supercomputing '93*, November 1993.
- [4] Rob F. Van der Wijngaart and Maurice Yarrow. RANS-MP: A portable parallel navier stokes solver. In *Computational Aerosciences Workshop, NASA Ames Research Center*, August 1996.
- [5] Raymond E. Gordnier and Miguel R. Visbal. Numerical simulation of the impingement of a stream-wise vortex on a plate. *AIAA Paper 97-1781*, June 1997.
- [6] Bruce Hendrickson and Robert Leland. The Chaco user's guide: Version 2.0. Technical Report SAND94-2692, Sandia National Laboratories, Albuquerque, NM, July 1995.
- [7] George Karypis and Vipin Kumar. METIS unstructured graph partitioning and sparse matrix ordering system, version 2.0. Technical report, Dept. Computer Science, University of Minnesota, August 1995.
- [8] Mark J. Lutton and Miguel R. Visbal. Time-accurate validation of the Chimera method for unsteady vortical flows. *AIAA Paper 96-2077*, June 1996.
- [9] Robert L. Meakin. On the spatial and temporal accuracy of overset grid methods for moving body problems. *AIAA Paper 94-1925*, June 1994.
- [10] J.S. Ryan and S.K. Weeratunga. Parallel computation of 3-D navier-stokes flowfields for supersonic vehicles. *AIAA Paper 93-0064*, January 1993.
- [11] Karen A. Tomko. Grid level parallelization of an implicit solution of the 3d navier-stokes equations. Technical report, 1996.
- [12] Jerry C. Yan, Dennis Jespersen, and Pieter Buning. Performance evaluation of OVERFLOW/PVM on a network of workstations. In *Computational Aerosciences Workshop, NASA Ames Research Center*, August 1996.

**A STUDY OF THE PARTICULATE EMISSIONS OF A WELL-STIRRED
REACTOR**

**Max Trueblood
Assistant Professor
Cloud and Aerosol Sciences Laboratory**

**University of Missouri, Rolla
G-7 Norwood Hall
Rolla, MO 65409**

**Final Report for:
Summer Research Program
Wright Laboratory**

**Sponsored by:
Air Force Office of Scientific Research
Bolling Air Force Base, Washington, DC**

And

Wright Laboratory

September 1997

A STUDY OF THE PARTICULATE EMISSIONS OF A WELL-STIRRED REACTOR

Max B. Trueblood
Research Assistant Professor
Melissa R. Wilson
Graduate Student
Cloud and Aerosol Sciences Laboratory

Abstract

A well-stirred reactor system was constructed and a preliminary study of its particulate emissions was made using the University of Missouri-Rolla Mobile Aerosol Sampling system. The test matrix included hydrogen and hydrocarbon fuels where the fuel to air equivalence ratios were varied between lean stoichiometric and rich. Preliminary results indicate that particulate concentrations increased by several orders of magnitude as the equivalence ratio approached 1.0 compared to those for either lean or rich regimes. The size distributions were linear in shape between particle diameters of 10 and 250nm, with the peak at the smaller diameter. Results from this preliminary study were presented at the NASA Workshop on Aerosols, Cleveland Ohio, July 29-30 1997.

A STUDY OF THE PARTICULATE EMISSIONS OF A WELL-STIRRED REACTOR

Max B. Trueblood

Introduction

The emission of particulates from jet engines has received significant interest from the atmosphere and emissions scientific community in recent years. Earlier this year, the EPA released a call-to-arms for particle characterization, citing the detrimental effects of small particulates on the human body¹⁻². This study was undertaken to examine the feasibility of using a well-defined laboratory experiment to represent data obtained from actual aircraft emission measurements, and to possibly provide a fuel formulation-based particle emission mitigation strategy. The Well-Stirred Reactor (WSR) was chosen as an appropriate lab-based test venue because it is currently the closest approximation available to an ideal, Perfectly-Stirred Reactor (PSR) i.e. a reactor in which mixing and transport effects have been minimized.

The data obtained at Wright-Patterson Air Force Base (WPAFB) this summer is an integral part of a much larger data set acquired with the University of Missouri, Rolla Mobile Air Sampling System (UMR/MASS) and other aerosol diagnostic tools employed as part of the following NASA sponsored projects: airborne field campaigns SONEX, POLINAT I & II, SNIFF and SUCCESS and ground-based measurement venues such as the AEDC and NASA LeRC PSL projects, SNIFF, and Air National Guard F-100 engine studies.³⁻¹³

Experimental

The UMR/MASS approach to aerosol characterization of combustion sources is well developed. A schematic diagram of the MASS is given in figure 1. It has been described extensively in the literature and has been used in many test venues. A description of the complete suite of measurements accessible with the UMR/MASS is given in Appendix 1. This preliminary study focused on total particle emissions as represented by the total differential concentration (TCN) and size distributions of particles emitted from the WSR using a range of fuels including H_2 , CH_4 , and Jet A. Additional data was collected on the soluble mass fraction, morphology, and elemental composition of the particle emissions.

The WSR (Figure 2) is a toroidal reactor in which the fuel is prevaporized and then premixed with air and injected into a toroidal combustion chamber. The fuel/air mixture undergoes tremendous turbulent mixing as combustion occurs. Characterization of mixing has been described elsewhere in the literature¹⁴. This stirring process makes the WSR a very good approximation of a PSR, and so a good model of ideal combustion conditions.

Progress

In the initial phase of this project, the final construction of the WSR was completed along with its interface to the UMR/MASS. Specifically the UMR team assisted Wright Lab personnel with the installation of (1) the oil-based temperature control system for the sampling probes; (2) the nitrogen delivery and control system; (3) the Horiba Emissions Analyzers, (4) type B, C and K thermocouples used in the experiment, and (5) the temperature control system for the heated

transfer lines used by UMR and Wright Labs. This installation process took approximately five weeks. All this installation work was essential prior to making particle measurements.

Calibration and Testing

When the reactor was completed, it was given several calibration runs, including one run with a 40% H₂ / 60% N₂ fuel, which was used to determine the system background particle emission level. The remaining calibrations used methane. Initial particle concentrations observed with methane were exceptionally high (30 million particles per cubic centimeter (pcc)); this was determined to be due to alumina particles baking off from the inside walls of the plug flow region (PFR). With continued heating of the internal surfaces of the reactor and the PFR these particle emissions were seen to fall to almost zero, at which point the tests began in earnest. Test fuels used were methane and Jet A. These fuels were varied in terms of fuel to air stoichiometric equivalence ratio ϕ at points below, at and above 1.

Results

Table 1

Fuel	Equivalence Ratio ϕ	TCN (particles pcc)
H ₂ N ₂	1	3.07
CH ₄	0.776	30,000
	1.00	1,700,000
	1.30	800,000
Jet A	1.00	18,000,000
	1.30	140,000,000

Discussion

The H_2/N_2 fuel mixture was studied approximately two weeks after the initial lighting of the WSR. Total particle concentrations, even at $\phi = 1$, were not above 5 particles pcc. This low concentration indicates little or no ablation occurred at the metal sampling probes which were inserted into the WSR. It also indicates no alumina was ablated off the ceramic lining in the WSR-PFR in the form of particulates, at least after the initial calibration runs with methane. In the hydrogen test the small concentrations precluded obtaining any meaningful size distribution data. It should be noted that the highest temperatures obtained with the hydrogen fuel were approximately 1000°C , much lower than the 1700°C typically seen during runs with methane and Jet A. Although a higher percentage of hydrogen would have yielded a higher temperature, this avenue was not pursued for safety reasons.

Methane was the most common fuel used during the present study because of cost, safety, and ease of use. A large set of this data was obtained: well over two hundred size distributions and more than thirty hours of total concentrations logged. The methane data presented in Table 1 were taken on 26 July, 1997 and are representative of data taken at other times. Inspection of Table 1 shows that as f increases from 0.776 to 1.3, the TCN goes from 30,000 to 1,700,000 to 800,000 pcc.

Size distributions obtained for methane (Figures 3 and 4) suggest high particle counts at the lower sizes, possibly even below 1 nm. To increase the sampling range of the MASS at those particle sizes, another pump was added to the system early in the test program. This enabled

particle characterizations at very low particle sizes (below 10 nm). The distributions were almost linear on a log-log plot, indicating the highest concentrations at the lowest sizes, a result often seen in jet exhaust for more conventional fuels.

Jet A was found to have much higher TCN's than methane, by an order of magnitude or more. This was an expected result, as Jet A is a complex mixture of hydrocarbons, which have a high carbon to hydrogen ratio and thus a greater sooting capacity. Methane is the simplest hydrocarbon, having only a single carbon to four hydrogens, and thus less carbon and less soot production capacity per mole of fuel.

The size distributions obtained for Jet A (Figs. 5 and 6) indicate a higher mean particle diameter, and demonstrate a more "log-normal" shape than the methane distributions. The concentrations peaked at 20-30 nm as opposed to the 10 nm and lower peaks observed for methane.

Deliquescence data, used to determine the soluble mass fraction, was taken on both methane and Jet A, and is currently being analyzed.

Conclusions

The following conclusions can be drawn from this preliminary study:

1. The WSR can readily be interfaced to the UMR/MASS thus lending the WSR to MASS type analysis.

2. It was possible to passivate the alumina surfaces within the WSR-PFR to spurious particle production. This was achieved by burning methane in the WSR while monitoring the rate of change of particle emission. Passivation is achieved when the particle emission rate falls to a constant value for a given equivalence ratio and fuel flow rate.
3. Following passivation, background emissions observed using a hydrogen flame were negligible.
4. Particle concentrations varied as a function of fuel to air equivalence ratio peaking at stoichiometric ratios.
5. Particle concentrations varied with fuel formulation increasing with decreasing hydrogen carbon ratios.
6. Size distributions for methane are linear in shape with peaks at low particle sizes. Distributions for Jet A are closer to "log-normal" shape.
7. These preliminary results clearly demonstrate that a valuable database on particle emissions can be developed with further studies where the MASS is interfaced to a WSR.
8. These are first of a kind and unique data where particle emissions from a well defined laboratory burner have been physically characterized in terms of concentration, size distribution, hydration and growth properties and chemical composition.
9. The preliminary results of this study have been presented at the NASA Workshop on Aerosols, Cleveland Ohio, July 29-30 1997, and will be presented at the American Chemical Society Regional Meeting, October 29 - November 1, 1997.

Appendix 1

Aerosol characteristics accessible with the UMR/MASS.

Total Number Concentration N_{tot} - Because of the relative importance of this measurement total particle concentrations are determined by two methods. First, directly, by sending the incoming sample directly to a CN counter. This is a realtime measurement where all particles of effective diameters $> 3\text{nm}$ are detected a minimum sample time of 1 sec. Secondly, the total aerosol concentration, N_{tot} , can be determined indirectly through the integral of the aerosol size distribution function (see subsection on size distributions below):

$$N_{tot} = \int_0^{\infty} (dN/dx) dx \quad (1)$$

Excellent agreement between the direct measurement and size distribution function integration methods is achieved. These data with concomitant CO_2 measurements permit the calculation of the aerosol-related emission index ($\text{EI} = \text{\#particles/kg fuel}$) for aerosols in any given sample taken from aircraft exhaust plumes or other combustion exhaust flow. The MASS has its own i.r. absorption CO_2 detector for realtime EI determination.

Non-Volatile Aerosol Concentration (N_{NVCN}) - This parameter is obtained both directly and indirectly as described for N_{tot} . In this case however the incoming sample is passed through an oven en-route to the CN counter. The temperature of the oven and the residence time of the

sample in the oven are controlled such that complete evaporation of all materials with boiling points below that of the oven temperature is assured. The incoming sample flow is split prior to the oven in order to permit simultaneous measurement of N_{tot} and N_{NVCN} and intercomparison of the two CN counters employed. The non-volatile component of the aerosol in exhaust flow is representative of the soot emissions of the source

Total Mass Concentration - Another primary aerosol parameter, total aerosol mass concentration, can likewise be extracted from the non-volatile CN size distribution, assuming an average density for soot:

$$M = \int_0^{\infty} \left(\frac{4\pi}{3} \right) \rho(x) x^3 (dN/dx) dx \quad (2)$$

This then, with concomitant CO_2 measurements permits the calculation of the mass-related emission index ($\text{EI} = \text{g aerosol/kg}$).

Size Distribution - The aerosol size distribution is an essential aerosol characteristic. The size distribution is the apportionment of aerosol into different size (diameter) categories. This is usually expressed in terms of the differential concentration, dN/dx , which normally is dependent on particle diameter x . $(dN/dx)dx$ represents the particle concentration in the diameter range from x to $x+dx$.

Aerosol sizing in the diameter range 3nm - 300nm is achieved using differential mobility techniques. For diameters >300nm optical particle sizing techniques are employed.

Fixed Size Aerosol Concentration N_{FIX} - The differential mobility technique is also used to monitor, in real time, a fixed size aerosol. In this case the incoming sample is split of into another channel where a fixed diameter is selected through differential mobility analysis. This concentration is as described above using a CN counter.

Reactivity (Growth and/or Hydration Properties) - The growth and/or hydration properties of the aerosol must be characterized. These properties will control the ability of the aerosols to condense water or other species when they are exposed to moisture and other jet exhaust products. The total aerosol mass is subject to rapid changes in response to humidity variations. In turn this condensed water will control the chemical reactivity of the hydrated particle and influence its final evolution in the atmosphere. The hydration properties are usually represented in terms of the dry aerosol's soluble mass fraction (the fraction of the particle's total mass which is soluble in water) or critical supersaturation. A particle's critical supersaturation identifies the relative humidity (greater than 100%) which will cause the particle to become a freely growing droplet. Aerosol hydration properties are usually measured by observing the aerosol's response to different supersaturations in a cloud chamber, i.e. their critical supersaturation spectrum, or to 100% relative humidity conditions in a haze chamber, the deliquescence. The latter approach is employed in the MASS.

Threshold Soluble Mass Fraction Aerosol concentration N_{TSMF} - In this case the deliquescence technique is employed to monitor in real time the concentration of aerosols of fixed dry size that have a threshold soluble mass fraction.

Particle Morphology, Elemental Composition, and Molecular Composition - Other physical and chemical characteristics of the exhaust aerosols will be accessed. These will include Particle Morphology, Elemental Composition, and Molecular Composition. Here the strategy will be to collect aerosol samples on slides and/or filters for subsequent analysis, employing techniques such as SEM, FTIR microscopy and ultra-trace analysis separations mass spectroscopy, at analytical laboratories at UMR.

Acknowledgments

The authors would like to thank the following people for their help and support during this study:

Cpt. Robert Mantz, Lt. Cary Baird, Dr. Melvin Roquemore, Mr. James Blust, Mr. Greg Tibbs, Mr. Greg Conrad (*AFWL*), Dr. Philip Whitefield, Dr. Donald Hagen (*UMR*), RDL.

References

1. <http://www.c-ka.com/naaqs.htm>
2. <http://www.envirobiz.com/newsdaily/961202e1.htm>
3. Hagen, D.E., and P.D. Whitefield, "Particulate Missions in the Exhaust Plume from Commercial Jet Aircraft Under Cruise Conditions", J. Geophys. Res. Atmos. 101, 19551-19557 (1996).
4. Arnold, F., J. Schneider, H. Schlager, P. Schulte, P. Whitefield, D. Hagen and P. Van Velthoven, "Observation of upper tropospheric sulfuric dioxide- and acetone-pollution: Potential implications for hydroxyl radical and aerosol formation", Geophys. Res. Letts. 24, 57-60 (1997).
5. Schlager, H., P. Konopka, P. Schulte, U. Schumann, H. Zereis, F. Arnold, D. Hagen, P. Whitefield and J. Ovarlez, "In situ Observations of Air traffic Emission Signatures in the North Atlantic Flight Corridor", J. Geophys. Res. 102, 10739-10750 (1997).
6. Hagen, D.E., P.D. Whitefield and Max B. Trueblood, "Particulate Characterization in the Near Field of Commercial Transport Aircraft Exhaust Plumes Using the UMR-MASS". Proceedings of the "International Scientific Colloquium on the Impact of Emissions From Aircraft and Space Craft Upon the Atmosphere," Cologne Germany, April 1994.
7. Experimental Characterization of Gas Turbine Emissions at Simulated Flight Altitude Conditions. Ed. Robert Howard, AEDC TR-96-3 June 1996.
8. Pollution from Aircraft Emissions in the North Atlantic Flight Corridor, Contract no. EV5V-CT93-0310(DG 12 DTEE) Ed. U. Schumann, Commission of European Communities Final Report August 1996.

9. Whitefield, P.D., and D.E. Hagen, "Particulates and Aerosols Sampling from Combustor rigs Using the UMR MASS". AIAA 95-0111 33rd Aerospace Sciences Meeting, Reno January 1995.
10. Lilenfeld, H.V., P.D. Whitefield and D.E. Hagen, "Soot Emissions from Jet Aircraft". AIAA 95-0110 33rd Aerospace Sciences Meeting, Reno January 1995.
11. Whitefield, P.D., M.B. Trueblood and D.E. Hagen, "Size and hydration Characteristics of Laboratory Simulated Jet Engine Combustion Aerosols". Particulate Sci. and Tech. 11, 25, 1993.
12. Lilenfeld, H.V., P.D. Whitefield and D.E. Hagen, "Soot Emissions from Jet Aircraft". (ICAS-96-4.1.3) 20th International Council Aeronautical Science Congress/AIAA Aircraft Systems Conference, Sorrento Sorrento Italy, September 1996.
13. Whitefield, P.D., D.E. Hagen, J. Paladino, M.B. Trueblood, and H.V. Lilenfeld, "Ground-based Measurements of Particulate emissions from Sub-sonic and Super-sonic Transports" Proceedings of the 30th Section Anniversary Technical meeting Central State Section of the Combustion Institute: Combustion Fundamentals and Applications (Paper #39), St. Louis May 1996.
14. Blust J. W., D.R. Ballal, and G.J. Sturgess, "Emissions Characteristics of Liquid Hydrocarbons in a Well Stirred Reactor," AIAA Paper No. 97-2710, 1997.

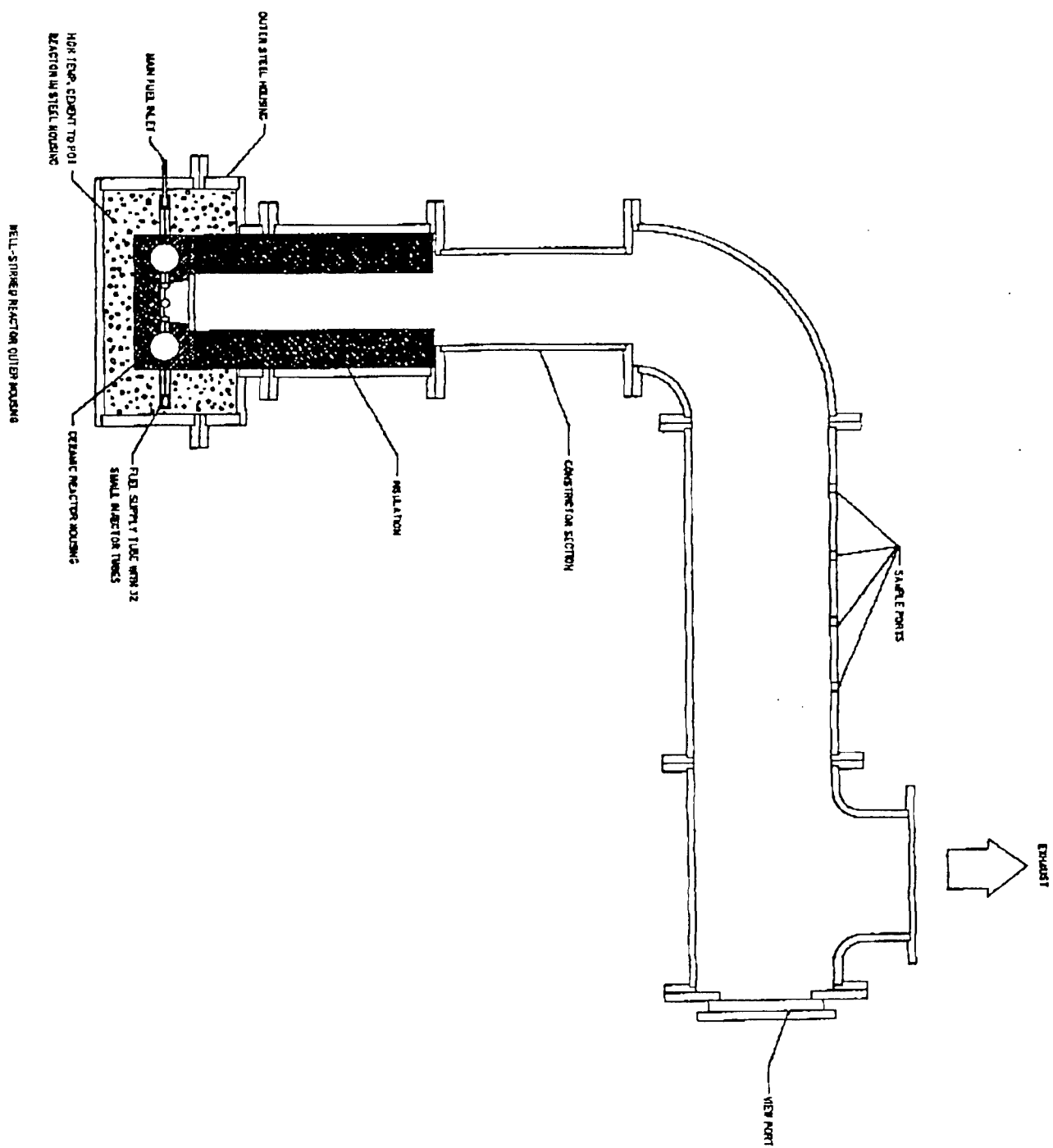
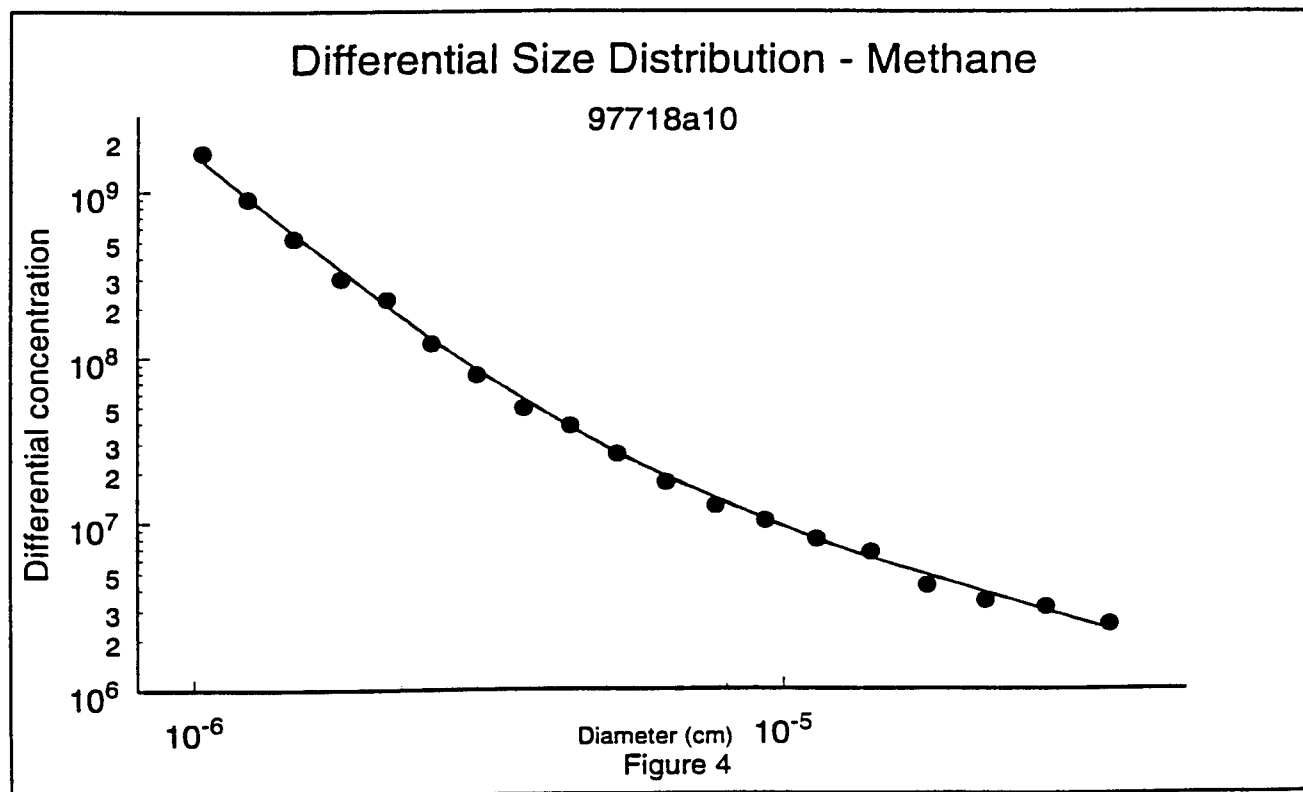
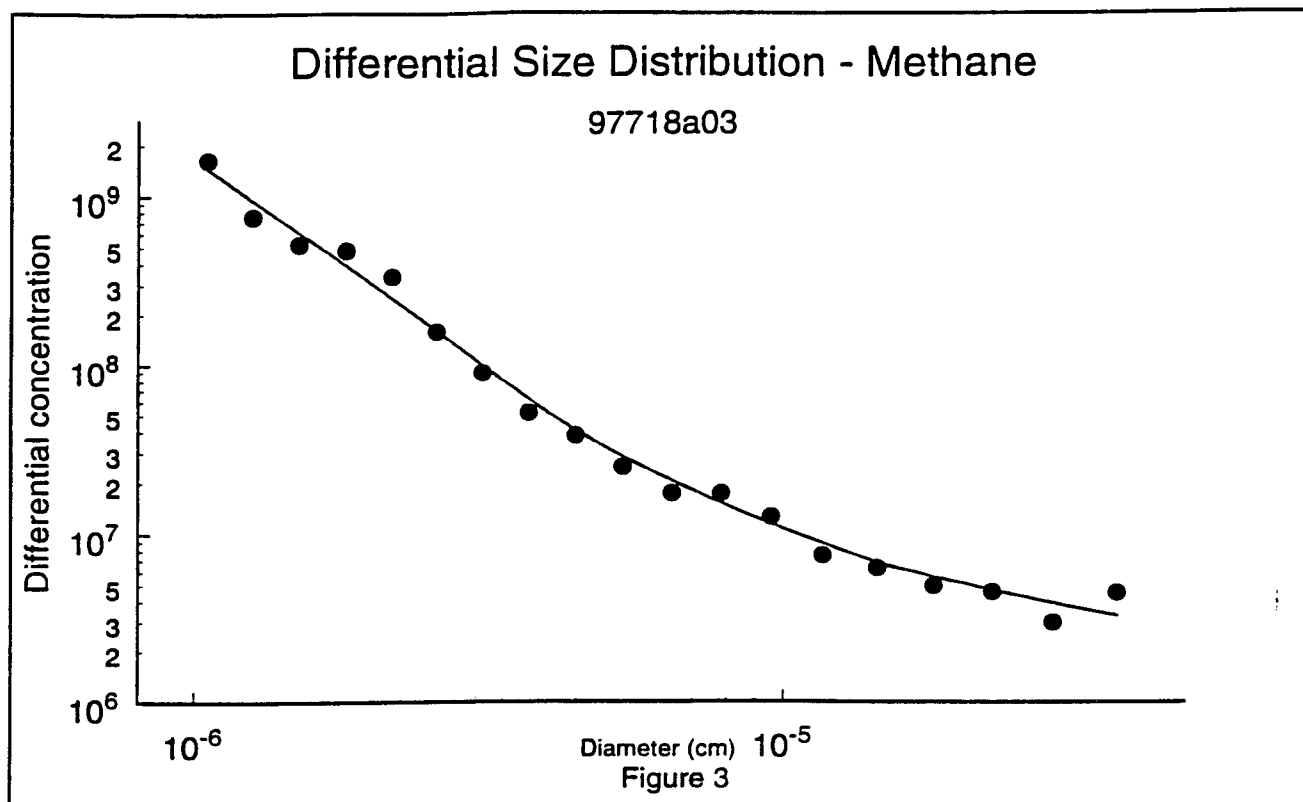
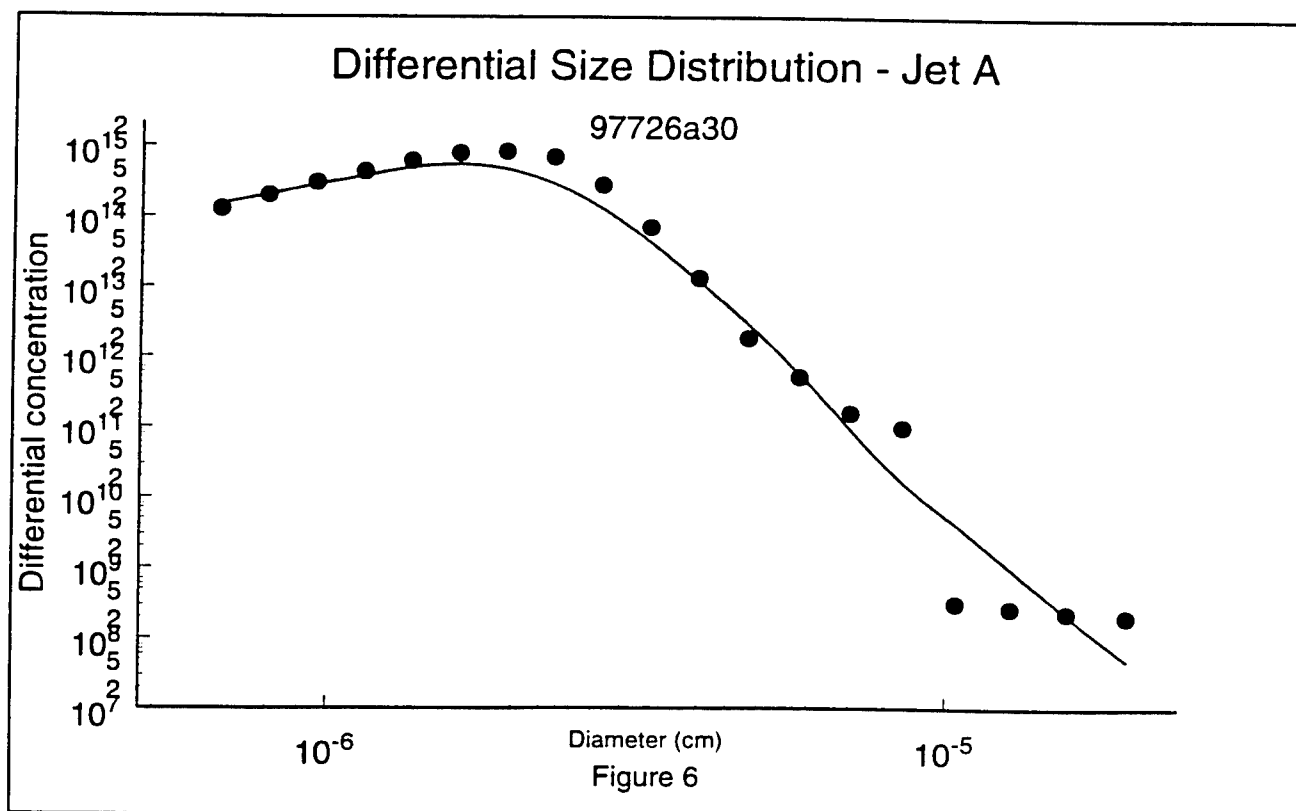
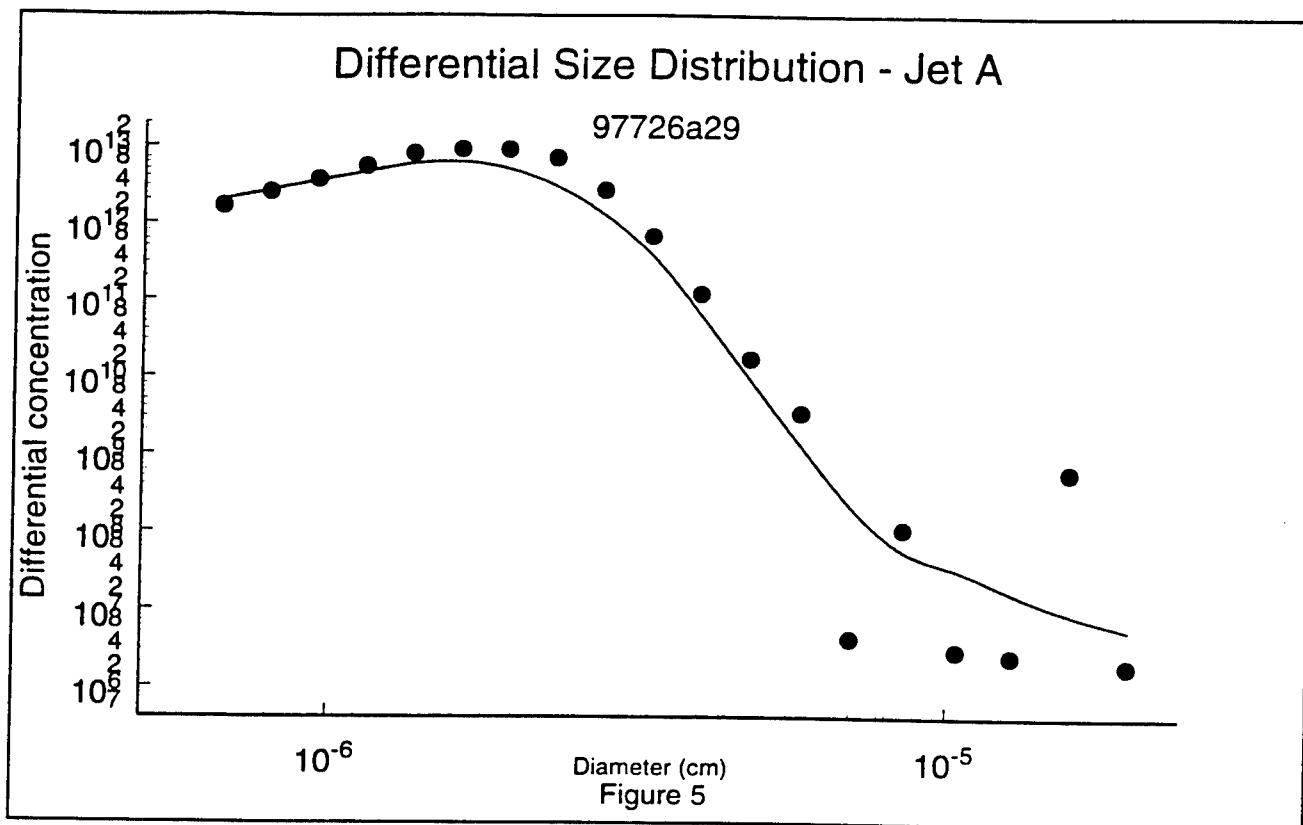


Figure 2





**DISLOCATION DYNAMICS IN HETEROJUNCTION BIPOLAR TRANSISTOR
UNDER CURRENT INDUCED THERMAL STRESS**

**C.T. Tsai
Associate Professor
Department of Mechanical Engineering**

**Florida Atlantic University
777 Glades Road
Boca Raton, FL 33431**

**Final Report for:
Summer Faculty Research Program
Wright Laboratory**

**Sponsored by:
Air Force Office of Scientific Research
Bolling Air Force Base, DC**

and

Wright Laboratory

August 1997

DISLOCATION DYNAMICS IN HETEROJUNCTION BIPOLAR TRANSISTOR UNDER CURRENT INDUCED THERMAL STRESS

C.T. Tsai
Associate Professor
Department of Mechanical Engineering
Florida Atlantic University

Abstract

The dislocation densities generated in the Heterojunction bipolar transistor (HBT) are caused by the current induced thermal stresses. A modified dislocation generation model is developed and then employed to calculate the increment of dislocation densities versus time in the HBT. Different stressing current densities and initial dislocation densities are used to verify the validity of this modified model. The results show that the increasing rate of dislocation density strongly depends on the stressing current density and lightly depends on the value of initial dislocation density.

DISLOCATION DYNAMICS IN HETEROJUNCTION BIPOLAR TRANSISTOR UNDER CURRENT INDUCED THERMAL STRESS

C.T. Tsai

Introduction

Heterojunction bipolar transistor (HBT) offers some attractive features such as high maximum oscillation frequency, high power handling capability and low $1/f$ noise. HBTs are now considered a strong contender in high frequency A/D converter, microwave high power amplifier, digital high speed communication. However, there are a number of failure mechanisms occurred in HBT that have become a great concern on device's reliability. One of the failure mechanisms is due to the dislocations generated in the HBT. In this study, we focus on the dislocation dynamics, i.e., the multiplication and movement of dislocation as functions of time, generated by the current induced thermal stress.

Dislocation is an important defect in semiconductor. Free carrier mobility is adversely affected by the presence of dislocation. The charge states at dislocation alter the occupation probability, and thus the Fermi level[1]. In field effect transistor (FET), dislocation proximity effect causes threshold voltage shift of a GaAs FET[2]. In p-n junction, dislocation is considered as a nonradiation recombination center. Therefore, it lowers the current gain of bipolar junction transistor and the conversion efficiency of solar cell[3]. The dark line defects (DLDs) observed in GaAs heterojunction laser and later the GaP light emitting diode are the prominent feature in the devices after hours of operation. DLD was also observed in HBT, and it is correlated to early failure of the device[4]. The results of these studies seem to suggest that DLD is

progressively generated by the current induced stress, and it is a common phenomenon occurred in minority injection devices including HBTs. The DLDs were found to be dislocation network[5]. Dislocation is the result of achieving a stable mechanical energy in the crystal under stresses. Therefore, the process-induced stress and the stress due to mismatched crystalline in the structure will affect its propagation and generation, in addition to the current induced stress. Another TEM observation of HBT after being subjected to current stress shows formation of dislocation and microtwin formation[6]. Using In-doped base in HBT to counter balance the C-dopant induced stress is found to be effective in slowing the degradation of the device, and the mean-time-to-failure (MTTF) has been demonstrated to be longer than 10^5 hours operating at 50 kA/cm^2 current density[6].

The majority of dislocation density are caused by excessive mechanical stresses. These include the thermal stress generated by the temperature change in the device during operation, and mismatched stress which are generated by the epitaxial layer grown on lattice-mismatched layer, and the metal- semiconductor interfaces. A constitutive equation which was developed originally by Haasen for relating the dislocation dynamics to plastic deformation, was employed by Tsai to develop a finite element model for predicting dislocation formation in semiconductor crystal growth from the melts[7]. In this study, a finite element model developed by Tsai is modified and applied to a HBT for calculating dislocation density generated by the current induced stress.

Finite Element Modeling. Results and Discussions

The HBT studied here is an axisymmetric structure so that a 2-dimensional axisymmetric finite element model can be used in this study. A total of 876 8-node axisymmetric elements are used to model the HBT structure shown in Fig. 1(a). Figs. 1(a)-1(d) show the default axisymmetric structure of a thermal shunt AlGaAs/GaAs HBT[8]. The active device has a diameter of $10\text{ }\mu\text{m}$. The collector, base and the wide band gap emitter layer thickness are 10000A, 1000A, 500A, respectively. The sub-emitter GaAs is 1000 A, and the nonalloyed contact layer thickness of InGaAs is 500 A. The thermal shunt thickness is $20\text{ }\mu\text{m}$, and the substrate thickness is $600\text{ }\mu\text{m}$. A total of 876 8-node axisymmetric elements are used to mesh the HBT structure shown in Fig. 1(a), where the total number of node is

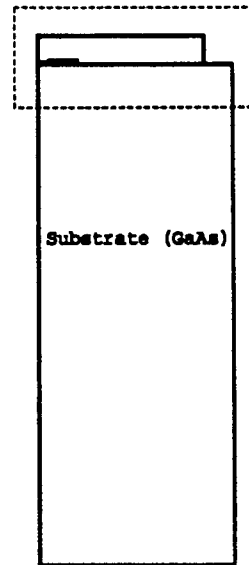


Fig. 1(a). Default structure of an axisymmetric AlGaAs/GaAs HBT.

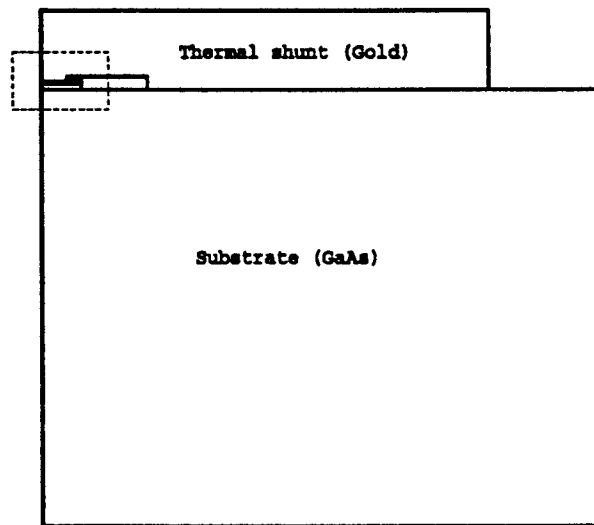


Fig. 1(b). Zoomed from the dashed box in Fig. 1(a).

2643. The temperature distribution is calculated using image approximation[9]. The default initial dislocation densities are nonuniform and assumed to be 10^4 cm^{-2} in GaAs, 10^5 cm^{-2} in AlGaAs and 10^6 cm^{-2} in InGaAs.

Three bias conditions giving current density of 50, 75 and 100 kA/cm^2 and a collector-emitter voltage of 2V were used in this calculation. Figs. 2(a) and 2(b) shows the temperature distribution in the default HBT (where e-b junction is located at the interface of base and collector) biased at 75 kA/cm^2 , where the maximum temperature of about 485°K is near the e-b junction. Figs. 3(a)-3(d) shows the evolution of the dislocation density distribution in the active device region at 75 kA/cm^2 at operation time of 2.4, 10.7, 48 and 200 hours, respectively. The dislocation density near the emitter-

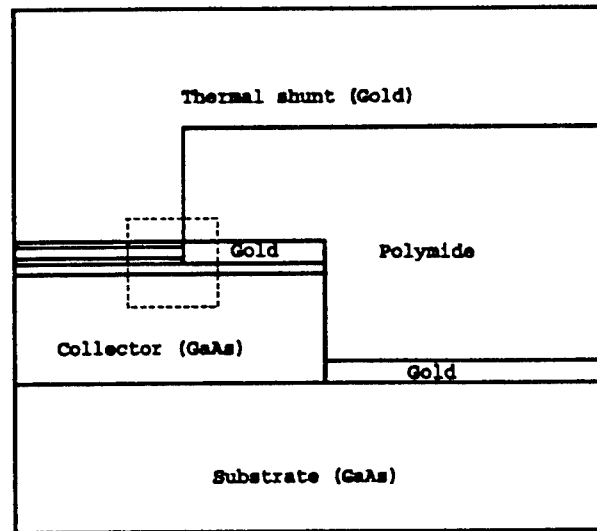


Fig. 1(c). Zoomed from the dashed box in Fig. 1(b).

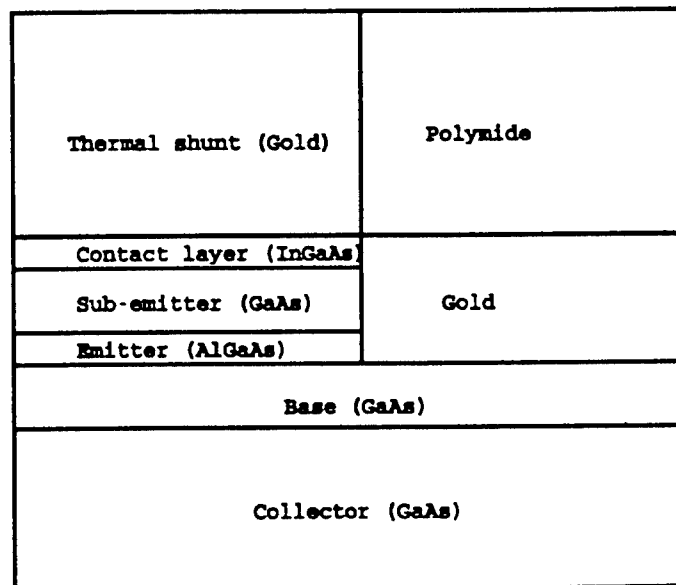


Fig. 1(d). Zoomed from the dashed box in Fig. 1(c).

base junction is initially maximum at the center of the junction as shown in Fig. 3(a). As time elapses, the dislocation density is progressively increases, and the maximum dislocation moves to the edge of the junction due to the stress redistribution from plastic deformation as shown from Figs. 3(b) to 3(d). Fig. 4 shows the dislocation density in the center of the emitter-base junction as functions of time for those three current densities. It shows that as current increases, both the dislocation generation rate and the stationary dislocation density are increased. The times to reach the stationary state are 0.8, 800, and 10^6 hours, for 100, 75 and 50 kA/cm², respectively. The stationary dislocation densities are 2, 1, and 0.4×10^8 cm⁻², for 100, 75 and 50 kA/cm², respectively. Since dislocation behaves as recombination center, this result infers that MTTF due to current degradation and the initial rate of current gain change is large at a large current density which is consistent with the experimental observation.

Finally, the results of the initial dislocation density dependency is shown in Figs. 4 and 5. The low initial dislocation density (10^4 cm⁻² uniformly across the entire structure) shows a similar results. The operation time to reach the stationary dislocation density and the final values of the stationary dislocation density are only slightly less compared to those for nonuniform higher initial dislocation density as shown in Fig. 4.

Summary

To summarize, the dislocation prediction in HBT under current stress taking into account the thermal stress and the heterostructure was conducted. It is found that the dislocation generation is strongly affected by the stressing current density. The dependence of the initial dislocation is also discussed. The latter result suggests that a sophisticated phenomenon of the

recombination enhanced defect diffusion may be important[10]. This is subjected to a further study. The effects due to structure and process parameters such as the thermal shunt thickness and the substrate thickness will also be followed.

References

1. R. M. Broudy and J. W. McClure, "Statistics of the Occupation of Dislocation Acceptors," **J. Appl. Phys.** vol. 31, pp. 1511-1516, 1960.
2. S. Miyazawa and K. Wada, "Mechanism for the Threshold Voltage Shift of a GaAs Field-Effect Transistor around Dislocations," **Appl. Phys. Lett.** vol. 48, pp. 905-907, 1986.
3. M. Yamaguchi, A. Yamamoto, and Y. Itoh, "Effect of Dislocation on the Efficiency of Thin-Film GaAs Solar Cells on Si Substrates," **J. Appl. Phys.** vol. 59, pp. 1751-1753, 1986.
4. T. Henderson, W. L. Chen and M. Sanna, "Reliability of GaAs-Based Heterojunction Bipolar Transistors," **Proceeding of GaAs MANTECH**, pp. 38-41, 1997.
5. P. W. Huchinson and P. S. Dobson, "Defect Structure of Degraded GaAlAs-GaAs Double Heterojunction Lasers," **Phil. Mag.** vol. 32, pp. 745-754, 1975.
6. H. Sugahara, J. Nagano, T. Nittono, and K. Ogawa, "Improved Reliability of AlGaAs/GaAs Heterojunction Bipolar Transistors with a Strained-Relaxed Base," **Proceeding of GaAs IC Symposium**, pp. 115-118, 1993.
7. L. Y. Li, C. T. Tsai, and C. S. Hartley, "Numerical Prediction of Dislocation Densities Generated in Si, GaAs and InP Crystals Grown from Melt," **Proceedings of the 15th Riso International Symposium on Materials Science**, pp. 393-398, 1994.
8. B. Bayraktaroglu, J. Barrette, L. Kehias, C. I. Huang, R. Fitch, R. Neidhard, and R. Scherer, **IEEE Electron Device Lett.** vol. 14, pp. 493, 1993.
9. L. L. Liou, T. Jenkins and C. I. Huang, "Dc Power Limitation of the Heterojunction Bipolar Transistor with Dot Geometry: Effect of Base Potential Distribution on Thermal Runaway," **Soli-State Electronics** vol. 41, pp. 871-877, 1997.
10. L. C. Kimerling, "Recombination Enhanced Defect Reactions," **Solis-State Electronis**, vol. 21, pp. 1391-1401, 1978.

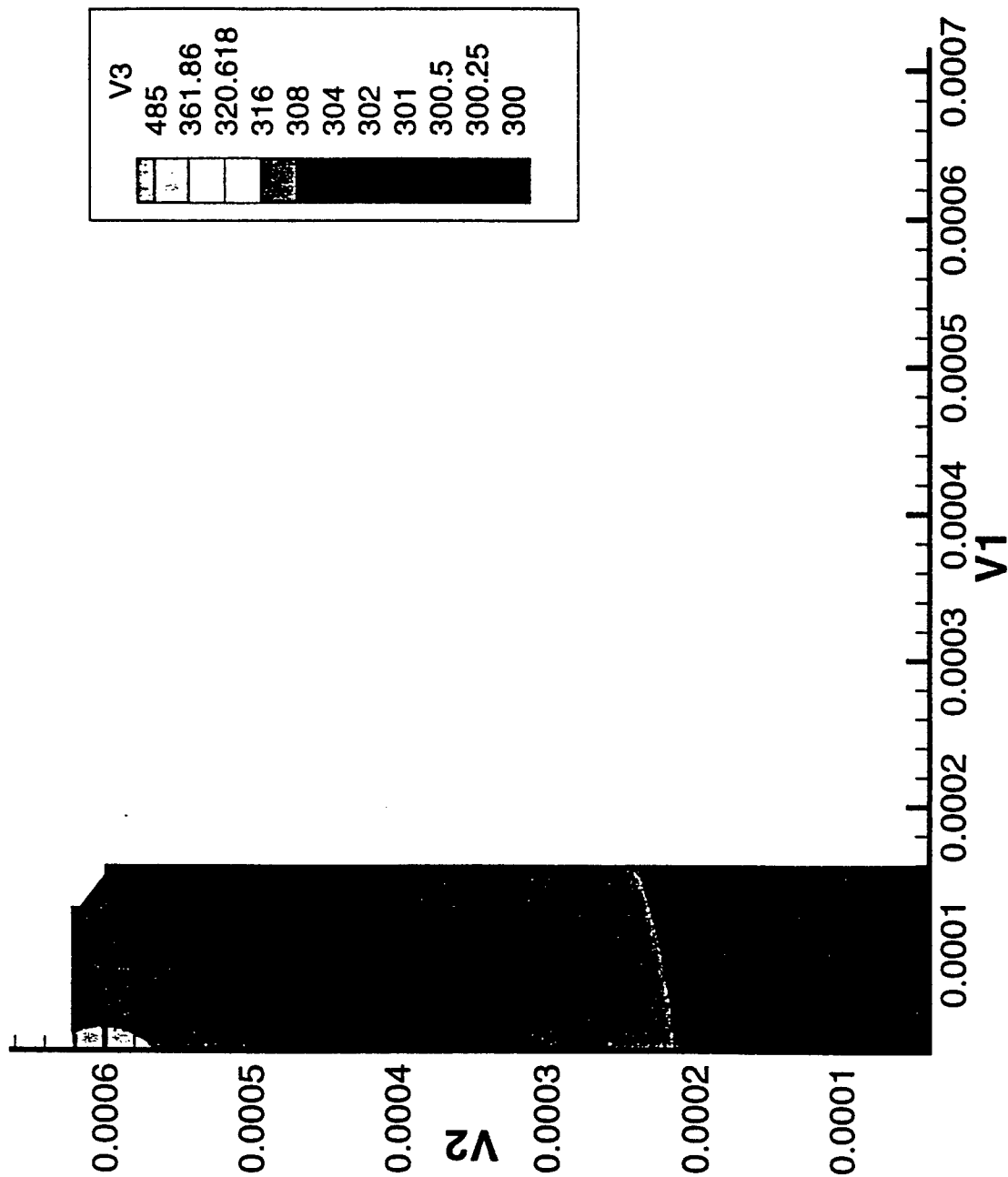


Fig. 2(a). Temperature distribution in the default HBT, V1 and V2 are the r and z coordinates in meter, V3 represents the absolute temperature.

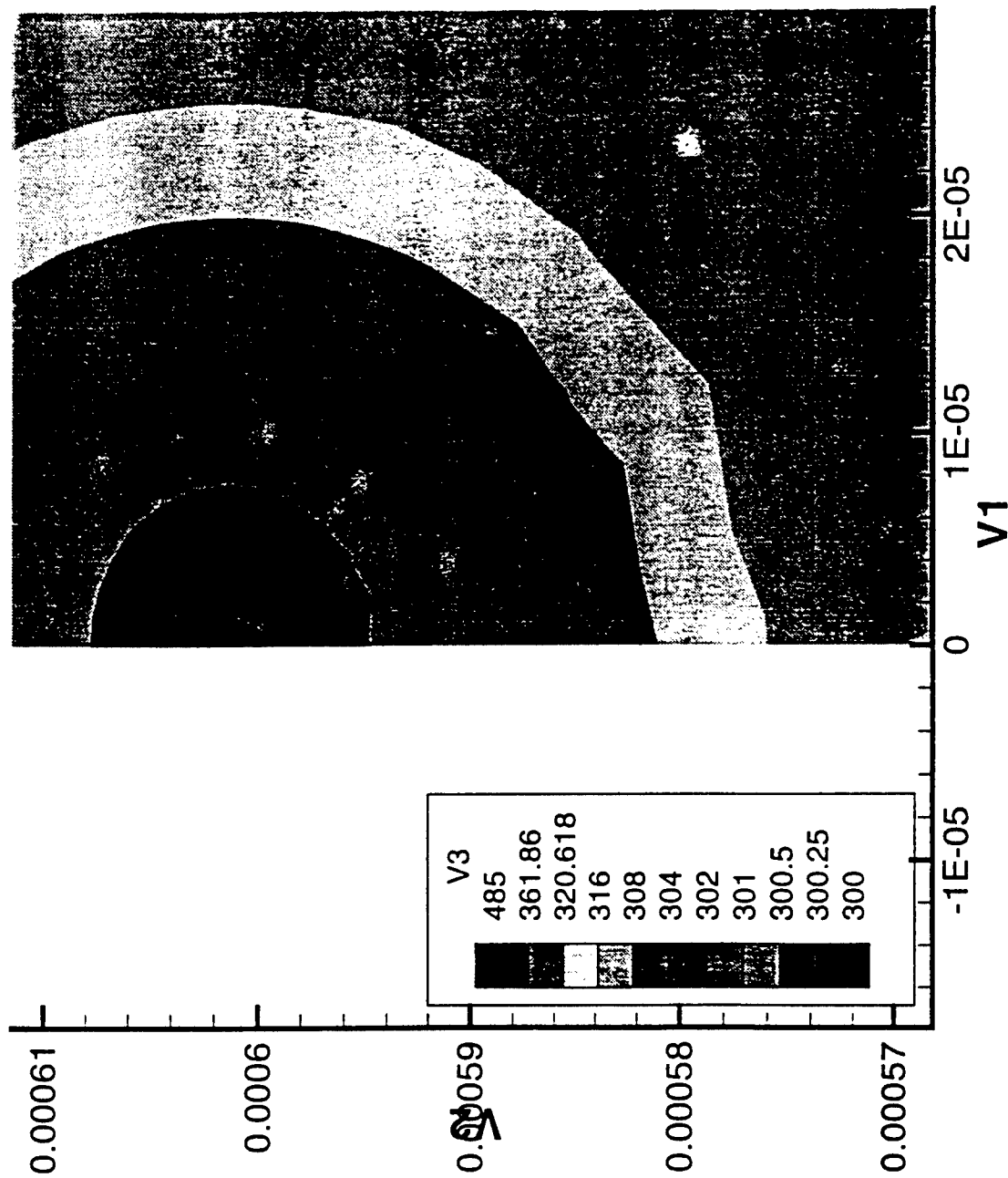


Fig. 2(b). Temperature distribution near the emitter-base junction of the default HBT, V1 and V2 are the r and z coordinates in meter, V3 represents the absolute temperature.

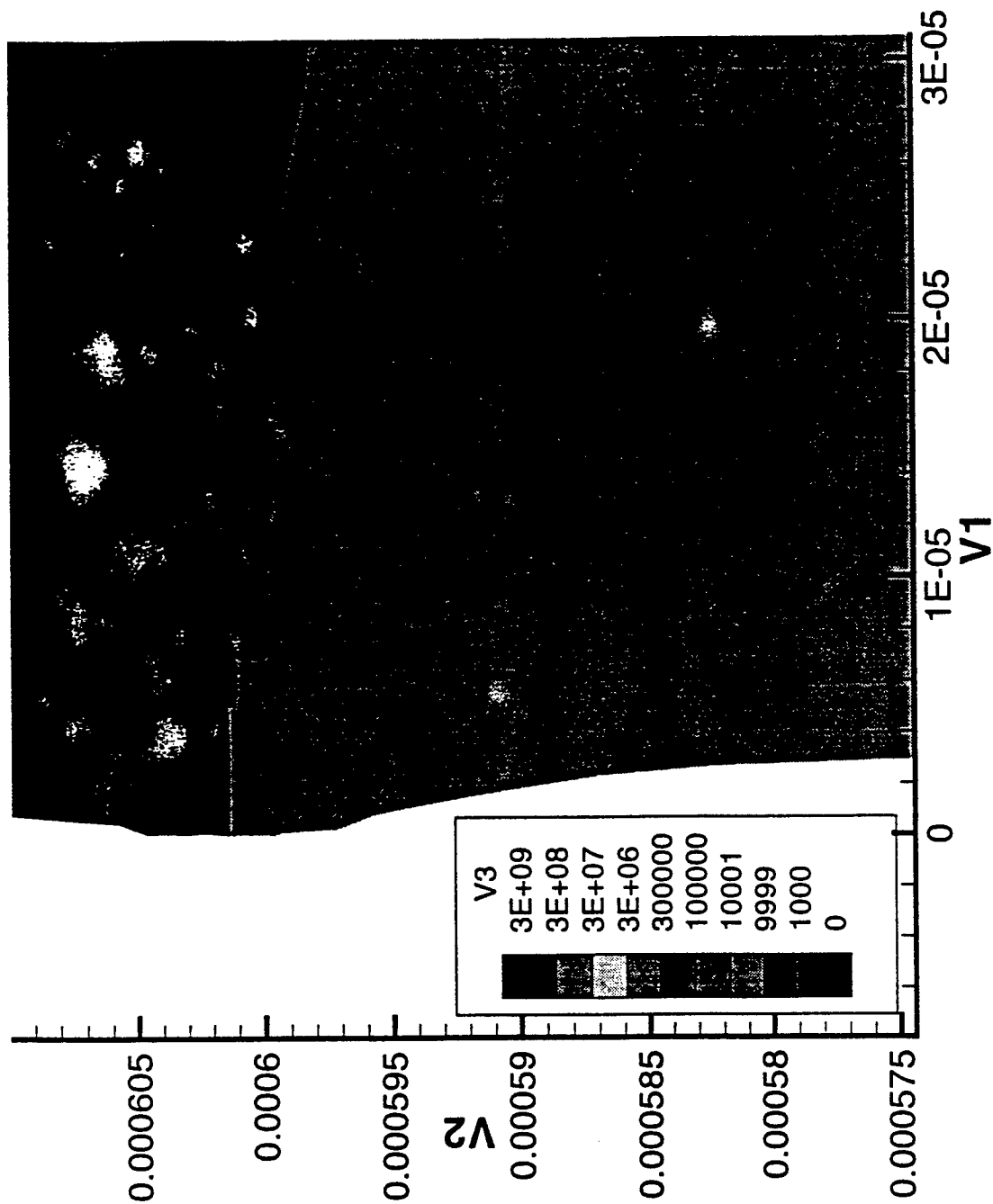


Fig. 3(a). Dislocation density contour plot at $75\text{kA}/\text{cm}^2$ after 2.4 hours of operation, $V1$ and $V2$ are the r and z coordinates in meter, $V3$ represents dislocation density per cm^2 .

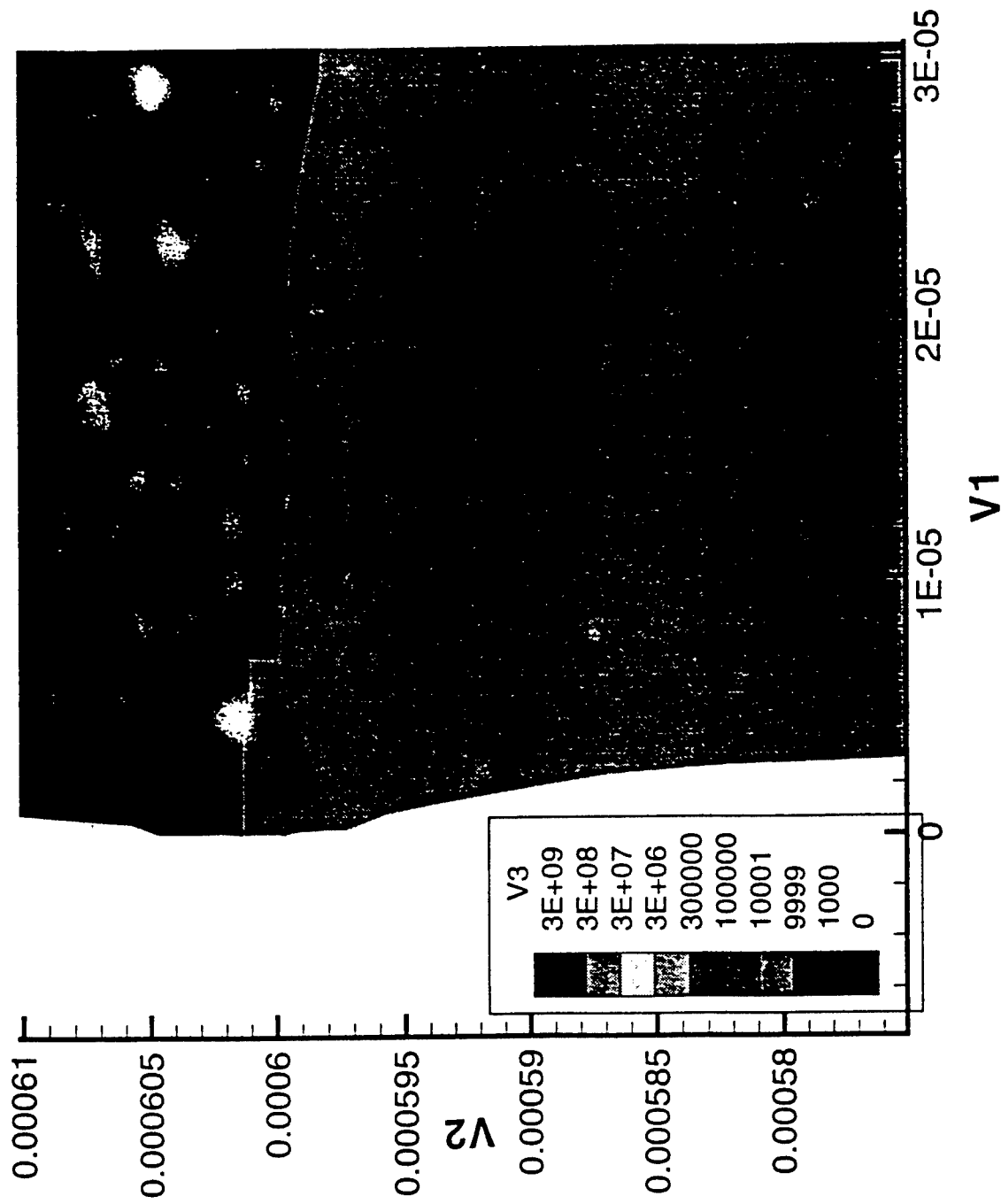


Fig. 3(b). Dislocation density contour plot at 75kA/cm² after 10.7 hours of operation, V1 and V2 are the r and z coordinates in meter, V3 represents dislocation density per cm².

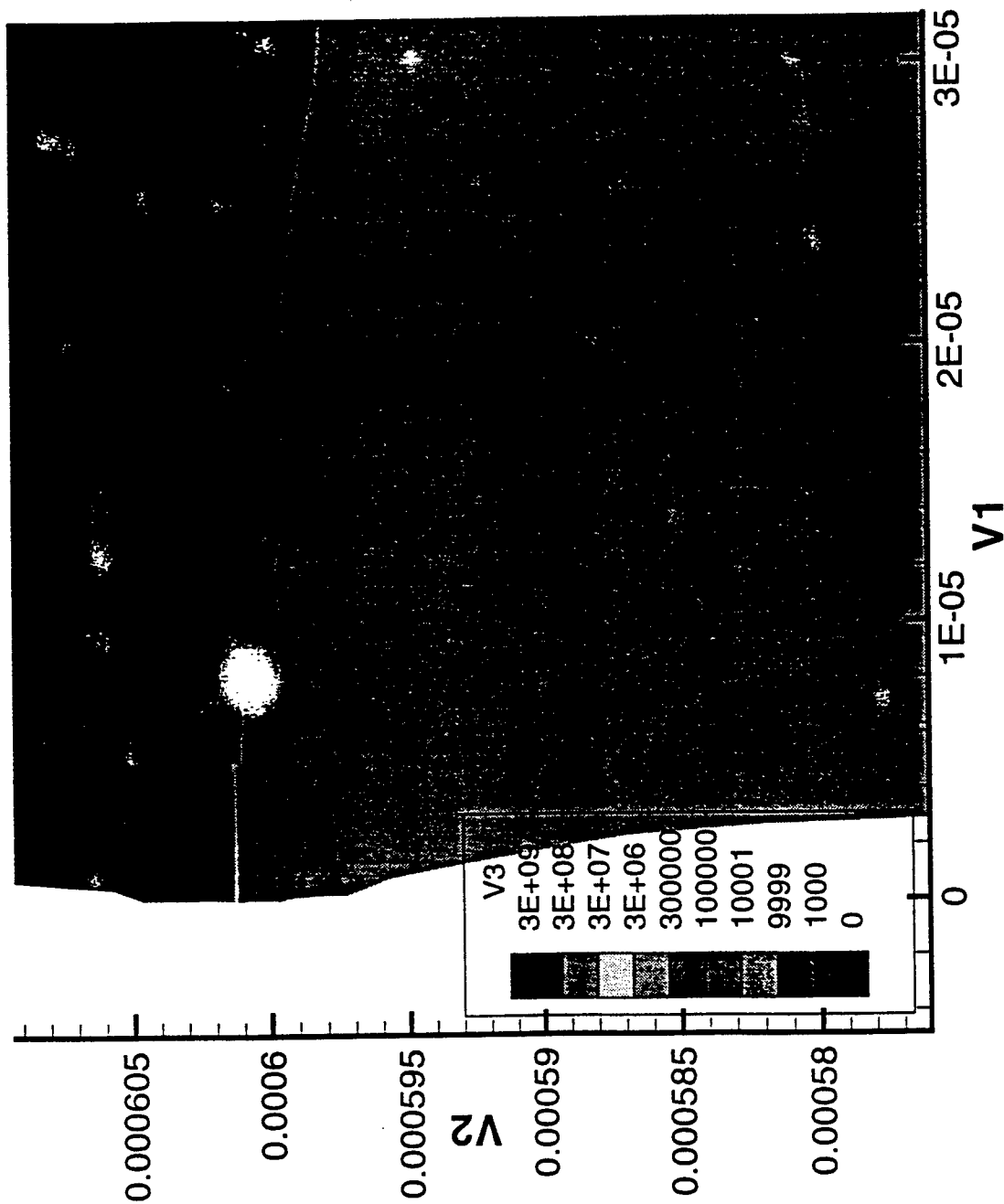


Fig. 3(c). Dislocation density contour plot at $75\text{kA}/\text{cm}^2$ after 48 hours of operation, V_1 and V_2 are the r and z coordinates in meter, V_3 represents dislocation density per cm^2 .

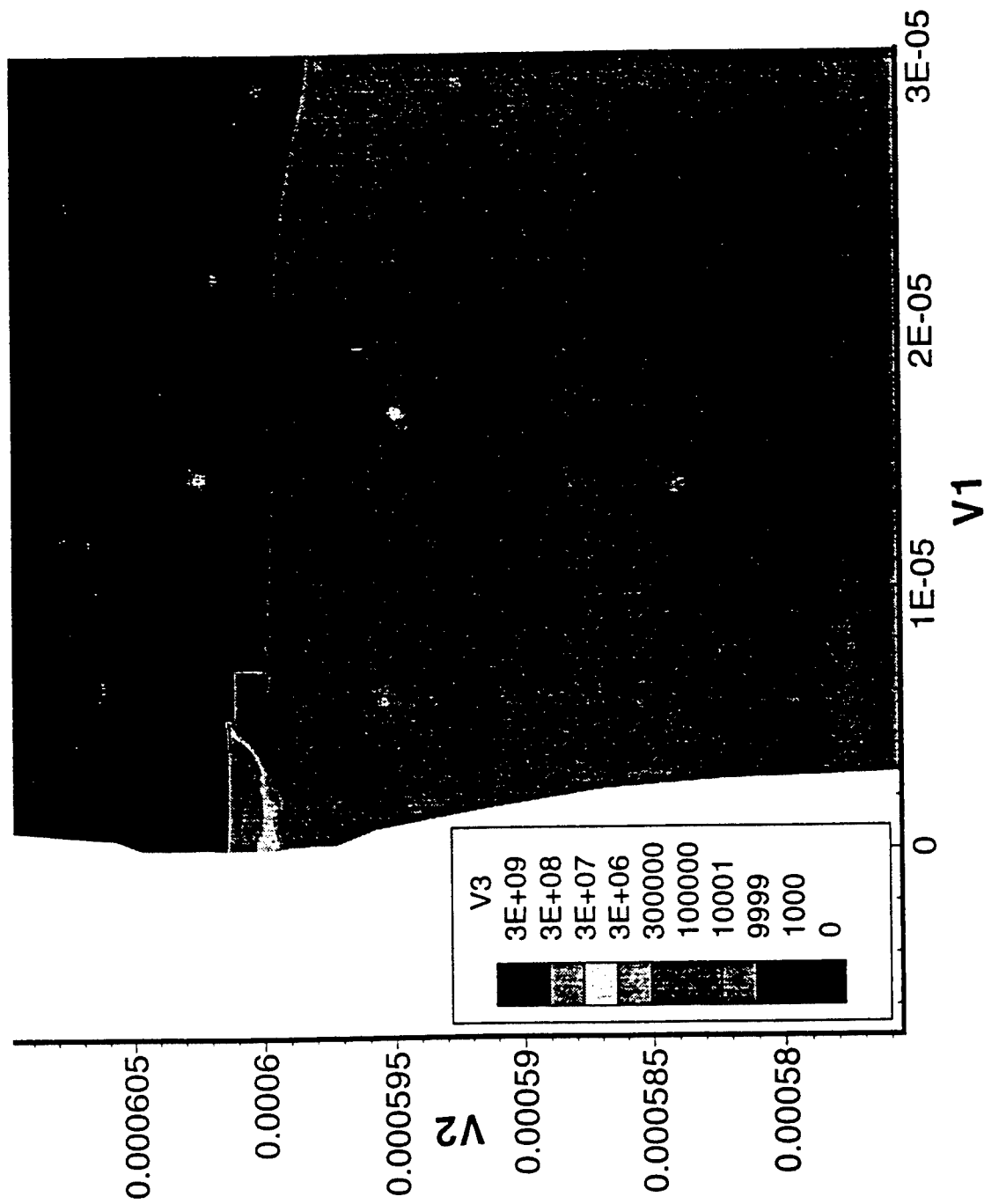


Fig. 3(d). Dislocation density contour plot at 75kA/cm² after 200 hours of operation, V1 and V2 are the r and z coordinates in meter, V3 represents dislocation density per cm².

initial Nd = 1e4, 1e5, 1e6

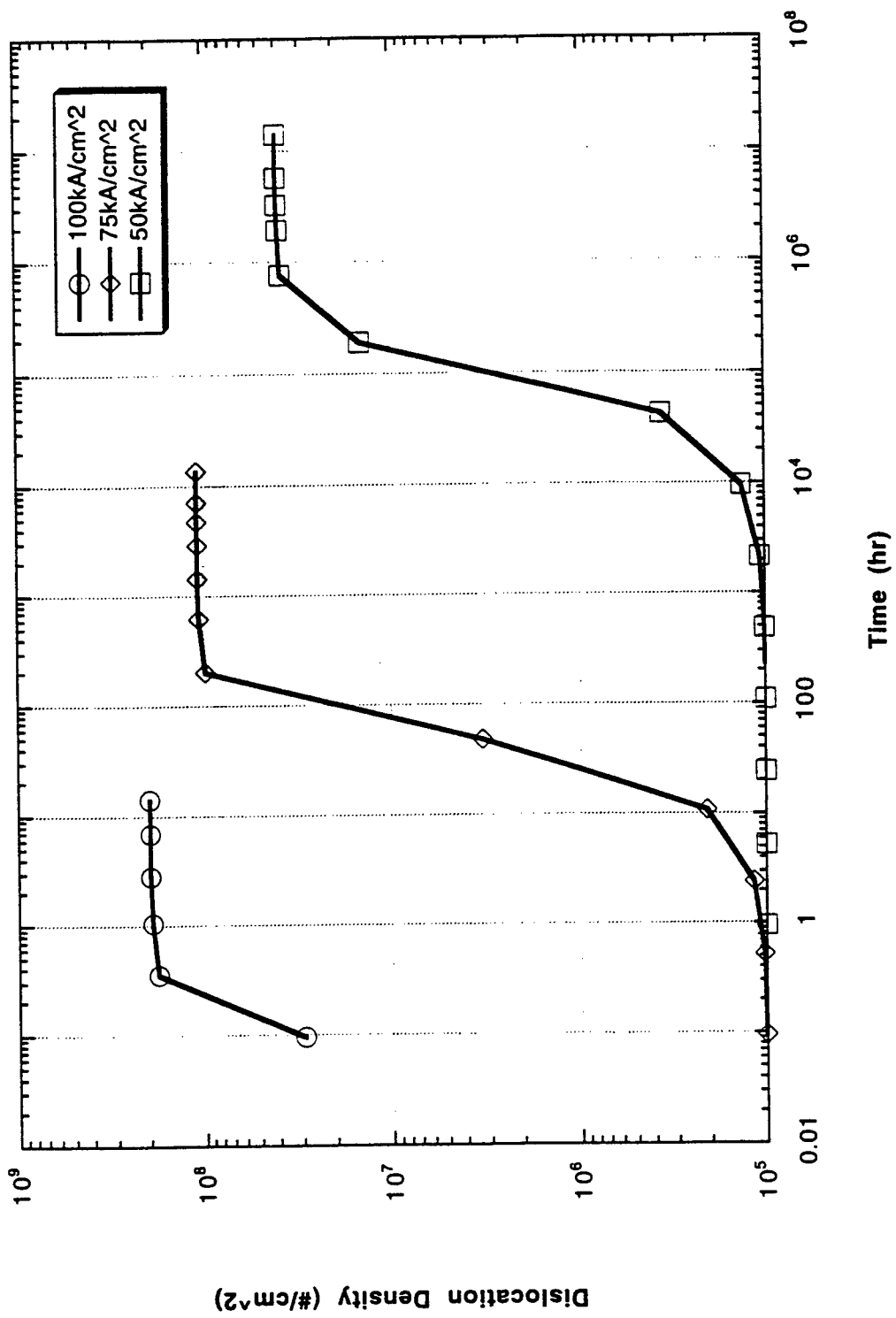


Fig. 4. Dislocation density versus time at the center of the emitter-base junction for nonuniform initial dislocation density of 10⁴, 10⁵ and 10⁵ cm⁻².

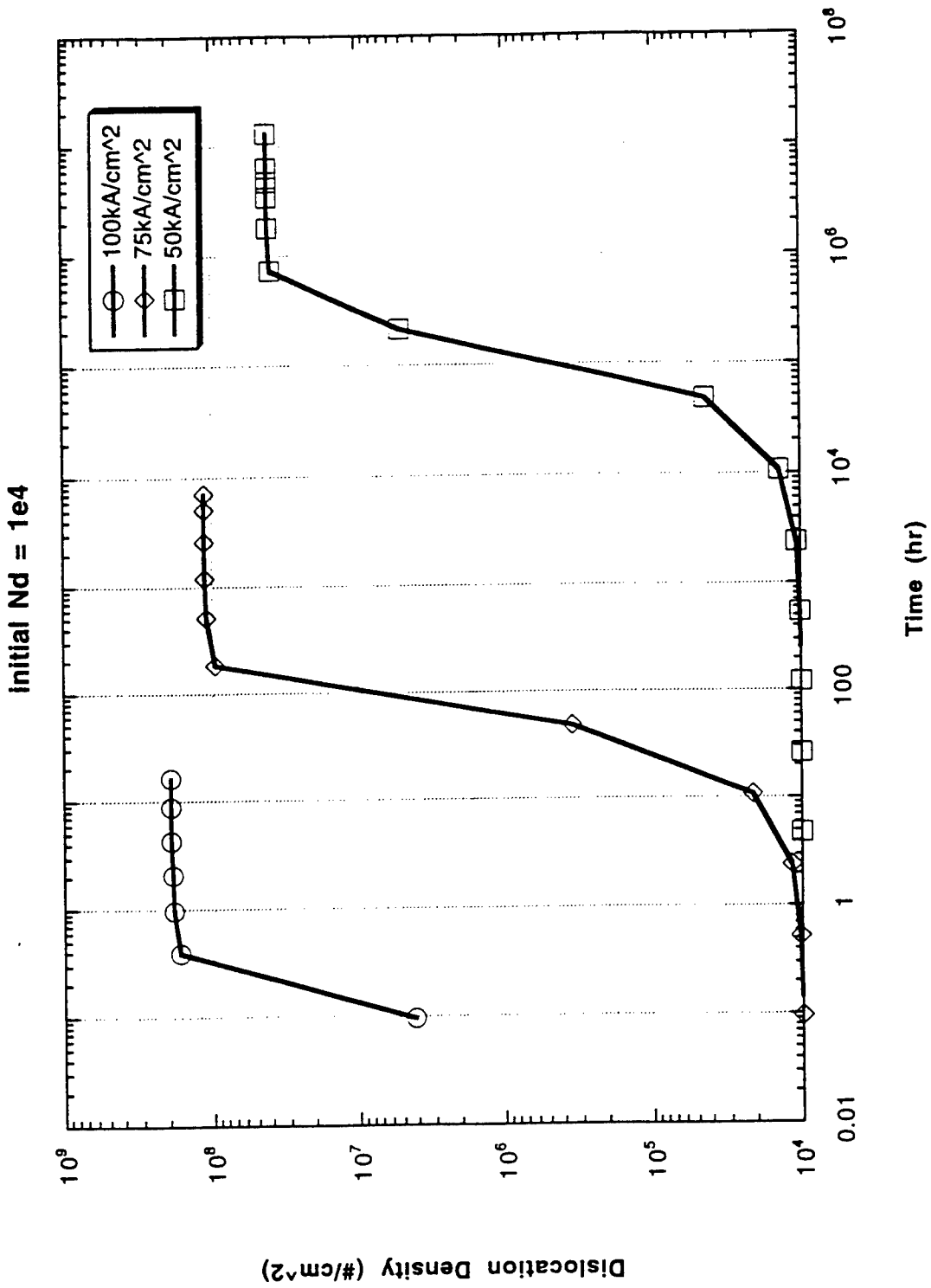


Fig. 5. Dislocation density versus time at the center of the emitter-base junction for uniform initial dislocation density of 10^4 cm^{-2} .

**TWO AXIS PNEUMATIC VORTEX CONTROL AT HIGH SPEED AND LOW
ANGLE-OF-ATTACK**

**John Valasek
Assistant Professor
Department of Aerospace Engineering**

**Texas A&M University
College Station, TX 77843**

**Final Report for:
Summer Research Program
Wright Laboratory**

**Sponsored by:
Air Force Office of Scientific Research
Bolling Air Force Base, Washington, DC**

And

Wright Laboratory

September 1997

TWO AXIS PNEUMATIC VORTEX CONTROL AT HIGH SPEED AND LOW ANGLE-OF-ATTACK

John Valasek
Assistant Professor
Department of Aerospace Engineering
Texas A&M University

Abstract

Forebody pneumatic vortex control has previously been demonstrated through full-scale flight test to be effective for directional control of aircraft at low Mach number and high angle-of-attack flight conditions. The objective of the present research was to investigate the suitability of two-axis (wing, and vertical tail) pneumatic vortex control on a current fighter-type aircraft at high Mach number and low angle-of-attack flight conditions. It was intended that the pneumatic effectors would both augment and replace the conventional aileron and rudder, and were used to control lateral/directional motions. The Lockheed F-16 XL was selected as the configuration to be studied, and evaluations were conducted on a high fidelity, nonlinear, six degree-of-freedom, non real-time simulation of this aircraft.

Evaluations consisting of a set of aggressive bank-to-bank maneuvers at various blowing coefficient levels, were conducted for pneumatic blowing as the primary control effectors with the conventional surfaces as augmenting effectors, and pneumatic blowing effectors only. A sample all pneumatic penetration strike mission was also investigated.

For the test cases studied, results demonstrate that by using pneumatic blowing at low blowing coefficient levels and with conventional effector augmentation, aileron and rudder activity and maximum deflections can be reduced. Progressively increasing the pneumatic control power demonstrated that at a realistic and attainable level of compressor bleed air, the aileron and rudder can be completely replaced by pneumatic devices yet allow the aircraft to complete aggressive bank-to-bank maneuvers. The simulated penetration strike mission test case demonstrated that successful completion of the mission is possible using only pneumatic lateral/directional effectors. Elevons were still used for pitch control since modeling did not permit the option of symmetrically blown ailerons.

TWO AXIS PNEUMATIC VORTEX CONTROL AT HIGH SPEED AND LOW ANGLE-OF-ATTACK

John Valasek

INTRODUCTION

Pneumatic vortex control (PVC) using either tangential slot blowing or nozzle blowing to control the forebody vortices generated by aircraft at high angles-of-attack is a generally well understood and mature technology. The viability of the concept for generating controllable yawing moments has been extensively tested in wind tunnels for several years [1-5]. More recently, the promise of PVC was successfully demonstrated in full-scale flight test to reduce the loss of directional control power on fighter type aircraft at high angles-of-attack [6-8]. The X-29A aircraft was fitted with compressed nitrogen gas bottles to power PVC nozzles mounted on each side of the forebody, essentially providing yaw augmentation only. The PVC nozzles were controlled manually by the pilot, i.e. open-loop, and not as part of the X-29A digital flight control system. The tests demonstrated that PVC was a viable means of generating well behaved yawing moments at high angles-of-attack and low Mach numbers. The time delays experienced in initiating a PVC event were small, and the responses to PVC inputs were generally fast and acceptable to the pilot. Specific recommendations for extending the PVC research program included using engine compressor bleed air to power the PVC nozzles, and closing the loop on the nozzles within the flight control system. All-PVC control, characterized by pneumatic devices completely replacing conventional aerodynamic effectors, provides the potential for significant reductions in radar detectability by eliminating control surface deflections altogether. To realize this potential in the operational context of low level strike/interdiction missions requires the use of pneumatics as multi-axis control effectors over the full subsonic/transonic flight envelope. Recent wind tunnel testing of PVC has expanded into the low angle-of-attack / high Mach number flight regime, and to other configurations such as the high speed civil transport [9-11]. Results indicated that with sufficient engine compressor bleed air, PVC devices are an attractive control effector for high speed / low angle-of-attack flight conditions. Other testing [12] successfully demonstrated wing-mounted PVC devices for generating multi-axis moments.

The remaining step prior to serious consideration of an all-pneumatic controlled aircraft is six degree-of-freedom evaluation of closed-loop multi-PVC (forebody, wing, and tail mounted devices) evaluated at low angle-of-attack / high speed flight conditions. The impact of PVC on flight performance, mission performance, and auxiliary systems (specifically engine engine compressor bleed air requirements) was the focus of the present research.

RESEARCH OBJECTIVES

The goal of the present research was to accomplish the following objectives through the use of a six degree-of-freedom flight simulation computer program:

1. Evaluate the feasibility of using PVC as the only type of control effector, and PVC augmented with conventional surfaces.

2. Extend the PVC concept to high speed, low angle-of-attack flight conditions which are representative of low level strike/interdiction missions.
3. Investigate the effects of multi-axis PVC, i.e. a suite of PVC devices mounted on the forebody, wing, and vertical tail which are capable of simultaneous operation.
4. Quantify the effect of various levels of engine compressor bleed mass flow rate on PVC performance.
5. Determine the threshold of engine compressor bleed mass flow rate required to completely eliminate conventional surfaces without degrading closed-loop vehicle performance.

PVC RESEARCH FLIGHT SIMULATION TOOL

Realistic evaluation of six degree-of-freedom closed-loop PVC on a high performance combat aircraft requires the use of a high fidelity flight simulation tool. The Lockheed F-16XL was selected as the baseline aircraft configuration to be studied (Figure 1). This aircraft is currently on flying status at the NASA Dryden Flight Research Center (DFRC) and is suitable for modification into a flying testbed for PVC research. In addition, the DFRC maintains both real-time and non real-time high fidelity, nonlinear, six degree-of-freedom simulations of this aircraft.

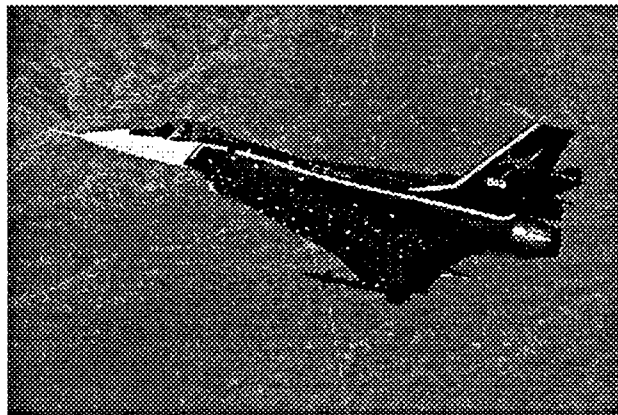


Figure 1 F-16XL External Physical Characteristics

An F-16XL flight simulation computer program provided by the NASA DFRC was installed at Wright Laboratory and used to generate the results presented in this report. The Wright Laboratory version of the F-16XL flight simulation is a high fidelity, non real-time, nonlinear six degree-of-freedom aircraft simulation. It contains full flight control system, engine, and aerodynamic models. The flight control system model contains both analog and digital implementations of the F-16XL control laws. The digital flight control system runs multi-rate with gain scheduling. All limiters and nonlinearities in the actual flight control system are present. The aerodynamic data base contains nonlinear, steady aerodynamic data for up-and-away flight at angles- of-attack up to 40 degrees. The aerodynamic data base was obtained from wind tunnel data and is corrected with flight test data, including flexibility

effects. The engine model is nonlinear and is representative of the F-16XL powerplant. User interface to the simulation is through input and output files. The input files contain initial attitude and flight condition, and pilot commands in the form of longitudinal and lateral stick position, rudder, and throttle time histories. Output files consist of tabular time history data which is plotted using standard plotting routines. Any special processing such as filtering or estimation is performed within the simulation itself when possible.

Unlike the X-29 flight research program which used PVC devices open-loop to augment the primary conventional control effectors, a specific goal of the present research was to investigate the benefit of using PVC devices as the *primary* control effectors, with conventional effectors used for augmentation in a closed-loop flight control system. The scope of the present research effort did not permit modifying or re-synthesizing the existing command augmentation system, labeled CAS in Figure 2. Instead, a control allocation/mixing scheme was devised to integrate the PVC devices into the existing F-16XL flight control system.

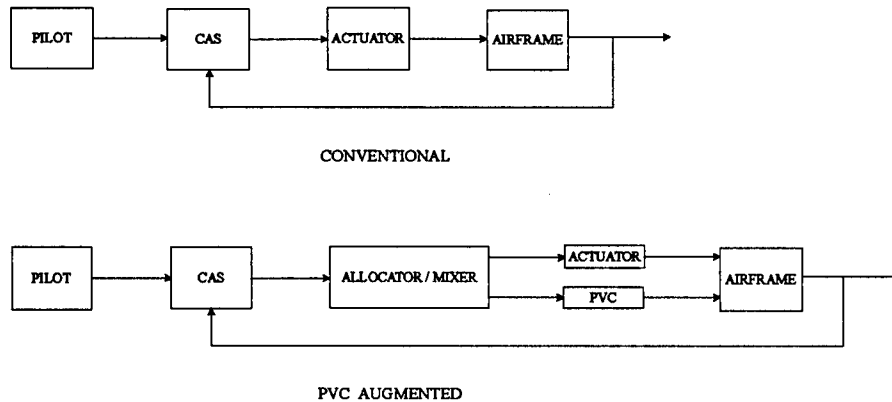


Figure 2 F-16XL Flight Control System Representations

This allocator/mixer receives surface deflection commands from the CAS, and upon filtering according to some designed-in logic, re-directs the commands in various proportions to both the conventional effectors and the PVC effectors. An illustration of the allocation/mixing algorithm logic flow using directional only PVC operation follows. As a response to internal (pilot) and/or external (gust) inputs, the CAS commands a rudder deflection $\delta_{r,comm}$. This commanded rudder deflection is then used to calculate the commanded (or required) yawing moment

$$C_{n,required} = C_{n_{\delta_r}} \delta_{r,comm}$$

Coefficient values were used since the aerodynamic data base and the coefficient buildup in the simulation use coefficient values. The required yawing moment is then set equal to the yawing moment which can be generated by the PVC device, and the PVC deflection required to generate the commanded value of yawing moment coefficient is solved for:

$$\delta_{PVC} = \frac{C_{n_{required}}}{C_{n_{\delta_{PVC}}}}$$

If the required yawing moment is greater than the yawing moment which can be generated by the PVC device, then the rudder deflection required to augment the PVC device up to the full required level is solved for:

$$\text{IF } C_{n_{required}} > C_{n_{\delta_{PVC}}} \delta_{PVC} \text{ THEN}$$

$$\Delta C_{n_{required}} = C_{n_{required}} - C_{n_{\delta_{PVC}}} \delta_{PVC}$$

$$\delta_{r \text{ filtered}} = \frac{\Delta C_{n_{required}}}{C_{n_{\delta_r}}}$$

This filtered value of commanded rudder deflection is then sent to the rudder actuator. This allocation concept was also extended to controlling the wing mounted PVC device in lieu of using aileron as the primary lateral control effector. This allocation concept proved to be adequate for one-axis PVC control (either wing mounted or vertical tail mounted).

For multi-axis PVC control, additional allocation is required to effectively “mix” multiple PVC devices. For this research, simultaneous use of both the wing mounted and vertical tail mounted PVC devices was accomplished by directing aileron commands to the wing mounted PVC device and likewise directing rudder commands to the vertical tail mounted PVC device. The aileron command signal in fact commands non-symmetric aileron deflections since it is used to modulate both lateral and directional motions. The mixing scheme extracts the *symmetric* content of this signal and feeds it to the wing mounted PVC device according to the previously described allocation algorithm. Subsequent evaluation of the allocation/mixing scheme demonstrated that crossfeed signals like the aileron to rudder interconnect (ARI) must be disabled. This is because the original aircraft model attempts to couple the individual effectors in a perverse manner. Since the PVC devices have inherently different aerodynamic coupling properties than the conventional control effectors, the interconnect modeling is inappropriate and therefore must be deactivated. It will be shown in the results section that this action does not severely degrade control harmony. Although not a goal of the present research, complete redesign of the control laws to provide the correct crossfeed signals would realize the maximum performance and benefit of using the PVC devices.

PVC DEVICE MODELING

Pneumatic control devices on the forebody, wing, and vertical tail were modeled in the simulation with existing PVC wind tunnel data supplied by Wright Laboratory [12,13]. The data consists of increments to normal force, sideforce, pitching moment, rolling moment, and yawing moment. Data was available for either on/off operation of the devices (fixed magnitude of control power), or proportional control by varying the massflow through the nozzle. Both types of device operation were modeled. Consistent with experimentally determined data, the associated dynamics and time delays were modeled as first-order lags with a time constant of 0.1 seconds. Consistent with the concept of incorporating PVC devices alongside conventional types to form an overall control effector suite, the PVC devices were mechanized in the flight simulation in exactly the same fashion as the existing conventional effectors. Reduction of engine thrust due to bleed air usage was not modeled, since the low percentage of bleed used (less than 4 lbm/sec) made this a second order effect.

TEST DESIGN

The test case matrix was designed to highlight the parametric effect of PVC massflow on closed-loop maneuver performance of an aircraft equipped with PVC devices. The test case ensemble (Table 1) consisted of i) an aggressive 3/4 stick roll doublet performed at Mach 0.9 at 25,000 feet over a sweep of PVC massflow levels; ii) a test case to determine the threshold of PVC massflow at which pneumatics can completely replace conventional effectors with no change in closed-loop performance; and iii) a segment of a low-observable penetration strike mission using only pneumatics.

Table 1 Test Case Matrix

case #	\dot{m}_{wing} (lbm/sec)	\dot{m}_{tail} (lbm/sec)	conventional augmentation
0 nominal	/	/	
1	4	3	
2	4	2	
3	4	1	
4	8	6	
5	8	4	
6	8	2	
7	8	6	✓
8	4	3	✓
9	14	12	
10 mission	≤ 4	≤ 3	

The roll doublet evaluations were conducted for two lateral/directional control effector suites. The first suite used PVC wing and vertical tail mounted devices to completely replace all conventional lateral/directional control effectors, and the second suite used the same PVC devices as the primary control effectors with the conventional effectors as

secondary or augmenting effectors, using the control allocation scheme previously described. Lack of suitable forebody PVC device data prevented its use for these tests. Bandwidth limitations of the PVC effectors precluded their use for pitch control effectors without extensive modification of the existing F-16XL DFCS, which was beyond the scope of this research. Data collection runs for the generic F-16XL were performed at an aircraft weight of 32,019 (lbf); inertias of $I_{xx} = 18,000$ (slug-ft²), $I_{yy} = 101,000$ (slug-ft²), $I_{zz} = 116,000$ (slug-ft²), and $I_{xz} = -530$ (slug-ft²); and center of gravity location 45.31% MAC.

TEST RESULTS

Figure 3 shows the responses for Case 0, the nominal F-16XL roll doublet case. The bank angle response is precise, and both angle-of-attack and normal load factor deviate only slightly from the trim values, represented by the first two seconds of data. The digital flight control system feeds-in three degrees of rudder to coordinate the roll. The maximum roll rate generated by the ailerons is 150 degrees per second.

Figure 4 displays the responses for Case 7, which is wing and vertical tail blowing at eight and six lbf/sec respectively, and augmentation provided by the aileron and rudder. For an identical lateral stick input, the body-axis roll rate and bank angle responses are identical to the nominal case. There is a slight difference in the pitch axis responses, as the PVC devices inherently generate pitching moments which the aileron and rudder do not. Since the control allocation scheme does not have a dedicated pitch axis capability, the induced pitching moments are seen as disturbances by the pitch control system, and are subsequently damped out. Compared to the nominal case, use of PVC reduces maximum aileron deflections overall by roughly two degrees. Maximum rudder deflections are reduced overall by up to three degrees when the required deflections are small. But for larger commanded rudder deflections, use of PVC resulted in larger actual deflections and increased rudder activity. This behavior is due to the exceptionally strong cross-axis effects inherent to PVC devices compared to conventional elevons, ailerons, and rudders. Additionally, whereas the nominal F-16XL digital flight control system has been purposely designed to reduce cross-axis responses resulting from deflection of the elevon, aileron, and rudder, the control allocation scheme simply selects the particular PVC device which can generate the largest magnitude response for that particular commanded axis. The by-product PVC generated moments which show up in other axes, whether of beneficial sign or not, are not accounted for by the control allocation scheme and are therefore seen as disturbances by the nominal F-16XL digital flight control system. Note that implementation of a dedicated PVC flight control system would alleviate this problem. For this maneuver, adverse yawing moments were generated by the PVC devices and rudder was used to cancel them out. The plots of PVC device activity indicate that with conventional effector augmentation, the devices are capable of generating the steady-state forces and moments required to initiate and sustain the maneuver without using the maximum level of blowing coefficient available ($C_{\mu} = .0015$ wing, $C_{\mu} = .0011$ tail). However, the PVC devices appear to lack the bandwidth necessary to smoothly arrest the roll acceleration, thereby resulting in some excessive activity characterized by "waviness" near the end of the maneuver.

The results of the other augmentation test case (Case 8, not shown) demonstrated that halving the wing and tail nozzle massflow levels did not affect the bank angle and body axis roll rate responses, but did result in slightly degraded pitch responses. The most significant difference was in the directional axis, where reduced PVC control power required extra rudder deflection to satisfy the demands of the maneuver. Both the maximum rudder deflections and the rudder activity were significantly increased compared to the nominal test case. The conclusion to be drawn from these test cases is that even with conventional effector augmentation, PVC devices must possess adequate control power or else overall system performance (in terms of the deflections and activity of the conventional effectors) may in fact be *worse* compared to a purely conventional control effector suite. Of course, the quality of the control allocation scheme will have a strong effect on this result, but even the best control allocation scheme needs effectors with large, uncoupled control power, regardless of the type of effector used.

An important part of this investigation was to eliminate the augmentation provided by the aileron and rudder, and repeat the maneuver using only PVC devices. Figure 5 displays the results for Case 4, which used the same massflow levels as Case 7 above. Compared to the nominal Case 0, the system was unable to achieve the full commanded bank angle displacement because the PVC devices were able to generate less than half the required body axis roll rate. A noteworthy result was that the pitch axis was virtually unaffected during the maneuver, unlike the strong effects observed for the augmented system in Cases 7 and 8. Likewise, the low-observables benefit of zero aileron and rudder deflections was achieved at the cost of saturated PVC devices. PVC device bandwidth was not an issue for this test case since the PVC devices simply could not generate large roll accelerations. However, in some scenarios, trading roll performance for increased survivability is beneficial.

Another objective of this research was to determine the threshold level of PVC device massflow required to *completely* replace the conventional effectors. A parametric study showed that 15 lbm/sec ($C_\mu = .0028$) supplied to both the wing and tail PVC devices generated sufficient control power to successfully complete the roll doublet maneuver with no appreciable degradation in closed-loop performance. The bank angle response was virtually identical to the nominal Case 0. Naturally, the control allocation scheme could not completely eliminate the cross-axis effects, but overall closed-loop performance was very close to Case 0.

A sample penetration strike mission was flown with an ingress consisting of a 90 degree evasive turn to the right, followed by a 90 degree evasive left turn onto the initial point, a short weapons release run, and an egress consisting of a 180 degree heading change. The entire 125 second mission segment was successfully flown using pneumatics only, with massflow levels of 4 lbm/sec for the wing ($C_\mu = .00074$) and 3 lbm/sec for the vertical tail ($C_\mu = .00056$). The mission performance in terms of time of exposure to hostile defenses can be improved by increasing the massflow to the PVC devices, thereby increasing the maximum turn rate.

SUMMARY AND CONCLUSIONS

A high fidelity batch-type computer simulation tool of the F-16XL aircraft incorporating forebody, wing, and vertical tail mounted pneumatic vortex control devices was built for evaluating lateral/directional closed-loop performance, required PVC massflow levels, and penetration strike mission performance. Eleven test cases, including a segment of a penetration strike mission were evaluated, and based upon the results it is concluded that:

1. Signature characteristics, as measured by peak aileron and rudder deflection, can be improved by using pneumatic devices operated at low blowing coefficient levels (≈ 0.0012) and minimal massflow levels (4 lbm/sec). The effector suite used to accomplish this reduction consists of pneumatic devices as the primary control effectors, with augmentation provided by conventional (elevon and aileron) effectors. For the particular test cases studied, maximum aileron and rudder deflections could be reduced up to three degrees compared to a conventional F-16XL for the same maneuver.
2. Significant and usually adverse cross-axis responses can be expected when using multiple-axis PVC devices. X-29A flight testing showed similar cross-axis coupling resulting from open-loop use of forebody PVC devices. This problem can be alleviated by use of a dedicated PVC integrated flight control system.
3. Conventional ailerons and rudder can be *completely* replaced by purely pneumatic devices operating at realistic and attainable levels of engine compressor bleed air and blowing coefficients (14 lbm/sec, $C_{\mu} = .0028$), while still maintaining closed-loop system performance during aggressive roll doublet maneuvers. This feature can significantly improve signature characteristics by completely eliminating control surface deflections.
4. The simulated penetration strike mission test case demonstrated that successful completion of the mission is possible using only pneumatic lateral/directional effectors at low blowing coefficient levels (≈ 0.00074), provided the required turn rates are not large. Large turn rates are defined here as those which are approximately 80% - 100% of the maximum full-performance turn rates which can be achieved by conventionally equipped aircraft.

RECOMMENDATIONS FOR FUTURE PVC RESEARCH

Based upon the results and conclusions detailed above, the following recommendations are proposed for continued future research of this technology:

1. Employing rigorous and sophisticated control allocation methods to incorporate the PVC devices into the existing F-16XL digital flight control system.
2. Extend the test cases begun in the present research to true multi-axis PVC including forebody blowing and closed-loop pitch control. Suitable forebody PVC data was not available for the tests conducted in the present research, and the pitching moment capability of PVC was not taken advantage of because of restrictions prohibiting re-design of the digital flight control system. Incorporating these two aspects will provide the "full picture".
3. Synthesize a new and completely PVC dedicated de-coupled digital flight control system using either a model predictive variable structure control scheme, or a model reference adaptive control scheme. The controller would use on-line system identification to handle the robustness problem associated with the control power generated by the PVC devices, and would also autonomously handle the stability augmentation function for the pitch axis. This could potentially reduce the level of massflow required.

REFERENCES

- [1] Ericsson, L.E., "Control of Forebody Flow Asymmetry A Critical Review," AIAA-90-2833-CP.
- [2] Malcolm, Gerald N., and Ng, T. Terry, "Aerodynamic Control of Fighter Aircraft by Manipulation of Forebody Vortices," AGARD-CP-497, Maneuvering Aerodynamics, Nov. 1991, pp. 15-1 to 15-22.
- [3] Guyton, Robert W., Osborn, Russell F., and LeMay, Scott P., "Forebody Vortex Control Aeromechanics," AGARD-CP-497, Maneuvering Aerodynamics, Nov. 1991, pp. 16-1 to 16-14.
- [4] Celik, Zeki Z., and Roberts, Leonard, "Vortical Flow Control on a Wing-Body Combination Using Tangential Blowing," AIAA-92-4430-CP.
- [5] Iwanski, Kenneth P., and O'Rourke, J., "F-15 Forebody Vortex Flow Control Using Jet Nozzle Blowing," AIAA Journal of Aircraft, Volume 33, Number 3, May-June 1996, pp. 491-498.
- [6] Walchli, Lawrence A., Guyton, Robert W., Luria, Frank, and Gillard, William J., "High Angle-Of-Attack Control Enhancement On A Forward Swept Wing Aircraft," AIAA-92-4427-CP.
- [7] Hancock, Regis, and Fullerton, Gordon, "X-29 Vortex Flow Control Tests," 1992 Report To The Aerospace Profession, Thirty-Sixth Symposium Proceedings, Beverly Hills, CA, Sept. 1992, pp. 209-219.
- [8] Luria, Frank, et. al, "Final Test Report: X-29A Vortex Flow Control (VFC) Flight Test Results," WL-TR-93-3106, Flight Dynamics Directorate, Wright Laboratory, 1993.
- [9] Eidson, Robert C., and Mosbarger, Neal A., "Forebody Pneumatic Devices at Low Angles of Attack and Transonic Speed," AIAA-97-0042-CP.
- [10] Parker, Brian A., Eidson, Robert C., and Takahashi, Timothy t., "Forebody Vortex Flow Control on a High Speed Transport Configuration," AIAA 97-0044-CP.
- [11] Takahashi, T., Eidson, R.C., and Heineck, J.T., "Aerodynamic Characteristics of a Supersonic Transport with Pneumatic Forebody Flow Control," AIAA-97-0043-CP.
- [12] Langan, Kevin J., and Samuels, Jeffrey J., "Effects of Wing Jet Blowing on the SHARC 55%-Scale Fighter Configuration," AIAA-97-0039-CP.
- [13] Maines, B.H., and Peters, S.E., "Pneumatic Aerodynamic Device Development (PADD)," WL-TR-96-3141, May 1996.

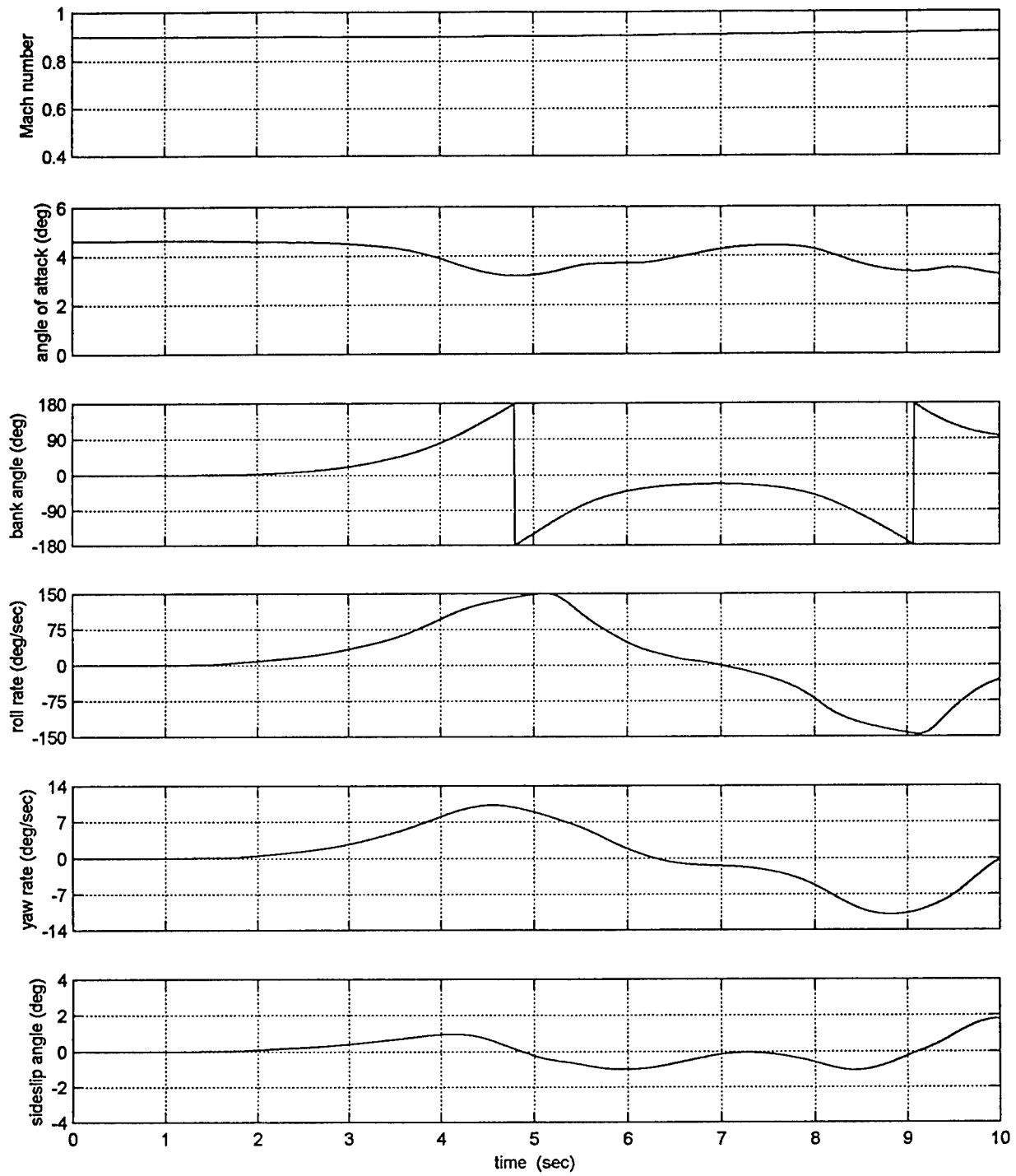


Figure 3 Case 0, Roll Doublet Response, Nominal Configuration F-16XL, 0.9/25k

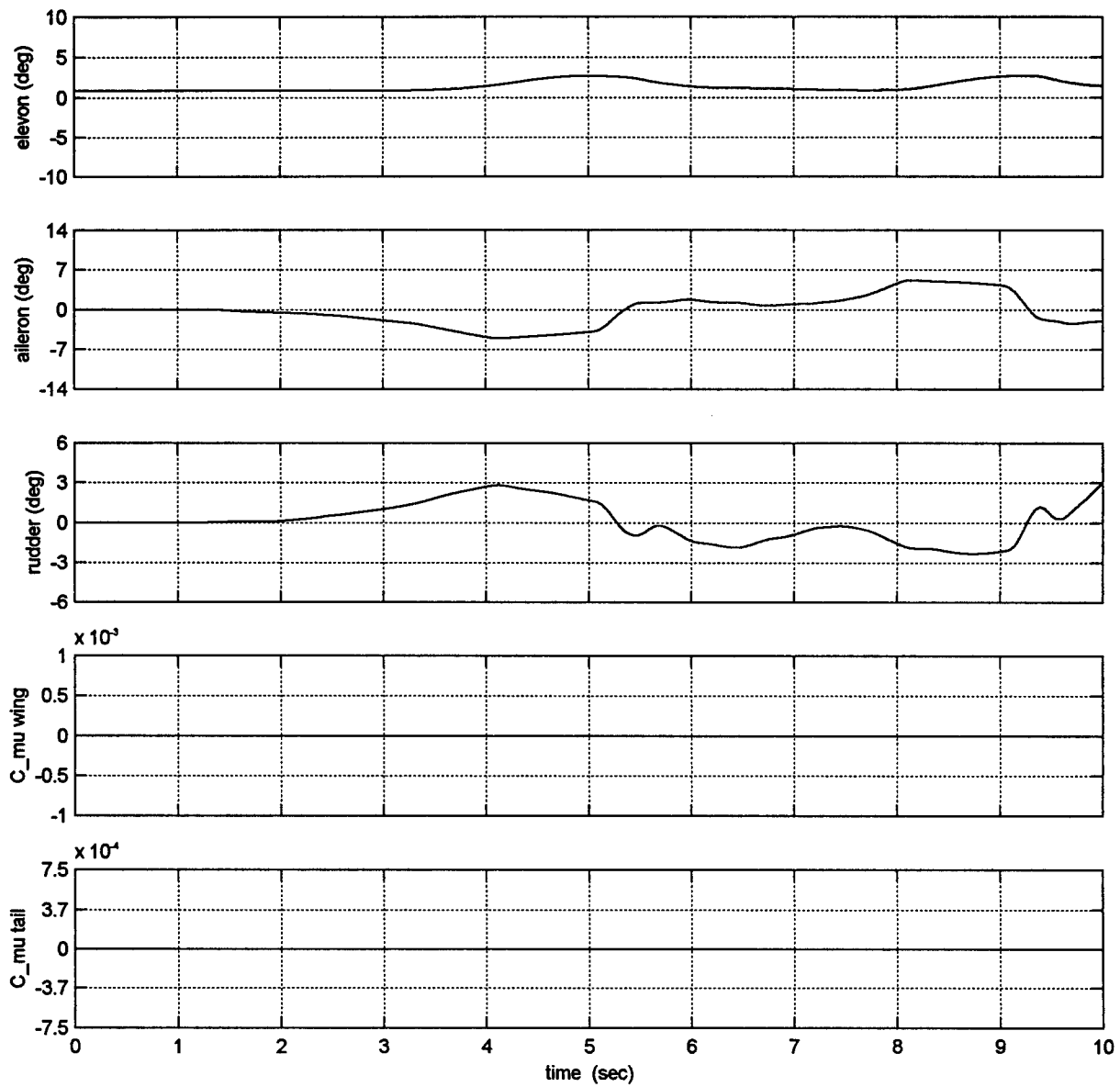


Figure 3 (continued) Case 0, Roll Doublet Response, Nominal Configuration F-16XL, 0.9/25k

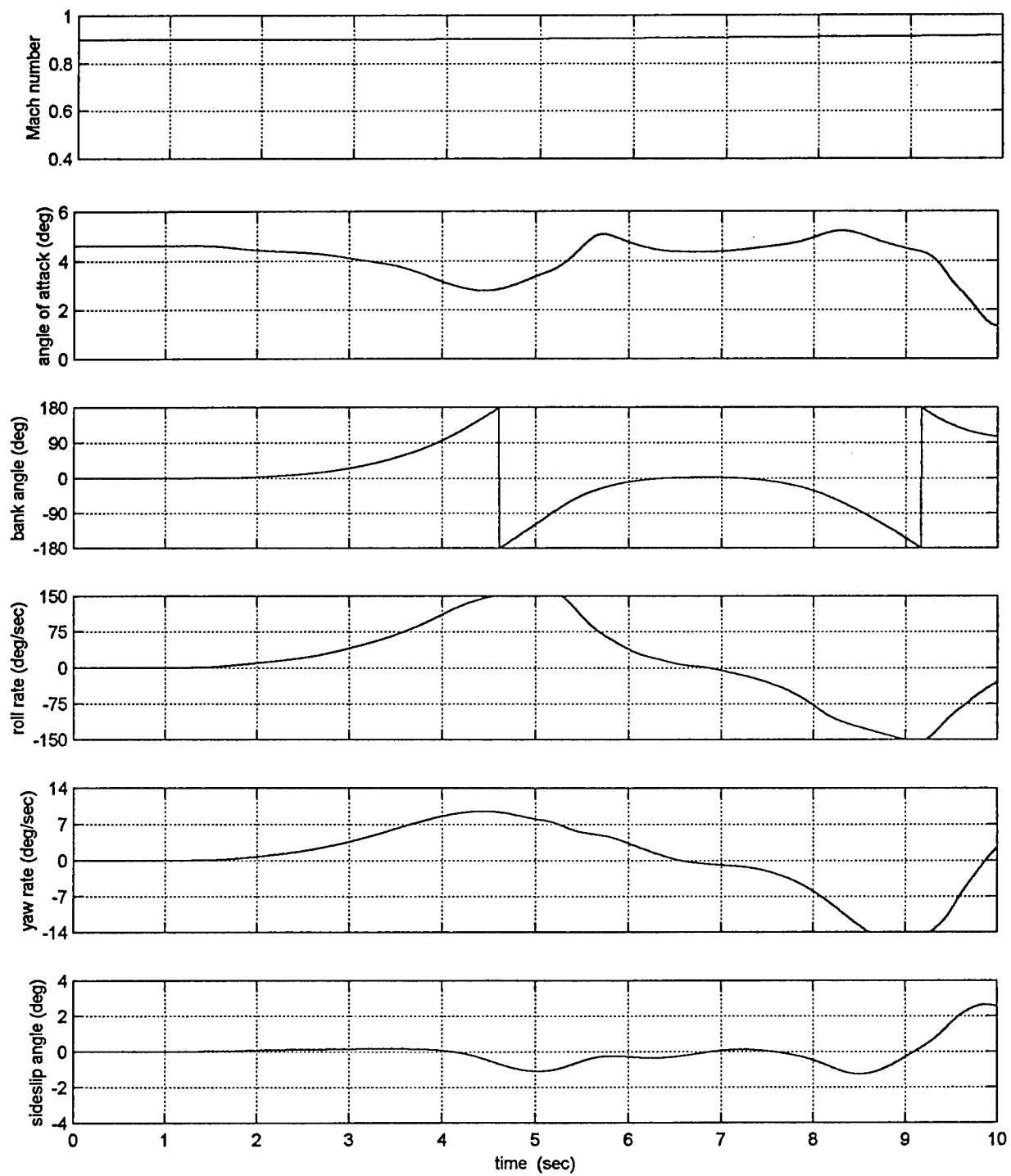


Figure 4 Case 7, Roll Doublet Response, PVC + Augmentation F-16XL, 0.9/25k

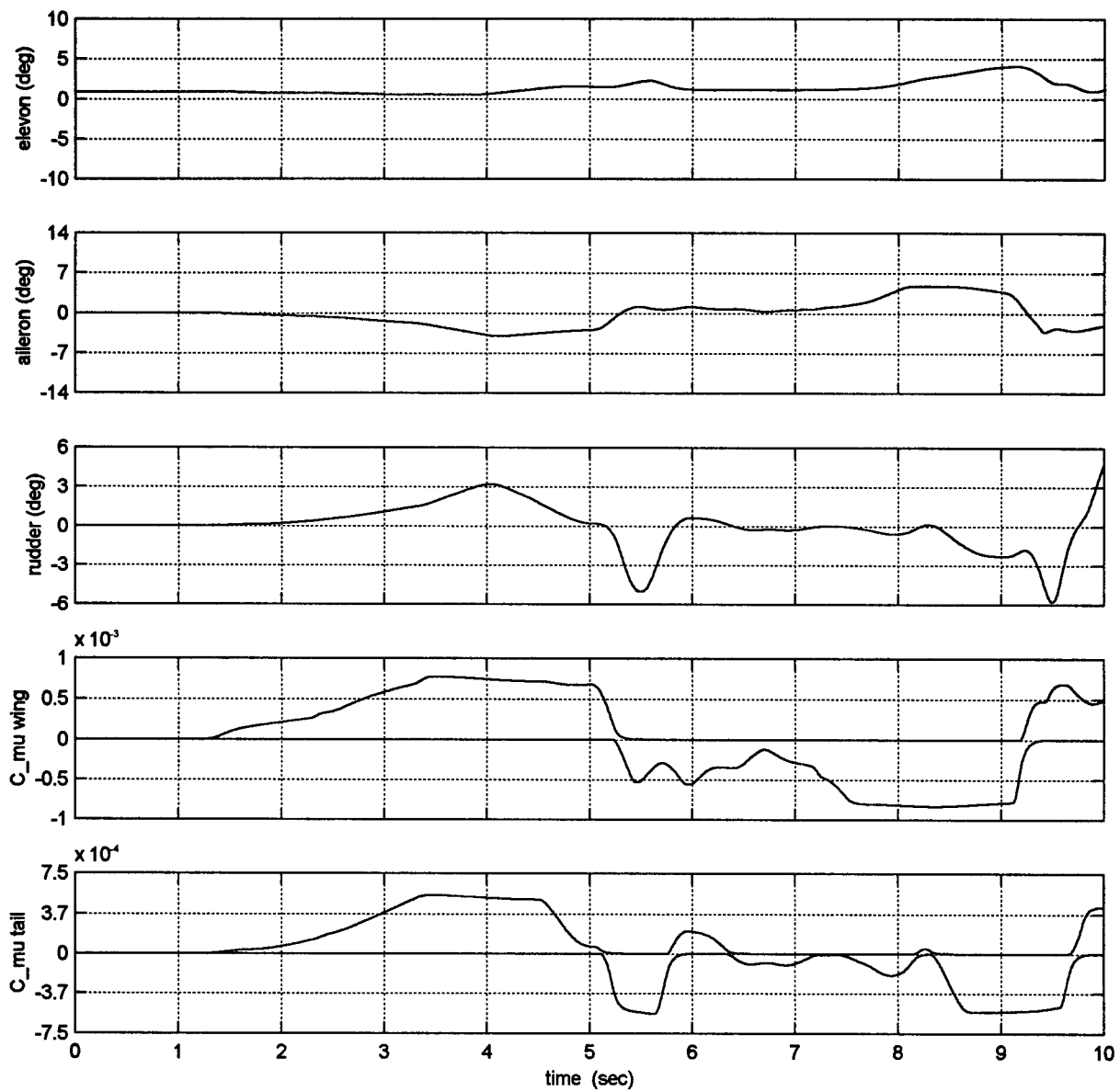


Figure 4 (continued) Case 7, Roll Doublet Response, PVC + Augmentation F-16XL, 0.9/25k

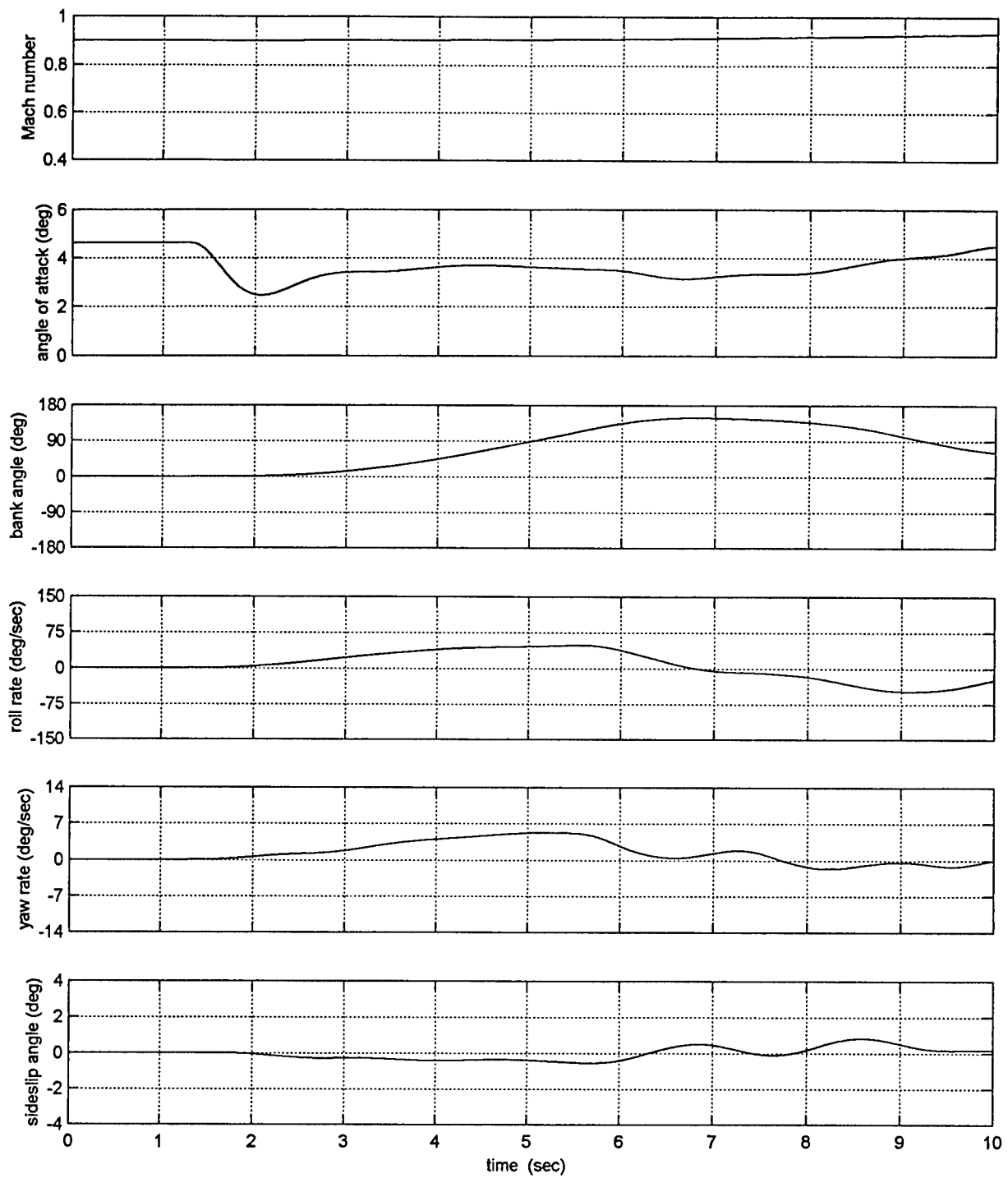


Figure 5 Case 4, Roll Doublet Response, PVC Alone F-16XL, 0.9/25k

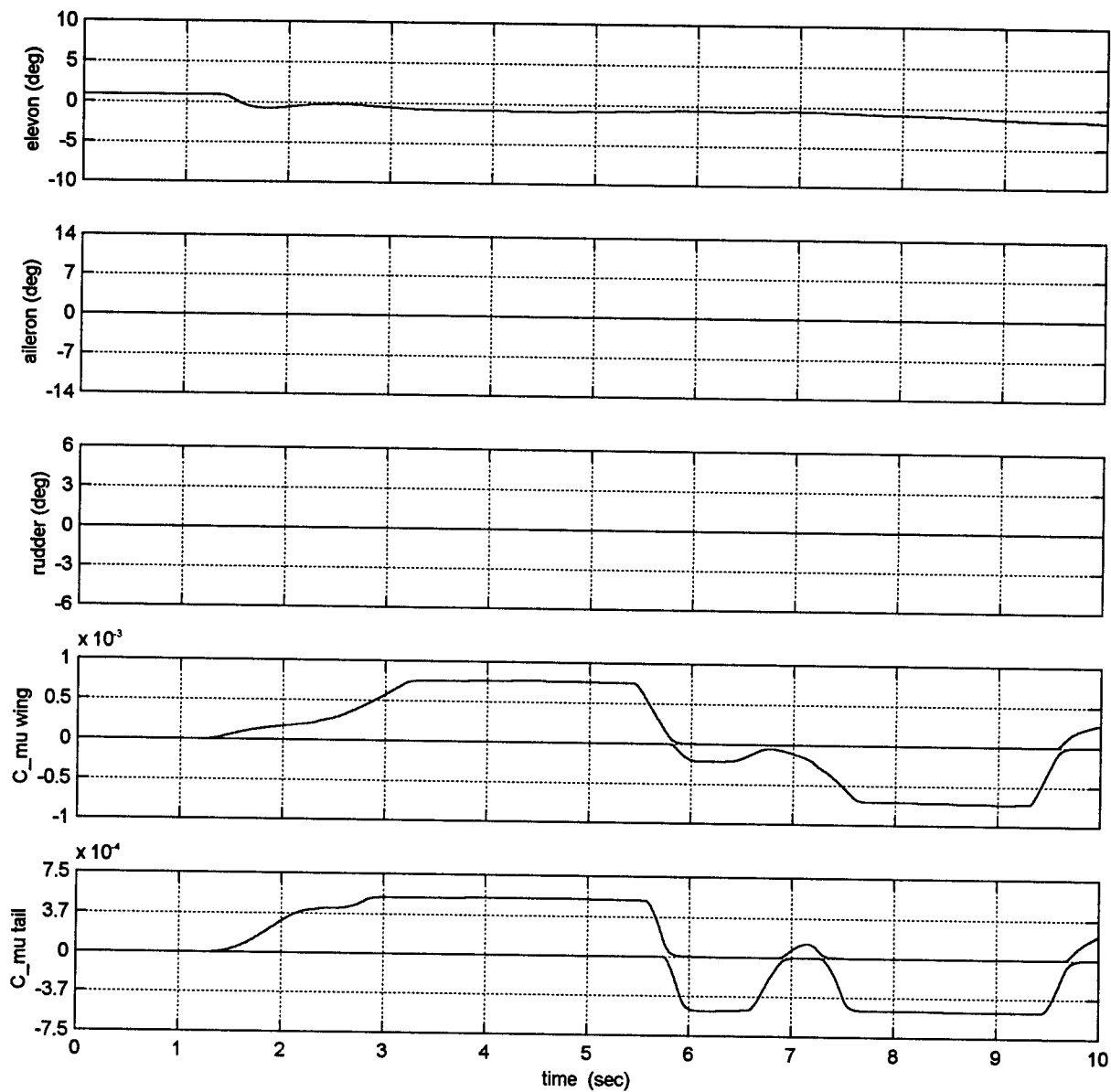


Figure 5 (continued) Case 4, Roll Doublet Response, PVC Alone F-16XL, 0.9/25k

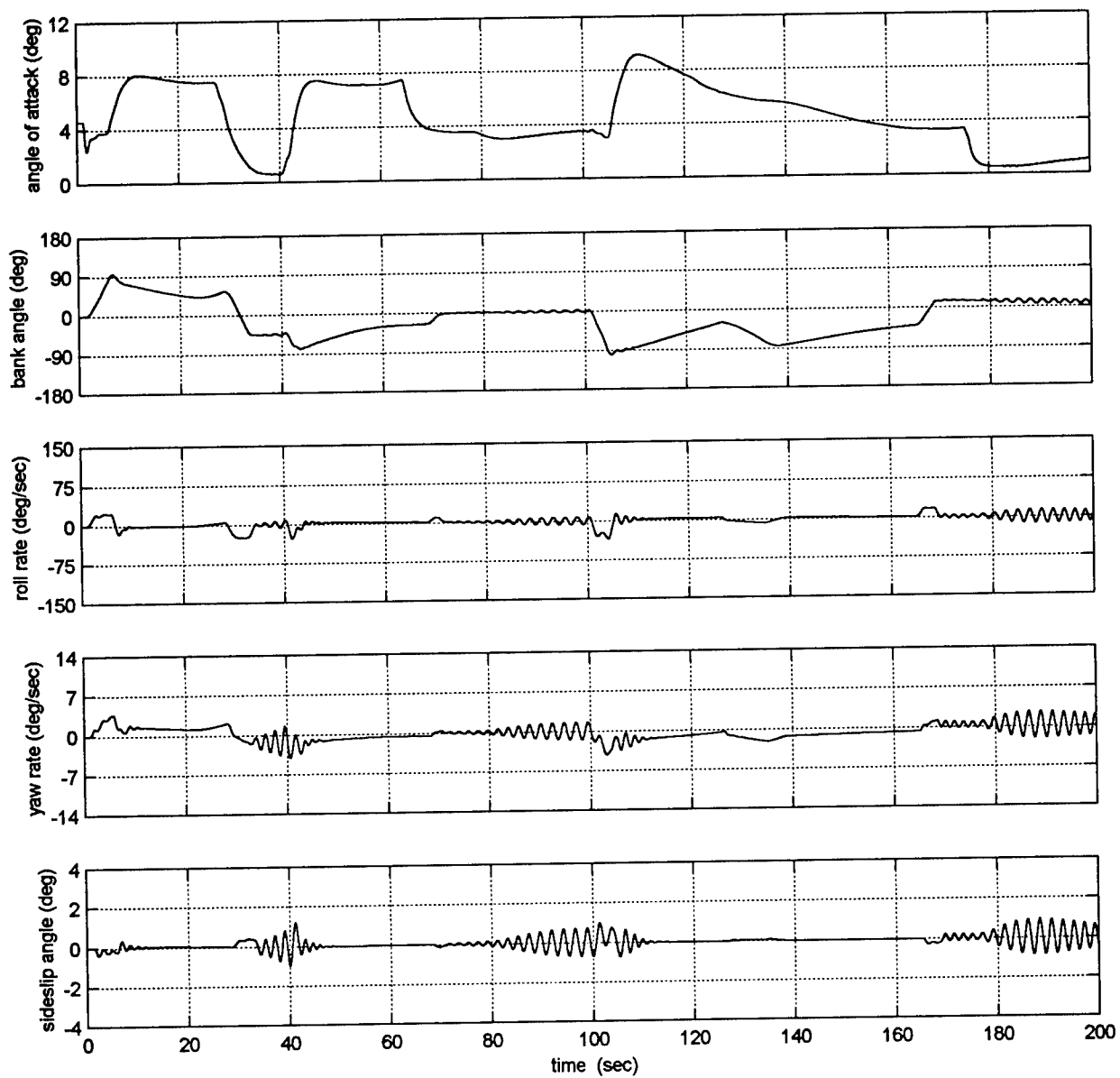


Figure 6 Penetration Mission, PVC Alone F-16XL, 0.9/25k

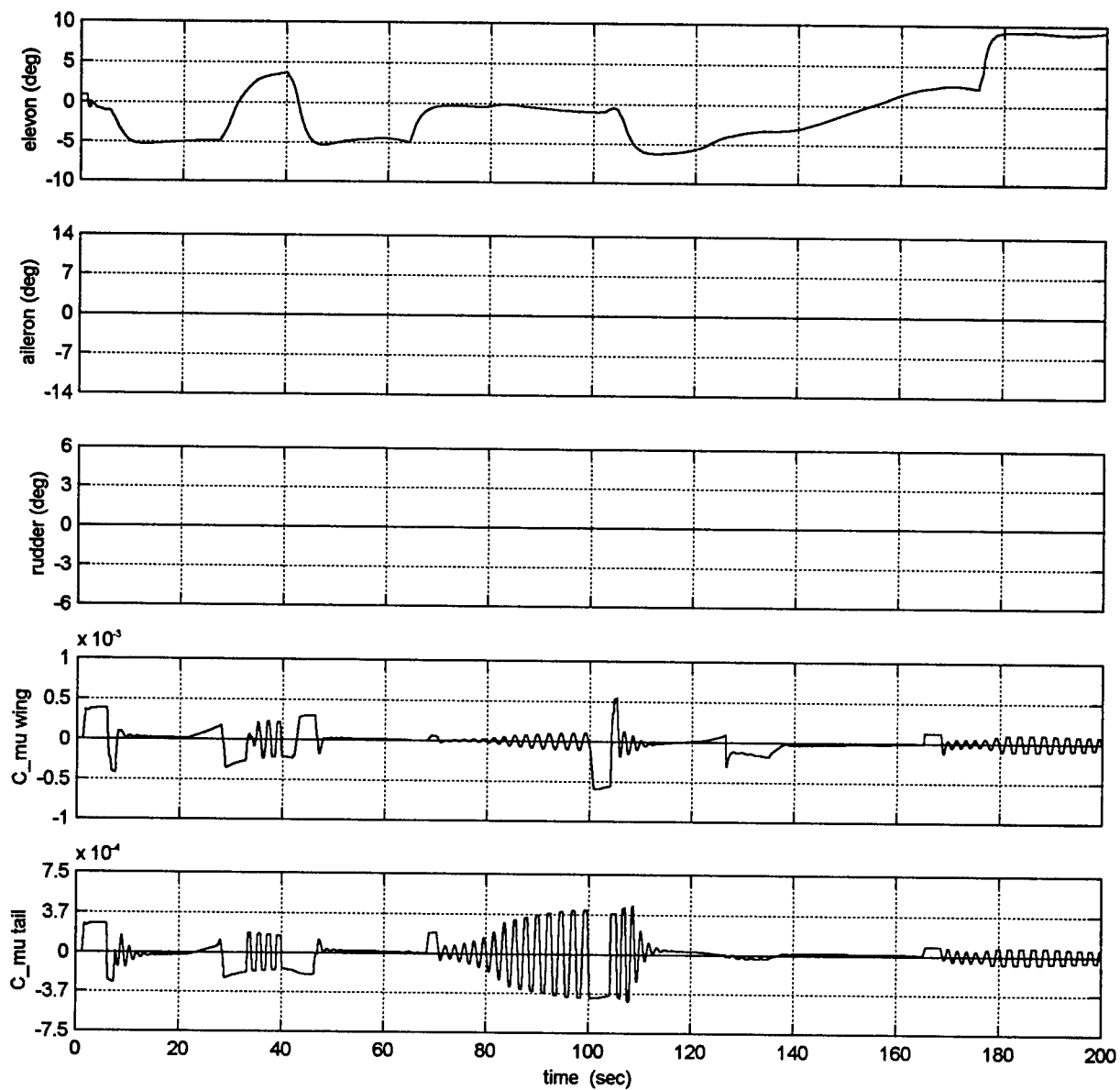


Figure 6 (continued) Penetration Mission, PVC Alone F-16XL, 0.9/25k

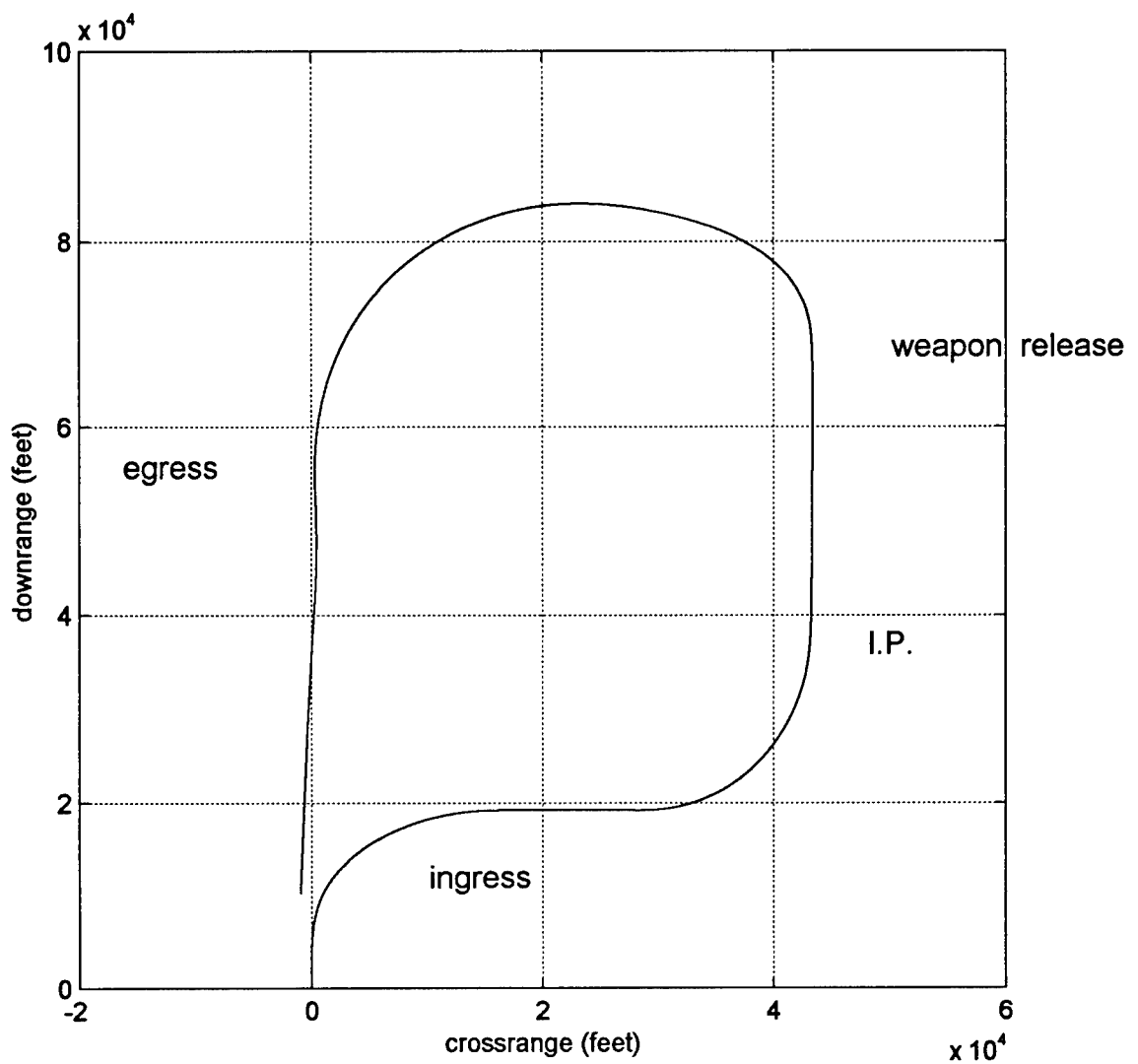


Figure 6 (continued) Penetration Mission Trajectory, PVC Alone F-16XL, 0.9/25k

**AN EXPERIMENTAL AND COMPUTATIONAL ANALYSIS OF THE
UNSTEADY BLADE ROW POTENTIAL INTERACTION IN A TRANSONIC
COMPRESSION STAGE**

**J. Mitch Wolff
Assistant Professor
Department of Mechanical and Material Engineering**

**Wright State University
3640 Colonel Glenn Highway
Dayton, OH 45435**

**Final Report for:
Summer Research Program
Wright Laboratory**

**Sponsored by:
Air Force Office of Scientific Research
Bolling Air Force Base, Washington, DC**

And

Wright Laboratory

September 1997

AN EXPERIMENTAL AND COMPUTATIONAL ANALYSIS OF THE UNSTEADY BLADE ROW POTENTIAL INTERACTION IN A TRANSONIC COMPRESSION STAGE

Danielle E. Brown
Graduate Student

J. Mitch Wolff
Assistant Professor

Department of Mechanical and Materials Engineering
Wright State University

Abstract

A computational and experimental investigation is performed to investigate the unsteady upstream traveling forcing function from a high speed, highly loaded compression rotor. The IGV unsteady surface pressures are experimentally measured for a near-stall transonic operating point to determine the forcing function. The data is analyzed in both the time and frequency domain based on the blade pass frequency. The experimental configuration is computationally modeled with a nonlinear unsteady viscous vane/blade interaction 2D code for comparisons with the experimental data in both the time and frequency domain.

Significant upstream traveling pressure effects were both measured and predicted. A detached bow shock is caused by the increased back pressure consistent with a near stall operating point. The bow shock is shown to impact the IGV blades. Its strongest effect is at the trailing edge of the IGV's with a 3.4 psia fluctuation. The nonlinear viscous unsteady vane/blade interaction computational analysis showed excellent agreement with the experimental results in both the time and frequency domain. Significant higher harmonic content was evident near the trailing edge of the IGV's. This is important, in light of recent trends toward use of linearized Euler and Navier-Stokes models for turbomachinery designs. The results of this research indicate the importance of higher harmonics, therefore extreme caution should be taken when designing transonic compression stages with linearized methods.

AN EXPERIMENTAL AND COMPUTATIONAL ANALYSIS OF THE UNSTEADY BLADE ROW POTENTIAL INTERACTION IN A TRANSONIC COMPRESSION STAGE

Danielle E. Brown
J. Mitch Wolff

Introduction

Gas turbines are a vital energy source for both military and industrial applications with recent research focusing on identifying high cycle fatigue unsteady flow mechanisms. There is a constant need for an improved understanding of the flow physics through the various components. This greater understanding leads to the ability of manufacturers to achieve higher levels of performance and a more efficient system. As technology increases, there are continually increasing demands on gas turbine engines involving greater durability, reduced noise levels, reduced size and greater thrust. A jet engine consists of several distinct components; the inlet, compressor, combustor, turbine, and exit nozzle. A considerable portion of the recent research involves the unsteady interaction between adjacent blade rows in both the compressor and turbine sections.

The two principle types of blade row interaction are usually referred to as wake and potential flow interactions.¹ Wake interaction is the effect upon the flow through a downstream blade row of the vortical and entropic wakes shed by one or more upstream rows. Potential flow interaction results from the variations in the velocity potential or pressure fields associated with the blades of a neighboring row and their effect upon the blades of a given row moving at a different rotational speed. This type of interaction is of serious concern when the axial spacing between adjacent blade rows is small or the flow Mach number is high.

Recently, computational work has been initiated to develop nonlinear, time-accurate, inviscid (Euler) and viscous (Navier-Stokes) solution techniques for unsteady flows through isolated and aerodynamically coupled blade rows (see Verdon, 1992 for a review). For coupled systems of rotating and

stationary blade rows, the relative motions between adjacent rows give rise to unsteady aerodynamic excitations which can initiate blade vibrations, generate discrete-tone noise, and degrade aerodynamic efficiency. Two categories of numerical procedures have recently been developed for determining the effects of relative motion between adjacent blade rows. In the first category of numerical procedures, incoming wakes are specified at the inlet of isolated blade rows.² In these methods, the wakes are usually assumed to be parallel with uniform pressure and prescribed total enthalpy and/or velocity variations. In the second category of numerical analyses, both blade rows are modeled and the relative position of one blade row is varied to simulate blade motion.^{3,4,5}

Some joint computational and experimental investigations have been made into vane/blade interactions. These investigations have been primarily on turbine configurations, with the experimental data acquired in generally two different types of experimental rigs. First, large scale turbine rigs are used to simplify the experimental investigation. The large scale of the rig is a distinct advantage because it permits the use of extensive instrumentation on both the stationary and rotating blades. The large scale also has the advantage of giving Reynolds numbers which are typical of high pressure turbines at nominal model running conditions⁶, but it can not simulate transonic flow phenomena. Full-scale transonic turbines are being tested using blow down or shock tube facilities.⁷ These facilities are beneficial for testing actual hardware components with research issues being miniature measurement techniques and short test duration times.

In summary, little research has been directed at vane/blade interaction in a compressor section. Thus, relatively little is known about the unsteady IGV/blade interactions which occur within a compression system. Since these unsteady aerodynamic interactions can lead to high vibratory stresses, models must be developed to analyze vane/blade interaction. In addition, relevant experiments are needed to assess the validity of these models and direct future research efforts.

The objective of this research is to investigate and quantify the fundamental vane/blade interaction phenomena relevant to the upstream potential forcing function of a downstream rotor in a compression system. This is accomplished by performing a series of experiments in the Compressor Aero Research Lab

(CARL), a high speed, highly loaded compression stage facility. IGV unsteady surface pressures are experimentally determined for a near-stall transonic operating point. The data is analyzed in both the time and frequency domain based on the blade pass frequency. In addition, a two dimensional nonlinear viscous unsteady multi-blade row computational (CFD) analysis is compared with the experimental data in both the time and frequency domain.

Compressor Aero Research Laboratory (CARL)

The Compressor Aero Research Lab facility at Wright Patterson Air Force Base's Wright Laboratory is a full scale, high speed, highly loaded compression stage. The single stage compressor facility consists of an open or closed loop (currently open) tunnel system with an upstream venturi flow meter to measure the mass flow rate. The test compressor is driven by a 2,000 hp electric motor with a variable speed range of 6,000 to 21,500 rpm.

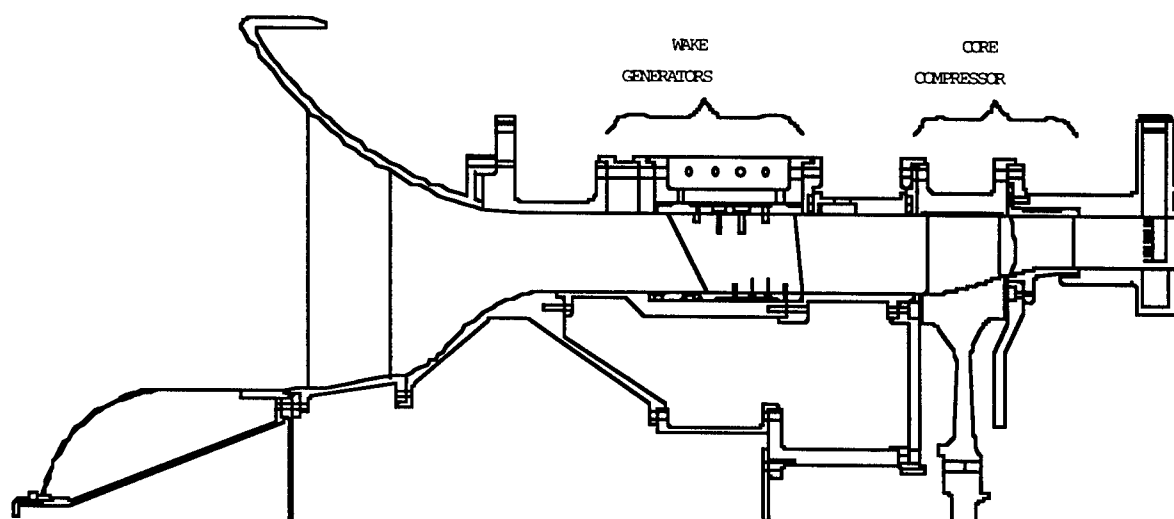


Figure 1. Schematic of SMI Compressor Rig.

The research compressor, Figure 1, was designed by CARL personnel and manufactured by Pratt & Whitney Aircraft Engines. The primary intent for this research compressor is for a Stage Matching Investigation (SMI), characterizing overall compressor performance. Therefore, a single stage core compressor consisting of a rotor and stator with 33 and 49 airfoil blades respectively is used. The outer

diameter for both the rotor and stator is 19 inches. The SMI's core compressor design results in a transonic rotor.

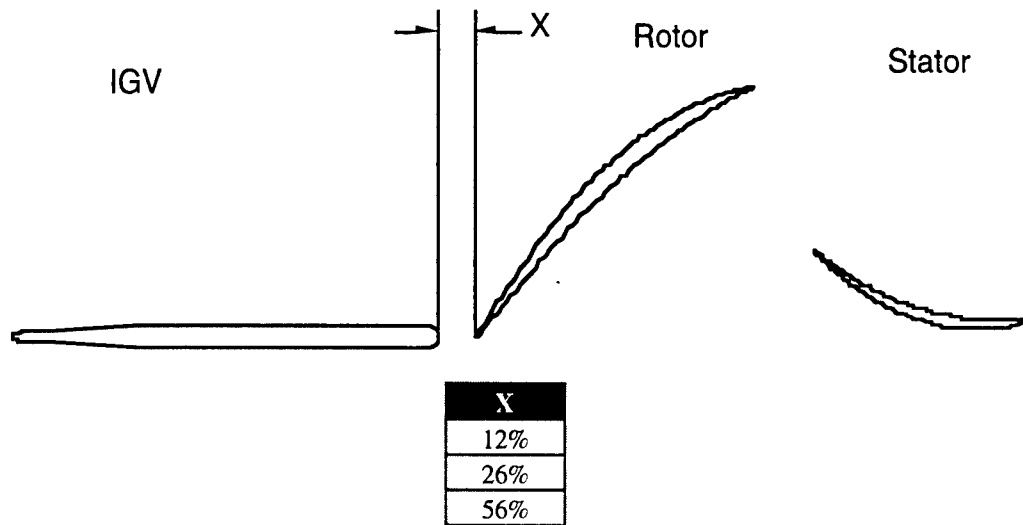


Figure 2. Flow path through SMI Compressor Rig

To study the effect of different upstream stages, an IGV assembly is placed upstream of the rotor section. The IGV's were designed by Pratt and Whitney with the purpose of creating a propagating wake consistent with a modern technology, highly loaded, low aspect ratio stage, therefore they are sometimes referred to as Wake Generators. This term along with Inlet Guide Vanes (IGV) will be used interchangeably. The wake generators do not turn the flow as would a normal IGV assembly. They have a constant solidity (spacing to chord ratio) along the span and have no aerodynamic loading in order to achieve a uniform two dimensional wake. With this design, several ways are utilized to modify the wake profile generated. First, the number of IGV blades in the upstream passage can be varied. A split ring assembly is used for installation and three different numbers of IGV blades can be utilized 12, 24, and 40. It is also possible to vary the axial spacing between the IGV's and the rotor, Figure 2. Three different spacings are possible 12%, 26%, and 56% of the rotor chord from the IGV trailing edge to the rotor leading edge. In this research, only the 24 IGV and 26% spacing data set has been examined.

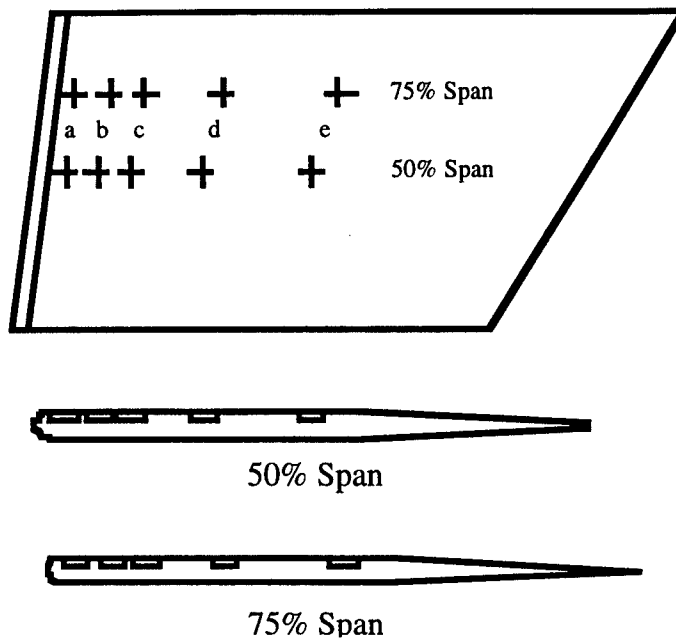


Figure 3. Transducer Locations on IGV

IGV Surface Pressure Instrumentation

The wake generators are instrumented with miniature Kulite pressure transducers. Figure 3 shows the locations of these pressure transducers. Two different blades are instrumented with 10 pressure transducers each. To investigate three dimensional effects, two different spanwise locations are instrumented, 50% and 75% as shown. The blade surface is machined to allow the pressure transducers to be mounted flush. To protect the pressure sensor, a thin layer of RTV was placed over the diaphragm. Grooves for the lead wires are also machined to ensure no disturbance to the flow. The lead wires are bundled and fed out of the casing.

Two adjacent wake generators are instrumented giving data for one flow passage. Surface pressure data is collected for only the 24 wake generator case. Flow periodicity is assumed with one blades data phase shifted to the other blade for analysis purposes.

LQ-125 miniature pressure transducers from Kulite are used for the surface pressure measurements. The pressure transducers are manufactured directly on the blades using chip on technology. The pressure sensing element is 0.060 inches in diameter. It has an internally compensated temperature range of 30 to 130°F. The natural frequency of the pressure transducer is 300 kHz, giving a usable frequency range of 60

kHz. During initial testing, it was discovered that one pressure transducer was bad so the experimental data could not be collected at the 75% span 50% chord location.

Calibration of the transducers for sensitivity and offset was achieved in the following manner. Before installation of the instrumented wake generator, the transducers were subjected to variable pressures at a nominal temperature of 70°F and an elevated temperature of 110°F. The results of this study indicated for this range of temperature transducer sensitivity was 0.01% per degree F. However, offset was influenced by temperature variation and the magnitude of the shift varied from a high of 0.017 psia/degree F to a low of 0.001 psia/degree F.

Based on this bench calibration, no special procedures were established to control sensitivity with inlet air temperature shifts. However, to control transducer offset variation, the transducers' amplifiers were re-balanced at atmospheric conditions for any inlet temperature shift of 3°F or greater.

From these procedures, offset and precision errors were established as ± 0.06 psi and ± 0.04 psi, respectively. In addition, a zero response data set was recorded. The data was then processed in the same manner as the actual test data. Therefore, this signal is representative of the actual static pressure uncertainty due to noise influences. The measured random uncertainty was a ± 0.1 psia fluctuation in static pressure. This value includes precision error due to random noise and temperature changes.

Computational Analysis

In 1992, a nonlinear unsteady Euler/Navier-Stokes vane blade interaction model, VBI 2D, was developed by Rao et al⁸ for turbine configurations. This analysis models the relative motion of adjacent blade rows by allowing one row to move with respect to the other. The VBI code is utilized for the IGV/rotor interaction in the compression stage by modeling both the IGV and rotor. A brief overview of the VBI code will now be given.

Grid Generation

Two separate grids are generated using VGRID, an H and O grid for each blade row. The two grids are then embedded to form a composite grid by a chimera scheme called PEGSUS.⁹ PEGSUS creates the appropriate hole boundaries and interpolation stencils involved in the communication of embedded grids.

The embedding process eliminates problems with cell skewness near the leading and trailing edges of the airfoils. The transition from the inflow and outflow boundaries to the airfoil leading and trailing edges causes this problem. The PEGSUS results are read directly into the VBI code.

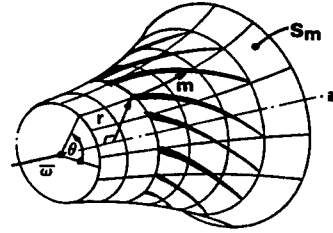


Figure 6. Coordinate system used in VBI formulation

Numerical Method

The VBI code solves the Euler/Navier Stokes equations using an explicit runge kutta scheme in quasi-three-dimensional space. Figure 6 represents the coordinate system used in the formulation.⁸ The Baldwin-Lomax¹⁰ model for turbulence and transition is utilized within the code. The governing equations for flow on a blade-to-blade surface of revolution will now be given:⁵

$$\frac{\partial Q}{\partial t} + \frac{\partial E}{\partial m} + \frac{\partial F}{\partial \theta} = H \quad (1)$$

where:

$$H = H_i - H_v + \frac{\partial E_v}{\partial m} + \frac{\partial F_v}{\partial \theta}$$

$$Q = rb \begin{bmatrix} \rho \\ \rho u \\ \rho v \\ \rho e \end{bmatrix}$$

$$E = rb \begin{bmatrix} \rho u \\ \rho u^2 + p \\ \rho uv \\ u(\rho e + p) \end{bmatrix}$$

$$F = b \begin{bmatrix} \rho v \\ \rho uv \\ \rho v^2 + p \\ v(\rho e + p) \end{bmatrix}$$

$$E_v = \frac{rb}{Re} \begin{bmatrix} 0 \\ \sigma_{11} \\ \sigma_{12} \\ E_4 \end{bmatrix}$$

$$F_v = \frac{b}{Re} \begin{bmatrix} 0 \\ \sigma_{12} \\ \sigma_{22} \\ F_4 \end{bmatrix}$$

$$H_i = rb \begin{bmatrix} 0 \\ \left(\rho v^2 + p \right) \frac{1}{r} \frac{dr}{dm} + p \frac{1}{b} \frac{db}{dm} \\ -\rho uv \frac{1}{r} \frac{dr}{dm} \\ 0 \end{bmatrix}$$

$$H_v = \frac{rb}{Re} \begin{bmatrix} 0 & \sigma_{22} \frac{1}{r} \frac{dr}{dm} + \sigma_{33} \frac{1}{b} \frac{db}{dm} \\ -\sigma_{12} \frac{1}{r} \frac{dr}{dm} & 0 \end{bmatrix}$$

The following equations represent the energy components

$$e = \frac{p}{\rho(\gamma-1)} + \frac{1}{2}(u^2 + v^2) \quad (2)$$

$$E_4 = u\sigma_{11} + v\sigma_{12} + \frac{1}{\gamma-1} \frac{\mu}{Pr} \frac{\partial a^2}{\partial n} \quad (3)$$

$$F_4 = u\sigma_{12} + v\sigma_{22} + \frac{1}{\gamma-1} \frac{\mu}{Pr} \frac{1}{r} \frac{\partial a^2}{\partial \theta} \quad (4)$$

where E_4 and F_4 are the viscous terms from the energy equation. It is now necessary to represent the shear stress equations:

$$\sigma_{11} = 2\mu \frac{\partial u}{\partial n} + \lambda \nabla \cdot V \quad (5)$$

$$\sigma_{12} = \mu \left(\frac{\partial v}{\partial m} - \frac{v}{r} \frac{dr}{dm} + \frac{1}{r} \frac{\partial u}{\partial \theta} \right) \quad (6)$$

$$\sigma_{22} = 2\mu \left(\frac{1}{r} \frac{\partial v}{\partial \theta} + \frac{u}{r} \frac{dr}{dm} \right) + \lambda \nabla \cdot V \quad (7)$$

$$\sigma_{33} = 2\mu \frac{u}{b} \frac{db}{dm} + \lambda \nabla \cdot V \quad (8)$$

For this analysis, it is assumed that Stokes' hypothesis is true. For turbulent results, the viscosity is represented in an appropriate form. The laminar and turbulent viscosity's are accounted for with the turbulent viscosity found from the Baldwin-Lomax eddy-viscosity model.

Frequency Analysis

A fast fourier transform algorithm (FFT) was added to the VBI source code to allow frequency comparisons to be made between the experimental and computational results, as suggested by Probasco et al⁹. The fundamental use of FFT algorithms are for computing the discrete Fourier transforms of sequences. The FFT algorithm utilized in this source code was developed with the help of an existing algorithm by Pickering.¹⁰ The algorithm is based on blade pass frequency and calculates the first five harmonics of both the magnitude and phase of the unsteady delta pressure for each chord location along the entire surface of the IGV blade. A frequency analysis is required for any forced response analysis, because it is the unsteady pressure phase response which determines the flutter stability of the cascade. The addition of a frequency

capability makes the VBI code a more useful tool in high cycle fatigue analysis. Originally the code only calculated unsteady envelopes (i.e., maximum and minimum unsteady distributions).

Results

The results discussion is divided into two sections, experimental and computational. A series of experiments were performed in the Compressor Aero Research Lab SMI compression stage to investigate the IGV unsteady surface pressure response due to the upstream traveling potential field generated by the downstream rotor. A computational study was then completed utilizing the VBI code with comparisons made to the experimental data.

Experimental Data Reduction

The experimental data was recorded on a 28 channel analog tape recorder with a flat response up to 80kHz. The data was digitized off-line at an effective sample rate of 500 kHz. Anti-aliasing was achieved using a Precision Filters TD6B Linear Phase Time Delay Filter. A cutoff frequency of 132 kHz was used for the data reduction. This gives a 1% attenuation of the signal at 77 kHz. The blade pass frequency is 7.8 kHz. Therefore, the first 11 blade pass harmonics are resolved without aliasing. Data was digitized for a time record of 68 milliseconds, which gives approximately 16 rotor revolutions. Ensemble averaging was performed on the data in order to average out any inconsistencies that may exist from one rotor blade to the next. The ensemble averaging was accomplished based on the rotor blade pass frequency, since the rotor has 33 blades, about 520 records were ensemble averaged.

Computational Analysis Parameters

Four thousand time steps were used per rotor blade pass with a time step of approximately 2.9×10^{-8} seconds being used. Figure 7 represents a pressure time history for one node of the flow field. A total of 37 rotor blade passes were analyzed to reach a nearly periodic solution as shown in Figure 7. There appears to be a possible low frequency rotating stall cell present in the computational solution. This is not seen in the experimental data, but the experimental results are obtained with a downstream stator section included, while the computational analysis did not model the downstream stator blade row. The consequences of this difference will be discussed later when the computational Mach number contours are presented. For the

quasi-three-dimensional effects, a 20% streamtube contraction through the rotor is input into the VBI code to take care of the spanwise direction component of the three dimensional analysis. Finally, an algebraic turbulence model is utilized to model viscous effects in the computational results presented.

Discussion of Results

A comparison of computational results and experimental data will be shown. The operating point used for this comparison is 105% corrected speed and a near stall throttle setting on the performance curve. This operating point is shown in Figure 8. The inlet guide vane assembly can be located either 12%, 26% or 56% of rotor chord away from the rotor leading edge and with either 12, 24, or 40 vanes. The data and results discussed here are for the 26% rotor chord spacing and 24 vane configuration. The computational results shown are the last two blade passes of thirty-seven.

Figure 9 represents the computational Mach contour lines for six rotor blades and four inlet guide vanes. For this operating point, a bow shock at the leading edge of the rotor is known to exist. The high back pressure needed to operate at this low of a flow rate forces the bow shock upstream of the rotor leading edge. In the computational analysis, the bow shock is clearly evident in the plot and can be seen to progress upstream. The upstream shock interaction causes a significant unsteady pressure force on the IGV blades which is not considered in typical turbomachinery compressor designs. The separation near the trailing edge can be accounted in two manners. First, the downstream stator stage is not modeled, therefore, the exit pressure for the rotor is not known. A rise in the exit pressure would provide a more favorable pressure gradient for the flow removing the trailing edge separation. Secondly, the computational analysis is 2-D. The streamtube contraction method of modeling the 3-D flow within the actual rig may not include all the flow physics to keep the flow attached. Finally, the primary interest of this research is the upstream traveling potential blade row effect. So, a separated flow region at the trailing edge of the rotor is not of major importance to the upstream solution.

Figure 10 represents a comparison of the unsteady normalized difference (upper surface - lower surface) pressure for the computational and experimental results at the 50%, 70%, 83%, 89%, and 95% chord locations on the Inlet Guide Vanes. This figure will be discussed from the trailing edge forward, since

the strongest interaction is at the trailing edge. At the 95% chord location, there is excellent agreement between the experimental and computational blade pass response. The upstream traveling bow shock is the dominating feature of both the experimental and computational response. The computational analysis models the nonlinear shock interaction extremely well in both magnitude and phase. For the 89% chord location, the shock structure is less evident but is still the dominating phenomenon. The computational analysis slightly over predicts the unsteady magnitude response with the phase in excellent agreement. At 83%, the shock structure has disappeared. The computational analysis again over predicts the unsteady magnitude response with an excellent phase agreement. The general character of the unsteady response at the 70% chord location is modeled by the computational analysis. The magnitude and phase are in reasonable agreement with experimental data, but the shape of the response is slightly off. Finally, at the 50% chord location, the magnitude is modeled adequately, but the phase is about 180° off.

It is evident in Figure 10 the effect of moving farther away from the rotor has on the unsteady response. At the 50% chord location the unsteady pressure response is about 1/4th of the response at the trailing edge. At the trailing edge, the net pressure fluctuation acting on the IGV blades is 3.4 psia. The unsteady response at the trailing edge is dominated by the rotor bow shock which is traveling upstream. It is encouraging for the turbomachinery designer, the agreement found between the experimental and computational results. These results definitely increase the designer's confidence in the computational design tools available.

Figure 11 represents a comparison of the magnitudes of the first five harmonics for the computational results and experimental data versus chord position. The first harmonic computational results are generally lower than the experimental results. The computational results show a very high response at the 98% chord location. Since there was not any instrumentation at this location, it is unknown if this response is actual. The second harmonic response in general has much better agreement with the experimental results. It is important to note the magnitude of the 2nd harmonic response near the trailing edge. At the 98% chord position, the 2nd harmonic response is greater than the 1st. If the shock wave is hitting the IGV at the 98% chord location, then this kind of behavior would be expected. The 3rd through

5th harmonic response show negligible response except at the trailing edge. Again, this is consistent with a shock interaction at the trailing edge.

These results have significant implications for turbomachinery design models. For transonic compressor design the shock interaction upstream of the rotor is significant. By the nature of this shock wave, the interaction is highly nonlinear. Therefore, to properly model a transonic compressor design a nonlinear analysis is required. Current trends in turbomachinery design systems is toward linearized methods, either linearized Euler or Navier-Stokes models. These linearized methods are quite computationally efficient, but they only consider the 1st harmonic response. As the above results show, the designer should be extremely cautious about using linearized design tools for transonic compressor designs.

Conclusions

A computational and experimental investigation was performed to investigate the unsteady upstream traveling forcing function from a high speed, highly loaded compression rotor. The IGV unsteady surface pressures were experimentally measured for a near-stall transonic operating point to determine the forcing function. The data was analyzed in both the time and frequency domain based on the blade pass frequency. The experimental configuration was computationally modeled with a nonlinear unsteady viscous vane/blade interaction 2D code for comparisons with the experimental data in both the time and frequency domain.

Significant upstream traveling pressure effects were both measured and predicted. A detached bow shock is caused by the increased back pressure consistent with a near stall operating point. The bow shock is shown to impact the IGV blades. Its strongest effect is at the trailing edge of the IGV's with a 3.4 psia fluctuation. The nonlinear viscous vane/blade interaction computational analysis showed excellent agreement with the experimental results in both the time and frequency domain. Significant higher harmonic content was evident near the trailing edge of the IGV's. This is important, in light, of recent trends toward use of linearized Euler and Navier-Stokes models for turbomachinery designs. The results of this research indicate the importance of higher harmonic, therefore extreme caution should be taken when designing transonic compression stages with linearized methods.

Acknowledgments

The authors would like to thank all of the personnel at CARL. In particular, Dr. Randy Chriss and Dr. Bill Copenhaver for help in analyzing the experimental data. Also, Dr. Rolf Sondergaard and Charles Stevens from WL/POTT are thanked for help with the computational results. In addition, the authors would like to acknowledge the support of Doug Probasco, a Wright State University Master's student, who was instrumental in the successful completion of this research. Finally, this work was supported in part by a grant of HPC time from the DoD HPC Center, MSRC at Wright Patterson Air Force Base through the use of the HPC07 and CFS01 machines.

References

¹Verdon, Joseph M, "Unsteady Aerodynamic Methods for Turbomachinery Aeroelastic and Aeroacoustic Applications," *AIAA Paper No. 92-0011*, 1992.

²Suddhoo, A., Giles, M.B., and Stow, P, "Simulation of Inviscid Blade Row Interaction Using a Linear and a Non-Linear Method," *AIAA Paper No. 91-7049*, 1991.

³Giles, M.B., "Stator/Rotor Interaction a Transonic Turbine," *AIAA Paper No. 88-3093*, 1988.

⁴Rai, Man Mohan, "Three-Dimensional Navier-Stokes Simulations of Turbine Rotor-Stator Interaction; Part I-Methodology," *Journal of Propulsion*, Vol. 5, No. 3, 1989, pp. 305-311.

⁵Rao, K.V., and Delaney, R., "Investigation of Unsteady Flow Through Transonic Turbine Stage; Part 1: Analysis," *AIAA Paper No. 90-2408*, 1990.

⁶Dring, R.P., Joslyn, H.D., Hardin, L.W., and Wagner, J.H., "Turbine Rotor-Stator Interaction," *Journal of Engineering for Power*, Vol. 104, 1982, pp. 729-742.

⁷Dunn, M.G., Bennett, W.A., Delaney, R.A., and Rao, K.V., "Investigation of Unsteady Flow Through a Transonic Turbine Stage: Data/Prediction Comparison for Time-Averaged and Phase-Resolved Pressure Data," *Journal of Turbomachinery*, Vol. 114, 1992, pp. 91-99.

⁸Rao, K.V., Delaney, R.A., and Topp, D.A., "Turbine Vane-Blade Interaction," *Interim Report WL-TR-92-2002*, 1992.

⁹Probasco, D.P., Wolff, J.M., Copenhaver, W.W., and Chriss, R.M., "Unsteady Blade Row potential Interaction in a Compression Stage," *AIAA Paper No. 97-3285*, 1997.

¹⁰Pickering, M., "An Introduction to Fast Fourier Transform Methods for Partial Differential Equations, with Applications," 1943, pp 163.

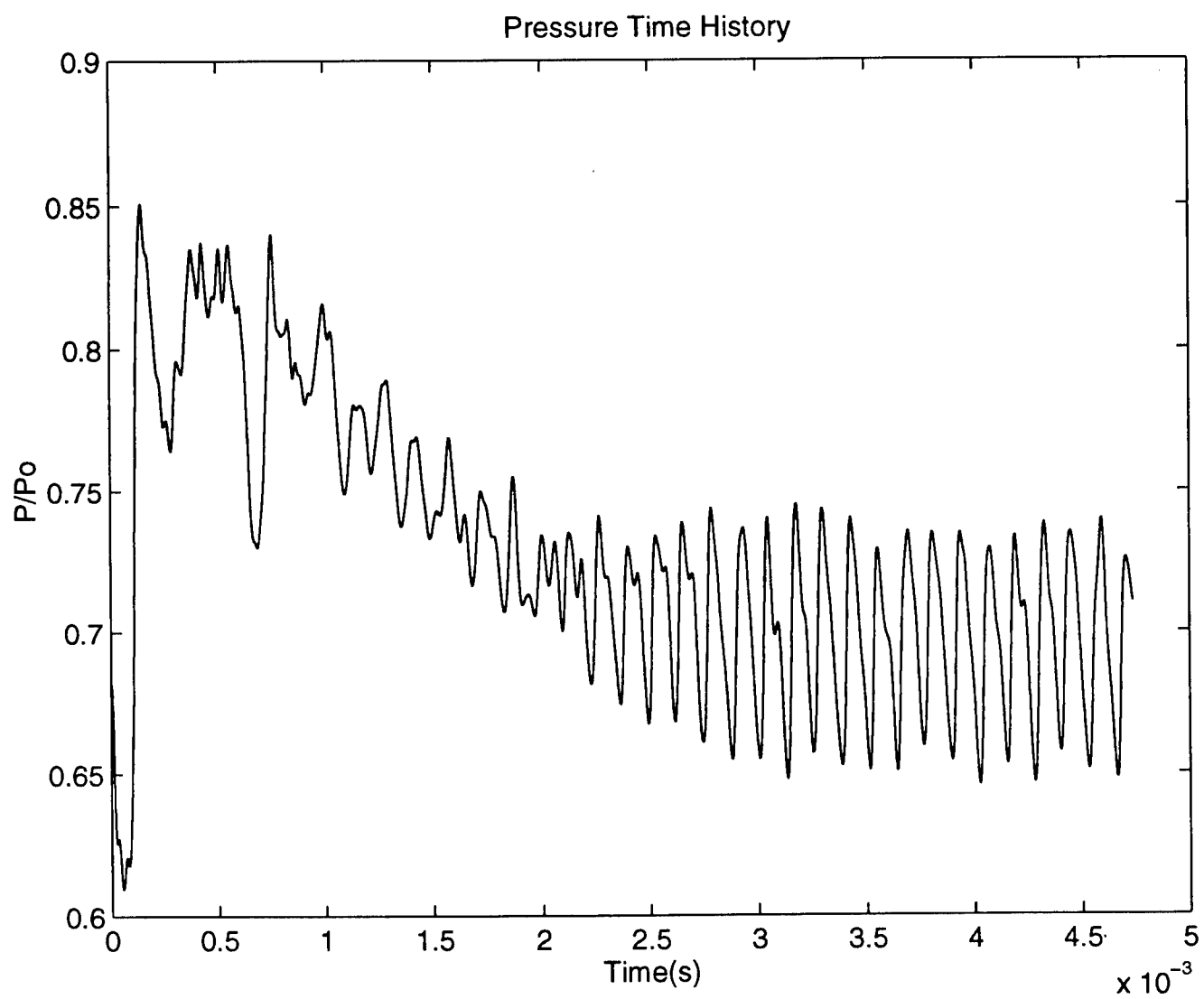


Figure 7. Pressure Time History

Compressor Performance Map

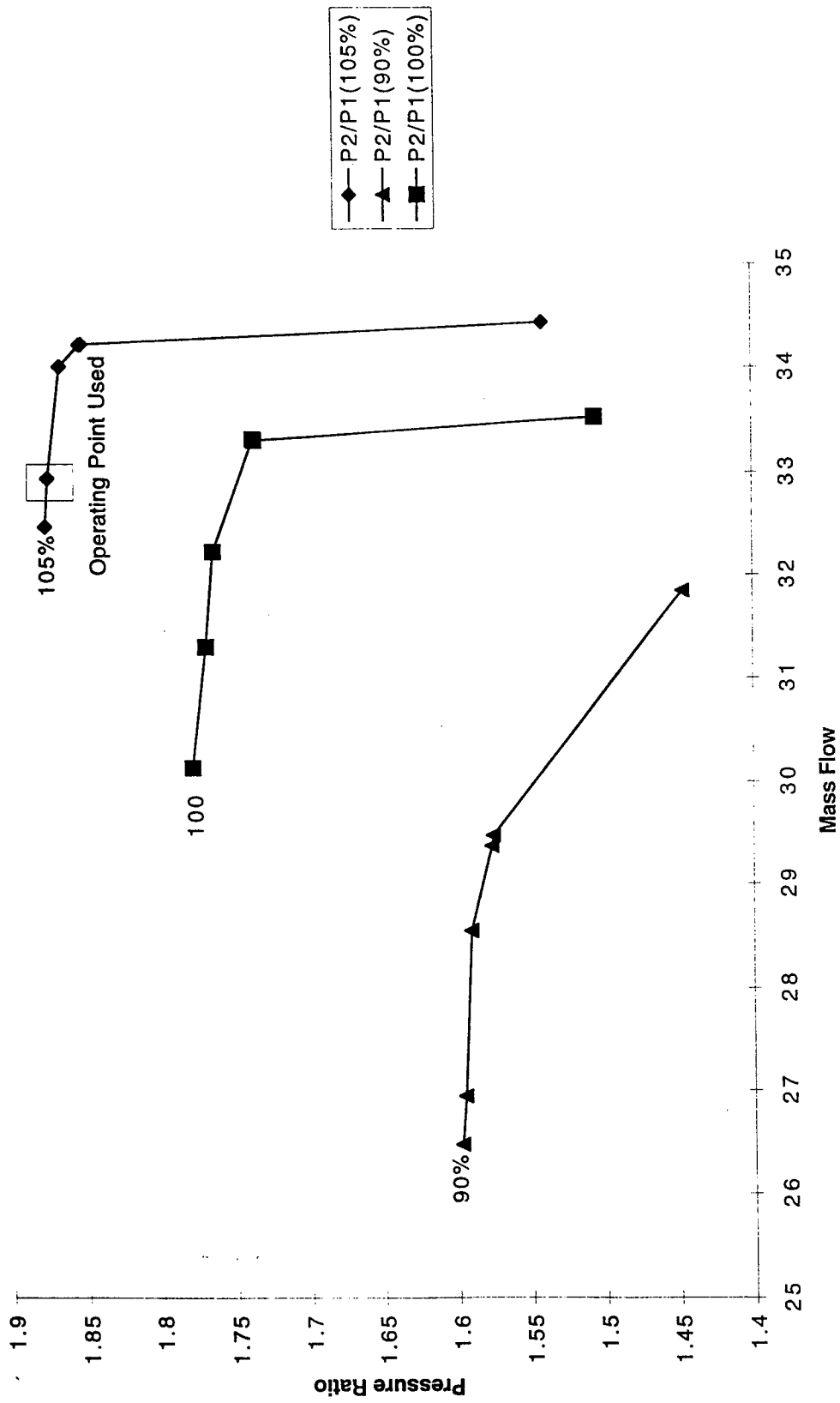


Figure 8. Compressor Performance Map SMI Rotor

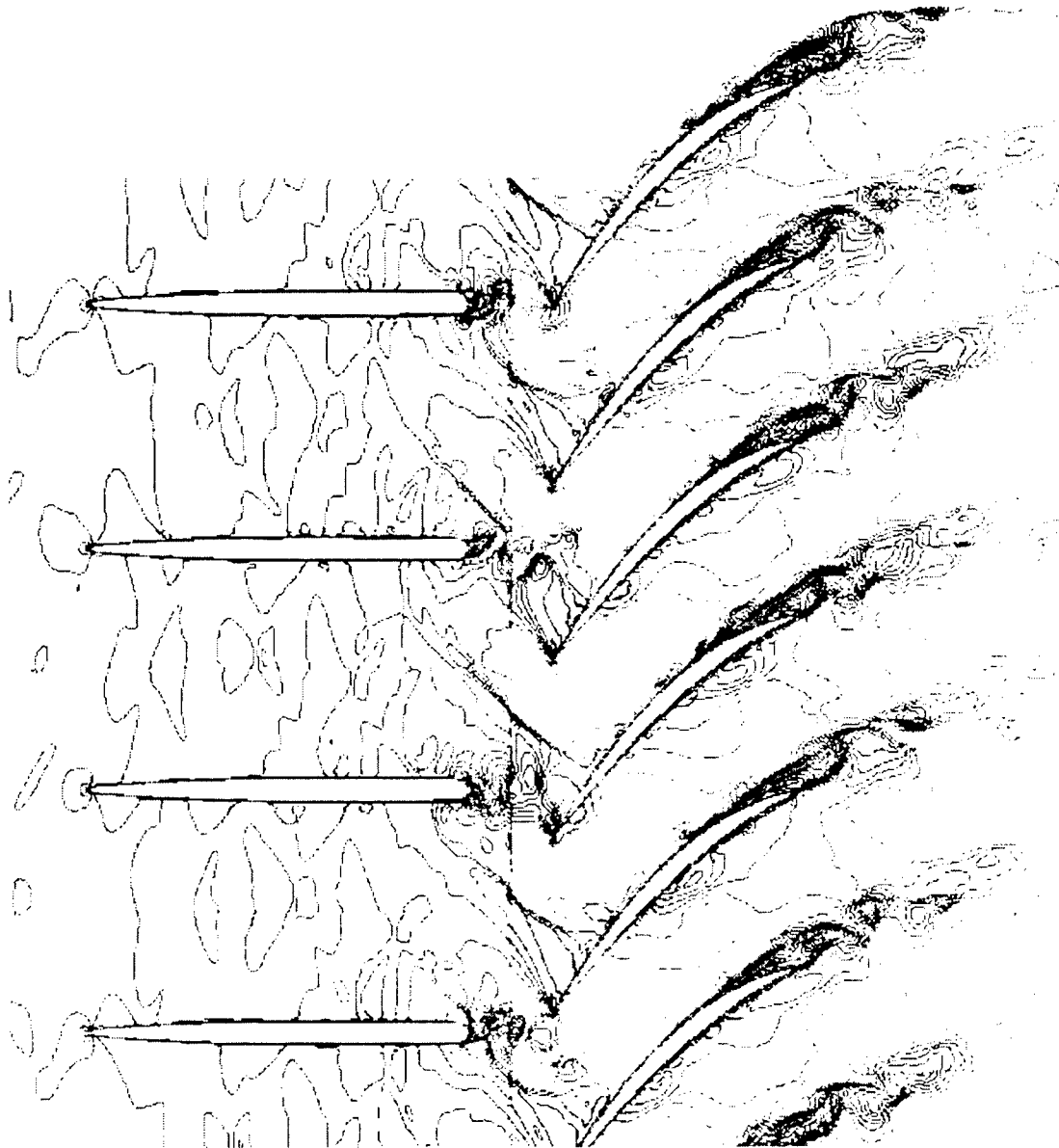


Figure 9. Snap Shot of Mach Number Contours

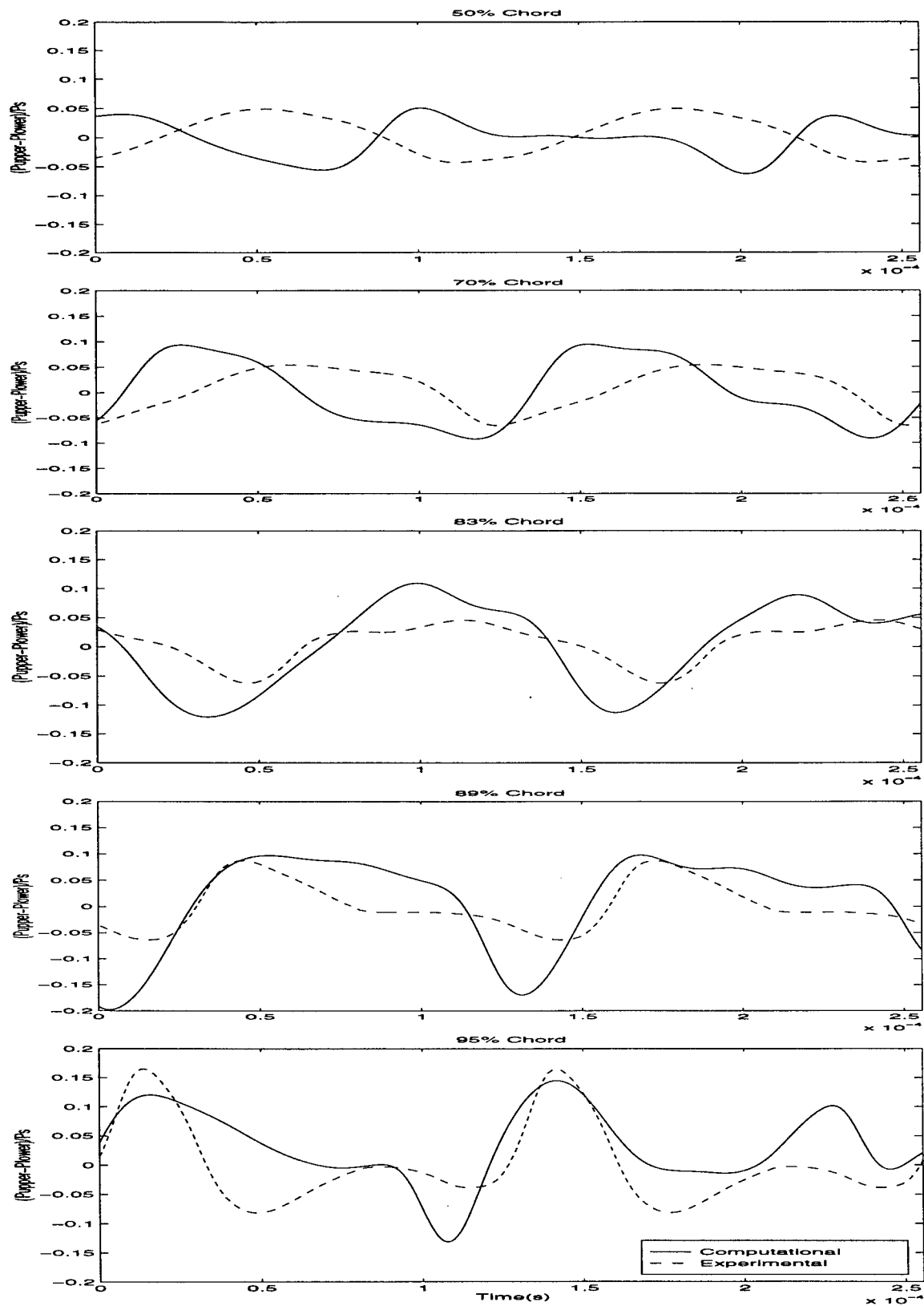


Figure 10. Unsteady Delta Pressure Comparison for 5 Chordwise Locations

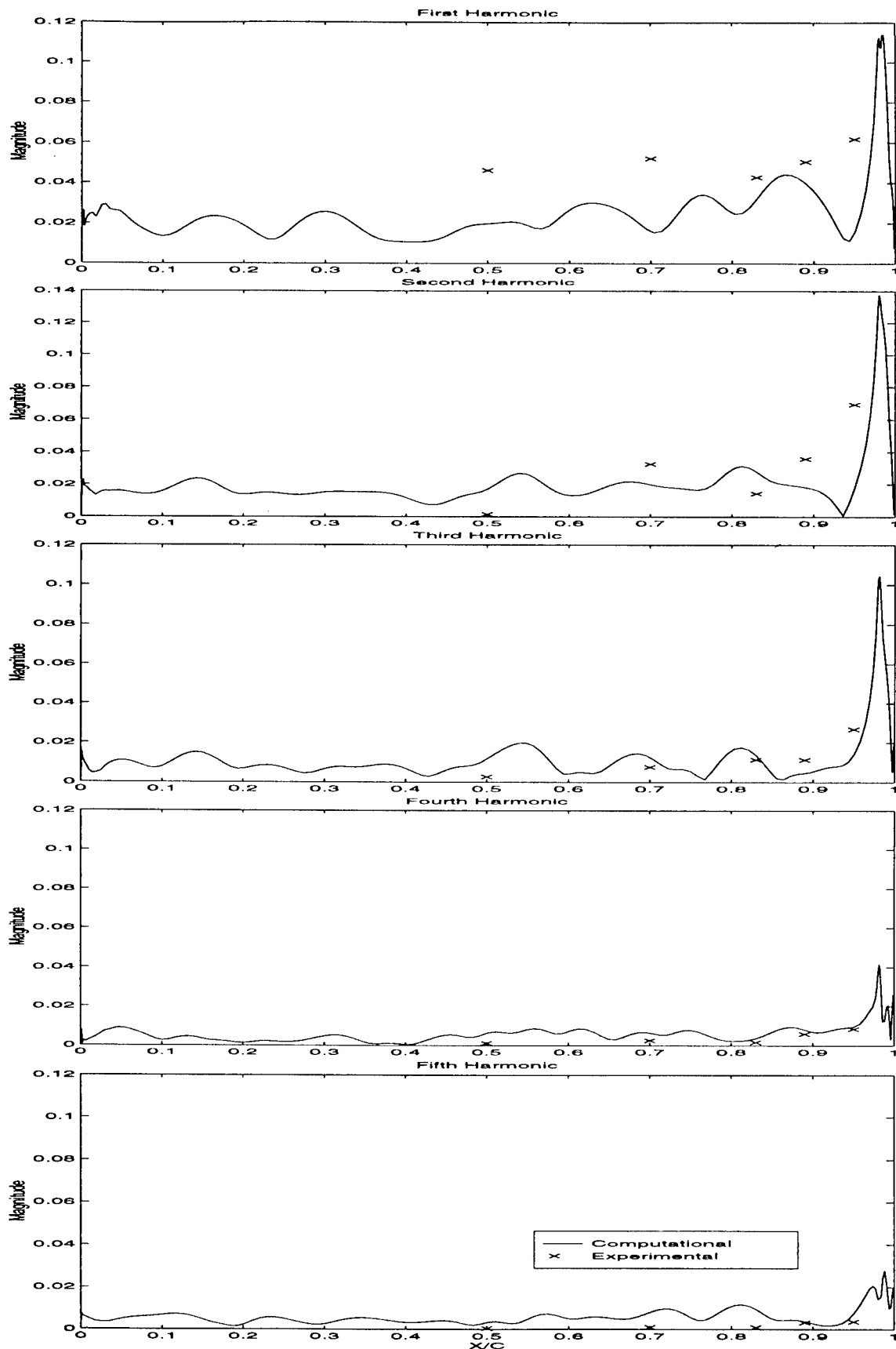


Figure 11. Unsteady Delta Pressure Magnitude Harmonic Response

IMPROVED AIRCRAFT ROLL MANEUVER PERFORMANCE USING
SMART DEFORMABLE WINGS

R. K. Yedavalli
Professor
Department of Aerospace Engineering

Ohio State University
Columbus, OH. 43210

Final Report for:
Summer Faculty Research Program
Wright Laboratory

Sponsored by:
Air Force Office of Scientific Research
Bolling Air Force Base, DC

And

Wright Laboratory

September, 1997

IMPROVED AIRCRAFT ROLL MANEUVER PERFORMANCE USING SMART DEFORMABLE WINGS

R. K. Yedavalli

Professor

Department of Aerospace Engineering,
Applied Mechanics, and Aviation.

The Ohio State University
Columbus, Ohio 43210-1276

Abstract

In the research during the Summer Faculty Research Program, the aspects of modeling and control design methodology for improving roll maneuver performance in aircrafts (for achieving a desired roll rate) by deforming a flexible wing with piezoelectric actuation and sensing are studied. An integrated finite element model of a laminated composite plate embedded with smart piezo actuators and sensors subject to aerodynamic loading giving rise to a steady roll rate is developed. The resulting model in the generalized coordinates which has nonsymmetric aerodynamic damping matrix and a nonsymmetric stiffness matrix (due to aerodynamic stiffness) is then transformed to real but nonorthogonal modal coordinates and a reduced order model is developed. A new control design algorithm based on 'Reciprocal State Space' framework is then developed to achieve the desired roll rate and to simultaneously suppress the flexible mode vibrations. The research carried out clearly delineates the relationship and interaction between the structural, aerodynamic and piezo actuation based control subsystems and underscores the importance, potential and the vast scope of the proposed integrated approach to improve aircraft maneuver performance.

IMPROVED AIRCRAFT ROLL MANEUVER PERFORMANCE USING SMART DEFORMABLE WINGS

R. K. Yedavalli

1 Introduction:

In recent years, design and control of smart structures has become an active topic of research due to the significant potential of these structures to actively deform for control purposes thereby improving the performance of various types of flight vehicles. In particular, piezoelectric actuation and sensing is gaining lot of attention due to the distributed nature of these 'smart' materials. Federal Research Laboratories such as Wright Laboratory, DARPA and industries such as Northrop Grumman are actively engaged in research and development of this challenging multidisciplinary area with extensive applications [1][2]. Typically, the modeling of the vibrational motion of these structures is done using finite element procedures, which yield, in the linear range, simultaneous, ordinary differential equations of second order in the 'configuration or generalized' coordinates, which we call the Matrix Second Order Systems involving Mass, Damping and Stiffness matrices. Most of the previous modeling and control design research in this multidisciplinary area is confined to integration of any two subdisciplines such as structures and control, control and smart materials, structures and smart materials. Lately aeroelastic control involving structures, aerodynamics and controls has become an active area of research but in this research the actuation is assumed to be point actuation with discrete devices. Only recently the truly integrated problem of incorporating all four subdisciplines, namely structures, aerodynamics, smart materials and control system design is being attempted. This type of pure and straightforward integration of these four disciplines is realized to be a complicated task requiring expertise in all of these disciplines. In addition, for applications involving aircraft maneuvers one should even add another subdiscipline, namely flight mechanics! One of the first attempts to incorporate structures, aerodynamics, control and flight mechanics (addressing specifically the roll maneuver) are the series of papers by WL and Northrop Grumman researchers Khot, Eastep, Kari Appa and their colleagues [3][4]. In this

summer research, an attempt is made, perhaps for the first time, to achieve integration of all the above five disciplines! In this research, efforts are undertaken to model and control the aeroelastic dynamics of a flexible wing structure embedded with piezo material for actuation and sensing so that a roll maneuver with a desired roll rate is achieved by actively deforming the wing. This modeling is done using finite element method in the 'generalized' coordinates. Because of the coupling between these subsystems, the resulting 'Matrix Second Order System' of equations consists of a symmetric positive definite mass matrix but a nonsymmetric and indefinite damping (which includes aerodynamic damping) and stiffness (that includes aerodynamic and piezo material stiffness, in addition to the standard structural stiffness) matrices! The piezoelectric voltages serve as the Control variables. This large model in the generalized coordinates is then transformed to a set of 'nonorthogonal modal' coordinates and model reduction is carried out in these modal coordinates. This model is then converted to the 'state space' form. This standard state space form is then transformed to a new framework called 'Reciprocal State Space' framework and control design is carried out in this new framework. This new modeling and control design methodology is illustrated with the help of an example and its efficacy clearly demonstrated.

2 Integrated Modeling for Smart Flexible Deformable Wings:

In Kari Appa, Khot et al [5], the matrix second order equations of motion are first derived using the 'orthogonal modal' coordinates of the pure structural dynamic system and the aerodynamic pressure distribution to achieve roll motion is assumed to be known along these 'modal coordinates' which is the typical procedure currently followed by most aeroelastic studies. However, in this summer research, attempts are made to obtain a more generic model that is applicable not only to the present problem of roll maneuvers but also to the future applications involving pitch, roll and yaw maneuvers. With this in mind, it is argued that this type of generic maneuver model can be developed easier in the 'generalized' coordinates rather than in the orthogonal modal coordinates. In the orthogonal modal coordinate approach it is difficult to simultaneously consider the influence or coupling of the other subsystems such as aerodynamics, controls, flight mechanics and smart material actuation and sensing whereas this is possible in the direct 'generalized' coordinates. Of course there is a price to be paid later for this generality! It is that when model reduction

is required for control design, the necessary step of converting to the modal coordinates involves 'nonorthogonal' modal coordinates! However, it is felt that this is a smaller price to pay considering the 'true integration' achieved when modeling is done in the 'generalized' coordinates. So in what follows, we develop a finite element model with nodal displacements as the 'generalized' coordinates and simultaneously incorporate the aerodynamic pressure distribution as well as piezo actuation directly integrated into this finite element model.

2.1 Finite Element Modeling of a Smart Material (Piezoelectric) Wing Subject to Aerodynamic Loads:

The constitutive equations for a piezoelectric material are expressed as [6]

$$\{T\} = [c]\{S\} - [e]^T\{E\} \quad (1)$$

$$\{D\} = [e]\{S\} + [\epsilon]\{E\} \quad (2)$$

where

$$\{T\} = [\sigma_{xx} \ \sigma_{yy} \ \sigma_{zz} \ \sigma_{yz} \ \sigma_{zx} \ \sigma_{xy}]^T ; \text{stress vector}$$

$$\{S\} = [\varepsilon_{xx} \ \varepsilon_{yy} \ \varepsilon_{zz} \ \gamma_{yz} \ \gamma_{zx} \ \gamma_{xy}]^T ; \text{strain vector}$$

$$\{E\} = [E_x \ E_y \ E_z]^T ; \text{electric field vector}$$

$$\{D\} = [D_x \ D_y \ D_z]^T ; \text{electric displacement vector}$$

$$[c] = \begin{bmatrix} C_{11} & C_{12} & C_{13} & 0 & 0 & 0 \\ C_{12} & C_{11} & C_{13} & 0 & 0 & 0 \\ C_{13} & C_{13} & C_{33} & 0 & 0 & 0 \\ 0 & 0 & 0 & C_{44} & 0 & 0 \\ 0 & 0 & 0 & 0 & C_{44} & 0 \\ 0 & 0 & 0 & 0 & 0 & C_{44} \end{bmatrix}$$

$$[e] = \begin{bmatrix} 0 & 0 & 0 & 0 & e_{15} & 0 \\ 0 & 0 & 0 & e_{24} & 0 & 0 \\ e_{31} & e_{32} & e_{33} & 0 & 0 & 0 \end{bmatrix}$$

$$[\epsilon] = \begin{bmatrix} \epsilon_{11} & 0 & 0 \\ 0 & \epsilon_{11} & 0 \\ 0 & 0 & \epsilon_{33} \end{bmatrix}$$

2.2 Finite Element Model using Coupled 8-node Brick Elements

In order to generate the finite element formulation of a flexible wing, 8-node coupled brick elements (Fig. 1) are employed. The shape functions of the elements are expressed as

$$N_i = \frac{1}{8}(1 + \xi\xi_i)(1 + \eta\eta_i)(1 + \zeta\zeta_i) \quad (3)$$

Each node of the element has four degrees of freedom which are spatial displacements (u, v, w) and voltage (V). These displacements and voltage are coupled to each other according to the constitutive equation (Eq. 2). The displacement fields with the shape functions in the finite element model are expressed as

$$\mathbf{u} = [\mathbf{N}_q]\{\mathbf{q}_i\} = [\mathbf{N}_q]\mathbf{q} \quad (4)$$

$$\varphi = [\mathbf{N}_\varphi]\{\varphi_i\} = [\mathbf{N}_\varphi]\varphi \quad (5)$$

where

$$\begin{aligned} [\mathbf{N}_q] &= \begin{bmatrix} N_1 & 0 & 0 & N_2 & 0 & 0 & N_3 & 0 & 0 & \dots \\ 0 & N_1 & 0 & 0 & N_2 & 0 & 0 & N_3 & 0 & \dots \\ 0 & 0 & N_1 & 0 & 0 & N_2 & 0 & 0 & N_3 & \dots \end{bmatrix} \\ [\mathbf{N}_\varphi] &= \begin{bmatrix} N_1 & N_2 & N_3 & \dots \end{bmatrix} \\ [\mathbf{q}] &= \begin{bmatrix} u_1 & v_1 & w_1 & u_2 & v_2 & w_2 & u_3 & v_3 & w_3 & \dots \end{bmatrix}^T \\ [\varphi] &= \begin{bmatrix} V_1 & V_2 & V_3 & \dots \end{bmatrix}^T \end{aligned}$$

Then, the strain and electric fields are written as

$$S = [L_q][N_q]\{q_i\} = [B_q]q \quad (6)$$

$$E = [L_\varphi][N_\varphi]\{\varphi_i\} = [B_\varphi]\varphi \quad (7)$$

where

$$[B_q] = \begin{bmatrix} \frac{\partial N_1}{\partial \xi} & 0 & 0 & \frac{\partial N_2}{\partial \xi} & 0 & 0 & \frac{\partial N_3}{\partial \xi} & 0 & 0 & \dots \\ 0 & \frac{\partial N_1}{\partial \eta} & 0 & 0 & \frac{\partial N_2}{\partial \eta} & 0 & 0 & \frac{\partial N_3}{\partial \eta} & 0 & \dots \\ 0 & 0 & \frac{\partial N_1}{\partial \zeta} & 0 & 0 & \frac{\partial N_2}{\partial \zeta} & 0 & 0 & \frac{\partial N_3}{\partial \zeta} & \dots \end{bmatrix}$$

$$[B_\varphi] = \begin{bmatrix} \frac{\partial N_1}{\partial \xi} & \frac{\partial N_2}{\partial \xi} & \frac{\partial N_3}{\partial \xi} & \dots \\ \frac{\partial N_1}{\partial \eta} & \frac{\partial N_2}{\partial \eta} & \frac{\partial N_3}{\partial \eta} & \dots \\ \frac{\partial N_1}{\partial \zeta} & \frac{\partial N_2}{\partial \zeta} & \frac{\partial N_3}{\partial \zeta} & \dots \end{bmatrix}$$

2.3 Modeling of Aerodynamic Pressure Distribution Generating Roll Maneuver

We now consider the modeling of aerodynamic pressure distribution on the flexible wing structure. According to the piston theory [7][8] the aerodynamic pressure on the surface of a wing for a high Mach number ($M > 1.6$) is expressed as

$$\Delta p = - \left[\lambda \left(\frac{\partial w}{\partial x} \right) + g \left(\frac{\partial w}{\partial t} \right) \right] \quad (8)$$

where

$$\lambda = \frac{2q}{(M^2 - 1)^{0.5}}, \quad g = \frac{\lambda}{U_a} \frac{M^2 - 2}{M^2 - 1}, \quad q = \frac{1}{2} \rho_a U_a^2$$

ρ_a : air density

U_a : air velocity

Fig. 2 shows a 32 degrees of freedom brick element with aerodynamic loads. According to the Eq. 8, the loads are changing by the vertical displacements of nodes and varied with x coordinate and time. It is assumed that the pressure difference between upper and lower surfaces of the wing acts on the upper surface.

By substituting Eq. 4 into Eq. 8, the Eq. 8 can be written as

$$\Delta p = -\lambda [N_a]_{,\xi} \mathbf{q} - g [N_a] \dot{\mathbf{q}} \quad (9)$$

where

$$[N_a] = \begin{bmatrix} 0 & 0 & 0 & 0 & 0 & 0 & 0 & 0 & 0 & \dots \\ 0 & 0 & 0 & 0 & 0 & 0 & 0 & 0 & 0 & \dots \\ 0 & 0 & N_{1,\zeta=1} & 0 & 0 & N_{2,\zeta=1} & 0 & 0 & N_{3,\zeta=1} & \dots \end{bmatrix}$$

It is seen from Eq. 9 that the aerodynamic loads are expressed in terms of the generalized coordinates of the element. The principal advantage of this approach is that, in the equation of motion of the system, one can easily identify the damping and stiffness contributions due to aerodynamics alone. After assembling the required terms we obtain the well known matrix second order system of equations given by [9]

$$\begin{bmatrix} M & 0 \\ 0 & 0 \end{bmatrix} \begin{bmatrix} \ddot{\mathbf{q}} \\ \ddot{\varphi} \end{bmatrix} + \begin{bmatrix} C_A & 0 \\ 0 & 0 \end{bmatrix} \begin{bmatrix} \dot{\mathbf{q}} \\ \dot{\varphi} \end{bmatrix} + \begin{bmatrix} K_q + K_A & K_{q\varphi} \\ K_{\varphi q} & K_{\varphi\varphi} \end{bmatrix} \begin{bmatrix} \mathbf{q} \\ \varphi \end{bmatrix} = \begin{bmatrix} 0 \\ \mathbf{Q} \end{bmatrix} \quad (10)$$

where

$$\begin{aligned} M &= \int_{-1}^1 \int_{-1}^1 \int_{-1}^1 \rho [N_q]^T [N_q] |J| d\xi d\eta d\zeta \\ C_A &= \int_{-1}^1 \int_{-1}^1 g [N_q]_{\zeta=1}^T [N_a] |J_a| d\xi d\eta \\ K_q &= \int_{-1}^1 \int_{-1}^1 \int_{-1}^1 [\mathbf{B}_q]^T [\mathbf{c}] [\mathbf{B}_q] |J| d\xi d\eta d\zeta \\ K_A &= \int_{-1}^1 \int_{-1}^1 \lambda [N_q]_{\zeta=1}^T [N_a] |J_a| d\xi d\eta \\ K_{q\varphi} &= \int_{-1}^1 \int_{-1}^1 \int_{-1}^1 [\mathbf{B}_q]^T [\mathbf{e}]^T [\mathbf{B}_\varphi] |J| d\xi d\eta d\zeta \\ K_{\varphi q} &= K_{q\varphi}^T \\ K_{\varphi\varphi} &= \int_{-1}^1 \int_{-1}^1 \int_{-1}^1 [\mathbf{B}_\varphi]^T [\mathbf{e}] [\mathbf{B}_\varphi] |J| d\xi d\eta d\zeta \end{aligned}$$

and J and J_a are the Jacobian matrices for converting from global coordinates to local coordinates.

2.4 Torsional Motion of Piezo-electric Continua

With the model developed above, it is observed that it is difficult to achieve roll motion as the above piezoelectric actuation model does not produce any significant twisting motion in the wing that is necessary to generate the roll motion. It is clear that aerodynamic load is varied by changing the local angle of attack, α , achieved by the twisting motion of the wing. Thus, twisting motion is essential for roll direction are needed to produce twisting moment of wing [10][11] (fig. 3(b)). However, the piezoelectric constant, $[e]$ (Eq. 2), does not have e_{36} constant which produces this shear strain, γ_{xy} by voltage actuation in z direction. Thus, a skew angle, θ , is introduced [10] to generate a nonzero e_{36} constant(Fig. 4).

Incorporating the modified piezo-electric constant, a torsional motion is produced As shown in Fig. 4, two layers, bottom and upper layers, with opposite skew angles are required to generate a torsional mement in the wing. The maximum shear strain, γ_{xy} is obtained when the skew angles are $\frac{\pi}{4}$.

3 Model Reduction in Nonorthogonal Modal Coordinates

From Eq. 10, the equation of motion with voltage actuation is written as

$$M\ddot{\mathbf{q}} + C_A\dot{\mathbf{q}} + (K_q + K_A)\mathbf{q} = -K_{q\varphi}\varphi \quad (11)$$

By premultiplying M^{-1} for both side of Eq. 11, the Eq. 11 is expressed as

$$\ddot{\mathbf{q}} + M^{-1}C_A\dot{\mathbf{q}} + M^{-1}(K_q + K_A)\mathbf{q} = M^{-1} - K_{q\varphi}\varphi \quad (12)$$

The modal equation motion of the system can be obtained with a similarity transformation that diagonalizes the integrated stiffness matrix [12].

Let

$$\mathbf{q} = T\boldsymbol{\eta} \quad (13)$$

where

$$T = [t_1 \ t_2 \ t_3 \ ...t_n] \quad t_i : \text{eigen vector of } M^{-1}(K_q + K_A)$$

Then, Eq. 12 can be written as

$$\ddot{\eta} + C_{\eta}\dot{\eta} + \Lambda\eta = F_{\eta}\varphi \quad (14)$$

where

$$\begin{aligned} \eta &= [\eta_r \ \eta_{f1} \ \eta_{f2} \ \dots] \\ C_{\eta} &= T^{-1}M^{-1}C_AT \\ \Lambda &= T^{-1}M^{-1}(K_q + K_A)T = \text{diag}(\Lambda_r, \Lambda_{f1}, \Lambda_{f2}, \dots) \\ F_{\eta} &= T^{-1}M^{-1} - K_{q\varphi} \end{aligned}$$

But the model in this (nonorthogonal) modal coordinates is too large for meaningful control design. For this purpose, we carry out a transformation to the nonorthogonal (but real) modal coordinates clearly identifying the roll mode and all the flexible modes. The corresponding state space form of Eq. 14 is written as

$$\begin{aligned} \begin{bmatrix} \dot{\eta} \\ \ddot{\eta} \end{bmatrix} &= \begin{bmatrix} 0 & I \\ -\Lambda & -C_{\eta} \end{bmatrix} \begin{bmatrix} \eta \\ \dot{\eta} \end{bmatrix} + \begin{bmatrix} 0 \\ F_{\eta} \end{bmatrix} \varphi \\ \dot{x} &= Ax + Bu \end{aligned} \quad (15)$$

State space representation is a useful tool to design controllers for linear systems and many control design methods in state space framework are available for achieving stabilization and regulation of the state variables. However, for our particular problem at hand namely to achieve a desired constant roll rate, it turns out that it is cumbersome to use state space based control design because the steady state constant roll rate implies infinite roll displacements as time progresses. Therefore, the closed loop system is considered unstable. To overcome this problem and still design a simple controller using available control system software for this desired roll rate achievement problem, we propose a new framework called the ‘Reciprocal State Space’ framework [13]. This is discussed in the next section.

4 Full State Derivative Feedback Control Design using Reciprocal State Space Representation

The reciprocal state space representation of the system is expressed as

$$\begin{aligned} \dot{x} &= G\dot{x} + Hu \\ u &= K\dot{x} \end{aligned} \tag{16}$$

where

$$G = A^{-1}, \quad H = -A^{-1}B$$

The closed loop system is then given by

$$\begin{aligned} \dot{x} &= (G + KH)\dot{x} \quad \text{or} \\ \dot{x} &= G_c\dot{x} \end{aligned} \tag{17}$$

In the reciprocal state space representation, the steady state constant roll rate implies zero roll acceleration. It means that the closed loop G matrix then becomes asymptotically stable. Consequently, the reciprocal state space representation is a better framework to handle the 'roll rate' control design problem.

From Eq. 17, the performance index to be minimized is expressed as

$$PI = \int_0^\infty [\dot{x}^T Q \dot{x} + u^T R u] dt \tag{18}$$

where Q and R are positive semidefinite and positive definite matrices, respectively.

As discussed in [13], using the above new 'Reciprocal State Space' framework, the control gain K can simply be determined by employing the standard Linear Quadratic Regulator (LQR) algorithm of the standard state space framework! Thus the gain K is simply given by

$$K = -R^{-1}H^T S \tag{19}$$

where the matrix S can be obtained from the associated Algebraic Matrix Riccati equation given by

$$0 = SG + G^T S - SHR^{-1}H^T S + Q \tag{20}$$

5 Illustrative Example

A PVDF plate wing with two layers and eight elements(Fig. 5) is used to illustrate the proposed modeling and control design methodology to achieve the desired constant roll rate well as to suppress flexible mode vibration. Each layer has opposite skew angle to generate torque of the wing. The plate has eight 8-node brick elements with the total number of nodes being 30. In other words, the system has 120 degree of freedom, 90 for structural and 30 for electrical degrees of freedom. Roll motion is achieved by constraining the spatial displacements at the nodes along the center line to zero and thus the eventual number of nodes with nonzero displacements is reduced to 114. The rigid body motion, which is equivalent to the roll motion, can be isolated from the system through the modal coordinate transformation. In vibration problems, the lower frequency modes including rigid body modes are always dominant in the system responses. A reduced order model is then obtained that includes one rigid body mode, which is roll motion, and three flexible modes. A simple coordinate transformation is performed to convert the problem of achieving a specific roll velocity, into a regulation problem .

Let

$$\begin{aligned}\dot{\xi} &= \dot{x} + \mathcal{P} \\ \xi &= x + \mathcal{V}\end{aligned}\tag{21}$$

where

$$\begin{aligned}\mathcal{P} &= \begin{bmatrix} p_d & 0 & 0 & 0 & 0 & 0 & 0 & 0 \end{bmatrix}^T \\ \mathcal{V} &= \begin{bmatrix} p_d t & 0 & 0 & 0 & 0 & 0 & 0 & 0 \end{bmatrix}^T\end{aligned}$$

p_d : desired roll velocity

By introducing Eq. 21 into Eq. 17, the transformed reciprocal state space representation of the system is expressed as

$$\begin{aligned}\xi &= G\dot{\xi} + Hu \\ u &= K\dot{\xi}\end{aligned}\tag{22}$$

For our present example problem, the system matrix G is determined to be

$$G = \begin{bmatrix} 0.52964 & 0 & 0 & 0 & 2.92527 & 0 & 0 & 0 \\ 0 & 0 & 0 & 0 & 0 & -0.00011 & 0 & 0 \\ 0 & 0 & 0 & 0 & 0 & 0 & -0.00004 & 0 \\ 0 & 0 & 0 & 0 & 0 & 0 & 0 & -0.00003 \\ 1 & 0 & 0 & 0 & 0 & 0 & 0 & 0 \\ 0 & 1 & 0 & 0 & 0 & 0 & 0 & 0 \\ 0 & 0 & 1 & 0 & 0 & 0 & 0 & 0 \\ 0 & 0 & 0 & 1 & 0 & 0 & 0 & 0 \end{bmatrix}$$

It is observed that the open loop system is unstable. Usually, a pure structural system is neutrally stable. But, the structure in the aerodynamic field is no longer stable because of the presence of the nonconservative aerodynamic field which contributes some stiffness as well as damping. By applying the proposed control design technique, the closed loop system is not only stabilized but also a desired constant roll rate of 1.5 rad/sec is achieved.

Fig. 6 shows, for a selected set of weighting matrices, the roll velocity response. From this figure, it is clear that the desired roll velocity of 1.5 rad/sec is achieved by the controller. The corresponding roll displacements are shown in Fig. 7. The roll displacements gradually increase as expected. The rest of the flexible mode responses are shown in Fig. 8 and Fig. 9. It is easily seen that all flexible mode vibrational motion is suppressed. Fig. 10 shows the control input voltage histories at the node-1.

6 Conclusions:

In this summer research, an attempt is made, perhaps for the first time, to model the dynamics of a smart flexible wing involving the integration of five disciplines, namely structures, aerodynamics,

smart materials, control and flight mechanics! The control objective is to sustain a roll maneuver with a desired roll rate and to suppress the flexible mode vibrations by actively deforming the wing. Modeling of this dynamics is done using finite element method in the 'generalized' coordinates. Because of the coupling between these subsystems, the resulting 'Matrix Second Order System' of equations consists of a symmetric positive definite mass matrix but a nonsymmetric and indefinite damping (which includes aerodynamic damping) and stiffness (that includes aerodynamic and piezo material stiffness, in addition to the standard structural stiffness) matrices! The piezoelectric voltages serve as the Control variables. This large model in the generalized coordinates is then transformed to a set of 'nonorthogonal modal' coordinates and model reduction is carried out in these modal coordinates. This model is then converted to the 'state space' form. This standard state space form is then transformed to a new framework called 'Reciprocal State Space' framework and control design is carried out in this new framework. This new modeling and control design methodology is illustrated with the help of an example and its efficacy clearly demonstrated.

6.1 Future Research That Needs AFOSR Support:

There is clearly a need to carry out further research in the following important areas. Firstly more research should be undertaken to come up with improved control design algorithms, in the lines of present research proposed in this report. Secondly the traditional integrated optimization ideas need to be expanded to include the interactions between the five subdisciplines mentioned before. Last but not least is the need to continue the analytical studies such as those presented in this report to more general flight maneuvers involving not only roll but pitch and yaw motions as well and also a combination of these maneuvers using smart deformable wings. Of course, in addition to analytical studies, considerable effort should be expended in conducting application studies to realistic scenarios involving software and hardware issues for industrial structures such as real wings. Finally the importance of conducting experimental studies to validate the theories can not be overemphasized. Thus a long term commitment for research in 'Flight Control with Smart Deformable Wing Structures' must be of high priority for Universities such as The Ohio State University and Air Force (WL) and Aircraft Industries to reap the benefits of this exciting research.

References

- [1] J.Kudva, K.Appa, C. Martin, and P.Jardine et al. Design, fabrication and testing of the darpa/wl smart wing wind tunnel model. *38th AIAA SDM Meeting*.
- [2] C.L.Hustedde, G.W.Reich, M.A.Hopkins, and K.E. Griffin. An investigation of the aeroelastic tailoring for smart structures concept. *37th AIAA SDM Meeting*.
- [3] N.S.Khot, F.E.Eastep, and R.M. Kolonay. Optimization of a composite wing structure for enhancement of the rolling maneuver. *AIAA-96-3998-CP*.
- [4] N.S.Khot, F.E.Eastep, and R.M. Kolonay. Wing twist and camber for the rolling maneuver of a flexible wing without ailerons. *38th AIAA SDM Meeting*.
- [5] K. Appa and N. S. Khot et. al. Feasibility assessment and optimization study of smart actuation systems for enhanced aircraft maneuver performance. *Pre Print*.
- [6] H. S. Tzou. Piezoelectric shell; distributed sensing and control of continua. *Solid Mechanics and Its Applications, Kluwer Academic Pub.*, 19, 1993.
- [7] Holt Ashley and Garabed Zartarian. Piston theory - a new aerodynamic tool for the aeroelastician. *Journal of Aeronautical Sciences*, 23:1109-1118, December 1956.
- [8] Maher N. Bismarck-Nasr. Finite element analysis of aeroelasticity of plates and shell. *Applied Mechanics Reviews*, 45(12):461-482, December 1992.
- [9] Anjali M. Diwekar and Rama K. Yedavalli. Smart structure control in matrix second-order form. *Journal of Smart Structures and Materials*, 5:429-436, 1996.
- [10] C.-K. Lee and F. C. Moon. Laminated piezopolymer plates for torsion and bending sensors and actuators. *Journal of Acoustical Society of America*, 85(6):2432-2439, June 1989.
- [11] Ron Barrett. All-moving active aerodynamic surface research. *Journal of Smart Structures and Materials*, 1995.
- [12] L. Meirovitch. Computational methods in structural dynamics. *Sijthoff Noordhoff*, 1980.

- [13] Yuan-Wei Tseng and R.K.Yedavalli. Control design of linear dynamic system with matrix differential equations for equations for aerospace applications. *Ph.D Dissertation*.

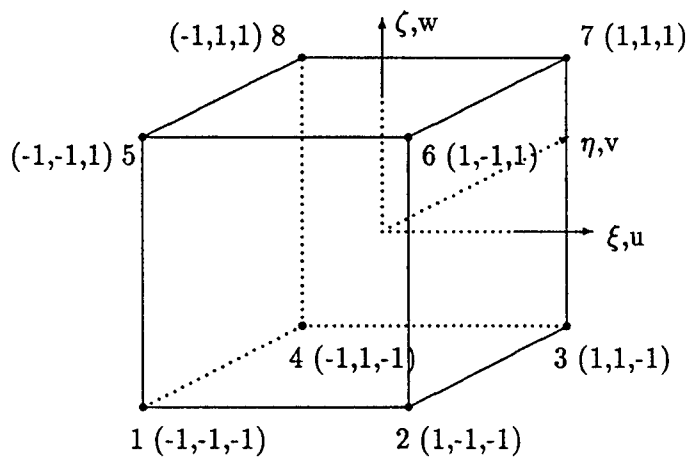


Figure 1: Coupled 8 Nodes 3-D Solid

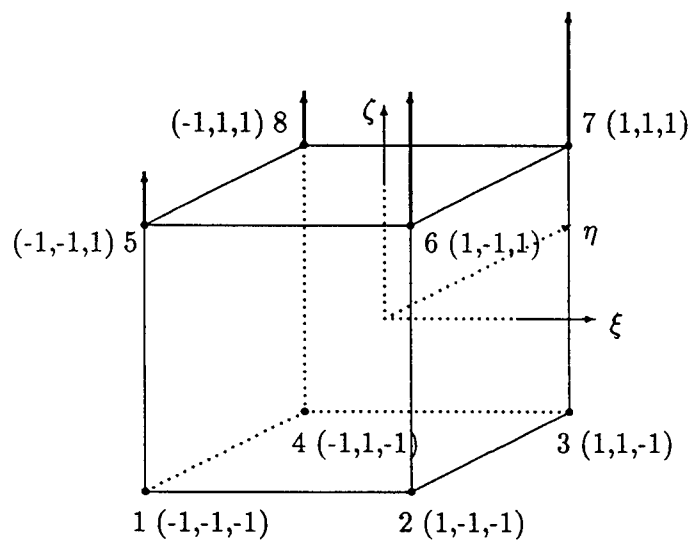


Figure 2: Coupled 8 Nodes 3-D Solid with Aerodynamic Load

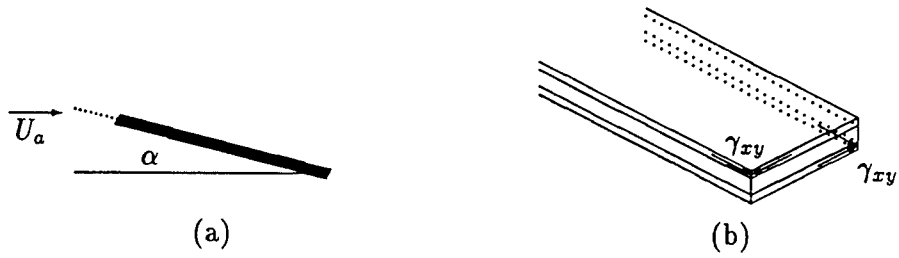


Figure 3: Torsional Motion of Cross Section of a Wing

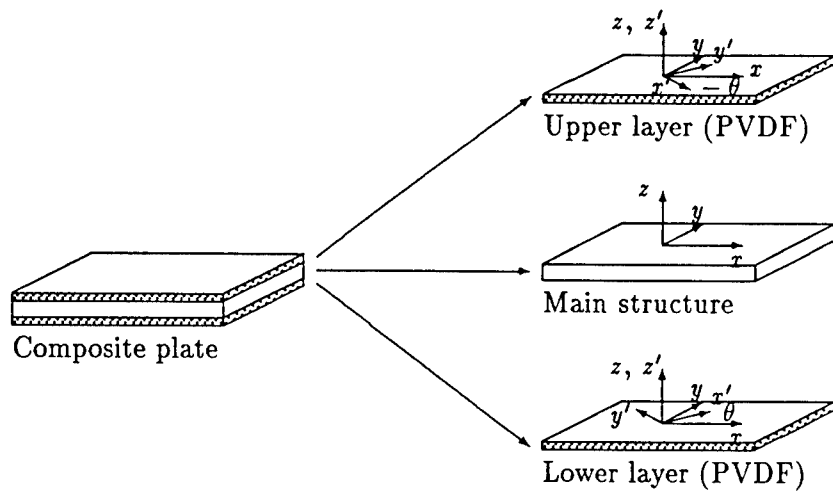


Figure 4: Skew Angle

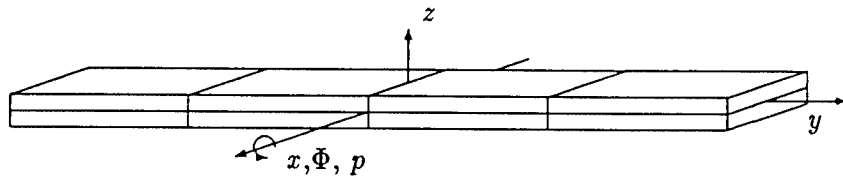


Figure 5: Wing Plate (PVDF)

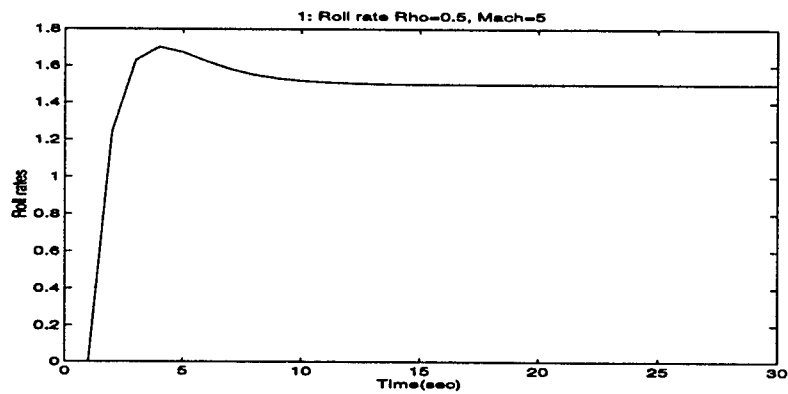


Figure 6: Roll Velocity Response

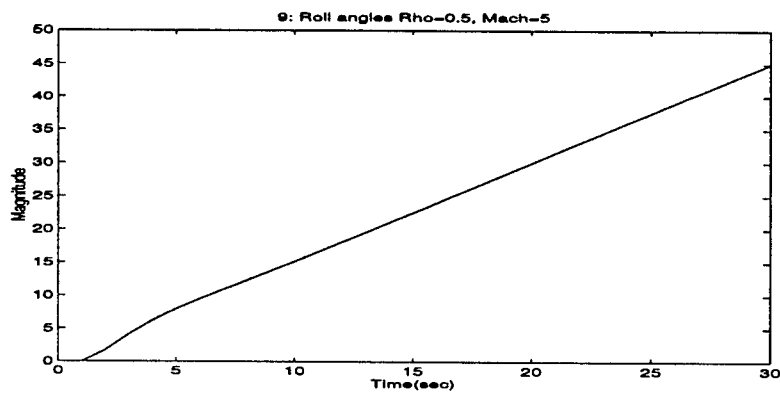


Figure 7: Roll Displacement Response

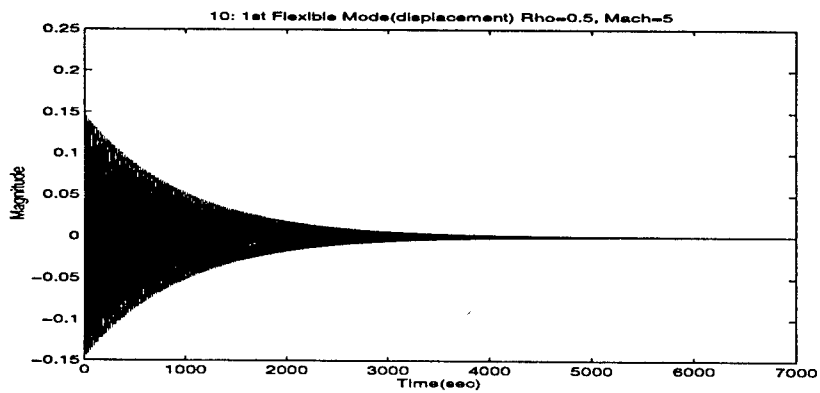


Figure 8: Displacement Response : 1st Flexible Mode

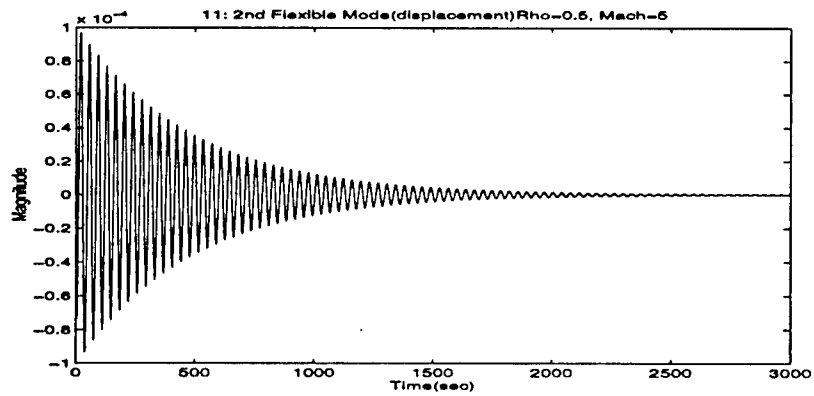


Figure 9: Displacement Response : 2nd Flexible Mode

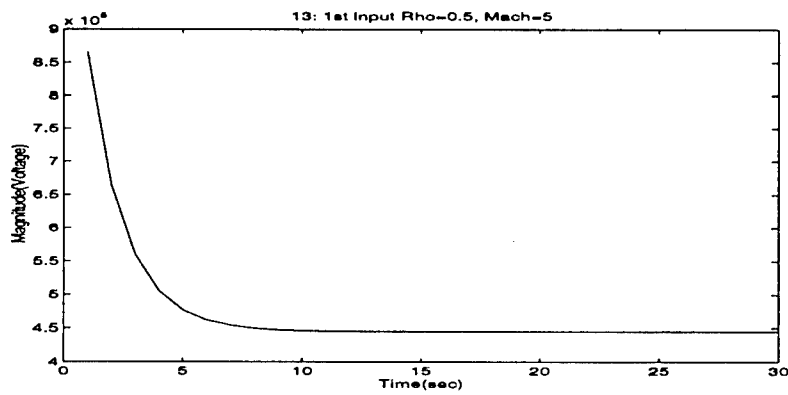


Figure 10: 1st Input